

AFRL-ML-WP-TR-1999-4162

**SMART MATERIALS AND STRUCTURES –
SMART WING
VOLUMES I, II, III, AND IV**

**CHRISTOPHER A. MARTIN, JAYANTH N. KUDVA, FRED
AUSTIN, A. PETER JARDINE, LEWIS B. SCHERER, ALLEN J.
LOCKYER, AND BERNIE F. CARPENTER**



**NORTHROP GRUMMAN CORPORATION
ONE NORTHROP AVENUE
HAWTHORNE, CALIFORNIA 90250**

DECEMBER 1998

FINAL REPORT FOR PERIOD 01 DECEMBER 1994 – 01 SEPTEMBER 1998

Approved for public release; distribution unlimited.

**MATERIALS AND MANUFACTURING DIRECTORATE
AIR FORCE RESEARCH LABORATORY
AIR FORCE MATERIEL COMMAND
WRIGHT-PATTERSON AIR FORCE BASE, OH 45433-7750**


REPORT DOCUMENTATION PAGE				Form Approved OMB No. 0704-0188	
Public reporting burden for this collection of information is estimated to average 1 hour per response, including the time for reviewing instructions, searching existing data sources, gathering and maintaining the data needed, and completing and reviewing this collection of information. Send comments regarding this burden estimate or any other aspect of this collection of information, including suggestions for reducing this burden to Department of Defense, Washington Headquarters Services, Directorate for Information Operations and Reports (0704-0188), 1215 Jefferson Davis Highway, Suite 1204, Arlington, VA 22202-4302. Respondents should be aware that notwithstanding any other provision of law, no person shall be subject to any penalty for failing to comply with a collection of information if it does not display a currently valid OMB control number. PLEASE DO NOT RETURN YOUR FORM TO THE ABOVE ADDRESS.					
1. REPORT DATE (DD-MM-YYYY) 01-12-1998		2. REPORT TYPE Final Report		3. DATES COVERED (FROM - TO) 01-12-1995 to 01-09-1998	
4. TITLE AND SUBTITLE Smart Materials and Structures-Smart Wing Volumes I, II, III, and IV Unclassified				5a. CONTRACT NUMBER F33615-95-C-3202	
				5b. GRANT NUMBER	
				5c. PROGRAM ELEMENT NUMBER	
6. AUTHOR(S) Martin, Christopher A. ; Kudva, Jayanth N. ; Austin, Fred ; Jardine, A. P. ; Scherer, Lewis B. ;				5d. PROJECT NUMBER	
				5e. TASK NUMBER	
				5f. WORK UNIT NUMBER	
7. PERFORMING ORGANIZATION NAME AND ADDRESS Northrop Grumman Corporation One Northrop Avenue Hawthorne, CA90250				8. PERFORMING ORGANIZATION REPORT NUMBER	
9. SPONSORING/MONITORING AGENCY NAME AND ADDRESS Materials and Manufacturing Directorate Air Force Research Laboratory Air Force Materiel Command Wright-Patterson AFB, OH45433-7750				10. SPONSOR/MONITOR'S ACRONYM(S)	
				11. SPONSOR/MONITOR'S REPORT NUMBER(S)	
12. DISTRIBUTION/AVAILABILITY STATEMENT APUBLIC RELEASE					
13. SUPPLEMENTARY NOTES BLOCK #3: Dates covered should be from 1 Dec 1994.					
14. ABSTRACT This final report of the DARPA-sponsored, Air Force Research Laboratory administered Smart Wing Phase 1 program documents key results and conclusions reached in the application of smart materials to both subsonic and transonic adaptive wing development. The program effort for the subsonic regime targeted an F/A-18 class vehicle, and examined 1) variable wing twist effected by a nickel titanium (NiTi) shape memory alloy (SMA) torque tube and 2) hingeless, smoothly contoured trailing edge control surface deployment using SMA wires. Two 16% scale wing wind tunnel models were fabricated, one with SMA actuated control surfaces and the other of conventional design, and tested at NASA Langley Research Center (LaRC). Up to and greater than a 10% increase in lift and rolling moment versus a conventional flap and aileron was demonstrated for the Smart Wing design. Program development for the transonic effort, on the other hand, was focused on commercial aircraft, and examined two approaches for gaining fuel savings by optimizing transonic cruise: 1) an adaptive wing that employed TERFENOL-D linear actuators in the wing box structure (between the spars) to optimize airfoil shape, and 2) camber modification with smoothly contoured trailing edge, also powered by a TERFENOL-D linear wave actuator. The latter approach was downselected and program studies showed that fuel savings of 5% were achievable equating to cost savings up to \$7 billion per year for US-based commercial jet fleets. The work performed under this contract is being continued under an on-going Phase 2 effort. This work will be completed in early 2001 and is expected to lead to flight testing on unmanned aircraft, leading the way for near-term technology transition to operational flight vehicles.					
15. SUBJECT TERMS Adaptive / Aeroelastic Wing; Aircraft; Aircraft Control Surfaces; Aircraft Performance; Aerodynamics; Smart Materials; Smart Structures; Smart Wing; Wind Tunnel Testing					
16. SECURITY CLASSIFICATION OF:		17. LIMITATION OF ABSTRACT		18. NUMBER OF PAGES	
		Same as Report (SAR)		531	
19. NAME OF RESPONSIBLE PERSON Fenster, Lynn lfenster@dtic.mil					
a. REPORT Unclassified	b. ABSTRACT Unclassified	c. THIS PAGE Unclassified	19b. TELEPHONE NUMBER International Area Code Area Code Telephone Number 703767-9007 DSN 427-9007		
				Standard Form 298 (Rev. 8-98) Prescribed by ANSI Std Z39.18	

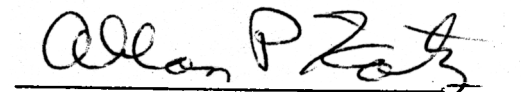
NOTICE

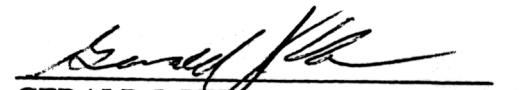
WHEN GOVERNMENT DRAWINGS, SPECIFICATIONS, OR OTHER DATA ARE USED FOR ANY PURPOSE OTHER THAN IN CONNECTION WITH A DEFINITELY GOVERNMENT-RELATED PROCUREMENT, THE UNITED STATES GOVERNMENT INCURS NO RESPONSIBILITY OR ANY OBLIGATION WHATSOEVER. THE FACT THAT THE GOVERNMENT MAY HAVE FORMULATED OR IN ANY WAY SUPPLIED THE SAID DRAWINGS, SPECIFICATIONS, OR OTHER DATA, IS NOT TO BE REGARDED BY IMPLICATION OR OTHERWISE IN ANY MANNER CONSTRUED, AS LICENSING THE HOLDER OR ANY OTHER PERSON OR CORPORATION, OR AS CONVEYING ANY RIGHTS OR PERMISSION TO MANUFACTURE, USE, OR SELL ANY PATENTED INVENTION THAT MAY IN ANY WAY BE RELATED THERETO.

THIS REPORT IS RELEASABLE TO THE NATIONAL TECHNICAL INFORMATION SERVICE (NTIS). AT NTIS, IT WILL BE AVAILABLE TO THE GENERAL PUBLIC, INCLUDING FOREIGN NATIONS.

THIS TECHNICAL REPORT HAS BEEN REVIEWED AND IS APPROVED FOR PUBLICATION.


GEORGE P. SENDECKY
Ceramics Development & Materials
Behavior Branch
Metals, Ceramics & NDE Division


ALLAN P. KATZ, Chief
Ceramics Branch
Metals, Ceramics & NDE Division
Materials & Manufacturing Directorate


GERALD J. PETRAK, Asst Chief
Metals, Ceramics & NDE Division
Materials & Manufacturing Directorate

IF YOUR ADDRESS HAS CHANGED, IF YOU WISH TO BE REMOVED FROM OUR MAILING LIST, OR IF THE ADDRESSEE IS NO LONGER EMPLOYED BY YOUR ORGANIZATION, PLEASE NOTIFY, AFRL/MLLN, WRIGHT-PATTERSON AFB OH 45433-7817 TO HELP US MAINTAIN A CURRENT MAILING LIST.

COPIES OF THIS REPORT SHOULD NOT BE RETURNED UNLESS RETURN IS REQUIRED BY SECURITY CONSIDERATIONS, CONTRACTUAL OBLIGATIONS, OR NOTICE ON A SPECIFIC DOCUMENT.

REPORT DOCUMENTATION PAGE			Form Approved OMB No. 0704-0188	
Public reporting burden for this collection of information is estimated to average 1 hour per response, including the time for reviewing instructions, searching existing data sources, gathering and maintaining the data needed, and completing and reviewing the collection of information. Send comments regarding this burden estimate or any other aspect of this collection of information, including suggestions for reducing this burden, to Washington Headquarters Services, Directorate for Information Operations and Reports, 1215 Jefferson Davis Highway, Suite 1204, Arlington, VA 22202-4302, and to the Office of Management and Budget, Paperwork Reduction Project (0704-0188), Washington, DC 20503.				
1. AGENCY USE ONLY (Leave blank)		2. REPORT DATE DECEMBER 1998		3. REPORT TYPE AND DATES COVERED FINAL REPORT FOR 01 DEC 1994 – 01 SEP 1998
4. TITLE AND SUBTITLE SMART MATERIALS AND STRUCTURES – SMART WING VOLUMES I, II, III, AND IV			5. FUNDING NUMBERS C: F33615-95-C-3202 PE: 62102 PR: 4Y10 TA: 03 WU: 00	
6. AUTHOR(S) CHRISTOPHER A. MARTIN, JAYANTH N. KUDVA, FRED AUSTIN, A. PETER JARDINE, LEWIS B. SCHERER, ALLEN J. LOCKYER, BERNIE F. CARPENTER				
7. PERFORMING ORGANIZATION NAME(S) AND ADDRESS(ES) NORTHROP GRUMMAN CORPORATION ONE NORTHROP AVENUE HAWTHORNE, CALIFORNIA 90250			8. PERFORMING ORGANIZATION REPORT NUMBER NOR 00-804	
9. SPONSORING / MONITORING AGENCY NAME(S) AND ADDRESS(ES) MATERIALS AND MANUFACTURING DIRECTORATE AIR FORCE RESEARCH LABORATORY AIR FORCE MATERIEL COMMAND WRIGHT-PATTERSON AIR FORCE BASE, OH 45433-7750 POC: GEORGE SENDECKYJ, AFRL/MLLN, (937) 255-4490			10. SPONSORING / MONITORING AGENCY REPORT NUMBER AFRL-ML-WP-TR-1999-4162	
11. SUPPLEMENTARY NOTES				
12a. DISTRIBUTION AVAILABILITY STATEMENT APPROVED FOR PUBLIC RELEASE; DISTRIBUTION UNLIMITED			12b. DISTRIBUTION CODE	
13. ABSTRACT (Maximum 200 words) This final report of the DARPA-sponsored, Air Force Research Laboratory administered Smart Wing Phase 1 program documents key results and conclusions reached in the application of smart materials to both subsonic and transonic adaptive wing development. The program effort for the subsonic regime targeted an F/A-18 class vehicle, and examined 1) variable wing twist effected by a nickel titanium (NiTi) shape memory alloy (SMA) torque tube and 2) hingeless, smoothly contoured trailing edge control surface deployment using SMA wires. Two 16% scale wing wind tunnel models were fabricated, one with SMA actuated control surfaces and the other of conventional design, and tested at NASA Langley Research Center (LaRC). Up to and greater than a 10% increase in lift and rolling moment versus a conventional flap and aileron was demonstrated for the Smart Wing design. Program development for the transonic effort, on the other hand, was focused on commercial aircraft, and examined two approaches for gaining fuel savings by optimizing transonic cruise: 1) an adaptive wing that employed TERFENOL-D linear actuators in the wing box structure (between the spars) to optimize airfoil shape, and 2) camber modification with smoothly contoured trailing edge, also powered by a TERFENOL-D linear wave actuator. The latter approach was downselected and program studies showed that fuel savings of 5% were achievable equating to cost savings up to \$7 billion per year for US-based commercial jet fleets. The work performed under this contract is being continued under an on-going Phase 2 effort. This work will be completed in early 2001 and is expected to lead to flight testing on unmanned aircraft, leading the way for near-term technology transition to operational flight vehicles.				
14. SUBJECT TERMS Adaptive / Aeroelastic Wing, Aircraft, Aircraft Control Surfaces, Aircraft Performance, Aerodynamics, Smart Materials, Smart Structures, Smart Wing, Wind Tunnel Testing			15. NUMBER OF PAGES 534	
			16. PRICE CODE	
17. SECURITY CLASSIFICATION OF REPORT UNCLASSIFIED	18. SECURITY CLASSIFICATION OF THIS PAGE UNCLASSIFIED	19. SECURITY CLASSIFICATION OF ABSTRACT UNCLASSIFIED	20. LIMITATION OF ABSTRACT SAR	

Standard Form 298 (Rev. 2/89) (EG)
Prescribed by ANSI Std. Z39.18
Designed using Perform Pro, WHS/DIOR,
Oct 94

Table of Contents

Volume I	Smart Wing Phase 1 Final Report..... I-i
Volume II	Transonic Cruise Optimization..... II-i
Volume III	Wind Tunnel Test ResultsIII-i
Volume IV	Pre-Test and Stress ReportsIV-i

ABSTRACT

This final report of the DARPA-sponsored, Air Force Research Laboratory-administered Smart Materials and Structures - Smart Wing Phase 1 program (F33615-95-C-3202) documents key results and conclusions reached in the application of smart materials to both subsonic and transonic adaptive wing development. The program effort for the subsonic regime targeted an F/A-18 class vehicle and examined (1) variable wing twist effected by a nickel titanium (NiTi) shape memory alloy (SMA) torque tube and (2) hingeless, smoothly contoured trailing edge control surface deployment using SMA wires. Two 16 percent scale wing wind tunnel models were fabricated, one with SMA-actuated control surfaces and the other of conventional design, and tested at NASA Langley Research Center (LaRC). Up to and greater than a 10 percent increase in lift and rolling moment versus a conventional flap and aileron was demonstrated for the Smart Wing design. Program development for the transonic effort, on the other hand, was focused on commercial aircraft, and examined two approaches for gaining fuel savings by optimizing transonic cruise: (1) an adaptive wing that employed TERFENOL-D linear actuators in the wing box structure (between the spars) to optimize airfoil shape and (2) camber modification with smoothly contoured trailing edge, also powered by a TERFENOL-D linear wave actuator. The latter approach was downselected, and program studies showed that fuel savings of 5 percent were achievable equating to cost savings up to \$7 billion per year for US-based commercial jet fleets.

The work performed under this contract is being continued under an on-going Phase 2 effort. This work will be completed in early 2001 and is expected to lead to flight testing on unmanned aircraft, leading the way for near-term technology transition to operational flight vehicles.

The report is organized into four volumes. Volume I, "Smart Materials and Structures - Smart Wing Phase 1 Final Report" details the design, fabrication, and testing of the SMA torque tube and SMA flap and aileron in the NASA LaRC 16 ft TDT, exclusively (except for Section 1). Volume II, "Transonic Cruise Optimization," describes the transonic cruise concept effort in its entirety. Volume III, "Wind Tunnel Test Results," provides a compilation of the entire wind tunnel test results from both Test 1 (May 1996) and Test 2 (July 1998). Volume IV, "Pre-Test and Stress Reports," contains the summary reports that describe the model, the model design, and the test plan.

FOREWORD

The research and development effort reported herein was performed under the DARPA / AFRL program (Contract Number F33615-95-C-3202), entitled “Smart Materials and Structures – Smart Wing Phase 1.” The program manager at DARPA (DSO), the funding agency, was Dr. Robert Crowe who initiated the Smart Materials and Structures programs at DARPA. The Air Force Research Laboratory at Dayton, Ohio was the monitoring agency, and Dr. George Sendekyj (AFRL/ MLLN) was the contract monitor.

Northrop Grumman Corporation, Integrated Systems and Aerostructures Sector, was the prime contractor for the program with Lockheed Martin Astronautics, Mission Research Corporation, F & S Inc., ETREMA Products, Inc., Georgia Institute of Technology, University of California at Los Angeles, and University of Texas at Arlington, as subcontractors. Key contributors include:

Northrop Grumman Corporation:

Dr. Jayanth N. Kudva	Program Manager and Principal Investigator
Dr. Kari Appa	Aeroelastic Analysis and Design
Mr. Jonathan Bartley-Cho	Structural Analysis
Mr. John Flanagan	Wind Tunnel Model Design and Fabrication
Dr. A. Peter Jardine	SMA Torque Tube Design and Fabrication
Mr. Larry Jasmin	Wind Tunnel Model Design
Mr. Allen Lockyer	Technology Transition and Documentation
Mr. Christopher Martin	Wind Tunnel Model Design and Analysis
Mr. Lewis Scherer	Wind Tunnel Test
Dr. Fred Austin	PI, Transonic Cruise Optimization Concept (TCOC)
Dr. Chien Huang	System Control and Analysis (TCOC)
Dr. Mike Siclari	CFD Analysis (TCOC)

Subcontractors:

Dr. Bernie F. Carpenter (LM)	SMA Smart Trailing Edge Development
Mr. Mark West (MRC)	Instrumentation and Control Surface Development
Mr. Paul Duncan (F & S)	Fiber Optic Sensors
Dr. Nick Weisensel (ETREMA)	TERFENOL-D Linear Wave Actuator Development
Dr. Chris Lynch (Georgia Tech)	Piezo-actuators
Dr. Greg Carman (UCLA)	SMA Characterization
Dr. Shiv Joshi (UTA)	Smart Actuator Research

The wind tunnel models were tested at the NASA Langley Research Center’s Transonic Dynamics Tunnel. Ms. Anna R. McGowan was the lead test engineer from NASA; Dr. Robert Moses was the assistant test engineer for the first entry and Ms. Renee Lake for the second entry.

ACKNOWLEDGEMENTS

Several people, across all the organizations and companies involved in this program contributed to program success; in particular, the authors would like to acknowledge and thank:

- Dr. Bob Crowe (DARPA); Dr. George Sendeckyj, Mr. Terry Harris, and Dr. Mark Hopkins (AFRL); Dr. Janet Sater (IDA); Dr. Tom Noll and Dr. Boyd Perry (NASA); and Dr. Bob Badalian (NRL) for their guidance and support throughout the program
- Ms. Jennifer Pinkerton-Florance, Ms. Carol Wieseman, Mr. Tony Rivera, Dr. Al Burner, Mr. Gary Fleming, and Mr. Rex Nutter, of NASA LaRC, who provided pivotal support during both wind tunnel tests
- Mr. Robert Froom who helped develop the fabrication, manufacturing, and attachment process for the SMA torque tube
- Mr. John Bacon III, Mr. Rich Votava, Mr. Carl Griffitts and Mr. Mel Daniels whose experience and guidance aided in the design, fabrication, and testing of the wind tunnel models
- Ms. Carlene Lau and Mr. Joe Salinas who reduced and plotted all the wind tunnel test data
- Ms. Kari Miyamoto and Mr. José Bilderbeck who patiently made revisions and format updates to this final report
- Mr. Jerry Draper and Ms. Kristi Mederos who helped fabricate and assemble the SMA flap and aileron
- Dr. Kent Murphy, Mr. Mark Jones, and Dr. Kevin Shinpaugh who provided expertise and test support for the fiber optic sensors.

VOLUME I

SMART WING PHASE 1 FINAL REPORT

Table of Contents

VOLUME I SMART WING PHASE 1 FINAL REPORT

1.	Introduction and Program Objective	I-1
1.1	Program Team	I-2
1.2	Lift and Maneuver Enhancement Concept	I-2
1.3	Transonic Cruise Concept	I-3
1.4	Summary of Key Program Accomplishments	I-4
1.5	Wind Tunnel First Entry Test Results	I-5
1.6	Wind Tunnel Second Entry Test Results	I-6
1.7	Report Roadmap	I-8
2.	SMA Torque Tube Design Development	I-9
2.1	Technology Description	I-9
2.2	SMA Torque Tube Design	I-10
2.3	Torque Tube Manufacturing	I-12
2.4	Torque Tube Training	I-13
2.5	SMA Torque Tube Connection and Integration	I-15
2.6	Torque Tube Control	I-18
2.7	Torque Tube Lab Tests	I-19
2.8	Summary and Lessons Learned	I-19
3.	SMA Wire-Actuated Flap and Aileron	I-20
3.1	Technology Description	I-20
3.2	SMA Flap and Aileron Preliminary Design	I-21
3.3	Detailed Design and Manufacturing	I-27
3.4	Flap and Aileron Control System Development	I-30
3.5	Flap Delamination	I-34
3.6	Summary and Lessons Learned	I-40
4.	Model Design and Fabrication	I-41
4.1	Wind Tunnel Model Design	I-41
4.2	Smart Actuator Control Surface Integration	I-52
4.3	Test Setup Instrumentation	I-55
4.4	Accomplishments and Summary	I-57

Table of Contents (continued)

5.	Wind Tunnel Test Results	I-58
5.1	Test Program Overview and Goals	I-59
5.2	Wind Tunnel Test Configuration and Setup	I-61
5.3	Program Wind Tunnel Test Results	I-70
6.	Conclusions and Technology Transition.....	I-83
6.1	Program Self-Assessment	I-83
6.2	Final Word on Progress and Technology Transition	I-84
7.	References.....	I-86

Table of Figures

VOLUME I

SMART WING PHASE 1 FINAL REPORT

Figure	Page
1-1. Smart Wing Concepts	I-1
1-2. ETEMA TERFENOL-D Linear Motor	I-2
1-3. TERFENOL-Powered Smart Trailing Edge	I-2
1-4. Smart Wing Team Members.....	I-3
1-5. Program Technology Payoffs and Risks	I-4
1-6. Wind Tunnel Pressure Distribution Measurements	I-6
1-7. Rolling Moment Comparison – Contoured vs. Conventional Aileron.....	I-6
1-8. Photograph of Smart Wing Model and Installation Schematic	I-6
1-9. Summary of Results for Wind Tunnel Tests 1 and 2.....	I-7
 2-1. Torsional SMA Actuators.....	 I-11
2-2. Torque Tube Design Limits	I-12
2-3. Initial Electrodischarge Machining Pattern for SMA Torque Tube	I-13
2-4. Electrodischarge Machining of SMA Torque Tube	I-13
2-5. SMA Torque Tube Training Apparatus	I-14
2-6. Torque Tube Connection Scheme	I-16
2-7. First Entry: Torque Tube Connection Scheme	I-16
2-8. Transmission to Model Attachment	I-17
2-9. Improved Transmission Rod Design for Test 2.....	I-17
2-10. Torque Tube Testing Prior to Installation	I-18
2-11. Torque Tube Wire Heater Elements.....	I-18
 3-1. Shape Memory Alloy Control Surface Concept.....	 I-20
3-2. Antagonistic Actuation	I-21
3-3. Requirements for SMA Control Surfaces	I-22
3-4. Planform View of Wind Tunnel Model Showing Location of Control Surfaces.....	I-22
3-5. Leading Edge Inboard Control Surface.....	I-23
3-6. Leading Edge Outboard Control Surface	I-23
3-7. Trailing Edge Inboard (Flap) Control Surface.....	I-24
3-8. Trailing Edge Outboard (Aileron) Control Surface.....	I-24
3-9. Finite Element Model (FEM) Results for SMA Control Surface	I-25
3-10. Wire Density Studies for Inboard TE Flap	I-26
3-11. Streamwise Cross-Section Cuts for FEM Results.....	I-26
3-12. Facesheet Detail Showing Tubes and SMA Wire Placement	I-28
3-13. SMA Flap Segment Layout	I-29
3-14. SMA Aileron Segment Layout.....	I-29
3-15. Photos of Completed Flap.....	I-30
3-16. Distributed Control Approach	I-30

Table of Figures (continued)

3-17.	Control System Block Diagram.....	I-31
3-18.	Typical Power Amplifier Used on Program.....	I-31
3-19.	Step Tuning Procedure.....	I-33
3-20.	Antagonistic Control Software.....	I-33
3-21.	Location of Flap Delamination.....	I-34
3-22.	Applied Loads.....	I-36
3-23.	Flatwise Tension Test Setup.....	I-36
3-24.	Facesheet Orientation for Smart Wing Test.....	I-37
3-25.	Flatwise Tension Results.....	I-37
3-26.	Flatwise Tension Test Results Comparison With Analytical Results.....	I-38
3-27.	Photograph of Tested 7.5 Degree Facesheet Specimen.....	I-38
3-28.	Simultaneous Wire Operation.....	I-39
4-1.	Planform View of Wind Tunnel Model with Upper Skin Removed.....	I-42
4-2.	Typical Model Design Aspects.....	I-43
4-3.	Model Design Process.....	I-44
4-4.	Wind Tunnel Model Internal Structure.....	I-45
4-5.	Planform View of Finite Element Model.....	I-46
4-6.	Pressure Distribution for the Wind Tunnel Model from ATROS Trim Analysis.....	I-47
4-7.	Maximum Individual Loads at Balance Face for Test 2.....	I-47
4-8.	Transverse Stress (σ_{xy}) for Lower Wing Skin.....	I-48
4-9.	Sand Bag Locations for Proof Load Test.....	I-49
4-10.	Proof Load Test of SMA Flap Prior to Test 2.....	I-50
4-11.	Comparison of Measured and Predicted Twist Angle for Various Loading Conditions.....	I-50
4-12.	Accelerometer Locations for Test 2 Ground Vibration Test.....	I-51
4-13.	Table of Results from Analysis and NASA-Performed Ground Vibration Test.....	I-51
4-14.	Frequency Response of Smart Wing Model.....	I-52
4-15.	Summary of Improvements Made to SMA Torque Tube from Test 1 to Test 2.....	I-53
4-16.	Torque Tube Failure Modes, Consequences, and Safety Features.....	I-53
4-17.	SMA Flap Connection Detail.....	I-54
4-18.	Trailing Edge Control Surface Improvements from Test 1 to Test 2.....	I-54
4-19.	Torque Tube Failure Safety Issues and Consequences.....	I-55
4-20.	Block Diagram of Instrumentation for Smart Wing Model.....	I-56
4-21.	Instrumentation Summary for Test 2.....	I-56
5-1.	Summary of Aerodynamic Performance Improvements.....	I-59
5-2.	Conventional and Smart Wind Tunnel Models.....	I-60
5-3.	Contoured Control Surface Concept.....	I-60
5-4.	Test 2 Overview.....	I-61
5-5.	Plan View of TDT Facility.....	I-62

Table of Figures (continued)

5-6.	TDT Cutaway of Test Section Area	I-63
5-7.	Plan View of Wing Model and Tunnel Installation	I-64
5-8.	Wing Model Configuration in TDT	I-64
5-9.	Static Pressure Ports for Conventional and Smart Models	I-66
5-10.	Contour Position Measurement	I-66
5-11.	NASA Langley Video Model Deformation System	I-67
5-12.	NASA Langley PMI System	I-68
5-13.	Program Test Sequence	I-69
5-14.	Smart Wing Wind Tunnel Test Conditions	I-69
5-15.	Baseline Repeatability – Test 1 (Q = 90 psf, Mach = 0.25)	I-71
5-16.	Baseline Repeatability – Test 2 (Q = 90 psf, Mach = 0.25)	I-72
5-17.	Wing Twist Effects – Test 1 (All Control Surfaces = 0 degrees, Runs 113 vs 89, Q = 120 psf, Mach = 0.29)	I-73
5-18.	Wing Twist Effects – Test 2 (Flap = 0 degrees, Q = 90 psf, Mach = 0.25)	I-74
5-19.	Wing Twist Effects – Increased Leading Edge Suction	I-74
5-20.	Spanwise Twist Distribution Due to SMA Torque Tube	I-75
5-21.	Wind Tunnel Pressure Distribution Measurements	I-76
5-22.	Pressure Plot – Flap Deflected 7.5 Degrees	I-76
5-23.	Rolling Moment Comparison – Contoured vs. Conventional Aileron	I-77
5-24.	Flap Only – Lift – Test 1 (Runs 100 vs 75, Q = 60 psf, Mach = 0.2)	I-77
5-25.	Flap Only – Pitching Moment – Test 1 (Runs 100 vs 75, Q = 60 psf, Mach = 0.2)	I-78
5-26.	Aileron Effectiveness – Test 1 (Runs 105 vs 22, Q = 90 psf, Mach = 0.25)	I-78
5-27.	Aileron Effectiveness – Rolling Moment – Test 2 (Runs 119 vs 41, Q = 90 psf, Mach = 0.25)	I-79
5-28.	Aileron Effectiveness – Deflection 10 Degrees – Test 2 (Q = 90 psf, Mach = 0.25)	I-80
5-29.	Aileron Effectiveness – Alpha Variation (Q = 90 psf, Mach = 0.25)	I-80
5-30.	Flap and Aileron Combined – Pitching Moment (Runs 105 vs 22, Q = 90 psf, Mach = 0.25)	I-81
5-31.	Rolling Moment Increase for Combined Wing Twist and Contoured Aileron Deflection	I-82
5-32.	Summary of Aerodynamic Improvements	I-82
6-1.	Program Requirements vs Performance	I-84

1. INTRODUCTION AND PROGRAM OBJECTIVE

Documented below is the final report for the (Contract Number F33615-95-C-3202) DARPA/AFRL “Smart Materials and Structures - Smart Wing Phase I” program. The overall objective was to apply smart material technology to improve flight characteristics and performance of military and commercial aircraft and to establish system payoffs.^{1,2,3,4} Summarized here, a variety of smart material concepts for performance enhancements have been investigated and have been taken further in a follow-on program. Both subsonic and transonic flight regimes are addressed. For subsonic applications, these include:

- Variable wing twist effected by nickel titanium (NiTi) shape memory alloy (SMA) torque tube for enhanced lift and maneuver control
- Hingeless, smoothly contoured trailing edge control surface deployment using NiTi SMA wires, also for enhanced lift and maneuver control
- Real-time pressure distribution data using embedded fiber-optic sensors for feedback control.

Program development for transonic flight features transonic cruise optimization concepts for commercial aircraft discussed in detail in “Smart Materials and Structures - Smart Wing Final Report Volume II,” entailing^{5,6,7}:

- Adaptive wing that employs TERFENOL-D linear wave actuator motors in the wing box structure to optimize airfoil shape
- Modifying camber with smoothly contoured trailing edge powered by TERFENOL-D linear wave actuators.

Figure 1-1 illustrates the subsonic smart wing concepts that have undergone wind tunnel testing in NASA Langley’s Transonic Dynamics Tunnel (TDT) on a 16 percent scale model. Figure 1-2 and Figure 1-3 depict the transonic cruise optimization concept employing TERFENOL-D actuators.

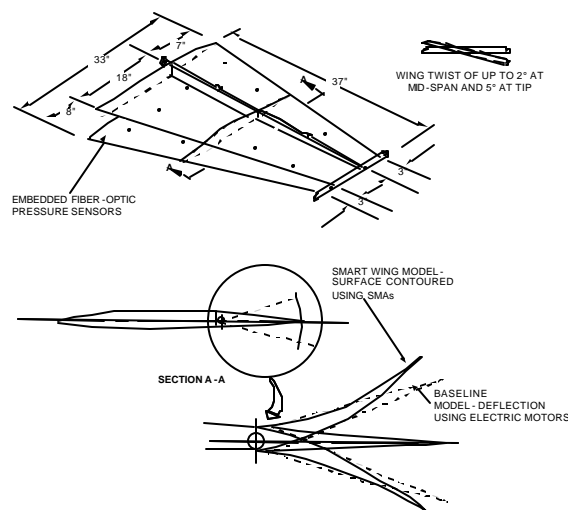


Figure 1-1. Smart Wing Concepts

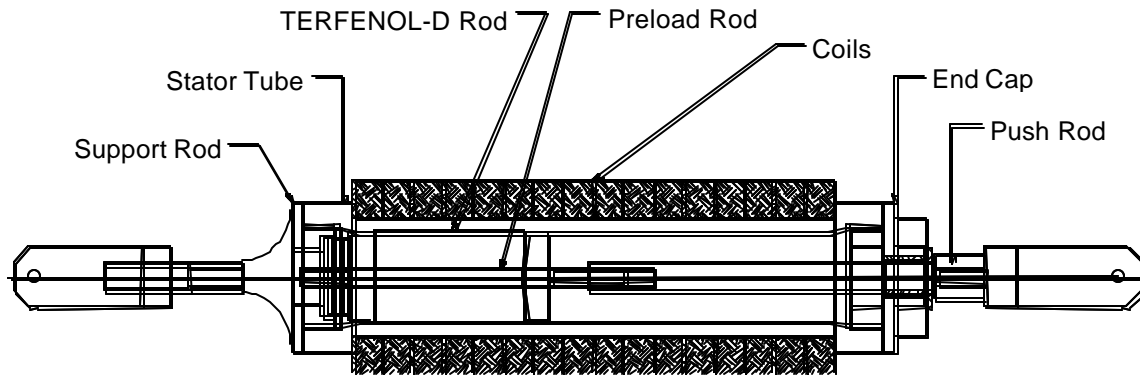


Figure 1-2. ETREMA TERFENOL-D Linear Motor

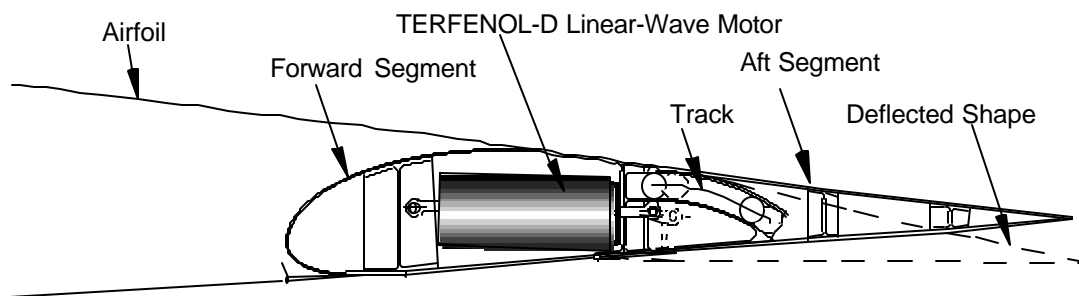


Figure 1-3. TERFENOL-Powered Smart Trailing Edge

1.1 PROGRAM TEAM

The Smart Wing Team comprises aerospace companies, small innovative research enterprises and universities with complementary strengths in all aspects of the program. Figure 1-4 shows the key team members as well as their areas of expertise and responsibilities.

1.2 LIFT AND MANEUVER ENHANCEMENT CONCEPT

The research and development pursued on this program was engendered by two earlier program efforts. While these efforts were not fully successful from a practical overall aircraft integration standpoint, they were nevertheless indispensable steps toward the ultimate goal of employing adaptive structures for improved aerodynamic performance. Both programs produced real hardware that validated earlier theoretical predictions showing that wing contour could indeed produce the anticipated enhancements. The first effort, the Mission Adaptive Wing (MAW)^{8,9,10,11} program, used a modified General Dynamics F-111 to prove the aerodynamic benefits but suffered system complexity and weight penalties incurred by the mechanical actuation system used. The second, the Active Flexible Wing (AFW)^{12,13} program, solved the weight problems by reducing wing stiffness requirements and compensated for the subsequent decrease in flutter speed and roll control effectiveness by using active leading edge and trailing edge control surfaces; however, high drag penalties were incurred that mitigated the anticipated benefits.

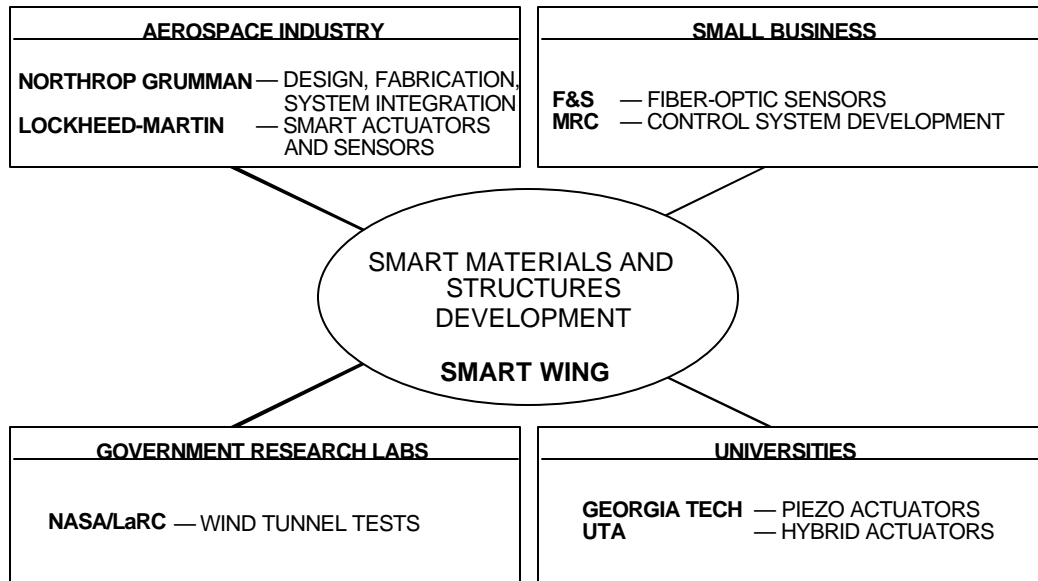


Figure 1-4. Smart Wing Team Members

The current program overcomes many of the earlier deficiencies by employing separate mechanisms to twist the wing and for control surface actuation, using the latest advances in “smart” shape memory alloy and magnetostrictive material technology. Figure 1-5 highlights some of the top level payoffs, risks, and issues that the program addressed.

1.3 TRANSONIC CRUISE CONCEPT

Northrop Grumman in Bethpage, NY, has been specializing in the development of adaptive wings to improve aircraft performance during transonic cruise by using a TERFENOL-D motor to extend or retract a trailing edge flap to optimize wing shape for various cruise conditions. Reducing drag in this way requires smaller motions and less weight than the originally proposed adaptive rib concept. This concept uses a TERFENOL-D linear motor to move the trailing edge, thus changing the wing shape and reducing shock-induced drag on the wing. The off-design cruise case is of serious concern for transport aircraft because wings are typically optimized for a single cruise condition and, therefore, usually have a much higher drag when operating at non-optimized conditions.

TECHNOLOGIES	PAYOFFS	RISKS/ISSUES
1. TWIST ADAPTIVE WING DESIGN	<ul style="list-style-type: none"> • PROVIDES HIGH LIFT - SHORT TAKEOFF AND LANDING - SHORT RUNWAYS - SHORT DECKS - INCREASED PAYLOADS (PASSENGERS/WEAPONS) 	<ul style="list-style-type: none"> • LIMITED TORQUE ACTUATION BY SMA • FATIGUE LIFE NOT WELL ESTABLISHED • MATERIAL FAB IS DIFFICULT
2. ADAPTIVE LE AND TE CONTROL SURFACES	<ul style="list-style-type: none"> • PROVIDES OPTIMAL L/D RATIO AT MULTIPLE FLIGHT CONDITIONS • ENHANCED MANEUVER CAPABILITIES • PROVIDES MINIMUM DRAG FOR MULTIPLE CRUISE CONDITIONS - INCREASED RANGE - DECREASED OPERATING COST 	<ul style="list-style-type: none"> • ALL OF THE ABOVE • REQUIRED ACTUATION RATES FOR MANEUVER (UP TO ≈ 10 Hz) DIFFICULT TO ACHIEVE • THERMAL MANAGEMENT NEEDS TO BE ADDRESSED
3. DISTRIBUTED FIBER-OPTIC SENSORS FOR PRESSURE MEASUREMENTS	<ul style="list-style-type: none"> • IMPROVED FLIGHT CONTROL SYSTEM STABILITY MARGINS • REDUNDANCY FOR OPERATION OF DAMAGED AIRCRAFT 	<ul style="list-style-type: none"> • MULTIPLEXING, FABRICATION AND DATA PROCESSING OF LARGE ARRAY OF SENSORS BEYOND PROGRAM SCOPE
4. LOAD ALLEVIATION	<ul style="list-style-type: none"> • ENLARGED FLIGHT ENVELOPE • IMPROVED RIDE QUALITY • IMPROVED MANEUVERABILITY - ROLL RATE, PITCH RATE, SUSTAINED G LEVELS 	<ul style="list-style-type: none"> • HYBRID SMA / PIEZOELECTRIC ACTUATORS WITH HIGH ACTUATION RATES (50-100 Hz) AND HIGHER POWER NEED TO BE DEVELOPED
5. TRANSONIC CRUISE OPTIMIZATION	<ul style="list-style-type: none"> • DRAG REDUCED IN TRANSONIC REGION ALLOWING SHOCK-FREE CRUISE 	<ul style="list-style-type: none"> • DETERMINING SHAPE FOR LOWEST DRAG AT CRUISE CONDITIONS
"SMART WING" DESIGN INCORPORATING 1 THROUGH 5	<ul style="list-style-type: none"> • ALL OF THE ABOVE • REDUCED STRUCTURAL WEIGHT • MAY ELIMINATE NEED FOR VARIABLE SWEEP WING 	<ul style="list-style-type: none"> • SEVERE A/C OPERATING ENVIRONMENT • OPTIMAL INTEGRATION OF ABOVE TECHNOLOGIES

Figure 1-5. Program Technology Payoffs and Risks

It was determined that imparting small motions to the wing's control surface could optimize the wing shape for various flight conditions, thus lowering drag and increasing range. Because of its reliability, fail-safe operation, high stiffness, and other properties, a TERFENOL-D elastic-wave linear motor was an excellent candidate to deploy the trailing edge control surface. The goal of the Transonic Cruise portion of the Smart Materials and Structures Development - Smart Wing Phase 1 program was to employ TERFENOL-D, a material that deforms in the presence of a magnetic field, to modify the wing shape during flight to achieve optimum wing performance over a range of flight Mach numbers. A detailed explanation of the concept is given in Volume II of the Smart Wing Phase 1 Final Report.

A summary of the key program accomplishments is given below while further details of the Smart Wing Phase 1 program progress for the subsonic concepts are detailed in Sections 2, 3, 4, and 5.

1.4 SUMMARY OF KEY PROGRAM ACCOMPLISHMENTS

Highlights of the progress are summarized below for all of the smart wing concepts. The subsonic effort established proof of concept to a degree by ground and wind tunnel testing whereas the transonic effort was largely analytical.

Key program accomplishments are:

- Requirements and concepts defined for control surface contouring and wing twist
- SMA-based hingeless, contoured control surfaces demonstrated with approximately ± 10 degrees of deflection and 8 to 12 percent increase in rolling moment compared to conventional designs
- 3,200 in-lb of torque achieved using a 1.125-inch diameter, 0.060-inch wall thickness, and 4-inch-long SMA torque tube; 5 degrees of wing twist demonstrated, which provided approximately 8 percent increase in rolling moment
- 1.5-inch stroke using 1.8-inch diameter TERFENOL-D linear wave motor demonstrated
- Methods to automatically optimize wing shape for transonic cruise developed and analytically validated.

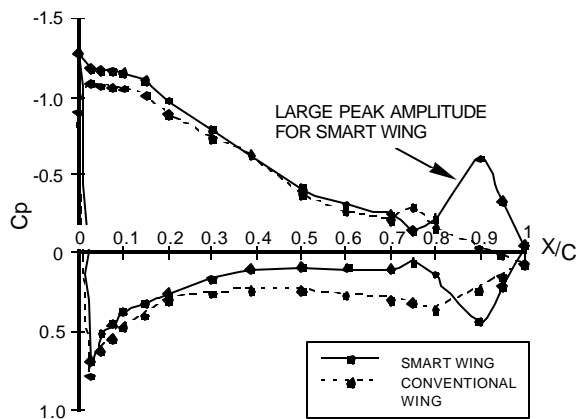
1.5 WIND TUNNEL FIRST ENTRY TEST RESULTS

Two wind tunnel models were tested in the NASA Langley TDT facility. One model was a baseline conventional wing, utilizing standard hinged trailing edge control surfaces, and the other model (Figure 1-2 and Figure 1-3) was the smart wing incorporating hingeless contoured control surfaces and distributed fiber optic sensors to monitor aerodynamic pressure.

Figure 1-6 illustrates the pressure distribution across the wing for both conventional (shown as a dashed line) and for smart configuration (solid line) employing a smoothly contoured SMA embedded flap. Aerodynamic pressure coefficient, C_p , is plotted along the vertical axis versus normalized chord length x/c along the abscissa so that pressure distribution from leading to trailing wing edges may be examined. Note that a large, fairly broad, peak suction pressure occurs at the trailing edge (TE) flap, for the smart hingeless case, far in excess of the amplitudes recorded for the conventional wing model. The modest pressure value for the conventional case is due to unwanted aerodynamic flow separation at the hinge line. For the smart flap, the point of flow separation moves further aft, much closer to the wing TE. Also, increased suction pressure for the smart configuration predominates in general across the entire wing chord span – the solid line is almost always above the dashed line in Figure 1-6.

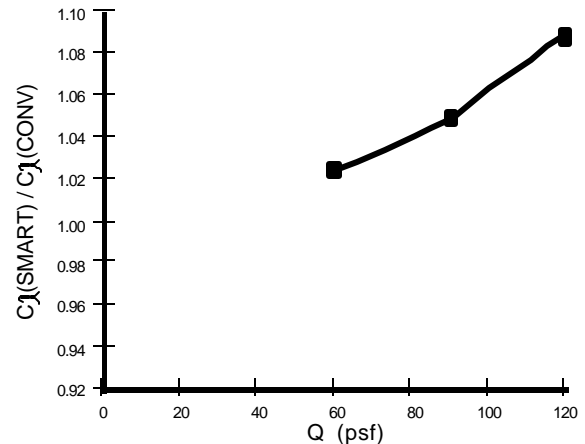
The importance of these results should not be overlooked. For the first time ever it was demonstrated and recorded by measurement that aerodynamic efficiency can be greatly enhanced using new smart material actuation systems. Furthermore, the result was confirmed by computational fluid dynamics (CFD) simulation (for brevity not shown) on the Smart Wing Phase 1 program. Figure 1-7 illustrates the aerodynamic efficiency for the contoured hingeless wing model normalized to the conventional value showing a 8 to 12 percent improvement in roll rate with increasing dynamic pressure. Similarly, encouraging results were obtained for the SMA torque tube concept. An 8 percent increase in the wing rolling moment due to an SMA actuated wing twist of approximately 1.25 degrees along the span was demonstrated and quantified. Such efficiency values are likely to increase as technology matures for the new program and will benefit future UAV and/or manned tactical aircraft.

Further details of progress are provided in the following sections.



T96-2/70/B

Figure 1-6. Wind Tunnel Pressure Distribution Measurements



T96-2/54

Figure 1-7. Rolling Moment Comparison - Contoured vs. Conventional Aileron

1.6 WIND TUNNEL SECOND ENTRY TEST RESULTS

The second round of wind tunnel tests was a reiteration of Test 1 except with improved fidelity in the testing and design upgrades to the smart actuator systems. Figure 1-8 shows the smart wing model wind tunnel model installed in the NASA TDT and a line drawing of the installation detail.

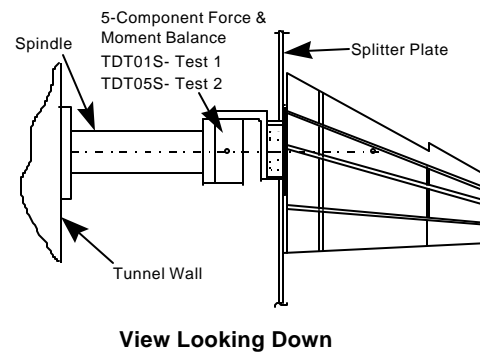
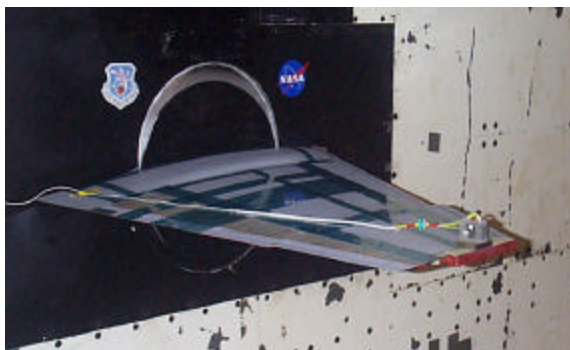


Figure 1-8. Photograph of Smart Wing Model and Installation Schematic

Figure 1-9 provides a summary of all of the aerodynamic improvements for the single effects of flap, aileron, and wing twist and the combined effects of flap with aileron and wing twist with aileron. For each configuration the deflection or twist is listed in degrees, and the delta lift and roll aerodynamic improvements are tabulated both in absolute and percentage terms. As a general comment, it can be seen that percentage improvements of the smart technology approached or exceeded 10 percent for the single effects and ranged between 15 and 17 percent for combined effects. It should be pointed out that percentages are relative to a typical takeoff condition where angle of attack (AOA) is 8 degrees and the dynamic pressure is 90 pounds per square foot (psf), ~200 mph.

In more tangible practical terms, a ten percent improvement in the lift and roll performances afforded by the smart technology would translate to:

- A 2000-pound increase in takeoff gross weight (TOGW) for a 40,000-pound fighter attack aircraft, e.g., a Joint Direct Attack Munition (JDAM)-equipped Mk 84 stores equivalent
- An increase in steady rolling rate from 120 degrees/sec to 135 degrees/sec for the equivalent conventional and contoured aileron deflection.

Configuration	Deflection or Wing Twist (deg)	Lift DC_L	Roll DC_ℓ	% Improvements	
				Lift	Roll
Flap Only (Test 1)	7.5	0.058	0.019	9.7	10.2
Flap and Aileron Combined (Test 1)	7.5	0.092	0.039	17.6	17.1
Aileron Only (Test 1)	5.0		0.015		8.0
Aileron Only (Test 2)	10.0		0.019		10.5
Wing Twist at Tip (Test 2)	3.0	0.034	0.019	8.0	10.0
	5.0	0.050	0.030	11.5	15.6
Wing Twist at Tip (Test 1)	1.4	0.041	0.022	10.0	12.8
Combined Aileron and Wing Twist (Test 2)	+ 10.0	0.057	0.031	15.3	17.3
	+ 4.5				

Figure 1-9. Summary of Results for Wind Tunnel Tests 1 and 2

A significant improvement over the Test 1 effort came in the updated single torque tube design that permitted the target 5-degree twist angle to be realized. However, across the board, all of the smart control surface concepts benefited from considerable design improvements over the configurations used in the first test. Model design enhancements unilaterally equated to higher deflection angles, improved fatigue characteristics and more uniform control surface deflections as reflected in Figure 1-8. The only setback in Test 2 was that a disbond in the flap occurred during preliminary wind tunnel flutter clearance runs, precluding further data acquisition for the flap performance in addition to the Test 1 data. Details of the failure are reported in Subsection 3.5. Nevertheless, very good data were obtained with the aileron that exhibited similar results to the Test 1 effort as described in Subsection 5.3.4.

1.7 REPORT ROADMAP

The report is organized into four volumes. This volume, Volume I, “Smart Materials and Structures - Smart Wing Phase 1 Final Report,” details the design, fabrication and testing of the SMA torque tube and SMA flap and aileron in the NASA Langley 16-foot TDT^{14,15}. Volume II, “Transonic Cruise Optimization,” describes the transonic cruise concept effort in its entirety. Volume III, “Wind Tunnel Test Results,” provides a compilation of the entire wind tunnel test results from both Test 1 and Test 2. Volume IV, “Pre-Test and Stress Reports,” contains the summary reports that describe the model, the model design, and the test plan. These reports were required by NASA before testing could begin.

2. SMA TORQUE TUBE DESIGN DEVELOPMENT

Before delving into the design details, it should be emphasized that shape memory alloy (SMA) torque tube development is focused on adaptive control of spanwise wing twist, specifically to improve aircraft landing and takeoff capabilities rather than maneuver performance. Today's inherent limitation of SMA material to respond quickly (a few Hz or higher), without highly aggressive active thermal management, limits its use as a primary control surface that could respond to fast maneuvers in aircraft applications. The real near-term benefit of the technology lies in low-rate wing twist optimization. Prior to the current program, research and development work had focused on little more than miniature applications or very small-scale applications of full-scale designs (i.e., helicopter rotor tab). The program, through a concentrated research and development effort, brought the technology up in scale and demonstrated that high-torque SMA torque tubes could be designed and applied.

Technical issues and strategies addressed in the program to promote and exploit SMA torque tubes for real-world manned aircraft (or UAV) applications were (1) analytical simulation and modeling of tube performance, (2) tube fabrication, (3) training methodologies of the SMA material to obtain the desired twist angle, and (4) the tube structural integration and attachment for maximum transmitted torque.

For quick reference, this section has been organized into the following topic areas:

- Technology description overview
- Torque tube design features
- Torque tube manufacturing
- Highlights of torque tube SMA material training
- Torque tube structural attachment considerations
- Torque tube control features
- Torque tube laboratory testing
- Summary and conclusions.

Though a degree of breadboard testing and prototyping was carried out in the laboratory, considerable design evolution transpired as a result of the first wind tunnel test (Test 1) as described in Section 5. Essentially, a dual tube approach configured inboard and outboard of the smart wing model was replaced by a single tube configuration that met the program goal of 5 degrees of twist.

2.1 TECHNOLOGY DESCRIPTION

A brief review of the important material phase changes that make SMAs so attractive for adaptive structures is first appropriate. The shape memory effect is due to a first order phase transformation from a low-modulus martensitic to a high-modulus austenitic phase. Temperatures at which the phase change occurs are denoted M_f (martensitic finish temperature), below which the material is fully martensitic, and A_f (austenitic finish temperature), above which the material is fully austenitic. The elastic modulus changes very dramatically as the material becomes martensitic; e.g., for Nickel Titanium (NiTi), which were the SMAs used in this program, it changes from approximately 12×10^6 pounds per square inch (psi) to 5×10^6 psi (83 GPa to 34.5 GPa). However, macroscopically, when the material attains the martensitic state, it is easily deformed, as would be required for an adaptive structure, and can accommodate up to 8 percent maximum strain and 4 percent practical strain. When heated through the transformation, the material reverts to its so-called hot shape, which is set by constrained annealing at 920°F (500°C).^{16,17}

The use of shape memory materials as a torsional actuator did not receive much attention prior to this program, owing partly to application difficulties and, until recently, a shortage of material stock.¹⁸ However, the use of NiTi SMAs for wing actuation is attractive for several reasons:

- SMA torsional actuators have potential to be lighter and less cumbersome than electric or hydraulic counterparts.
- Lack of moving parts provides innate simplicity.

The wing planform used was a 16 percent scale fighter attack aircraft that had at its widest point at the root a thickness of only 1.60 inches, and required over 2,000 in-lb to be applied to effect 1.25 degrees of twist. The SMA torque tube was configured to interact with the wing box, which acted as a bias spring for reacting against actuator twist. Prior to installation within the wing, the torque tube has to be trained and the SMA material prepared to provide twisting actuation. After installation of the actuator into the wing (installed configuration has to be carefully designed a priori), twisting movement by material phase change is achieved by indirect application of heat via a heater wire that is wrapped around the length of the torque tube. On heating, the tube reverts to its high-temperature (untwisted) state, which acts against the wing box stiffness, thereby generating the required wing twist of several degrees.

2.2 SMA TORQUE TUBE DESIGN

In simple terms the torque tube actuator may be described as a hollow cylindrical piece of SMA that is trained to provide 10 to 15 degrees of twist at anywhere between 500 and 3,500 in-lb of torque.¹⁹ There are three main design characteristics that can be varied in the design of the torque tube:

- Tube length, which determines the twist available or “stroke,” of the actuator
- Tube diameter, which determines the torque output
- Tube wall thickness, which determines primarily the tube stiffness and actuation bandwidth.

Figure 2-1 gives an overview of the torque tube concept. As described in the technology description section, initially the torque tube has no inherent twist. Prior to installation in the wind tunnel model, a pre-twist is physically applied to the torque tube which must be administered in such a manner that the tube will reliably “untwist” and return to its original state in a repeatable fashion when heat is applied. Therefore, once the pre-twist is successfully applied and the tube is installed in the model, heating the tube recovers the strain that was originally applied.

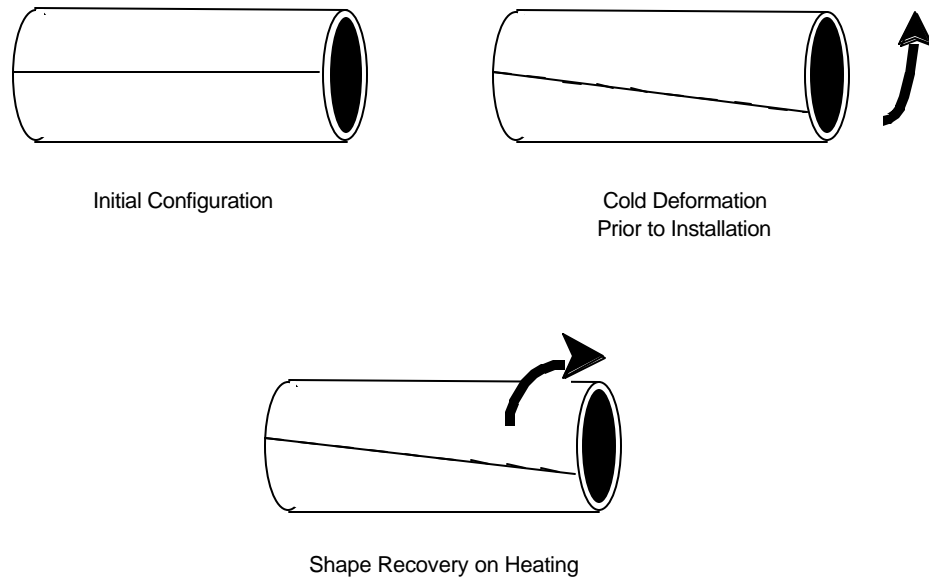


Figure 2-1 Torsional SMA Actuators

The torque tube was analytically modeled by assuming that the tube is a series of concentric circular shells that can recover 3.6×10^4 psi (250 MPa) of shear stress. The torque from each shell is then integrated together giving the total available torque for a particular diameter tube. The equations below can be used to determine the available torque:

$$F(r) = \left(\frac{F_{sa} * \ell}{R} \right) r dr$$

where F_{sa} = shear stress allowable = 3.6×10^4 psi

ℓ = tube length

R = tube outside radius

r = local radius

$$\Gamma(r) = \sum F(r) \bullet r dr$$

where $\Gamma(r)$ = output torque.

Results from this reasonably straight-forward modeling approach are plotted in Figure 2-2. This graph is plotted for a wall thickness inner diameter (ID) of 90 percent of the outer diameter (OD). Families of curves were assembled to facilitate torque tube ID and OD selection for a specified torque. While curves that relate tube diameters to available torque are an important step in the overall torque tube design process, other key factors include (1) heat transfer, (2) input power and (3) material phase change temperature transition relationship with stress. The latter phenomena were evaluated using Clapeyron equations, which are able to characterize such effects as the increase in martensite-to-austenite transition temperature with applied stress and plastic deformation. Applied stress at higher values will eventually cause plastic deformation instead of the strain recovery, a critical limiting feature for SMA applications. Other questions that needed to be resolved on the program were: are there upper limits to the model, and what are reasonable actuation times? As can be seen from Figure 2-2, a theoretical torque of 10,000 in-lb for a 1.7-inch-OD tube is possible. However, the limiting factor for higher torque performance lies in the provision of reliable structural connections as described in Subsection 2.5.

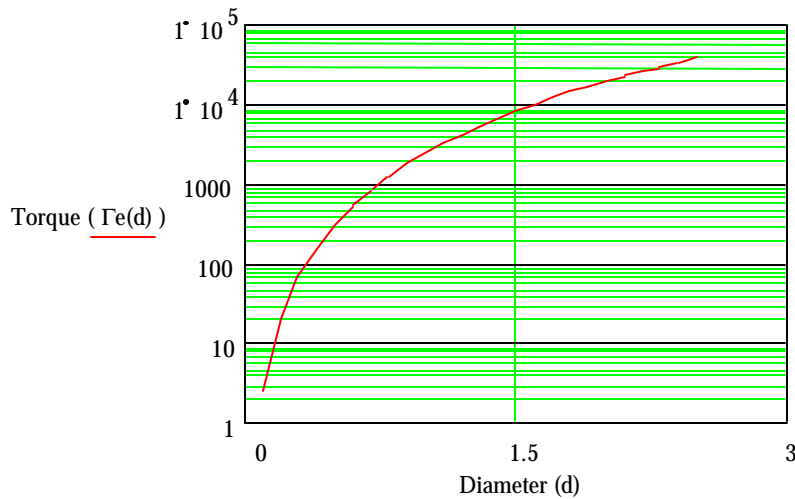


Figure 2-2. Torque Tube Design Limits

The analytical curve in Figure 2-2 is valid for thin-walled applications but only directly addresses the length and diameter effects of the torque tube's properties and performance. Equally important is wall thickness. Higher thicknesses bode well for structural load-carrying capability but are not optimal for SMA performance. It takes longer to heat and cool the material, leading to bandwidth and power efficiency problems, and as a general guideline, wall thicknesses with an inside-to-outside diameter ratio less than 80 percent should be avoided. Because of power problems and the fact that the design tools break down at diameter ratios less than 80 percent, a conservative ratio of 90 percent was employed for the tubes used in both wind tunnel tests.

To begin the torque tube design process, a critical factor that should be noted is configuration-specific maximum torque. The maximum torque determines the tube's outside diameter, with the 90 percent diameter ratio used to determine the wall thickness. In addition to tube diameter and wall thickness, the maximum angle through which torque is applied must be known in order to complete the design. This value, a typical pre-strain of 5 percent applied in the cold state, determines the tube's length. Sufficient data were generated during the program to establish design guidelines and accurate torque tube sizings.

Using a combination of analytical modeling in conjunction with considerable design experience and laboratory trial and error, torque tubes of 3,600, 2,000, and 500 in-lb were successfully designed and tested on the program, both in the laboratory and in the wind tunnel environment. These were the largest known designed, built, and tested SMA torque tubes at the time of writing and may be considered one of the many program firsts.

2.3 TORQUE TUBE MANUFACTURING

The SMA tube was manufactured from a hot-rolled Unimet metal rod obtained from Special Metals Company, with an A_f of 203 °F (95 °C). Because of the inherent difficulty in machining the SMA material, the rods were cut into 5.1-inch lengths by saw, followed by electrodischarge machining (EDM) to maximize utilization of the material. This is shown Figure 2-3, where three 1.15-inch diameter rods are cut out of the 2.50-inch diameter rod. After the smaller rods are cut out, they are gun-drilled to produce a rough tube. This is followed by further EDM (Figure 2-4) to finish the surface and obtain the final outside surface of the tube. The internal surface of the tube was then through wire EDMed to produce a tube that had a wall thickness of 0.065 inch. In Test 1, there was a problem in producing the final finish on the inside of the tube. With the Test 1 tubes, the EDM wire was used to cut the wall thickness to final depth, but this produced locations rough to the touch and contained several thinner areas of tube attributable to an initial overcut and

slight misalignments between the center of the tube and the machine. This nonuniformity caused the tube to buckle due to the torsion but still produced torque. For Test 2, the tube was bored out to its final size instead of being finished with the EDM wire, which gave a better inner surface and more consistent wall thickness.

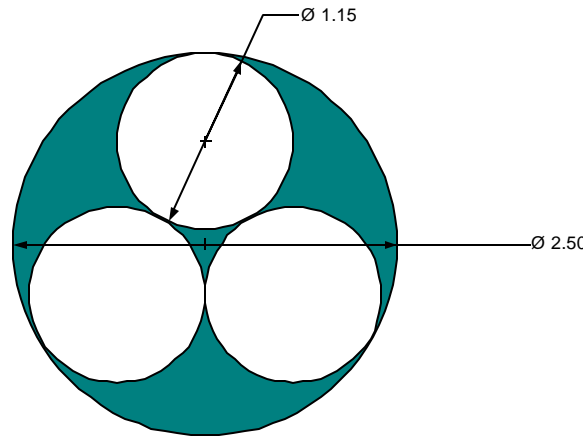


Figure 2-3. Initial Electrodischarge Machining Pattern for SMA Torque Tube

In Test 1, the 1-inch diameter material used for the final torque tube fabrication was produced with a 0.060-inch wall thickness, and the 0.5-inch diameter material was produced with a 0.050-inch wall thickness. The tube used in Test 2 was produced with a 1.125-inch diameter and a 0.060-inch wall thickness. After fabrication, the tube was annealed at 920 °F (500 °C) for 20 minutes to set the hot shape of the material, providing a large recovery stress.

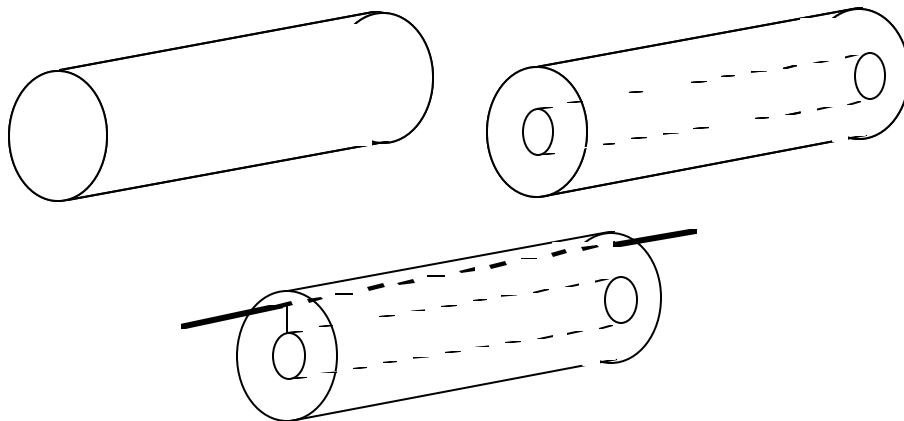


Figure 2-4. Electrodischarge Machining of SMA Torque Tube

2.4 TORQUE TUBE TRAINING

While SMA wire (discussed in Section 3, SMA Wire-Actuated Flap and Aileron) and linear element training had been practiced to an extent prior to the current program, tube training for torsional SMAs was in its infancy and had not been documented. Therefore, torsional characterization in the required torque range of 500 to 3,500 in-lb on the program had yet to be developed. In simplistic terms, let us review the training procedure before describing the torque tube training apparatus:

- The device (tube) is first heated up and annealed at $\sim 920^{\circ}\text{F}$ (500°C) for 20 minutes to relieve stresses and set “hot” or austenitic shape.
- The device is then cooled and torsional stress is applied in its cold state, providing the necessary pre-strain.
- Applying heat once more to the device, it “remembers,” or returns, to its annealed, untwisted state.
- The above sequence is repeated many times until the device is said to be trained.

The torque tube training apparatus used on the program is shown in Figure 2-5. Tubes were trained in the laboratory before wind tunnel testing; however, the apparatus was taken to NASA LaRC for the first wind tunnel tests, in case real-time adjustments had to be made.

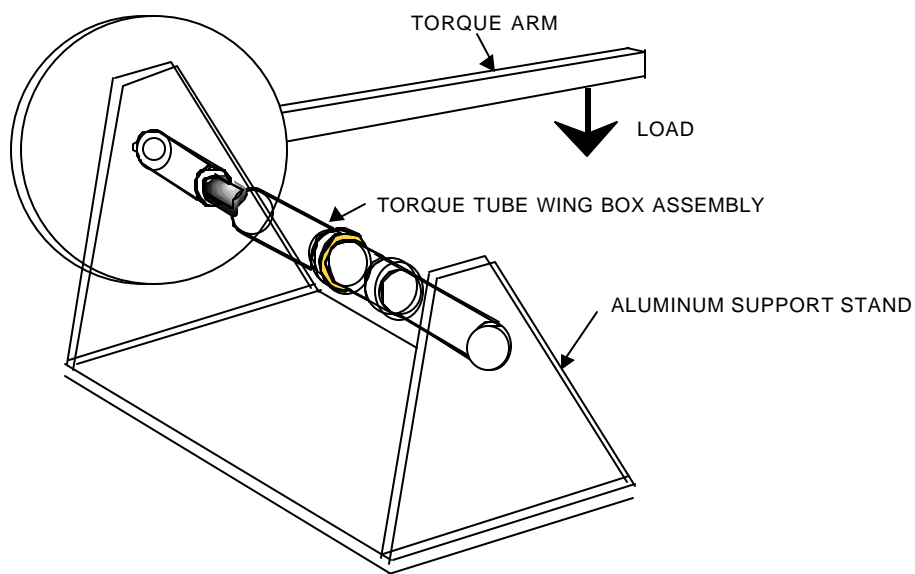


Figure 2-5. SMA Torque Tube Training Apparatus

Once the torque tubes had been manufactured, they were connected to a torque transmission rod that also had to be installed in the wing to transfer load. Heating of the SMA tube was accomplished via Nicrome wire (wire that becomes extremely hot when current is passed through it) encased in fiberglass tubing, which was then wrapped tightly around the tube. Application of heat during the training was identical to the method later to be used in the wind tunnel testing. A rotary sensor was attached to the end of the connection rig for deflection measurements. This in turn was attached to a loading arm with three holes at positions at 12, 18, and 24 inches from the center of rotation. The holes served to locate a weight pan, onto which the weights were loaded, providing an applied torque that could be applied repeatably and readily varied for maximum flexibility.

During the training process, torques were applied in the cold state to provide deflections with the load on, and the tube was heated to its austenitic state at temperatures up to 500 °F. Training was carried out by initially loading the 1-inch-diameter demonstration tubes to a relatively small load of 500 in-lb, and the device was cycled repeatedly to begin texturing the microstructure. Once recovery twists under load were observed, loads were added incrementally and cycled a number of times until the performance at each incremental step was satisfactory. With sufficient training, the 1-inch-diameter tube achieved 1,990 in-lb of torque and 5.3 degrees of twist whereas the 0.5-inch diameter torque tube provided 520 in-lb of torque and 14 degrees of twist. The weights of the tubes were 2 ounces and 1 ounce, respectively, demonstrating that large actuation energy density is available from these materials.

2.5 SMA TORQUE TUBE CONNECTION AND INTEGRATION

The structural connectivity of the actuator was one of the most challenging parts of the torque tube integration into the wind tunnel model smart wing configuration that tapered spanwise from a depth of 1.8 inches at the root to 0.375 inches at the tip. The first design used in Test 1 was a dual tube approach for inboard and outboard wing twist operation while Test 2 utilized a single tube installation.²⁰ In both cases, there were fundamentally two parts to the torque tube connection that required considerable attention:

- Torque tube to the transmission rod attachment
- Transmission rod to model attachment.

All torque tube connections had to withstand the required torque loads and needed to fulfill other integration requirements:

- Able to transmit torque values of 3,600, 2,000, or 500 in-lb
- Allow for clamping without slipping, be symmetric around axis of twist, and be able to take thermal loads
- Provide flexibility of adjustment for various applied pre-strains
- Fit within tight confines of the wing box.

The SMA torque tube to the transmission rod connection proved to be a far greater challenge than the team had first supposed. The problem stemmed from lack of integration experience in torque tubes of the program application's scale and dimension. In the past, on smaller tubes, the device had been secured to structure via a simple locking mechanism, employing a through-hole and shear pin. This type of connection, which relies on the steel shear pin bearing on the SMA torque tube to transmit torque, was initially tried for the larger-diameter tubes used on the program. Unfortunately, because of the large bearing stress and incomplete transformation to the high-strength phase for the ends of the tubes, the pin holes tended to elongate.

To get around this problem, a technique sometimes used in fastening hydraulic lines to cylindrical shapes was adopted. The idea entails using stainless steel crimps pressed onto the tube previously embedded with a tapered spline as demonstrated Figure 2-6. The benefit of the crimp is to apply a radial force that prevents the tube from slippage. Such a force had to be quite large for successful clamping since previous experiments in actuation (conducted at UCLA) had shown that accompanying the more familiar rotation is a secondary effect of longitudinal expansion. For Test 2, a shape memory effect (SME) hydraulic line clamp alternative to the stainless steel crimp method was investigated. While the method met with some success at lower torque values (up to 2,000 in-lb), it failed at the higher torque values that would be experienced during the second group of wind tunnel tests. The former mechanical method demonstrated with success during Test 1 for slip-free functioning of the SMA torque tube, was therefore retained for Test 2.

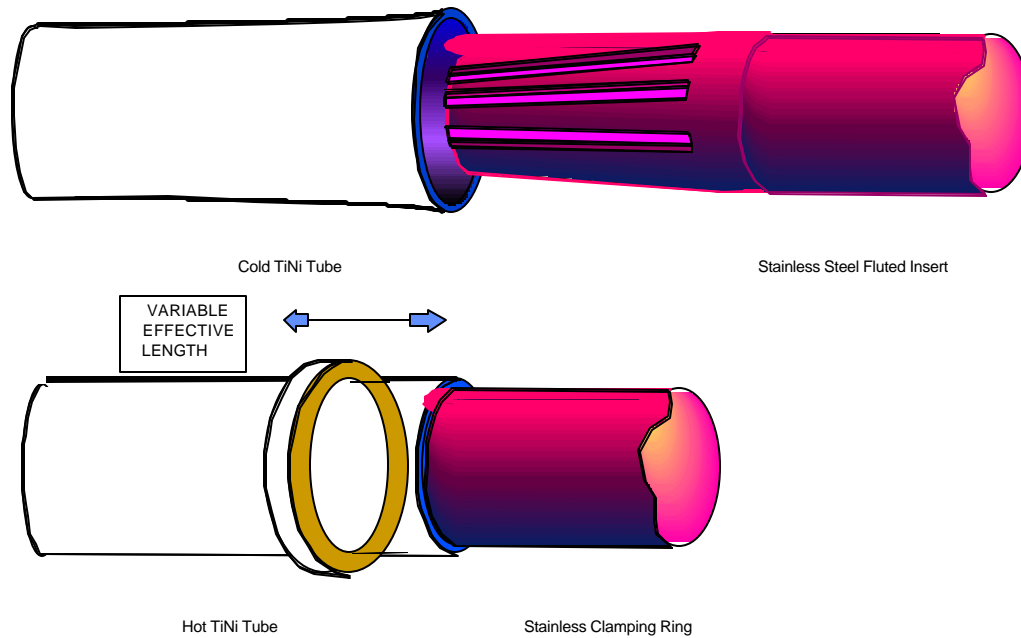


Figure 2-6. Torque Tube Connection Scheme

Further sophistication was added to the transmission rod and transmission rod connection for Test 2. The method used in Test 1 for the first dual tube design is illustrated in Figure 2-7. The design included structurally integral tangs at the wing root, mid- and tip ribs that corresponded to interference fit slots in the torque tube connector transmitting the required twist to the structure. Adjustments to the length (to allow installation and removal) and to the angle of pre-twist were accommodated using two stainless steel shafts connected together with a threaded rod. One shaft connected to the SMA tube using the connection scheme shown in Figure 2-6, while the other shaft attached to the wing rib using a slot and pin. A keyway was used to allow for length adjustments, and five holes drilled at 5-degree offsets were used to allow for angular adjustments as shown in Figure 2-7. Inspection showed that the weak spots for this design were the offset holes, and this portion of the connection was improved in the Test 2 design.

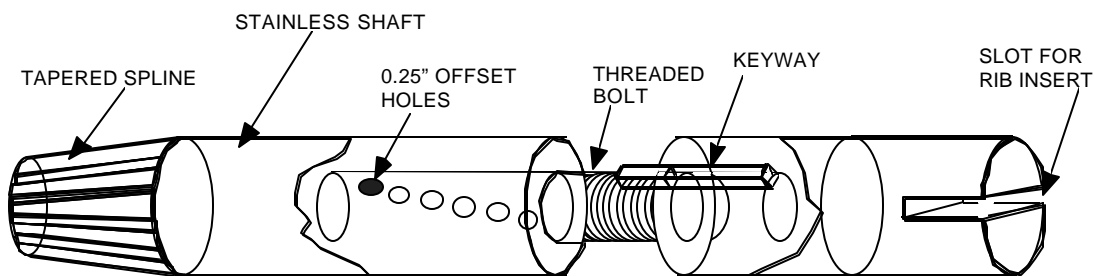


Figure 2-7. First Entry: Torque Tube Connection Scheme

The preceding attachment weaknesses were eliminated for Test 2, with yet another revised method. The new technique was an upgrade incorporating: (1) improved provision for torque tube pre-twist variation, (2) easier torque tube actuator removal and replacement, and (3) a torsionally stiffer connection. Figure 2-8 shows a schematic of the transmission shaft, SMA torque tube, and other details that make up the complete torque tube actuator assembly for the Test 2 design. In Test 2, a mesh gear was used to allow various torque tube pre-twists to be set. This kind of mesh gear involves a set of two gears that have radially cut teeth at 15-degree intervals. In the center of the gears are holes for bolts that lock the teeth together to prevent them from slipping. As a general observation for both connection schemes, it was determined early in the program that it was easier to design and build a connection method that permitted various different pre-twist angles to be set while the SMA tube was fitted with the crush couplers, instead of removing the couplers and torque tube, readjusting the coupler and SMA tube and then reattaching it.

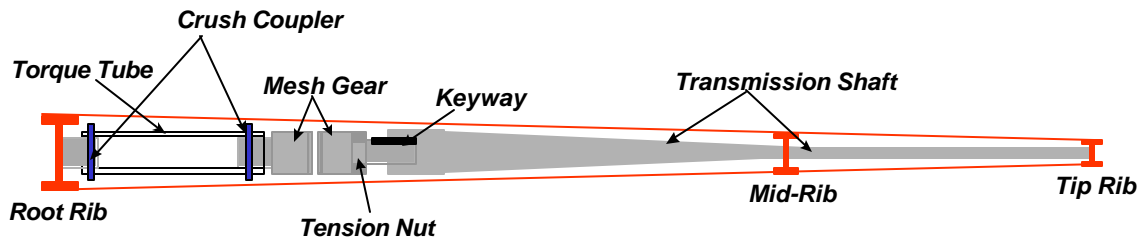


Figure 2-8. Transmission to Model Attachment

Another aspect of the design that proved challenging was minimization of the wind-up twist in the transmission rod. The torque tube has only a limited amount of available twist that it can output, and we did not want it wasted on twisting the transmission rod. The most structurally efficient transmission rod, with respect to limiting twist losses, would have been a circular cross-section. Due to size constraints inside the model, a circular cross-section was not feasible so a design using another shape was used. This design, shown in the figure below, was a tube that transitioned into a flattened ellipse. With this design, wind-up twist was reduced to less than 4.5 degrees. Figure 2-9 shows a planform view of the transmission rod illustrating the transition from circular to ellipsoid cross-section.

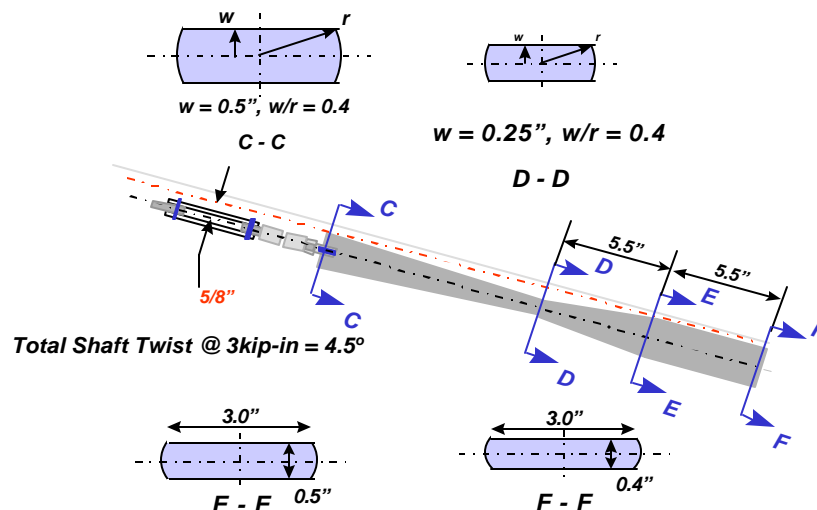


Figure 2-9. Improved Transmission Rod Design for Test 2

2.6 TORQUE TUBE CONTROL

The torque tube controller was tested prior to installation in the model as illustrated in Figure 2-10. Further details of the wind tunnel installation are provided in Sections 4 and 5. As mentioned earlier, the torque tubes were heated by Nicrome wire heaters, and the temperature of each torque tube was individually controlled from separate programmable HP 6024A power supplies. These in turn were controlled from a 486 PC running a Labview macro, which controlled the National Instruments digital-to-analog and analog-to-digital boards. Wing twist measurements were read from an external wing deformation measurement system developed by NASA Langley. Further details of the wind tunnel measurements are provided in Section 5.

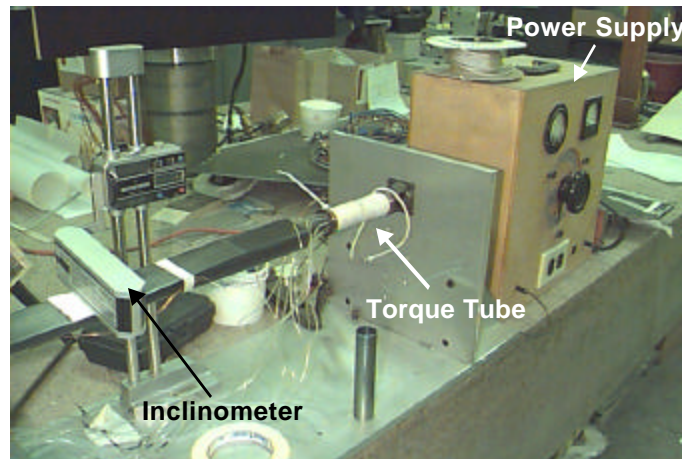


Figure 2-10. Torque Tube Testing Prior to Installation

The Nicrome wire was slipped into a fiberglass jacket to electrically insulate it from the rest of the model and wrapped around the tube as shown in Figure 2-11. The Labview control system was then regulated by a remote power supply that supplied the necessary heater current to the Nicrome wire. In Test 1, feedback or intermediate control over the torque tube behavior was very rudimentary. The power was merely routed to the appropriate tube in the tandem tube set up (inboard, outboard or both) on a “go/no-go” basis. Control features for Test 2, however, were vastly improved by incorporating power and time-versus-twist relationships that allowed intermediate twist positions to be selected. Also, information from two different types of tilt sensors (one an Advanced Orientation Systems Inc. electrolytic-type and the other a NASA-developed micro-electrical-mechanical-system (MEMS) sensor) was recorded, and an interface with the NASA TDT wind tunnel data acquisition system was established.

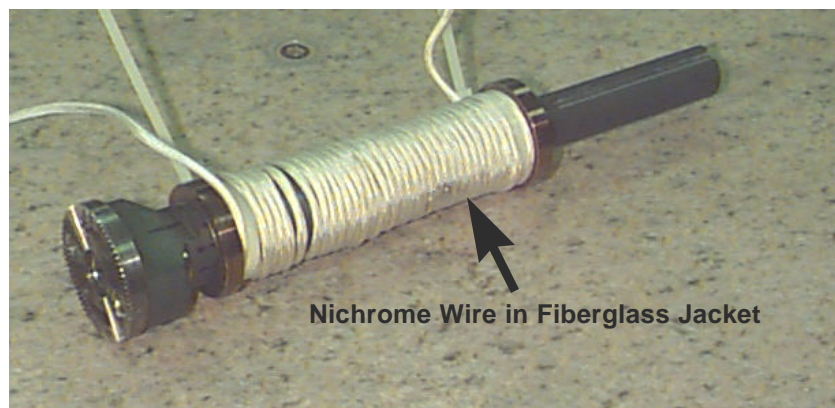


Figure 2-11. Torque Tube Wire Heater Elements

2.7 TORQUE TUBE LAB TESTS

In addition to training the tube, laboratory tests were necessary to verify twist output and connection mechanisms and gain further insight into performance prior to installation in the model. These tests included operation against a spring that simulated the torsional stiffness of the wind tunnel model. Once these tests were complete, the tubes and transmission rod were installed in the model. Then a second set of laboratory tests was performed prior to the wind tunnel testing. The laboratory tests performed before Test 1 included tests with the two torque tubes installed but with the upper skins not attached. This provided a functionality check on the tube and connections. Prior to Test 2, tests were also performed to bear out the functionality of the tube and the improved connection design. In these tests, the wind tunnel model was fully assembled, and a twist of 5.2 degrees was measured on the bench, which was also the twist obtained during the wind tunnel testing.

A good deal of effort was also put into laboratory testing to obtain detailed data on torque tube response and actuation times. As discussed before, the tube must be sized for the vehicle wing stiffness, and as indicated in Figure 2-2 considerable torque can be developed from a 1-inch-diameter tube, up to 5,000 in-lb and beyond if required. Of course, the great challenge is the thermal mass and the demands it would place on an aircraft thermal management system. These issues, along with others, would have to be resolved before the technology could compete with hydraulic or electrohydrostatic actuation for control surface deployment for maneuvers. Laboratory experiments, later substantiated by wind tunnel measurements, showed that actuators sized for 100 in-lb of applied torque took 5 to 10 seconds (i.e., < 0.2 Hz bandwidth) whereas 30 seconds was more realistic for higher torque actuators (e.g., $> 3,000$ in-lb) because of the increased volume of material that needed heating. Further details of the torque tube performance, which varied in design and results from the first wind tunnel entry (Test 1) and the second batch of measurements (Test 2), are provided in Section 5.

2.8 SUMMARY AND LESSONS LEARNED

The first demonstration of large-scale SMA torsional actuators integrated into a complex wing surface producing up to 5 degrees of twist and aerodynamic benefits in the 8 to 12 percent range for lift and rolling moment has been achieved. The torque tubes themselves, measuring 1.125 by 4 inches (active actuator length), were the largest (known) fabricated at the time of writing. The program experimentation with thin-walled torque tube materials, behavior, and properties has established an accurate design guide for sizing in the subject application. Torque tube actuation proved to be a viable method for torque applications less than 5,000 in-lb, though the thermal mass encountered is likely to limit actuation bandwidth to less than 0.2 Hz for near-term applications. A variety of command positions were successfully demonstrated on the program, using straightforward electronics and software, paving the way for successful proportional feedback control in future applications of the concept.

On the lessons-learned front, the actuator proved to be surprisingly stable during the hot state, at temperatures of 400 °F, and a potential problem was solved with no further development effort. It was also learned that a good deal of care must be applied in torque tube manufacture to prevent buckling although even a buckled tube can perform with some degree of success. Axial rotation for driven tandem tubes does not add up linearly, and the structural integration and connection scheme is all important. Proximity of the tube and driven surface is a very critical factor in terms of the overall actuator efficiency. However, in general for the torque tube structure interaction, simple loading paths gave expected results, and simple connection schemes, such as the one described earlier in this section, were found to be the most effective. Modeling efforts were useful for sizing, but accounting for the SMA structural behavior was not a straightforward (or useful) exercise.

In summary, it has been shown on the program that torque tubes can be successfully applied to adaptive wing features and to produce aerodynamic benefits. The most appropriate near-term application, however, is for low-bandwidth, torsional actuation.

3. SMA WIRE-ACTUATED FLAP AND AILERON

An important Smart Wing Phase 1 program goal was to demonstrate that operational capabilities of aircraft can be enhanced by incorporating advanced material adaptive structures. The main focus and development for Phase 1 centered on the SMA materials. While the torque tube actuation was described elsewhere (Section 2), this section describes an alternative SMA approach. An altogether different configuration using linear SMA wires was applied on the program to compliant aircraft wing control surfaces. Such configurations can be attached to the leading and trailing edges of a wing for hingeless, smoothly contoured control surface actuation.

The primary program objective, to develop compliant control surfaces for the 16 percent scale fighter/attack aircraft wing and establish concept feasibility, was fulfilled. The basic approach described below used SMA wires as embedded actuator elements for inboard flap and outboard aileron control surfaces. Controlled changes (by adding or dissipating heat) in control surface curvature were used to independently camber the flap and aileron to quantify performance improvements of the Smart Wing design in two iterations of wind tunnel testing. This section describes the program development under the separate headings of (1) Technology Description, (2) SMA Flap and Aileron Design, (3) SMA Flap and Aileron Manufacturing, and (4) SMA Control Development.

3.1 TECHNOLOGY DESCRIPTION

Much of the pioneering research performed by Lockheed Martin in SMA design for marine control surface applications proved useful to the program.^{21,22} The underlying physical principles of operation were, of course, the same. However, formidable challenges in terms of load levels, dynamics, confined space, weight, and a host of other structural and integration, power, and cooling issues had to be addressed.

Figure 3-1 illustrates how a series of SMA wires can be distributed along the control surface and by heating the wires in a particular manner and sequence, can produce actuation of the surface. An SMA wire has the useful property of producing a large strain (≈ 8 percent) when undergoing a phase change from the martensitic to austenitic states. While the more familiar linear coefficient of thermal expansion causes a wire to lengthen with temperature, the phase change that takes place for SMA does just the opposite. Therefore, to contour a surface downwards, wires on the bottom of the surface are hotter than those on the top. The surface may be contoured upwards by reversing the effect.

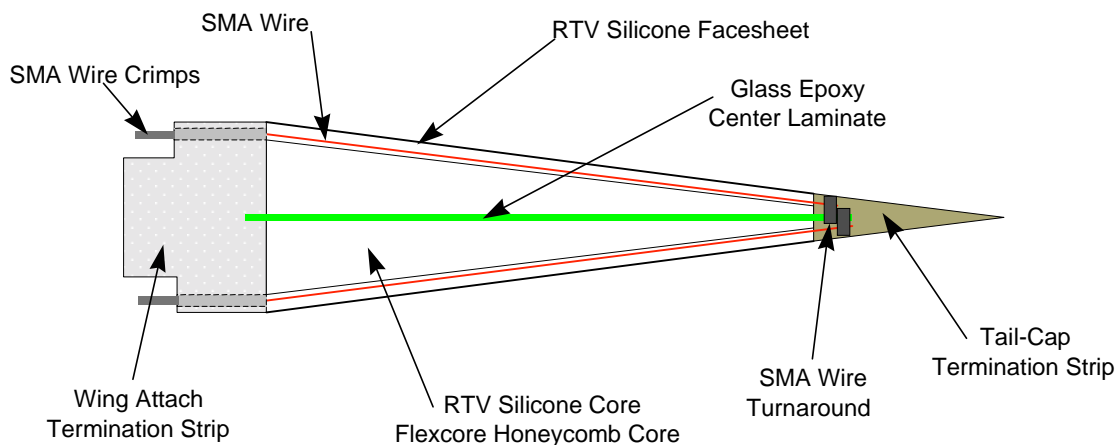


Figure 3-1. Shape Memory Alloy Control Surface Concept

By a judicious choice in the amount of pre-strain in the wires and employing antagonistic actuation – a technique used in hydraulic systems – balanced forces can be used to maintain a desired controlled surface position and made fail-safe (power-off position is neutral). Figure 3-2 illustrates the technique. A conventional composite laminate is bonded in the center of opposing core material layers with silicone facesheets, which have embedded SMA wires, bonded to both airfoil section outer surfaces. The fabricated shape is the neutral airfoil position, and actuation is accomplished by independently controlling the SMA wires at different temperatures. The maximum amount of length change in the wire, and thus control surface deflection, is dependent on the pre-strain applied during fabrication. To obtain the required cambered positions, the SMA wires on the bottom surface of the flap are activated while those on the top surface remain inactive. SMAs are capable of recovering up to 8 percent strain in the phase transition, but strain levels this high limit the fatigue life of the wire. For the Phase 1 program, pre-strain levels of less than 2 percent were used.

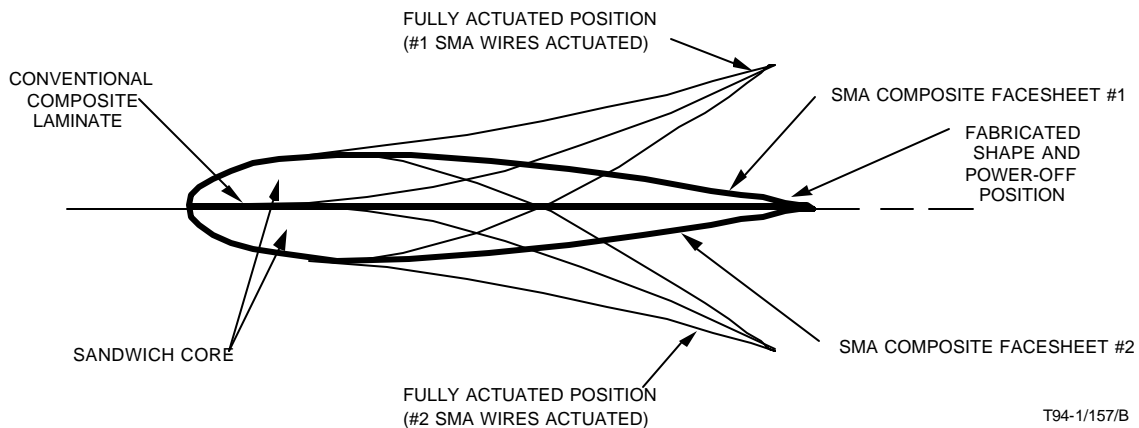


Figure 3-2. Antagonistic Actuation

3.2 SMA FLAP AND AILERON PRELIMINARY DESIGN

Going into the design activity some important constraints and guidelines in the overall approach were immediately apparent if the control surfaces were to fit the 16 percent scaled wing planform and achieve the required actuation. Briefly, these were:

- Despite total domain width of 8 percent, wire strain was restricted to ± 1.4 percent to limit fatigue and increase reliability/repeatability.
- Sufficient wire length must be embedded to meet tip deflection and surface curvature requirements.
- Parallel wires (Figure 3-1) are mechanically terminated at end points and must meet force and load requirements.
- A 0.02-inch wire diameter was selected based on trade-offs between thermal capacity (thicker wires heat up more, which leads to bandwidth problems), force requirements, and crimping (overcrimping adversely affects manufacturing).
- Actuator must “fight against” not only structural stiffness and air loads but also opposing wires (antagonistic actuation).

The solution to all of the foregoing key points will be addressed in the remainder of this subsection, which has been divided into (1) design requirements, (2) preliminary design and finite element modeling and (3) detailed design considerations.

3.2.1 SMA Control Surface Design Requirements

The performance requirements for the compliant control surfaces were driven by the 16 percent scale models used in both the wind tunnel tests. Figure 3-3 shows the top-level requirements. The team selected an antagonistic actuation approach to satisfy the requirements in Figure 3-3 and to meet the fail-safe requirement. However, it should be remembered that the actuator (in this case the SMA wires), in balancing the control surface position, “works against itself.”

Pressure Load	1.5 psi
Operating Temperature	< 50° C
Control Surface Deflection	Trailing Edge Flap $\pm 10^\circ$ Trailing Edge Aileron $\pm 10^\circ$
Maximum Hinge Moments	Trailing Edge Flap 160 in-lb Trailing Edge Aileron 40 in-lb
Control Surface Rates	<0.2 Hz
Physical Restrictions	Model Outer Mold Line (if Possible)
Fail-Safe Position	Neutral (0° Deflection)

Figure 3-3. Requirements for SMA Control Surfaces

Other table entries such as the pressure load, hinge moments, and operating temperature would change quite significantly in a real-world full-scale aircraft (most likely increase) but are representative for first proof-of-concept wind tunnel measurements. The most telling requirement is the control surface rate. This rate, less than 0.2 Hz, is determined by the ability to heat and (more importantly) cool the SMA wires. Though appropriate for takeoff and landing, with today’s level of technology readiness, SMA actuation alone cannot respond rapidly enough to meet realistic maneuver requirements.

3.2.2 Preliminary Design and Finite Element Modeling

During the preliminary design phases of the program, four control surfaces were selected as potential candidates for SMA actuation. These are identified in Figure 3-4, which shows the surfaces installed in the baseline model wing configuration. For the sake of completeness, both the leading and trailing edge inboard and outboard configurations studied are depicted in Figures 3-5, 3-6, 3-7, and 3-8. Plan dimensions and thickness details are shown in the figures; however, the leading edge configurations were not pursued and were considered to be out of scope for this program because of their higher load requirements and restricted available space.

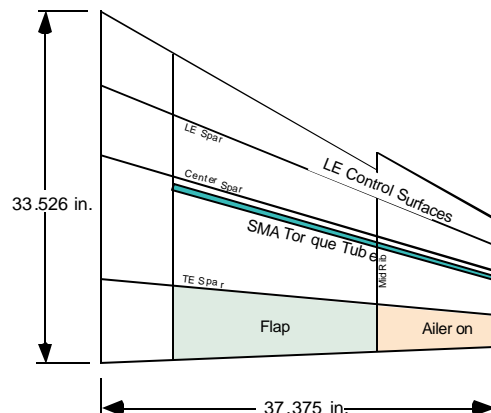


Figure 3-4. Planform View of Wind Tunnel Model Showing Location of Control Surfaces

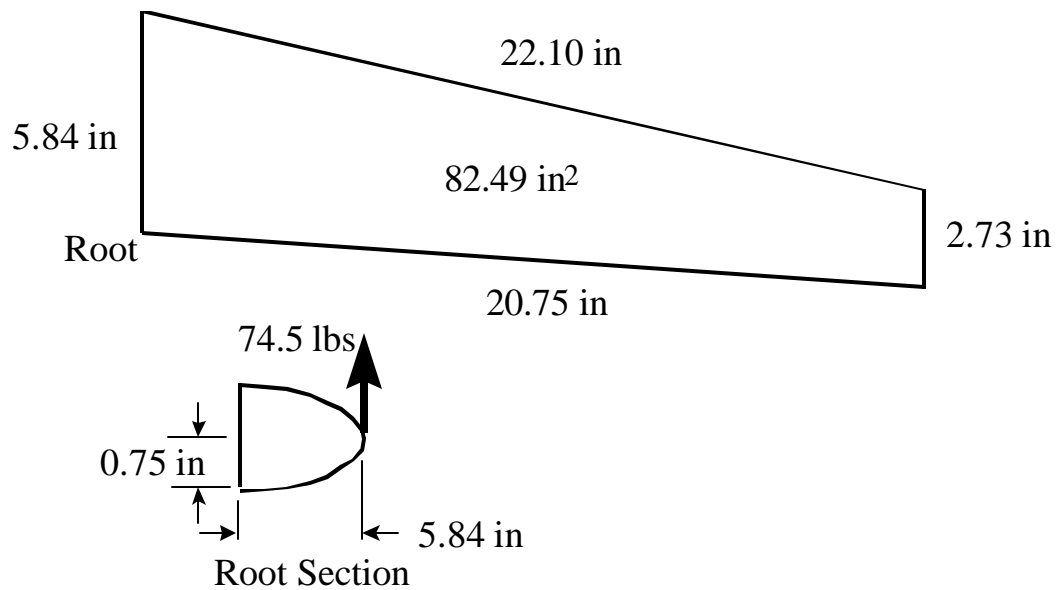


Figure 3-5. Leading Edge Inboard Control Surface

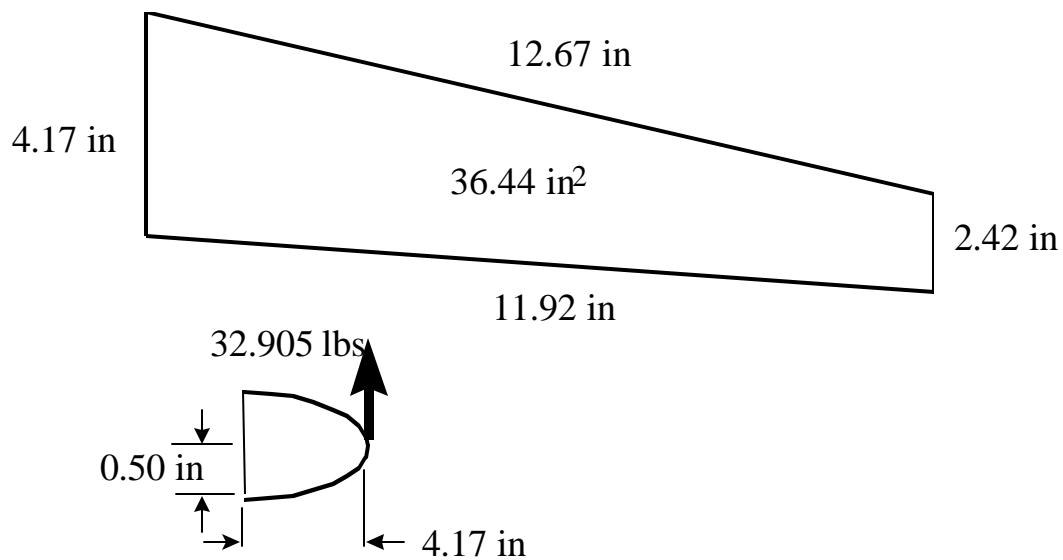


Figure 3-6. Leading Edge Outboard Control Surface

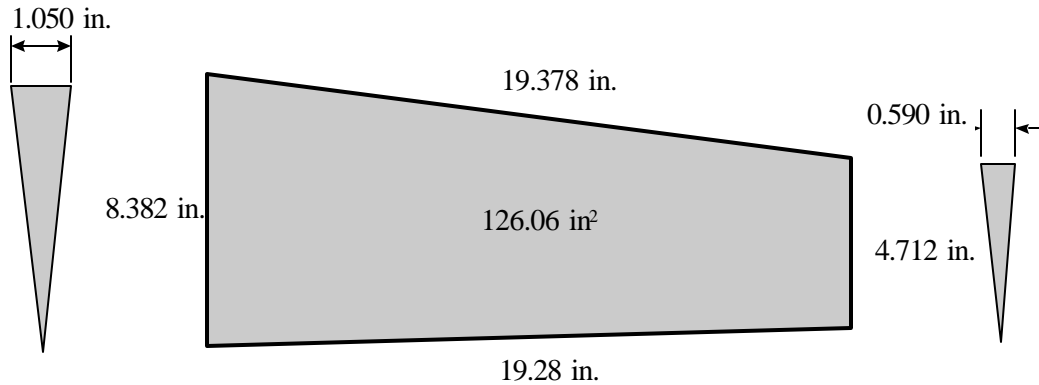


Figure 3-7. Trailing Edge Inboard (Flap) Control Surface

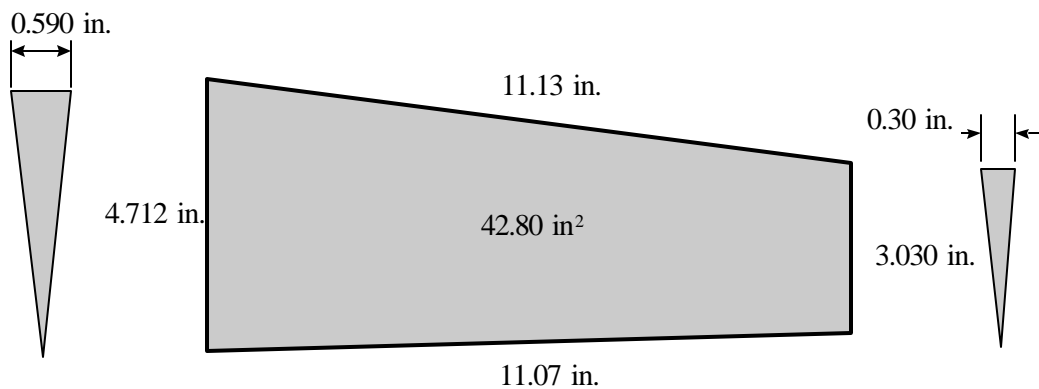


Figure 3-8. Trailing Edge Outboard (Aileron) Control Surface

An iterative finite element (FE) study was also performed by the team during preliminary design to optimize SMA wire strain and stress, to satisfy deflection and structural stiffness requirements, and most of all to determine wire density. Specifically, the optimum number, length, and termination characteristics had to be determined early in the program. The analytical model contained all the components that were used in the final control surfaces tested during the two wind tunnel tests. The critical control surface components analyzed were:

- Silicone facesheets with embedded SMA wires
- Fiberglass/epoxy composite center laminate
- Hexcel Flexcore honeycomb or cast silicone core interposed between the center laminate and facesheets
- Rigid terminations at the trailing edge and at the wire termination.

Deflection analysis performed on the inboard trailing edge was conducted assuming antagonistic actuation and a maximum of 4 percent strain in the compliant facesheets. Figure 3-9 shows an early model with an approximate 1 psi pressure load uniformly applied over the compliant trailing edge area. In this model, the SMA wires are oriented parallel with the chord edges of the compliant surface to allow termination along the wing box spar and provide efficient load transfer from the wires to the compliant structure. Strain, representative of the contraction of the wires, was input to the model, resulting in the deformation shown in the Figure 3-9.

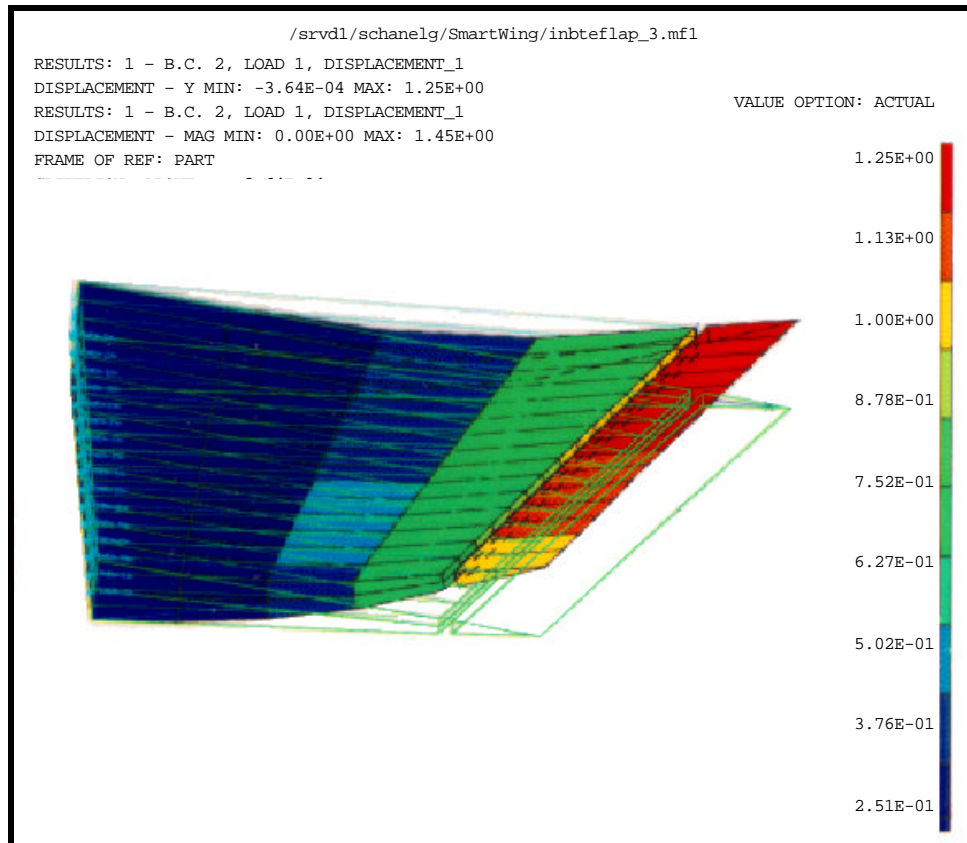


Figure 3-9. Finite Element Model (FEM) Results for SMA Control Surface

Representing the above component part list as realistically as possible, the FEM was developed. The FE analysis was conducted as a linear superposition of the deformation due to the SMA wire contraction and the 1 psi pressure loading. Deflection angle due to wire contraction was scaled such that an overall deflection angle of 14 degrees was maintained over the entire span. The analytical approach assumed linear behavior of the compliant control surface based on prior experience:

- Test conducted on a previous program verified linearity of the sandwich construction over similar range of deflection and load.
- Prior tests on an antagonistic wedge section showed a linear relationship between tip deflection and wire strain.

Essential modeling results are presented in Figure 3-10 in terms of the wire strain, axial force, and number of wires per inch for the worst-case 14-degree surface deflection angle. It should be emphasized that 4 to 7 pounds of additional force must be added to the load values to account for the force required to elongate the opposing SMA wires (necessary for antagonistic actuation). This is generally regarded as a reasonable “penalty” for fail-safe operation. In order to ensure that a minimum operating stress of 64,000 psi is maintained, the optimum number of wires per inch is six for a wire diameter of 0.020 inches. There are two characteristics that should be noted about fabricating the control surfaces using SMA wires. Firstly, the deflection cannot be increased by increasing the number of wires. This stems from the fact that the force generated by the SMA wire is a function of total wire cross-section, which depends on total number of wires and the wire diameter. The amount of deflection is directly related to the wire lengths and the

available strains, which are fixed to fit the planform. More strain, and hence deflection, cannot be achieved by adding wires. Additional wires will only translate to increased force and higher power. Secondly, increasing the number of wires at reduced diameter leads to crimping and manufacturing problems.

Model	Number of SMA Wires per Inch	Angle (°)	Strain (%)	Wire Axial Force (lb)
FLAP_3WPI	3	14.5	1.20	14.9
FLAP_6WPI	6	14.4	1.25	8.50

Angle Defined by Arctan (Tip Deflection / Chord)

Normal Surface Pressure of 1 psi Applied to Top Surface of Model

- Max Working Wire Strain: 1.4 %
- Max Working Wire Force: 25 lb
- Min Wire Reset Force: 3 lb

Figure 3-10. Wire Density Studies for Inboard TE Flap

The primary driving factor then in the design and configuration of compliant control surfaces is strain. In its native state, the alloy used in the program, NiTi, can accommodate 8 percent strain; however, repetitive use at this level introduces fatigue problems. To extend SMA wire life and facilitate reliability and repeatability, a maximum strain of 4 percent is recommended, which translates to ± 2 percent to account for antagonistic operation.

Further results from the finite element studies are depicted in Figure 3-11, which illustrates a streamwise cross-section cut of the inboard trailing edge control surface for various facesheet strain levels. The program settled on the deflection profile corresponding to a 2 percent strain as explained above. The three-dimensional view in Figure 3-9, however, illustrates another design challenge. Note the chord length variation with span. As the control surface must be changed by wire contraction traveling inboard to outboard, the wire pre-strain must also vary accordingly. The pre-strain in each wire must be set individually to obtain a constant deflection angle as the chord length varies. This is not readily accomplished, and earlier versions of the trailing edge surfaces suffered fatigue and deflection uniformity problems as described in Subsection 3.3.

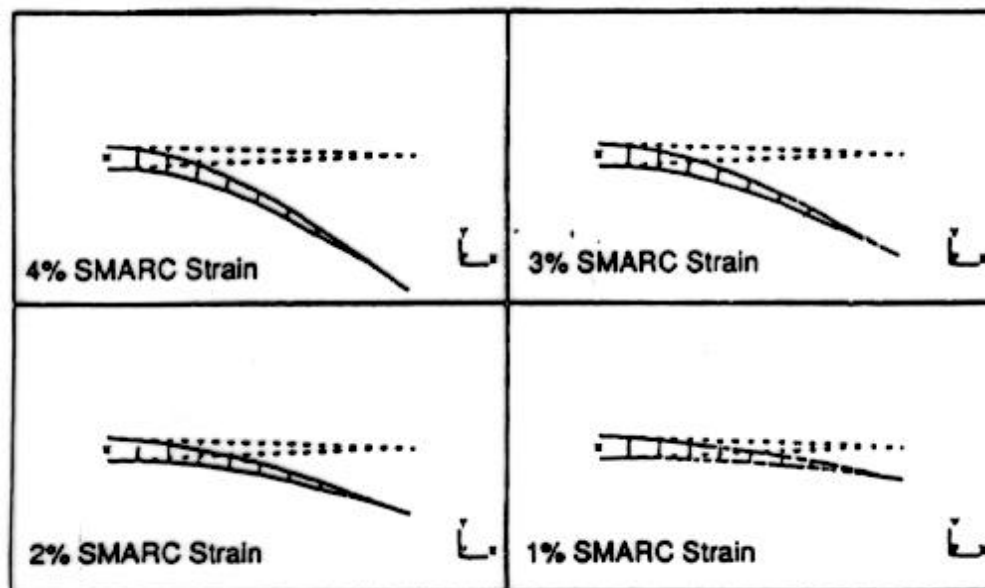


Figure 3-11. Streamwise Cross-Section Cut of FEM Results

3.3 DETAILED DESIGN AND MANUFACTURING

This subsection first reviews by component some important aspects of the control surface construction, which were essentially the same for both flap and aileron, but will concentrate on the flap since it was more complex. Additional design and manufacturing changes that resulted from the first wind tunnel test experience are reviewed later in the subsection.

3.3.1 Key Design Considerations by Smart Flap Component

The basic structural configuration for both flap and aileron control surfaces is of sandwich construction and is shown in Figure 3-1. A brief description of the prime features of each component follows, and references to issues arising, or uncovered, during the wind tunnel testing are brought out where appropriate.

Center Laminate. The center laminate is a 0.035-inch-thick glass/epoxy sheet attached to two termination strips. It is a prime load-carrying component and provides necessary stiffness to prevent in-plane buckling. Other functions include:

- Resistance to in-plane forces from SMA wire
- Resistance to aerodynamic forces
- Provision of restoring force to aid “opposite side” wires for extending contracted wires after actuation.

Termination Strips. These provide proper SMA wire termination and are attached to both ends of the center laminate. During Test 1 (the first wind tunnel entry), both the wing attach and tail-cap strips were made of Torlon, which was selected for its combined properties of structural robustness, high thermal conductivity, and low electrical conductivity. This material, however, did not perform as expected; towards the end of Test 1, the Torlon strip fatigued at the wire wraparound termination, resulting in loss of wire pre-strain.

This problem was solved prior to Test 2 by developing a new aluminum tail-cap termination strip. The fix is described below in some detail since it is typical of the engineering effort required to move the hardware toward flight worthiness:

1. An arrowhead-shaped piece of aluminum of exact dimensions was first machined and drilled with oversized holes.
2. The holes were filled with epoxy resin.
3. A new 0.1-inch hole was drilled in the center of the filled hole.
4. A steel pull-rievet was then installed in the 0.1-inch hole.
5. The rivet heads were then ground to make the rivet flush with the model outer mold line.

The above sequence of steps was necessary to ensure a rigid assembly, and the epoxy resin plug was required for electrical isolation of the wires. The wing attach termination strip for Test 2 was the same as for Test 1 and consisted of a Torlon strip. The wing attachment was made using 0.112-inch-diameter fasteners through the skin into Keen and Helicoil inserts set into the Torlon strip. These inserts were interspersed with the wire crimps and were a grounding concern before the first wind tunnel test.

The above method of attaching the control surface through the skin was successful and became the final solution after considerable discussion and analysis. Initially, installation of streamwise posts, which penetrated through the wing spar for quick removal and attachment of the control surface, appeared to be a viable approach. However, model size restrictions rendered the concept impractical. The thickness (0.3 inch) of the model aft outboard spar limited the post size for handling the required air loads.

Core. This component is bonded to both sides of the center laminate. For Test 1, the core consisted of a cast piece of room temperature vulcanizing (RTV) silicone bonded to the center laminate and facesheets. While the component functioned well, it was a prime candidate for weight reduction owing to the high density of the RTV silicone material. For Test 2, the core was replaced with Hexcel Flexcore aluminum honeycomb (H/C). However, the revision necessitated alternative facesheet attachment methods. In Test 1, the outer facesheets were bonded directly to the RTV honeycomb core using an RTV-based adhesive/sealant. For Test 2 Dow Corning Silastic J silicone rubber was used to bond the facesheet to the core. The problem in bonding the facesheets to the core is that most adhesives that would provide a good bond do not adhere to RTV, and the adhesives that do adhere to RTV are RTV-based and lack strength.

Facesheets. The primary role of the facesheet is to house the SMA wires and provide an aerodynamic cover for the control surface. Each facesheet consists of a cast sheet of silicone with polyurethane tubes cured in the silicone material at regular and fairly precise intervals in the streamwise direction. The SMA wires are then threaded through the tubes to “lace” the control surface as shown in Figure 3-12. The facesheet also keeps the wires constrained against the honeycomb. During Test 2, the facesheet-to-honeycomb joint suffered a disbond due to a combination of factors, with further details given in Subsection 3.5.

SMA Wires. The NiTi SMA wires were heated via Joule heating, i.e., passing current directly through the wires and using their inherent resistance to dissipate power as heat, causing the required control surface shape change. The wire diameter selected for the program was 0.020 inch. Smaller-diameter wires could have been used, but to avoid manufacturing difficulties it was necessary to limit the number of crimps. The mechanical crimps are placed at the end of the wire after it has been cut to the required length and pre-strained the appropriate amount. The selection of mechanical crimps for wire fastening was governed by the extreme difficulty of welding or brazing the NiTi alloy wire material. A single wire length runs from the wing attach termination strip down to the tail-cap termination strip and back. Each segment is then soldered together to provide electrical continuity. This step in the process is labor-intensive and requires specialized tooling and jigs to achieve the precision required for the control surfaces.

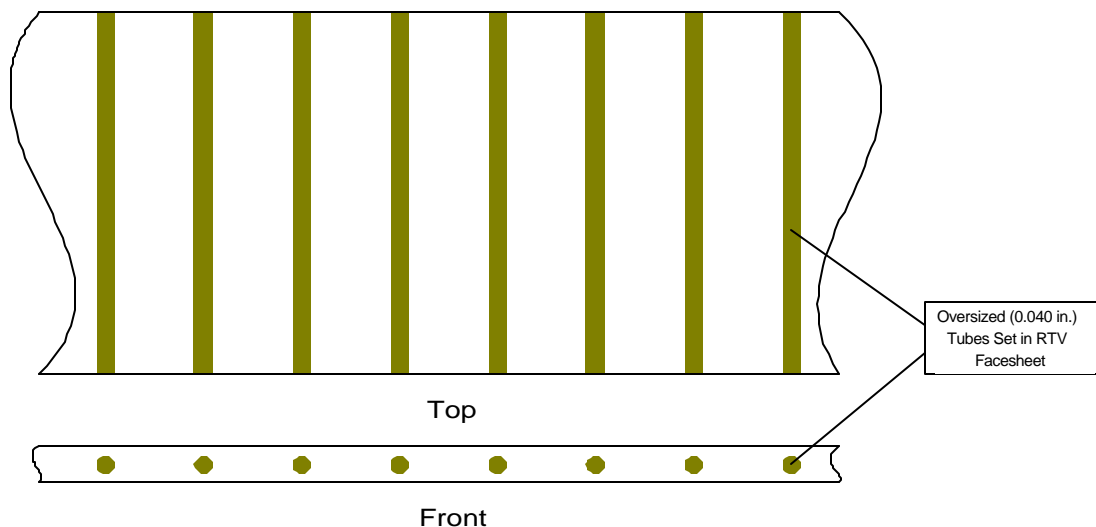


Figure 3-12. Facesheet Detail Showing Tubes and SMA Wire Placement

3.3.2 Further Design and Manufacturing Considerations

As described elsewhere, the top and bottom of the flap and aileron are separate and can be activated to move the control surface up or down depending on the wires selected. However, in Test 1, each control surface had only one controllable segment, which was physically one continuous circuit with all the wires connected in series. While the surface was actuated and gave reasonable results (Wind Tunnel Test Results, Section 5), the design was far from optimum for the following reasons:

- Wires and terminations fatigued more than expected.
- Available deflection varied spanwise across the control surface for a given current.
- This led to a non-uniform spanwise variation in deflected shape by Test 1 completion (e.g., when inboard deflection was 6.3 degrees, outboard deflection was only 3 degrees).

A solution to the non-uniformity was instituted by Lockheed Martin prior to Test 2. Their solution was to build multiple circuit segments with independent control – six for the flap and two for the aileron (Figure 3-13 and Figure 3-14). To limit system complexity during testing, pairs of adjacent segments were jointly controlled, reducing the total number of independent control units to three for the flap and one for the aileron. This provided sufficient spanwise shape control. Figure 3-15 shows close-up photographs of the flap final construction.

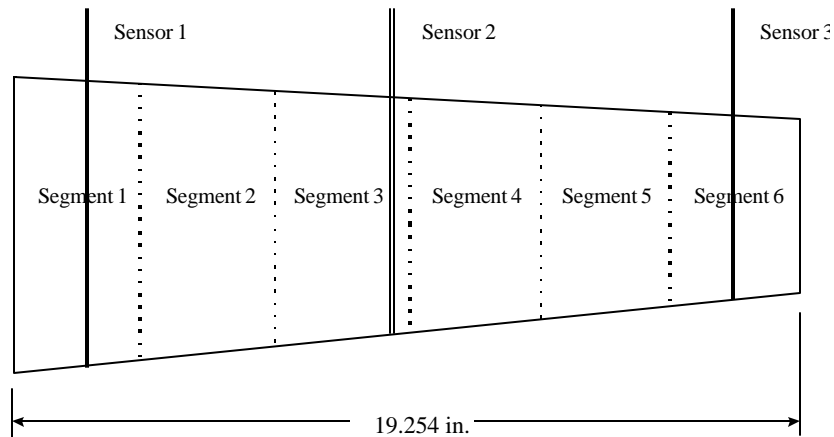


Figure 3-13. SMA Flap Segment Layout

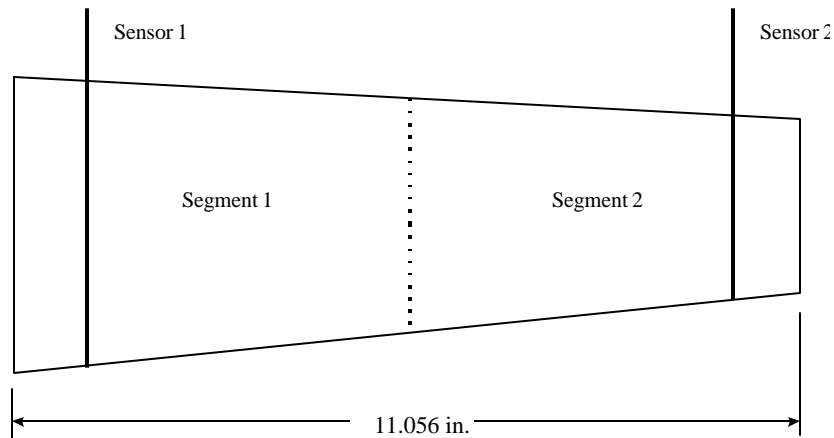


Figure 3-14. SMA Aileron Segment Layout

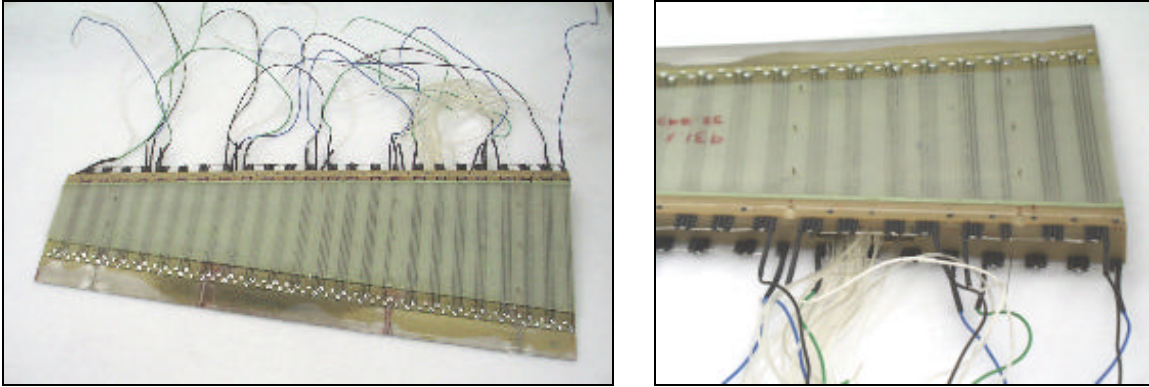


Figure 3-15. Photos of Completed Flap

The current ratio of values corresponding to each segment was also varied in Test 2 to account for fatigue and possible drift. This was accomplished by dedicating linear potentiometers to each segment to measure the tip deflection. As each user-defined tip deflection was input to the controller, the control system adjusted the appropriate current level for each individual segment to maintain a uniform deflection. This system was a significant improvement on the Test 1 design and provided a constant deflected shape with little spanwise variation.

3.4 FLAP AND AILERON CONTROL SYSTEM DEVELOPMENT

Figure 3-16 illustrates the distributed control setup across the wing span to provide segmented articulation of the control surface. Each segment operates from a desired set point, which is compared with a sensed displacement; by proportional control the wire current is moderated through an amplifier that trims the system for constant camber.

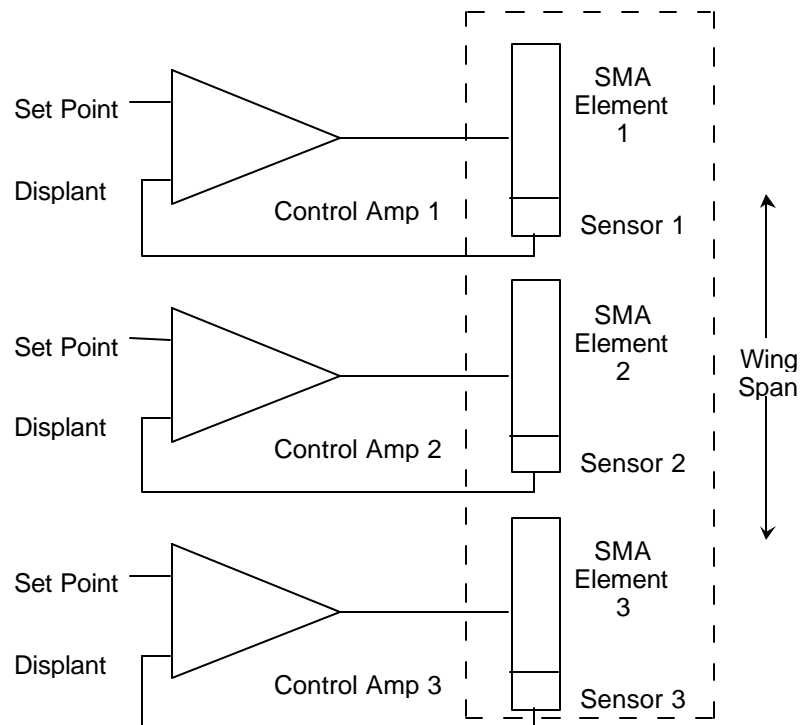


Figure 3-16. Distributed Control Approach

Antagonistic feedback control was achieved in principle by the functional operation of the circuit depicted in Figure 3-17. An analog-to-digital converter translates displacement signals from the sensed and user external commands, and a digital-to-analog converter translates the signal back into analog form after processing. Power amplifiers (Figure 3-18), operating from ± 70 V DC rails, provided sufficient current to move the surfaces as commanded by the control system. The power amplifiers were controlled by the analog signals routed through a two-tier isolation circuit. Control surface movement was achieved by resistive heating (and phase changes) of the SMA wires. The total power required for a 10-degree deflection of the aileron is 250 watts to initially deflect surface and less than 20 watts to maintain the deflection.

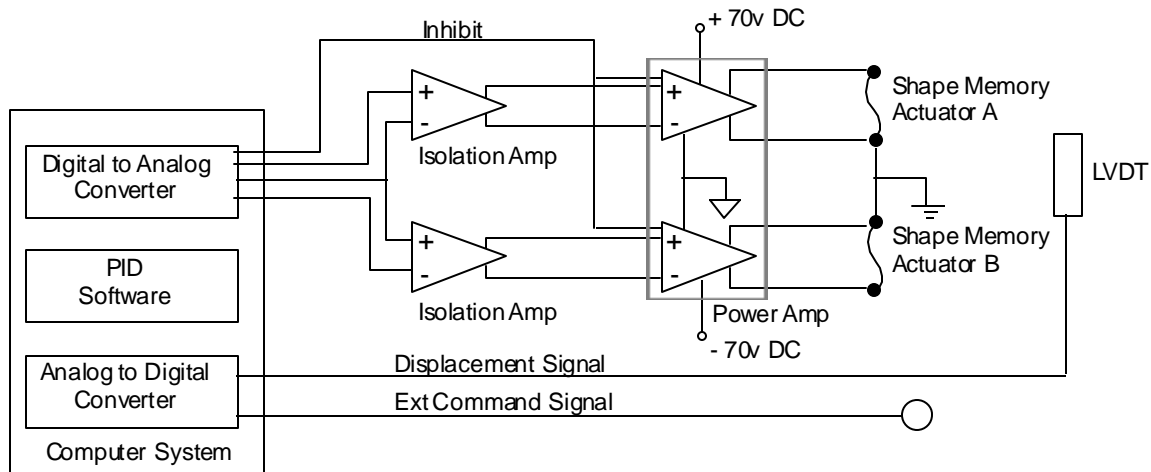


Figure 3-17. Control System Block Diagram

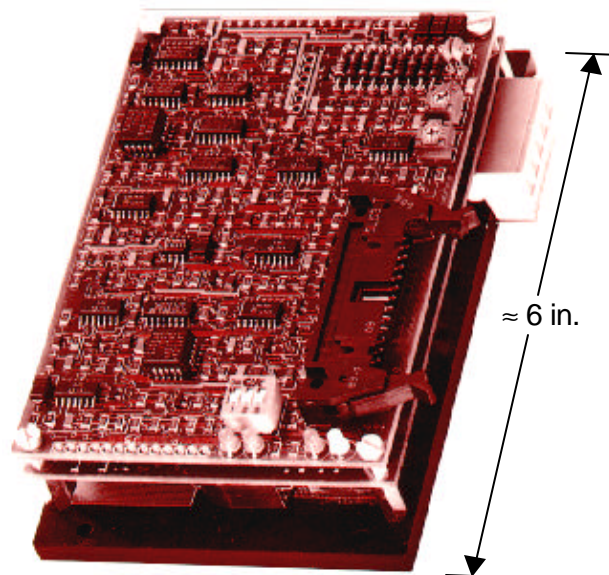


Figure 3-18. Typical Power Amplifier Used on Program

The control system (Figure 3-17) allows for modification of current flow to SMA actuators (wires) based upon feedback of measured displacement. Command signals are input as user-defined set points. An error signal is generated from the difference between the set point and the measured variable, namely the control surface tip displacement. A proportional integral differential

(PID) algorithm then calculates the output signal based on the magnitude of the error signal. The PID controller has four key components: (1) a derivative filter, (2) the proportional algorithm, (3) an output limiting capability, and (4) the integral action. The equations comprising the PID are executed in the order below:

1. Derivative Filter:

$$y = y + \Delta t * (PV - y) / (\Delta t + D/K_d)$$

2. Proportional Algorithm:

$$m = b + (100/P) * (SP - PV - K_d * (PV - y))$$

3. Output Limiting:

$$\begin{aligned} \text{if } m > m_h, \text{ then } m &= m_h \\ \text{if } m < m_l, \text{ then } m &= m_l \end{aligned}$$

4. Integral Action:

$$b = b + \Delta t * (f - b) / (\Delta t + I)$$

where

P	Proportional band in percent (a negative value indicates forward action)
I	Integral (reset) in minutes per reset
D	Derivative (rate) in minutes per repeat
K_d	Derivative gain limit (range 0 to 1)
PV	Process variable in percent
SP	Setpoint in percent
m	Manipulated variable (output of controller) in percent
m_h	High limit for manipulated variable
m_l	Low limit for manipulated variable
M	Manipulated variable in manual mode in percent
e	Error (difference between set point and process variable) in percent
b	Bias in percent
y	Output of derivative filter in percent
f	Feedback signal for the integral term in percent
L	Linearity parameter for the error-squared controller
Δt	Cycle time for algorithm in minutes.

The above calculations are performed at a rate of 2,000 to 5,500 Hz depending on graphical update requirements. The resulting output is provided to a programmable DC power supply (power amplifier) regulating current flow to the specified SMA wire circuit. The amplifiers update their output at a rate of 750 Hz or approximately 100 times faster than the response time of the control surface.

An open-loop (step test) tuning procedure was necessary to establish the magnitude of the proportional band and reset variables in terms of response time as shown in Figure 3-19. The procedure was based on the flap and aileron being modeled as first order lag and pure dead time. A step change in output was made while noting the resulting change in tip displacement as a function of time. From this data, T_d (dead time), T (constant), and K (process gain = percent change in output/percent change in PV) were determined. These measured values were multiplied by semi-empirically determined constants to derive the tuning parameters. PID commands were implemented on the SMA wires embedded in Facesheet A while applying a constant current on the SMA wires embedded in Facesheet B. This command structure was valid for all actuation cases between the neutral and maximum positive positions.

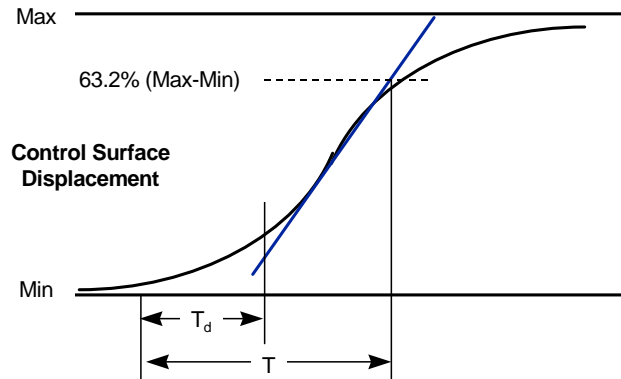
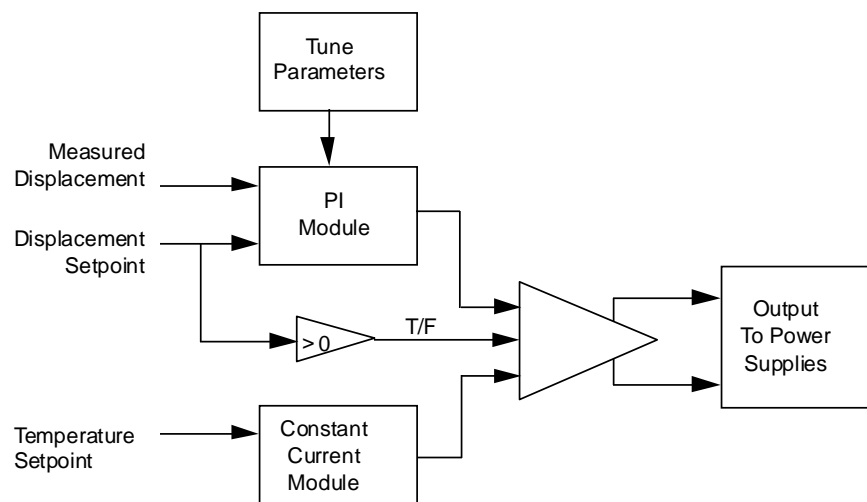


Figure 3-19. Step Tuning Procedure

As explained earlier, antagonistic control required that a maximum pre-strain of 2 percent be introduced to center the operational limits within the austenite/martensite domain width. This pre-strain was introduced at 70°C, slightly above the austenitic finish temperature of the alloy. Upon cooling to the operational temperature of the control surface (approximately 20°C) the two-way memory effect causes the wires to relax. To maintain wire tension, this effect must be compensated for by introducing a constant amount of power (approximately 1 watt/inch, depending on the thermal environment) through the wire, heating it to 70°C. PID control functions are then implemented on the opposing wires, allowing surface deflection to occur at nearly constant stress. Tip deflection occurs by the reversion of martensite to austenite, in response to the Δt created by the PID function. The contraction of the PID wire is opposed by the second SMA wire in which austenite is transformed to martensite by applied stress.

To obtain negative deflections it is necessary to switch PID control to Facesheet B wires and apply a constant current to Facesheet A wires. This is accomplished through the use of a software switch that senses the sign of the set point and allows an inhibit command to be output to two independent DC power supplies (Figure 3-20). To avoid crossover distortion during switching, current is applied to both A and B wires, increasing the apparent stiffness of the wing section. This action prevents the control surface from reacting to aerodynamic variations while operating close to the neutral position.



Switching Logic:
 -If T, then Facesheet A under PI control and Facesheet B under constant current control.
 -If F, then Facesheet A under constant current control and Facesheet B under PI control.

Figure 3-20. Antagonistic Control Software

It should be pointed out that in Test 1 a fiber-optic strain sensor was tested as a feedback device. It was attached to the center laminate and was to provide data on the curvature of the control surface. Unfortunately, the use of only one sensor located near the inboard edge compromised repeatability and precluded its use as a reliable feedback sensor.

In Test 2, a linear potentiometer was used to measure the deflection of the trailing edge tip by measuring the in-plane tension change. Although these sensors had some repeatability and noise problems, they performed well overall. Sufficient accuracy of the measured deflections permitted full antagonistic operation of the control surfaces, and the sensor output correlated quite well with the external deflection measurement systems described in Section 5.

3.5 FLAP DELAMINATION

This section analyzes an unexpected flap delamination failure that occurred during Test 2. Although the failure was not a major setback in terms of overall program success (proof of concept had already been established for SMA wire actuation in the earlier scheduled tests), the performance failure prevented the team from taking further substantiating aerodynamic data and limited the number of data points that could be obtained.

As described earlier in Subsection 3.2, all the necessary pre-test checks to ensure test worthiness of the flap were performed and went according to plan. Up to this point there were no indications that the control surface facesheet would disbond or fail to produce the desired results. However, a problem was uncovered and observed during the first flutter clearance run, and the system was shut down. Closer inspection of the failed surface showed that the SMA flap had an unusual curve and that the cause was a disbond of the facesheet from the honeycomb core. Figure 3-21 shows the location of the failure.

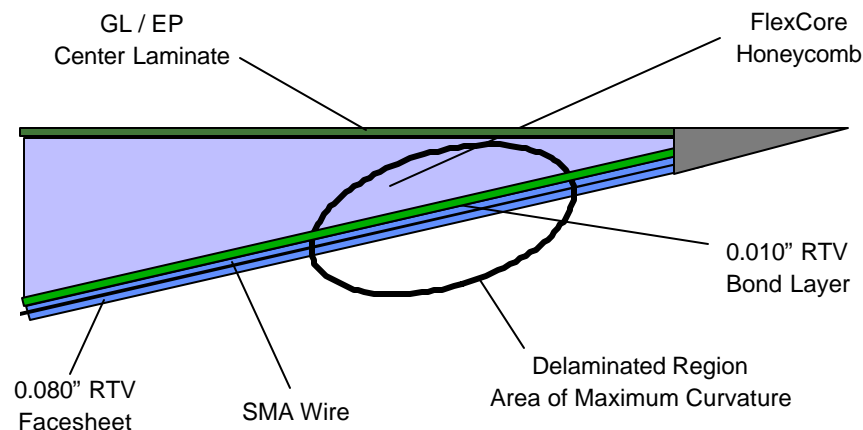


Figure 3-21. Location of Flap Delamination

The precise cause of the failure was not known at test time, but critical contributing factors were surmised to reside in a combination of the following factors:

- Inadvertent simultaneous actuation of the upper and lower wires pulling in opposite directions
- A suspect facesheet-to-aluminum honeycomb core bond joint.

The test was temporarily interrupted for flap inspection and repairs. However, further investigation of the problem to shed light on the unexpected failure was deferred until test completion.

3.5.1 Post Wind Tunnel Test Investigation

The investigation involved a closer examination of the (limited) data that had been taken before the failure and analysis and testing in three areas:

- Analysis to determine the loads applied to the facesheet and honeycomb core joint
- Flatwise tension tests on the flap material lay-up for comparison with analysis
- SMA wire investigation to see if simultaneous operation may have been the root cause of the delamination.

These are discussed in the following subsections.

3.5.2 Analytical Stress Calculations

To compare the wind tunnel model flap to results from the flatwise tension tests, the applied normal stresses attributable to the SMA wires needed to be determined. Since the wires were slipped through the facesheets as shown in Figure 3-12, the only force that the wires applied to the facesheet was a tension normal to the surface (Figure 3-22). Hence, straight-forward formulas to calculate the maximum load for a cable in tension may be used:

$$P = \frac{W}{2 \tan \theta} \Rightarrow W = P * 2 \tan \theta$$

$$W = 17.38 * 2 * \tan(-6.25^\circ) = 3.82 \text{ lb}$$

where P is the force applied by the SMA wire, W is the force normal to the core, and θ is the deflection angle (see Figure 3-22).

Spreading this load to a parabola, the following formula for the applied load (with respect to percent chord) is

$$(x - x_0)^2 = -2p(y - y_0)^2 \quad \text{where } y \text{ is the load and } x \text{ is position along the chord.}$$

Applying boundary conditions,

$$(x - 14.80)^2 = 0.0177 (y - 3.82)^2$$

Solving for y and integrating the curve to find the total applied load gives

$$y = -56.5x^2 + 1672.3x - 12371.3 \quad \text{where } y \text{ is the load normal to the surface at any point along the chord cross-section, and } A \text{ is the total applied load.}$$

$$A = \int_{14.54}^{15.06} (-56.5x^2 + 1672.3x - 12371.3) dy$$

Integrating the above equations and solving for the stress applied over the appropriate area yields a stress that is extremely close to the failure values for the facesheet orientation used:

$$\sigma = \frac{A}{l * w} * 4 = \frac{1.33 \text{ lb}}{0.52 \text{ in} * 0.40 \text{ in}} * 4 = 25.4 \text{ lb/in}^2 \quad \text{where } \sigma \text{ is the stress, and } l \text{ and } w \text{ are the dimensions of a section of facesheet (area).}$$

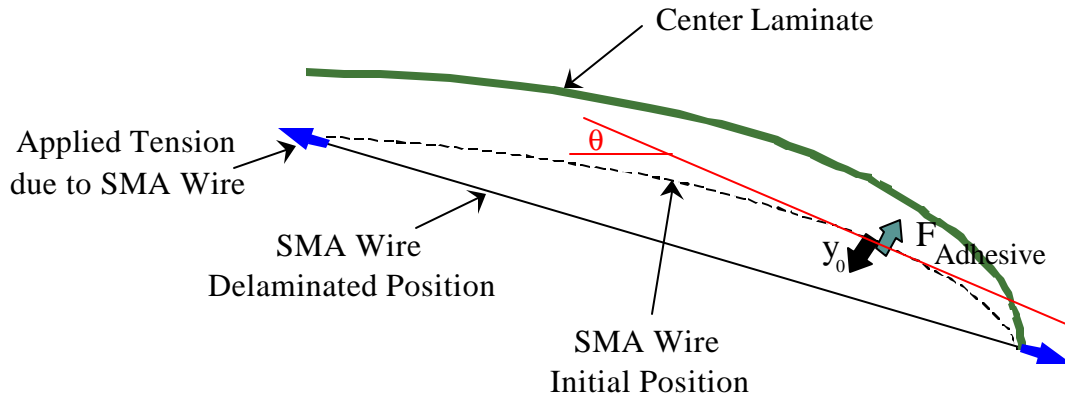


Figure 3-22. Applied Loads

3.5.3 Flatwise Tension Test and Evaluation

Flatwise tension tests were performed as per ASTM C297 to determine the effect of different facesheet orientations on the bond strength between the RTV facesheet and Hexcel Flex Core honeycomb.

The tests were carried out on 2- by 2-inch square specimens with the test grips and adhesives used for each bond joint shown in Figure 3-23. Four different facesheet arrangements were tested:

- Flat, with the facesheet on top
- Flat, with the facesheet on the bottom
- Inclined 7.5 degrees, with the facesheet on the top (Figure 3-24)
- Inclined 7.5 degrees with the facesheet on the bottom.

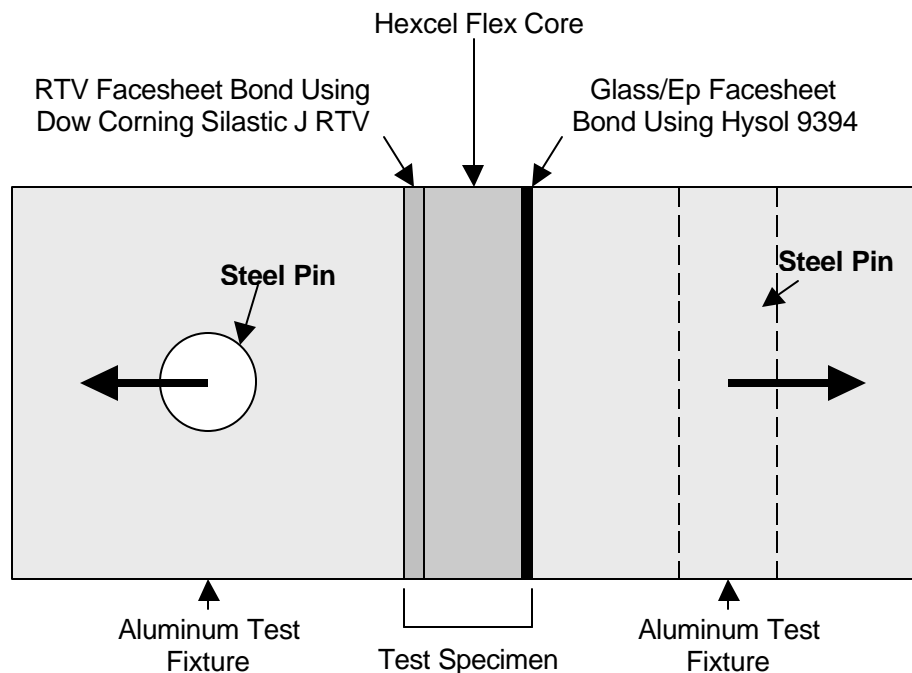


Figure 3-23. Flatwise Tension Test Setup

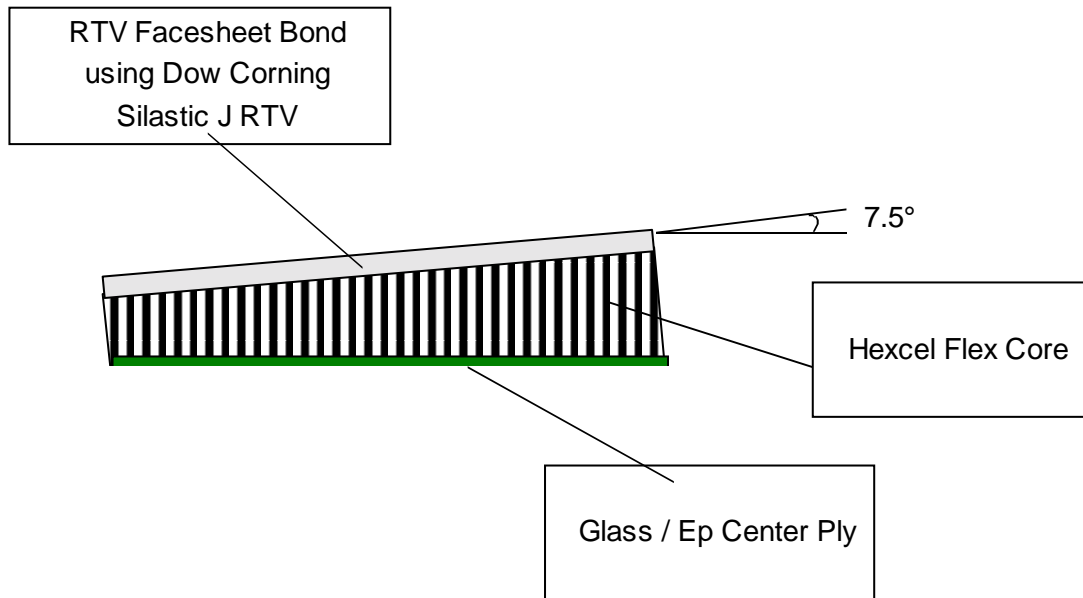


Figure 3-24. Facesheet Orientation for Smart Wing Test

The 7.5-degree angle is important because it is the taper angle for the trailing edge control surface. For each configuration the load rate was 0.05 inch/minute until the test specimens failed. The stress at failure was then calculated by dividing the applied force by the surface area of the test specimens. Figure 3-25 summarizes all the forces and loads for the four different facesheet arrangements, along with the average stress and the standard deviation. Figure 3-26 shows graphically a comparison of the average failure stresses. All of the flatwise tension results showed that the failures all occurred, as expected, at the joint between the RTV facesheet and honeycomb.

Flat Up	Force	Stress	
1	87	21.75	
2	140	35.00	
3	135	33.75	
4	115	28.75	
5	123	30.75	Std Dev
Averages	120	30.00	4.67

Flat Down	Force	Stress	
1	183	45.75	
2	157	39.25	
3	134	33.50	
4	163	40.75	
5	123	30.75	Std Dev
Averages	152	38.00	5.33

7.5° Up	Force	Stress	
1	102	25.50	
2	106	26.50	
3	104	26.00	
4	107	26.75	
5	102	25.50	Std Dev
Averages	104.2	26.05	0.51

7.5° Down	Force	Stress	
1	114	28.50	
2	129	32.25	
3	114	28.50	Std Dev
Averages	119	29.75	1.77

Analysis Results	
Applied	Stress
17.38	25.41

Figure 3-25. Flatwise Tension Test Results

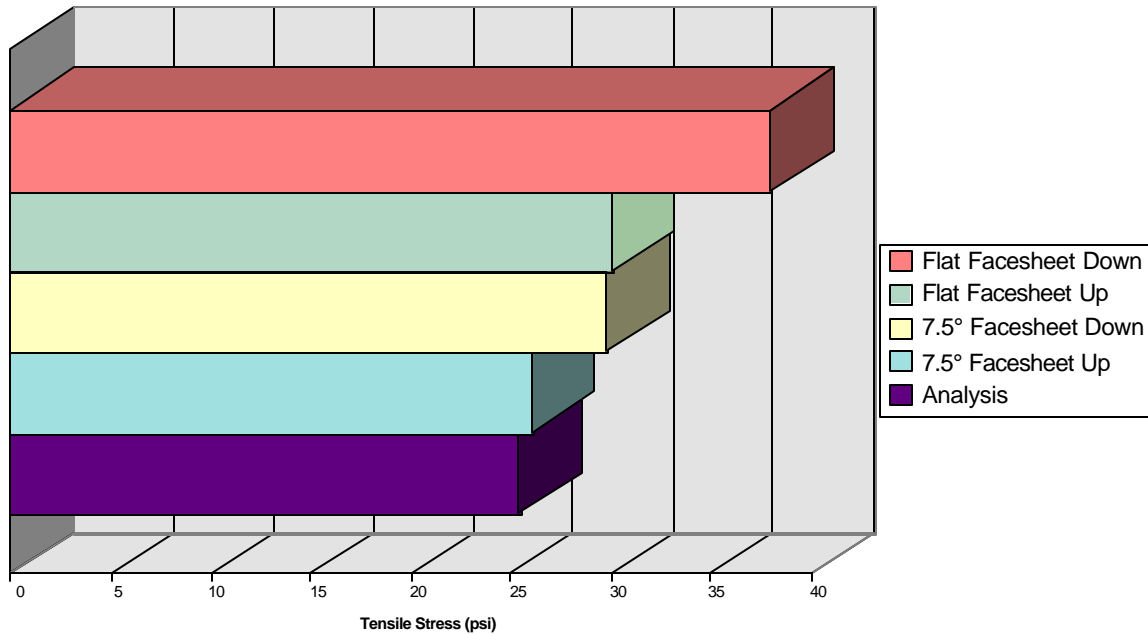


Figure 3-26. Flatwise Tension Test Results Comparison With Analytical Results

Figure 3-27 shows a photograph of the failed 7.5-degree facesheet-up specimen. A close inspection of the pieces after testing revealed some interesting conclusions:

- The RTV sealant used to bond the facesheet to the core left very little material inside the cells after failure, meaning that the failure was almost completely in the adhesive.
- Most importantly, the failure load was very dependent on the orientation of the facesheet to the core during manufacture.

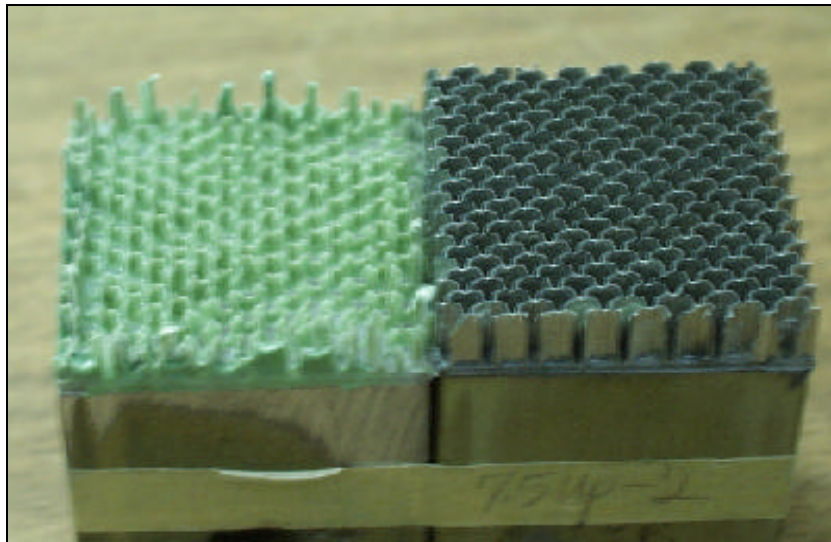


Figure 3-27. Photograph of Tested 7.5 Degrees Facesheet Specimen

In the flap and aileron used for the wind tunnel test, the facesheet was oriented so that the facesheet and core were at 7.5 degrees up. This angle, seemingly small, contributed greatly to the bond joint strength. The reason for such a large dependence of facesheet orientation to bond strength stems from cure time of the sealant/adhesive that is used to attach the facesheet to the core. Dow Corning Silastic J is a two-part, room-temperature-cure silicone rubber. It has the desired properties of adhering to both RTV and to aluminum. Unfortunately, the material is also very susceptible to contamination during the manufacturing process. Any grease, oil or surface dirt can have a strong negative effect on the curing of the compound. It also has a 24-hour room-temperature cure time. This allows the adhesive to flow after assembly and affects the shape, and thus the strength, of the fillets.

3.5.4 Simultaneous Wire Operation

Close inspection of Figure 3-28 indicates that both the upper and lower surface wires were operating at the same time and pulling the joint apart. In the figure, a large step occurs where the current is turned on to the bottom surface of the flap. A closer look reveals that the opposite surface was also being activated at the same time (albeit at a much lower power level). This would tend to compress the control surface directly back toward the aft spar and would cause the radius of curvature to become smaller, thus increasing the normal force and pull-off stress and exacerbating any failure initiation. To get around this problem, better and more consistent electrical ground needs to be maintained so that no unwanted residual current flows in the opposite side wires. Also, better electrical separation is needed across the amplifier to prevent ambiguous states (either on or off).

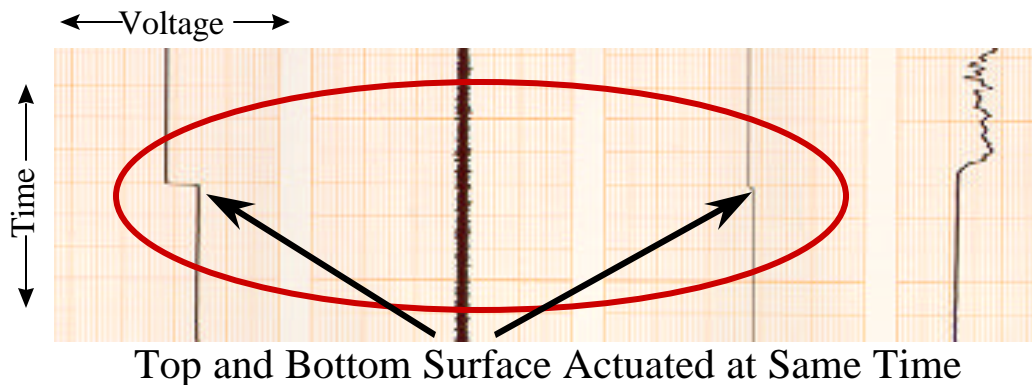


Figure 3-28. Simultaneous Wire Operation

3.5.5 Conclusions

The team's initial suspicions that the failure was partly due to a top facesheet honeycomb core joint failure exacerbated by unwanted simultaneous SMA wire activation were confirmed by subsequent test and analysis. The exact quantitative contribution of each was difficult to establish, but the manufacturing anomaly was most probably the dominant culprit. Steps to ensure that a similar failure does not occur for any follow-on work are as follows:

1. Improved manufacturing processes, especially preparation and cleaning of honeycomb, for the honeycomb-to-facesheet joint
2. Expanded search for better adhesives to bond silicone facesheet to aluminum honeycomb
3. Extensive specimen tests prior to control surface fabrication to verify joint strength
4. Curing in flat configuration to minimize adhesive creep
5. Improved control system to eliminate ambiguous states.

3.6 SUMMARY AND LESSONS LEARNED

The key program accomplishment was a first demonstration of SMA alloy application to smoothly contoured surfaces for aircraft. Considerable progress was made from program start-up to Test 1 and on through Test 2 in the design, manufacturing, and control of surfaces made using SMA wire as the actuation mechanism. For example, the core fabrication of the adaptive control surface was revised from a workable but heavy RTV silicone construction to a more aircraft-compatible aluminum material. Also, fatigue limiting aspects of the initial designs developed for Test 1 were addressed and incorporated into the Test 2 design. Among these were control of multiple sections on the control surface and improvements in the tip termination strip.

A good start was made in terms of sensor evaluation. Challenges such as linearity issues, installation, and rendition of absolute (rather than relative) sensing for use as the feedback element for hingeless control surfaces need further research. Devices such as linear potentiometers and DC linear variable displacement transducers (LVDTs), while accurate, were restricted because of the size of the model being tested.

Impressive progress was made with the SMA wire control system design. A distributed system emerged on the program and was shown to be the best solution in controlling current to a number of coupled circuit segments. The control algorithms were successfully incorporated to provide a uniform distribution and deflection of the control surfaces, and straight-forward “proportional control” at the amplifier level proved to be the correct strategy. From the SMA processing standpoint, meeting the challenge of antagonistic control with two-way memory led to improved SMA wire actuators.

4. MODEL DESIGN AND FABRICATION

An important aspect of this program was model fabrication and preparation.^{23,24} The control features (e.g., SMA torque tube and adaptive control surface) tested had to be integrated into a model suitable for the feature under investigation, and the model itself had to replicate a real aircraft (albeit scaled) as much as possible. For this program, a mid-sized attack/fighter aircraft wing was the representative planform selected for model scaling. This section highlights details of the wind tunnel model design and fabrication for both Test 1 and Test 2 under the headings:

- Wind Tunnel Model Design
 - Model Design Requirements
 - Design Process and Scaling
 - Model Loads and Layout Determination
 - Model Stress Determination and Assembly
 - Static Proof Load Testing
 - Model Dynamics Verification
- Smart Actuator Control Surface Integration
- Test Setup Instrumentation
- Accomplishments and Summary.

There were some differences between the two tests in the Smart Wing model construction attributable to control surface design evolution; however, in all other respects the models were identical for both wind tunnel entries. Key differences will be brought out as appropriate. For further details too expansive for the body of the text, prior to each test a Pre-Test Report and a Stress Report were written and are included in Volume IV. Included in these reports are detailed analysis of all load-bearing structures and other general model details such as instrumentation and test conditions.

4.1 WIND TUNNEL MODEL DESIGN

Both the Conventional and Smart Wing models were used for data comparison and possessed identical gross features in terms of wing box construction. Yet the models differed, as would be expected, significantly in terms of the method used for control surface deployment. Figure 4-1 shows a plan view photograph of the design layout, which incorporated the following top level construction features and model differences:

- Identical wing box construction: three spars, four ribs, and chem-milled (chemically milled) aluminum skins
- Spars and ribs computer numerical control (CNC) machined from steel and aluminum
- Hingeless flap and aileron and SMA torque tube actuation incorporated in Smart Model
- Electric-motor-actuated flap and bracketed aileron used in Conventional Model.

The following subsections take the reader through most of the critical elements of the wind tunnel model design development, dwelling in some detail on critical areas.

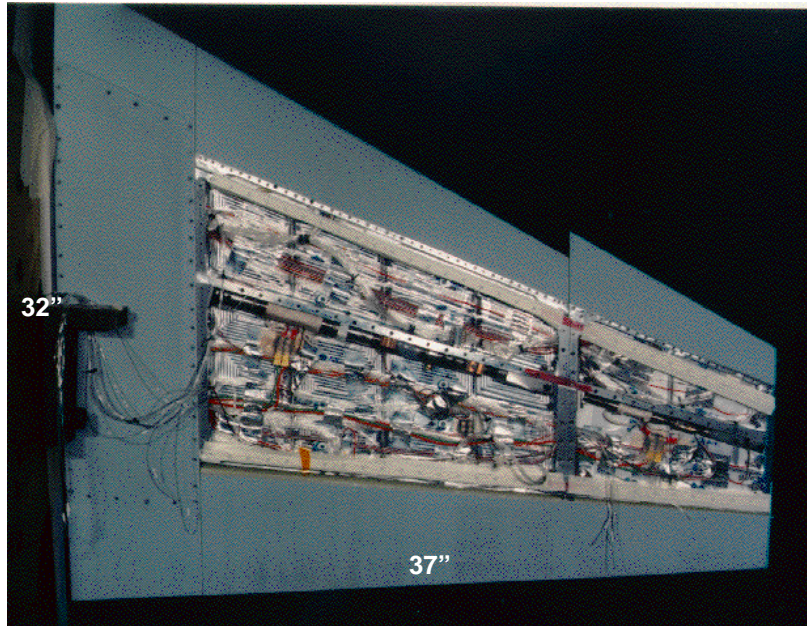


Figure 4-1. Planform View of Wind Tunnel Model With Upper Skin Removed

4.1.1 Model Design Requirements

One of the challenges facing this wind tunnel model design is the incorporation of contrasting features that are best handled by separate individual models. Two standard types of models are, specifically, (1) Force models, which are extremely stiff and inflexible, and (2) aeroelastic models, which are flexible and designed to capture dynamic characteristics. In the Smart Wing Phase 1 program, the models needed to incorporate aspects of both these types of models. For the trailing edge control surfaces, the model needed to be rigid for flap and aileron attachment, yet model flexibility was needed for the wing twist feature investigation to minimize torque requirements. Each class of model also has different construction techniques:

- Force models are typically CNC-machined from solid pieces of aluminum or steel
- Aeroelastic models typically use a single spar to simulate the scaled stiffness and are composed of lightweight foam cores with fiberglass shells to provide the required aerodynamic shape.

The smart wing model design was essentially a compromise between the foregoing conflicting requirements, and trade-offs were made to both requirement sets. Figure 4-2 provides an overview of the individual model requirements that were incorporated into the final smart wing model. For all of the wind tunnel performance measurements described in Section 5, comparisons were made between a “smart” model with the adaptive control feature (e.g., SMA flap, torque tube) and a baseline conventional model with traditional electric-motor-actuated control surfaces. These models also had to be sufficiently similar to ensure a strong basis for comparison.

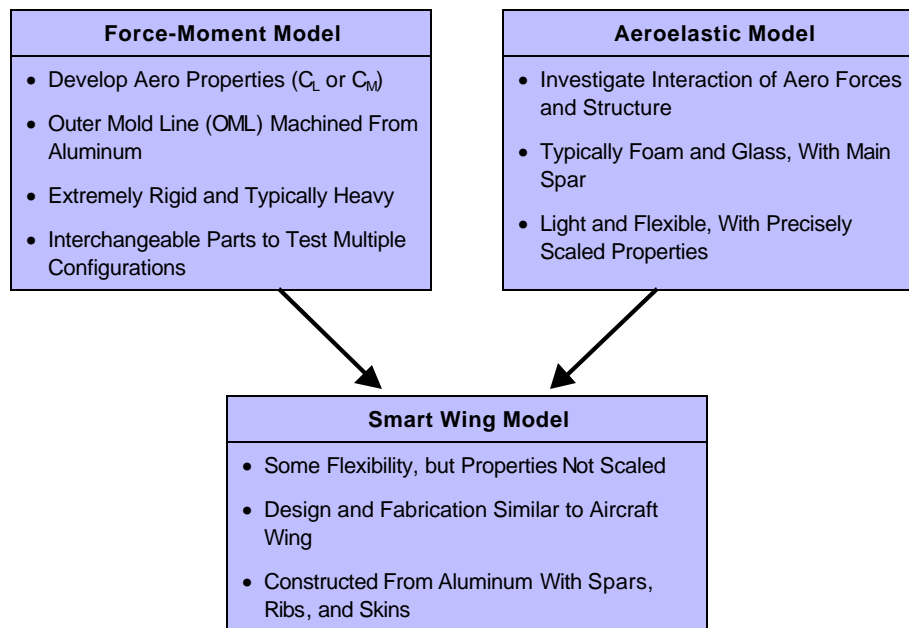


Figure 4-2. Typical Model Design Aspects

Top-level requirements in the model design were typical: the smart actuators had to be contained and tested in a wind tunnel environment, and most importantly the model and smart actuators had to complete testing with no damage to the tunnel facility or personnel. Additionally, NASA Langley Research Center, the facility provider, has its own requirements and stipulations:

- Factor of safety (FS) of four on all parts
- Dynamic pressure at which wing divergence occurs must be greater than two times the maximum test dynamic pressure (where dynamic pressure is defined as $\frac{1}{2} \rho v^2$; ρ is the density of the fluid and v is the fluid velocity)
- Dynamic pressure at which flutter occurs must be greater than two times maximum test dynamic pressure.

The above, and other requirements, are set out in the NASA LaRC “Wind Tunnel Model Systems Criteria” document.²⁵

4.1.2 Design Process and Scaling

The wind tunnel design process was conducted in parallel analytical and hardware development paths as indicated in Figure 4-3. The analytical effort began with ensuring flutter-free conditions and incorporating the applicable scaling in developing preliminary analytical models. However, the analytical modeling became more sophisticated from preliminary to detailed design; the effects of stiffness distribution and initial strength flutter dynamics were incorporated at first while finite element and dynamics analysis took on a more sophisticated role with program maturity. Specific component effects were also added as the analytical model developed. On the hardware track, static proof loading was first performed on a component-level basis, until the model hardware integration program phase, during which complete static and ground vibration and proof testing was conducted. It is important to note that several iterations between analysis and test took place before final model design freeze. The model instrumentation and test plan were

also portions of this design process since the test objectives and the sensors needed to achieve this objective were integral components of the model and the smart actuators systems.

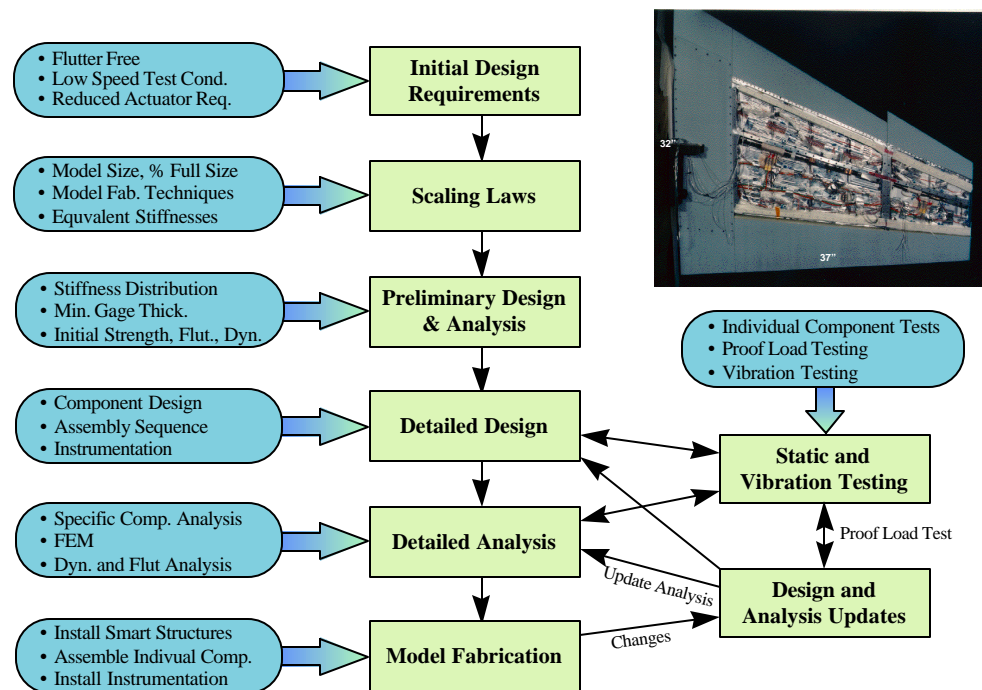


Figure 4-3. Model Design Process

From a smart technology perspective, the model needed to be small enough to minimize actuator force demands yet improved in scale and sophistication by an order of magnitude from tests conducted in the laboratory (university or industrial) prior to the program. Collaboration among NGC, Lockheed Martin, and NASA LaRC team members first analytically developed section lift and moment distributions. This was assessed using lift and pitch trim analysis methods in ASTROS. This analysis gave a pitch trim angle of attack (AOA) of 8.6 degrees for a load factor, N_z , of 2 and provided a preliminary testing range.

Using length and velocity, standard scaling laws were used to size the remaining critical characteristics of the model.²⁶ Other key calculations and assessments in the wind tunnel model design process will emerge in the following section.

4.1.3 Model Loads and Layout Determination

The compromise between rigidity and flexibility requirements and the construction material type drove the model stiffness. After the scale determination, initial trim loads were developed using aluminum minimum gage thicknesses, which were 0.020 inch and 0.030 inch for the skins and spar webs, respectively. However, the spar caps were required to accommodate rivetless nut plates for skin attach fasteners and had to be much thicker at 0.050 inch. For this exercise a panel aerodynamic plate model was superimposed on the structural finite element model, and trim loads were developed for a load factor of 2g. The internal loads from this condition showed that the minimum gage thickness was more than adequate to meet the safety factor requirements. Using the FEM with these minimum gage thicknesses, the requisite torque for 5 degrees of spanwise twist was determined. The overriding design factor in determining the use of minimum gage for the components was driven by the torque tube actuation requirement. The torque available from the SMA material, though state-of-the-art for the technology, was still limited for

wing design. Hence, with the load conditions previously described, the minimum gage was used for all components, and appropriate thicknesses were incorporated into the FEM to compute the deformations under air loads and torque tube control. Most importantly, from a safety standpoint, the static strength, divergence, and flutter instabilities were investigated.

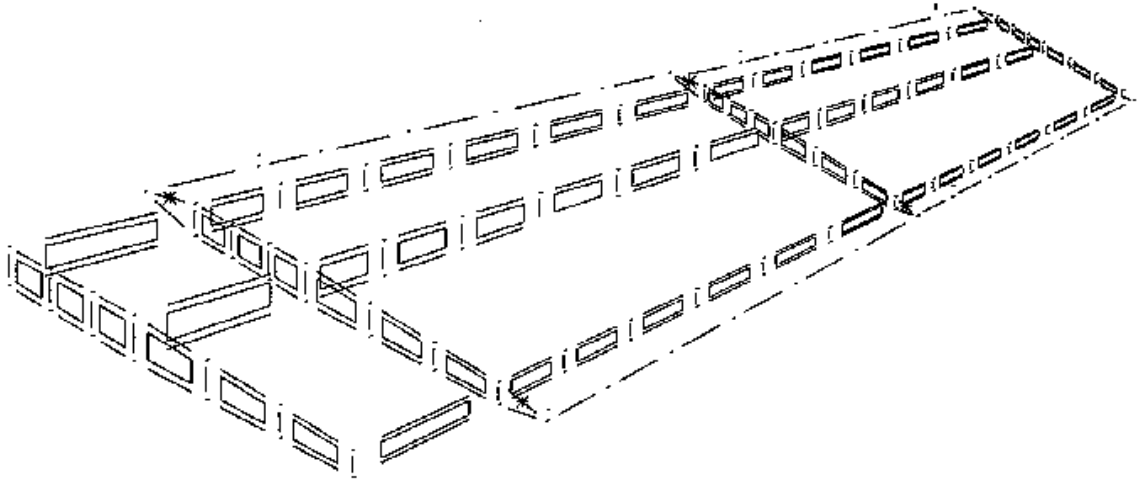


Figure 4-4. Wind Tunnel Model Internal Structure

At this point in the discussion it is appropriate to revisit the top-level model description provided in the section lead-in, expanding on component installation details. Figure 4-1 previously provided a plan view photograph of the component layout; however, Figure 4-4 provides a more detailed drawing showing the spars and ribs. The model component features in more depth are:

- Three continuous, spanwise spars machined from aluminum (0.030 in. web, 0.050 in. cap). The spars were CNC machined from UniGraphics (UG) files and provided the framework for the model.
- Four ribs, also CNC machined, composed of both steel and aluminum (two inboard from aluminum, two outboard from steel). The rib composition was dependent on size and thickness constraints. In outboard sections, tapped holes were used since there was insufficient space for inserts and aluminum does not hold threads well.
- Skins on the inboard section were constructed of glass/epoxy (0.150 inch thick) material. Glass/epoxy was used for convenience, opting for a simple mold and composite lay-up process in preference to a solid model approach that would have entailed complex tools and machinery.
- Skins on outboard section were aluminum (0.020 to 0.035 inch thick). Original attempts to employ a chem-mill process to manufacture the skin were thwarted because of tight tolerances so the fallback position of CNC machining was used.

- The conventional model used an electric Globe motor-driven flap and bracketed aileron to obtain settings. No “tunnel interruption for resetting” was necessary for the motor-driven flap. However, since size restrictions precluded motor actuation, the fallback variable bracket setting method was used for the aileron.
- The Smart Wing model contained the SMA torque tube discussed in Section 2 and the hingeless SMA actuated control surfaces described in Section 3.

With the foregoing level of model definition that included initial sizing performed for the skin thicknesses, spar cap depths, and spar web thicknesses, a more detailed FEM was developed. Figure 4-5 shows a planform view of the FEM. The model contained 369 grid points with over 4,000 degrees of freedom (DOF) and included over 1,000 elements (CQUAD4s, CBARs, CRODs, CTRIAs, and CONMs). Note: the SMA torque tube was modeled for its weight and stiffness contribution but not as an actuator, owing to the complexity and lack of reliable mathematical models (at the time of model development and fabrication) for SMA torque tube behavior. The applied torque from the SMA tube was simulated, however, using moments and force couples.

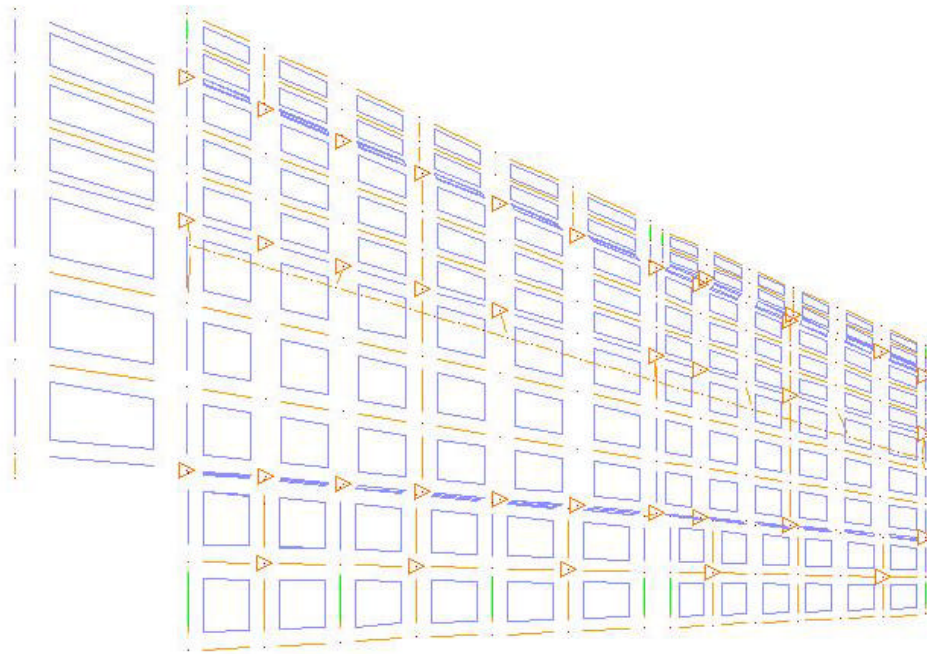


Figure 4-5. Planform View of Finite Element Model

Steady air loads were obtained using the USSAERO analytical tool in ASTROS.²⁷ Using all of the foregoing analytical tools, aeroelastically corrected air load distributions were predicted, together with the important displacements and stresses in all the relevant model structural components and members. Figure 4-6 through Figure 4-8 show a selection of the key outputs from the analysis. Figure 4-6 displays the pressure distribution across the wing as predicted by ASTROS (note the higher values in the leading edge area). Figure 4-7 shows the maximum individual forces and moments that the model exerted at the balance face. These maximums were derived from running a trim solution where the lift was equated with the scaled weight for a 2g maneuver at various dynamic pressures and control surface settings.

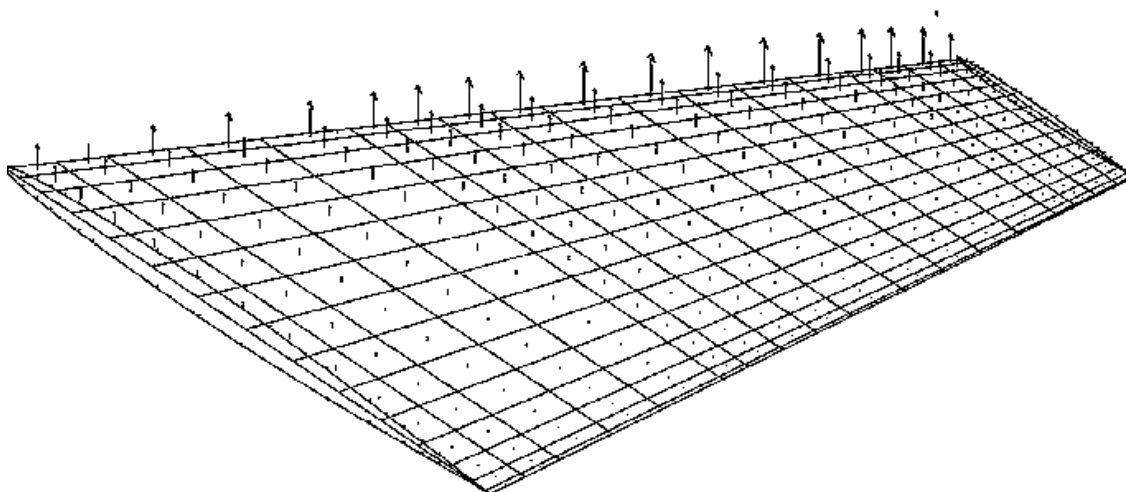


Figure 4-6. Pressure Distribution for the Wind Tunnel Model From ASTROS Trim Analysis

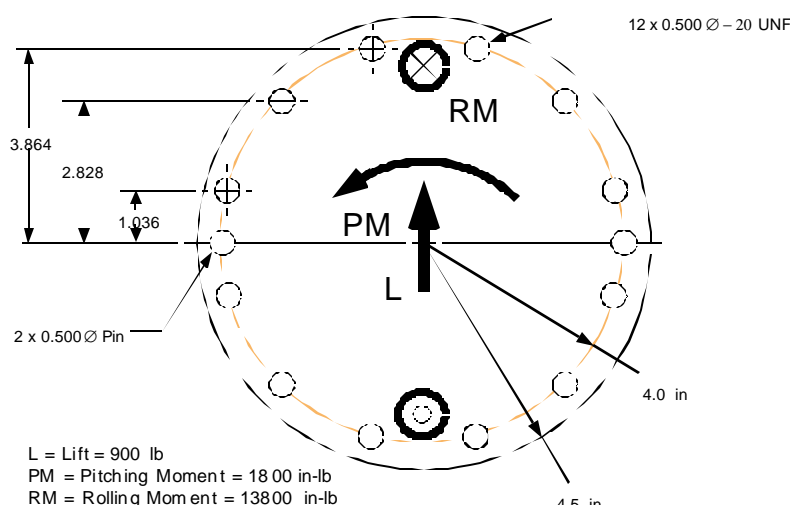


Figure 4-7. Maximum Individual Loads at Balance Face for Test 2

4.1.4 Model Stress Determination and Assembly

The FEM was also important for determining the critical areas for the model in terms of strength. Figure 4-8 shows the analytically predicted stresses for the combined air load and torque-tube-applied torsion load in the CQUAD4 elements that made up the skins. The stress levels were quite low, < 7,000 psi, but due to some large unsupported wing sections (11 by 5 inches), panel buckling became the critical condition for the skins and the dominant failure mode. To keep the skins from buckling, integral stiffeners were machined into the skins that provided the necessary stiffness, as mentioned earlier in this section. Other than the skin buckling, the stresses in the other regions were quite low, and the minimum gage was more than sufficient to meet the overall factor of four safety requirement.^{28,29}

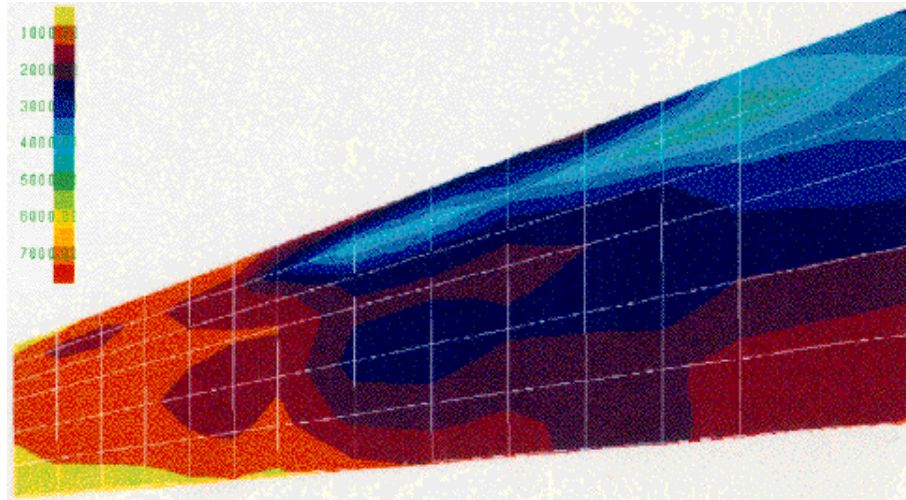


Figure 4-8. Transverse Stress (s_{xy}) for Lower Wing Skin

In practice, much of the preceding stress determination and part design took place iteratively. In fact, many changes and updates took place too quickly for management configuration to keep pace with the model changes and drawings until the final model assembly.

As the design progressed, a model assembly sequence was developed. The sequence was as follows:

1. Bulkhead at Y= 0.00
2. Three spars
3. Ribs and corner brackets
4. Lower skin panels
5. Torque tube assemblies
6. Drive trains, flaps and aileron
7. Inboard root section fiberglass skin
8. Attach leading edge control surfaces
9. Attach upper skin panels.

By using the above assembly sequence, a heavy, complex tool was not required to keep the models in rig when the upper skins were removed. This aided not only in simplifying the process of doing work in the wind tunnel test section by precluding the need for setting up tooling there but also helped ensure that the smart and conventional models were as identical as possible by creating a process that could be followed for both models.

4.1.5 Static Proof Load Testing

After model assembly, two static tests and one dynamic laboratory (non-wind-tunnel) test were performed to verify the analysis and design. These were (1) static proof load tests, (2) SMA torque tube actuation tests, and (3) a ground vibration test (GVT). With regard to the static load testing, there were two different tests necessary to validate the model wing box performance. First, it was necessary to verify that the analytically predicted strains and deflections for the entire model were correct. Second, proof loading of the smart control surfaces needed to substantiate that there would be no residual, or unwanted, deflections during the applied air loads where the surfaces needed to maintain a neutral position. For load test for the model itself, sand bags were used to simulate the applied air loads, and Figure 4-9 shows the locations where the sand bags were applied. Over 800 pounds of sand in 96 bags of varying weight composition were prepared and arranged to simulate the expected forces and moments (i.e., lift, and the pitching and rolling moments). Dial extensometers were used to measure deflection, and strain values were read from gages installed on all spars. The values matched well with the FEM results.

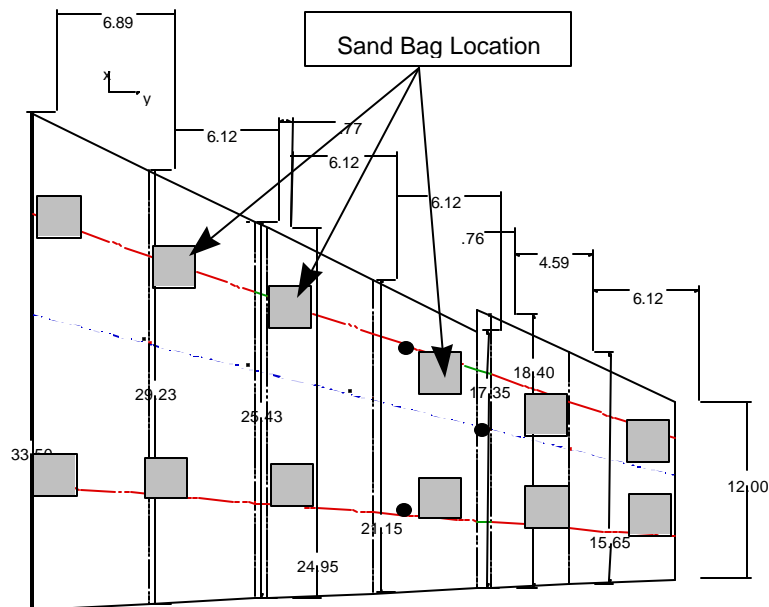


Figure 4-9. Sand Bag Locations for Proof Load Test

Also required before the wind tunnel testing were proof tests on the control surfaces. Aside from the no-load deflection issue discussed above, the strength of the control-surface-to-wing-box joint for the loaded condition, as well as the overall control surface stiffness, needed to be validated. Figure 4-10 shows a photograph of the model installed in the test section with twice the nominal air loads applied on the SMA flap. In the case of the flap and aileron smart control surfaces, a degree of extra caution was exercised in proof testing prior to performing wind tunnel runs because of the unknown and “exotic” nature of the SMA material.

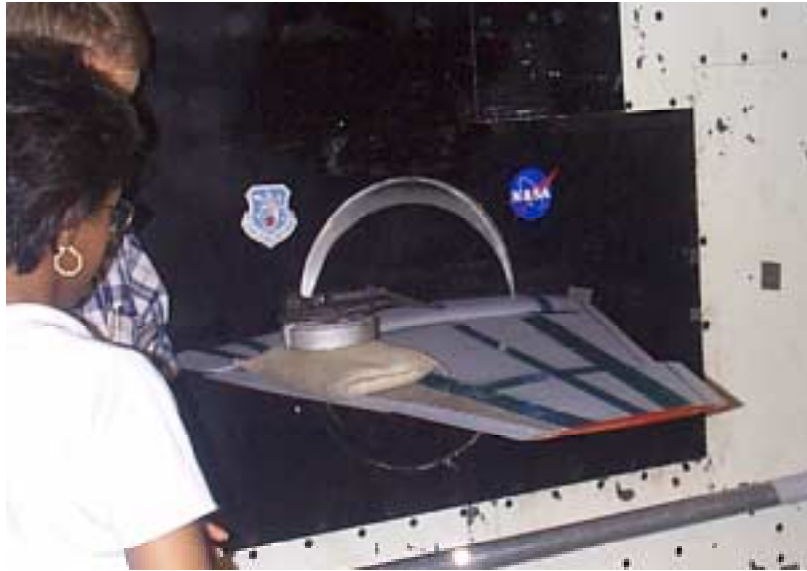


Figure 4-10. Proof Load Test of SMA Flap Prior to Test 2

Proof testing of the torque tube control component and ground tests to verify the finite element modeling were also performed. Some of the torque tube proof testing and evaluation has already been covered in Section 2, but other validation efforts were performed after the first wind tunnel entry (Test 1). Tests were run to confirm that the FEM matched the wind tunnel model's measured twist under load. Figure 4-11 shows that the measured twist and FE twist due to specific loads did in fact match very closely.

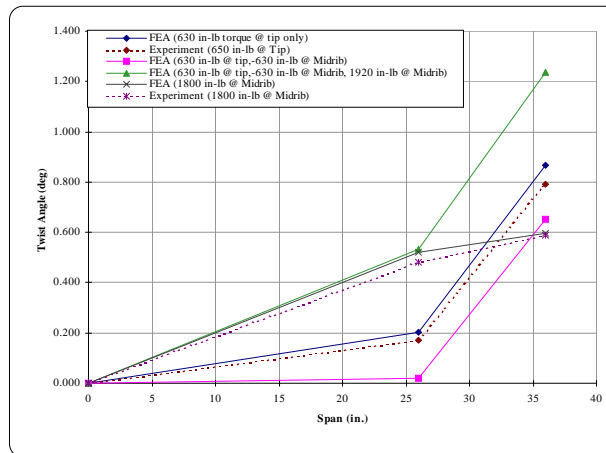


Figure 4-11. Comparison of Measured and Predicted Twist Angle for Various Loading Conditions

4.1.6 Model Dynamics Verification

The final model verification static test performed before wind tunnel measurements was the GVT. Briefly, a GVT is typically performed by placing an array of accelerometers on the wing to record the model response to random, broadband structural excitation supplied by an electric shaker. The accelerometer output frequency responses are processed to determine the excitation forces that drive the model to its first natural frequencies and fundamental mode shapes. The GVT was a mandatory NASA requirement, but it is a common practice for model integrity

checks and analysis validation that has become an indispensable tool for designing models and predicting wind tunnel model behavior. Figure 4-12 shows the accelerometer locations for Test 2, which were nearly identical to Test 1 except for numbering convention on the accelerometers.

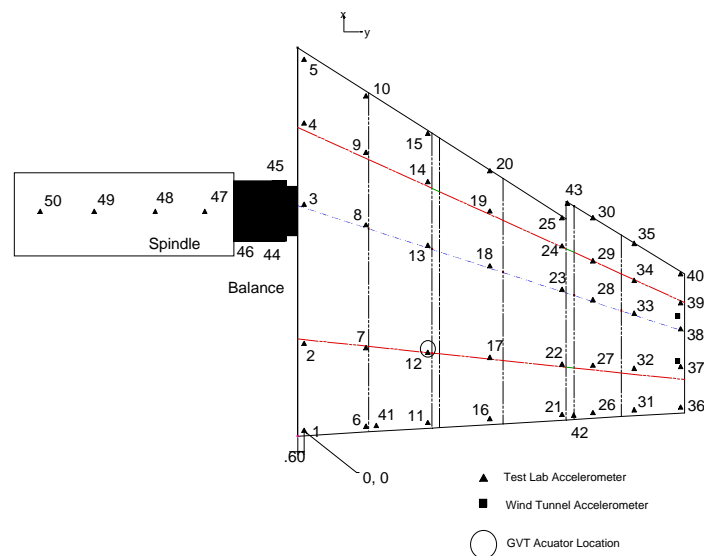


Figure 4-12. Accelerometer Locations for Test 2 Ground Vibration Test

Figure 4-13 shows a summary of the Smart Wing results for frequency versus dynamic pressure from Test 2. As the tables show, the frequencies correlate well (within 4 percent) for the first three modes, which are the critical modes for the model. Figure 4-14 shows how the frequency varies with dynamic pressure. These curves are important because they demonstrate that the frequency is stable throughout the dynamic pressure range where the Smart Wing Phase 1 models were tested. This stability is a key characteristic in assessing flutter and divergence.

Mode	Frequency (Hz)	Damping (%)	Shape
1	26.4	No Damping	1 st Bending
2	77.7	Assumed	1 st Torsion
3	106.0	in	2 nd Bending
4	156.8	Analysis	2 nd Torsion

ASTROS Analysis

Mode	Frequency (Hz)	Damping (%)	Shape
1	15.3	0.71	Spindle
2	27.6	0.71	1 st Bending
3	74.0	2.1	1 st Torsion
4	93.7	2.6	Control Surface
5	106.0	1.98	Control Surface
6	118.6	1.4	2 nd Bending

NASA Ground Vibration Test

Figure 4-13. Table of Results From Analysis and NASA-Performed Ground Vibration Test

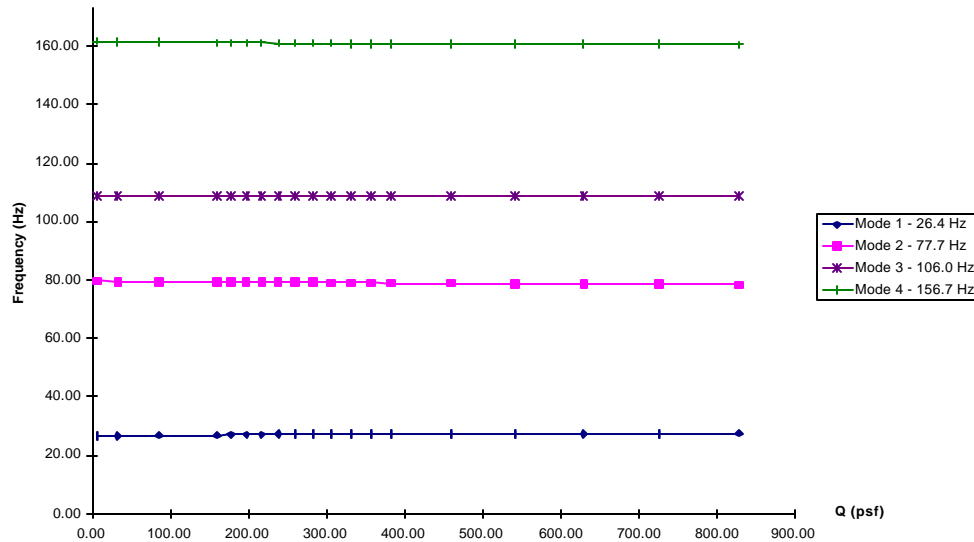


Figure 4-14. Frequency Response of Smart Wing Model

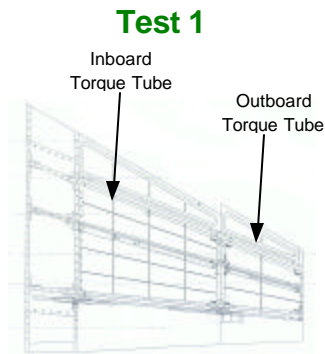
4.2 SMART ACTUATOR CONTROL SURFACE INTEGRATION

A vital consideration for the whole program was how the smart actuator components would integrate into a model that would replicate a real aircraft design as closely as possible. The model, designed with a wing box constructed using realistic spar and rib placement and stressed skins, did in many respects represent a real aircraft, making the lessons learned in the integration process all the more valuable. This section highlights some of the important integration issues.

4.2.1 SMA Torque Tube Model Integration

The torque tube, while relatively straight-forward in design and operation, had complexities beyond the attachment of the SMA material to the transmission rod discussed in Section 2. There were design revisions from a dual tube arrangement to a single tube configuration as discussed elsewhere, and important features and results of the two designs in both of the wind tunnel tests are summarized in Figure 4-15.

The overriding design challenge was that the torque had to be transmitted to the wing box structure with as little loss as possible. This was a design challenge because the internal height requirements limited the available sizes of the transmission rods. In Test 1, a circular cross-section rod could be employed to transmit the torque because each tube extended to only half the wing span and the torque values were lower. In Test 2, on the other hand, with over 3,000 in-lb of torque having to be transmitted in limited space, a flattened ellipse was designed. Subsection 2.4 expands on this description and includes a figure that shows a line drawing of the Test 2 torque transmission rod.^{30,31}



- Two SMA Torque Tubes
- Inboard – 1" Dia, 2,000 in-lb Torque
- Outboard – 0.5" Dia, 600 in-lb Torque
- Nicrome Wire Heater
- 1.25° Spanwise Twist Measured
- Twist Measurement Using NASA/LaRC video Model Deformation System

Test 2
SMA Torque Tube Shown in Test Rig



- One SMA Torque Tube
- TT – 1.25" Dia, 0.060" Wall Thickness, 3,600 in-lb Output Torque
- Nicrome Wire Heater
- 5° Spanwise Twist Measured
- Electrolytic Tilt Sensor, MEMS Sensor, and NASA LaRC Video Model Deformation System

Figure 4-15. Summary of Improvements Made to SMA Torque From Test 1 To Test 2

In meeting NASA's safety requirements for all models using the TDT facility, Figure 4-16 delineates the anticipated consequences for key failure modes. The rationale behind the list compilation was to make absolutely certain that there would be no real safety impact should any of the state-of-the-art control surface hardware exhibit unexpected failures.

TORQUE TUBE FAILURE MODE	CONSEQUENCES AND SAFETY FEATURES
SMA Torque Tube Buckles	Lose Applied Torque
Software "Runs Away" and Applies Too Much Current	SMA Tube Overheats, Re-anneals and Loses Torque
Mesh Gear Slips	Lose Applied Torque
Connection from Transmission Rod to Wing Box Fails	Lose Applied Torque, Main Wing Box Structure Unaffected

Figure 4-16. Torque Tube Failure Modes, Consequences, and Safety Features

The TDT facility maintains a power shut-off for protecting personnel, equipment, models, and the tunnel. The relatively large electrical power requirements (a maximum power of 400 watts for SMA torque tube and 600 watts for the SMA flap and aileron) also necessitated care in handling staff access to the tunnel as well as power-on restrictions.

4.2.2 SMA Flap and Aileron Model Integration

The SMA flap and aileron had very different design integration and attachment philosophies than those used for the SMA torque tube. Whereas the torque tube required essentially one large connection transferring all the load at one point, the SMA flap and aileron attachments were distributed connections using many fasteners to share the control surface and air loads.

As described in Section 3, the control surfaces were attached to the wing box via the termination strip. This attachment was accomplished using 0.112-inch-diameter fasteners through the skin into Keen and Helicoil inserts set in the Torlon®. Attaching the control surface through the skin was successful but was not the first concept investigated. Also discussed elsewhere, the initial goal was to install streamwise posts that would go through the wing rear spar and allow the control surfaces to be readily replaceable and removable. This was not possible because of model space limitations, which would not allow sufficient post size to achieve a connection with the requisite safety factor. Revisiting some of these concepts for improved maintainability and repairability (always key players in the life cycle cost reduction arena) would be a worthwhile activity on a future program.

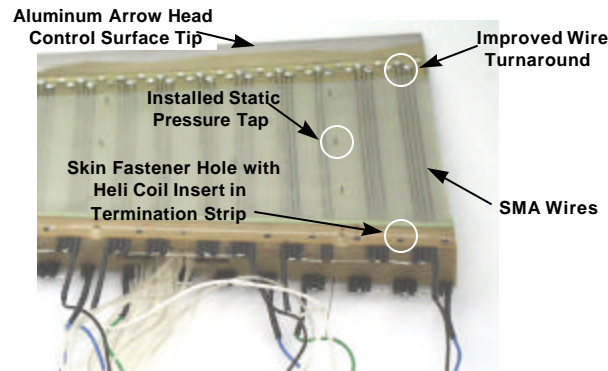


Figure 4-17. SMA Flap Connection Details

Figure 4-17 shows some of the attachment details of the trailing edge flap. It should also be emphasized that the flap and aileron had to be electrically isolated from the supporting structural framework (model spars and skins) and from any of the sensors that were needed for position monitoring, which adds a further degree of complexity as already described in Section 3. Figure 4-18 highlights some of the essential differences in the SMA trailing edge control surface improvements between the two scheduled wind tunnel tests, and most of them have been covered elsewhere. From a test monitoring perspective, a key difference was in the replacement of the fiber-optic and foil gages with a more reliable linear potentiometer method, as described in Subsection 3.4, but the fiber-optic approach should be retained for future programs.

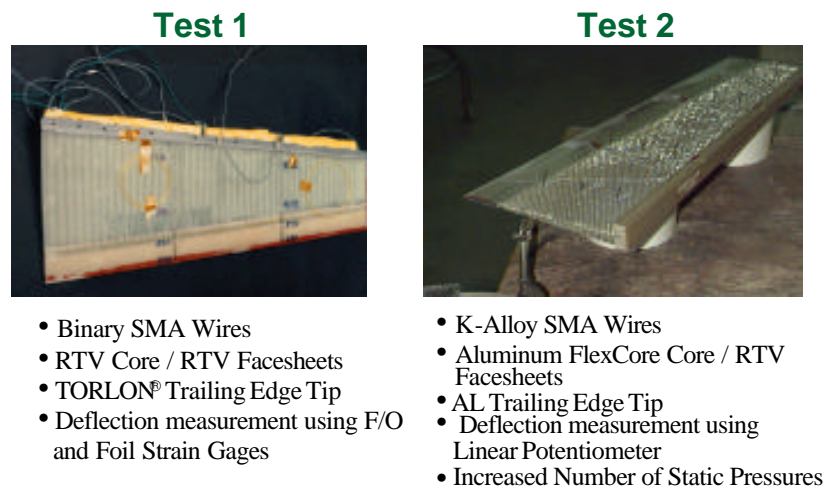


Figure 4-18. Trailing Edge Control Surface Improvements From Test 1 To Test 2

As with the torque tube, NASA required a failure analysis to be performed for all foreseeable contingencies. The results are depicted in Figure 4-19.

SMA FLAP AND AILERON FAILURE MODES	CONSEQUENCES AND SAFETY FEATURES
Control Room Computer Fails	No Input Condition to Flap- and Aileron-Zero Current
Power Supplies Overrun	Current to Control Surface Shut Off, Power Supplies Have Current Limiter Set at 2x Operation Value
One Side of Power Amp Fails (Creating Short Circuit)	Current to Control Surface Shut Off, Power Supplies Have Current Limiter Set at 2x Operation Value
Control Potentiometer Reads Incorrectly	Current to Control Surface Shut Off, Power Supplies Have Current Limiter Set at 2x Operation Value
Control Surface Grounded	Current to Control Surface Shut Off, Power Supplies Have Current Limiter Set at 2x Operation Value

Figure 4-19. Torque Tube Failure Safety Issues and Consequences

4.3 TEST SETUP INSTRUMENTATION

This section provides a snapshot of the wealth of instrumentation that is required to support a state-of-the-art investigation such as a research program of this kind. Much of the hardware instrumentation highlighted in this section had to be brought to the scene of the investigation by team members, specifically Northrop Grumman, Lockheed Martin, Fiber and Sensors, and Mission Research. In addition, there is all of the resident instrumentation provided by the wind tunnel facility itself, which is overviewed in Subsection 5.2.3.

Figure 4-20 shows a functional block diagram of the wind tunnel setup with the host of instrumentation supporting the wind tunnel activity. The “MODCOMP patch panel” (Figure 4-20), located on the model side of the tunnel east wall, was the main interface between the Smart Wing model and the NASA tunnel facility control room. The instrumentation included individual tilt sensors, accelerometers, linear potentiometers, feedback power amplifiers, strain gages, fiber-optic sensors, thermocouples, and other devices, all of which provided information on (1) the aerodynamic state of the models under test or (2) provided feedback or information on the smart actuator performance. Standard 120V AC power was provided by the facility, but any special-purpose power, such as the supplies used to power the SMA control surfaces, had to be brought in by the various team members as indicated in the figure. Further details of the east-wall MODCOMP channels are listed in the figure.

4.4 ACCOMPLISHMENTS AND SUMMARY

In terms of the first order of business, namely to design, build, and test a 16 percent scale model of a fighter attack aircraft wing, the program objective was achieved. The critical elements of the design process were: scaling and loads determination, model strength design and analysis, dynamic analysis and hardware check-out (GVT), instrumentation, and most importantly, integration of the smart actuator control surfaces.

It should also be pointed out that an appropriate (and intensive) level of instrumentation for monitoring the wing model was configured into the test setup, and that the data was accurately recorded, establishing the program's aerodynamic benefits. In addition, all of NASA's and other "best practice" wind tunnel safety standards were met. While loss of a key component of the smart actuators was disappointing, the safety of the test facility and model was never compromised.

From a model design perspective, the crowning achievement was the team's ability to integrate the state-of-the-art SMA material in two separate applications for control surface deployment in a realistic aircraft wing structure, solving all the problems on the way. While the difficulty of efficiently transferring torque from the SMA tube to the wing box did pose problems, these were solved by finding suitable attachment methods. For the SMA wire control surfaces, difficulty of attachment and electrical isolation with the limited size and safety constraints was considerable. Smart actuator scale-up (and -down) issues were addressed, and the difficulties of applying electrical power to effect and control surface movement, coupled with appropriate thermal management schemes, were nontrivial challenges for a wind tunnel test setup environment.

5. WIND TUNNEL TEST RESULTS

This section describes details of the wind tunnel testing and compares results for conventional and smart wing configurations for each adaptive (smart) wing feature.^{32,33} The specific adaptive concepts investigated in the Smart Wing Phase 1 program involved actuation of the flap and aileron, wing twist, and combined effects. Two wind tunnel models were tested in the NASA Langley Research Center's (LaRC) Transonic Dynamics Tunnel (TDT) facility on two separate occasions during the program at different levels of adaptive concept technology maturity. One model was a baseline conventional wing, utilizing standard hinged trailing edge control surfaces, and the other model was the smart wing incorporating hingeless contoured control surfaces and distributed fiber-optic sensors (Test 1 only) to monitor aerodynamic pressure.³⁴ Taking full advantage of the 16-foot TDT in the early and latter phases of the program, NGC coordinated with its NASA counterparts to schedule two tests for maximum risk reduction:

- **Test 1:** First demonstration of smart wing – validating aerodynamic benefits for a preliminary proof of concept, performed in May 1996
- **Test 2:** Second iteration of integrated smart wing concept demonstration – quantifying aerodynamic benefits and establishing technology integration payoffs/issues, performed in June 1998.

Figure 5-1 provides a summary of all of the aerodynamic improvements for the single effects of flap, aileron, and wing twist and the combined effects of flap with aileron and wing twist with aileron. For each configuration the deflection or twist is listed in degrees, and the aerodynamic lift and roll improvements are tabulated both in absolute and percentage terms. As a general comment it can be seen that percentage improvements of the smart technology approached or exceeded 10 percent for the single effects and ranged between 15 and 17 percent for combined effects. It should be pointed out that percentages are relative to a “safe maneuver” of 8 degrees AOA, 2g turn force, and a dynamic pressure of 90 pounds per square foot (psf) (~190 mph). Delineating percentage improvements as a measure of merit at the extremities of AOA for either cruise or high-g maneuver is not always useful or credible.

In more tangible practical terms, a 10 percent improvement in the lift and roll performances afforded by the smart technology would translate to:

- A 2,000 pound increase in takeoff gross weight (TOGW) for a typical 40,000-pound fighter/attack aircraft
- An increase in steady rolling rate from 120 degrees/second to 132 degrees/second for the equivalent conventional and contoured aileron deflection.

The Test 2 flap results (due to the failure) are an obvious table entry omission from Figure 5-1. The absence of any real flap data in Test 2 precluded a direct comparison between wind tunnel entries for this particular function; however, in all other respects Test 2 gave encouraging results and moved the technology further forward.

Configuration	Deflection or Wing Twist (deg)	Lift DC_L	Roll DC_ℓ	% Improvements	
				Lift	Roll
Flap Only (Test 1)	7.5	0.0581	0.0193	9.7	10.2
Flap and Aileron Combined (Test 1)	7.5	0.0916	0.0387	17.6	17.1
Aileron Only (Test 1)	5.0		0.0150		8.0
Aileron Only (Test 2)	10.0		0.0189		10.5
Wing Twist at Tip (Test 2)	3.0	0.0344	0.0193	8.0	10.0
	5.0	0.0502	0.0296	11.5	15.6
Wing Twist at Tip (Test 1)	1.4	0.0406	0.0218	10.0	12.8
Combined Aileron and Wing Twist (Test 2)	+ 10.0	0.0567	0.0310	15.3	17.3
	+ 4.5				

Figure 5-1. Summary of Aerodynamic Performance Improvements

The remainder of the section revisits the wind tunnel testing overview and goals and details further specifics of the testing effort under the following topics:

- Test program overview and goals
- Test configuration and setup
- Test results structured into (1) baseline repeatability, (2) wing twist, (3) flap, (4) aileron performance, (5) wing twist and aileron, and (6) flap and aileron
- Summary and conclusions.

Key wind tunnel test results only are discussed in this section. For a more complete account of all the Phase 1 wind tunnel testing, the reader may consult Volumes III and IV, “Wind Tunnel Test Results” and “Pre-Test and Stress Reports,” respectively.

5.1 TEST PROGRAM OVERVIEW AND GOALS

It is appropriate to restate the program goals, which were to demonstrate the use of smart materials to improve on the aerodynamic qualities of conventional wings. Specifically, this came down to demonstrating the use of SMA material to replace conventional actuator mechanisms (e.g., hydraulic) for control surface movement and to demonstrate that SMAs also have applications for wing twist. Wind tunnel measurements with scaled models (16 percent full-scale F/A-18) provided test beds for concept evaluation and enabled a close representation of real operational flight conditions. Figure 5-2 highlights the basic configuration differences between the conventional and smart models tested.

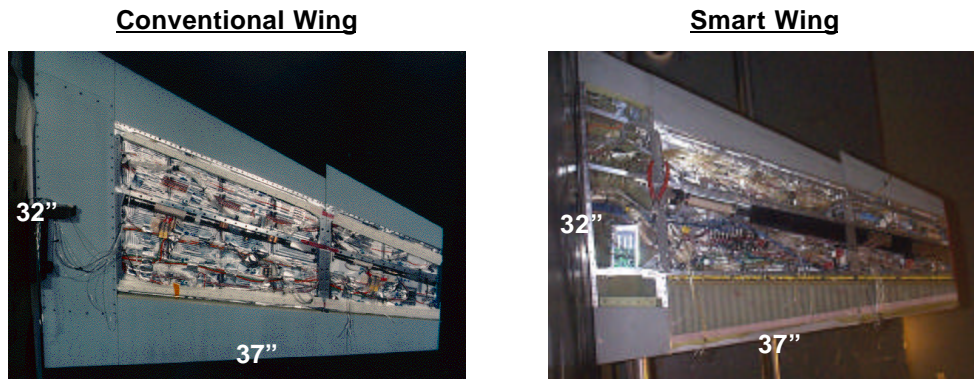


Figure 5-2. Conventional and Smart Wind Tunnel Models

The critical aerodynamic wing parameters tested and quantified were (1) lift for takeoff and landing configurations and (2) low-speed maneuver benefits in terms of increased roll effectiveness and pitching moment. As discussed previously, aerodynamic improvement derives from a smoothly contoured control surface deployment as illustrated in Figure 5-3. The aerodynamic flow pressure distribution is improved by delayed trailing edge flow separation and a generally distributed increased upper wing surface suction. Both effects result in superior flying qualities in terms of:

- Increased lift and reduced drag
- Improved pitching and rolling moment.

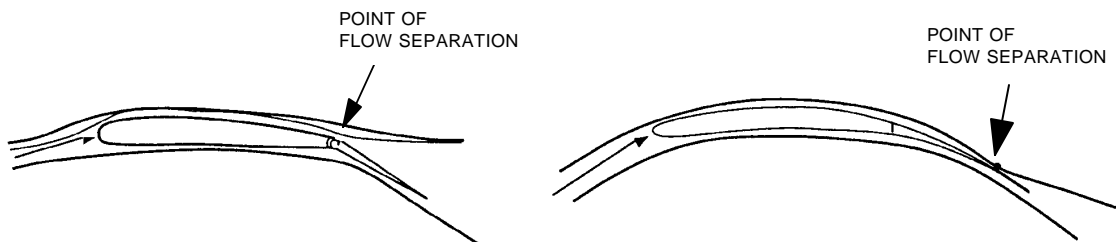


Figure 5-3. Contoured Control Surface Concept

Test 1 represented a significant breakthrough in the technology. SMA actuated surfaces were integrated into a smart technology wing and compared with conventional methods for the first time under experimentally controlled flight conditions. The relevant phenomena investigated during the first entry were (1) wing twist, (2) flap deflection, and (3) aileron deflection. Resulting improvements were encouraging and are depicted in Figure 5-1. Some restrictions in test setup and performance, however, arose due to limitations of scope. Issues and factors restricting the Test 1 execution included:

- SMA wire fatigue problems at termination of control surface trailing edge
- Limited deflection capability: flap ± 7.5 degrees, aileron ± 5 degrees
- Nonuniform deflection of flap and aileron, particularly in the spanwise direction
- Maximum wing twist of 1.25 degrees, short of the 5-degree goal

All of the foregoing limitations were corrected in the second iteration of wind tunnel testing (Test 2), which went entirely according to plan except for the flap failure. Figure 5-4 highlights the achievements, results, and benefits attributed to the program Test 2 effort. Perhaps the greatest improvement came in the updated single torque tube design that permitted the target 5-degree twist angle to be realized. However, across the board, all of the smart control surface concepts benefited from considerable design improvements over the configurations used in the first test. Model design enhancements unilaterally equated to higher deflection angles, improved fatigue characteristics, and more uniform control surface deflections.

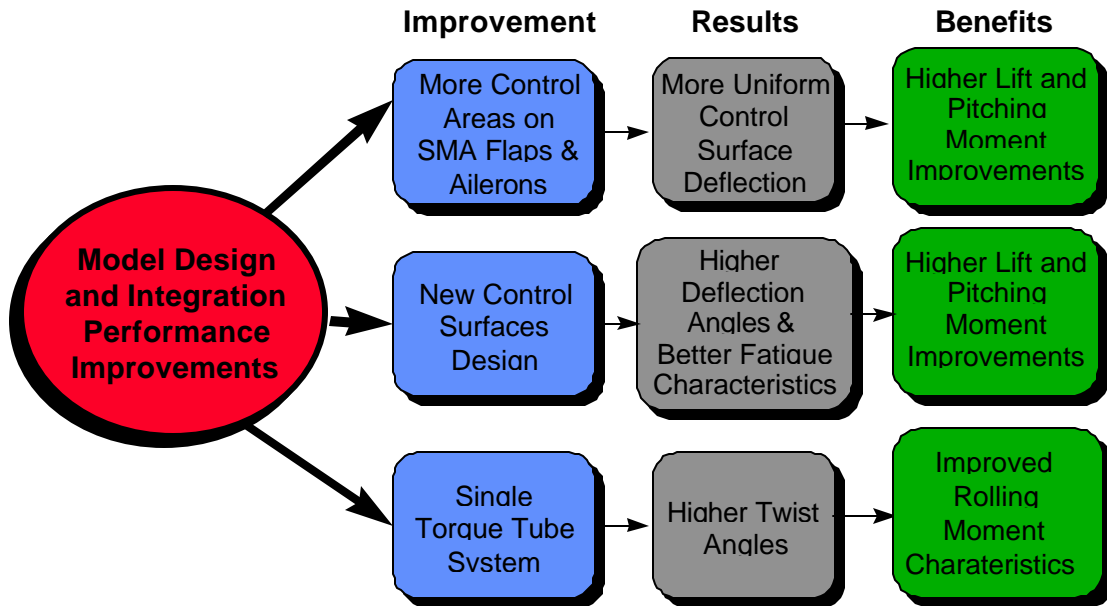


Figure 5-4. Test 2 Overview

5.2 WIND TUNNEL TEST CONFIGURATION AND SETUP

Prior to any detailed presentation of the results, critical items are reviewed in the test performance that depended heavily on the contributions of the NASA Langley wind tunnel facility. Test model installation, monitoring, and sequence details are also presented in this section.

5.2.1 NASA Langley Wind Tunnel Test Facility

The NASA LaRC TDT was used to test and quantify the aerodynamic performance benefits of both wind tunnel models. The TDT (planform shown in Figure 5-5) is a unique facility in that it is designed primarily for aeroelastic research and for validating vehicle performance for safe operation with respect to aeroelastic instability.³⁵ It is important to understand that the models used for the Smart Wing program were not designed to study aeroelastic effects; however, since their construction was similar to actual aircraft wings, there was concern of possible dynamic effects on the models while under air loads. The TDT's test section is 16 by 16 feet and easily accommodated the test models (Figure 5-6). The facility can provide variable tunnel total pressure from near vacuum to one atmosphere from Mach numbers of 0.1 to above the speed of sound at Mach 1.2. The facility also has the unique capability of using either air or R-134a high density gas, which greatly assists in the scaling of aeroelastic models. The high density gas, however, was not required for testing on the Phase 1 program.

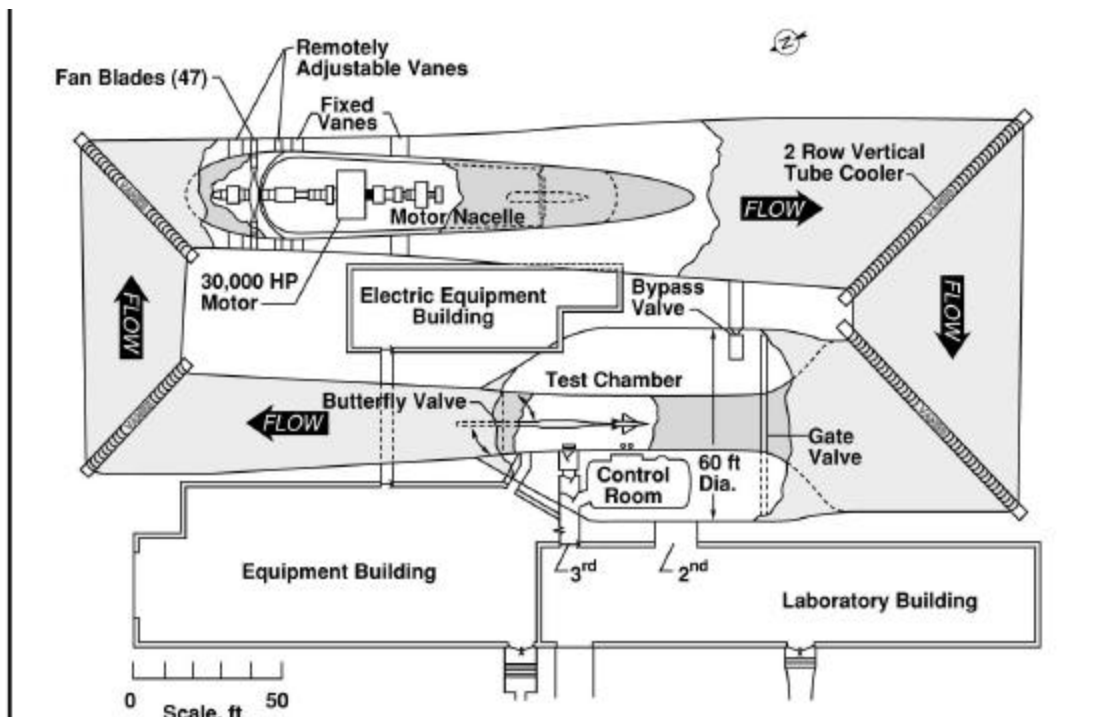


Figure 5-5. Plan View of TDT Facility

Other special features of the TDT facility include, but are not limited to:

- **Bypass Valve:** A unique safety feature uses four bypass valves connecting the test chamber (plenum) of the tunnel to the return leg of the wind tunnel circuit (Figure 5-5). In the event of model instabilities (flutter), the valves can be readily opened.
- **Air Stream Oscillator System:** For gust alleviation investigations, a set of oscillating vanes located upstream from the test section can be driven sinusoidally to simulate atmospheric turbulence or gusts.
- **Control Room:** The control room is strategically placed for maximum observation and communication with the test section within the same pressure shell of the test chamber plenum.
- **Test Section Isolation:** Butterfly and gate valves (Figure 5-5) isolate the test chamber from the remainder of the tunnel to allow quick access and reduce gas (R-134a) processing time.
- **Cooling Coils:** A set of cooling coils is located internal to the test circuit at the turning vanes immediately downstream of the drive motor ensures stable temperature at high dynamic pressures.
- **Test Versatility:** Four decades of diverse vehicle types have been tested, including phenomena such as flutter, divergence, buffet, gust loads, rotorcraft aeroelasticity and loads, unsteady pressure measurements, ground wind loads, dynamic response, atmospheric reentry loads and dynamics, aileron reversal, control surface buzz, active structural mode control, maneuver load control, active buffet alleviation, and a host of others.

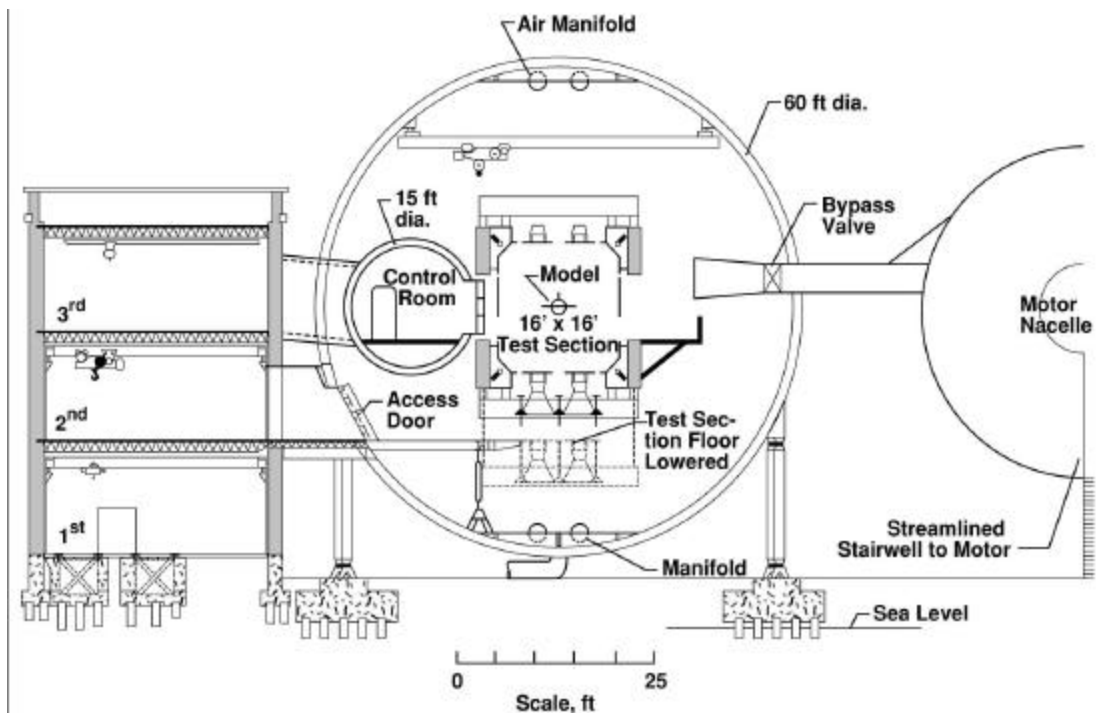


Figure 5-6. TDT Cutaway of Test Section Area

5.2.2 Smart Wing Tunnel Installation

Figure 5-7 is representative of both Test 1 and Test 2 and shows a plan view of the smart wing demonstration article as installed in the test chamber of the Langley TDT. As described in Section 4, for both wind tunnel tests (Test 1 and 2), two semispan wings were tested that were based on a typical fighter/attack wing. Construction of both the conventional and smart wing were almost identical with the exception of the trailing edge surfaces. The conventional wing had a standard hinged flap and aileron, while the smart model employed smooth trailing edge surfaces of the same size but actuated with SMA wires. The actuation was effected in the upper and lower wing skins by application of an electric current. The smart wing additionally had two SMA torque tubes in Test 1 and a single torque tube system to provide up to 5 degrees of twist (for Test 2) at the wing tip.

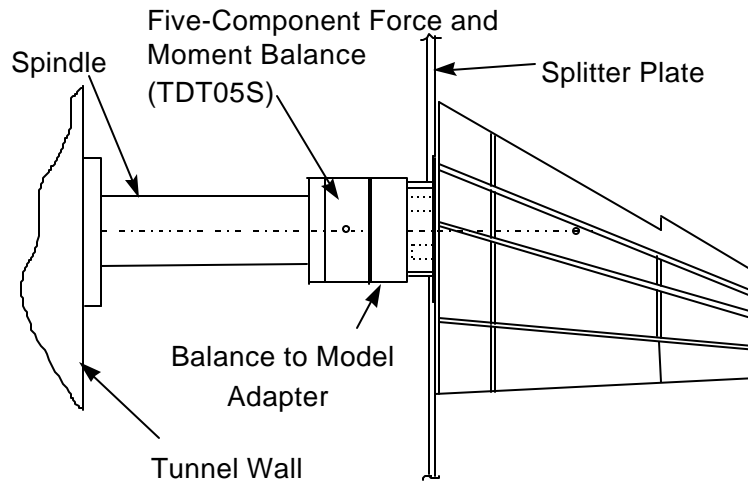


Figure 5-7. Plan View of Wing Model and Tunnel Installation

Each model was mounted approximately three feet off the wall on a splitter plate, shown in Figures 5-7 and 5-8, which moved the model out of the wall boundary layer and toward the center of the tunnel where air flow was more uniform. The splitter plate ensured that test conditions were minimally affected by tunnel wall boundary layer effects. Each model was firmly supported on the NASA Langley semispan turntable system, which extended through the tunnel wall. The turntable provided the capability for the model to be pitched through an angle of attack range of ± 30 degrees if required.

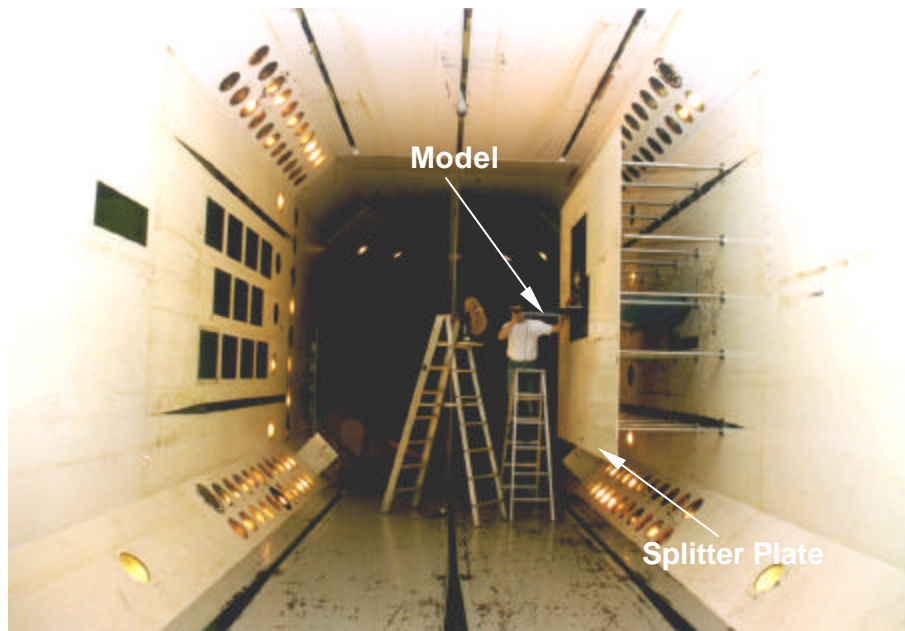


Figure 5-8. Wing Model Configuration in TDT

Critical setup items also depicted in Figure 5-7 were the spindle and balance. To obtain adequate support for the model, located well toward the tunnel center, the spindle was necessarily rigid. Details of the model balance are provided in the following subsection.

5.2.3 Test Instrumentation and Monitoring

Each model was extensively instrumented during both Test 1 and Test 2 to record the test conditions and results. The main differences were the replacement of fiber-optic sensors for wing surface deflection and pressure measurements with alternative nonintrusive methods mentioned in Section 2 (electrolytic and MEMS tilt sensors) and an upgraded test support strain-gaged five-component balance. The model instrumentation employed may be broadly divided into three categories:

- Aerodynamic force and moment measurement and pressure instrumentation
- Surface contour deflection and wing twist
- Safety and routine test condition monitoring.

The aerodynamic monitoring was performed by variously configured model balances to obtain the required program aerodynamic data. In Test 1 a two-piece balance was used (TDT-01S) that while adequate for a first proof-of-concept investigation of these smart actuators did not quite measure up to the program accuracy and repeatability requirements. For Test 2, NASA constructed a one-piece design that improved accuracy, reduced hysteresis, and provided a mounting flange that isolated local stresses caused by bolt tightening. These features, together with improved data reduction algorithms, led to more accurate and reliable data during Test 2. The refined balance for Test 2, NASA Langley's TDT-05S, was a five-component force and moment balance capable of recording the primary aerodynamic forces and moments: lift, drag, pitching moment, rolling moment, and yawing moment. This new balance provided an improvement in accuracy of almost 50 percent on each of the five monitored components and also had a significantly better repeatability.

Each of the models had four chordwise rows of static pressure taps as shown in Figure 5-9. The pressure tubes were routed through the splitter plate, "canoe" fairing and tunnel wall into the tunnel plenum. Each of the pneumatic tubes was connected to a port on one of the PSI modules. Four of the modules contained ± 1 pound per square inch differential (psid) rated transducers. The remaining module was ± 5 psid rated. The static pressure taps on the upper leading edge surface in each chordwise row were connected to the ± 5 psid rated module. The modules were operated and calibrated online by the PSI 8400 Control System. Because the transducer modules are extremely sensitive to temperature, a water-cooled plate surrounded by a thermally isolated box was used to house them. This maintained a stable temperature that minimized transducer drift and the need for frequent recalibration of the modules while running. Ports 1 and 32 on each PSI module were connected to a known pressure for verification and PSI system health monitoring during the test. In Test 2, two additional partial rows of static pressures for the smart flap and aileron (Figure 5-9) were used to more accurately characterize local flow of the smoothly contoured control surfaces. Additionally in Test 1, Extrinsic Fabry-Perot Interferometer (EFPI) fiber-optic sensors were investigated for their utility in providing pressure data that could be used for wind tunnel monitoring or could be actually installed in a future aircraft wing to augment the flight control system, but the concept was not used in Test 2. Briefly, difficulties in attachment, reliability, separating the monitored quantities (e.g., pressure, deflection, etc.) and cost deferred this development to another program.



Internal	External (Primary)
<ul style="list-style-type: none"> • Potentiometers – Surface Position and Control • MEMS Sensors – Wing • Tilt Sensors – Wing 	<ul style="list-style-type: none"> • NASA Langley Video Model Deformation (VMD) System • NASA Langley Projection Moiré Interferometry (PMI) System

Figure 5-10. Contour Position Measurement

I-66

To measure angle of attack, a Q-Flex inclinometer was mounted on the spindle pitch mechanism and an NGC-provided Scheavitz inclinometer was mounted at the root of each model to measure the angle of attack. Other internal devices were investigated for their ability to measure wing rotation due to twisting. MEMS sensors developed at NASA LaRC and tilt sensors manufactured by Advanced Orientation Systems, Inc., both attractive for small-scale installation, were used on the outboard wing sections. The MEMS sensors performed well within the ± 0.25 degrees static accuracy requirement but deteriorated to as high as ± 5.0 degrees under dynamic conditions. The electrolytic tilt sensors behaved well under dynamic conditions but also suffered from reliability problems with respect to discrepancies in the measured slope between positive and negative angles. The key focus of all of the internal sensors was to provide accurate position data for the contoured surfaces and spanwise twist that could be used in wind tunnel measurements or in flight. (Developing and using sensors for real-time feedback to be used for the flight control system is an extension of the previous idea that should be further pursued on a follow-on program, and all of the methods in the left-hand column of Figure 5-10, though lacking in maturity, should be encouraged for further development.)

External methods, on the other hand, were much more successful for measuring control surface position and twist. The NASA Langley optical video model deformation (VMD)⁵⁶ system was the primary system for measuring SMA flap and aileron position and wing twist. The method employs a series of small retroreflective tape discs carefully placed at several spanwise rows as shown in Figure 5-11. The discs serve as targets, which when illuminated generate a high-contrast image in a strategically located CCD camera. Image processing is used to automatically locate the targets. Photogrammetry is then used (after calibration) to determine the motion of the targets in the pitch plane and hence compute angular changes at the various spanwise target locations. The system is able to provide angular deflection in “near real time” with updates in angle a few seconds after triggering.

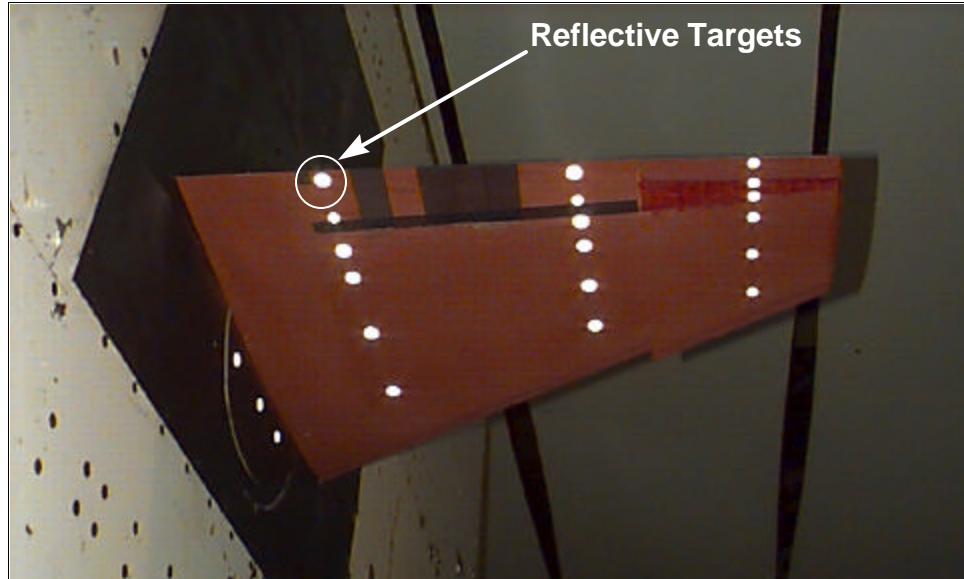
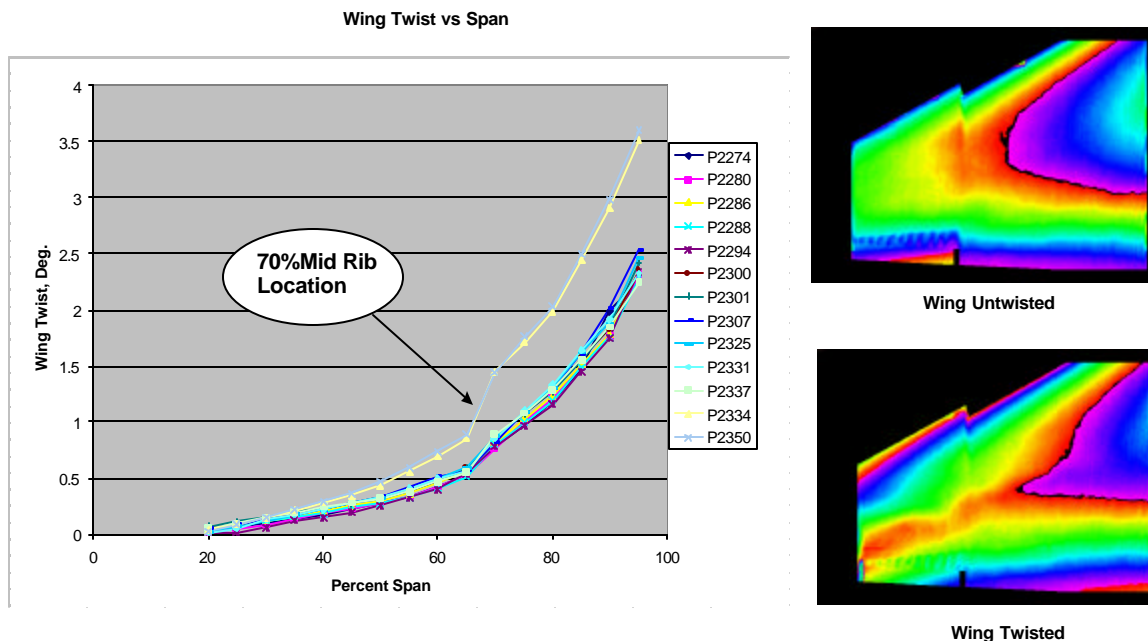


Figure 5-11. NASA Langley Video Model Deformation (VMD) System

Projection Moiré interferometry (PMI) was a second external optical diagnostic technique used to measure wing surface shape and deformation. The PMI system used an infrared, pulsed laser to project a series of equispaced, parallel lines onto the lower surface of the model. Images of the projected grid lines were captured using a CCD camera and frame grabber in reference (wind-off) and wind-on conditions. Image processing techniques were then used to reconstruct the model surface shape and/or deformation under aerodynamic load. Figure 5-12 shows PMI-measured quantitative wing surface shape measurements for the smart wing in nonactuated and torque-tube-actuated conditions. The PMI measurements were spatially continuous at a resolution of 0.055 inch per pixel (1.4 mm per pixel), far exceeding that of the VMD system. However, at its current state of development for wind-tunnel testing, PMI does not possess the high degree of accuracy demonstrated by VMD, and quantitative real-time output is not possible.



The third category of monitoring during wind tunnel testing relates to instrumentation used to monitor the safety of the models. As to be expected, reliable and conventional instrumentation was used for this task. The location of these sensors is shown in Figure 5-9, and the sensors include accelerometers, strain gages, and thermocouples. Three accelerometers were installed in each of the wing tips of the conventional and smart wing models in both Test 1 and Test 2. Data from these devices were monitored in real time using a frequency analyzer and a strip chart throughout the test. A change in the dynamic characteristics could possibly be a sign that something has happened to the model. An example of this could have been if one of the wing spar connections had come free, the stiffness of the model would have changed, causing the natural frequencies to move. The strain gage rosettes, mounted inboard and outboard on each of the three wing spars, provided real-time model dynamics and structural load monitoring. Thermocouples were installed on the SMA torque tube to monitor its temperature. They were also colocated with the strain gages to provide temperature compensation for the strain, if necessary, and determine the effect on the internal temperature throughout the model due to torque tube actuation.

As the analysis predicted, during the course of testing no instabilities or failures occurred that would threaten model or personnel safety. The only unexpected failure that occurred happened to the SMA flap in Test 2 and was a localized phenomenon. The instrumentation installed on the

model to measure tip deflection did not sense the visually apparent change in control surface shape and because of the type of failure that occurred (a delamination of the RTV skin) the other parameters being measured to ensure safety were not affected. This type of failure would only have been sensed if a technique were available that measured the tip deflection by using the shape of the control surface in real time. The sensors available on the program either measured the tip deflection only at discrete locations that could (and did) provide ambiguous readings or required some offline processing to determine the control surface shape.

5.2.4 Program Test Sequence and Conditions

A similar test sequence was used for both Test 1 and Test 2, and the essential elements of the procedure and conditions are depicted in Figure 5-13 and Figure 5-14. Common to both tests was a flutter clearance run to ensure model stability prior to recording any actual wing model performance data (a normal safety precaution for wind tunnel testing). The model was taken slowly to increasing dynamic pressures and Mach numbers, and angle of attack was varied between 0 and 10 degrees. The reason for doing this was to clear the test envelope and verify that the model behaved dynamically as expected in the test range.

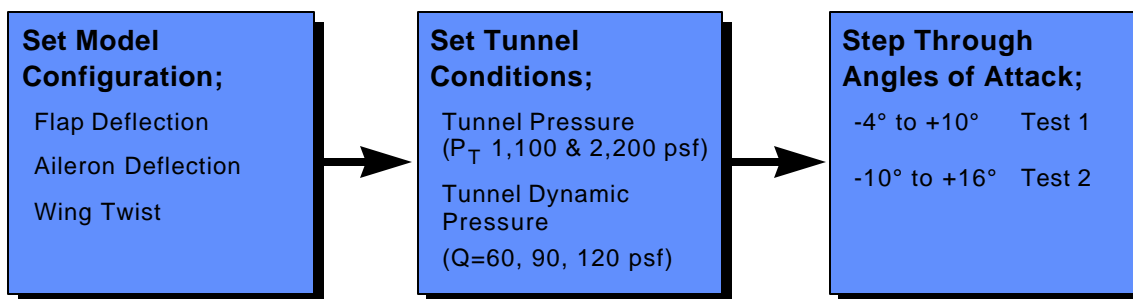


Figure 5-13. Program Test Sequence

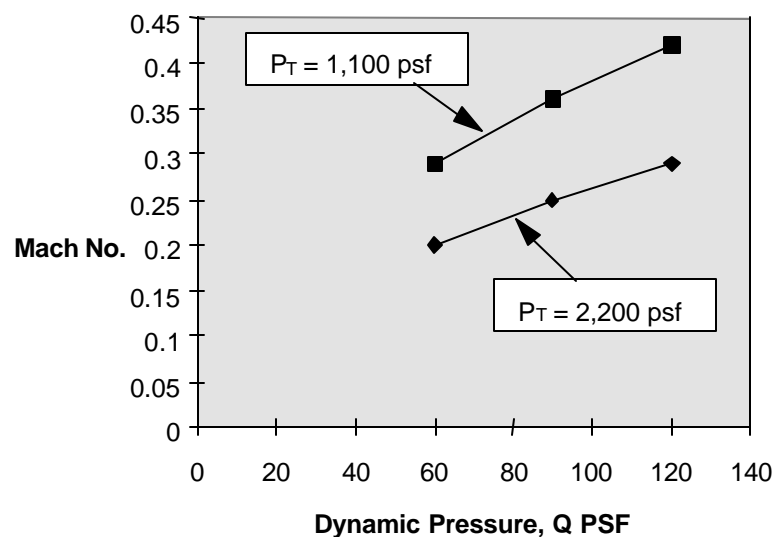


Figure 5-14. Smart Wing Wind Tunnel Test Conditions

In Test 1, the models were tested at a constant tunnel total pressure of one atmosphere (sea level or 2200 psf) and dynamic pressures of 60, 90, and 120 psf, which corresponded to Mach numbers of 0.2, 0.25, and 0.29 respectively. Data were recorded at specified, fixed angles of attack starting at -4 degrees and increasing to +10 degrees in fixed increments of 2 degrees except around the 0-degree point where the increment was 1 degree. Run polars, plots of aerodynamic coefficients (C_L , C_M , etc.) versus AOA, were generated at various total pressures and Mach numbers with fixed wing twist and control surfaces. The means of measurement in Test 1 were as follows:

- TE flap deflection angle on conventional model was set with an electric motor and calibrated with a rotary potentiometer.
- Aileron deflection angle was set with fixed brackets.
- Smart wing SMA trailing edge deflection was measured optically (described previously).

The key differences in test conditions between Test 1 and Test 2 were that the later test matrix included higher Mach numbers, lower total pressures, and higher angles of attack, up to 16 degrees (Figure 5-13).

5.3 PROGRAM WIND TUNNEL TEST RESULTS

A top-level discussion of the wind tunnel test results was presented in the section overview and briefly summarized in Figure 5-1. This section reviews in more detail each individual function tested. The wind tunnel results are discussed by adaptive concept investigated, and where appropriate, differences in the progression from Test 1 to Test 2 are brought out in the text or figures. This order of topics presents a clearer picture than a chronological presentation of data. Hence, subsections are structured into:

- Baseline Test Repeatability
- Wing Twist Performance
- Wing Flap Performance
- Wing Aileron Performance
- Combined Effects on Wing Performance.

The above delineation and separation of functions permits a rapid review of each individual effect on the aerodynamic qualities of the wing, and the combined effects (wing twist and aileron together) may also be readily examined. Detailed descriptions of the adaptive features may for the most part be found in other sections; however, some degree of repetition is included to make the current section “stand alone” and to clarify interpretation of the wind tunnel results.

5.3.1 Baseline Test Repeatability

An important aspect of testing in general is the repeatability of data, and in particular the baseline must always be as constant as possible since variations in the performance data could be attributable to baseline shift rather than the particular parameter (e.g., twist) under investigation.^{37,38} Since there were considerable model differences and changes in the test configuration (e.g. balance and smart control surfaces) from Test 1 to Test 2, model baseline repeatability checks were performed prior to each test entry and were established in the same sequence in each test case – directly after the safety compliance flutter runs and prior to actual recording of performance data.

Both baseline repeatability runs were performed at the midrange dynamic pressure and Mach number, namely Mach = 0.25 and $Q = 90$ psf, since this is where the bulk of the data collection

was performed. During each test entry, a comparison was performed to verify that the models were identical in outboard shape and to verify proper installation. Individual plots in Figure 5-15 show the comparison of the lift, pitching moment, and rolling moment for the undeflected case (i.e., no adaptive features applied) for both the conventional and smart wing models. Note that the curves are almost completely superimposed except for the rolling moment, and all plots were well within accuracy and repeatability limits for the TDT-01S balance (± 9 lb lift, ± 100 in-lb roll moment and ± 160 in-lb pitching moment). The errors are within the values for the balance, but because the forces and moments that were measured were less than 10 percent of the balance maximum, these balance inaccuracies proved to be in some places greater than the measured forces and moments.

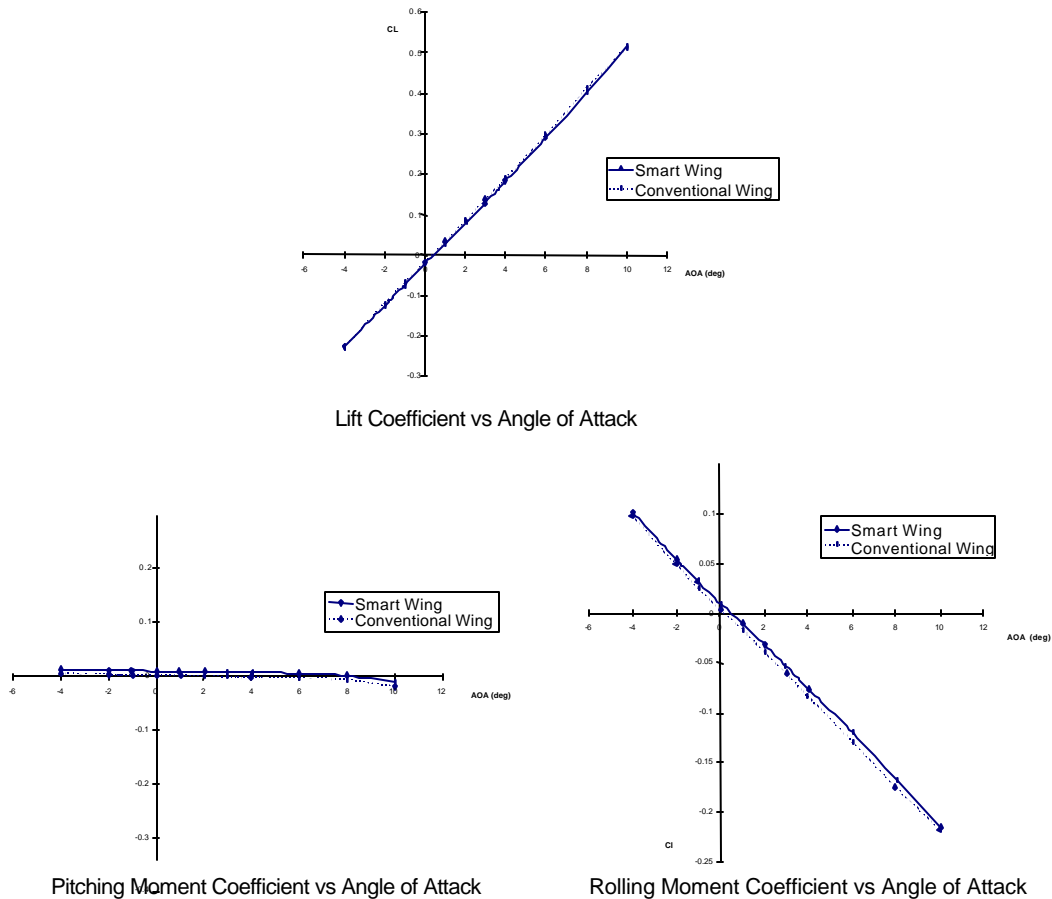


Figure 5-15. Baseline Repeatability – Test 1 (Q = 90 psf, Mach = 0.25)

The same individual plots for lift, pitching moment, and rolling moment under identical conditions as Test 1 show the baseline repeatability for Test 2 (Figure 5-16). As in Test 1, a series of alpha polars were run for model accuracy and installation. Note that all of the individual plots in Figure 5-16 are virtually superimposed, including the rolling moment coefficient versus angle of attack. This indicates that the new TDT-05S balance, specially constructed for Test 2, provided markedly improved accuracy and repeatability characteristics.

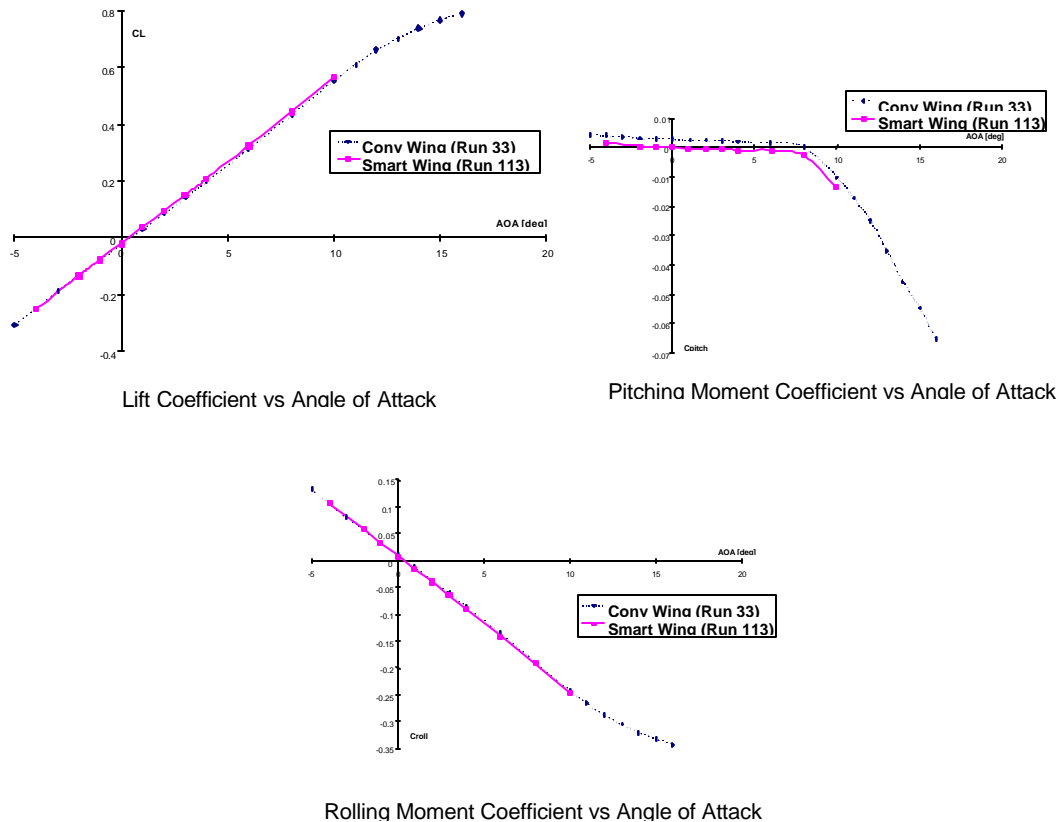


Figure 5-16. Baseline Repeatability – Test 2 (Q = 90 psf, Mach = 0.25)

5.3.2 Wing Twist Performance

In validating the torque tube performance, experimental data recorded from Test 1 proved to be a valuable learning experience. Design revisions put into practice after Test 1 enabled radical concept improvements to be instituted before the second tunnel entry. Test 1 was notable for the first chronicled demonstration of wing twist characteristics using “smart materials.” Specifically, serial SMA torque tubes were used to vary the spanwise twist of a scaled wing surface (detailed in Section 2 and Section 4). Two thousand in-lb of torque were achieved using a 1-inch-diameter, 4-inch-long SMA torque tube that provided approximately 1.25 degrees of twist and an increase in rolling moment of approximately 8 to 12 percent. It should, perhaps, be emphasized that a relatively small amount of twist can produce a significant rolling moment improvement. On the other hand, with the enhanced torque tube design (Section 2 and Section 4), the Test 2 model exceeded the target goal and verified that 5.2 degrees of twist (first recorded under laboratory conditions) could also be accomplished in a realistic wind tunnel environment. Other (known) technology achievements during Test 2 relate to the magnitude of the actuation torque developed, the high degree of load transfer for the integrated configuration within the wing, the ability to select and sustain predetermined twist angles, and active cooling hardware. Test 2 advanced the learning curve still further, and gave valuable and surprising insight on future torque tube implementation.

Figure 5-17 indicates the improved lift and a 12 percent rolling moment benefit due to the relatively modest spanwise twist of 1.25 degrees afforded by the earlier SMA torque tube. Note that all control surfaces are in the neutral (undeflected) state, and the data taken at Q = 120 psf and Mach = 0.29 are typical of the lower Mach values conservatively used for measurement recording during the first exploratory proof-of-concept tests. Validation at higher Mach numbers was to be deferred until Test 2. Tunnel data recorded at Run 113 and Run 89, depicted on the

figure, relate to data taken in the twisted and untwisted conditions respectively. As stated in the overview, all of the figures in the current sections are selected examples of typical runs, and the reader interested in more complete characterization of wing twist, or any other adaptive feature tested, should consult Volume III.

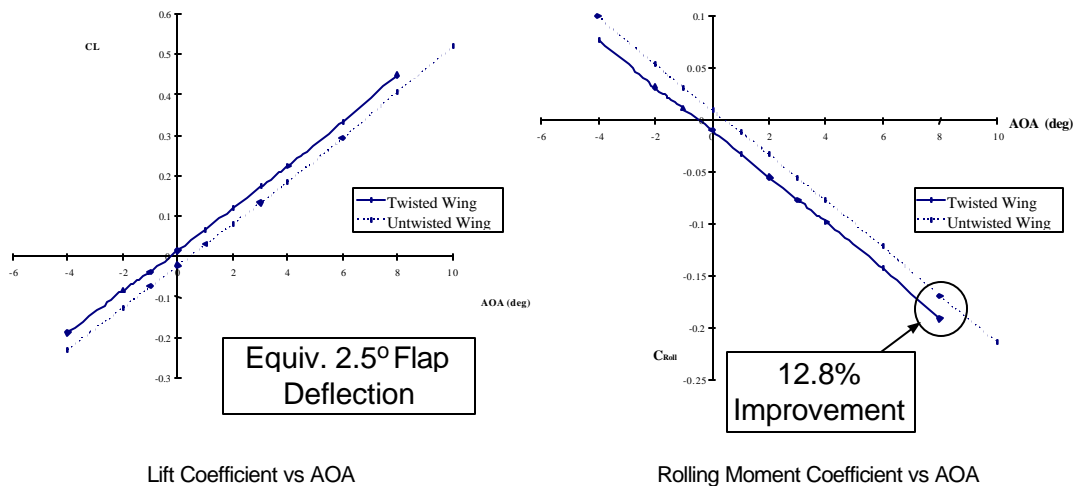


Figure 5-17. Wing Twist Effects – Test 1
(All Control Surfaces = 0 degrees, Runs 113 vs 89, Q = 120 psf, Mach = 0.29)

As a means of comparison with the alternative SMA flap adaptive method for providing enhanced lift capability (discussed in the following sections), the lift coefficient vs AOA for an “equivalent flap deflection” is also graphically displayed in Figure 5-17. Note that a spanwise twist of 1.25 degrees (or 2,500 in-lb total applied torque for both tubes) produces the equivalent lift as a 2.5-degree deflection of the flap control surface with little or no increase in drag at the low dynamic pressures tested. Recalling the first prototype torque tube design from Section 2, the total twisting effect in Test 1 was facilitated by a combination of two (mid-rib to inboard and outboard) sections of the model as shown in Figure 2-7. This dual tube configuration, however, was replaced by a single tube design during Test 2.

Before embarking on further Test 2 wing twist results, a few words of explanation for the non-aerodynamic-specialist on how this adaptive feature provides lift and at what phases of an aircraft’s mission it could be applied are appropriate. The resulting spanwise twist enabled by the concept may seem at first glance to be counterproductive since it promotes “wash in” conditions. Wing wash-out – where the wing root AOA exceeds the wing tip, is usually the more desirable condition for alleviating undesirable stall characteristics and facilitating maneuver control after wing root stall. Wash-in conditions however, occur during takeoff and landing. Twisting the wing to cause wash in provides substantially more lift while maintaining the same wing root (i.e., fuselage) angle of attack. This adaptive feature should therefore be reserved for takeoff and landing only where the most benefit can be derived.

Test 2, with the revised single torque tube design, was successful in achieving the 5-degree twist angle program goal as evidenced by Figure 5-18. Also, the wing twist adaptive feature provided a beneficial increase in aerodynamic suction pressure at the wing leading edge, as illustrated in Figure 5-19. However, a quite surprising result is observed in comparing the lift coefficient and rolling moment with the Test 1 data. Despite almost quadrupling the twist angle and meeting the 5-degree program goal, the Test 2 results are only slightly better than Test 1. This initially caused some consternation but led to some important conclusions about future implementation of the torque tube adaptive feature, which will be covered in the remainder of this subsection.

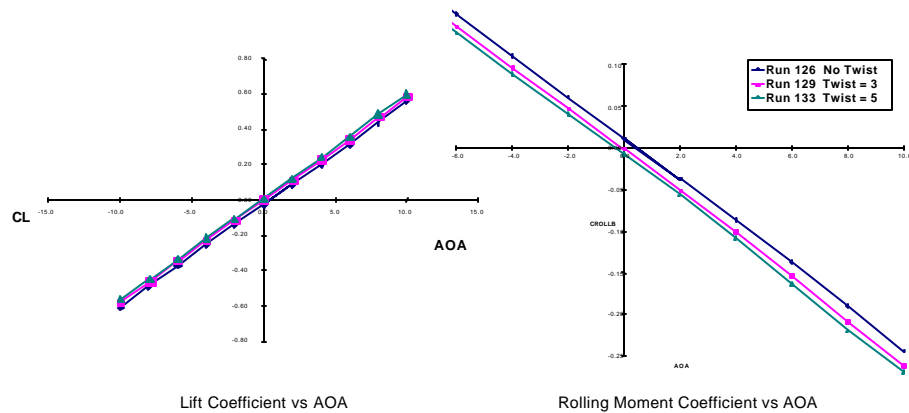


Figure 5-18. Wing Twist Effects – Test 2
(Flap = 0 degrees, $Q = 90$ psf, Mach = 0.25)

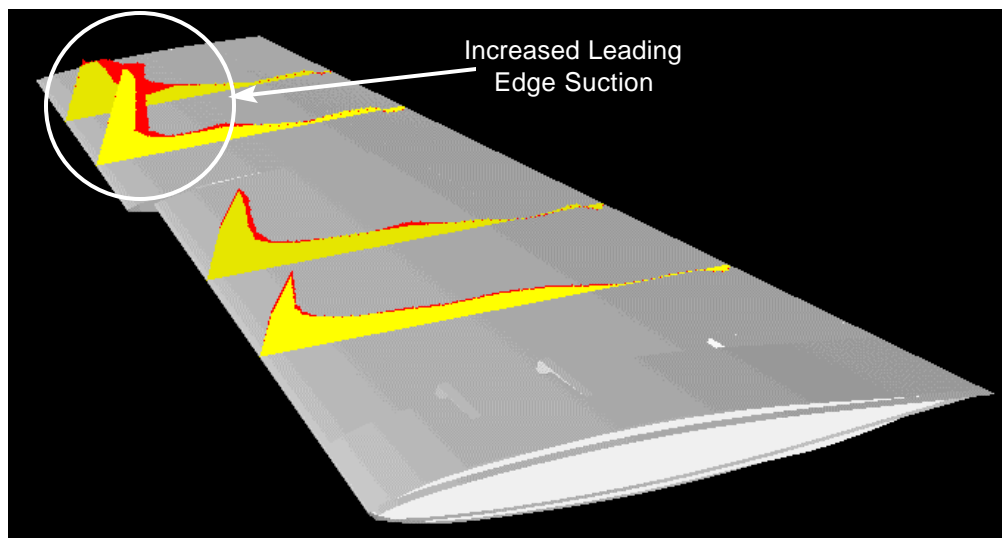


Figure 5-19. Wing Twist Effects – Increased Leading Edge Suction

For an answer, we must review some of the torque tube lessons learned and design changes discussed elsewhere but reiterated here for completeness. The dual torque tube setup of Test 1 fell short of the program twist angle goal because:

- Outboard tube “worked against” the inboard tube, limiting the total twist to 1.25 degrees.
- Outboard tube was limited in size to 0.6 inches outside diameter.
- Size limitation reduced maximum torque capability to modest value of 600 in-lb.

The single-tube revised design overcame all of these shortcomings, met the program goal, provided an impressive stall torque of 3,200 in-lb, and was fully expected to yield superior results. The apparent discrepancy was resolved under close inspection of the data and found to be related to inherent wing stiffness, wing elastic axis location, and twist distribution. The twist for Test 1, where approximately 2,000 in-lb of torque was applied at the mid-section and 600 in-lb at the tip, meant that the inboard portion of the wing predominated. The tip section would ordinarily twist more due to the inherent torsional stiffness of a tapered wing that decreases with outboard travel. However, inability of the outboard actuator to provide sufficient torque nullified this effect. For the single torque tube installation, on the other hand, where a higher torque was evenly distributed, the effects of the taper were realized, causing the tip to twist quite appreciably, while the inboard section recorded low twist and AOA deflection.

The corollary to this investigation is that area and twist section location are all important. During Test 2, the inboard section of the model out to the mid-rib accounts for over 73 percent of the total planform area (see Figure 5-20), and was at a lower relative angle of attack than in Test 1. The net result was little difference in the overall wing lift and rolling moments, despite the Test 2 model spanwise twist at the tip exceeding its Test 1 counterpart by a factor of 4.

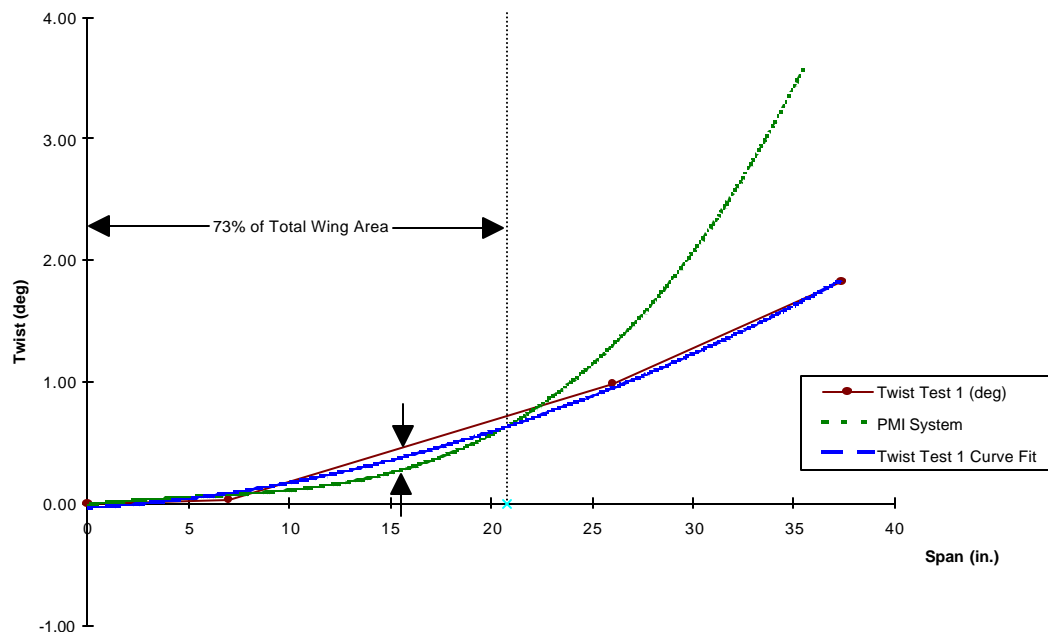


Figure 5-20. Spanwise Twist Distribution Due to SMA Torque Tube

5.3.3 Wing Flap Performance

The performance benefit afforded by the SMA actuated flap, versus a hinged configuration, is perhaps one of the most critical results and achievements of the Smart Wing Phase 1 program. Figure 5-21 illustrates the pressure distribution across the wing for both conventional (shown as a dashed line) and for smart configuration (solid line) employing a smoothly contoured SMA embedded flap. Aerodynamic pressure coefficient, C_p , is plotted along the vertical axis versus normalized chord length x/c along the abscissa so that pressure distribution from leading to trailing wing edges may be examined. Note that a large, fairly broad, peak suction pressure amplitude occurs at the TE flap for the smart hingeless case, far in excess of the amplitudes recorded for the conventional wing model. The modest pressure value for the conventional case is due to unwanted aerodynamic flow separation at the hinge line. For the smart flap, the point of flow separation moves further down, much closer to the wing TE. Also, increased suction pressure for the smart configuration predominates in general across the entire wing chord span – the solid line

is almost always above the dashed line in Figure 5-21. This effect can be seen at different locations in the spanwise direction along the wing in the three dimensional graphic depicted in Figure 5-22.

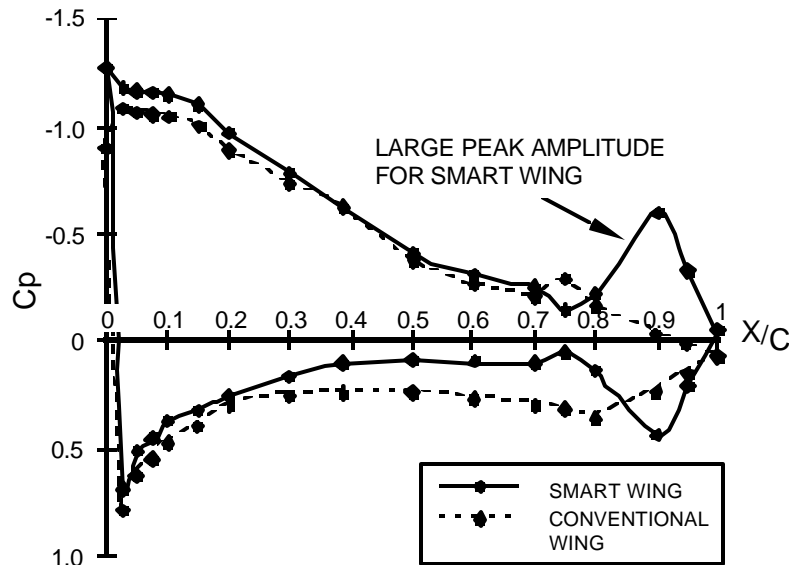


Figure 5-21. Wind Tunnel Pressure Distribution Measurements

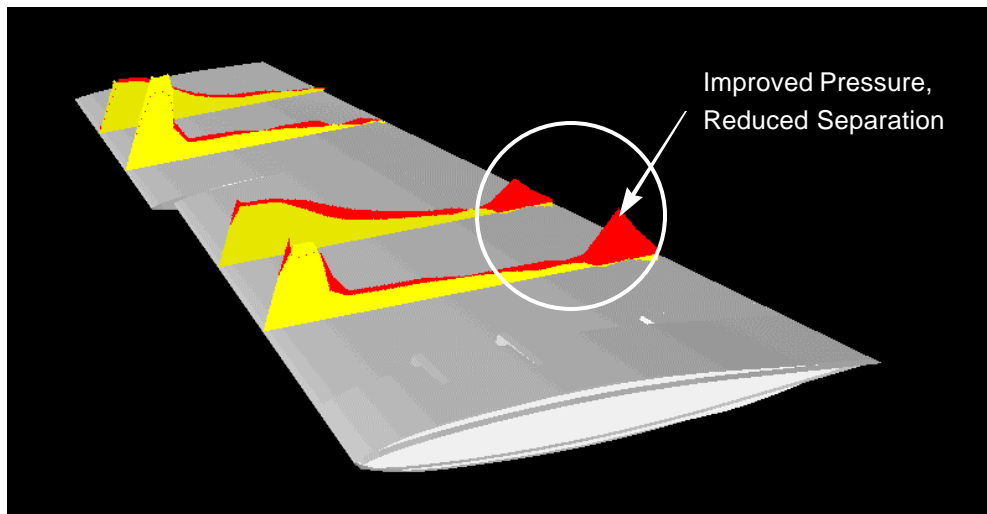


Figure 5-22. Pressure Plot – Flap Deflected 7.5 Degrees

The importance of these results should not be overlooked. For the first time ever it was demonstrated and recorded by measurement that aerodynamic efficiency can be greatly enhanced using new smart material actuation systems. Prior to wind tunnel testing, a computational study of a smooth contoured trailing edge surface versus a conventional hinged trailing edge was undertaken. A NASA Ames-developed CFD code, ENSAERO was used in this study. Two identical wing models were compared, with the exception of one having a conventional hinged trailing edge control surface and the second a seamless contoured control surface. The results, included in Volume III, show the same trends as seen in the wind tunnel data.

Figure 5-23 illustrates the aerodynamic efficiency for the contoured hingeless wing model normalized to the conventional value, showing an 8 to 12 percent improvement in roll rate with increasing dynamic pressure, which translates directly into a more efficient lifting surface and improved aircraft speed.

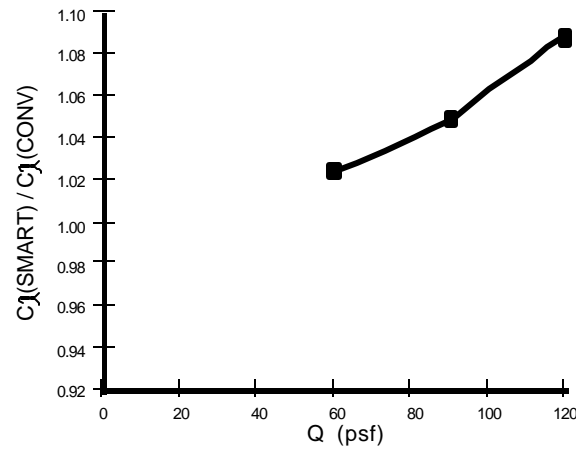
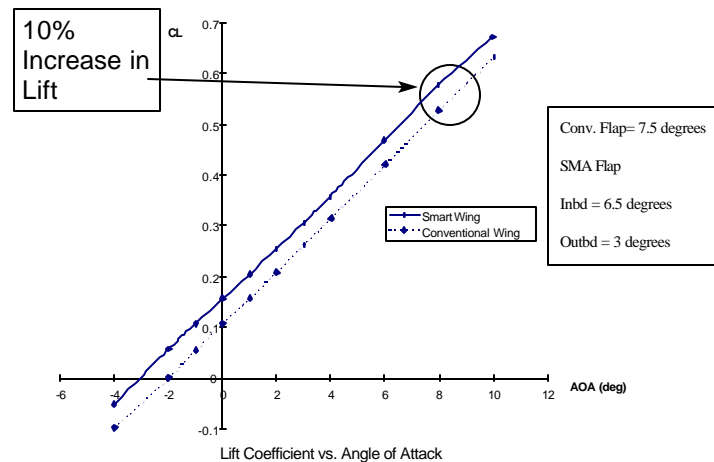


Figure 5-23. Rolling Moment Comparison – Contoured vs Conventional Aileron

The increased lifting and pitching moment can be seen by the delta shifts depicted in Figure 5-24 and Figure 5-25, respectively. Such an increase in lift or pitching moment per angle of attack equates directly with improved aerodynamic performance per angle of deflection for the smart wing. The lift benefit translates to greater weight-carrying capacity for a given aircraft at takeoff, or a shorter takeoff or landing distance. For a given weight, the smart flap requires less deflection and therefore less drag, which shortens the takeoff distance. The benefit is thus realizable by an increased capacity to carry fuel or stores, smaller, lighter engines, or lighter overall vehicles.



**Figure 5-24. Flap Only – Lift – Test 1
(Runs 100 vs 75, Q = 60 psf, Mach = 0.2)**

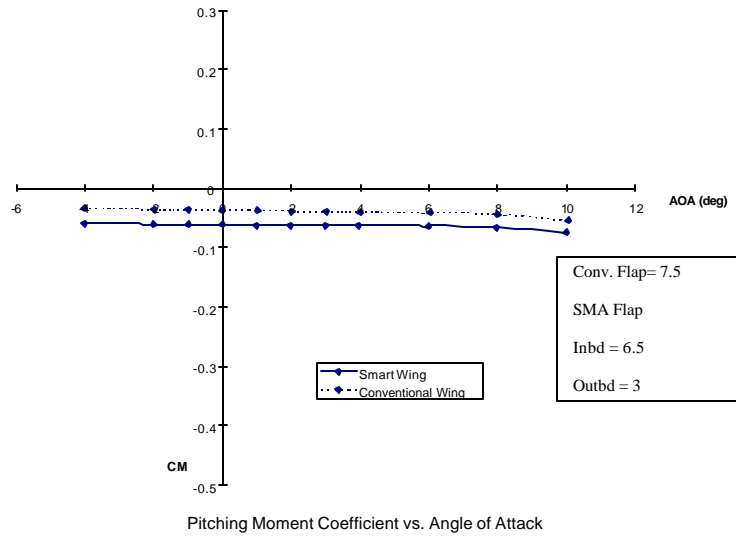


Figure 5-25. Flap Only – Pitching Moment – Test 1
(Runs 100 vs 75, Q = 60 psf, Mach = 0.2)

The above result was recorded during Test 1, and considerable planning went into the Test 2 effort to obtain more data points and more accurate characterization of the benefit. Unfortunately this could not be completed because of the Test 2 flap failure, but further definition will be pursued on the Smart Wing Phase 2 program.

5.3.4 Wing Aileron Performance

Figure 5-26 shows the improved rolling moment by the shift in the rolling moment coefficient plotted against angle of attack recorded during Test 1 for the combination of flap and aileron. This simulates a landing or takeoff configuration for the aircraft.

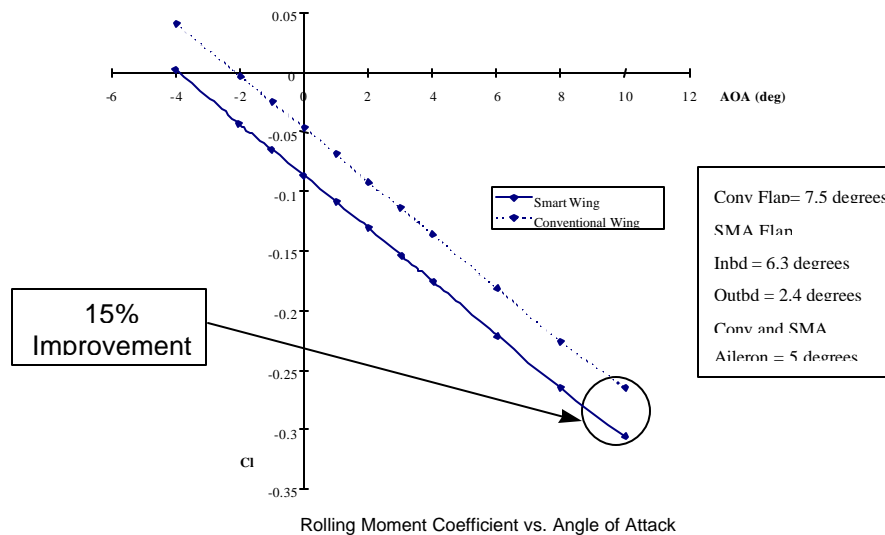
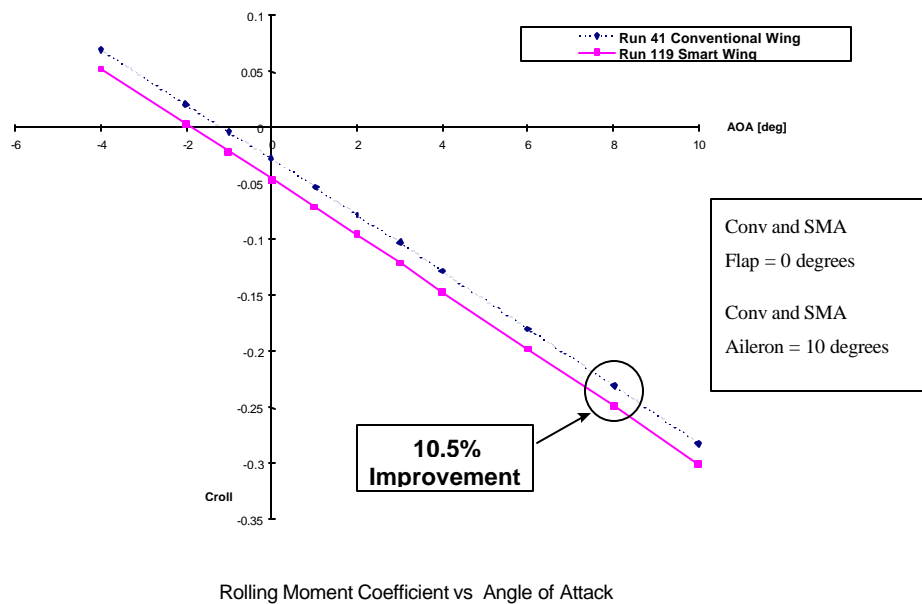


Figure 5-26. Aileron Effectiveness – Test 1
(Runs 105 vs 22, Q = 90 psf, Mach = 0.25)

In Test 1 both the aileron and flap performances were hampered by uneven spanwise trailing edge deflection due to controllability of the wires. This was caused by manufacturing and control difficulties as described in Section 3. The net effect was an observed lack of uniformity in spanwise deflection. Fatigue caused SMA wires to lose their pre-strain properties (a bias characteristic essential for efficient actuation in a nonuniform and somewhat random manner). It was also observed that the outboard wires lost their controllable surface deflection ability sooner than their inboard counterparts. This phenomena was clearly due to the shorter outboard wire lengths undergoing higher strain for the same deflection and thus larger stresses on the wire termination strips, leading in turn to more rapid fatigue. However, it should be emphasized that during Test 1, even with less than ideal wire control, a rolling moment increase of 8 percent was possible and demonstrated. These improvements in roll moments lead directly to higher roll rates and faster turns.

During the program interim period between Tests 1 and Test 2, the wire termination fatigue characteristics were markedly improved by a superior design that was validated in the Test 2 aileron performance test data. Figure 5-27 and Figure 5-28 show similar graphics for the rolling moment versus AOA characteristic and pressure distribution benefits in the case of the adaptive aileron, as described for the flap in the previous section. Again, the benefit in flying qualities equates to enhanced roll moment and reduced flow separation at the trailing edge. A more uniform spanwise deflection of the smart aileron attributable to design upgrades led to an overall 11 percent aileron effectiveness benefit and a 3 percent delta improvement over the Test 1 results. No doubt a similar delta improvement would have been seen if full testing of the flap characteristics had been possible, but such results still require substantiation by further flap testing during the Smart Wing Phase 2 program.



**Figure 5-27. Aileron Effectiveness – Rolling Moment – Test 2
(Runs 119 vs 41, Q = 90 psf, Mach = 0.25)**

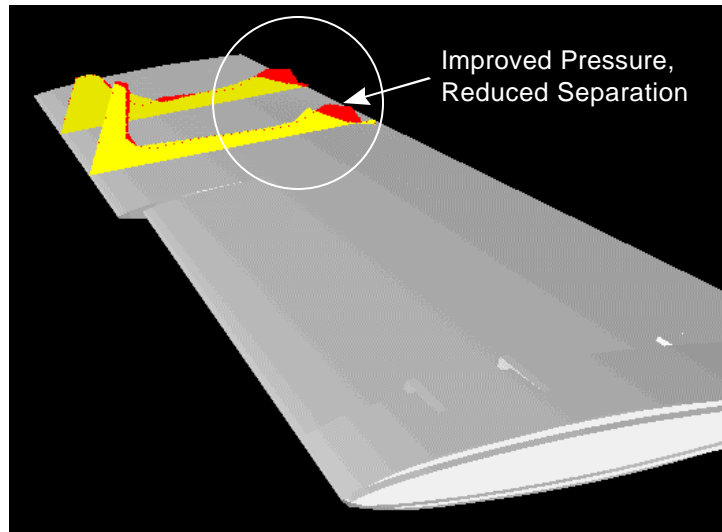


Figure 5-28. Aileron Effectiveness – Deflection 10 Degrees – Test 2
($Q = 90$ psf, Mach = 0.25)

An alternative method of visualizing the aileron effectiveness is illustrated in Figure 5-29. Here the rolling moment coefficient caused by aileron deflection is plotted for different angle of attack, namely at $\alpha = 6, 8$, and 10 degrees. Two important features are shown on this graphic. First, at zero degrees deflection, the rolling moments are very close, which would indirectly verify the consistency between the models. The second is the increase in performance improvement with increasing control surface deflection angle. This shows that the separation reduction at the contoured aileron provides an improved lifting surface and a lower deflection angle to obtain the same lift as a conventional wing.

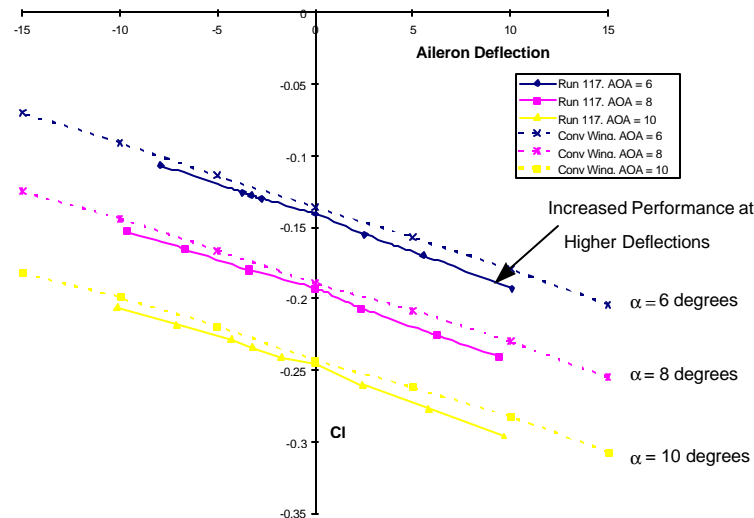


Figure 5-29. Aileron Effectiveness – Alpha Variation
($Q = 90$ psf, Mach = 0.25)

The first result is to be expected since the surface was not deflected and could be viewed as an indirect method of verifying consistency between the models. The second performance improvement feature derives from the aerodynamic benefit of reduced flow separation borne out by Figure 5-28. As before, the separation reduction of the smart aileron provides an improved lifting surface, resulting in smaller aileron deflection requirements to obtain an equivalent rolling moment to the conventional hinged surface case.

5.3.5 Combined Effects on Wing Performance

It is important to appreciate that of all of the adaptive effects discussed so far it is unlikely that any one of them will be used exclusively in isolation for a complete mission. There will be many instances in which effects will be combined, such as during takeoff and landing where the flap and aileron will be actuated simultaneously or a combination of wing twist with flap and aileron. Under such conditions, questions can be posed. Are the effects additive? Can we assume linear superposition? When does it make sense to combine effects?

During Test 1 with the limited time available, combined effects were investigated for deployment of the flap and aileron together in terms of both pitching and rolling moment. Figure 5-30 shows the pitching moment versus angle of attack. In general terms it can be seen that both effects worked well together, accruing essentially additive components. All conditions for the smart and conventional models were identical to the cases where data were taken on the individual adaptive feature, making the basis for comparison quite valid. Improvements discussed throughout this section were once again seen for the combined conditions. Note, as before, the varying angles of deflection from the inboard section of the flap are evident in the plots, which are attributable to the SMA wire controllability issue that caused a nonuniform spanwise deflection as discussed earlier.

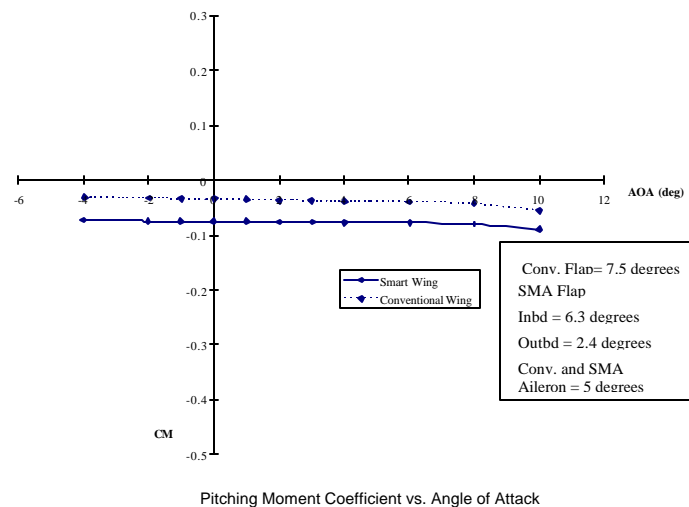


Figure 5-30. Flap and Aileron – Pitching Moment
 (Runs 105 vs. 22, Q = 90 psf, Mach = 0.25)

The Test 2 combined effects investigation was similarly limited in terms of scope but concentrated on assessing the combined wing twist and aileron behavior since the twist adaptive feature was left out of the equation in the Test 1 assessment. Figure 5-31 once again substantiates that adaptive features tend to support each other, though not necessarily in a completely linear fashion, and essentially provide a superposition of flying qualities benefits.

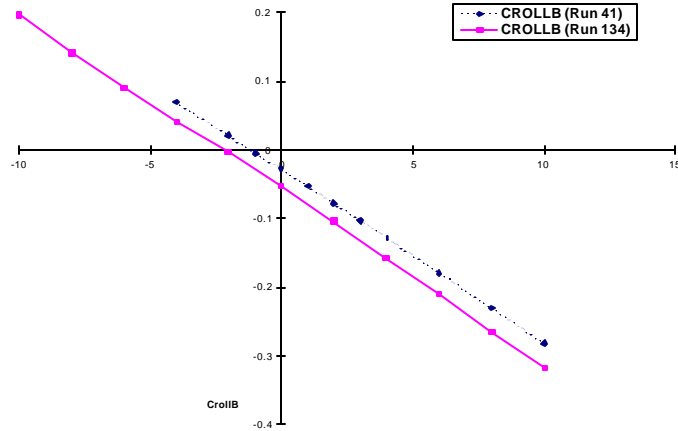


Figure 5-31. Rolling Moment Increase for Combined Wing Twist and Contoured Aileron Deflection

5.4 CONCLUSIONS

The results of the first and second entries of the Smart Wing Phase 1 program demonstrated the improvements in aerodynamic performance due to integration of smart materials. Design limitations of scope and integration issues from the first entry were successfully addressed in Test 2. Figure 5-32, a restatement of Figure 5-1, summarizes the significant and repeatable improvements in aerodynamic performance due to the smart material actuators.

Configuration	Deflection or Wing Twist (deg)	Lift DC_L	Roll DC_ℓ	% Improvements	
				Lift	Roll
Flap Only (Test 1)	7.5	0.0581	0.0193	9.7	10.2
Flap and Aileron Combined (Test 1)	7.5	0.0916	0.0387	17.6	17.1
Aileron Only (Test 1)	5.0		0.0150		8.0
Aileron Only (Test 2)	10.0		0.0189		10.5
Wing Twist at Tip (Test 2)	3.0	0.0344	0.0193	8.0	10.0
	5.0	0.0502	0.0296	11.5	15.6
Wing Twist at Tip (Test 1)	1.4	0.0406	0.0218	10.0	12.8
Combined Aileron and Wing Twist (Test 2)	+ 10.0	0.0567	0.0310	15.3	17.3
	+ 4.5				

Figure 5-32. Summary of Aerodynamic Improvements

6. CONCLUSIONS AND TECHNOLOGY TRANSITION

Completion of the Smart Wing Phase 1 Program heralded the first government-sponsored activity to demonstrate that (as of this writing) smart materials are reaching a level of maturity for inclusion in adaptive wing technology and that benefits over conventional approaches are substantial and real. The challenge for the program resided as much in vehicle integration and in manufacturing as in concept development itself. Issues such as the torque tube integration, the SMA wire fatigue, and attachment problems were all addressed cost-effectively and were greatly facilitated by the program's appropriate scheduling of wind tunnel test sequences into the concept design development cycle.

Lessons learned, summaries, and recommendations for improvements for each concept have been discussed throughout the text and at the termination of the preceding sections. Further details will not be repeated in great depth here, but key developments and issues will be reiterated for completeness. Also, it is appropriate to revisit the very ambitious group of tasks that were included in the "wish list" at program inception, some of which had to be curtailed or deferred to a follow-on activity, and to reflect on the overall program progress.

6.1 PROGRAM SELF-ASSESSMENT

Figure 6-1 takes stock of the program's accomplishments, including those activities that proved beyond the state of technology, and provides an overall rating for all smart concepts examined. High marks are given for all of the wind tunnel subscale model testing that collectively established proof of concept for (1) the development of the SMA torque tubes to demonstrate spanwise twist, and (2) SMA wire-actuated trailing edge flap and aileron. Torque tube development was taken to a new level in terms of the training and torque levels (up to 3,200 in-lb); the installation difficulties were overcome and the program goal of 5 degrees of spanwise twist was achieved. Similarly, suitable SMA flap and aileron models were developed and anticipated aerodynamic benefits established. Figure 6-1 shows that requirements were fully met for the first wind tunnel test; progress for the second wind tunnel test is rated "partially covered" since, while there were improved control surface fatigue characteristics that resulted in design improvements, the facesheet failure inhibited further characterization of flap performance.

On the debit side, three requirements in Figure 6-1 – the contoured leading edge, a distributed fiber-optic sensor array for active flight control, and aeroelastic control – stand out as areas where the program fell short of original expectations. While given an "X" or "~" rating because they could not be accomplished with the funding available, these activities are nevertheless candidates for further effort. A more specific discussion of these areas is provided in the following paragraphs.

Contoured Leading Edge. A lack of wing depth, combined with higher model air loads compared to the trailing edge requirement, proved to be the stumbling block. As stated earlier, the SMA design requires a certain wire length to achieve appreciable deflection for the control surface for a given stiffness. Because the structure had to be much stiffer at the leading edge to resist air loads and the thickness to chord ratio of the plan form chosen was prohibitively small ($t/c = 0.06$), a wire long enough to provide significant deflection could not be readily incorporated into the model.

Distributed Array of Fiber-Optic Sensors for Active Control. In this activity the original program plans were thwarted on two counts. Fiber-optic pressure sensors were built, installed, and tested in the first wind tunnel test. And while the sensor fiber-optic data correlated quite well with colocated standard static pressures taken by conventional instruments, the processing time and control law complexities proved to be the Achilles' heel.

Aeroelastic Control. Aeroelastic and maneuver load control proved an ambitious goal for the Smart Wing Phase 1 program. Actuator rate and controllability proved too much to overcome where basic issues such as torque tube fabrication and smart actuator integration still needed to be solved. While the design, integration, and testing of slow-rate SMA trailing edge control surfaces and torque tubes proved successful, a solution to increase actuation rate is a task to be addressed in Phase 2.

<u>Requirement</u>	<u>Rating</u>	<u>Remarks</u>
1 st Wind Tunnel Test	✓	Successfully Completed Test in May 1996
SMA Torque Tubes	✓	Fabricated, Trained, Installed, and Tested Two High-Torque Tubes in Model
Contoured Leading Edge	X	Wing Depth and Large Air Loads Made Design Prohibitive
SMA Flap and Aileron	✓	Fabricated and Tested Control Surfaces, Demonstrated Aero Improvements
Distributed Fiber-Optic Pressure Sensor Array	~	Tested Partial System, Sensor/Control System Integration Still Required
2 nd Wind Tunnel Test	✓	Successfully Completed Test in July 1998
SMA Torque Tubes	✓	Improved Wing Twist to >5 deg, Increased Available Torque
SMA Flap and Aileron	~	Improved Fatigue and Deflected Shape, Facesheet Failure on Flap
Aeroelastic Control / Flutter Suppression	X	Control Surface Actuation Rate Not Where Required for Active Control, High-Rate Control Surfaces in Phase 2
Legend ✓ : Full ~ : Partially Covered X : Not Covered		

Figure 6-1. Program Requirements vs Performance

6.2 FINAL WORD ON PROGRESS AND TECHNOLOGY TRANSITION

Recapping once more the program accomplishments and reflecting on some of the important developments and lessons learned, it can be confidently stated that the major program goals were achieved. At the highest level, a 16 percent scale wind tunnel model of a fighter attack aircraft, to be used as a proof-of-concept smart adaptive test bed, was successfully designed, fabricated, and tested at NASA LaRC TDT wind tunnel facility. NASA participation was indispensable, and the team worked effectively in pulling together resources from the government, industry and academia.

Some of the more detailed program accomplishments, lessons learned, and knowledge assimilated include, but are not limited to:

- Design, fabrication, training, and testing of various sized SMA torque tubes, with torque ranging from 500 to 3,200 in-lb, was performed.
- Tube design database encompassing rules and curves was developed that is valid for all designs up to 10,000 in-lb.

- Methods of connecting SMA torque tubes to the structure were developed. It was confirmed that NiTi cannot be welded or brazed so mechanical methods of transmitting the large torques had to be developed. For small-scale model configurations, this issue is even more challenging because of the wing depth restrictions.
- While no leading edge applications were demonstrated, the trailing edge concepts were highly developed. Flap and aileron control surfaces were successfully built and tested for both wind tunnel tests.
- It became apparent after the first wind tunnel test that flap and aileron performance could be improved in spanwise variation of deflection and fatigue properties:
 - Spanwise variation of the deflection – Control issues and control surface fatigue problems prevented the ability to preserve a uniform, spanwise deflected angle. This problem was solved and demonstrated in the second wind tunnel entry by supplying independent power control to separate and multiple control surface sections. This permitted small corrections of tip deflection to be sensed and also equated to constant tip deflection.
 - Fatigue properties of the close-out tip – In Test 2, the Torlon tip was replaced by aluminum, which greatly diminished fatigue degradation of the control surface.
- Failure in the flap during the second wind tunnel entry curtailed further flap data acquisition, but subsequent analysis and tensile tests contributed to a greater understanding of the flap facesheet applied forces, which will lead to improvements in future designs.
- Reported variously throughout the document, performance improvements were shown in the 10 to 15 percent range in lift, pitch, and roll moment, and drag levels were too low to quantify. While the actual numbers will be aircraft configuration dependent, it should be recognized that these improvements are scaleable and applicable to almost all air vehicles.
- The combined effects of the TDT flow conditions, model size, and balance used during the testing precluded accurate and repeatable axial force measurements needed to quantify drag improvements.

The overriding conclusion for technology transition is that the current design of the SMA flap and aileron, while suitable for low-rate applications, is limited for high-speed maneuvers. The use of SMA wires with today's technology limits actuation frequency to around 1 to 3 Hz maximum. In follow-on programs, hybrid systems that use the force from SMA materials with the high frequency of the piezoelectrics should be employed. The SMA torque tube has niche applications for which high torque and low rate are required with the minimum of weight impact. To realize the promise of the technologies and concepts developed here on full-scale operational aircraft, issues related to power supplies, cost, system reliability, and overall system integration need to be addressed.

Several of the above issues and important limitations encountered in Phase 1, such as low actuation bandwidth, restricted range of deflections, and limited number and range of test parameters, are being addressed in Phase 2. At the end of Phase 2, the technology readiness level is expected to be significantly higher and perhaps sufficient to perform flight testing, paving the way for the eventual development of a revolutionary "smart air vehicle."

7. REFERENCES

1. Kudva, J. N., et al., "Adaptive smart wing design for military aircraft: requirements, concepts and payoffs," Paper No. 2447-04, SPIE North American Conference on "Smart Structures and Materials," San Diego, California, February 26 - March 3, 1995.
2. Crowe, C. R. and Sater, J. M., "Smart Aircraft Structures," AGARD Conference on Future Aerospace Technology in the Service of the Alliance, Affordable Combat Aircraft Symposia, AGARD-CP-600, Vol. 1, Paper A20, April 14-17, 1997.
3. Kudva, J. N., Lockyer A. J., and Appa, K., "Adaptive Aircraft Wing," Paper No. 9, AGARD Lecture Series 205, Smart Structures and Materials: Implications for Military Aircraft of New Generation, Invited Paper presented at AGARD Meetings in Philadelphia, Amsterdam, and Paris.
4. Kudva, J. N., "Exploiting Smart Structures Technologies for Military Aircraft Applications – Perspective on Development of a Smart Air Vehicle," AIAA - SDM St. Louis, MO, 13 - 15 April 1999.
5. Redeker, G., Wichmann, G., and Oelker, H-C., "Aerodynamic Investigations Toward an Adaptive Airfoil for a Transonic Transport Aircraft," Journal of Aircraft, Vol. 23, No. 5, pp. 398-405, May 1986.
6. Spillman, J. J., "The use of variable camber to reduce drag, weight and costs of transport aircraft," *Aeronautical Journal*, Jan. 1992, pp. 1-9.
7. Fielding, J.P., and Vaziry-Zanjany, M.A.F., "Reliability, Maintainability, and Development Cost Implications of Variable Camber Wings," *Aeronautical Journal*, pp. 183-195, May 1996.
8. Wong, K.J., "AFTI/F111 Mission Adaptive Wing Lift and Drag Flight Test Results," AFFTC-TR-86-42, Final Report, March 1987.
9. Cogburn, L.T., "AFTI/F111 Mission Adaptive Wing Flutter and Aeroservoelastic Test Program," AFFTC-TR-86-42, Final Report, April 1987.
10. Hall, J.M., "Executive Summary AFTI/F-111 Mission Adaptive Wing," WRDC-TR-89-3083, September 1989.
11. Bonnema, K. L. and Lokos, W. L., "AFTI/F-111 Mission Adaptive Wing Flight Test Instrumentation Overview," *Proceedings of the 35th International Symposium of the Instrumentation Society of America*, April-May 1989.
12. Miller, G.D., "Active Flexible Wing (AFW) Technology," AFWAL-TR-87-3096, February 1988.
13. Buttrill, C., et al., "Simulation and Model Reduction for the AFW Program, AIAA-92-2081, presented at AIAA Dynamics Specialists Conference in Dallas, Texas, April 16-17, 1992

14. Kudva, J.N., et al., "Overview of the ARPA/WL 'Smart Structures and Material Development – Smart Wing' Contract," Paper No. 2721-02, SPIE North American Conference on "Smart Structures and Materials," San Diego, CA, February 26-29, 1996.
15. Kudva, J. N., et al., "Overview of the DARPA/AFRL/NASA Smart Wing Program," Paper No. 3674-26, SPIE Symposium on Smart Structures and Materials, Newport Beach, CA, March 1-4, 1999.
16. Funakubo, H., *Shape Memory Alloys*, Gordon & Breach Science Publishers, ISBN No. 2-88124-136-0, 1986.
17. Jackson, C.M., Wagner, H.J., and Wasilewski, R. J., "55_Nitinol, The Alloy With a Memory: Its Physical Metallurgy, Properties and Applications," NASA-SP-5110, 191, p. 91.
18. Jardine, A. P., et al., "Shape Memory Alloy TiNi Actuators for Twist Control of Smart Wing Designs," Paper No. 2716-10, SPIE North American Conference on "Smart Structures and Materials," San Diego, California, February 26 - February 29, 1996.
19. Jardine, A. P., Flanagan, J., Jasmin, L., and Carpenter, B. F., "Smart Wing Shape Memory Alloy Actuator Design and Performance," Paper No. 3044-04, SPIE North American Conference on "Smart Structures and Materials," San Diego, CA, March 3-6, 1997.
20. Jardine, A. P., et al., "Improved Design and Performance of the SMA Torque Tube for the Smart Wing Program," Paper No. 3674-29, SPIE Symposium on Smart Structures and Materials, Newport Beach, CA, March 1-4, 1999.
21. Misra, M.S., et al., "Adaptive Structure Design Employing Shape Memory Actuators," Paper No. 15, AGARD-CP-531, presented at the 75th meeting of the AGARD Structures and Materials Panel, Lindau, Germany, 5-7 October 1992.
22. Maclean, B.J., Carpenter, B.F., Draper, J. S., and Misra, M.S., "A Shape Memory Actuated Compliant Control Surface," SPIE, Vol. 1917, "Smart Structures and Intelligent Systems," 1993, pp. 809-818.
23. Martin, C. A., Jasmin, L., Appa, K., and Kudva, J. N., "Smart Wing Wind Tunnel Model Design," Paper No. 3044-03, SPIE North American Conference on "Smart Structures and Materials," San Diego, CA, March 3-6, 1997.
24. Martin, C. A., et al, "Design and Fabrication of Smart Wing Model and SMA Control Surfaces," Paper No. 3674-27, SPIE Symposium on Smart Structures and Materials, Newport Beach, CA, March 1-4, 1999.
25. NASA Langley Research Center, "Wind Tunnel Design Criteria," Report Number LHB 1710.15, May 1992.
26. Bisplinghoff R. L., Ashley, H., Halfman, R. L., *Aeroelasticity*, Addison-Wesley, Cambridge, MA, 1955.
27. Johnson, E.H., and Venkayya, V. B., "Automated Structural Optimization System (ASTROS)," Vol. I, II and III, AFWAL-TR-88-3028, December, 1988.

28. Bruhn, E. F., *Analysis and Design of Flight Vehicle Structures*, Jacobs Publishing, Indianapolis, IN, 1973.
29. Peery, D. J. and Azar, J. J., *Aircraft Structures*, McGraw-Hill, Inc., New York, 1982.
30. Shigley, J. E., *Mechanical Engineering Design*, McGraw-Hill, Inc., New York, 1963.
31. Roark, R. and Young, W., *Formulas for Stress and Strain, Fifth Edition*, McGraw-Hill, Inc., New York, 1975.
32. Scherer, L. B., Martin, C. A., Appa, K., Kudva, J. N., and West, M., "Smart Wing Wind Tunnel Test Results," Paper No. 3044-05, SPIE North American Conference on "Smart Structures and Materials," San Diego, CA, March 3-6, 1997.
33. Scherer, L. B., et al., "DARPA/AFRL/NASA Smart Wing Second Wind Tunnel Test Results," Paper No. 3674-28, SPIE Symposium on Smart Structures and Materials, Newport Beach, CA, March 1-4, 1999.
34. Duncan, P. G., Jones, M. E., Shinpaugh, K. A., Poland, S. H., Murphy, K. A., and Claus, R. O., "Optical Fiber Pressure Sensors for Adaptive Wings", Paper No. 3042-41, SPIE North American Conference on "Smart Structures and Materials," San Diego, CA, March 3-6, 1997.
35. NASA Langley Research Center, "The Langley Transonic Dynamics Tunnel," NASA Langley Working Paper LWP-799, 1969.
36. Burner, A. W., Martinson, F. D., "Automated Wing Twist and Bending Measurements Under Aerodynamic Load," 19th AIAA Advanced Measurement and Ground Testing Conference, New Orleans, LA, AIAA 96-2253, June 1996.
37. Rae, W. H. Jr., Pope, A., *Low-Speed Wind Tunnel Testing*, John Wiley and Sons, New York, 1984.
38. Alexander, M., "Subsonic Wind Tunnel Testing," Report Number WL-TR-91-3073, 1991.

VOLUME II

TRANSONIC CRUISE OPTIMIZATION

Table of Contents

VOLUME II TRANSONIC CRUISE OPTIMIZATION

1.	Introduction.....	II-1
2.	Terfenol-D Powered Elastic-Wave Linear Motor Overview.....	II-3
3.	Adaptive Wing for Efficient Transonic Cruise.....	II-6
	3.1 Aircraft Selection for Adaptive Wing Investigation.....	II-6
	3.2 Preliminary Pay-off Studies	II-7
	3.3 Adaptive Wing Shape-Control Concept	II-8
	3.4 Computation of Airfoil Shapes	II-9
4.	Terfenol-D Powered Smart Trailing Edge for Transonic Cruise.....	II-13
	4.1 Concepts and Trade Studies	II-14
	4.2 Preliminary Design Optimization of Smart Trailing Edge	II-16
	4.3 Smart Trailing Edge With Combined Motion	II-19
	4.4 Navier-Stokes Comparison Studies.....	II-20
5.	Linear Motor Development	II-23
	5.1 Material Behavior	II-23
	5.2 Magnetic Analysis	II-23
	5.3 Phase 1 Motor Testing	II-26
6.	Phase 2 Program	II-44
	6.1 Mechanical.....	II-44
	6.2 Magnetic	II-44
	6.3 Power.....	II-45
	6.4 Thermal Design	II-45
	6.5 Tribology.....	II-45
	6.6 Modeling	II-45
7.	Conclusions	II-46
8.	References.....	II-47

Table of Figures

VOLUME II TRANSONIC CRUISE OPTIMIZATION

Figure	Page
1-1. TERFENOL-D Powered Smart Trailing Edge	II-2
1-2. TERFENOL-D Elastic -Wave Linear Motor	II-2
2-1. Linear Actuator Principle	II-3
2-2. Example of a 4-2 Shift Pattern.....	II-4
3-1. Drag and Thrust Match for Gulfstream III.....	II-7
3-2. Gulfstream III Range Sensitivities	II-8
3-3. Method of Controlling Airfoil Shape	II-9
3-4. Cambered Airfoil at $M_\infty = 0.78$ and $CL = 0.60$	II-10
3-5. Baseline $M_\infty = 0.78$ and $CL = 0.50$ Airfoil Design and 50% Flexed Design at an Off-Design $M_\infty = 0.80$ Using 4 Control Points	II-11
3-6. Drag Reduction Characteristics Versus Number of Control Points and the Extent of Upper Surface Adaptation at an Off-Design Condition of $M_\infty = 0.80$	II-12
3-7. Drag Reduction Characteristics of the $CL = 0.50$ Cambered Baseline Airfoil Design at the Off-Design Lift Coefficients and Mach Number Using 4 Control Points.....	II-12
4-1. TERFENOL-D Powered Smart Trailing Edge	II-15
4-2. Segmented Multi-Flap System.....	II-15
4-3. Drag Reduction with TERFENOL-D Powered Smart Trailing Edge.....	II-17
4-4. Multi-Point Optimized Segmented Flap Solution.....	II-17
4-5. Comparison of the Computed GRUMFOIL Pressure Distribution for the Baseline Airfoil and an Optimized Compromise Flap System at Two Different Mach Numbers and Lift Coefficients	II-18
4-6. Percent Decrease in UAV Fuel Consumption for Constant Range	II-19
4-7. Percent Increase in UAV Loiter Time and Range for Constant Fuel.....	II-19
4-8. Drag Comparison with and Without Optimized Three-Segment Flap ($Re = 20$ Million).....	II-20
4-9. Geometry of the Three-Segment Flap Configuration at the Highest Lift in Each Range	II-21
4-10. Comparison of the Navier-Stokes and GRUMFOIL Predicted Drag Reduction with the Optimized Flap Deployment for a Two-Segment Smart Trailing Edge ($Re = 5$ Million)	II-22

Table of Figures (continued)

5-1.	Effect of Improved Construction on Magnetic Field.....	II-24
5-2.	Typical Coil Trade Study	II-24
5-3.	Superposition of Coil Fields to Achieve Approximate Square-Wave Excitation	II-25
5-4.	Coil Thermal Analyses	II-25
5-5.	POC-1 Elastic-Wave Linear-Motor Testing.....	II-26
5-6.	Typical Motor Test Results.....	II-27
5-7.	Linear Motor Designs for Phase 1 (POC-1) and Phase 2 (POC-2)	II-27
5-8.	Smart Trailing Edge Experiment.....	II-28
5-9.	Sweep Frequencies as a Function of Speed Voltage and Pattern.....	II-29
5-10.	Pattern 4-2 Retracting Under an 8 lb Tension Load.....	II-29
5-11.	Summary of Runs at Speed Settings of 1.5 and 2 Volts.....	II-30
5-12.	Speed vs Load at 2.2 in. Displacement	II-31
5-13.	Speed vs Frequency at 2.2 in. for No Load and Various Pattern (Retraction Velocities are Shown Positive to Compare with Extension)	II-32
5-14.	Speed vs Frequency at 2.2 in. for Retraction with an 8-4 Pattern for the Unloaded Case and a 4 lb. Tension Load	II-32
5-15.	Speed at 2.2 in. vs Frequency for a 4-2 Pattern for Various Opposing Tension Loads	II-33
5-16.	Variation of Retraction Speed at 2.2 in. with Sweep Frequency for the 2-1 Pattern for Various Tension Loads	II-33
5-17.	Variation of Retraction Speed with Tension Load for Various Speed Voltage Settings.....	II-34
5-18.	Stall Force/Blocked Armature Testing Matrix	II-35
5-19.	Retraction – Blocked Actuator Force at a Displacement of 1.875 in. for Various Sweep Patterns and Speed Voltage Settings	II-36
5-20.	Extension – Blocked Actuator Force at a Displacement of 1.953 in. for Various Sweep Patterns and Speed Voltage Settings	II-36
5-21.	Retraction – Blocked Actuator Force at a Displacement of 2.24 in. for Various Sweep Patterns and Speed Voltage Settings	II-37
5-22.	Extension – Blocked Actuator Force at a Displacement of 2.311 in. for Various Sweep Patterns and Speed Voltage Settings	II-37
5-23.	Retraction – Blocked Actuator Force at a Displacement of 3.077 in. for Various Sweep Patterns and Speed Voltage Settings	II-38
5-24.	Extension – Blocked Actuator Force at a Displacement of 3.154 in. for Various Sweep Patterns and Speed Voltage Settings	II-38
5-25.	Retraction – Blocked Actuator Force for Various Patterns and Speed Voltage Settings as a Function of Position.....	II-39
5-26.	Blocked Actuator Force as a Function of Sweep Pattern for Various Sweep Speed Voltages.....	II-39
5-27.	Comparison of Effectiveness of Pattern Modification upon Speed at Different Compressive Loads	II-40
5-28.	Comparison of Load-Handling Capability of Special Pattern to a Standard Pattern	II-40

Table of Figures (continued)

5-29.	Blocked Force of Repaired Actuator as a Function of Sweep Pattern for Various Sweep Speed Voltages	II-41
5-30.	Variation of Mean Velocity with Actuator Usage.....	II-42
5-31.	Degradation in Average Speed Over Full Stroke, 4/13/98 to 5/12/98	II-43

1. INTRODUCTION

Transport aircraft as well as manned and unmanned attack and surveillance aircraft generally have multiple cruise requirements. Transports may cruise at slower speeds to minimize fuel usage, or at higher speeds to maximize the number of daily trips or make up for schedule delays. Attack and surveillance aircraft dash to the battle zone, then loiter to detect and attack enemy targets, or gather information at a speed and altitude consistent with optimum sensor performance. After burning most of its fuel and possibly releasing its munitions, the vehicle returning from a long flight can weigh only a fraction of its takeoff weight. Also, large variations can occur in commercial aircraft passenger and cargo loads. Consequently, the wing must accommodate large changes in lift. A single wing profile cannot be optimum for all of these flight conditions. In the transonic region strong shocks develop when the wing shape is not optimum for the flight condition, and the resulting increased drag can have a significant adverse effect on the aircraft's performance. Consequently, with today's technology, a larger engine and additional fuel must be provided to accommodate nonoptimal flight. However, by small modifications to the wing's surface, it is possible to maintain a near-optimum wing shape as the flight condition changes so that drag is minimized and cruise performance is significantly improved. Our studies show that fuel savings on the order of 5 percent are realizable. Since commercial jets use 13 billion gallons of fuel each year, at an annual cost of \$7 billion, saving even a small portion of this fuel would provide significant economic and ecological benefits. The goal of the Transonic Cruise portion of the Smart Materials and Structures Development Program is to employ TERFENOL-D, a smart material, to modify the wing shape during flight to achieve optimum wing performance. TERFENOL-D is an alloy of the rare earth elements, terbium and dysprosium, with iron. The material is magnetostrictive; i.e., it deforms in the presence of a magnetic field.

Since it is impractical to deform the stiff ribs that comprise the wing's structural frame by using smart materials to apply loads to the structure, our initial concept involved the use of truss-type smart ribs that change geometry. Linear actuators comprised the triangular truss members that would change the truss's shape by extending and retracting. The upper and lower wing covers are sheet material that is attached to the ribs, and the covers bend easily as the ribs change shape. It was shown analytically and demonstrated experimentally that, by this technique, it is possible to achieve desired wing shapes with very high surface accuracy. A TERFENOL-D elastic-wave linear motor was being developed for use as the variable-length truss member. However, during the wing development program, it became apparent that, with near-term technology, additional drag induced as a result of the system weight increase caused primarily by the large number of required actuators would offset the benefits of the adaptive-wing concept. The approach could be used in the future if sufficiently light actuators could be developed that met the system requirements.

Alternatively, it was found that a TERFENOL-D powered smart trailing edge could affect the shock waves in the transonic region, thus reducing drag such that optimum performance would be maintained over all required flight conditions. The trailing edge concept is relatively light in weight and can increase range, reduce the time to reach the threat, and increase loiter times with smaller engines and less fuel capacity.

The TERFENOL-D powered sSmart trailing edge is shown in Figure 1-1. Instead of deforming wing structure, TERFENOL-D elastic-wave linear motors are used in conjunction with a mechanism to provide a combination of translational as well as rotational motion to maintain a smooth upper-wing surface. If additional control of the shape of the upper surface is needed, several flap segments, each powered by a TERFENOL-D motor, can be employed in tandem. Drag is further minimized by locating the actuator and associated hardware completely within the contour of the airfoil. By using speed and fuel-flow measurements, the smart trailing edge constantly adjusts itself to minimize drag.

The TERFENOL-D elastic-wave linear motor is shown in Figure 1-2. It has only one moving component, a rod of TERFENOL-D, which is held in a stator tube by a shrink fit. By exciting a magnetic wave in the coils, an elastic wave is induced in the TERFENOL-D rod, causing it to move within the tube. In this program, a proof-of-concept Phase 1 (POC-1) motor has been developed and successfully demonstrated. The POC-1 motor is 9 inches long when contracted, has a travel of 1.5 inches, and can exert a maximum force of 28 pounds. When the motor is fully developed, it will be an excellent actuator for the transonic cruise application. Moreover, with only one moving part, it can be made highly reliable. It automatically locks in the event of a power failure and, therefore, has a natural fail-safe feature. It has no slop or end play; consequently, flap flutter is eliminated and accurate control can be easily accomplished. It also fits in with the Air-Force's all-electric aircraft initiative.

The motor and its operating principle are described in Section 2. The adaptive-wing concept is discussed in Section 3. The smart trailing edge is discussed in Section 4. Motor development and testing are described in Section 5. Section 6 contains a brief discussion of the Phase 2 follow-on program.

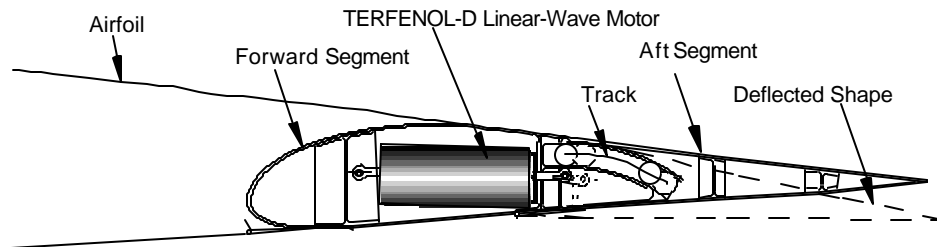


Figure 1-1. TERFENOL-D Powered Smart Trailing Edge

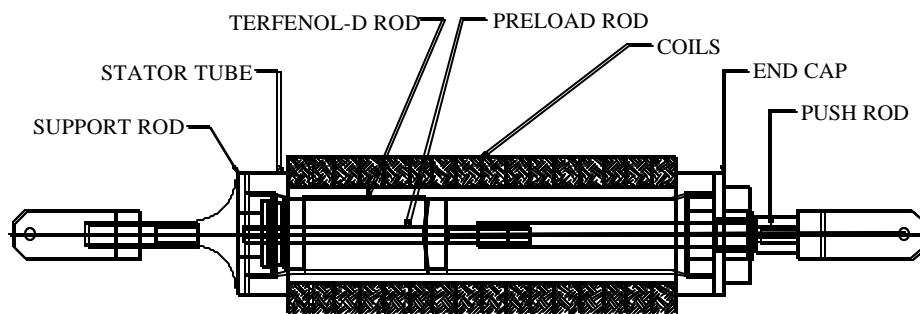


Figure 1-2. TERFENOL-D Elastic-Wave Linear Motor

2. TERFENOL-D POWERED ELASTIC-WAVE LINEAR MOTOR OVERVIEW

TERFENOL-D motors have the potential to meet the Smart Wing transonic-cruise program requirements. Currently in development is an ETEMA TERFENOL-D[®] linear motor, which uses the natural phenomenon of conservation of volume as TERFENOL-D undergoes strain in a magnetic field. Accordingly, as the rod elongates, its diameter decreases slightly. The TERFENOL-D is placed in a stator tube of nonmagnetic material. By carefully fabricating the stator and the rod to high tolerances, the TERFENOL-D has an interference fit in the stator when no field is present and has a clearance fit when the field is present. Using this characteristic, the portion of the rod that is not affected by the localized magnetic field provides a very high locking force while the segments of the rod that are affected provide the actuation force. As shown in Figure 2-1, if many small coils are used along the length of the motor instead of one full-length coil, they can be turned on sequentially in a wave motion that will cause the TERFENOL-D rod to move in the direction opposite to that of the magnetic wave. In the beginning of a cycle, this wave will cause the left end of the rod to fit loosely and extend while the remainder of the material to the right is held in a shrink fit. Then the left end is held in a shrink fit as material to the right is progressively loosened and moved left. Finally, the right-most material moves left to complete the cycle. This concept was discovered in Germany by Dr. Lothar Kiesewetter at the University of Berlin.

In practice, the coils are energized in groups to optimize performance. The group energization sequence is called the “shift pattern.” An example of a 4-shift-2 pattern (abbreviated “4-2”) is shown in Figure 2-2 for a motor with 16 coils. Initially, the first 4 coils are energized. Then coils 1 and 2 are turned off and coils 5 and 6 are turned on. At successive intervals, the group of 4 energized coils is shifted by 2 coils. A complete cycle requires eight time intervals, i.e., eight shifts.

The speed of the motor is determined by the frequency at which the coils are energized, the shift pattern, the magnetic design, and the applied voltage. The holding power, to withstand aircraft maneuver loads, is also a function of these parameters as well as the length and number of rod sections.

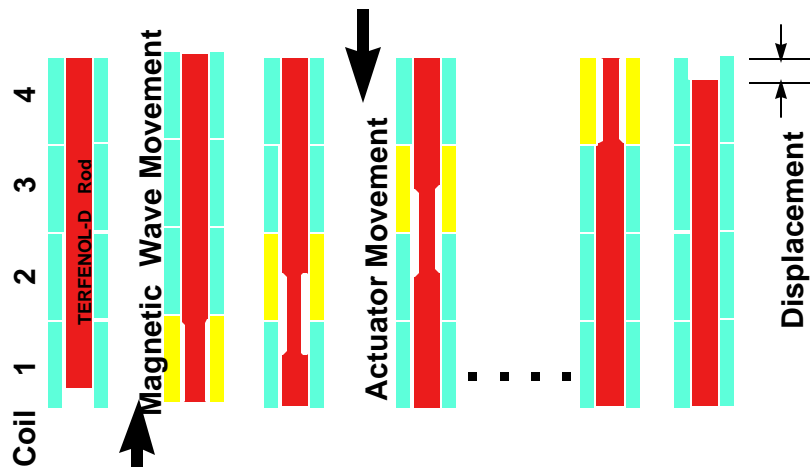


Figure 2-1. Linear Actuator Principle

Time Interval Index	Binary Control Signal	Active Coils
1	0000000000001111	1-4
2	0000000000111100	3-6
3	0000000011110000	5-8
4	0000001111000000	7-10
5	0000111100000000	9-12
6	0011110000000000	11-14
7	1111000000000000	13-16
8	1100000000000011	1,2,15,16

Figure 2-2. Example of a 4-2 Shift Pattern

There are benefits and characteristics of both the magnetostrictive TERFENOL-D smart material and the elastic-wave linear motor concept that make this combination attractive for the Smart Wing program. The benefits include:

- Only one moving part
- Fail-safe lock-up upon power loss
- Zero backlash / end play
- Long stroke
- Micro-positioning
- High holding force
- Self-contained
- High stiffness
- Low voltage
- Lightweight
- High reliability
- Potential for low power consumption

The proof-of-concept TERFENOL-D motor, POC-1, shown in Figure 1-2, was constructed for the Smart Wing program. The motor is 9 inches long when contracted, has a travel of 1.5 inches, and can exert a force of 28 pounds. The maximum velocity is 0.05 inch/second. Motor development is described in References 1 through 5 and Section 5.

Tests have established coefficients of friction (static and dynamic) between TERFENOL-D and several candidate materials for use in the motor. Also, strength, wear resistance, thermal-expansion coefficient, weight, machinability, and cost comparisons have been completed for different tube materials. In the first test motor, 304 SS steel was used for the tube; however, to better match the thermal expansion of the tube to the TERFENOL-D, HAYNES[®] Alloy 242[™] was used in the POC-1 motor.

A second area of analysis was the design of the coil system which supplies the moving magnetic field in the motor. Calculations and tests determined the number of coils, the size of the coils and their time constants, switching frequencies, and field strengths needed to achieve the desired performance. Sixteen coils are used in POC-1. Size, weight, and power estimates were iterated with material choices and calculations of forces. The concept can be scaled to larger or smaller proportions.

The experimental motor has been used to extrapolate the characteristics of full-scale actuators. If necessary, ETREMA can grow TERFENOL-D to a diameter of 3 inches, which will be able to supply over 7,000 pounds of force. The design has only one moving part and will be able to operate over a wide range of temperatures. With power off, the system is locked and, therefore, meets the fail-safe requirement to hold position in the event of a power failure.

3. ADAPTIVE WING FOR EFFICIENT TRANSONIC CRUISE

In this section, the development of aircraft lifting surfaces that change shape to enable relatively shock-free performance throughout a range of design points in the transonic region is described. This type of reduced-drag airfoil has the potential to increase range, decrease fuel expenditure, increase cruising speed, increase lift, or accomplish a combination of these desirable effects. Preliminary payoff studies on a Gulfstream III aircraft with a hypothetical smart wing show that if 1,000 pounds were added to the weight of the aircraft to incorporate smart wing technology and the coefficient of drag C_D could be decreased by 20 counts (0.0020), 5 percent less fuel would be required or the range could be increased by 5 percent with the existing fuel. However, as discussed in Subsection 4.2, until it becomes technologically possible to substantially reduce the weight of the actuation system and structure, the expected benefits cannot be achieved with the adaptive wing. An alternative concept described in Subsection 4.2, however, does provide significantly enhanced performance.

In this section, airfoil shapes are computed with a stochastic optimization method based on simulated annealing using drag as the variable. Drag reduction is presented as a function of flight condition, region of surface control, and number of actuators. Design and development of an experimental TERFENOL-D actuator to provide the variable airfoil shape required for optimum performance are also discussed. Our work in the exploration of adaptive wings to improve aircraft performance during transonic cruise is described in detail in References 6 through 11. The required shape changes to maintain optimum performance as the flight condition changes are small and, therefore, are potentially achievable.

The shape of the wing can only be varied between the spars, the longitudinal beams comprising the wing structural frame; consequently the benefits are limited by these constraints. We have investigated a method to control airfoil shapes between the spars of a two-spar wing. The ribs are trusses employing, as diagonal members, linear actuators that expand and retract to vary the structural shape. The shape control-system gain matrix uses a finite-element model of the structure with the actuators absent; therefore, the procedure is simplified since it does not require models of complex actuators. The control system minimizes the error between the desired and achievable shapes.

3.1 AIRCRAFT SELECTION FOR ADAPTIVE WING INVESTIGATION

There are two broad categories of aircraft: transport and reconnaissance aircraft with their long cruise requirements, and fighter and attack aircraft with maneuverability as well as cruise requirements. Both categories must operate at multiple performance points. Fighter and attack aircraft require cruise, maneuver, and dash capability. Transport and reconnaissance aircraft also must be designed for a significant variation of flight conditions since payload variations and fuel consumed during cruise can reduce weight (and hence required lift) by 30 to 40 percent.

The multiple design requirements for fighter and attack aircraft, high speed with maximum range and maneuvering, are the most diverse. However, although many newer fighter and attack aircraft have internal stores, some carry external stores or pods, with drag contributions that may be much greater than that of the wing. Compared to a transport, a drag reduction for the fighter wing translates into a smaller fraction of the total aircraft drag. In addition, the utilization of fighter and attack aircraft is lower relative to commercial aircraft. Thus, a benefit in reduced wing drag for a fighter translates into a smaller dollar savings.

Transport aircraft do little else but cruise, with the drag due to the wing being the primary component. They have a high utilization rate, so that a drag benefit for the aircraft would translate into significant dollar savings. Thus, reducing the drag of the wing can provide a significant mission performance improvement. Since smart structures technology allows independent multiple cruise-point optimization, a transport aircraft offers greater quantifiable benefits. Relative to

fighter and attack aircraft, a transport will provide more fuel savings for a wing drag reduction. Although a generic transport aircraft could have been designed for the purposes of this study, it was decided to base the analysis on a real aircraft.

The Gulfstream III has been selected as the candidate aircraft for studying smart wing performance in Phase 1. Its wing is representative of commercial and military transports, and it employs supercritical wing technology. It was designed at Northrop Grumman; consequently, we are familiar with the weight and structure of the aircraft. In anticipation of future flight experiments, it is a modest-size aircraft that could be equipped with a smart wing and flight tested at a moderate cost.

3.2 PRELIMINARY PAY-OFF STUDIES

3.2.1 Background

For a fixed wing shape, drag increases for increased lift and higher speeds. The increase in drag with speed is the *drag rise*. There is a rapid increase in drag at transonic speeds because of shock formation. This rapid increase is the *drag divergence* and develops more quickly for thicker wings or higher lift. The large drag increase for a small increase in speed is the primary effect limiting the speed for high-speed dash or efficient cruise.

A performance model of the Gulfstream III was developed. Figure 3-1 illustrates the drag (C_D) and thrust (C_T) match for this model. Each lift coefficient (C_L) has a different subsonic drag level and drag rise. The thrust lines represent maximum available thrust, hence the intersection with a drag line would be the maximum level flight speed for that lift coefficient. The match point would be different for cruise since a thrust somewhat lower than the maximum available thrust is employed to achieve a compromise between high speed and low fuel expenditure, but the effect of the drag rise is essentially the same. The smart wing design challenge is to move all C_L curves to the right to enable higher speed cruise at lower drag.

Typically, as wing thickness increases, wing weight is reduced, but the transonic drag divergence is more severe. Thus, the usual compromise in a wing design is to balance the opposing effects of maximizing the wing thickness while minimizing drag. Smart wing technology offers the additional benefit of reducing drag with larger wing thickness.

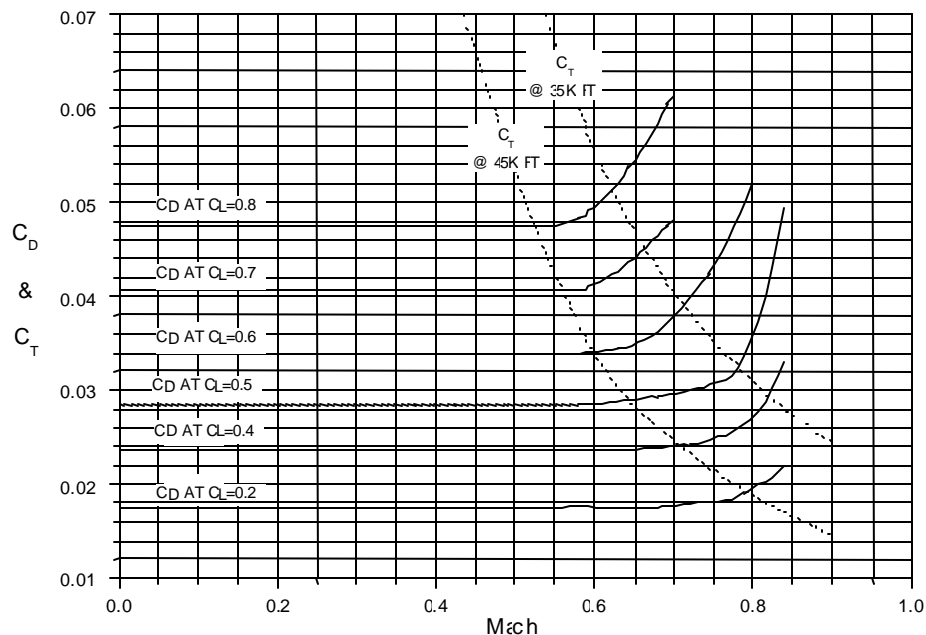


Figure 3-1. Drag and Thrust Match for Gulfstream III

3.2.2 Performance Estimates

To determine the benefits of shock-free cruise and include the influence of the weight added to incorporate smart wing technology, range sensitivities to weight and drag changes were calculated with the performance model of the Gulfstream III. The reference conditions for the sensitivities are a takeoff gross weight (TOGW) of 67,800 pounds, 27,900 pounds of fuel, and a range of 4,029 nm. The range calculations include takeoff, climb, cruise at best Mach number and altitude, and 30 minutes loiter at sea level. Efficient cruise conditions were determined by the program. Cruise altitude varied from 41,800 to 45,000 feet, with corresponding cruise Mach numbers ranging from 0.74 to 0.72.

Figure 3-2 summarizes the results. The nominal conditions are shown in the first line of the table. As indicated, a drag reduction of 0.0020 (20 counts) increases the range 6.8 percent, while combining the drag reduction with 1,000 pounds of added weight increases the range 4.8 percent. Also, the fuel required can be reduced by 1,000 pounds with a range increase of 4.6 percent if the cruise drag coefficient is reduced by 0.0030. The results are approximately linear, so that the consequences of other variations in weight, fuel, and drag can be estimated from the table.

Instead of increasing range or decreasing fuel expenditure, the smart wing technology could be used to increase speed or to achieve a combination of these effects. From the table, it can be determined that if the technology required a 1,000 pound structural weight increase and a drag reduction of 0.0020 could be achieved, approximately 5 percent less fuel would be required to travel the same range; i.e., 1 percent of the fuel could be saved for each 4 count decrease in drag. Since commercial jets use 13 billion gallons of fuel per year, at an annual cost of \$7 billion, the savings of a small percentage of this fuel translates into a significant economic and ecological benefit.

DTOGW (lb)	DFUEL (lb)	DC_D	TOGW (lb)	FUEL (Lb)	RANGE (NM)	DR/R_{REF} (%)
0	0	0	67,800	27,900	4,029	0
0	0	-0.0020	67,800	27,900	4,301	6.75
+1,000	0	-0.0020	68,800	27,900	4,223	4.79
+2,000	0	0	69,800	27,900	3,887	-3.53
+2,000	0	-0.0020	69,800	27,900	4,146	2.90
+2,000	0	-0.0030	69,800	27,900	4,290	6.47
0	-1,000	0	67,800	26,900	3,816	-5.29
0	-1,000	-0.0030	67,800	26,900	4,213	4.57

Figure 3-2. Gulfstream III Range Sensitivities

3.3 ADAPTIVE WING SHAPE-CONTROL CONCEPT

The method of controlling the airfoil shape is illustrated in Figure 3-3. A two-spar wing is used with truss-type ribs. The diagonal elements are linear actuators that extend and contract to control the shape. Theoretical and experimental results confirm that highly accurate shapes can be obtained by this method.⁹



Figure 3-3. Method of Controlling Airfoil Shape

3.4 COMPUTATION OF AIRFOIL SHAPES

Optimum baseline airfoils were first designed for a given lift coefficient at a design Mach number with a specified thickness profile. A specified segment of the upper surface was then allowed to adapt to a change in-flight conditions. The perturbed airfoil shapes were developed with cubic splines that pass through the actuator-surface connection points. We refer to these connection points as *control points*.

3.4.1 Stochastic Method – Simulated Annealing

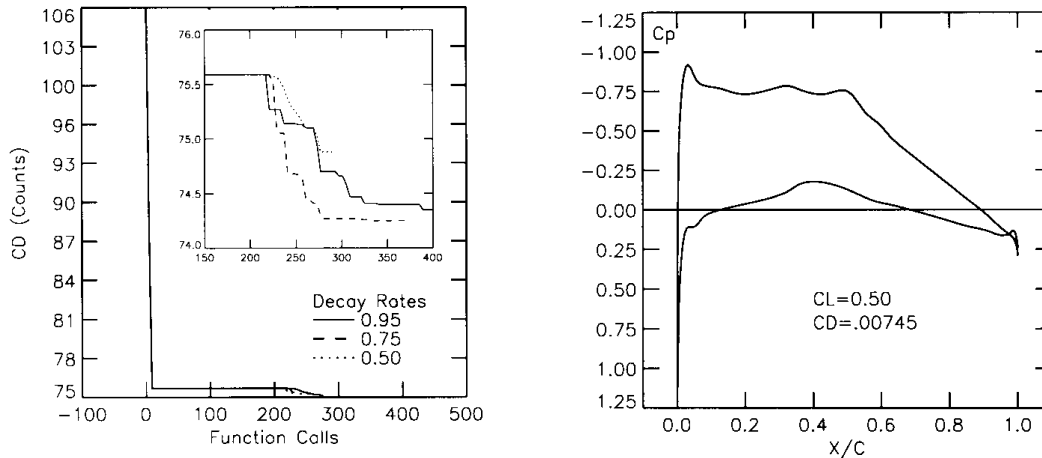
For the computation of optimum airfoil shapes, gradient methods experience difficulties when used with numerically generated sensitivity derivatives. Other difficulties arise due to numerically generated local minima as well as real local minima. Consequently, a simulated annealing method, that was modified to enhance convergence was used to obtain optimum airfoils. The method, called Simulated Annealing With Domain Decay (SADD), reliably computes near optimal airfoils.^{12,13} In SADD, the bounds of the design variable hyperspace are allowed to decay. The design space tracks and is centered about the optimum as the decay of the domain takes place. Convergence occurs when the design space boundaries meet a specified tolerance.

Since the thickness variation of the boundary layer affects the optimum airfoil shape, it was necessary to include viscous effects in the analysis. To efficiently incorporate viscosity, GRUMFOIL,¹⁴ a full potential inviscid/viscous integral turbulent boundary layer code was adapted to this design problem. GRUMFOIL was used successfully in conjunction with simulated annealing to routinely design both baseline airfoils and variable-shape airfoils with minimum drag. Shockless minimum-drag airfoils were achieved by specifying the drag as the objective function.

3.4.2 Baseline Airfoil Design

To obtain a basis of comparison for the variable-shape wings, the optimization procedure was used for designing a good baseline fixed-shape airfoil. A transonic flight Mach number of 0.78 was selected for the baseline design for a range of aircraft weights corresponding to lift coefficients that varied from 0.40 to 0.60. The thickest portion of the profile was constrained at 8 percent of the chord. For the baseline design, the thickness was held fixed at values similar to a 65A008 airfoil. A camber line, composed of fore and aft parabolas matched in the middle with a cubic function, was assumed. This shape function has four degrees of freedom, or four design variables, consisting of the locations and magnitude of the maximum displacements of the fore and aft parabolas.

Figure 3-4a shows the convergence of the objective function (drag) for the SADD scheme versus the number of analyses, or function calls, for a camber design at $C_L = 0.60$ and $M_\infty = 0.78$ initiated with the symmetric airfoil. Three curves are plotted in Figure 3-4a for three different decay rates of the domain. The inset in Figure 3-4a is an enlargement of the convergence plot for the last 150 function calls as the domain space begins to decay or converge on the locale of the optimized solution. All three solutions vary by only about 0.4 counts of drag. Figure 3-4b shows the pressure distribution for the optimum solution.



(a) SADD scheme convergence

(b) Surface pressures

Figure 3-4. Cambered Airfoil at $M_\infty=0.78$ and $C_L=0.60$

3.4.3 Adaptive Wing Airfoil Sections

Next, a portion of the airfoil is allowed to deflect in regions between 15 and 65 percent of the chord from the leading edge between the spars of an assumed two-spar wing design. The control points (actuator intersection points at the upper cover) are assumed to be evenly spaced. Preliminary computations indicated that deflecting a portion of the lower surface had a negligible effect on the drag; therefore, only the upper surface was deflected, and the lower surface remained fixed. By defining the problem in this way, both thickness and camber are affected by perturbations of the upper surface. A maximum allowable deflection of ± 0.005 of the chord is specified as a constraint to avoid major perturbations to the thickness distribution. Cubic splines define the airfoil surface between control points. A baseline airfoil is used as the initial guess and an off-design condition is used to evaluate the effectiveness of the adaptive wing concept.

The number of actuators were studied to determine the optimum number that are required to control the surface shape. This number will ultimately be used to trade actuator weight against performance. Another important parameter is the extent over which the surface shape is controlled. It must be determined whether the constraint that the airfoil surface can only be flexed (varied in shape) between rigid spars (e.g. from 15 to 65 percent of the chord) will significantly impact the drag reduction capability of the system.

Two baseline airfoils were designed at $M_\infty = 0.78$ at $C_L = 0.50$ and $C_L = 0.60$ to demonstrate the effectiveness of an adaptive wing at off-design conditions.

3.4.4 Effect of Extent of the Flexible Surface

Figure 3-5 illustrates the performance an adaptive airfoil shape designed with four evenly spaced control points between 15 and 65 percent of the chord. Figure 3-5a compares the baseline airfoil's surface pressures with that of the adaptive airfoil at $C_L = 0.50$ and an off-design Mach number of 0.80. In this case, the drag is reduced from 118 to 76 counts. The shock wave is not eliminated, but its strength is diminished. Figure 3-5b compares the shapes (enlarged vertically) of the baseline and flexed airfoils. The drag reduction process reduces the thickness over the flexed portion of the airfoil.

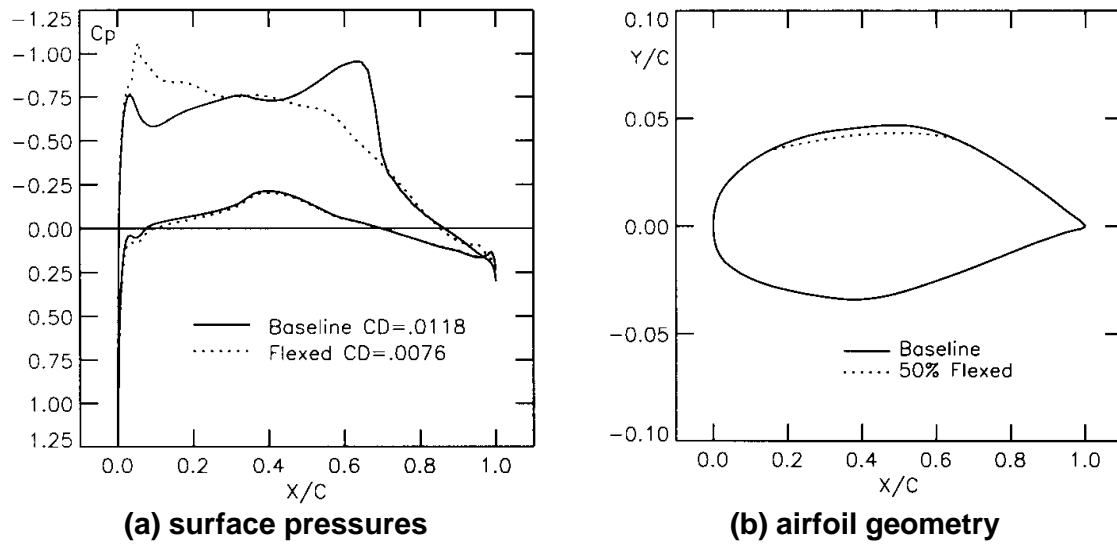
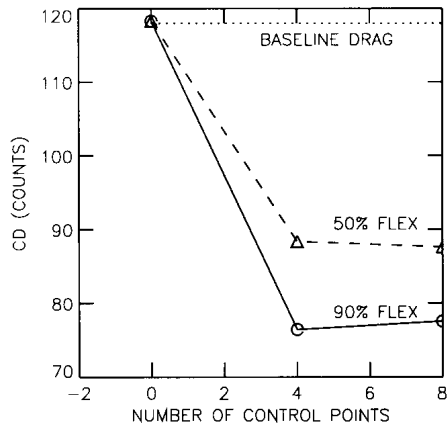


Figure 3-5. Baseline $M_\infty = 0.78$, $C_L = 0.50$ Airfoil Design and 50% Flexed Design at an Off-Design $M_\infty = 0.80$ Using 4 Control Points

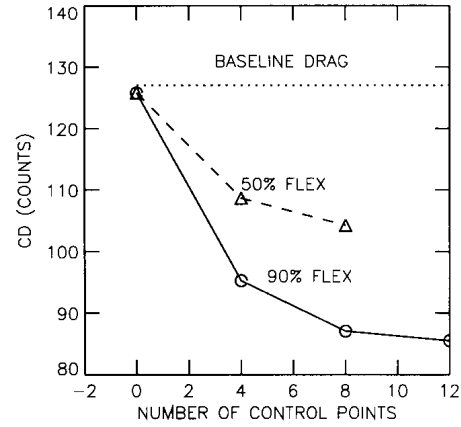
3.4.5 Summary of Adaptive Wing Behavior

Figure 3-6 illustrates the overall performance of the adaptive wing concept for the two baseline airfoils designed at $M_\infty = 0.78$ at $C_L = 0.50$ and 0.60 at an off-design condition of $M_\infty = 0.80$. Figure 3-6a shows the drag versus the number of control points used to adapt the surface for the $C_L = 0.50$ baseline airfoil. The baseline drag of 118 counts is indicated by the dotted line. In addition, two curves are plotted, one representing adaptation of 50 percent of the upper surface, and the other 90 percent of the upper surface. In the 50 percent adaptation, the surface is flexed between the forward and rear spars. In the 90 percent adaptation, the surface is flexed between 5 and 95 percent of the chord, and the results are shown for comparison purposes only. Only airfoils with four and eight control points were actually designed for this case and the resulting points were connected. For both 50 and 90 percent adaptation of the upper surface, the number of control points has negligible influence on the drag reduction for the baseline airfoil at $C_L = 0.50$. Flexing only 50 percent of the upper surface still yields 75 percent of the reduction gained when adapting 90 percent of the surface. For the $C_L = 0.60$ baseline airfoil, Figure 3-6b indicates a greater sensitivity to the number of control points used to adapt the surface.

Figure 3-7 shows the performance that can be achieved by adapting the baseline airfoil designed at $C_L = 0.50$ for a range of lift coefficients from 0.50 to 0.60 at the design Mach number of 0.78 and an off-design Mach number of 0.80 using only four control points. Both cases where the upper surface is flexed 50 and 90 percent are shown. In Figure 3-6a, at $C_L = 0.50$, negligible drag reduction is achieved due to the fact that this is the baseline airfoil's design point. As C_L increases, the baseline airfoil begins to show some drag rise which reaches a maximum increment of about 19 counts at $C_L = 0.60$. Adapting 90 percent of the upper surface reduces the drag rise to about three counts. Figure 3-6b shows a similar plot, but for off-design Mach number, $M_\infty = 0.80$. For this case, the baseline airfoil is inefficient at all values of C_L . Adaptation of 90 percent of the upper surface reduces the drag significantly for all lift coefficients with large increases in efficiency as the lift coefficient increases. At $C_L = 0.50$ to 0.55 , the drag values are near shockless levels. Adapting only 50 percent of the upper surface works well at all lift coefficients with approximately a uniform drag reduction of 30 counts over the lift-coefficient range. Flexing 50 percent of the upper surface at $C_L = 0.60$ retains slightly less than 50 percent of the drag reduction achieved for 90 percent adaptation.

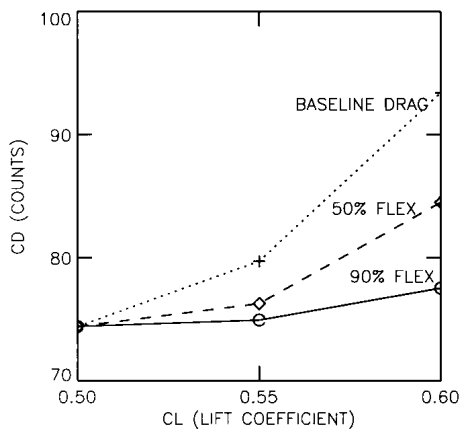


(a) $C_L = 0.50$ cambered airfoil

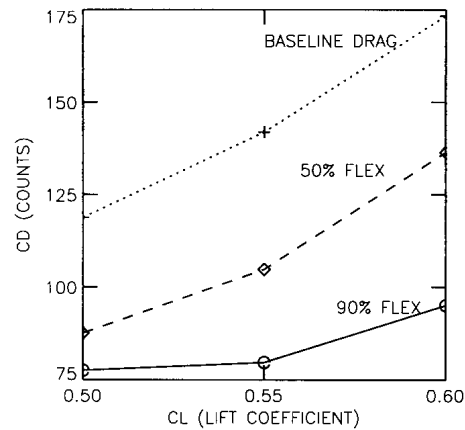


(b) $C_L = 0.60$ cambered airfoil

Figure 3-6. Drag Reduction Characteristics Versus Number of Control Points and the Extent of Upper Surface Adaptation at an Off-Design Condition of $M_\infty = 0.80$



(a) $M_\infty = 0.78$



(b) $M_\infty = 0.80$

Figure 3-7. Drag Reduction Characteristics of the $C_L = 0.50$ Cambered Baseline Airfoil Design Adapted at Off-Design Lift Coefficients and Mach Number Using 4 Control Points

Both baseline airfoils at the two lift coefficients have large supersonic zones terminating in a shock wave at about 65 to 70 percent of the chord. For the higher lift coefficients and higher Mach numbers, the shock wave is located near the end of the adaptable region of the 50-percent-flexed airfoil. This position of the shock wave may indeed have an influence on the efficiency of the surface adaptation and the loss of drag reduction (25 to 45 percent) when flexing only 50 percent of the upper surface.

4. TERFENOL-D POWERED SMART TRAILING EDGE FOR TRANSONIC CRUISE

In the previous section, we discussed a method to modify the airfoil shape throughout the cross-section to enable near shock-free cruise in the transonic region; however, in the current section, it is shown that varying the position of special flaps on the trailing edge is preferable for achieving in-flight wing shape optimization to improve transonic cruise performance. Consequently, we have redirected our effort toward the development of a smart trailing edge.¹⁵ This system has the potential to increase range, reduce the time-to-reach the threat, and increase loiter times with smaller engines and less fuel capacity.

In the smart trailing edge, TERFENOL-D linear motors move segmented flaps that continuously modify the trailing edge shape for optimum performance. The system is mechanized to maintain smooth upper-surface shapes. The flap sizes and geometric parameters were optimized with a modified simulated annealing technique. A full-potential solver coupled to an integral boundary-layer method is used to simulate the aerodynamics. Average drag improvements over the lift-coefficient range are 16 counts at Mach 0.815 and 46 counts at Mach 0.726. The results of the optimization are checked for validity and flow separation with a higher-fidelity Navier-Stokes solver. While the adaptive wing provides the most capability to change the structural shape to minimize shock-induced drag, it was determined that the smart trailing edge is the better concept when actuator- and structural-weight penalties were considered as well as reliability and maintenance. Numerical optimization of a simplified smart trailing edge determined the optimum configuration and optimum deflections for minimum drag. The system has the potential to extend the range of a small-fuselage, large-wing uninhabited air vehicle (UAV) bomber by 9 percent and increase its loiter time by 11 percent.

Kinematically adjusting trailing edges to enhance wing performance during cruise has been studied for many years, and a variety of innovative concepts have been proposed¹⁶⁻²⁰. Performance benefits have been verified and numerous variable camber concepts have been employed.¹⁷ For example, the AFTI/F-111 has a flap that is deformed by a complex mechanical system of links and cams, and the X-29A has a split flap with a second hinge aft of the main hinge. Hilbig and Wagner¹⁸ predicted a 5-percent reduction in required fuel for a complete aircraft by deflecting trailing edges at high C_L s at Mach 0.8. These predictions were obtained by extending wind-tunnel test results of a model with exchangeable parts to simulate Fowler flap travel. Szodruch¹⁹ quantified the drag improvements for a wing with a split flap for various settings of each of two flap components. Anderson and DeCamp²⁰ optimized the AFTI/F-111 camber setting to maximize the velocity during transonic cruise. Other optimum camber schedules have been developed by obtaining performance curves for a sequence of flap angles and employing the locus of the best responses (e.g., see Reference 19). However, in these studies only a single camber variable for the airfoil was optimized,^{18,19} or in the case of split flaps,¹⁹ the performance for a discrete set of flap-angle settings was determined, and a schedule was constructed so that the best setting could be employed during flight. However, the actual set of flap-angle settings is infinite, and significant shocks could arise at off-optimum conditions; consequently, a selected setting could be far from optimum.

While fuel savings ranging from 3 to 6 percent have been projected and validated by test, benefits have been limited because of the use of pivoted tabs which cause abrupt curvature changes, variation of only a single flap variable, which produces a limited shape change, or the use of the flap-scheduling method. A TERFENOL-D powered smart trailing edge is being developed to overcome these limitations. Using this device, the upper airfoil contour will have the smooth shape needed to reduce the shock strength without boundary layer separation. Peak performance is ensured by maintaining an optimal trailing edge shape with an optimization method that uses in-flight speed and fuel-flow measurements to continually adjust the flap segments for minimum drag.

The smart trailing edge that is being developed can optimize performance at a variety of flight conditions. By employing a combination of rotation and translation of its segments to change its shape, the smart trailing edge maintains the smooth upper surface required to reduce shock strength without boundary layer separation. In addition, the actuators are located completely within the contour of the airfoil to minimize the drag. Peak performance can be assured by maintaining an optimal trailing edge shape by a method that uses in-flight speed and fuel-flow measurements to continually adjust the flap segments for minimum drag.

Numerical optimization procedures are employed to verify the theoretical performance gains of such a trailing edge design. The hinge locations and the flap settings for various segmented flap configurations are optimized to minimize drag throughout different lift ranges at two transonic speeds, given a fixed airfoil volume.

4.1 CONCEPTS AND TRADE STUDIES

While the investigations are currently directed towards UAVs, in Phase I the Gulfstream III was used as the reference aircraft for the comparison of the adaptive wing with the smart trailing edge. TERFENOL-D elastic-wave linear motor actuators, under current development, were assumed to drive the shape-modification mechanism in each concept. With only one moving part and their trait of locking automatically in the event of a power failure, these actuators have potentially high reliability. They also have high stiffness and essentially zero backlash and end play. Therefore, they minimize the potential for trailing edge buzz or flutter.

4.1.1 Adaptive Wing

The adaptive wing concept, illustrated in Figure 3-3, was originally proposed to reduce fuel expenditure during transonic cruise. The concept is described in Section 3. To obtain optimum airfoil shapes for varying flight conditions, approximately 40 optimum airfoils were developed for a range of two-dimensional (2-D) transonic-cruise conditions from Mach 0.726 to Mach 0.815. (The equivalent three-dimensional (3-D) actual aircraft speeds are Mach 0.82 and 0.92, respectively). Two-dimensional lift coefficients ranged from 0.37 to 0.70. Some of the optimum airfoils for specific design conditions were developed by an inverse approach using potential-flow theory and checked using the GRUMFOIL code while other airfoils were developed by employing our SADD optimization program, coupled with GRUMFOIL for the analysis phase. GRUMFOIL and SADD are described in Subsection 3.4.1. The shapes of the more promising airfoils were varied throughout the off-design flight range.

4.1.2 TERFENOL-D Powered Smart Trailing Edge

The smart trailing edge design concept is illustrated in Figure 4-1. Rollers connected to the aft segment move in a track that is mounted to the forward segment. This roller-track system guides the trailing edge as it is moved by an actuator (the TERFENOL-D motor) and provides a combination of translational as well as rotational motion. By constructing the track so that its center of curvature coincides with the center of curvature of the upper surface of the aft segment at the point of contact with the forward segment, the two surfaces can always be tangent as the trailing edge is moved. The resulting smooth upper surface minimizes the strength of the shock during transonic flow, thereby minimizing airfoil drag. The lower surfaces separate; however, tabs close the gaps to maintain continuity. Drag is further minimized by locating the actuator and associated hardware completely within the contour of the airfoil. To provide additional control of the shape of the upper surface, several segments can be used as shown in Figure 4-2. In this case, a main actuator (not shown, but described in Reference 21) moves the forward segment of the smart trailing edge and provides the large flap motion needed for landing and takeoff. All-electric TERFENOL-D elastic-wave linear motors move the succeeding segments. By using speed and fuel-flow measurements, the smart trailing edge constantly adjusts itself to minimize drag.

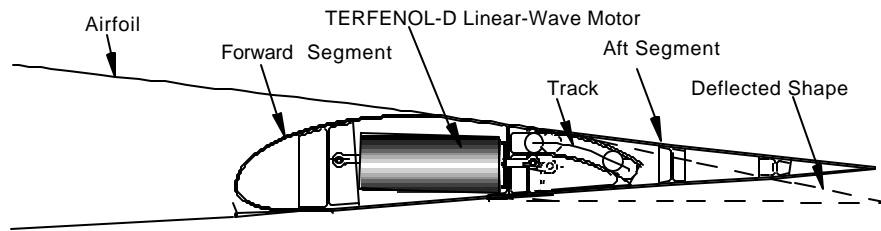


Figure 4-1. TERFENOL-D Powered Smart Trailing Edge

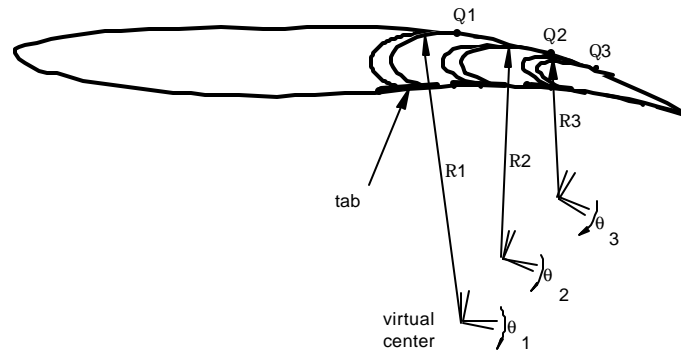


Figure 4-2. Segmented Multi-Flap System

4.1.3 Performance Results

A performance model of the Gulfstream III was used to compute fuel flow for a 4000 NM mission where the aircraft weight varied by approximately 30 percent because of fuel usage, requiring a significant variation of the lift coefficient and, therefore, the flight condition. To compare designs, it was assumed that the aircraft would travel at Mach 0.82 (3-D) 70 percent of the time and Mach 0.92 (3-D) 30 percent of the time.

To obtain a fair basis of comparison for smart trailing edge performance at a range of practical Mach numbers, we developed an efficient compromise, 8 percent thick, fixed-shape airfoil by using an inverse inviscid full-potential design method.²² This baseline airfoil performs far better than the older-technology existing Gulfstream III design. Preliminary structural and mechanical designs of the adaptive wing were generated. To accomplish the desired shape control in a Gulfstream III aircraft, 150 to 200 smart actuators were required per wing. In addition, structural design studies showed that the unconventional truss structure required additional reinforcement to meet a 3.5 G high-speed gust requirement. Production actuator weights were predicted assuming expected technology improvements over the next 5-year period. Without a weight penalty, the adaptive wing saved up to 11 percent of the fuel, depending on the flight condition. However, when the actuator and structural-weight penalty was incorporated, the fuel savings dropped to less than 1 percent.

By limiting the use of smart actuators to kinematically drive trailing edge segments, fewer than 10 actuators are needed per wing. Furthermore, since these actuators no longer are required to deform the structure and the smart trailing edge mechanism relieves a portion of the load, the actuator load requirements are dramatically reduced; consequently, the actuators can be much lighter. The wing structure can also be simpler and lighter because it is no longer subjected to shape-deformation stresses. Since far fewer and lighter actuators are required for a smart trailing edge and the wing structure can be lighter, significant performance benefits can be achieved. A

simplified, nonoptimum version of the smart trailing edge saved approximately 5 percent of the fuel. In addition, the smart trailing edge is easier to repair, has lower cost, and is more reliable. As a result, the TERFENOL-D powered smart trailing edge was selected as the configuration for further development.

4.2 PRELIMINARY DESIGN OPTIMIZATION OF SMART TRAILING EDGE

Preliminary design studies for comparing the smart trailing edge with the adaptive wing were performed with conventional flap hinges located midway between the upper and lower wing surfaces. The conventional flap hinges allow rotation but they do not allow translation. Results for the more sophisticated flaps that translate and rotate are presented in Subsections 4.3 and 4.4. To optimize the smart trailing edge it is necessary to determine the number and geometry of the actuated segments. Optimization techniques, with single and multi-point objectives, were exercised to determine the best compromise system with the most payback in performance for a challenging transonic cruise profile. The optimum hinge locations for one, two, and three segmented flaps and the segment settings to minimize drag throughout the flight regime were determined by numerical optimization. More details are presented in Reference 22.

4.2.1 Analysis and Optimization

Modern transports have the capability of cruising at Mach numbers of 0.9 and higher; however, they often are also required to cruise at lower speeds. The upper curves of Figure 4-3 show the baseline airfoil two-dimensional drag versus lift coefficients at the 2-D Mach numbers of 0.815 and 0.726 for the range of aircraft weights considered. These 2-D Mach are equivalent to actual 3-D Mach numbers of 0.92 and 0.82, respectively, for aircraft with a typical wing sweep of 28 degrees.

Next, the smart trailing edge parameters were optimized over the same mission profile. The optimization problem involves designing a segmented flap with fixed hinge locations such as that illustrated in Figure 4-2. As an example, we describe the development of a three-segmented flap configuration that maximizes the airfoil performance with the constraint that the length of the smart trailing edge system cannot exceed more than the 25 percent portion of the airfoil aft of the rear spar.

SADD was used for the design optimization procedure together with GRUMFOIL as the analysis tool. After the optimization method arrived at a set of optimal solutions, these solutions were further checked and analyzed with a Navier-Stokes solver to determine whether any major separation would occur. Separation is always a concern when dealing with a significant amount of trailing edge camber.

The geometry of the design problem was defined such that each flap segment can deflect independently. The deflection angles θ were defined mathematically such that the first deflection angle θ_1 rotates the entire flap system, the second deflection angle θ_2 , rotates the second and third segments, and the third deflection angle θ_3 , rotates the remaining flap segment. The flap-segment rotations result in slope discontinuities in the surface of the airfoil. In our later work, segment translation/rotation is incorporated into the program, enabling us to exploit the advantages of smoother surfaces.

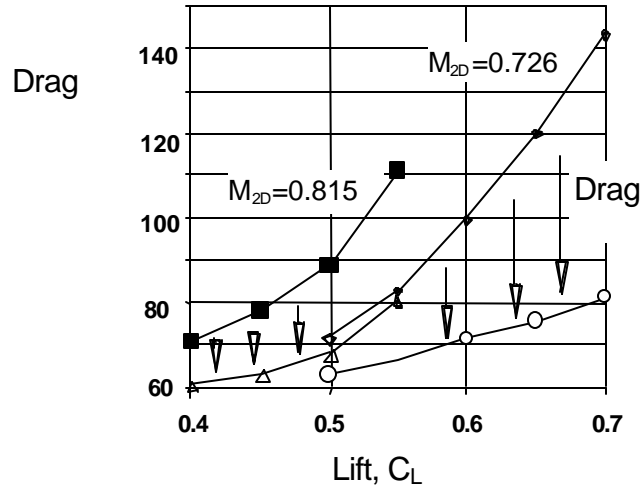


Figure 4-3. Drag Reduction With TERFENOL-D Powered Smart Trailing Edge

To achieve the best possible performance, we first include the hinge locations as variables in the optimization process. Since the hinge locations do not vary with flight condition, they are necessarily an optimal compromise at both Mach numbers. Determination of the best hinge locations required the solution of a multi-point optimization problem with nine design variables and two transonic analyses per objective-function evaluation. The design variables were the three deflection angles at each of the two design conditions and the three hinge locations. The objective was to minimize the combined drag at the 2 design conditions, namely, $M_{2D} = 0.815$ and $C_L = 0.55$ and $M_{2D} = 0.726$ and $C_L = 0.70$.

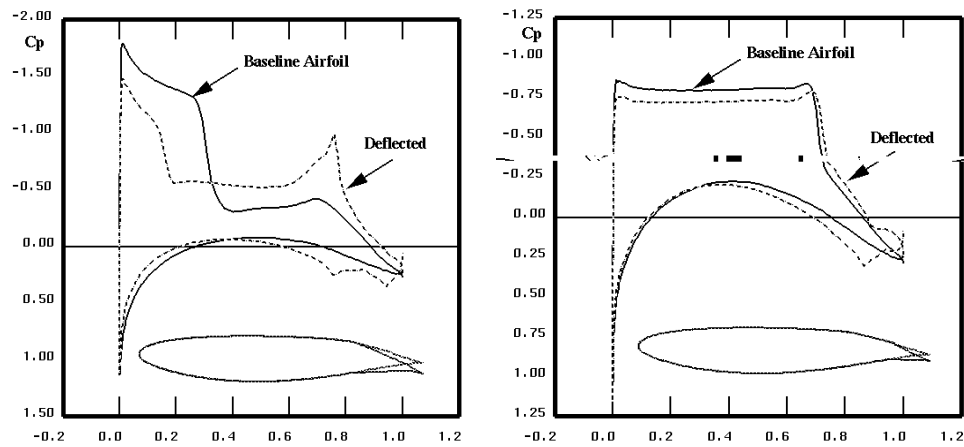
The resulting solution for the optimum segmented flap system is given in Figure 4-4. Each flight condition exhibits approximately the same drag, 82 counts. The forward hinge of the smart trailing edge system was located at about 75 percent of the chord.

Segment	Hinge Location (X/C)	$M_{2D} = 0.726$ $C_L = 0.70$ $C_D = 81.7$ Counts	$M_{2D} = 0.815$ $C_L = 0.55$ $C_D = 82.4$ Counts
		θ (deg.)	θ (deg.)
1	.7539	-4.00	-0.33
2	.8629	1.36	-4.64
3	.9385	-4.68	1.63

Figure 4-4. Multi-Point Optimized Segmented Flap Solution

Figures 4-5a and 4-5b compare the GRUMFOIL-computed pressure distributions for the optimized smart trailing edge with the baseline at a Reynolds number of 20 million. In these figures, the ordinates of the airfoil geometry are scaled by a factor of two for clarity. Figure 4-5a compares the pressure distributions and geometries at a Mach number of 0.726 and a lift coefficient of 0.70. The baseline airfoil at this off-design Mach number has a strong shock situated at about 30 percent of the chord. The effect of the flap deflection, which alters the aft camber of the airfoil, is to reduce the strength of the shock by creating two supercritical zones. The second supercritical region occurs at about 70 percent of the chord. Figure 4-5b compares the data at a Mach number of 0.815 and a lift coefficient of 0.55. The baseline airfoil has a strong shock located much farther downstream, relative to the lower Mach number, at about 70 percent

of the chord. When the solutions were verified using a Navier Stokes solver, it was found that the pressure distributions and incremental drags agreed well with the GRUMFOIL solutions and that flow separation was minimal.²²



(a) $M_{2D} = 0.726$, $C_L = 0.70$, $Re = 20M$ (b) $M_{2D} = 0.815$, $C_L = 0.55$, $Re = 20M$

Figure 4-5. Comparison of the Computed GRUMFOIL Pressure Distributions for the Baseline Airfoil and an Optimized Compromise Flap System at Two Different Mach Numbers and Lift Coefficients.

4.2.2 Preliminary Performance Improvements for Optimized Smart Trailing Edge

Drag improvements are illustrated in Figure 4-3 for a mission with a dash and loiter at two-dimensional Mach numbers of 0.815 and 0.726. The upper curves for each Mach number are the drag for the baseline airfoil. The lower curves are the drag for the airfoil with the optimum-geometry smart trailing edge and optimum flap positions throughout the lift range. The smart trailing edge reduces the drag over the entire flight envelope. The average drag coefficient is reduced by 19 counts at the higher, so-called dash, Mach number and by 32 counts at the loiter Mach number.

Decreasing fuel consumption by 3 to 6 percent, as reported in References 17-19, is quite dramatic. Improvements by wing drag reduction are limited because only a portion of the aircraft drag comes from the wing; the fuselage, empennage, and other components also contribute to the total drag. However, for a preliminary UAV fighter design, with the TERFENOL-D powered smart trailing edge, 7 percent less fuel is required during the loiter phase, and 5 percent less fuel is required during the dash phase (see Figure 4-6). For a proposed UAV bomber with a very clean wing and a small fuselage section, the results are even more impressive. Thirteen percent less fuel is required during loiter, and 10 percent less fuel is required during the dash phase. Consequently, instead of carrying extra fuel, the aircraft can carry extra payload instead of carrying extra fuel.

Alternatively, instead of reducing the fuel carried, the loiter time and range could be increased (see Figure 4-7) instead of reducing the fuel carried. With the smart trailing edge, the fighter can reach targets that are 4 percent more distant and then loiter 6 percent longer. The bomber can reach targets that are 9 percent more distant and then loiter 11 percent longer.

Assumes loiter at Mach 0.82 and dash at Mach 0.92

AIRCRAFT	LOITER TIME	DASH RANGE
Fighter	7.0	5.0
Bomber	12.8	10.1

Figure 4-6. Percent Decrease in UAV Fuel Consumption for Constant Range

AIRCRAFT	LOITER TIME	DASH RANGE
Fighter	6.0	4.2
Bomber	11.3	9.0

Figure 4-7. Percent Increase in UAV Loiter Time and Range for Constant Fuel

4.3 SMART TRAILING EDGE WITH COMBINED MOTION

In this section, the procedure for developing the smart trailing edge with combined rotational and translational motion is described. In addition to flap-segment lengths and flap angles, track hinge radii are also employed as design variables to determine the optimum trailing edge geometry. The optimization techniques, with multi-point objectives, were used to maintain near optimum performance as the aircraft travels at different Mach numbers and a range of aircraft weights. The detailed aerodynamic studies used to optimize the trailing edge are described in Reference 23 and are summarized in this section.

4.3.1 Optimization of Trailing Edge Geometry

The aerodynamic optimization problem involves designing a segmented aft-wing or smart trailing edge system for an optimized supercritical airfoil such as that illustrated in Figure 4-2. The solution will provide the optimum flap sizes and radii of curvature under the constraint that the flap system cannot exceed more than 25 percent of the aft portion of the airfoil because of the fixed rear spar position as well as constraints on the flap-deflection magnitudes.

As in Section 3, the trailing edge optimization was performed by using modified simulated annealing program, SADD with GRUMFOIL, to perform the aerodynamic analyses. After the optimization method arrived at a set of optimal solutions, the results were further checked with a higher-fidelity Navier-Stokes solver to determine whether any major flow separation would occur.

4.3.2 Multi-Objective Optimization for Construction Parameters

Three configurations were designed by varying the number of flap segments from one to three. For each configuration (one-, two-, or a three-segment arrangement), compromise optimal hinge line locations were first be designed. This was carried out by a multiobjective optimization or minimization of the drag at the two extreme highest lift conditions of required lift ranges for two cruise Mach numbers. The objective function that was minimized was the sum of the two drag coefficients at the design conditions of $M_\infty = 0.815$, $C_L = 0.55$ and $M_\infty = 0.726$, $C_L = 0.70$. For the three-segment configuration, a total of 12 design variables were employed: three hinge line locations, three radii of curvature, and six deflections (three for each Mach number). Once the trailing edge geometry parameters were determined by this optimization, additional optimizations were performed to determine the best flap deflections at lower lift coefficients with the fixed hinge-line locations and track radii arrangements.

4.3.3 Optimization Results

Figure 4-8 compares the performance of the airfoil with the three-segment optimized trailing edge with the baseline airfoil at the two cruise Mach numbers at various lift coefficients. The computations all were carried out at the flight Reynolds number of 20 million. In all of the optimization studies, the deflection of any individual flap segment was constrained to be less than 5 degrees down relative to the previous segment with no relative upward rotation permitted. The 5-degree deflection constraint did not appear to constrain the optimization since the optimum deflections were less than this upper bound. At all flight conditions, the flap configurations reduce the drag. In particular, the performance of the airfoil is increased dramatically through the use of flaps at the off-design Mach number of 0.726. Average drag improvements over the lift-coefficient range are 16 counts at Mach 0.815 and 46 counts at Mach 0.726. At the lower Mach number, the optimum airfoil would have more camber, and the flap serves this purpose. Figure 4-6 shows the optimized deflected flap design. It also gives the locations of the hinge lines (Xs) and the track radii of curvature (Rs).

The lower-surface gap covers or tabs are assumed to be linear surfaces covering the opening. As a result, the lower surface slope is discontinuous at the gaps; however, this discontinuity did not seem to affect the optimization or efficiency of the flap designs. This was verified by Navier-Stokes solutions.

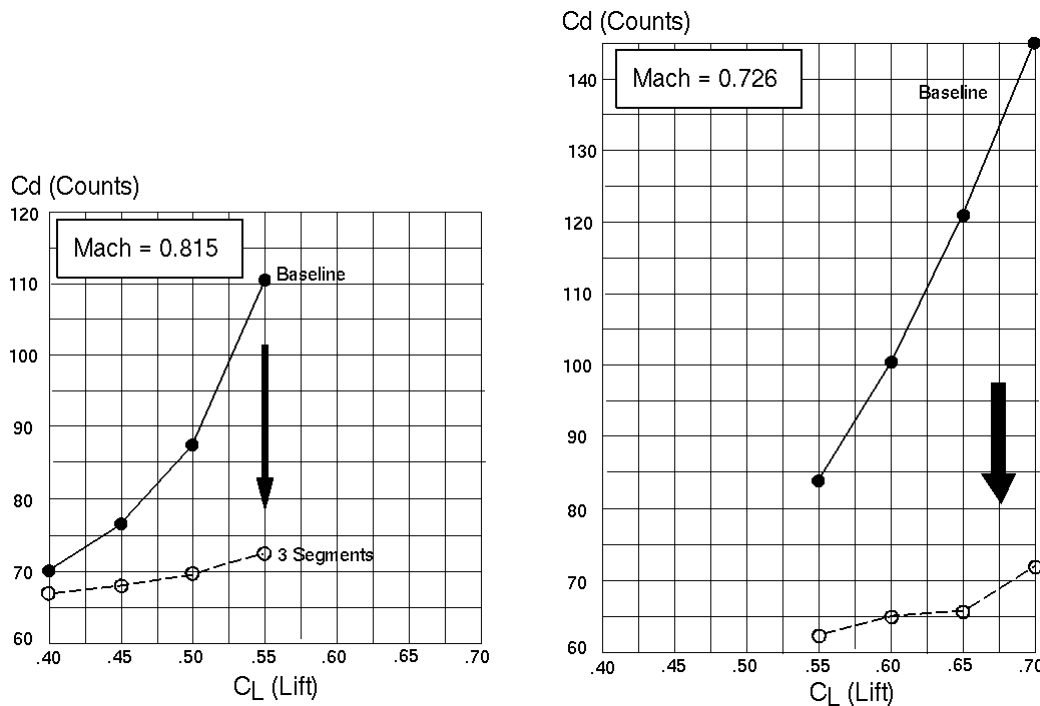


Figure 4-8. Drag Comparison With and Without Optimized Three-Segment Flap (Re = 20 Million)

4.4 NAVIER-STOKES COMPARISON STUDIES

Since the possibility of flow separation on the flap segments is a concern, the ability of GRUMFOIL to predict and avoid separated flow solutions was verified. The GRUMFOIL solutions were checked using a Navier-Stokes flow solver to determine whether any flow separation might occur for the optimal flap deflections and degrade performance of the overall system.

At the flight Reynolds number of 20 million, Navier-Stokes analyses require an extremely fine grid and a great deal of computer time. Also, Reynolds numbers that are this high cannot be achieved in a reasonable-size wind tunnel. Consequently, the optimum flap settings were analyzed at a lower Reynolds number (Re) of 5 million which is representative of a Reynolds number that could be achieved in a wind tunnel. For comparison, GRUMFOIL analyses also were performed at the highest lift coefficients with $Re = 5$ million, and it was found that the flap deflections for the three-segment configuration, which were optimum at $Re = 20$ million, no longer outperform the one- and two- segment configurations. These results indicate that the Reynolds number effect can be significant in designing an in-flight flap system. They also indicate that a full-scale in-flight optimization is required to maintain optimum flap settings; the settings cannot be determined from wind-tunnel testing. A parabolic-estimation method, using sensed fuel flow and aircraft speed, is being developed to implement in-flight optimization

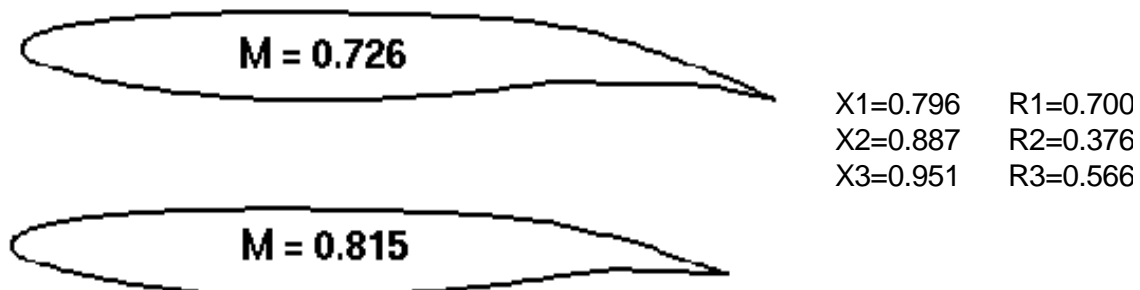


Figure 4-9. Geometry of the Three-Segment Flap Configurations at the Highest Lift in Each Range

The TLNS code²⁴ developed at NASA Langley was used to generate the turbulent Navier-Stokes solutions for the flap system. At all design conditions, the flap configurations exhibited an improvement to the baseline performance of the airfoil. However, the total drag as well as the drag reduction predicted by the Navier-Stokes solutions was significantly higher than that predicted by GRUMFOIL. The differences in the solutions are due to the weak shock assumptions in the potential flow portion of GRUMFOIL as well as small differences in pressure around the entire airfoil indicative of an overall boundary-layer displacement effect. However, the overall trend is correct; i.e., the smart trailing edge provided significant drag reduction over the baseline airfoil. Figure 4-7 shows a comparison of the predicted drag reduction attributed to optimized flap deployment at the two Mach numbers and range of lift coefficients for the two-segment configuration. In all cases, the drag reductions predicted by the Navier-Stokes solver for the optimized flap configurations are greater than those originally predicted by the full potential/boundary layer code GRUMFOIL. In Figure 4-10a, at the highest lift coefficient at Mach 0.815, the Navier-Stokes solver predicts a drag reduction of 30 counts in comparison to GRUMFOIL which predicts a reduction of only 18 counts. In Figure 4-10b, at the lower Mach number of 0.726, the Navier-Stokes solution predicts about 110 counts of drag reduction at the highest lift coefficient. This corresponds to more than a 30 percent reduction in drag. It should be kept in mind that the higher drag reduction encountered with the Navier-Stokes solver may be attributed to the higher overall drag predicted by the viscous solutions.

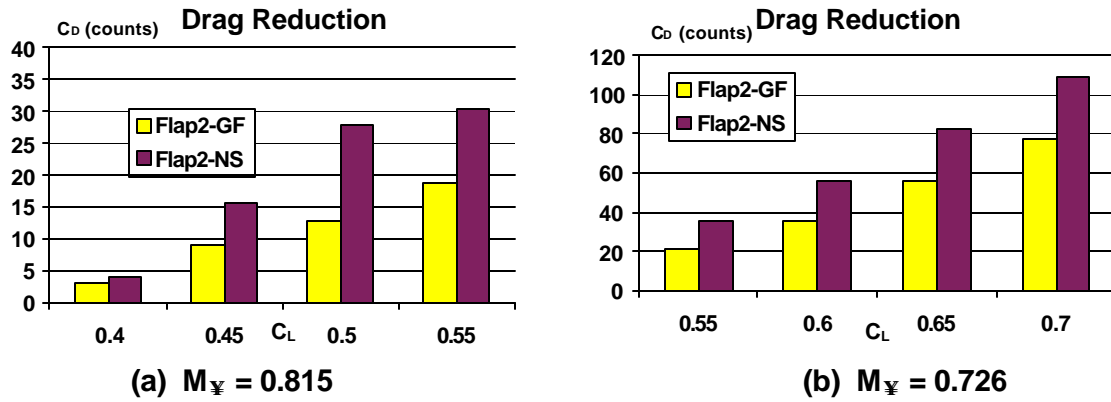


Figure 4-10. Comparison of the Navier-Stokes and GRUMFOIL Predicted Drag Reduction With Optimized Flap Deployment for a Two-Segment Smart Trailing Edge ($Re = 5$ million)

As a final evaluator of the success of the numerical optimization, the flow fields computed by the Navier-Stokes solver were inspected in detail to see if any flow separation was apparent. No significant flow separation was apparent on either the upper or the lower surfaces.

5. LINEAR MOTOR DEVELOPMENT

An experimental model of the TERFENOL-D elastic wave linear motor has been built and tested. Structural, mechanical, magnetic, thermal, and electronic analyses and testing were performed to develop the motor. Breadboards and components were built for the tests as well a complete experimental motor. This work is presented in detail in References 1 through 5. The basic material behavior, some of the magnetic finite-element analyses, and the thermal analysis are described in this section. Test results on the completed unit are also provided. Reference is frequently made to the shift patterns defined in Section 2.

5.1 MATERIAL BEHAVIOR

ETREMA TERFENOL-D[®] is a magnetostrictive material, i.e., it will change shape in the presence of a magnetic field with the degree of change increasing with the strength of the magnetic field. The strain and force available from TERFENOL-D are superior to other smart shape-change materials. As such, TERFENOL-D is characterized as a giant magnetostrictive material. With strains of well over 0.1 percent, TERFENOL-D has the ability to move an object with significant force through a relatively large distance.

In the presence of a magnetic field, a magnetostrictive TERFENOL-D rod expands in length and contracts diametrically, thereby conserving the volume of an essentially incompressible material. The magnetostrictive effect produces elastic forces in accordance with a generalized Hooke's Law. In the linear operating range of a magnetostrictive material, the transduction may be described by the fundamental pair of constitutive equations:

$$\begin{aligned} S &= s^H T + d H \\ B &= d T + \mu H \end{aligned}$$

where S is the strain, H is the magnetic field intensity, B is the flux density, T is the mechanical stress, s is the elastic compliance, d is the magneto-mechanical coefficient (which couples the magnetic and mechanical equations), and μ is the magnetic permeability. In practice, nonlinearities in the constitutive equations are important, and these are being modeled in the Phase 2 program.

5.2 MAGNETIC ANALYSIS

Figure 5-1 shows some of the ANSYS[®] finite-element modeling simulation results. The field intensity in the upper half of the TERFENOL-D rod is shown for the improved coil configuration and for the original coil configuration. The improved configuration concentrates the field under the energized coil while reducing the field under neighboring coils. In addition, experiments, in air, have shown that the field is increased by 60 percent under the energized coil and reduced from 45 to 25 percent under the adjacent coil. Further improvements to the magnetic design method, which will be used for the Phase 2 motor, are being developed.

The coil design will be improved by determining the configuration that gives maximum uniform magnetic field consistent with the constraints of motor envelope size, power budget, and manufacturability of the stator tube. In addition, it is desirable to lower the inductance of the coil to decrease the rise time which allows higher operating frequency and, therefore, higher motor speed. Since minimum coil power does not coincide with minimum rise time as shown in Figure 5-2, trade studies were employed to design the motor. We have also determined that it is possible to concentrate the field in the region desired by superimposing the fields from adjacent coils. A preliminary study of field superposition (Figure 5-3) indicates the promise of this method, and it will be fully developed in Phase 2.

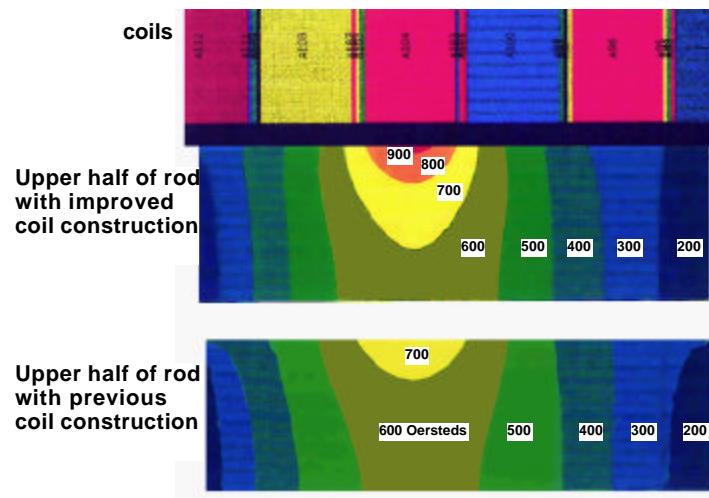


Figure 5-1. Effect of Improved Construction on Magnetic Field

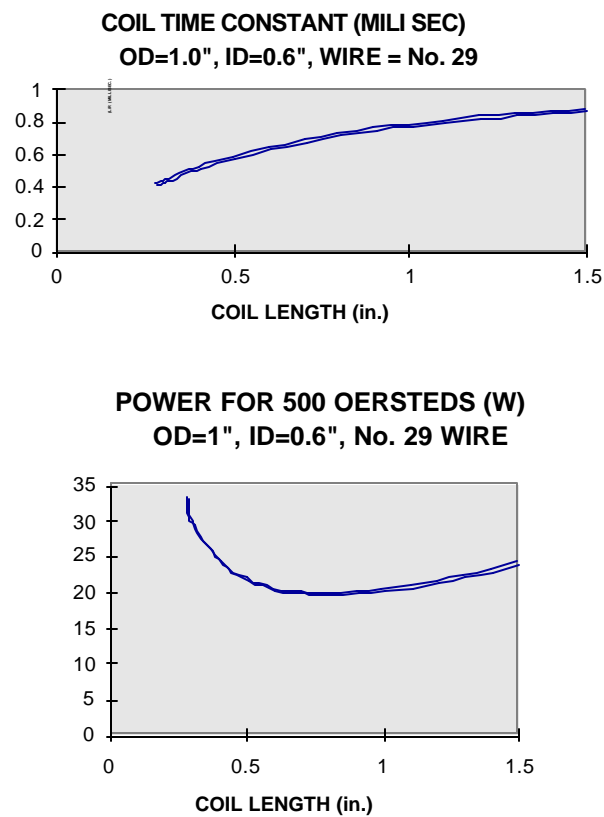


Figure 5-2. Typical Coil Trade Study

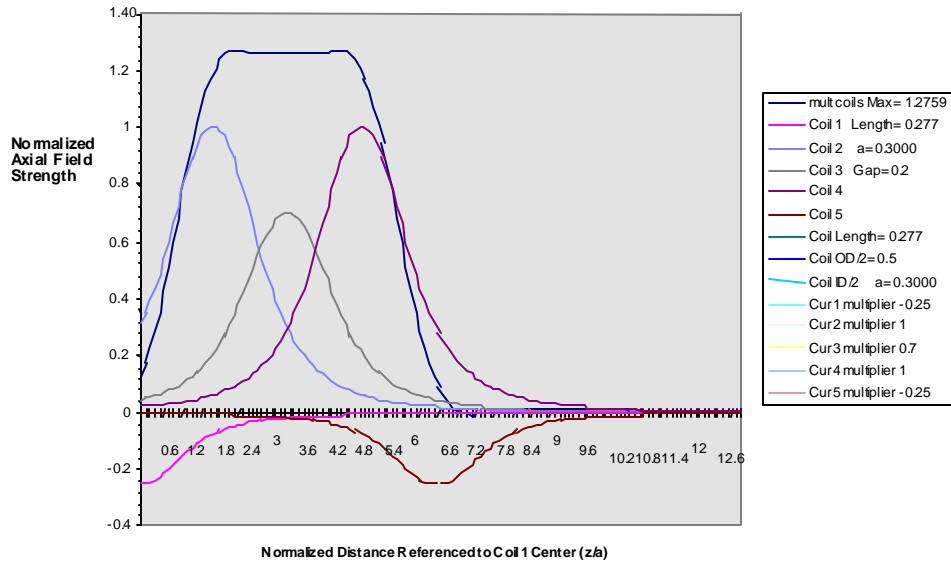


Figure 5-3. Superposition of Coil Fields to Achieve Approximate Square-Wave Excitation

5.2.1 Thermal Design and Analysis

Stator tube design must account for the important influence of thermal expansion for high-performance linear-motor operation. The tube used in the linear motor will absorb heat from the coils and thermal expansion of the tube will result. The TERFENOL-D rod inside the tube also expands, since it is heated by contact with the tube and by eddy currents. Measurements were made to characterize the coefficient of thermal expansion (CTE) of TERFENOL-D in different temperature regions for different types of TERFENOL-D. The average CTE of TERFENOL-D was measured as approximately 11 ppm/°C. HAYNES® Alloy 242™ was selected as the stator tube material since its CTE closely matches TERFENOL-D and because it provides the necessary strength, friction, durability, and corrosion resistant properties.

During actuator testing, coil currents were measured by a Hall effect probe, and oscilloscope traces were recorded. When the actuator was hot, the currents were measurably lower than the currents of the colder actuator at the start of the test. Further testing and circuit analysis revealed that the drop in current was due to increases in the coil resistances when they became hot. By assuming that all coils were at the same temperature and using the thermal resistivity coefficient for copper, the hot coil temperatures shown in the second and third column of Figure 5-4 were computed. Because of possible measurement errors, the highest temperatures (corresponding to the 8-4 shift pattern) are believed to be accurate within $\pm 20^{\circ}\text{C}$. Details of this analysis are provided in Reference 25.

Shift Pattern	Based on Electrical Analysis		Based on Thermal Analysis			
			Coil Nearest Cooling-Air Inlet		Coil Farthest from Cooling-Air Inlet	
	ΔT °C	Temp °C	ΔT °C	Temp °C	ΔT °C	Temp °C
2-1	11	32				
4-2	28	49				
8-4	51	72	53	74	90	112

Figure 5-4. Coil Thermal Analyses

To confirm these results, a simplified finite element analysis (FEA) thermal model of the ETREMA POC-1 elastic-wave linear motor coils was developed. A 5-watt-per-coil heat load was assumed, which is consistent with the highest-power coil excitation pattern, the 8-4 pattern. Results are shown in Figure 5-4. The coil temperature rise varied from 53 °C above the 21 °C ambient temperature at the cooling-air inlet to 90°C at the cooling air exit; consequently, the maximum computed coil temperature was 112°C. The 53°C-to-90°C temperature rises based on the crude FEA thermal model are higher than the average 51°C rise that was deduced from electrical measurements. The higher FEA temperatures are probably due to the FEA model assumptions that all power is dissipated in the coils and is transferred only to the cooling air, i.e., all other coil surfaces are perfectly thermally insulated. Nevertheless, even the lower calculated temperature levels are of concern for operation of the actuator. Details of this analysis are provided in Reference 26.

5.3 PHASE 1 MOTOR TESTING

The ETREMA TERFENOL-D[®] magnetostrictive elastic wave linear motor was received at Northrop Grumman on February 11, 1997. The motor was powered with 12 volts, from a supply capable of delivering 16 amperes enabling eight coils to be energized at once (as required for the 8-4 pattern). Extensive preliminary tests were performed to determine general motor performance. Various problems were identified and corrected including modifications to the feedback-sense logic, erratic operation near a stopping voltage caused by a very sensitive comparator that reacted to digital noise, and a short to the case that developed on one of the coil terminals. In each case, the motor was returned to ETREMA, and motor improvements were made to eliminate repetition of the problem.

The test fixture shown in Figure 5-5 was used to evaluate the proof-of-concept linear motor designed for Phase 1 (POC-1). Various weights can be applied at either end of the lever shown in the figure to load the motor in either compression or tension. Motor position is measured with an LVDT that is in parallel with the motor. Position data is acquired electronically and is stored in a computer for processing. Typical results are shown in Figure 5-6. Note that retraction speed increases in the negative, downward direction. Motor speed first increases with sweep frequency; however, at high frequencies it decreases since the time available for the field to build up becomes insufficient before coil shifting occurs. Consequently, a Phase 2 design goal will be to minimize the time constant, by decreasing the system inductance, to achieve more rapid response. Variations in speed with stroke are attributable to nonuniform dimensions in the tube and/or rod, resulting in a variation in the shrink fit.

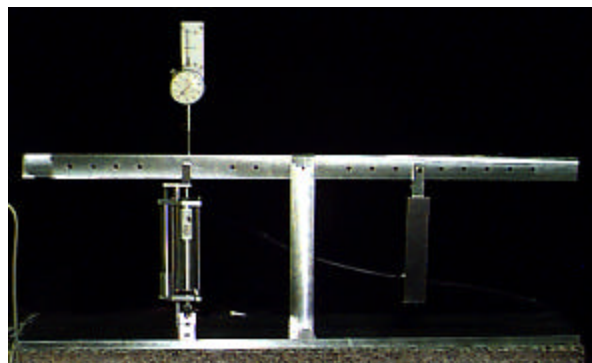


Figure 5-5. POC-1 Elastic-Wave Linear-Motor Testing

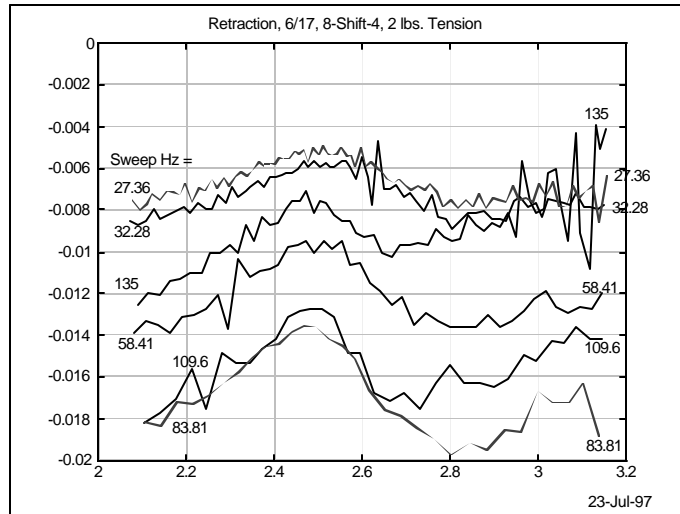


Figure 5-6. Typical Motor Test Results

5.3.1 Motor Performance

POC-1 has achieved the performance shown in Figure 5-7 under various loads, magnetic excitation patterns, and sweep frequencies. It has been used to successfully drive the model of the smart trailing edge shown in Figure 5-8.

Design Requirement	Units	POC-1 Design Performance	POC-2 Design Target*
Stall Force	lb	28	± 50
Holding Force	lb	67.5	TBD
Stroke	in	1.5	1.0
Speed (no load)	in/s	0.05	0.1
Length (retracted)	in	9.0	5.0
Diameter	in	1.6	0.8
Weight	lb	1.8	TBD
Power	W	10-20 (per coil)	35
EMI	G	-----	< 10

*preliminary

Figure 5-7. Linear Motor Designs for Phase 1 (POC-1) and Phase 2 (POC-2)

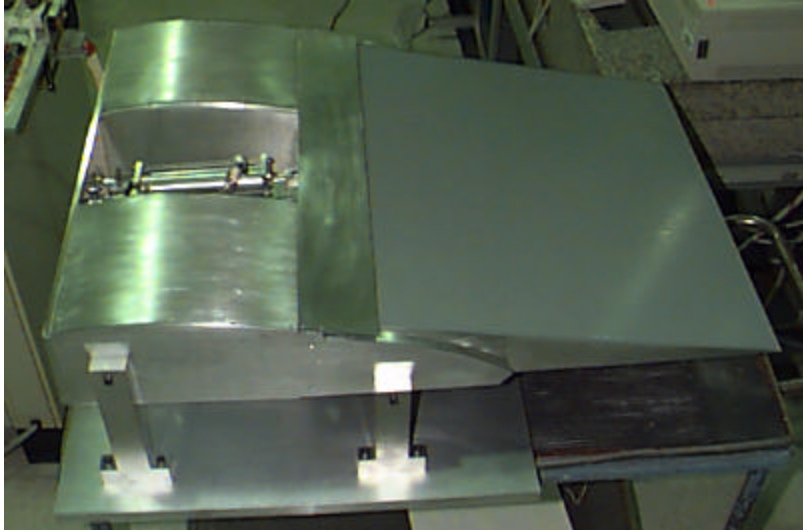


Figure 5-8. Smart Trailing Edge Experiment

5.3.2 Final Motor Testing

In order to learn how to develop an improved actuator, a relatively complete set of characterization tests were performed after a new TERFENOL-D rod was installed in March 1997. The outside diameter of the rod and the inside diameter of the tube must be held to extremely tight tolerances since motor performance is a strong function of the nature of the interference fit. Consequently, motor performance varies with rod position and wear. The variation in performance resulting from wear was measured and is discussed in Subsection 5.3.5. A primary effort on the Phase 2 development program will be to reduce the need for tight tube and rod tolerances and to reduce the sensitivity of the motor's performance to these tolerances. This goal can be achieved with the new split-tube design concept. Because of the sensitivity of the POC-1 motor to tolerances, the refurbished system with the new rod did not perform as well as the previous system; consequently, many of the above test results could not be duplicated. Nevertheless, they indicate that the motor is capable of producing, at least, the performance indicated above. Testing was conducted in two phases: (1) to determine speed, and (2) to determine load capability. In both phases, the unit was run in the automatic mode (unit commanded position is set by the CP potentiometer, and the motor moves and stops). The final set of motor test results are summarized in the following subsection. Additional details are presented in Reference 27.

5.3.3 Speed Tests With Applied Loads

Speed tests were performed during extension and retraction with opposing loads (compression and tension, respectively). For each case, four shift patterns were investigated: 2-1, 4-1, 4-2, and 8-4. For each of these combinations of motion direction, load, and shift pattern, tests were run at five sweep frequencies. The reference position for stroke measurements is at the upper surface of the motor housing assembly, and speed tests were performed over a range of approximately 1.9 to 3.1 inches, i.e., a stroke of 1.2 inches.

The following equations relate the measurements to the physical motor parameters. The stroke in inches is

$$x = 3.642 - 0.48077 * MP$$

where MP is the position measured by the LVDT in volts. The time that a single coil is excited, in seconds, is

$$\Delta T = 1 / (206.68910 * V + 19.010673)$$

where V is the speed voltage command in volts. The sweep frequency in Hz is

$$f = (206.68910 * V + 19.010673) / \text{Perfac}$$

where Perfac is a period factor that provides the sweep period when multiplied by the single-coil excitation-time interval:

$$\text{Perfac} = 16 / (\text{number of coils shifted})$$

e.g., Perfac = 4 for the 8-4 pattern, 8 for the 4-2 pattern, and 16 for the 2-1 pattern.

Sweep frequencies for various speed voltage settings and patterns are shown in Figure 5-9.

Speed Voltage Command (V)	0.5	1.0	1.5	2.0	2.5
Single Coil Time Active (msec)	16.35	8.86	6.08	4.63	3.73
8-4 Freq. (Hz)	30.6	56.4	82.3	108.1	133.9
4-2 Freq. (Hz)	15.3	28.2	41.1	54.0	67.0
2-1 Freq. (Hz)	7.6	14.1	20.6	27.0	33.5

Figure 5-9. Sweep Frequencies as a Function of Speed Voltage and Pattern

Typical performance under loaded conditions is shown in Figure 5-10. Note that for retraction, higher speeds are in the negative, downward direction. Once again, it is seen that speed increases with sweep frequency; however, when the sweep frequency is increased above a certain value, the speed begins to decrease since the field does not have sufficient time to build up before the shifting occurs. In the region of approximately 2.5 to 2.8 inches, the velocity decreases indicating poorer performance. Additional tests (see Reference 27) indicate that the cause is due to small variations in the dimensions of the rod outside diameter and/or the tube inside diameter causing too tight a fit in this region. This should not occur in the Phase 2 actuator, which will be relatively insensitive to tolerance variations.

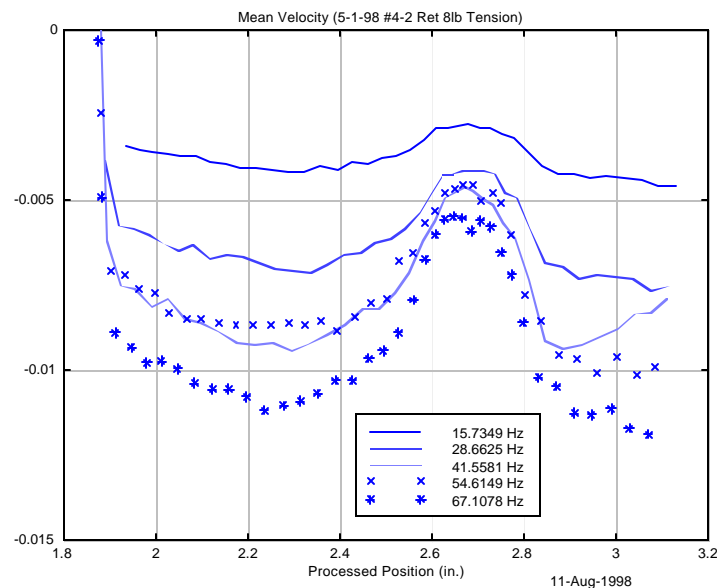


Figure 5-10. Pattern 4-2 Retracting Under an 8 Pound Tension Load

Testing under load is summarized in Figure 5-11 for 1.5 volts and 2.0 volts speed settings. The actuator had greater capability to retract under a tension load than to extend under a compression load. The lack of symmetry in retraction and extension performance under opposing loads is believed to be attributable to the location of TERFENOL-D particles in the tube.

		2 shift 1	4 shift 2	8 shift 4
1.5 volts	2 lb			ran
1.5 volts	4 lb	ran	ran	ran
1.5 volts	6 lb	ran	ran	ran
1.5 volts	8 lb	ran	ran	stalled
1.5 volts	10 lb		stalled	
2.0 volts	2 lb			ran
2.0 volts	4 lb	ran	ran	ran
2.0 volts	6 lb	ran	ran	stalled
2.0 volts	8 lb	ran	ran	
2.0 volts	10 lb	ran		

a. Retraction Under Tension

		2 shift 1	4 shift 2	8 shift 4
1.5 volts	2 lb	stalled	ran	ran
1.5 volts	4 lb		ran	ran
1.5 volts	6 lb		stalled	stalled
1.5 volts	8 lb			
1.5 volts	10 lb			
2.0 volts	2 lb		ran	ran
2.0 volts	4 lb		ran	stalled
2.0 volts	6 lb			
2.0 volts	8 lb			
2.0 volts	10 lb			

b. Extension Under Compression

Figure 5-11. Summary of Runs at Speed Settings of 1.5 and 2 Volts

Examinations of plots of speed versus position show that the speed is relatively uniform in the region of armature positions ranging from 1.9 to 2.4 inches. Where the speed is indicated at 2.2 inches displacement in the following plots, the average speed in the 1.9 to 2.4 inch region is used.

In Figure 5-12, the retraction and tension speeds under opposing loads are shown for three shift patterns for a speed setting of 1.5 volts. Speeds on the retraction curves are shown positive in order to better compare the retraction curves to the extension curves. In retraction, the 4-2 pattern achieves nearly half of the no-load speed of the 8-4 pattern, but the 2-1 pattern achieves far less than half of the 4-2 pattern speed. This result is consistent with a coupled structural/magnetostrictive finite-element analysis performed under Phase 2 where it was found that significantly less strain in the rods is induced for the 2-1 pattern because of reduced field strength when energizing only two coils. However, there is only a small reduction in field when energizing four coils compared to eight.

There is a very significant difference between extension and retraction speeds under opposing loads for the 8-4 pattern. More slippage occurs for the 8-4 pattern since the stronger field that energizes 8 coils simultaneously, tends to leak and contract more of the rod than desired; consequently, the performance of the 8-4 pattern is a strong function of the accuracy of the dimensions of the rod outside diameter and the tube inside diameter. As a result, its behavior is complex and difficult to predict. There are smaller differences between extension and retraction performance for the 4-2 and 2-1 patterns, and the differences increase with load. Retraction performance is superior to extension except for the 8-4 pattern with no load, and a 2-pound load. In fact, for these load levels 8-4 pattern extension speeds are significantly higher than retraction speeds.

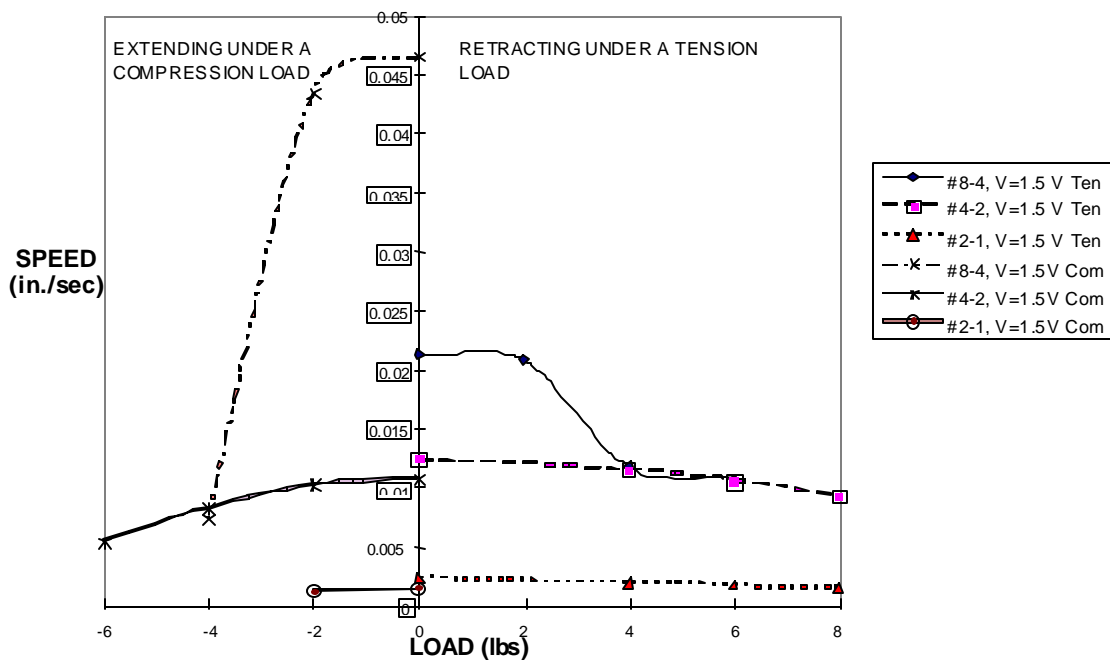


Figure 5-12. Speed vs Load at 2.2 Inches Displacement

As seen in Figure 5-13, except for the 8-4 pattern, there is very little difference between extension and retraction speeds at 2.2 inches under no load. Generally, the speeds are expected to increase with sweep frequency and then decrease at higher frequencies when the coil excitation time becomes too low to enable a sufficient buildup of the magnetic field. The 8-4 pattern first increases with sweep frequency, then decreases but then increases again. The final increase remains unexplained. Figure 5-14 shows that this unusual behavior does not occur under a 4 pound opposing load. Figure 5-11 shows the same unusual behavior for the 4-2 pattern but this time, with an 8 pound tension load.

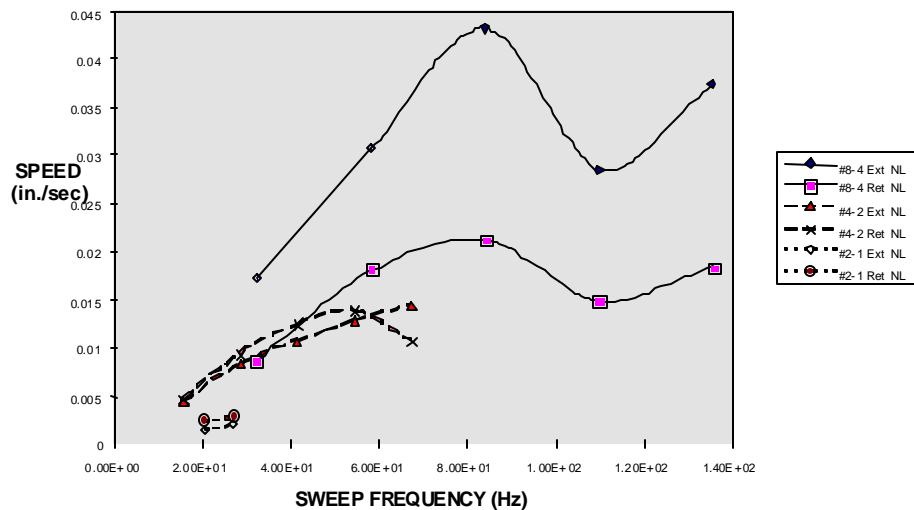


Figure 5-13. Speed vs Frequency at 2.2 inches for No Load and Various Patterns (Retraction Velocities Are Shown Positive to Compare with Extension)

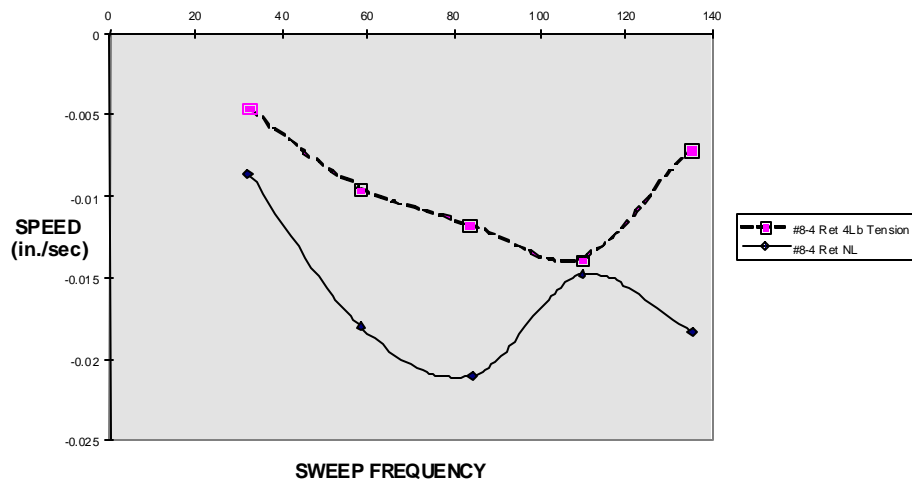


Figure 5-14. Speed vs Frequency at 2.2 inches for Retraction With an 8-4 Pattern for the Unloaded Case and a 4 Pound Tension Load.

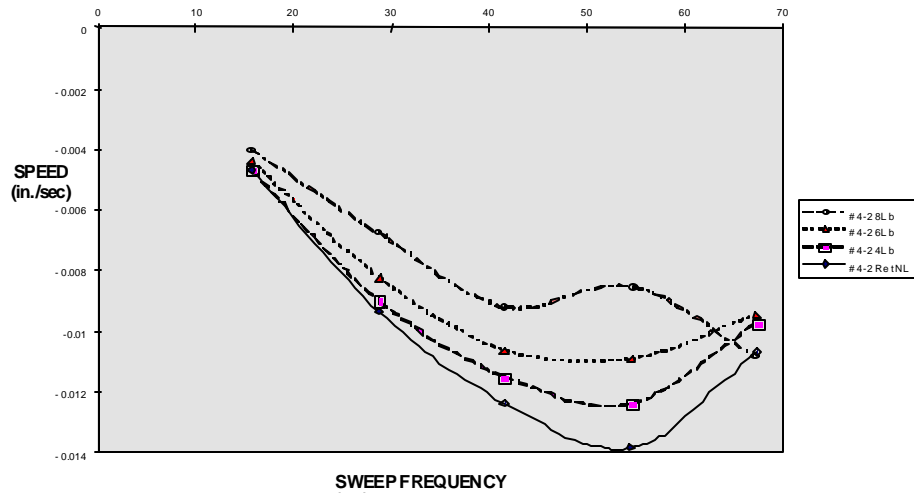


Figure 5-15. Speed at 2.2 inches vs Frequency for a 4-2 Pattern for Various Opposing Tension Loads

Figure 5-16 shows the speed variations with sweep frequency for the 2-1 pattern and various tension loads. Speed increases with sweep frequency; however, there is very little difference in speed between the 2.0 volt and 2.5 volt settings as shown in Figure 5-17.

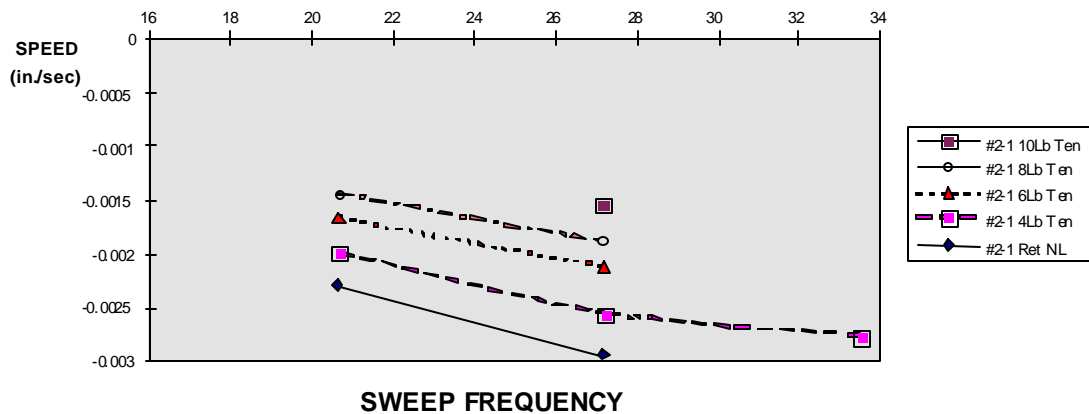


Figure 5-16. Variation of Retraction Speed at 2.2 in. With Sweep Frequency for the 2-1 Pattern for Various Tension Loads

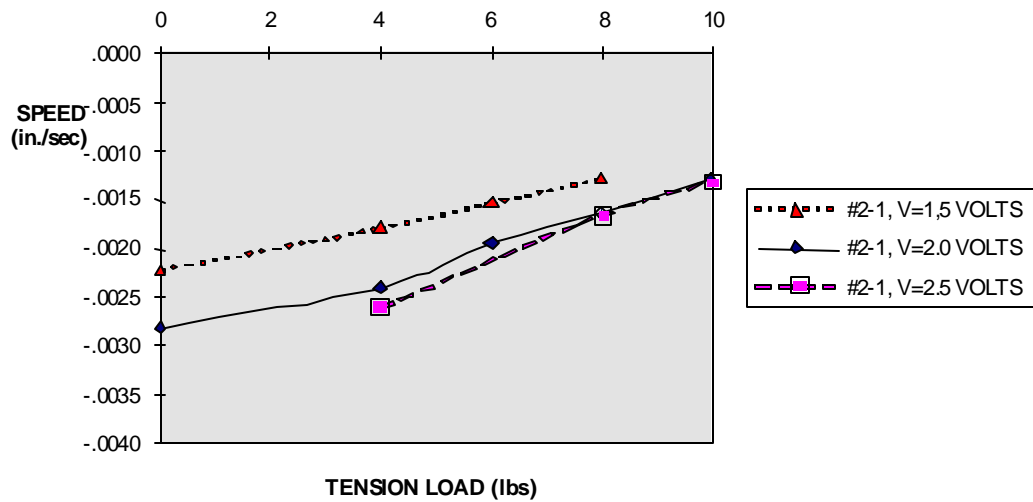


Figure 5-17. Variation of Retraction Speed with Tension Load for Various Speed Voltage Settings

5.3.4 Blocking Load Tests

The loads exerted by the blocked actuator were measured after the above speed tests were performed. The actuator had already been run a significant number of times and had accumulated wear that had resulted in deteriorated performance.

To test under a stalled/blocking load, the test apparatus was modified to include a load cell that locked the testing balance beam. The load cell was positioned at 7.5 inches on one side of the balance fulcrum, and the actuator was positioned at 7.5 inches to the other side of the fulcrum. The transducer was an Interface Force Transducer Model SM-250 (s/n C91845) with a 250 pound capacity. The readout device was a BLH Electronics Digital Strain Indicator Model 1200 (s/n 2307). The tests were conducted for the same combination of motion direction, shift pattern, and sweep frequency as the speed tests. Two additional shift patterns were investigated, 2-2a and 4-2a, where the suffix a designates a modification to the pattern that is described below. The tests were performed at three actuator displacements. Figure 5-18 shows the matrix of tests performed. MP (measured position) designates the actuator displacement.

Speed (Voltage)	Pattern				
	8-4	4-2	2-1	4-2a	2-2a
0.5	MP=3.7 MP=3.0 MP=1.0	MP=3.7 MP=3.0 MP=1.0	MP=3.7 MP=3.0 MP=1.0	MP=3.7	MP=3.7 MP=3.0 MP=1.0
1.0	MP=3.7 MP=3.0 MP=1.0	MP=3.7 MP=3.0 MP=1.0	MP=3.7 MP=3.0 MP=1.0	MP=3.7	MP=3.7 MP=3.0 MP=1.0
1.5	MP=3.7 MP=3.0 MP=1.0	MP=3.7 MP=3.0 MP=1.0	MP=3.7 MP=3.0 MP=1.0	MP=3.7	MP=3.7 MP=3.0 MP=1.0
2.0	MP=3.7 MP=3.0 MP=1.0	MP=3.7 MP=3.0 MP=1.0	MP=3.7 MP=3.0 MP=1.0	MP=3.7	MP=3.7 MP=3.0 MP=1.0
2.5	MP=3.7 MP=3.0 MP=1.0	MP=3.7 MP=3.0 MP=1.0	MP=3.7 MP=3.0 MP=1.0	MP=3.7	MP=3.7 MP=3.0 MP=1.0

Figure 5-18. Stall Force/Blocked Armature Testing Matrix

Patterns with the suffix “a” are modified patterns that energize the next set of coils before removing excitation from the coils to be turned off; i.e. the energized coils are advanced by the shift number before de-energizing the coils that are no longer required. For example, in a 2 - 2 regular pattern, Coils 1 and 2 are energized, and then on the next clock cycle coils 3 and 4 would be energized with coils 1 and 2 de-energized. The modified pattern would energize coils 1 and 2 as before but energize Coils 1 and 2 and 3 and 4 on the next clock cycle and on the third clock cycle just energize Coils 3 and 4. This process continues until the field sweeps the entire rod length. This requires more clock cycles to complete a sweep and therefore, produces a slower moving actuator response. It also increases total power consumption slightly. However, the modified patterns were investigated to determine whether they could produce higher loads.

Figures 5-19 through 5-24 show the blocked actuator stall forces at different actuator positions as a function of speed voltage command, and the variation of stall force with actuator position is shown in Figure 5-25. Although there is a small variation with position and speed voltage setting, the dominant variable is the pattern. The actuator generated higher loads with the 2-1 and 4-2 patterns than with the 8-4 pattern. The more extensive field required for the 8-4 pattern caused widespread contraction of the rod diameter resulting in slippage at lower loads. The effect of the pattern is isolated in Figure 5-26 which shows retraction at the 1.875-inch position and extension at the 1.953-inch position.

Generally, the unmodified pattern exerted higher loads than the corresponding modified pattern. This is most evident in the comparisons of corresponding patterns presented in Figures 5-27 and 5-28.

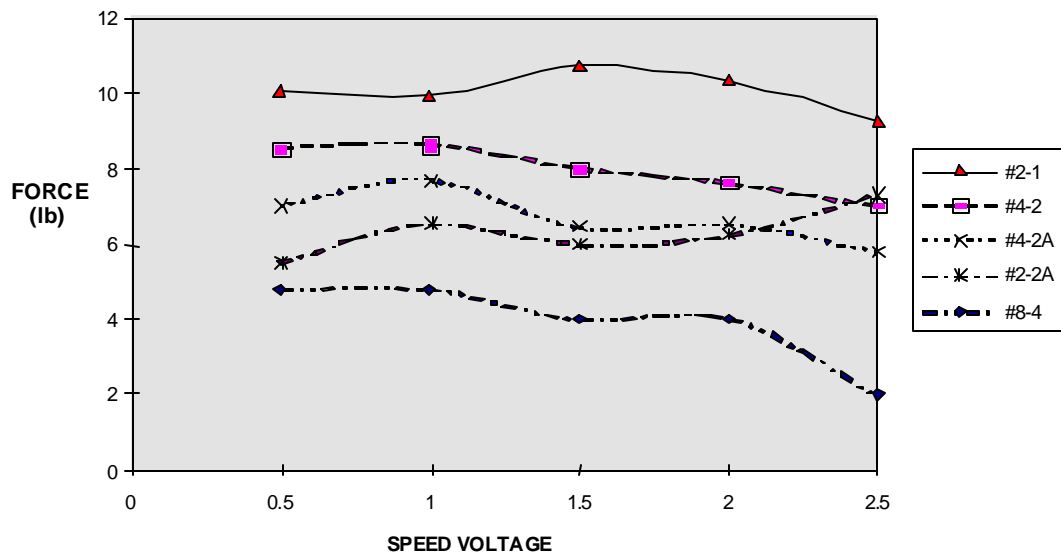


Figure 5-19. Retraction – Blocked Actuator Force at a Displacement of 1.875 inches for Various Sweep Patterns and Speed Voltage Settings

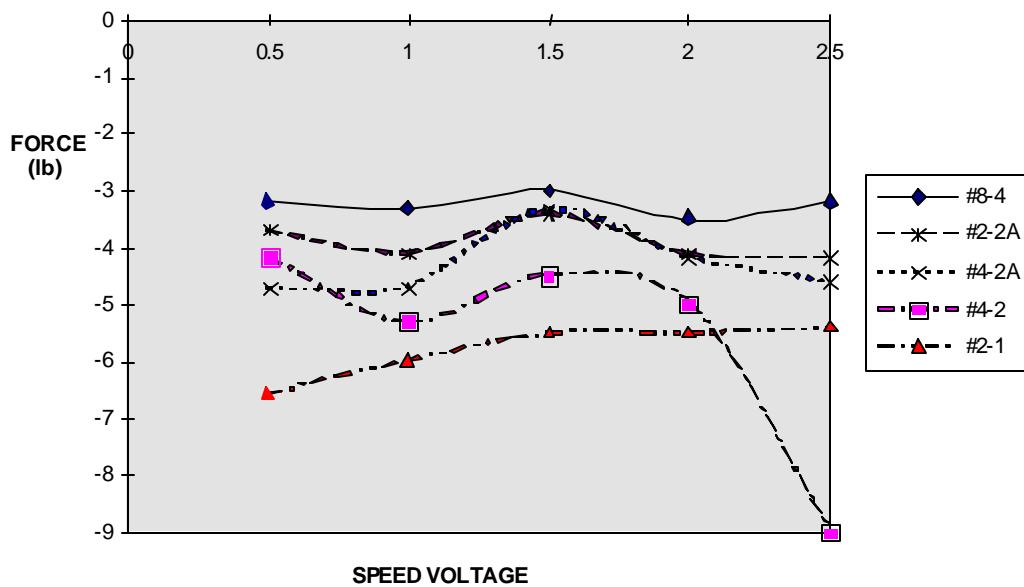


Figure 5-20. Extension – Blocked Actuator Force at a Displacement of 1.953 inches for Various Sweep Patterns and Speed Voltage Settings

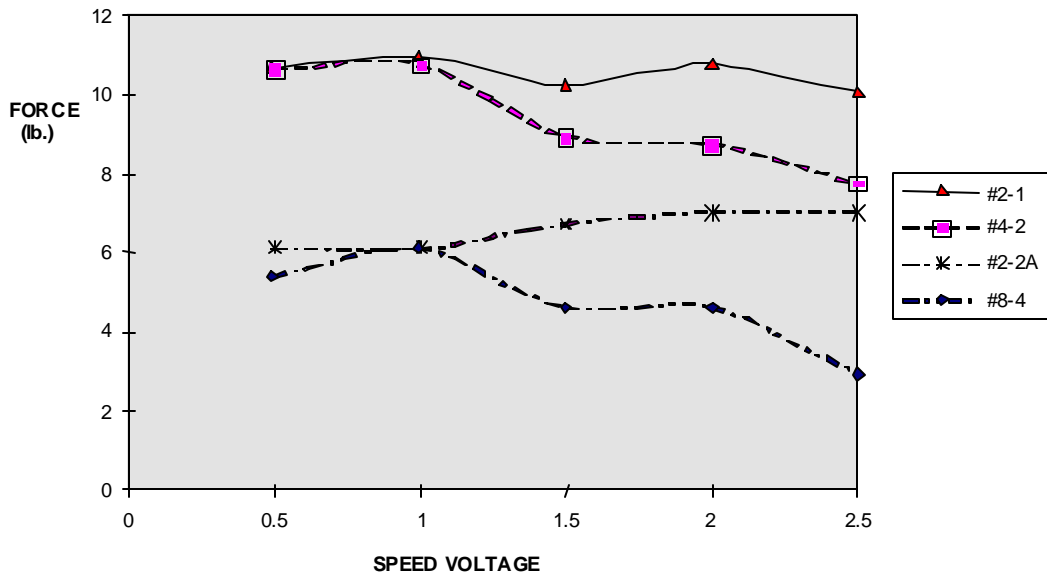


Figure 5-21. Retraction – Blocked Actuator Force at a Displacement of 2.24 Inches for Various Sweep Patterns and Speed Voltage Settings

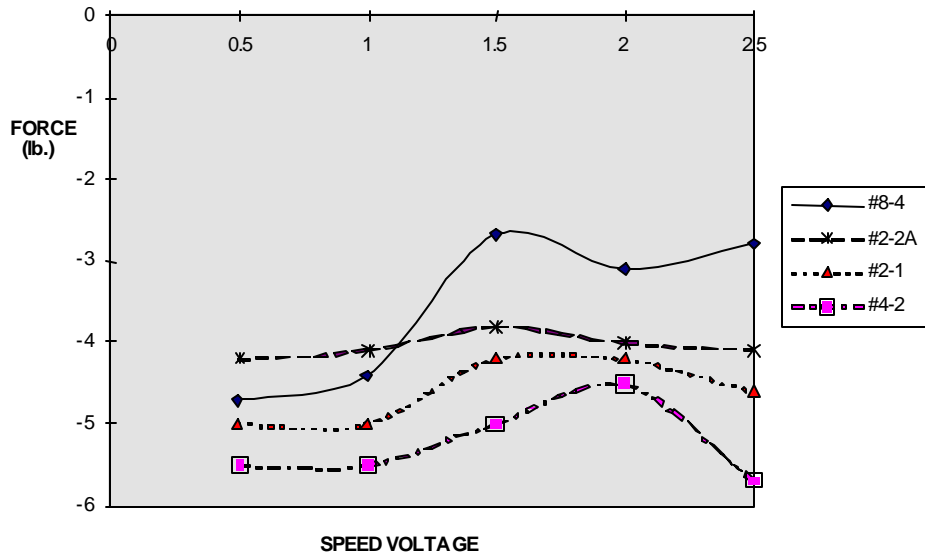


Figure 5-22. Extension – Blocked Actuator Force at a Displacement of 2.311 Inches for Various Sweep Patterns and Speed Voltage Settings

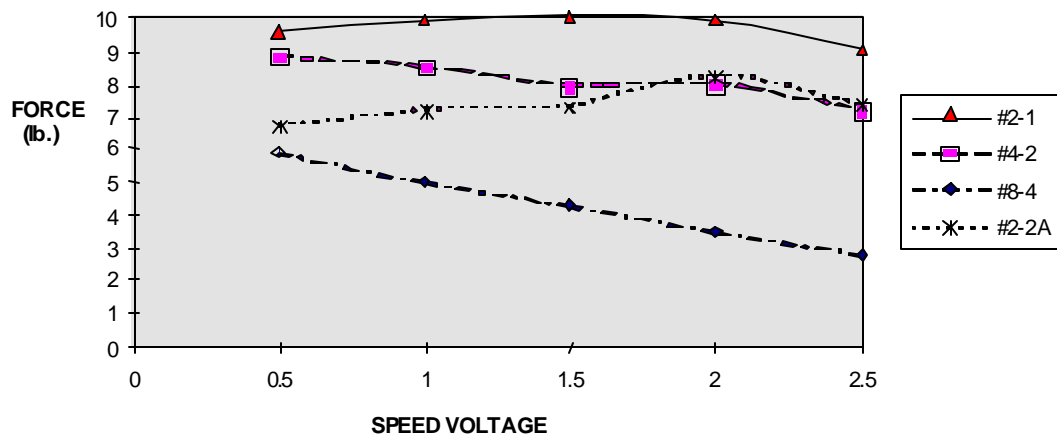


Figure 5-23. Retraction – Blocked Actuator Force at a Displacement of 3.077 Inches for Various Sweep Patterns and Speed Voltage Settings

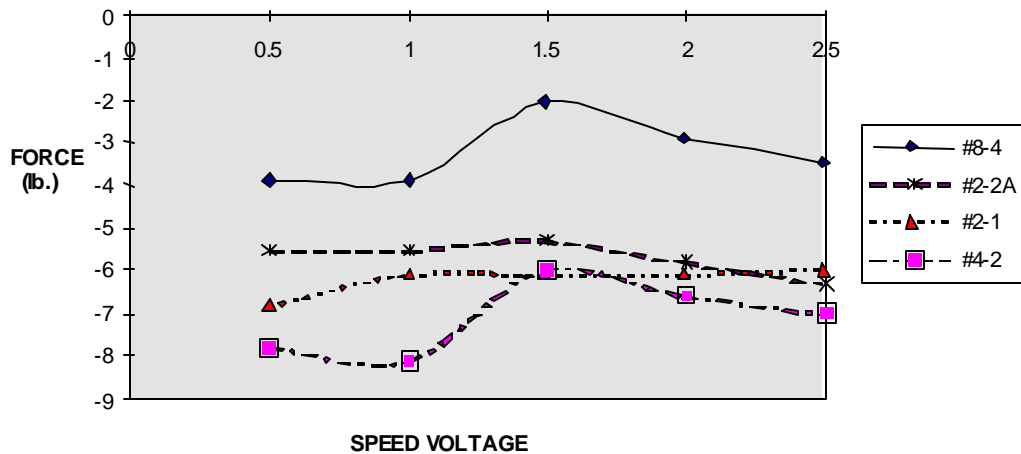


Figure 5-24. Extension – Blocked Actuator Force at a Displacement of 3.154 Inches for Various Sweep Patterns and Speed Voltage Settings

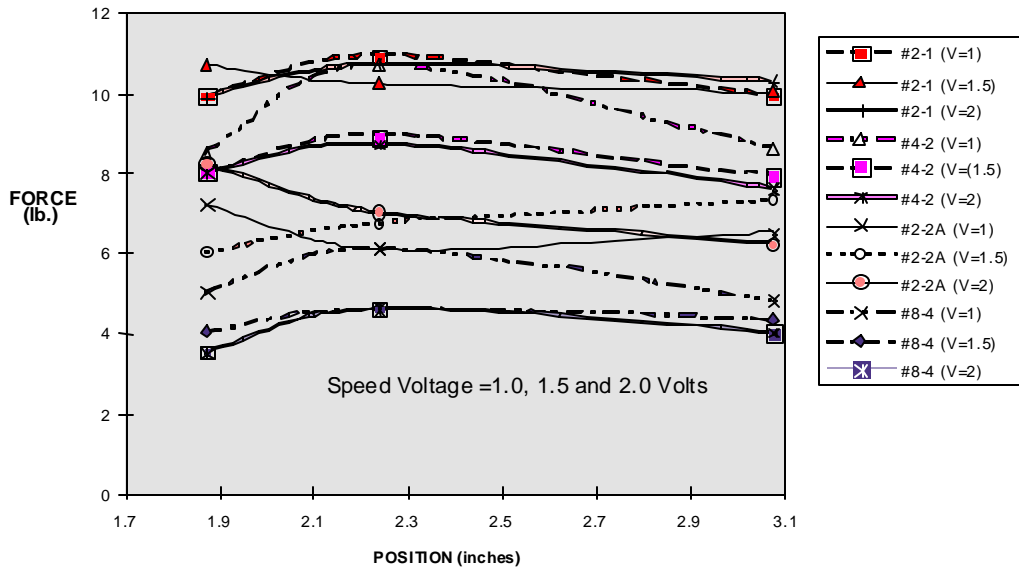
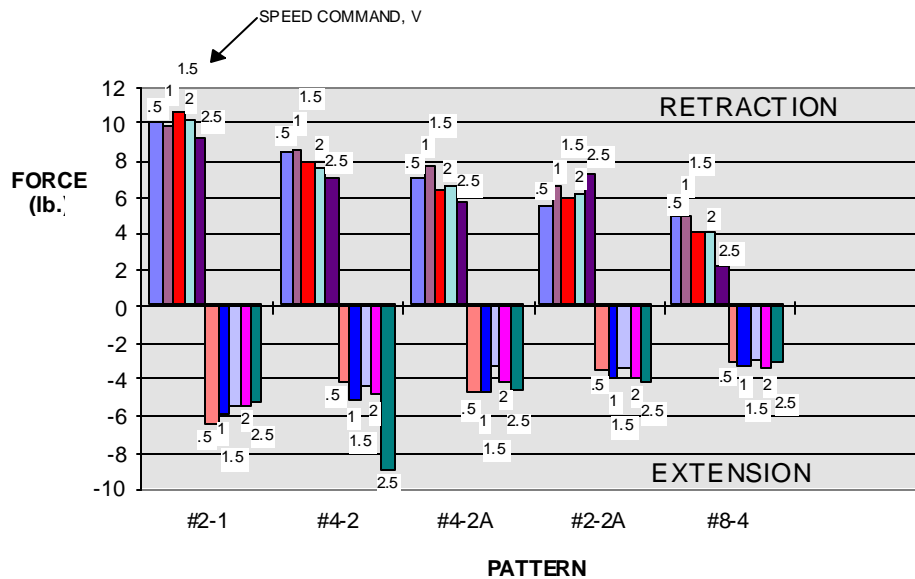


Figure 5-25. Retraction – Blocked Actuator Force for Various Patterns and Speed Voltage Settings as a Function of Position



Retraction is shown producing a positive (tension) stall force at 1.875 inches, and extension produces a negative (compression) stall force at 1.953 inches.

Figure 5-26. Blocked Actuator Force as a Function of Sweep Pattern for Various Sweep Speed Voltages

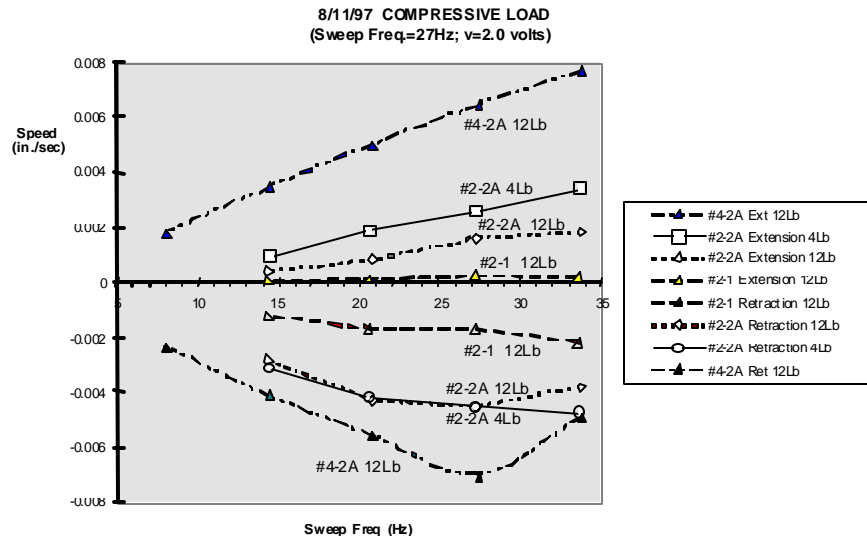
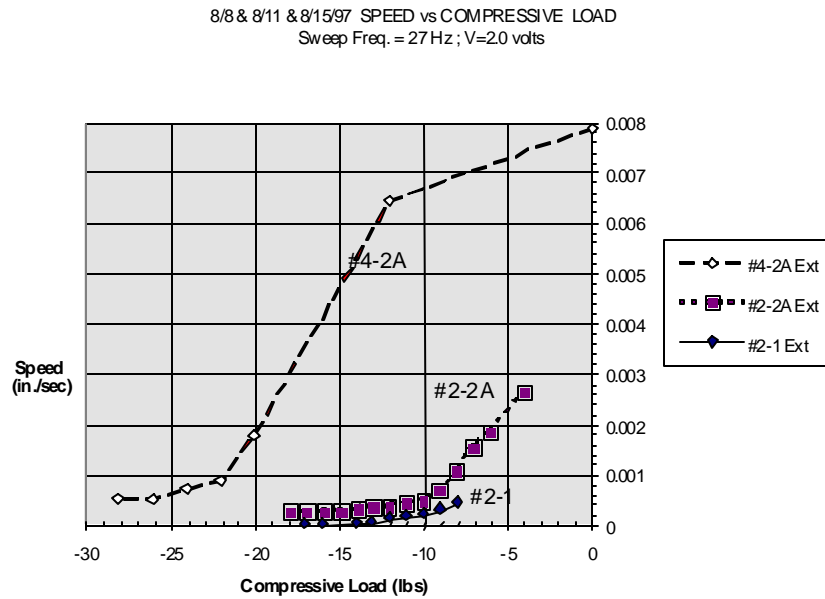


Figure 5-27. Comparison of Effectiveness of Pattern Modification Upon Speed at Different Compressive Loads

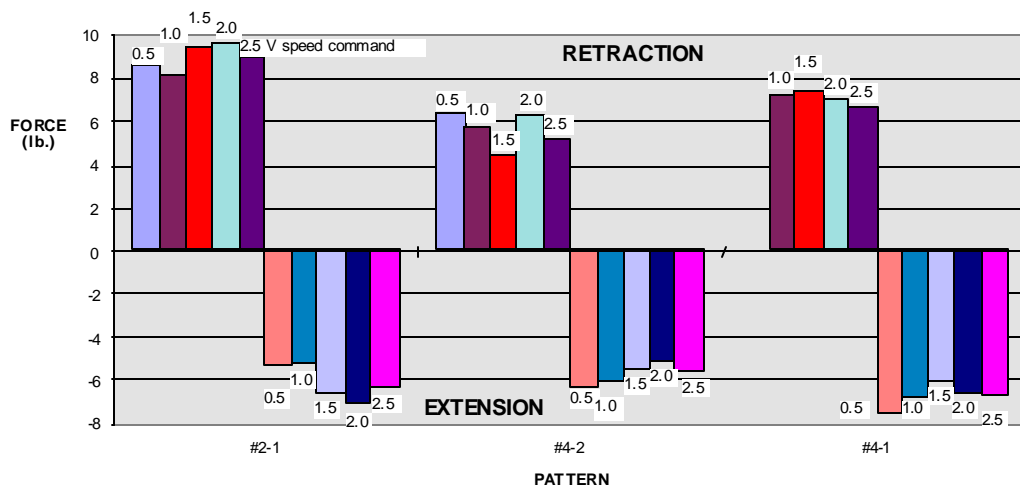


A no-load point taken from a different days data was added to 4-2a to complete the data

Figure 5-28. Comparison of Load-Handling Capability of Special Pattern to a Standard Pattern

At the end of the blocked actuator tests, motor performance was significantly degraded, and the motor was returned to ETREMA for inspection and repair. A polymer spacer between rod laminations shifted position, and a portion of the spacer, about 0.5" long, was found protruding from a lamination in the rod and was removed. The rod is laminated to reduce eddy currents. A small amount of dust on the contacting surfaces of the rod and tube was also removed. Motor wear is discussed in more detail in Subsection 5.3.5.

After the repair, some of the blocked motor tests were repeated. To minimize wear, the tests were restricted to 2-1 and 4-2 and a new 4-1 pattern. The overall results indicate a slightly reduced performance after the repairs. The data is summarized in Figure 5-29. The 2-1 pattern provided about 9 pounds instead of 10 pounds, and the 4-2 provided about 6 pounds instead of 7 pounds. The new 4-1 pattern was better in retraction than 4-2 but did not do better than the 2-1 pattern. Interestingly, the 4-1 pattern did do better than even the 2-1 pattern in extension. The extension characteristics show different trends than those of retraction. In general, the 4-1 pattern in extension provided the highest force.



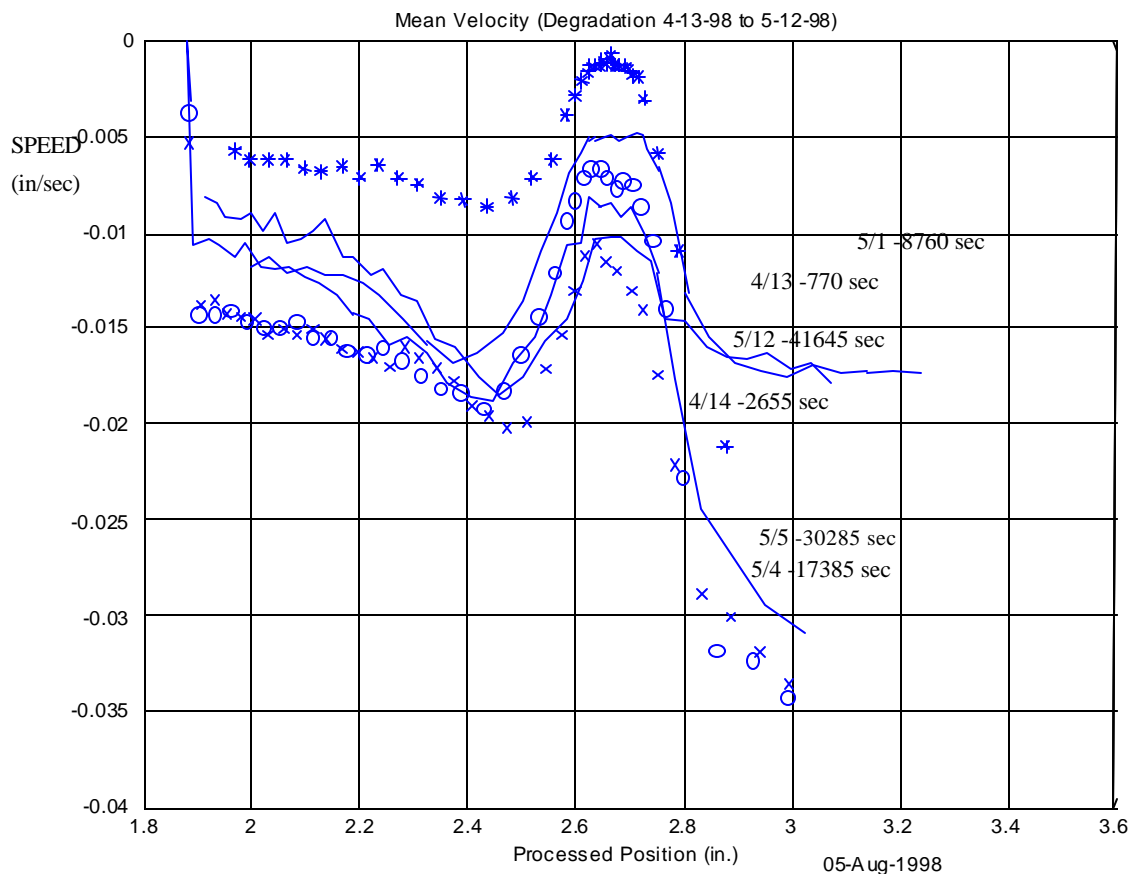
Retraction is shown producing positive (tension) stall force at 1.868 inches, and extension produces a negative (compression) stall force at 1.964 inches

Figure 5-29. Blocked Force of Repaired Actuator as a Function of Sweep Pattern for Various Sweep Speed Voltages

5.3.5 Motor Wear

During the period from October 1997 to October 1998, three motor stoppages resulted from wear, and a fourth stoppage (which occurred after motor-characterization tests were complete) was caused by shifting of the polymer spacer. In each case, small particles of TERFENOL-D were found on both the stator ID and TERFENOL-D rod. Generally, cleaning of the rod and tube corrected the problem. However, when the motor was disassembled after the second failure, some chipping was found at the end of the rod, and a new rod was manufactured. As a result, minimization of motor wear is a primary effort in the Phase 2 development program. We are investigating techniques such as coatings and the use of a split tube to eliminate the wear problem.

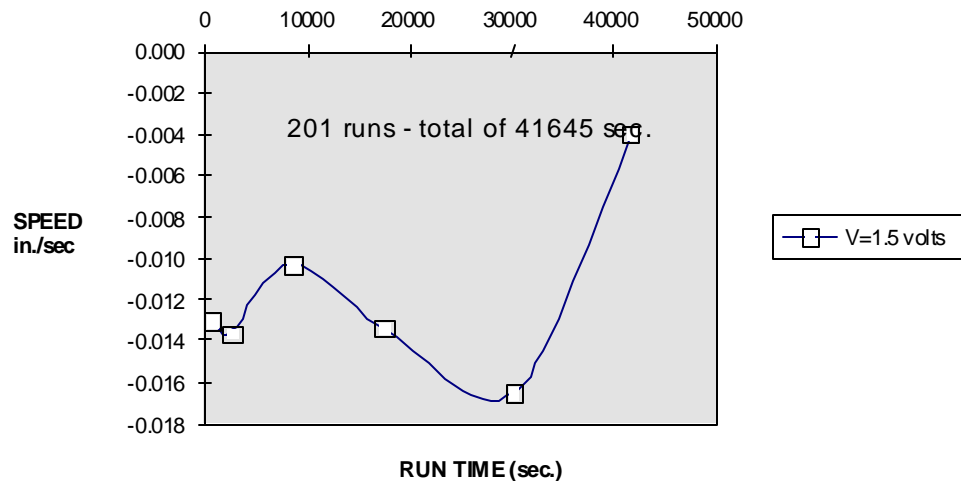
To quantify motor degradation, a baseline test was repeated four times on each test day. These tests were conducted at the start of each test the day, before lunch at the close of a morning testing session, at the start of an afternoon session, and at the end of the day's testing. This permitted any warming effects as well as degradation to be observed. In the baseline runs, the 8-4 pattern was used, and a 4 pound tension load was applied. The speed-voltage command was set at $V = 1.5$ volts. This value was selected because it provided the maximum speed over the entire span of the actuator for both the unloaded actuator and the case with the 4 pound tension load.



Baseline runs are retraction with a 4 pound tension load, an 8-4 pattern, and a sweep frequency of 84 Hz

Figure 5-30. Variation of Mean Velocity with Actuator Usage

There was notable degradation in performance during the testing on 5/12/98 (after 143 runs, 30,285 seconds of operation; and before accumulating 201 runs, 41,645 seconds). This degradation is evident in the end-of-day baseline plots of Figures 5-30 and 5-31. In the range of positions from 2.5 inches to 2.8 inches the armature slowed down and under certain conditions stalled. Differences were observed in both cold and hot performance, and some changes were noticed at specific armature locations.



From end-of-day baseline runs using an 8-4 pattern, a 4 pound tension load, and a speed voltage setting of 1.5 volts

Figure 5-31. Degradation in Average Speed Over Full Stroke, 4/13/98 to 5/12/98

6. PHASE 2 PROGRAM

Our Phase 2 program is now underway. We have selected Northrop Grumman's uninhabited combat air vehicle, a Mach 0.75 uninhabited fighter, to demonstrate the effectiveness of the TERFENOL-D powered smart trailing edge in a wind - tunnel. Magnetic and electronic revisions to the TERFENOL-D elastic-wave linear motor are being developed to reduce weight and increase load capacity and efficiency.

Significant cost savings are being achieved by implementing the technologies developed under this program and the related technologies described in Section 1 in a common wing design.

Under Phase 2, a finite-element method has been developed to enable us to optimize the geometry, structure, electro-magnetic design, and thermal design of the motor. Detailed motion of the Phase 1 actuator has already been using this program, and we feel confident that the program will lead to significant motor performance improvements.

Also, design variations are being considered that will eliminate the need for tight motor tolerances. ETREMA is now experimenting with a motor of approximately the same size as the Phase 1 actuator that has delivered 125 pounds of load at speeds of 5 inches/minute, and we feel confident that we can improve the performance.

The key design challenges being addressed under Phase 2 are discussed in the following subsections.

6.1 MECHANICAL

Since the linear motor working principle is based upon the worm-like motion of a TERFENOL-D rod inside a well-machined stator tube, diametrical tolerance, straightness, and surface finish are critical. Because this actuator depends upon an interference fit for operation, the mechanical design and tolerances affect the stroke, actuation and holding forces, speed, and power. The relationships between the active, locking, and total lengths of the TERFENOL-D rod, coil lengths, and rod diameter are highly interdependent and have a strong influence on the motor's performance. With our new finite-element tool, we will be able to determine optimum values of these parameters to maximize performance. Also, a new split-tube design is being investigated to eliminate the need for fine tolerances between the critical mating parts.

6.2 MAGNETIC

The magnetic field to activate a segment of the TERFENOL-D rod must be optimized to generate maximum magnetic field within the desired envelope and concentrated within the desired segment only. The concentration of the magnetic flux in the given segment maximizes magnetostriction in that segment and hence increases performance and lowers the power requirement and, therefore, the heat generation from the coils. The results of ANSYS® finite element modeling, as well as experimental measurements, indicate that the addition of magnetic field isolators and magnetic flux concentrators in the coils improve the flux maximization in the active rod segment while decreasing the magnetic flux in the inactive segments. In the Phase 2 motor, a new single component of soft magnetic material will be used to replace the magnetic field concentrator and magnetic field isolator.

The rod is hollow, and the size of the rod inside diameter (ID) can be varied to achieve a more uniform field, resulting in increased magnetostriction in the active region. The finite-element model will enable us to determine the optimum rod ID.

The coil design for maximum field output was limited by the linear motor envelope size and manufacturability of the stator tube. The coil design can be improved by using the best configuration that gives the maximum uniform magnetic field that is concentrated in the required location. This will lower the inductance of the coil as well as the rise time and allows higher operating frequency, meaning higher speed.

6.3 POWER

A method is being developed to minimize power consumption. Instead of dissipating the power delivered to each coil as heat, we are developing a circuit that will reuse much of the power to energize the next coils as the pattern is shifted. In addition to substantial efficiency improvements, this method will reduce the operating temperature of the motor.

6.4 THERMAL DESIGN

Stator tube design must account for the important influence of thermal expansion for high-performance linear-motor operation. The tube used in the linear motor will absorb heat from the coils, and thermal expansion of the tube will result. The TERFENOL-D rod inside the tube is also heated and expands. In Phase 1, a stator tube material was selected to match the thermal expansion coefficient of the TERFENOL-D. However, since the tube and rod temperatures may differ, the tube material selection will be revisited to determine whether a mismatch in the expansion coefficients would provide superior performance. Improved thermal management will be key to maintaining optimal operation of the Phase 2 linear motor over the range of environmental conditions. The approach is to (1) eliminate unwanted sources of heat generation, for example through design optimization and efficiency, and (2) manage those sources that remain, for example, through materials selection.

6.5 TRIBOLOGY

The friction characteristics of the materials in the drive rod and stator tube were studied in Phase 1. This investigation is being expanded in Phase 2 to include any new stator tube materials. In addition, the durability conditions will be more fully considered, and the wear characteristics will be measured. Durability improvements are expected through a combination of design configuration alternatives, materials selection, and, if needed, surface finishes and/or treatments.

6.6 MODELING

Modeling and simulation will play an important role in maximizing motor performance. TERFENOL-D presents a rich set of variables to achieve balanced and optimized designs. In addition, the elastic-wave linear motor concept adds even more design variables to manipulate. Efficiently trading off all these variables lends itself to use of analysis and credible models that integrate the features of the multiple physical systems involved. These models will become the tools to effectively complete parametric sensitivity studies, trade-offs, and optimization. It would be cost prohibitive to experimentally examine the large number of promising alternative design combinations.

Under Phase 2, a high-level code has been developed to enable us to use the ANSYS finite-element system to optimize the geometry, structure, electro-magnetic design, and thermal design of the motor. This finite element program enables analysis of systems with coupled structural, magnetic, nonlinear magnetostrictive, dynamic, and variable-contact effects. Thermal-strain effects are being incorporated. Detailed motion of the Phase 1 actuator has already been simulated with this program, and we feel confident that the program will lead to significant motor performance improvements.

7. CONCLUSIONS

Concepts for modifying wing shapes during flight were investigated. It was shown that, by doing so, drag can be constantly minimized in the transonic region as the flight condition changes, resulting in fuel savings exceeding 5 percent. Since commercial jets use 13 billion gallons of fuel each year, at an annual cost of \$7 billion, saving even a small portion of this fuel would provide significant economic and ecological benefits. Two approaches were examined: an adaptive wing that changes shape between the forward and rear spars, and a trailing edge that translates and rotates to maintain a smooth upper surface. The Gulfstream III was selected as a baseline aircraft for the Phase 1 study. A modified simulated annealing scheme was used, together with computational fluid dynamics codes, to obtain optimum designs of both the adaptive-wing and trailing edge systems. With the adaptive wing, drag reductions of up to 40 counts over baseline airfoils were achieved for certain flight conditions; however, it was found that the additional drag resulting from the weight of the actuators offsets the benefits of the adaptive-wing concept. In the future, if sufficiently light actuators could be developed, the adaptive wing could be used to provide optimum wing shapes throughout the transonic region. On the other hand, with the TERFENOL-D powered smart trailing edge, far fewer and lighter actuators are required; consequently, drag reductions exceeding 5 percent can be achieved. To drive the trailing edge, a proof-of-concept TERFENOL-D elastic-wave linear motor was developed. This first motor had a stroke of 1.5 inches, exerted a load of 28 pounds, and traveled at a speed of 3 inches/minute, which is more than adequate for the transonic cruise application. The motor has no backlash or end play, and with only one moving part, it has the potential for very high reliability. Several motor improvements were identified, and under Phase 2, we are already experimenting with a motor of approximately the same size that exerted a 125 pounds load at a speed of 5 inches/minute.

8. REFERENCES

1. R. Clifford and V. Kottamasu, "The ETREMA Terfenol-D[®] Based Linear Motor Design and Development Program, Phase 1 B Report," Nov. 1995.
2. R. Clifford and V. Kottamasu, "The ETREMA Terfenol-D[®] Based Linear Motor Design and Development Program, Phase 1 C Report," Dec. 1995.
3. G. N. Weisensel and V. Kottamasu, "The ETREMA Terfenol-D[®] Based Linear Motor Design and Development Program, Phase 1 D and 1 E Report," Sept. 1996.
4. G. N. Weisensel, V. Kottamasu, and K. Shoop, "The ETREMA Terfenol-D[®] Based Magnetostrictive Elastic Wave Type Linear Motor Design and Development Program, Operating Instruction Manual," Feb. 1997.
5. G. N. Weisensel and V. Kottamasu, "The ETREMA Terfenol-D[®] Based Linear Motor Design and Development Program, Final Report, Phase 1 F 1 G, 2 & 3," Feb. 1997.
6. F. Austin, M. J. Rossi, A. Jameson, W. Van Nostrand, J. Su, and G. Knowles, "Active rib experiment for adaptive conformal wing," Proceedings of the Third International Conference on Adaptive Structures, San Diego, CA, Nov. 1992, pp. 43-55.
7. F. Austin, W. Van Nostrand and M. J. Rossi, "Shape control of structures with semi-definite stiffness matrices for adaptive wings," Proceedings of the 1993 North American Conference on Smart Structures and Materials, Albuquerque, NM, Jan.-Feb. 1993.
8. M. Rossi, F. Austin and W. Van Nostrand, "Active rib experiment for shape control of an adaptive wing," AIAA paper 93-1700, Proceedings of the 34th Structures, Structural Dynamics, and Materials Conference, April 1993, pp. 3485-3489.
9. F. Austin, M. J. Rossi, W. Van Nostrand, G. Knowles, and A. Jameson, "Static Shape Control for Adaptive Wings," *AIAA Journal*, **32**, pp. 1895-1901, 1994.
10. F. Austin and W. Van Nostrand, "Shape control of an adaptive wing for transonic drag reduction," presented at the SPIE 1995 North American Conference on Smart Structures and Materials, San Diego, CA, Feb.-March 1995.
11. F. Austin, W. Van Nostrand, M. J. Siclari, P. Aidala, and R. Clifford, "Design and Performance Predictions of Smart Wing for Transonic Cruise," *Proc. of SPIE's 3rd International Symposium on Smart Structures and Materials 1996*, **2721**, pp. 17-25.
12. S. Aly, F. Marconi, M. Ogot, R. B. Pelz, and M. J. Siclari, "Stochastic Optimization Applied to CFD Design," AIAA- 95-1647, *12th AIAA CFD Conference*, 1995.
13. M. J. Siclari, W. Van Nostrand, and F. Austin, "The Design of Transonic Airfoil Sections for an Adaptive Wing Concept Using a Stochastic Optimization Method," *34th Aerospace Sciences Meeting & Exhibit, Reno, NV*, AIAA-96-0329, 1996.
14. H. R. Mead and R. E. Melnik, "GRUMFOIL: a computer code for the viscous transonic flow over airfoils," NASA CR 3806, Oct. 1985.
15. F. Austin, M. J. Siclari, W. Van Nostrand, G. N. Weisensel, V. Kottamasu, and G. Volpe, "Comparison of Smart wing Concepts for Transonic Cruise Drag Reduction," *Proc. of SPIE's 4th International Symposium on Smart Structures and Materials*, **3044**, pp. 33-40, March 1997.

- 16 E. Greff, "The Development and Design Integration of a Variable Camber Wing for Long/Medium Range Aircraft, *Aeronautical Journal*, pp. 301-312, 1990.
- 17 J. H. Renken, "Mission Adaptive Wing Camber Control Systems for Transport Aircraft", AIAA Paper, 1985.
- 18 H. Hilbig and H. Wagner, Variable Wing Camber Control for Civil Transport Aircraft, ICAS-84-5.2.1, 1984.
- 19 J. Szodruch, "The Influence of Camber Variation on the Aerodynamics of Civil Transport Aircraft", AIAA Paper, 1985.
- 20 L. T. Anderson and R. W. DeCamp, "Camber Control System," U.S. Patent 4741503, 1988.
- 21 A. Arena, "Linear Actuator System," patent application NGC No. P-1(10193), 1995.
- 22 M. J. Siclari, F. Austin, W. Van Nostrand, and G. Volpe, "Optimization of Segmented Flaps for In-Flight Transonic Performance Enhancement," *35th Aerospace Sciences Meeting & Exhibit*, AIAA-97-0516, 1997.
- 23 M. J. Siclari and F. Austin, "Optimization of a Realistic Flap Design for In-Flight Transonic Performance Enhancement," *36th Aerospace Sciences Meeting & Exhibit*, AIAA-98-0596, 1998.
- 24 V. N. Vatsa, M. D. Sanetrik, and E. B. Parlette, "Development of a Flexible and Efficient Multigrid-Based Multiblock Flow Solver," AIAA Paper No. 93-0677, Jan. 1993.
- 25 M. Kesselman, "Coil Temperature Estimates," Northrop Grumman IOM, Dec. 1997.
- 26 J. Klein, "Calculated Terfenol-D Actuator Coil Temperatures," Northrop Grumman IOM, Sept.. 1998.
- 27 M. Kesselman, "Summary of Data Taken May-August 1998, Loaded Testing of Repaired Armature TERFENOL Actuator", Northrop Grumman Memorandum, Aug. 1998.

VOLUME III

WIND TUNNEL TEST RESULTS

Table of Contents

VOLUME III

WIND TUNNEL TEST RESULTS

Introduction.....	III-1
Data Collection and Section Organization.....	III-1
Wind Tunnel Test 1	III-3
Wind Tunnel Test 2.....	III-95

Table of Figures

VOLUME III

WIND TUNNEL TEST RESULTS

Figure	Page
1-1. Program Test Sequence	III-1
1-2. Smart Wing Wind Tunnel Test Conditions.....	III-2
1-3. Test 1 Data Collected at Q = 60 psf, M = 0.20	III-3
1-4. Test 1 Data Collected at Q = 90 psf, M = 0.25	III-3
1-5. Test 1 Data Collected at Q = 120 psf, M = 0.29	III-4
2-1. Test 2 Data Collected at Q = 60 psf, M = 0.20	III-95
2-2. Test 2 Data Collected at Q = 90 psf, M = 0.25	III-95
2-3. Test 2 Data Collected at Q = 120 psf, M = 0.29	III-95

INTRODUCTION

Wind tunnel test results have been discussed in several sections throughout the report, and particularly in Section 5 where key results were highlighted to illustrate the program technology benefits. Inclusion of all of the relevant test data in the body of the report would have been extensive and overly cumbersome. This volume brings together all of the relevant wind tunnel data assimilated over a total of 130 test runs, with many different permutations of test conditions during the two wind tunnel test events. Accordingly, the data has been divided and compiled into two separate sections for each test series:

Test 1 Series – Smart Wing Phase 1, Test Entry 1, performed at NASA Langley’s TDT facility during May 1996.

Test 2 Series – Smart Wing Phase 1, Test Entry 2, performed at NASA Langley’s TDT facility during July 1998.

Figure 1-1 represents the overall approach followed during both of the wind tunnel test series in terms of the model configuration, tunnel pressure conditions and AOA ranges examined during data collection. Essentially the second wind tunnel test series exercised more developed and integrated smart wing concepts, through larger ranges of parameters (e.g., AOA) and/or more severe test conditions.

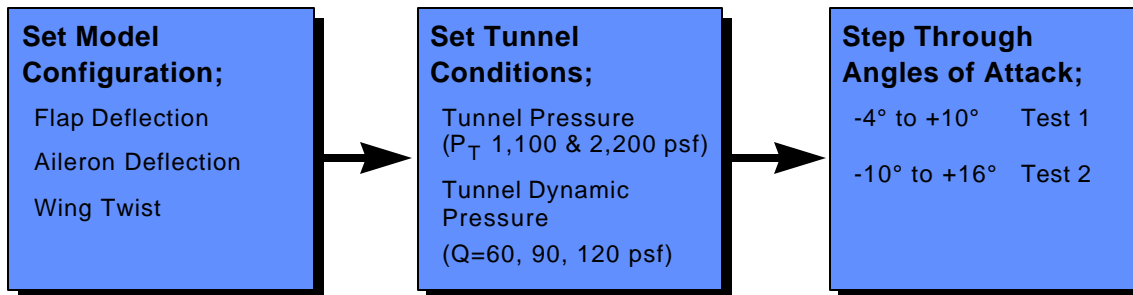


Figure 1-1. Program Test Sequence

Figure 1-2 shows overall tunnel conditions for both test series. The graph illustrates the dependence of Mach number and dynamic pressure (Q or $\frac{1}{2}\rho V^2$) on total tunnel pressure pressures (e.g., 1,100 and 2,200 pounds per square foot). The selection of two total pressure values reduced the amount of data collected and tunnel time required to a reasonable duration and gave adequate characterization for proof of concept rather than qualification.

DATA COLLECTION AND SECTION ORGANIZATION

The data for both the wind tunnel tests has been organized into tables and graphs. A closer inspection of Figure 1-1 not only reveals the general test sequence for performing tunnel measurements, but provides insight into how the data was assimilated for a particular test run. Essentially, runs were performed by holding the tunnel total pressure, dynamic pressure (and hence Mach number) constant while sweeping the angle of attack - usually taking eleven data points. Separate tunnel runs were iterated for variations in flap and aileron deflections and wing twist. An identical process was used for both the conventional wing and smart wing models so that legitimate comparisons could be made to establish the benefits of the smart technology. Also, it was important to make comparisons with the models with no control surfaces deflected to verify that they were identical and that the benefits came from the smart structures not in some difference in the models. Hence, the first runs performed for both models in both test entries were baseline runs (no control surface deflections or spanwise twist) to verify model similarity.

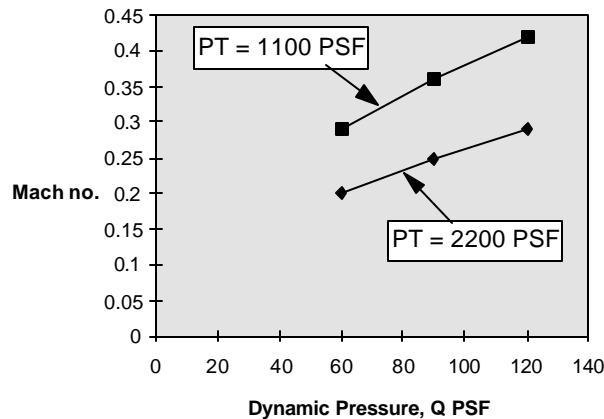


Figure 1-2. Smart Wing Wind Tunnel Test Conditions

All results have been plotted graphically so that a direct comparison between the conventional hinged wing and smart technology model can be readily made. Preceding both of the wind tunnel data compilation sections, tables identifying the specific run number used in data collection, and test conditions with respect to control surface orientation are delineated. The tables are also cross referenced to the appropriate section page number, graphs (usually) six to one page have been printed to save space.

There are fundamentally two distinct types of graphs displayed in the data compilation of the later sections relating to (1) pressure graphs, and (2) coefficient data. The pressure plots compare the pressure outputs for the differing rows of static ports that were installed on the model (See Volume I, Section 5). Quite unilaterally, it can be seen among all the curves that the contoured control surface gave favorable, and often marked improvements in pressure distribution, compared to the hinged control surface counterpart. This theme has been repetitively emphasized throughout the text due to its importance and advocacy for adaptive technology investigated on the program. For each run, there are eight pressure plots – four rows of pressure ports with the data being shown for two different angles of attack.

A quick perusal of the remaining graphical data will reveal that other graphs show another important measure-of-merit in aerodynamic assessment namely, aerodynamic coefficient data versus angle of attack (AOA). The coefficient specifics displayed are (1) lift versus AOA, (2) lift versus drag, (3) pitching moment versus AOA, and (4) rolling moment versus AOA. As to be expected for consistency, all plots comparisons were made for identical dynamic pressure (Q) and Mach number conditions. The interested reader is invited to examine all of the data to draw his own conclusions from the test cases recorded in both wind tunnel series. But, assuredly, an overriding conclusion should emerge from such study that the smart wing fared better, ranging from 10 to 15 percent improvement in efficiency than its conventional hinged wing counterpart. Such conclusions should bode well for the future applications of the technology.

1. WIND TUNNEL TEST 1

Run	Flap Deflection Angle (deg.)		Aileron Deflection Angle (deg.)		Comments	Page
	Conv	Smart	Conv	Smart		
Run 87 vs 17	0°	0°	0°	0°		6
Run 87 vs 69	0°	0°	0°	0°		8
Run 93 vs 6	5°	4.7°	0°	0°	missing data in run 74; used run 6	10
Run 93 vs 15 (partial)	7.5°	4.7°	0°	0°		12
Run 93 vs 75	7.5°	4.7°	0°	0°		14
Run 93 vs 80	10°	4.7°	0°	0°		16
Run 100 vs 6	5°	- 4°	0°	0°	inverted Smart Wing	18
Run 100 vs 75	7.5°	- 4°	0°	0°	inverted Smart Wing	20
Run 100 vs 80	10°	- 4°	0°	0°	inverted Smart Wing	22
Run 107 vs 18	0°	0°	5°	4°		24
Run 107 vs 30	0°	0°	10°	4°		26
Run 110 vs 44	0°	0°	- 5°	- 4°		28
Run 110 vs 56	0°	0°	- 10°	- 4°		30
Run 104 vs 23	5°	- 4°	5°	- 4°		32
Run 104 vs 24	7.5°	- 4°	5°	- 4°		34
Run 104 vs 35	5°	- 4°	10°	- 4°		36
Run 104 vs 39	10°	- 4°	10°	- 4°		38
Run 98 vs 87	N/A	0°	N/A	0°	inverted run vs. clean wing	40

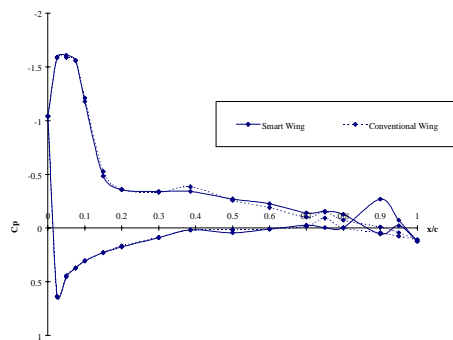
Figure 1-3. Test 1 Data Collected at Q = 60 psf, M = 0.20

Run	Flap Deflection Angle (deg.)		Aileron Deflection Angle (deg.)		Comments	Page
	Conv	Smart	Conv	Smart		
Run 88 vs 2	0°	0°	0°	0°		42
Run 94 vs 5	5°	4.7°	0°	0°		44
Run 94 vs 11	10°	4.7°	0°	0°		46
Run 94 vs 14	7.5°	4.7°	0°	0°		48
Run 101 vs 5	5°	- 4°	0°	0°	inverted Smart Wing	50
Run 101 vs 11	10°	- 4°	0°	0°	inverted Smart Wing	52
Run 101 vs 14	7.5°	- 4°	0°	0°	inverted Smart Wing	54
Run 108 vs 19	0°	0°	5°	4°		56
Run 108 vs 31	0°	0°	10°	4°		58
Run 111 vs 45	0°	0°	- 5°	- 4°		60
Run 111 vs 57	0°	0°	- 10°	- 4°		62
Run 105 vs 22	5°	- 4°	5°	- 4°		64
Run 105 vs 25	7.5°	- 4°	5°	- 4°		66
Run 105 vs 34	5°	- 4°	10°	- 4°		68
Run 105 vs 40	10°	- 4°	10°	- 4°		70
Run 99 vs 88	N/A	0°	N/A	0°	inverted run vs. clean wing	72
Run 113 vs 89	0°	0°	0°	0°	Both Torque Tubes, Wing Twist = 1.25° (inboard - 0.5°, outboard - 0.75°)	74

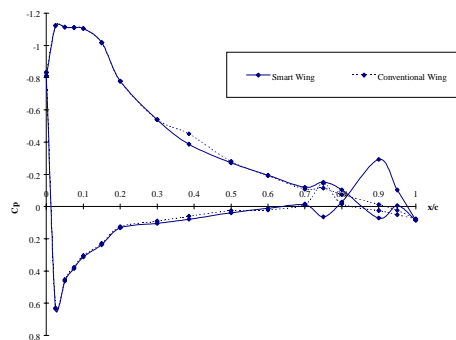
Figure 1-4. Test 1 Data Collected at Q = 90 psf, M = 0.25

Run	Flap Deflection Angle (deg.)		Aileron Deflection Angle (deg.)		Comments	Page
	Conv	Smart	Conv	Smart		
Run 89 vs 3	0°	0°	0°	0°	AOA = 10° instead of 8°	76
Run 103 vs 8	5°	- 4°	0°	0°		78
Run 103 vs 12	10°	- 4°	0°	0°		80
Run 103 vs 13	7.5°	- 4°	0°	0°	AOA = 10° instead of 8°	82
Run 106 vs 21	5°	- 4°	5°	- 4°	inverted Smart Wing	84
Run 106 vs 26	7.5°	- 4°	5°	- 4°	inverted Smart Wing	86
Run 106 vs 33	5°	- 4°	10°	- 4°	inverted Smart Wing	88
Run 106 vs 41	10°	- 4°	10°	- 4°	inverted Smart Wing	90
Run 109 vs 20	0°	0°	5°	4°		92
Run 112 vs 46	0°	0°	-5°	- 4°		94

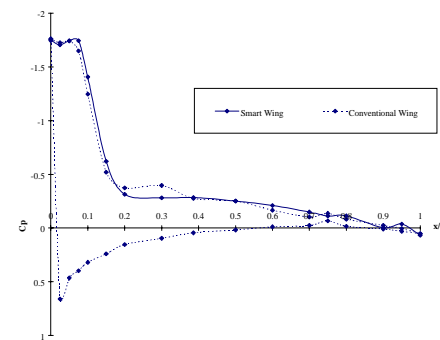
Figure 1-5. Test 1 Data Collected at Q = 120 psf, M = 0.29



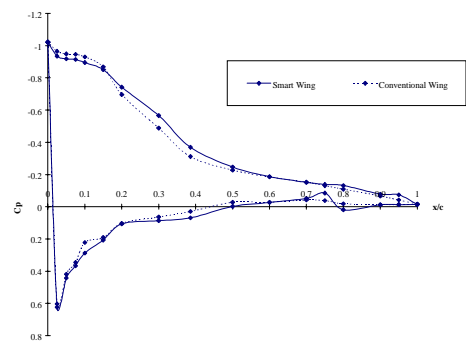
Row A, AOA = 8



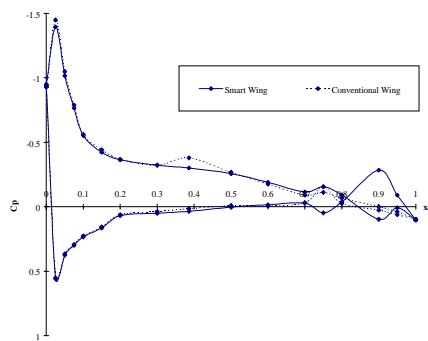
Row B, AOA = 8



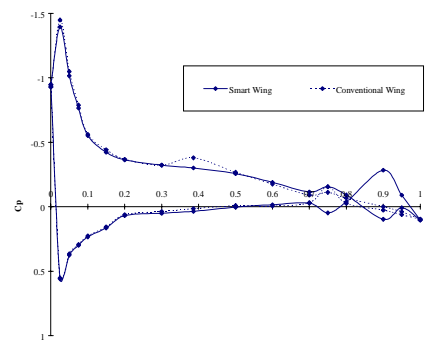
Row C, AOA = 8



Row D, AOA = 8

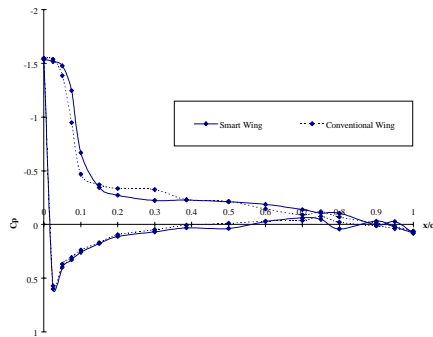
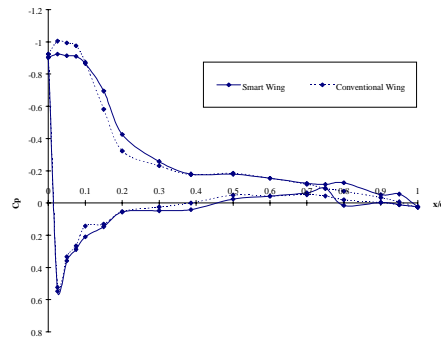
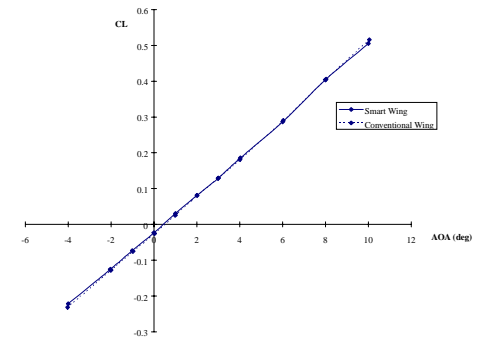


Row A, AOA = 6

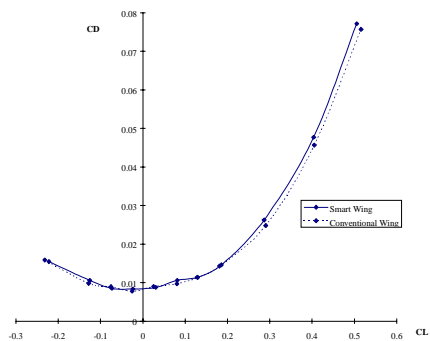


Row B, AOA = 6

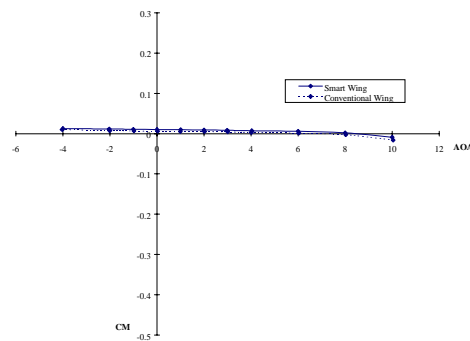
Run 87 vs 17
 $M = 0.20$, $Q = 60$ psf
 Conventional Flap = 0° Aileron = 0°
 Smart Flap = 0° Aileron = 0°

Row C, $AOA = 6$ Row D, $AOA = 6$ 

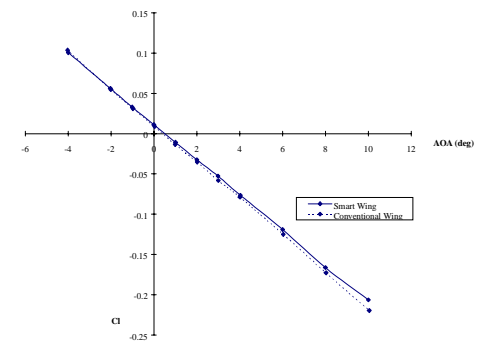
CL vs. AOA



CD vs. CL



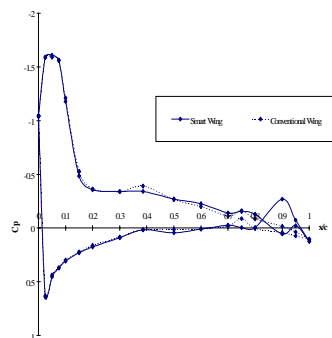
CM vs. AOA



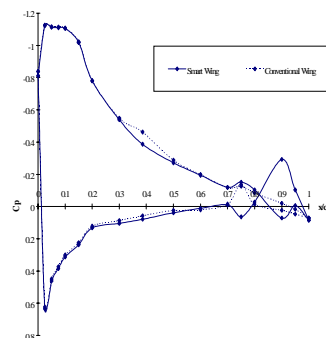
Roll Moment vs. AOA

Run 87 vs 17

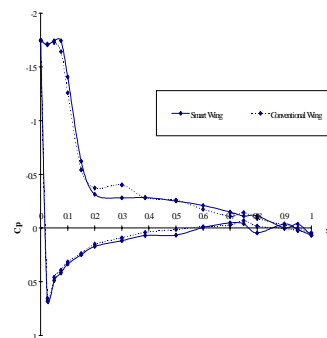
 $M = 0.20$, $Q = 60$ psfConventional Flap = 0° Aileron = 0° Smart Flap = 0° Aileron = 0°



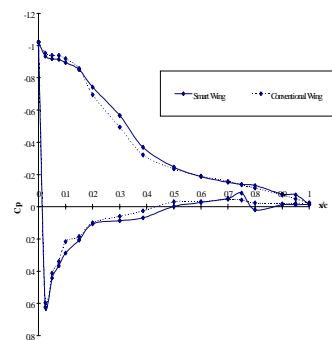
Row A, AOA = 8



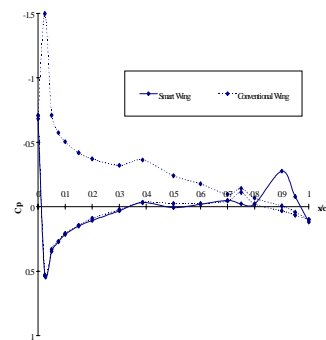
Row B, AOA = 8



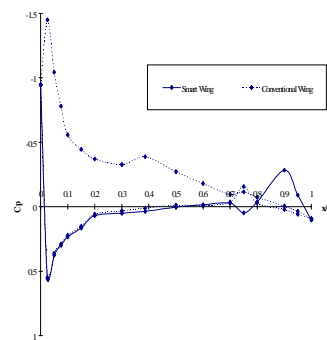
Row C, AOA = 8



Row D, AOA = 8

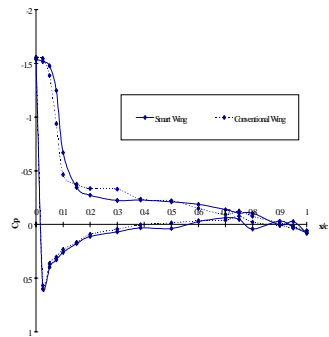


Row A, AOA = 6

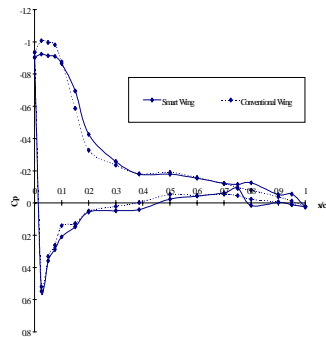


Row B, AOA = 6

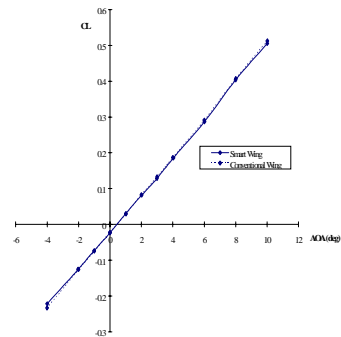
Run 87 vs 69
 $M = 0.20$, $Q = 60$ psf
 Conventional Flap = 0° Aileron = 0°
 Smart Flap = 0° Aileron = 0°



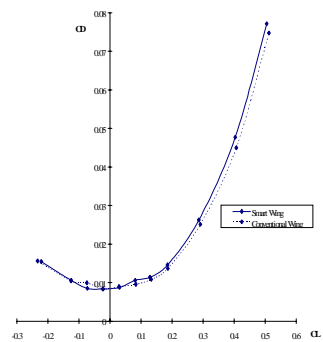
Row C, AOA = 6



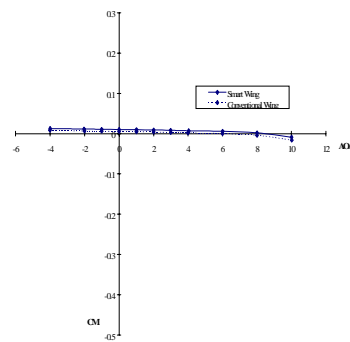
Row D, AOA = 6



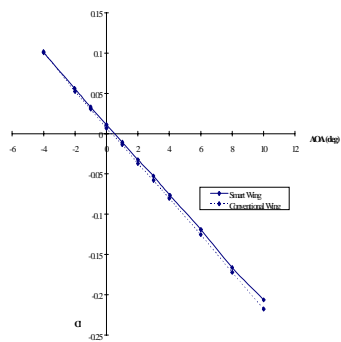
CL vs. AOA



CD vs. CL

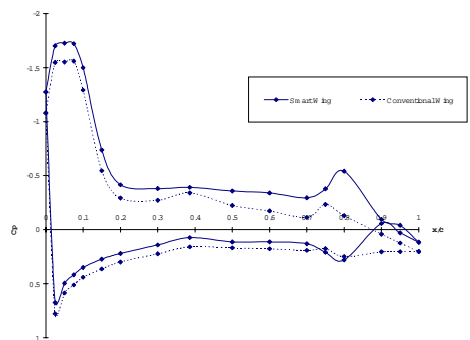


CM vs. AOA

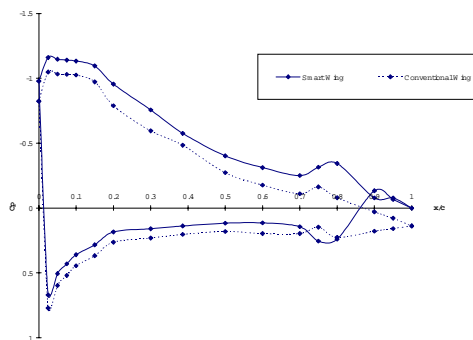


Roll Moment vs. AOA

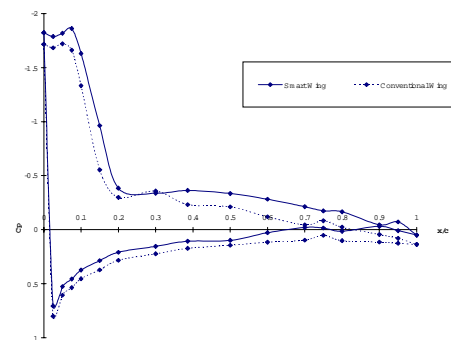
Run 87 vs 69
 $M = 0.20$, $Q = 60$ psf
 Conventional Flap = 0° Aileron = 0°
 Smart Flap = 0° Aileron = 0°



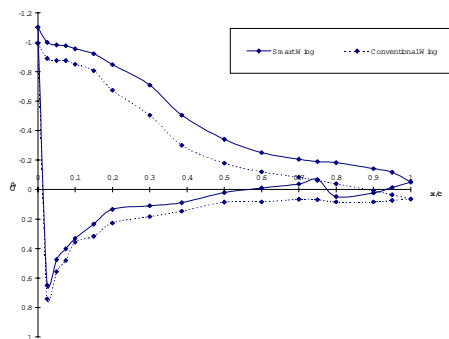
Row A, AOA = 8



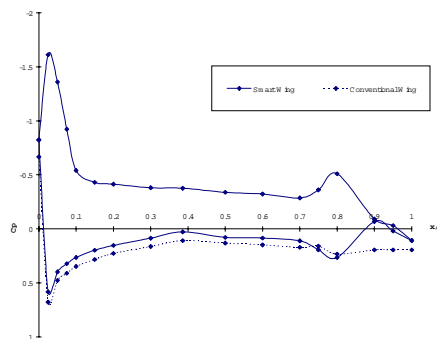
Row B, AOA = 8



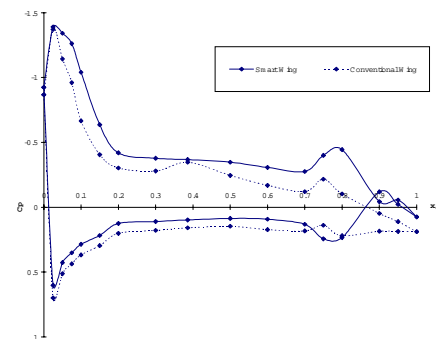
Row C, AOA = 8



Row D, AOA = 8

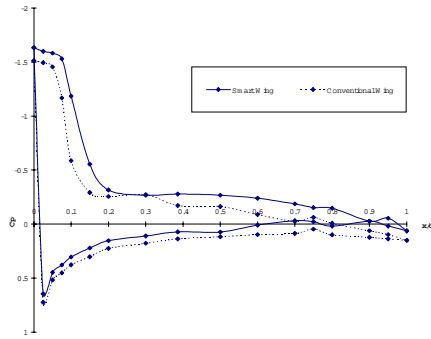


Row A, AOA = 6

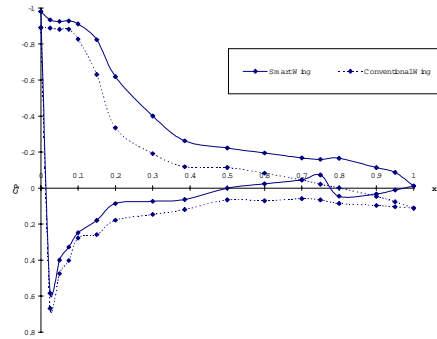


Row B, AOA = 6

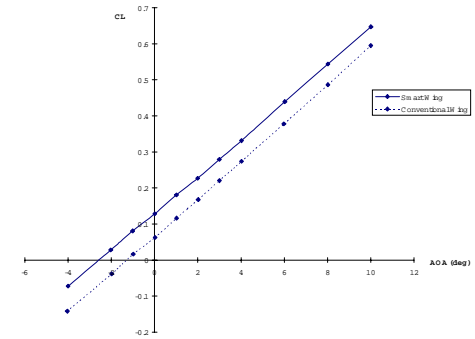
Run 93 vs 6
 $M = 0.20$, $Q = 60$ psf
 Conventional Flap = 5° Aileron = 0°
 Smart Flap = 4.7° Aileron = 0°



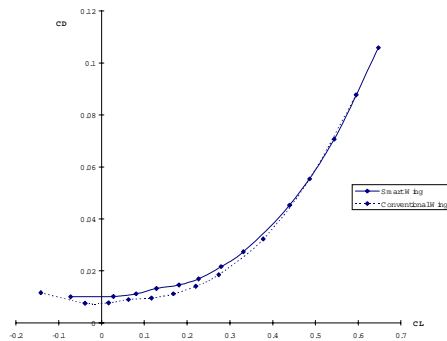
Row C, AOA = 6



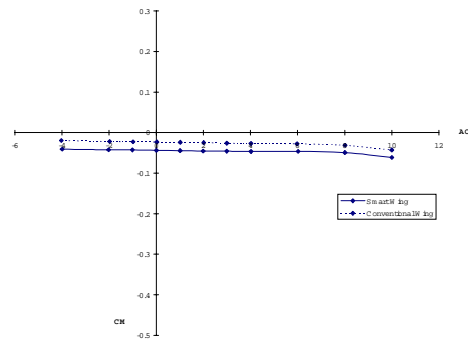
Row D, AOA = 6



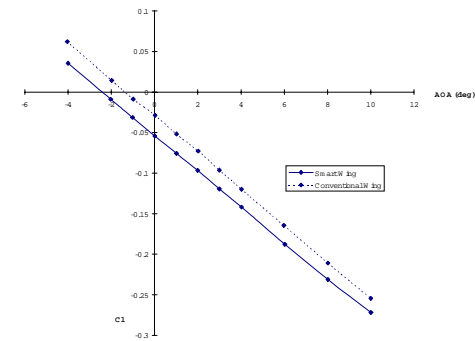
CL vs. AOA



CD vs. Cl

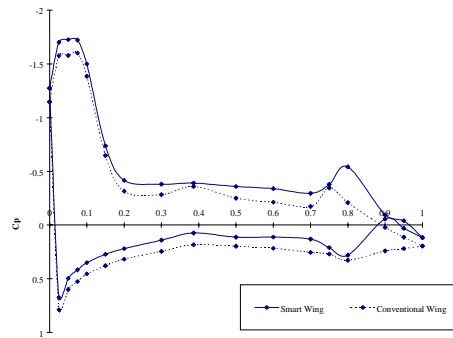


CM vs. AOA

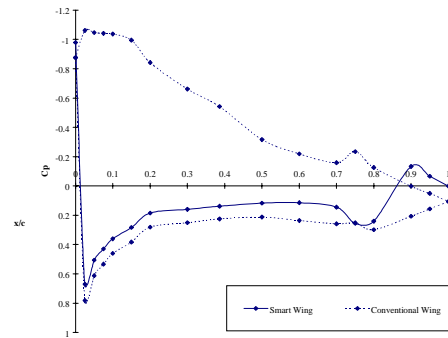


Roll Moment vs. AOA

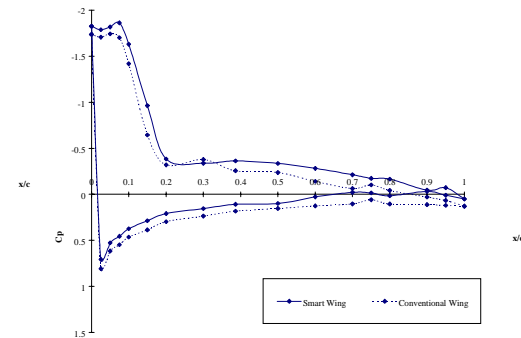
Run 93 vs 6
 $M = 0.20$, $Q = 60$ psf
 Conventional Flap = 5° Aileron = 0°
 Smart Flap = 4.7° Aileron = 0°



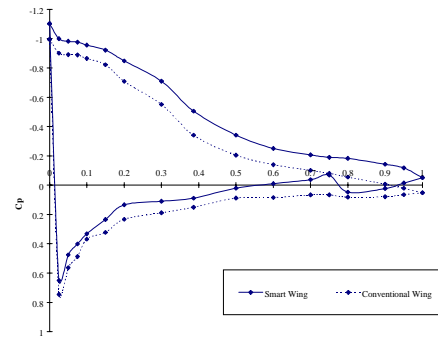
Row A, AOA = 8



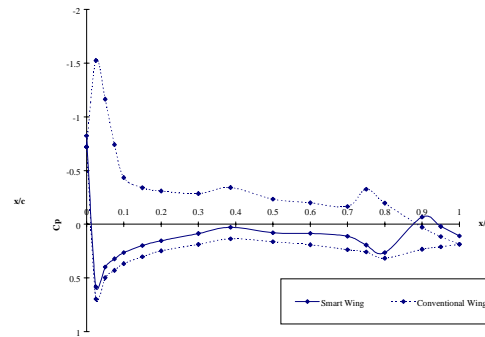
Row B, AOA = 8



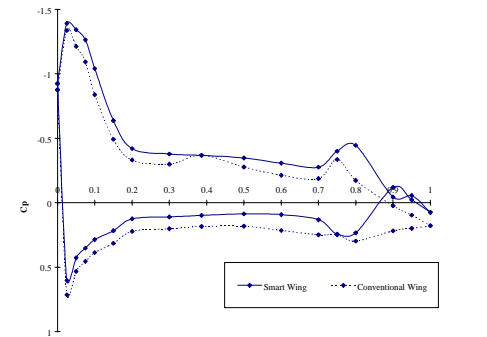
Row C, AOA = 8



Row D, AOA = 8

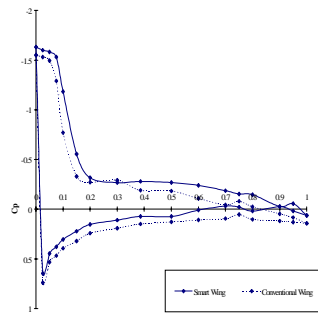


Row A, AOA = 6

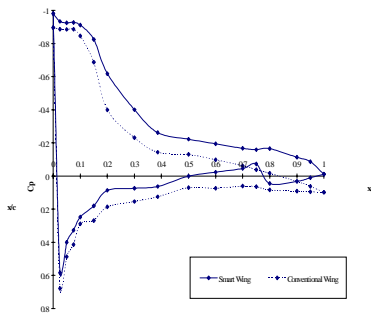


Row B, AOA = 6

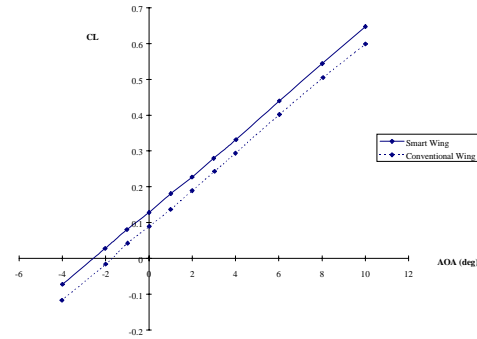
Run 93 vs 15 (partial)
 $M = 0.20$, $Q = 60$ psf
 Conventional Flap = 7.5° Aileron = 0°
 Smart Flap = 4.7° Aileron = 0°



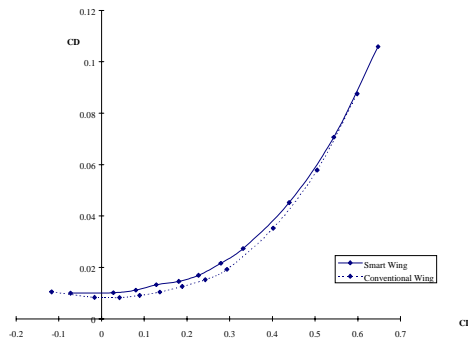
Row C, AOA = 6



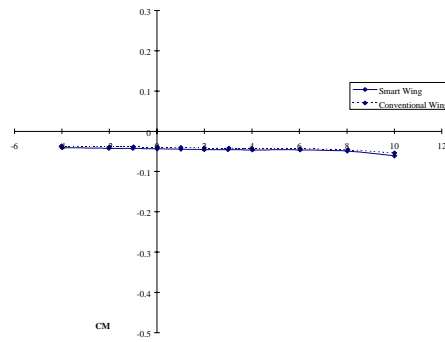
Row D, AOA = 6



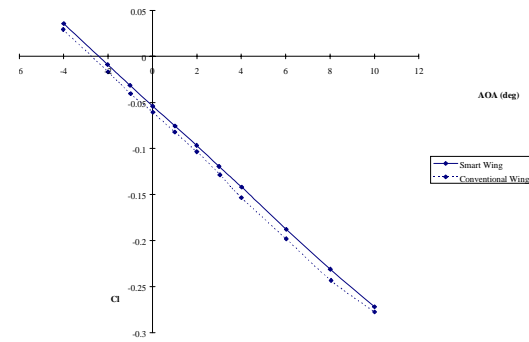
CL vs. AOA



CD vs. Cl

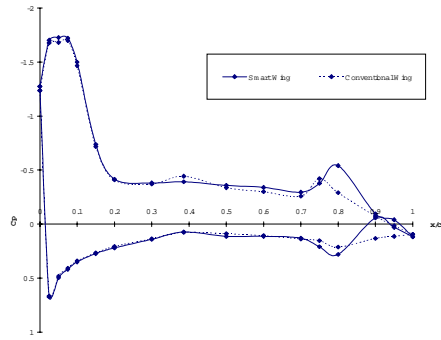


CM vs. AOA

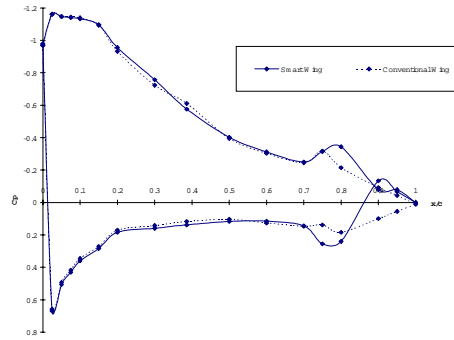


Roll Moment vs. AOA

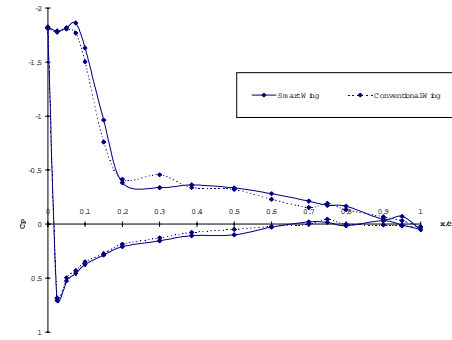
Run 93 vs 15 (partial)
 $M = 0.20$, $Q = 60$ psf
 Conventional Flap = 7.5° Aileron = 0°
 Smart Flap = 4.7° Aileron = 0°



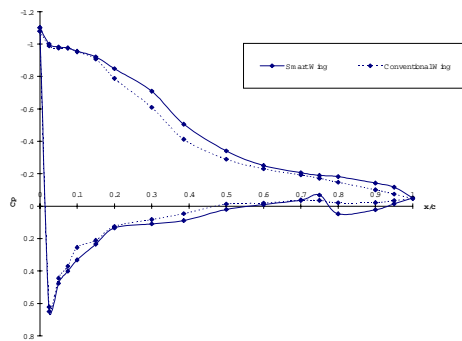
Row A, AOA = 8



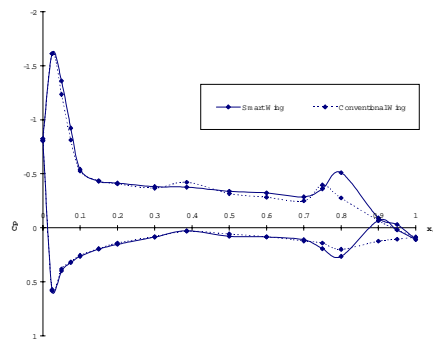
Row B, AOA = 8



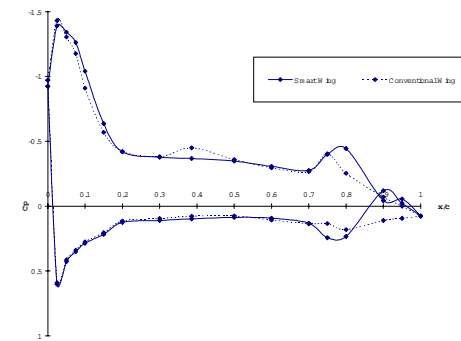
Row C, AOA = 8



Row D, AOA = 8

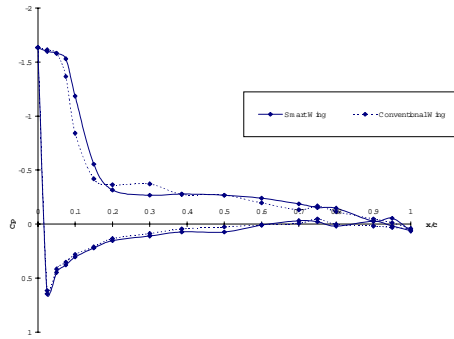


Row A, AOA = 6

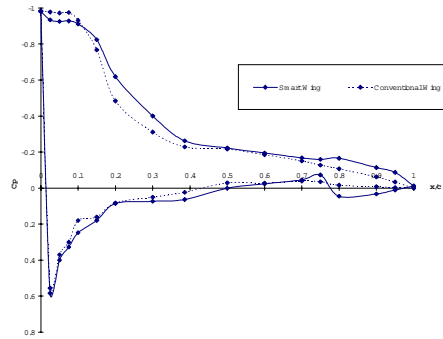


Row B, AOA = 6

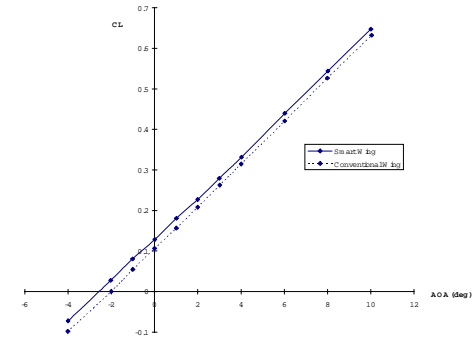
Run 93 vs 75
 $M = 0.20$, $Q = 60$ psf
 Conventional Flap = 7.5° Aileron = 0°
 Smart Flap = 4.7° Aileron = 0°



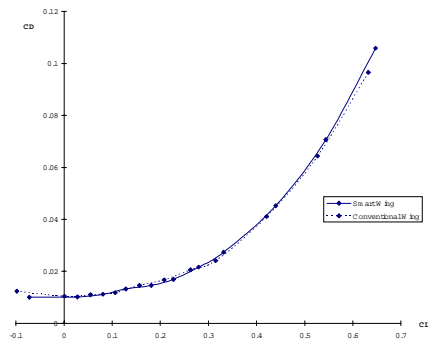
Row C, AOA = 6



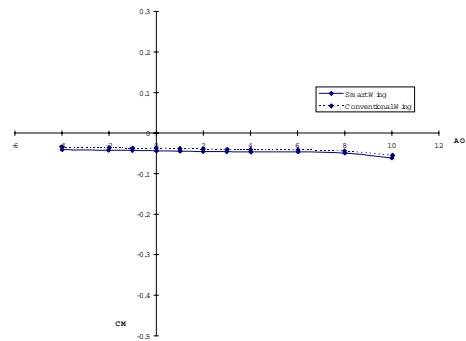
Row D, AOA = 6



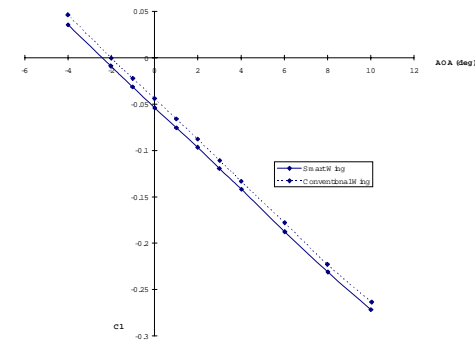
CL vs. AOA



CD vs. Cl

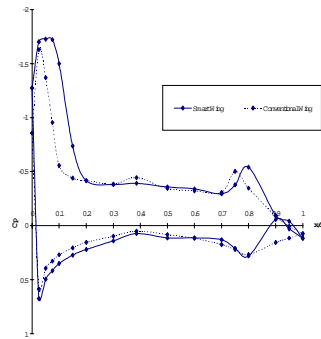


CM vs. AOA

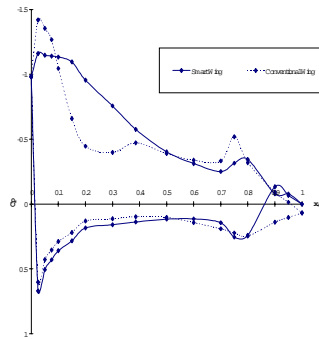


Roll Moment vs. AOA

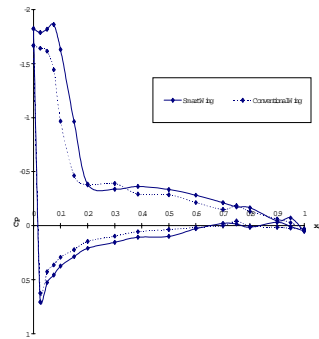
Run 93 vs 75
 $M = 0.20$, $Q = 60$ psf
 Conventional Flap = 7.5° Aileron = 0°
 Smart Flap = 4.7° Aileron = 0°



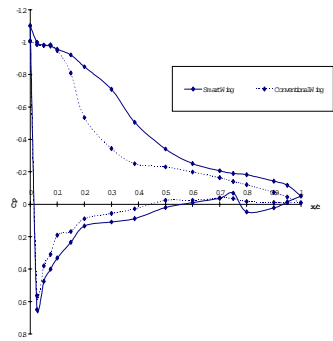
Row A, AOA = 8



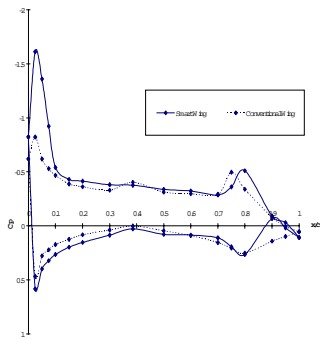
Row B, AOA = 8



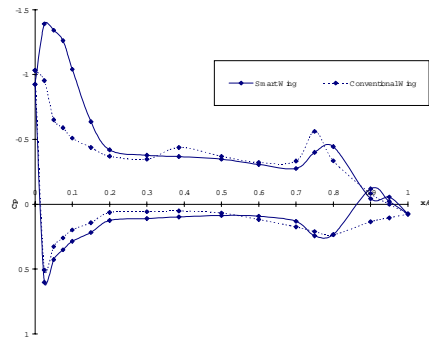
Row C, AOA = 8



Row D, AOA = 8

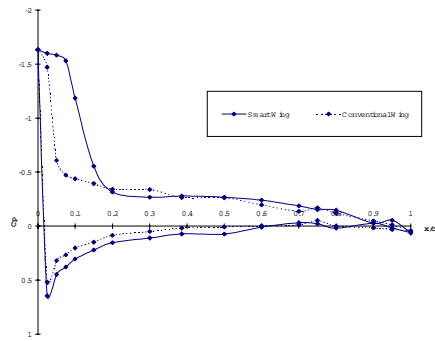


Row A, AOA = 6

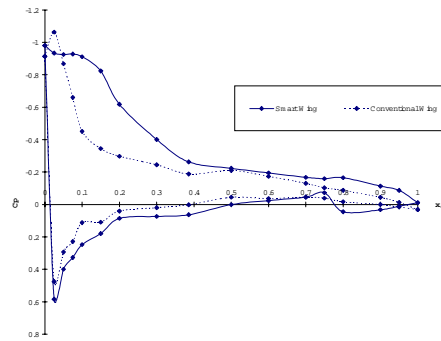


Row B, AOA = 6

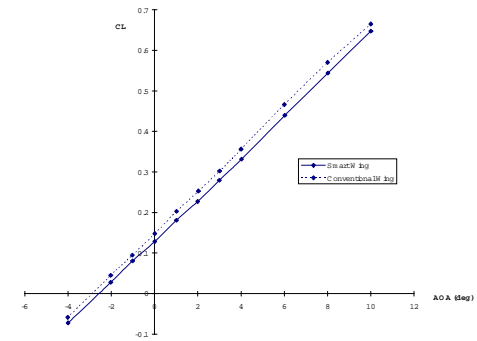
Run 93 vs 80
 $M = 0.20$, $Q = 60$ psf
 Conventional Flap = 10° Aileron = 0°
 Smart Flap = 4.7° Aileron = 0°



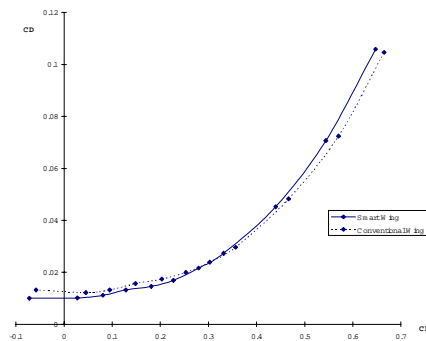
Row C, AOA = 6



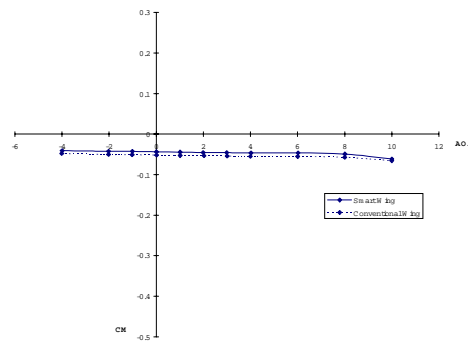
Row D, AOA = 6



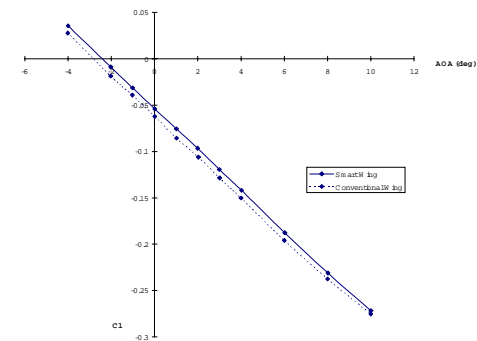
CL vs. AOA



CD vs. CL

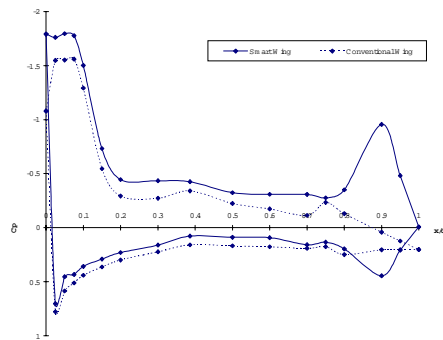


CM vs. AOA

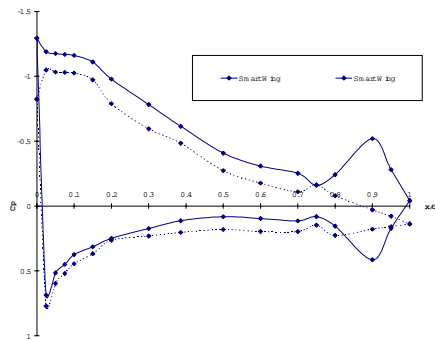


Roll Moment vs. AOA

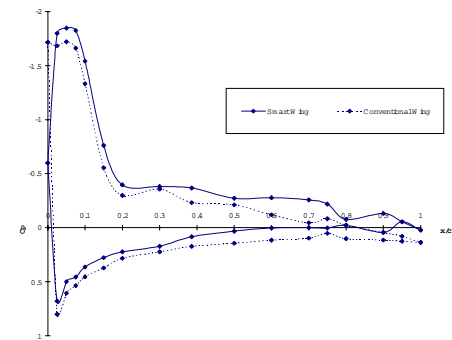
Run 93 vs 80
 $M = 0.20$, $Q = 60$ psf
 Conventional Flap = 10° Aileron = 0°
 Smart Flap = 4.7° Aileron = 0°



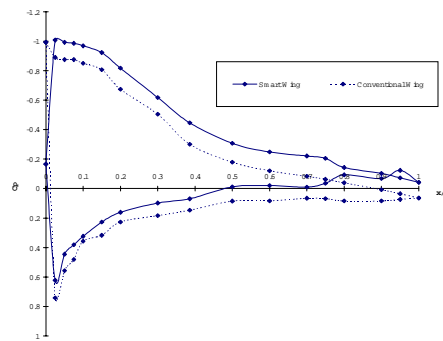
Row A, AOA = 8



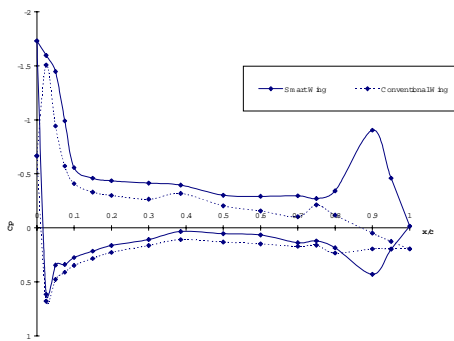
Row B, AOA = 8



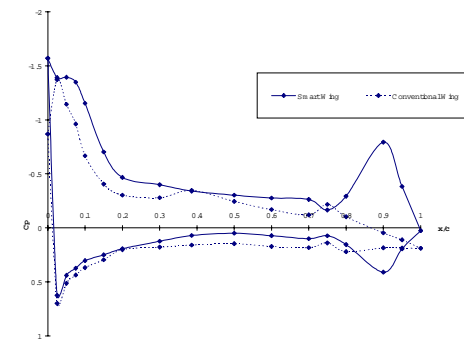
Row C, AOA = 8



Row D, AOA = 8

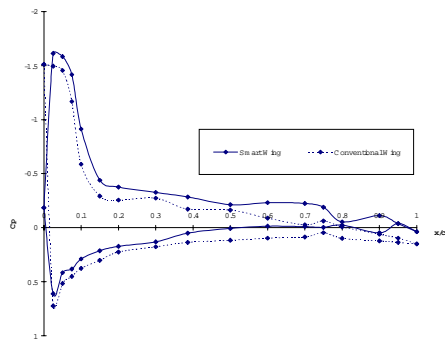


Row A, AOA = 6

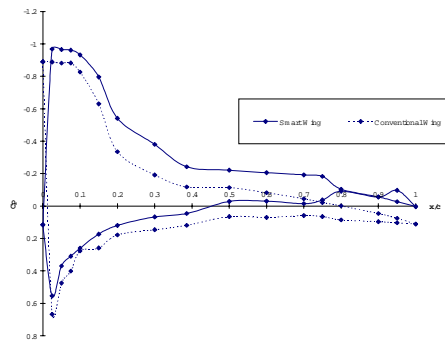


Row B, AOA = 6

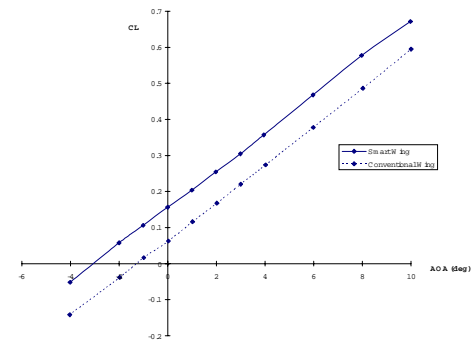
Run 100 vs 6
 $M = 0.20$, $Q = 60$ psf
 Conventional Flap = 5° Aileron = 0°
 Smart Flap = -4° Aileron = 0°



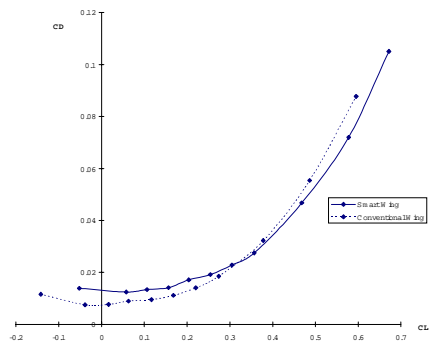
Row C, AOA = 6



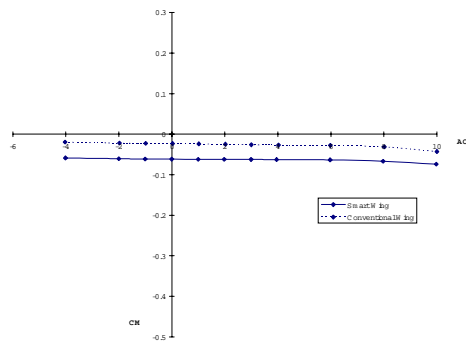
Row D, AOA = 6



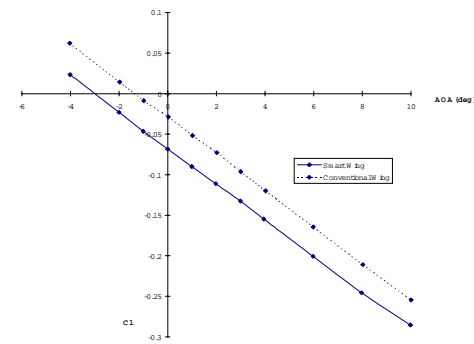
CL vs. AOA



CD vs. CL

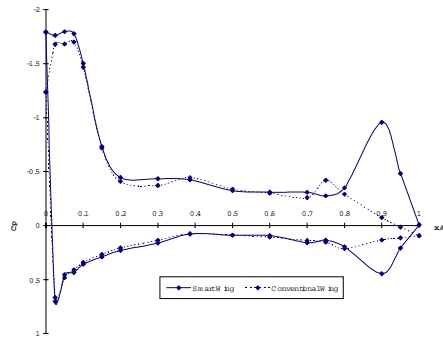


CM vs. AOA

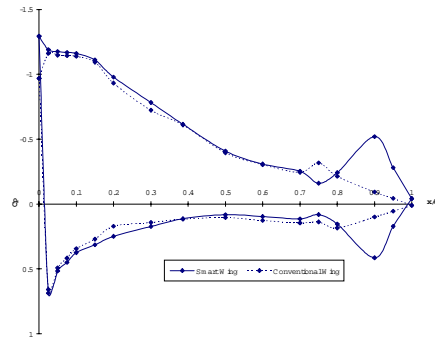


Roll Moment vs. AOA

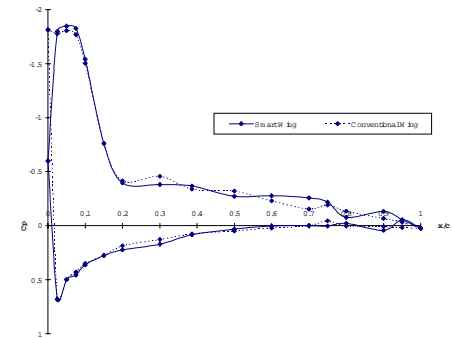
Run 100 vs 6
 $M = 0.20$, $Q = 60$ psf
 Conventional Flap = 5° Aileron = 0°
 Smart Flap = -4° Aileron = 0°



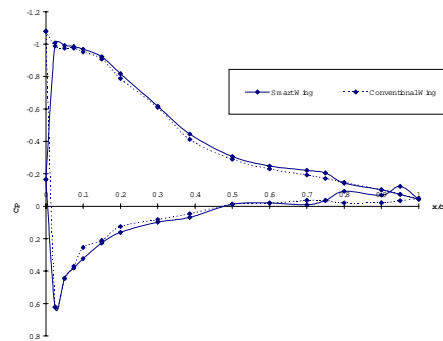
Row A, AOA = 8



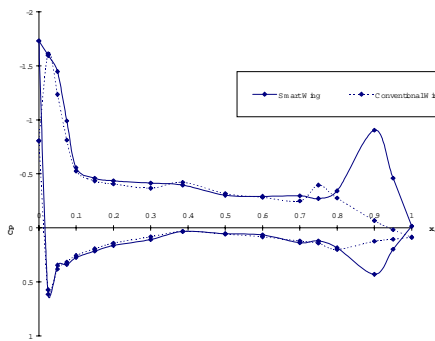
Row B, AOA = 8



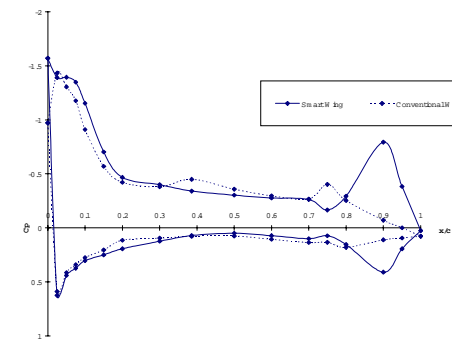
Row C, AOA = 8



Row D, AOA = 8

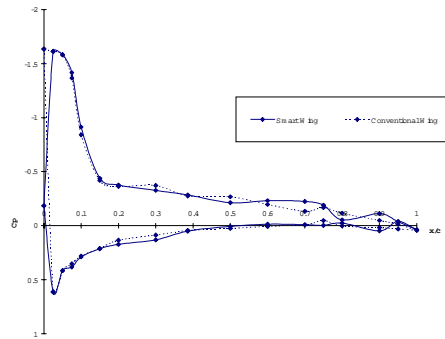


Row A, AOA = 6

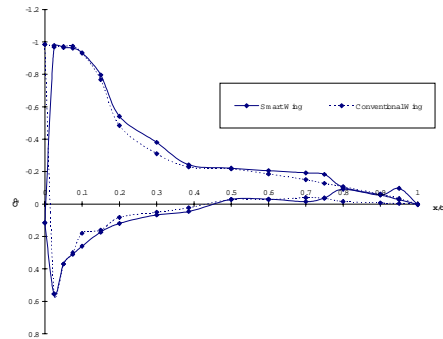


Row B, AOA = 6

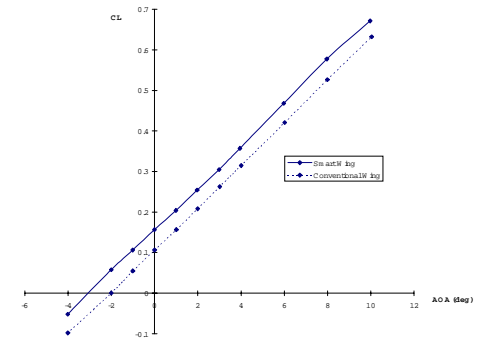
Run 100 vs 75
 $M = 0.20$, $Q = 60$ psf
 Conventional Flap = 7.5° Aileron = 0°
 Smart Flap = -4° Aileron = 0°



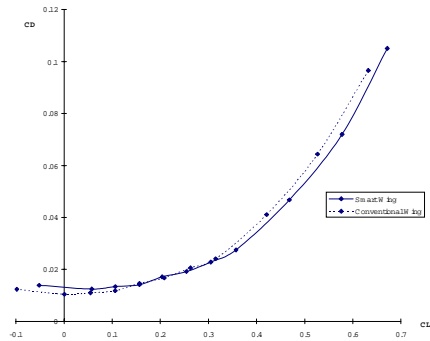
Row C, AOA = 6



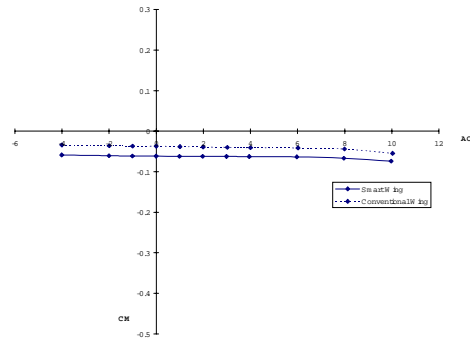
Row D, AOA = 6



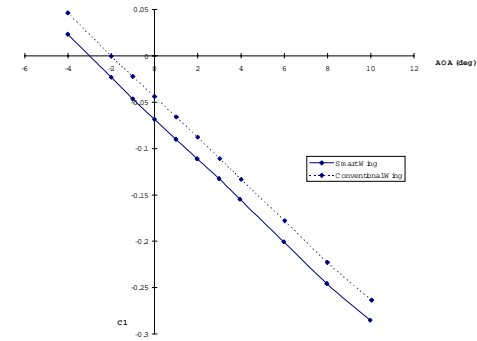
CL vs. AOA



CD vs. CL

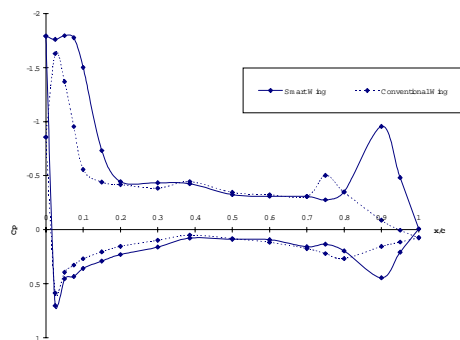


CM vs. AOA

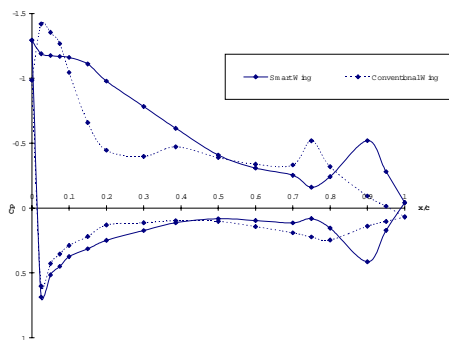


Roll Moment vs. AOA

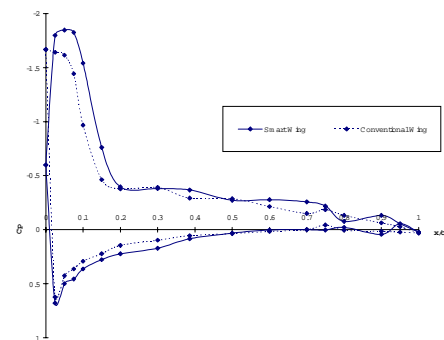
Run 100 vs 75
 $M = 0.20$, $Q = 60$ psf
 Conventional Flap = 7.5° Aileron = 0°
 Smart Flap = -4° Aileron = 0°



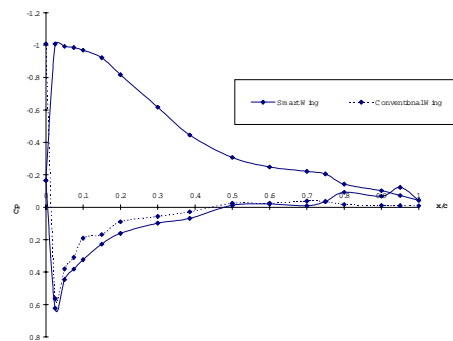
Row A, AOA = 8



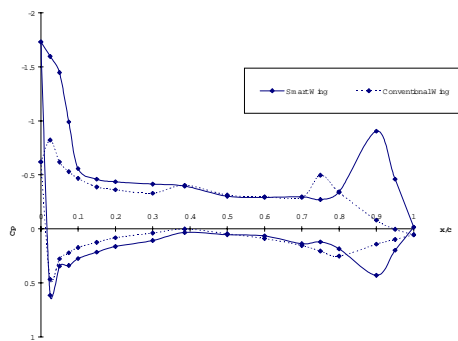
Row B, AOA = 8



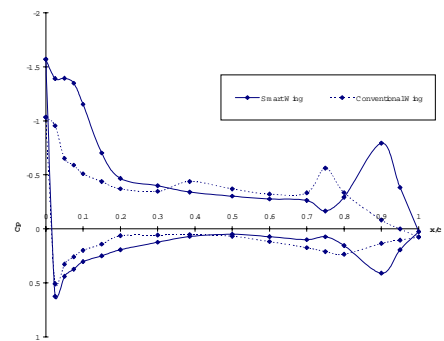
Row C, AOA = 8



Row D, AOA = 8

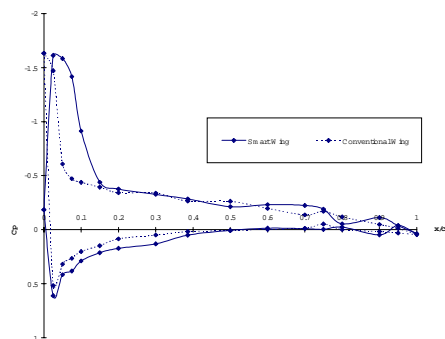


Row A, AOA = 6

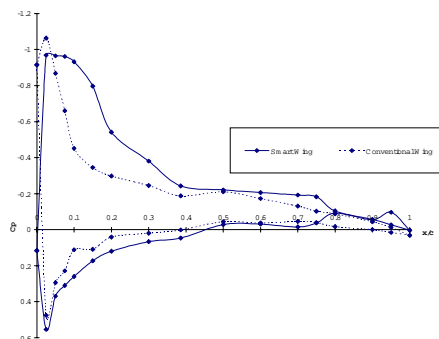


Row B, AOA = 6

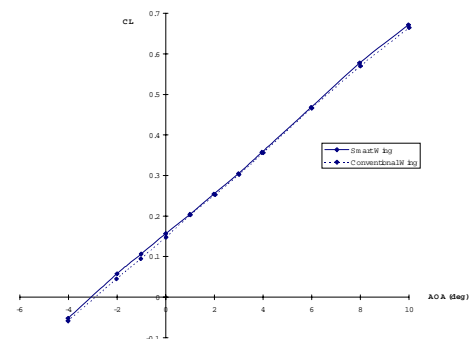
Run 100 vs 80
 $M = 0.20$, $Q = 60$ psf
 Conventional Flap = 10° Aileron = 0°
 Smart Flap = -4° Aileron = 0°



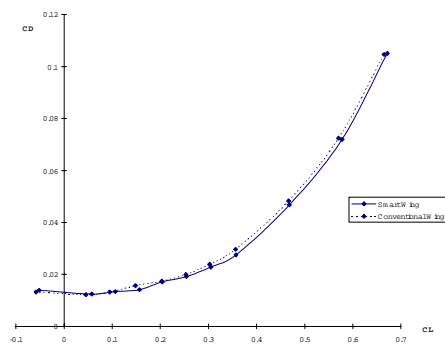
Row C, AOA = 6



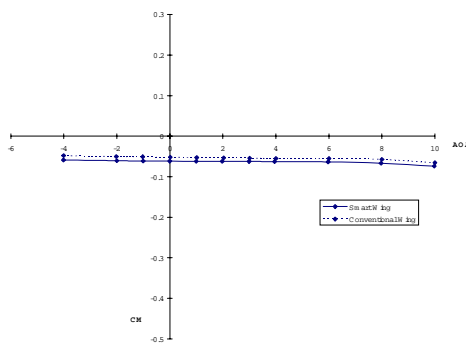
Row D, AOA = 6



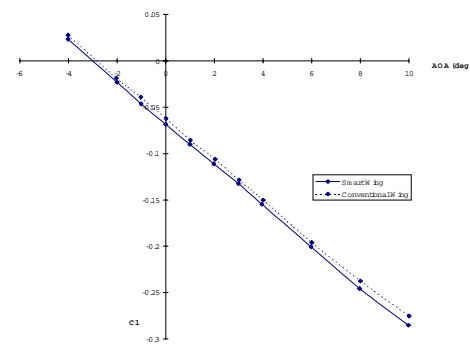
CL vs. AOA



CD vs. CL

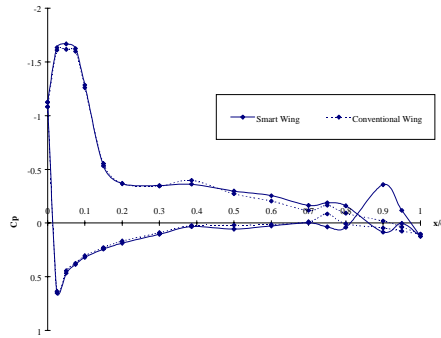


CM vs. AOA

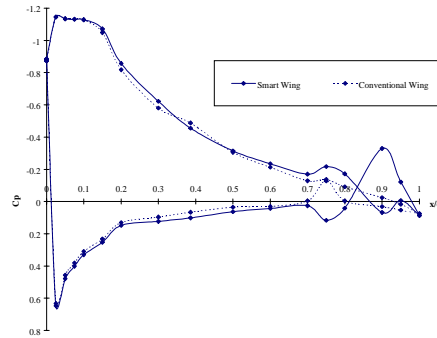


Roll Moment vs. AOA

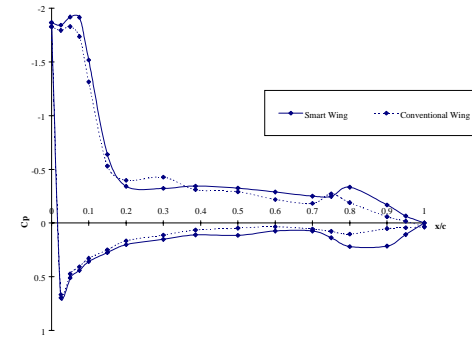
Run 100 vs 80
 $M = 0.20$, $Q = 60$ psf
 Conventional Flap = 10° Aileron = 0°
 Smart Flap = -4° Aileron = 0°



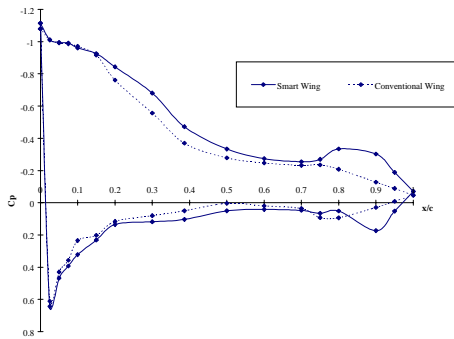
Row A, AOA = 8



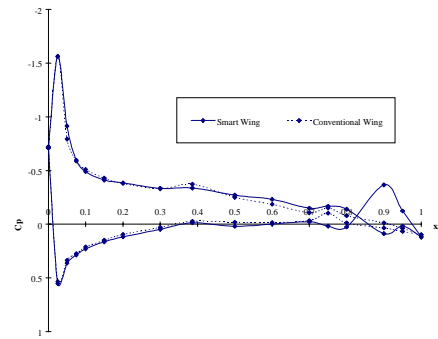
Row B, AOA = 8



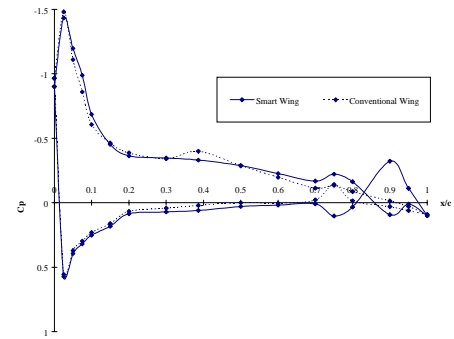
Row C, AOA = 8



Row D, AOA = 8

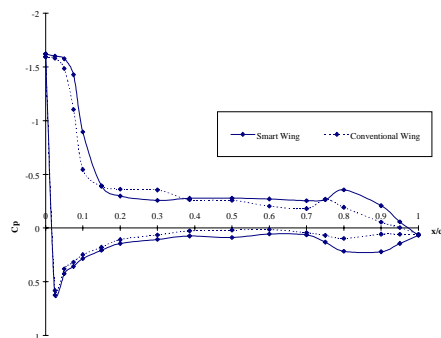


Row A, AOA = 6

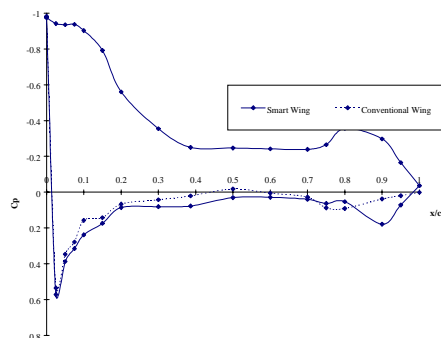


Row B, AOA = 6

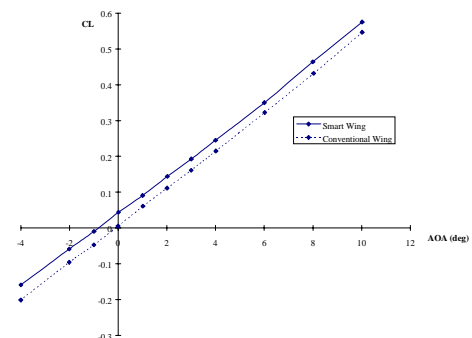
Run 107 vs 18
 $M = 0.20$, $Q = 60$ psf
 Conventional Flap = 0° Aileron = 5°
 Smart Flap = 0° Aileron = 4°



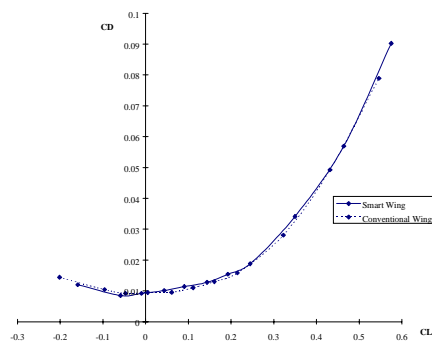
Row C, AOA = 6



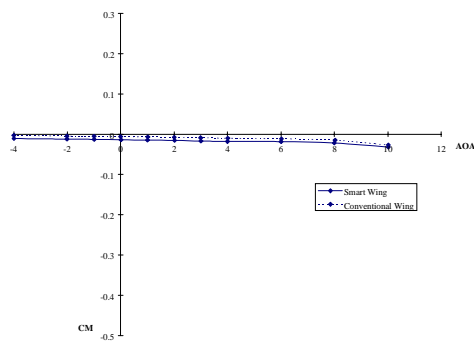
Row D, AOA = 6



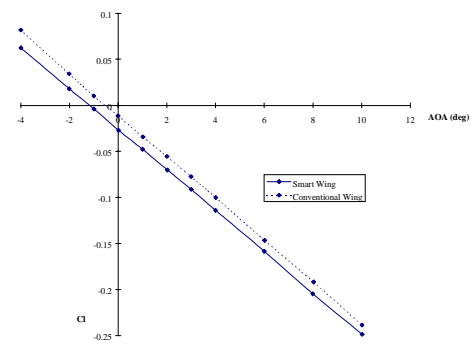
CL vs. AOA



CD vs. Cl

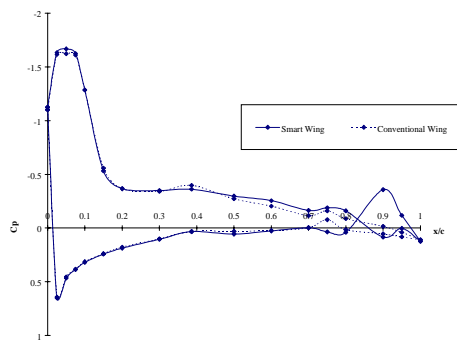


CM vs. AOA

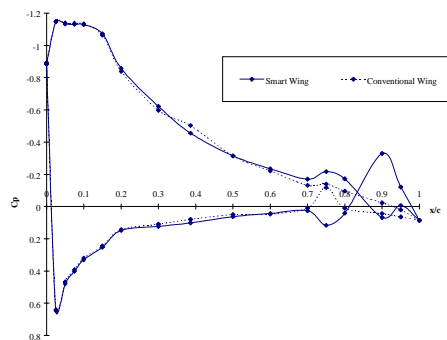


Roll Moment vs. AOA

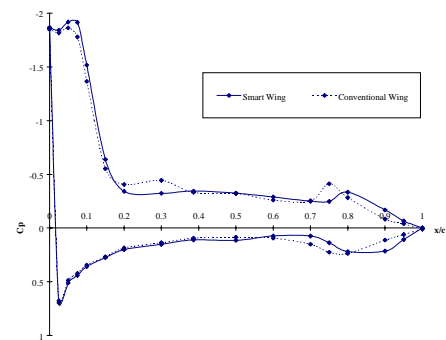
Run 107 vs 18
 $M = 0.20$, $Q = 60$ psf
 Conventional Flap = 0° Aileron = 5°
 Smart Flap = 0° Aileron = 4°



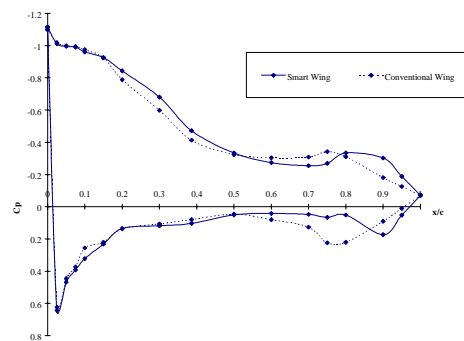
Row A, AOA = 8



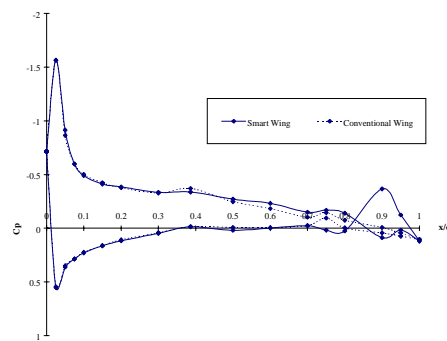
Row B, AOA = 8



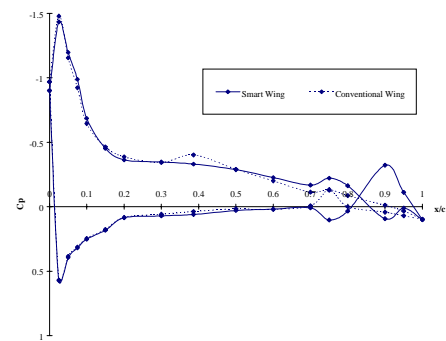
Row C, AOA = 8



Row D, AOA = 8

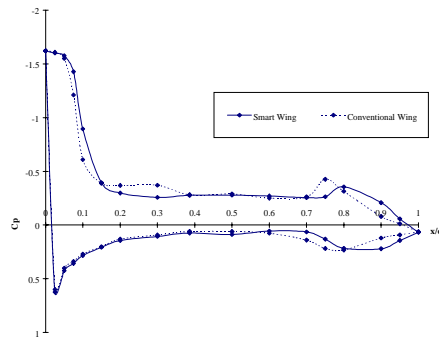


Row A, AOA = 6

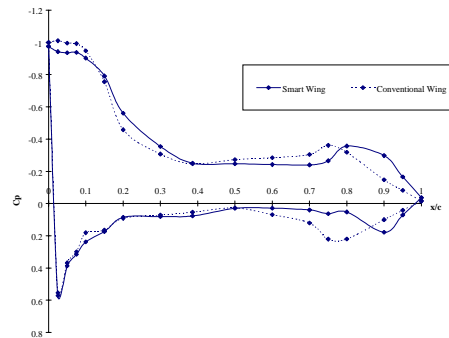


Row B, AOA = 6

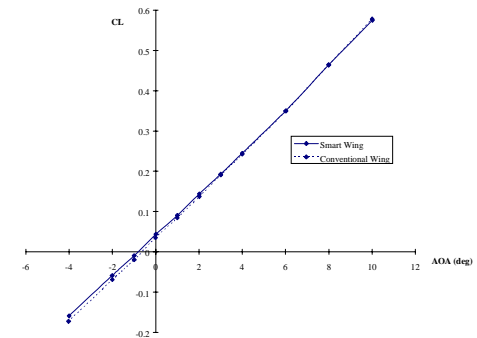
Run 107 vs 30
 $M = 0.20$, $Q = 60$ psf
 Conventional Flap = 0° Aileron = 10°
 Smart Flap = 0° Aileron = 4°



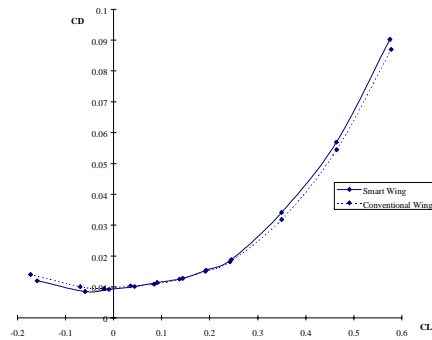
Row C, AOA = 6



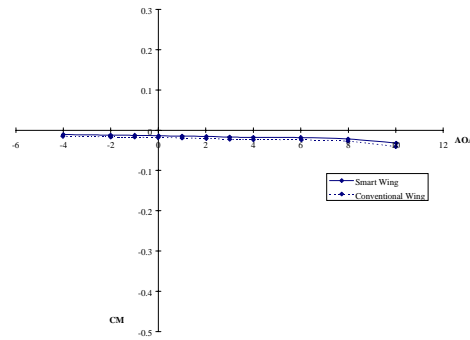
Row D, AOA = 6



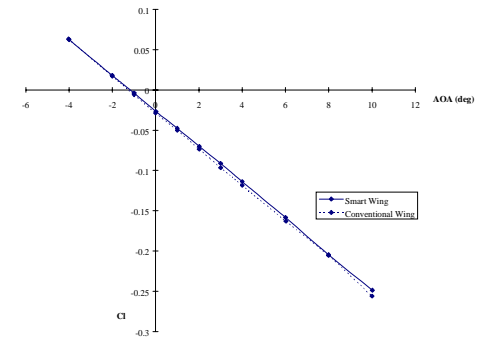
CL vs. AOA



CD vs. CL

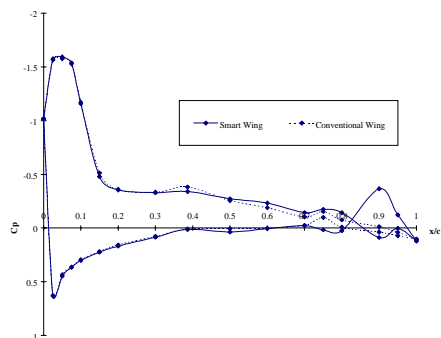


CM vs. AOA

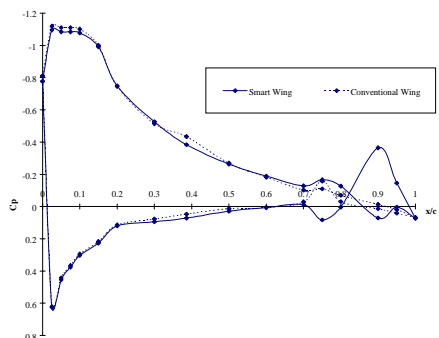


Roll Moment vs. AOA

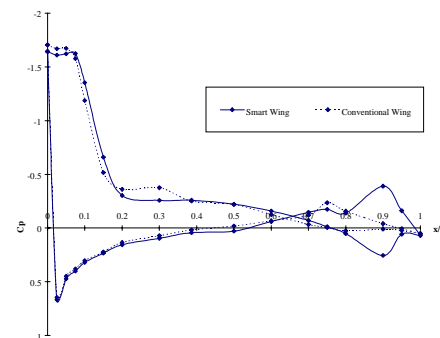
Run 107 vs 30
 $M = 0.20$, $Q = 60$ psf
 Conventional Flap = 0° Aileron = 10°
 Smart Flap = 0° Aileron = 4°



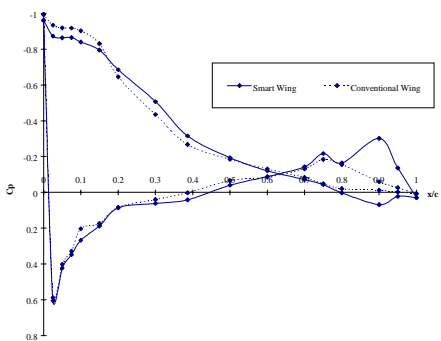
Row A, AOA = 8



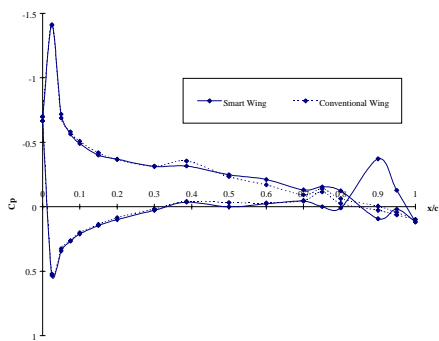
Row B, AOA = 8



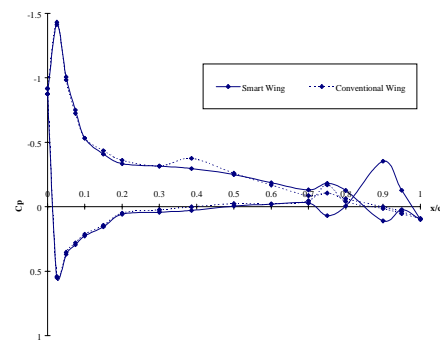
Row C, AOA = 8



Row D, AOA = 8

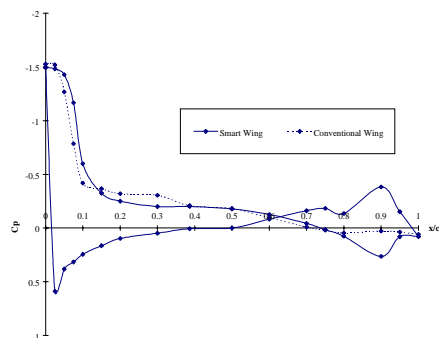


Row A, AOA = 6

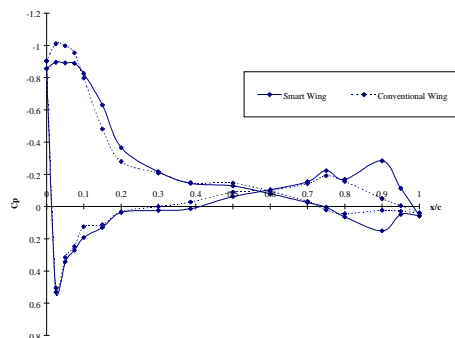


Row B, AOA = 6

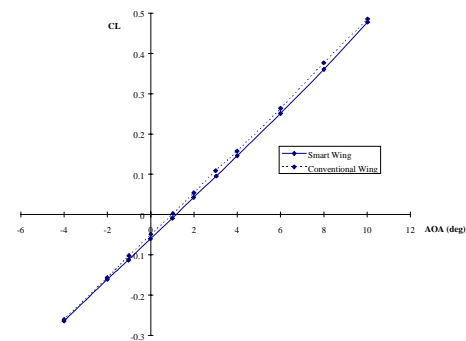
Run 110 vs 44
 $M = 0.20$, $Q = 60$ psf
 Conventional Flap = 0° Aileron = -5°
 Smart Flap = 0° Aileron = -4°



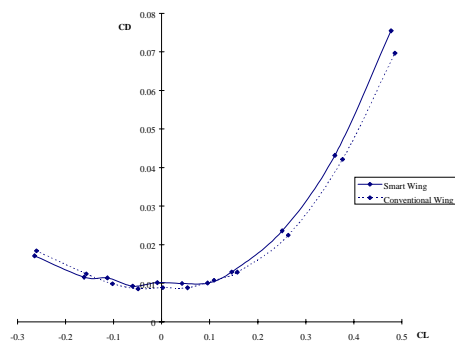
Row C, AOA = 6



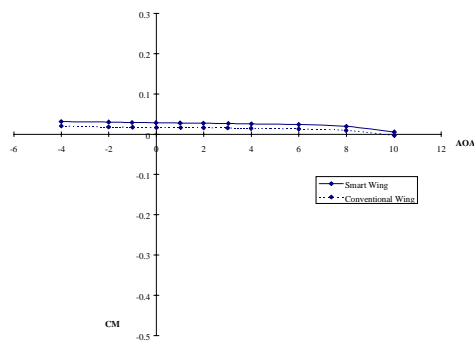
Row D, AOA = 6



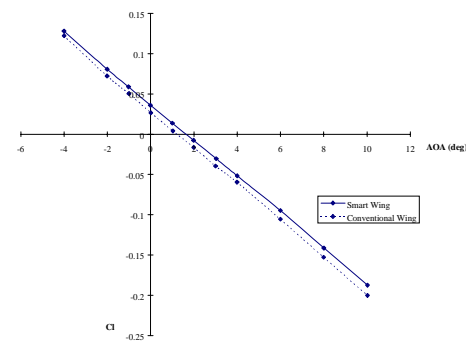
CL vs. AOA



CD vs. CL

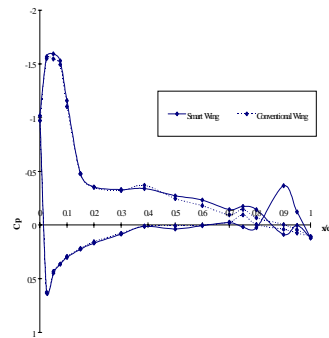


CM vs. AOA

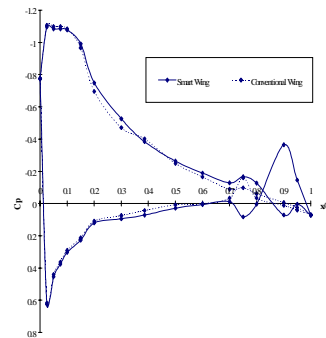


Roll Moment vs. AOA

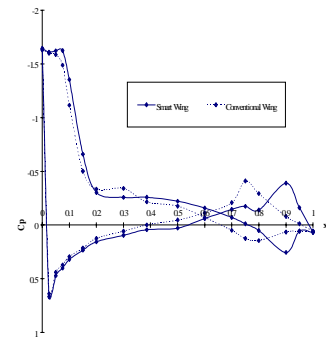
Run 110 vs 44
 $M = 0.20$, $Q = 60$ psf
 Conventional Flap = 0° Aileron = -5°
 Smart Flap = 0° Aileron = -4°



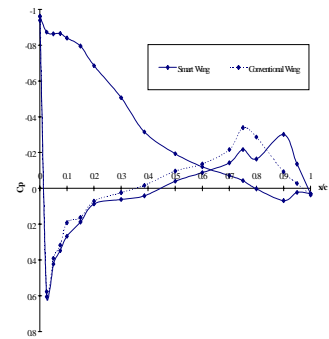
Row A, AOA = 8



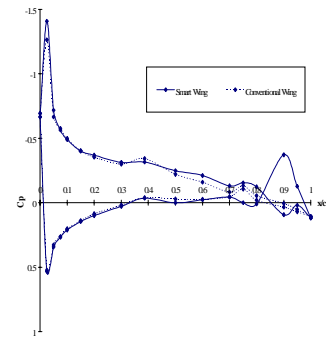
Row B, AOA = 8



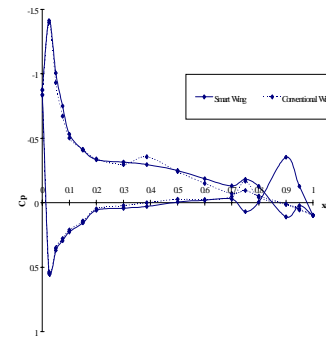
Row C, AOA = 8



Row D, AOA = 8

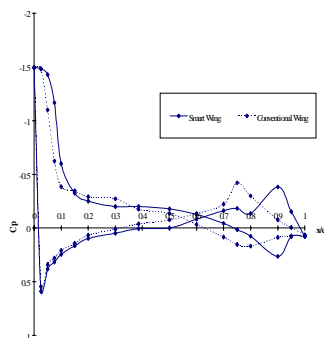


Row A, AOA = 6

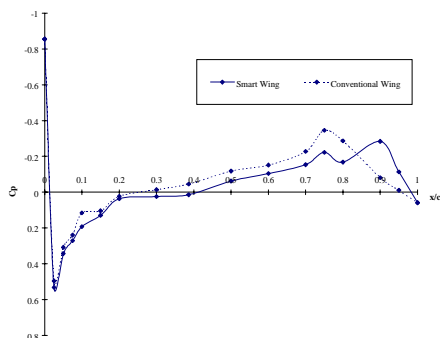


Row B, AOA = 6

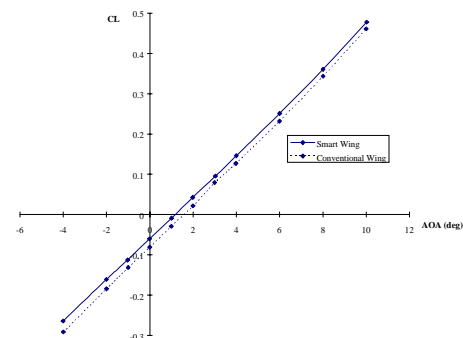
Run 110 vs 56
 $M = 0.20$, $Q = 60$ psf
 Conventional Flap = 0° Aileron = -10°
 Smart Flap = 0° Aileron = -4°



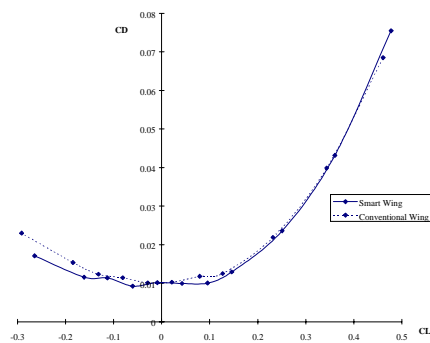
Row C, AOA = 6



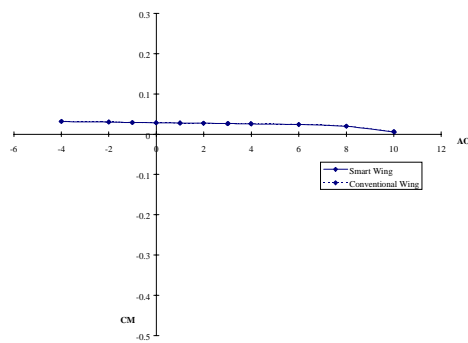
Row D, AOA = 6



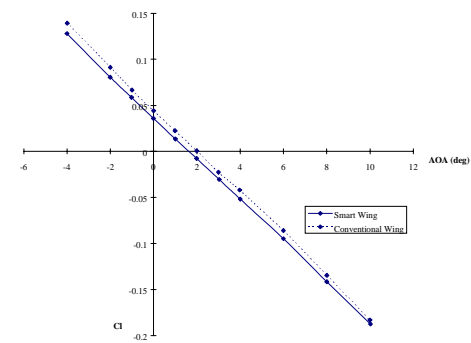
CL vs. AOA



CD vs. CL

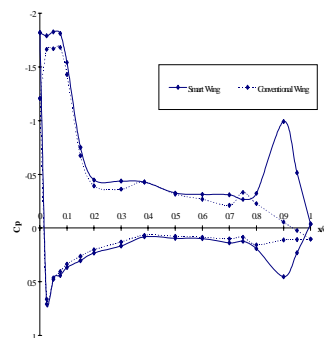


CM vs. AOA

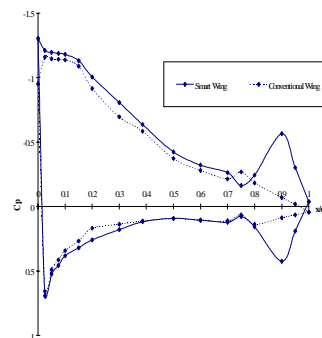


Roll Moment vs. AOA

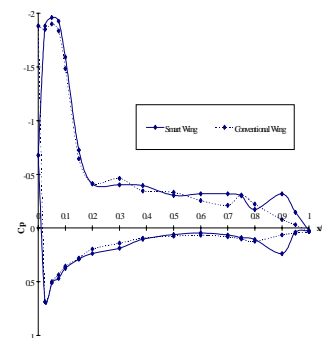
Run 110 vs 56
 $M = 0.20$, $Q = 60$ psf
 Conventional Flap = 0° Aileron = -10°
 Smart Flap = 0° Aileron = -4°



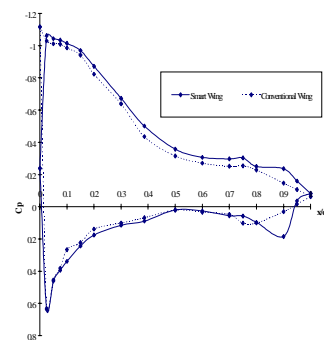
Row A, AOA = 8



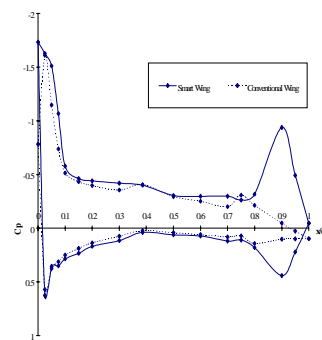
Row B, AOA = 8



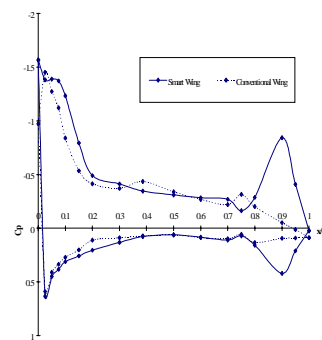
Row C, AOA = 8



Row D, AOA = 8

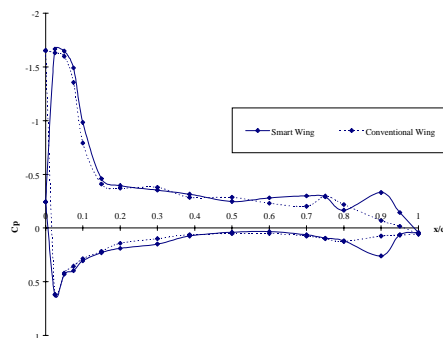


Row A, AOA = 6

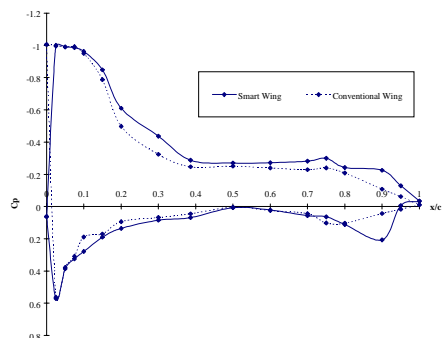


Row B, AOA = 6

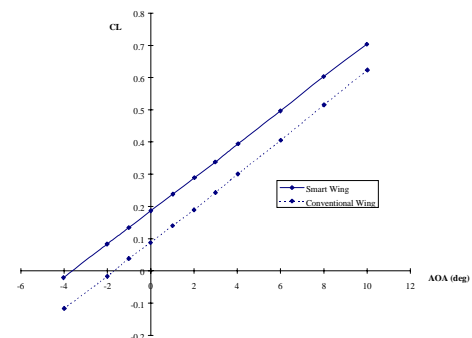
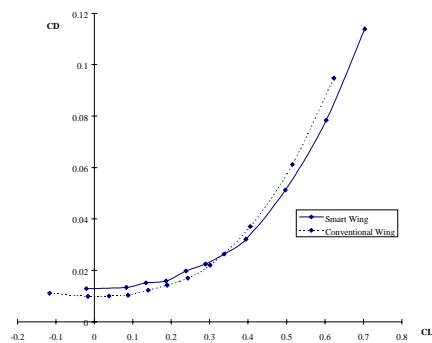
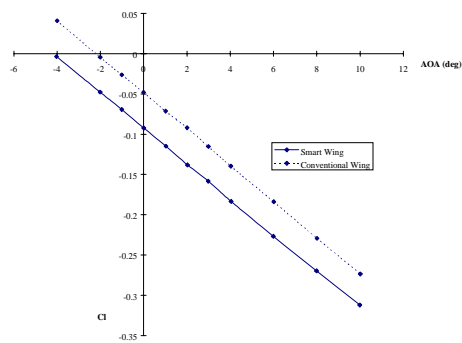
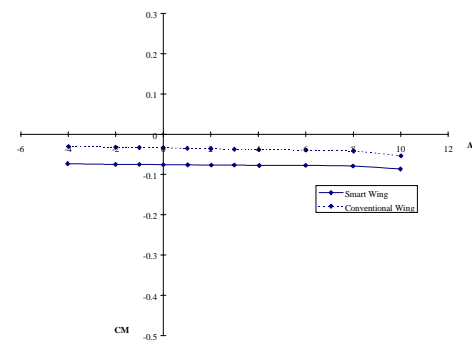
Run 104 vs 23
 $M = 0.20$, $Q = 60$ psf
 Conventional Flap = 5° Aileron = 5°
 Smart Flap = -4° Aileron = -4°



Row C, AOA = 6

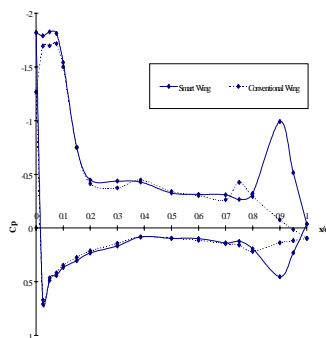


Row D, AOA = 6

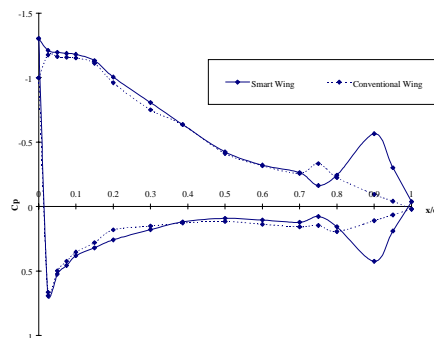
C_L vs. AOAC_D vs. C_LC_i vs. AOA

Roll Moment vs. AOA

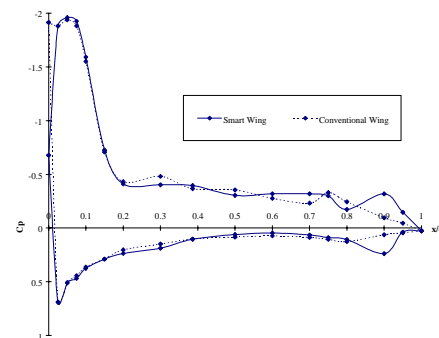
Run 104 vs 23
 $M = 0.20$, $Q = 60$ psf
 Conventional Flap = 5° Aileron = 5°
 Smart Flap = -4° Aileron = -4°



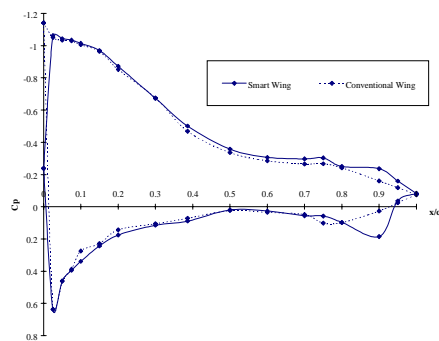
Row A, AOA = 8



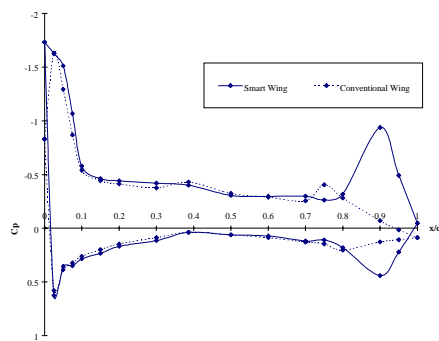
Row B, AOA = 8



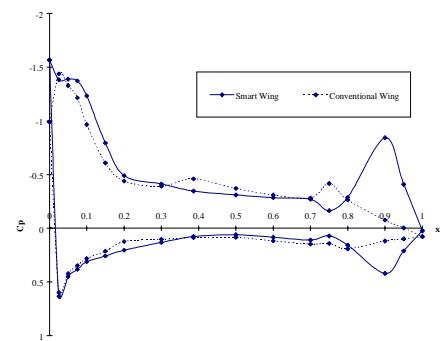
Row C, AOA = 8



Row D, AOA = 8

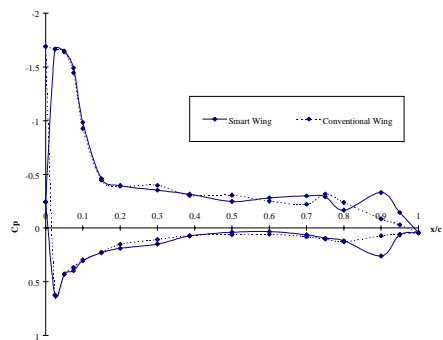


Row A, AOA = 6

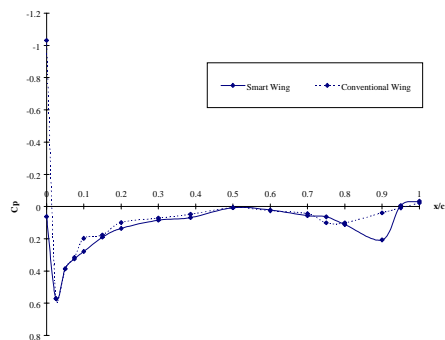


Row B, AOA = 6

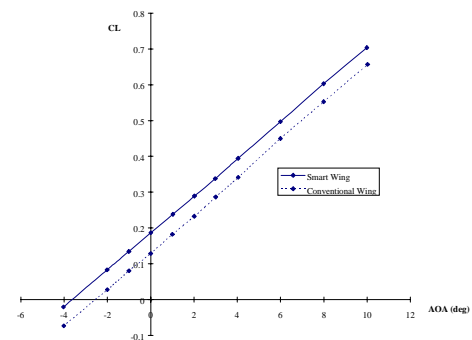
Run 104 vs 24
 $M = 0.20$, $Q = 60$ psf
 Conventional Flap = 7.5° Aileron = 5°
 Smart Flap = -4° Aileron = -4°



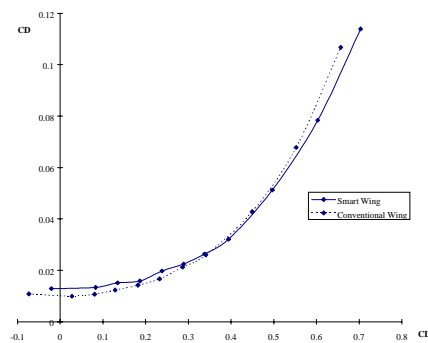
Row C, AOA = 6



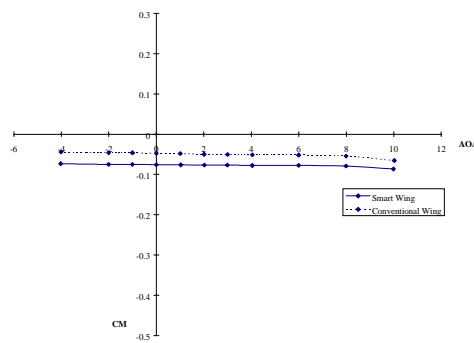
Row D, AOA = 6



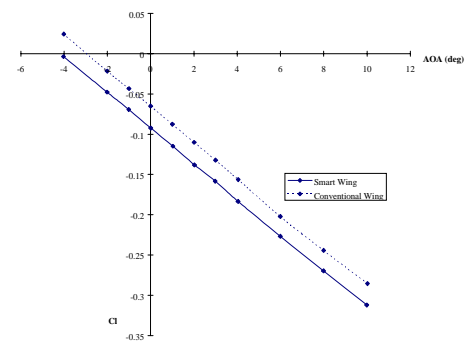
CL vs. AOA



CD vs. CL

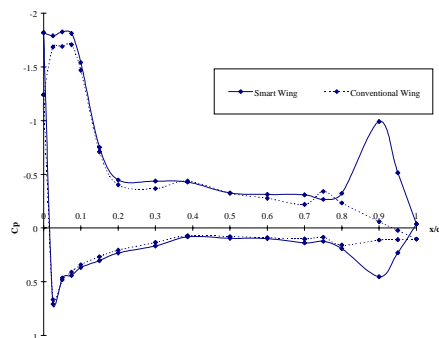


CM vs. AOA

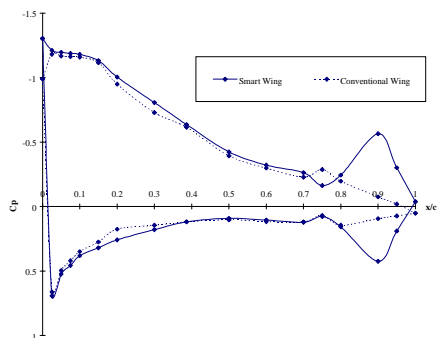


Roll Moment vs. AOA

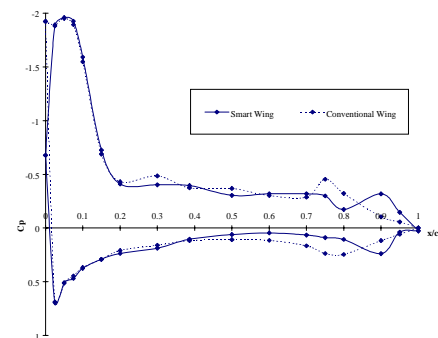
Run 104 vs 24
 $M = 0.20$, $Q = 60$ psf
 Conventional Flap = 7.5° Aileron = 5°
 Smart Flap = -4° Aileron = -4°



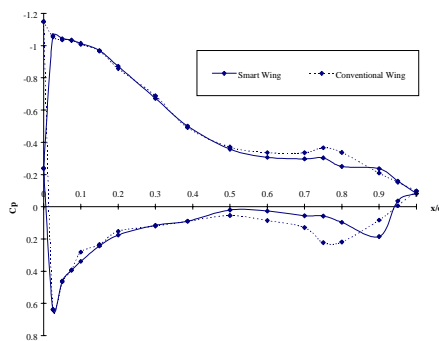
Row A, AOA = 8



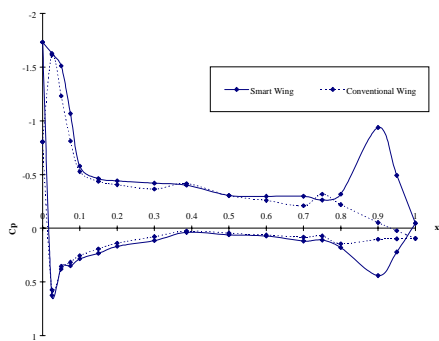
Row B, AOA = 8



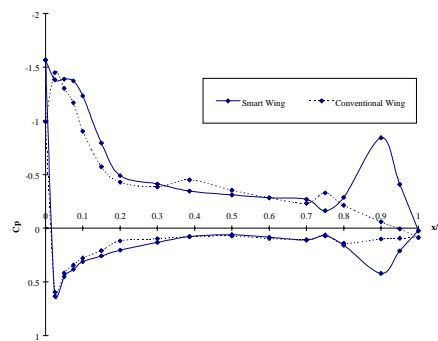
Row C, AOA = 8



Row D, AOA = 8

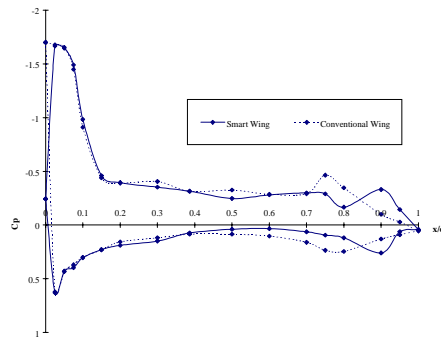


Row A, AOA = 6

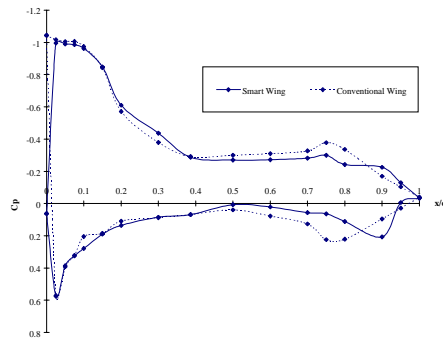


Row B, AOA = 6

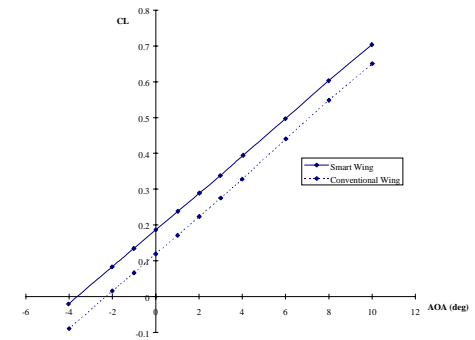
Run 104 vs 35
 $M = 0.20$, $Q = 60$ psf
 Conventional Flap = 5° Aileron = 10°
 Smart Flap = -4° Aileron = -4°



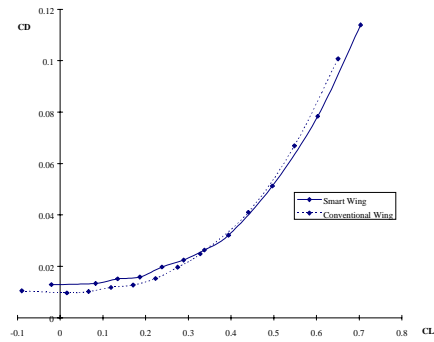
Row C, $AOA = 6$



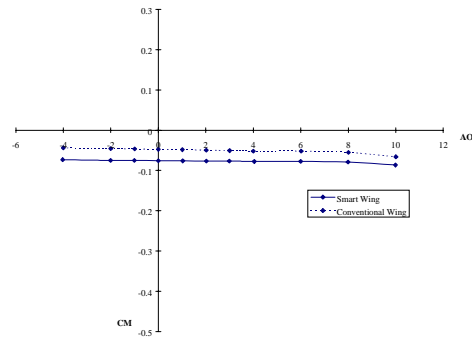
Row D, $AOA = 6$



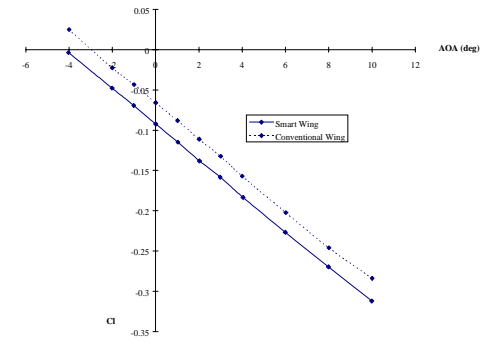
CL vs. AOA



CD vs. CL

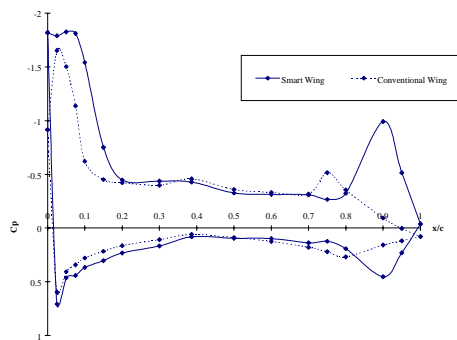


CM vs. AOA

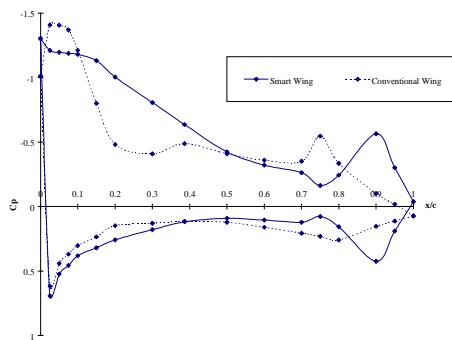


Roll Moment vs. AOA

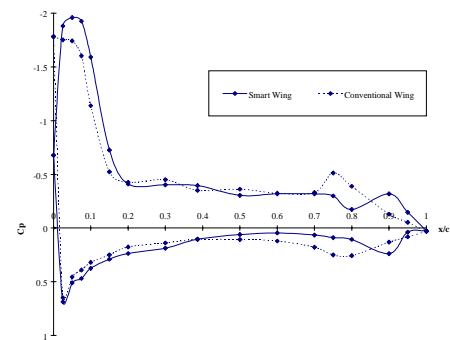
Run 104 vs 35
 $M = 0.20$, $Q = 60$ psf
 Conventional Flap = 5° Aileron = 10°
 Smart Flap = -4° Aileron = -4°



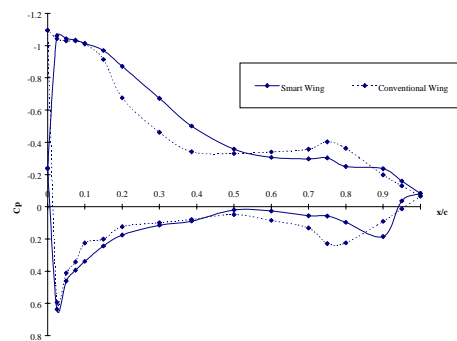
Row A, AOA = 8



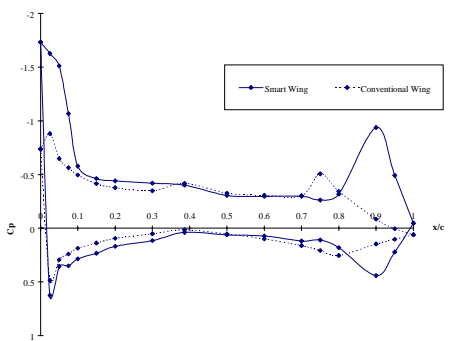
Row B, AOA = 8



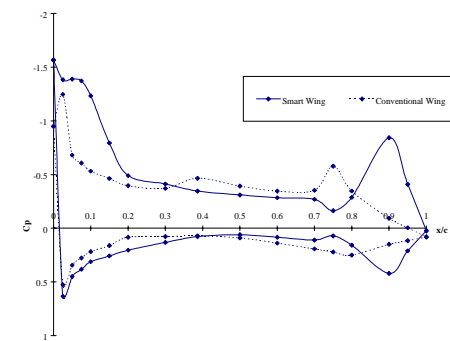
Row C, AOA = 8



Row D, AOA = 8

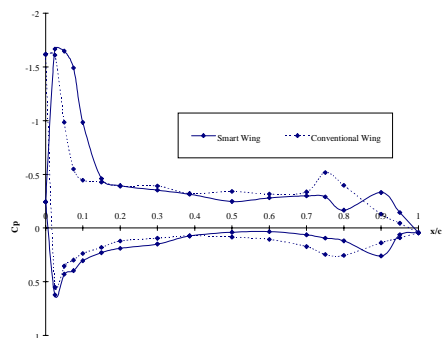


Row A, AOA = 6

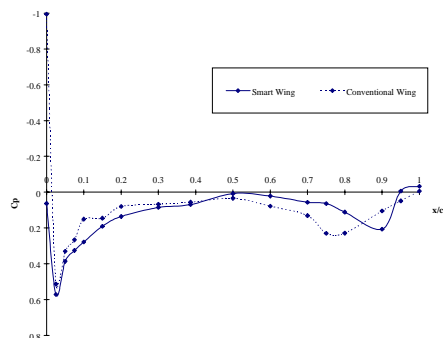


Row B, AOA = 6

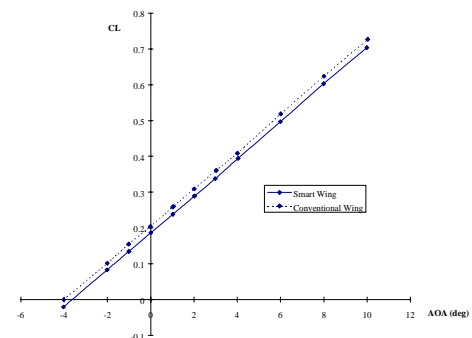
Run 104 vs 39
 $M = 0.20$, $Q = 60$ psf
 Conventional Flap = 10° Aileron = 10°
 Smart Flap = -4° Aileron = -4°



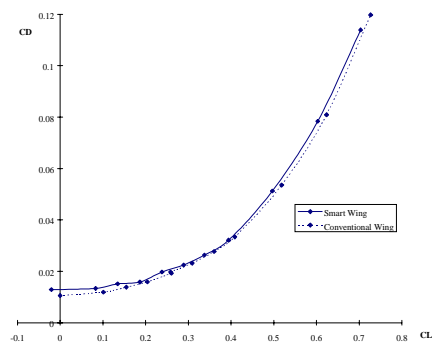
Row C, AOA = 6



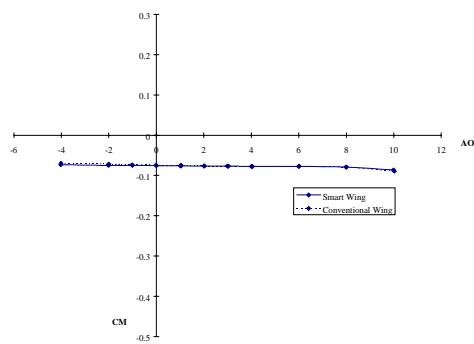
Row D, AOA = 6



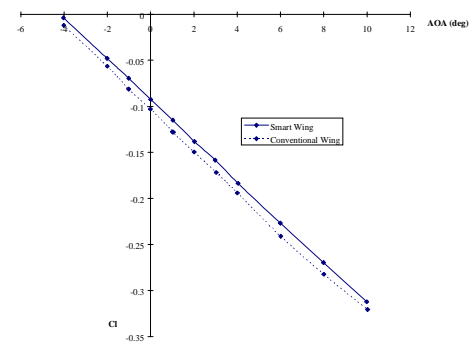
CL vs. AOA



CD vs. CL

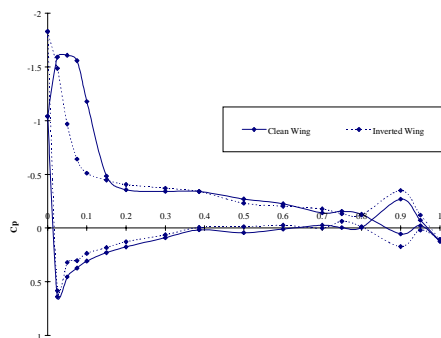


CM vs. AOA

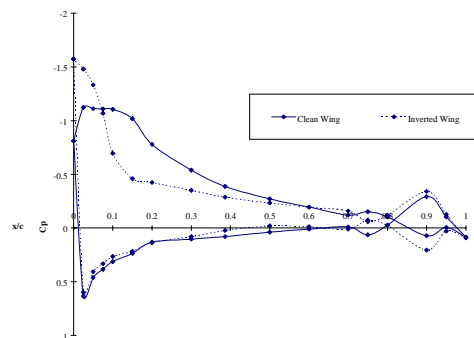


Roll Moment vs. AOA

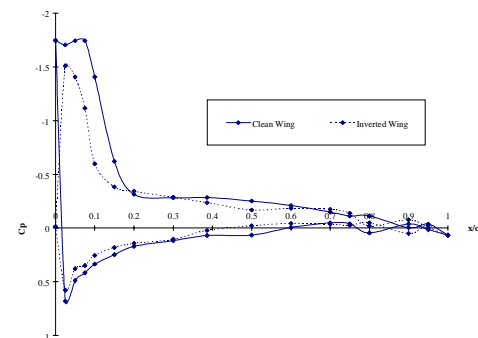
Run 104 vs 39
 $M = 0.20$, $Q = 60$ psf
 Conventional Flap = 10° Aileron = 10°
 Smart Flap = -4° Aileron = -4°



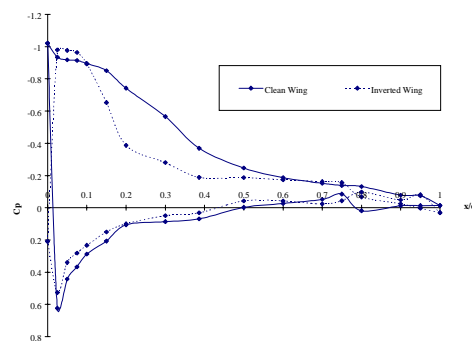
Row A, AOA = 8



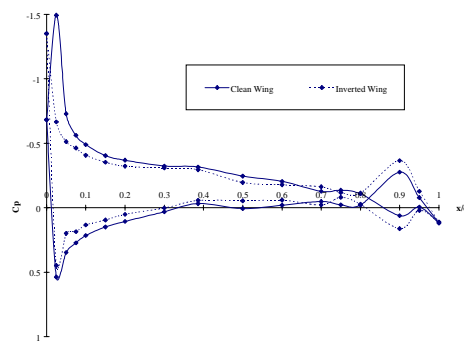
Row B, AOA = 8



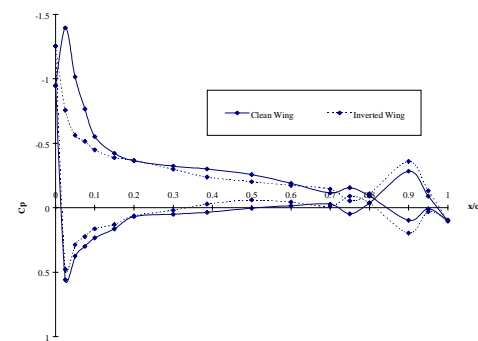
Row C, AOA = 8



Row D, AOA = 8

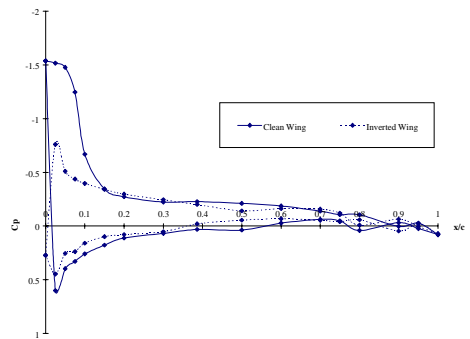


Row A, AOA = 6

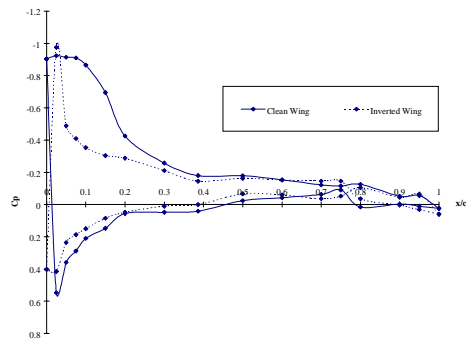


Row B, AOA = 6

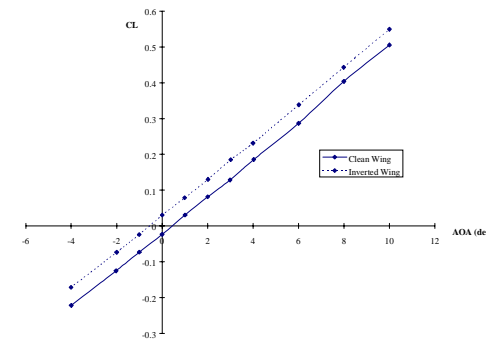
Run 98 vs 87
 $M = 0.20$, $Q = 60$ psf
 Conventional Flap = N/A Aileron = N/A
 Smart Flap = 0° Aileron = 0°



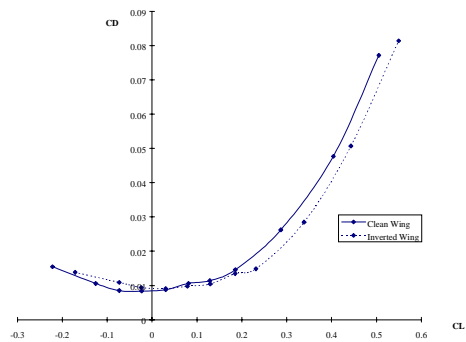
Row C, AOA = 6



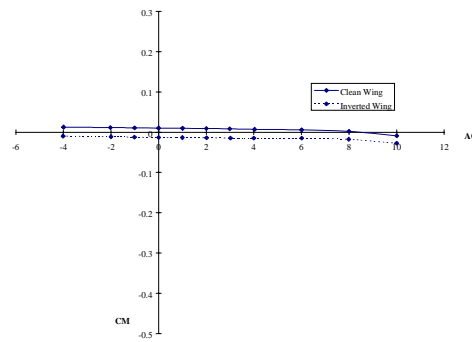
Row D, AOA = 6



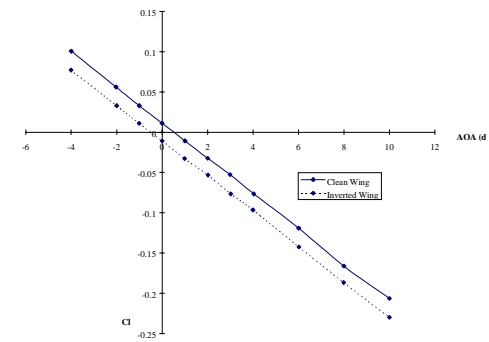
CL vs. AOA



CD vs. CL



CM vs. AOA



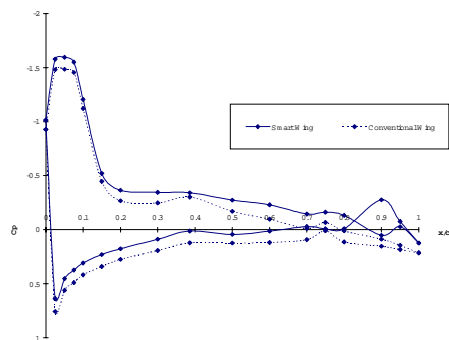
Roll Moment vs. AOA

Run 98 vs 87

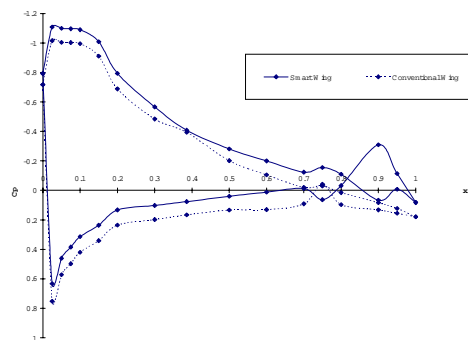
M = 0.20, Q = 60 psf

Conventional Flap = N/A Aileron = N/A

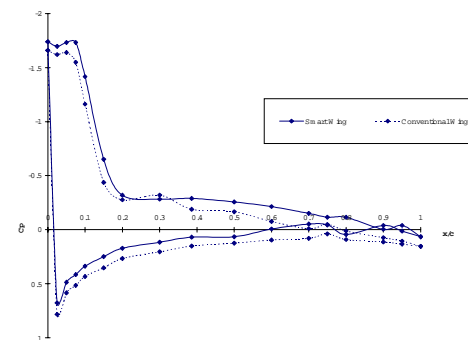
Smart Flap = 0° Aileron = 0°



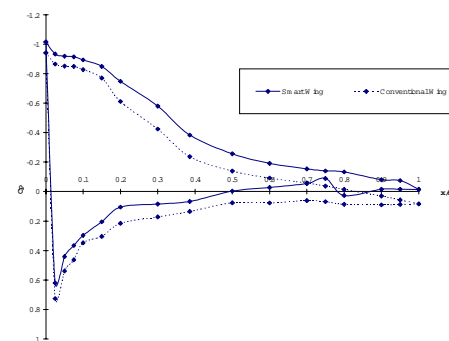
Row A, AOA = 8



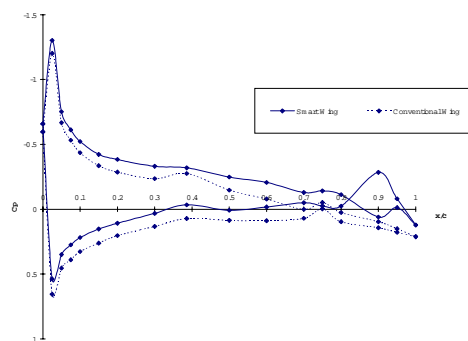
Row B, AOA = 8



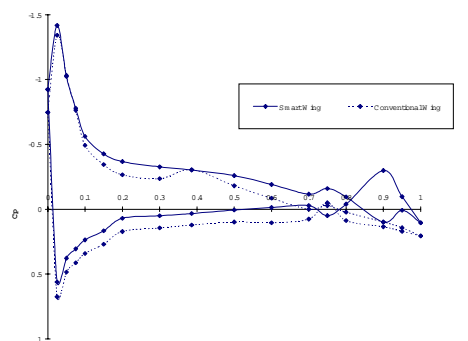
Row C, AOA = 8



Row D, AOA = 8

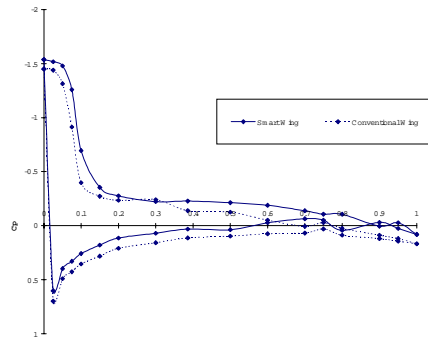


Row A, AOA = 6

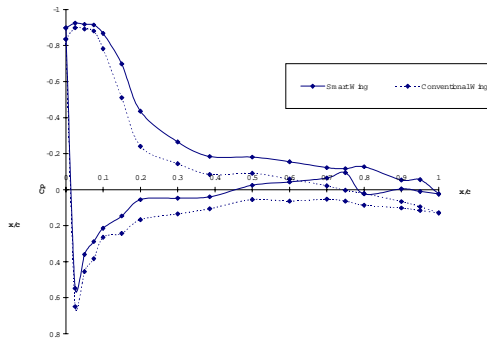


Row B, AOA = 6

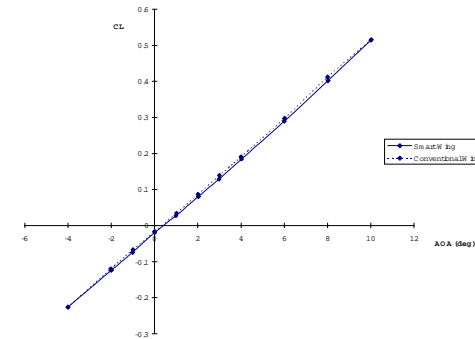
Run 88 vs 2
 $M = 0.25$, $Q = 90$ psf
 Conventional Flap = 0° Aileron = 0°
 Smart Flap = 0° Aileron = 0°



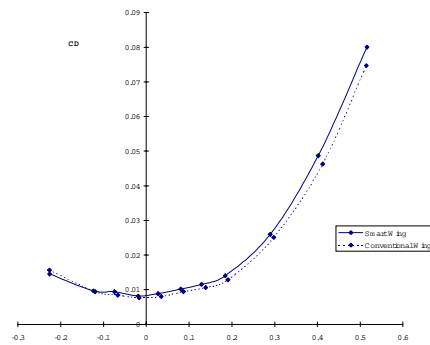
Row C, AOA = 6



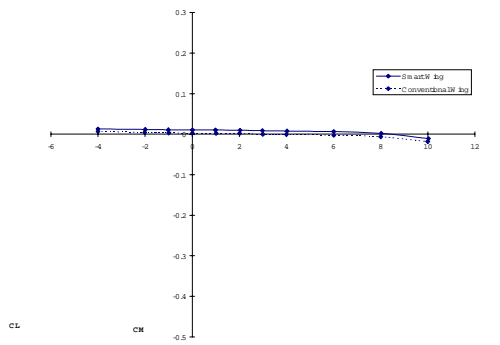
Row D, AOA = 6



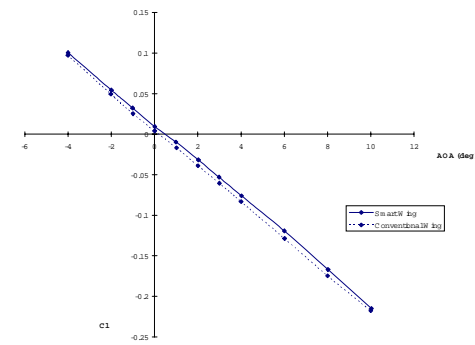
CL vs. AOA



CD vs. Cl

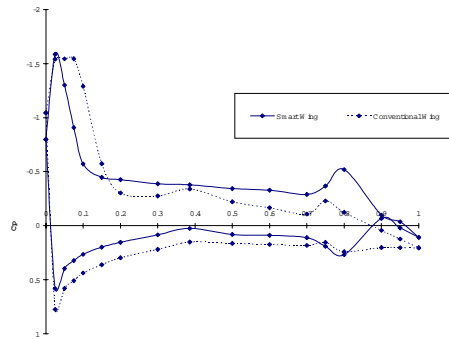


CM vs. AOA

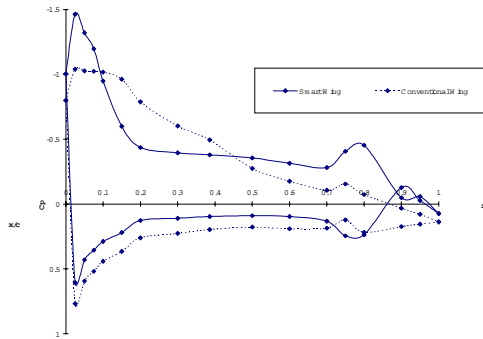


Roll Moment vs. AOA

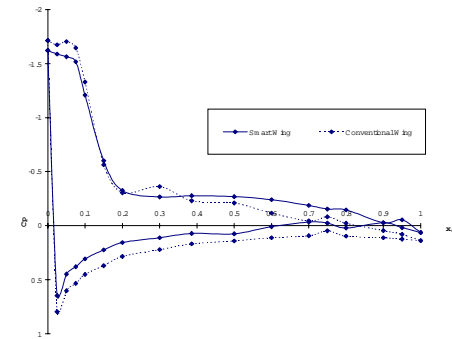
Run 88 vs 2
M = 0.25, Q = 90 psf
Conventional Flap = 0° Aileron = 0°
Smart Flap = 0° Aileron = 0°



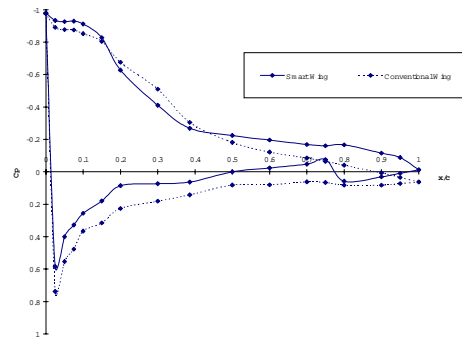
Row A, AOA = 8



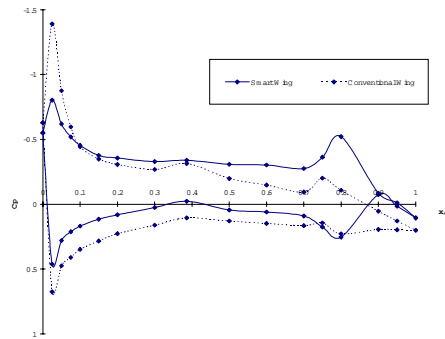
Row B, AOA = 8



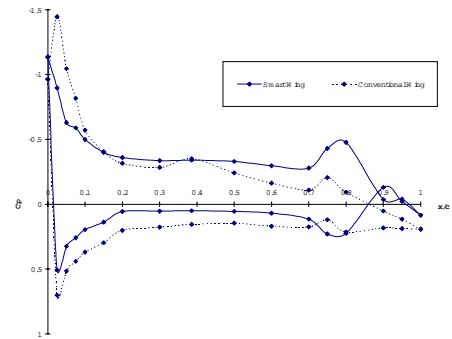
Row C, AOA = 8



Row D, AOA = 8

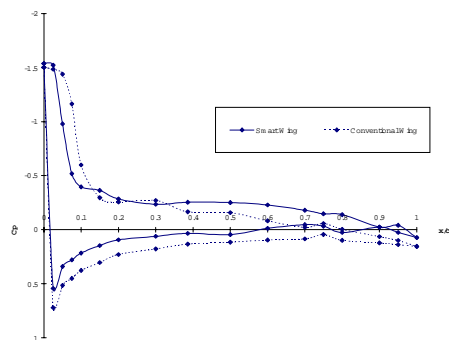


Row A, AOA = 6

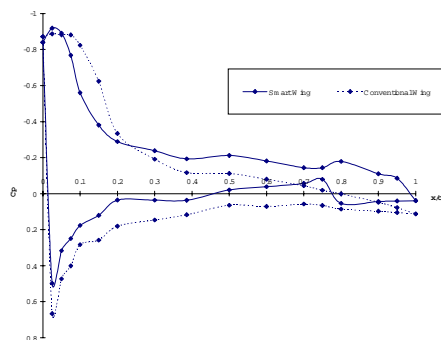


Row B, AOA = 6

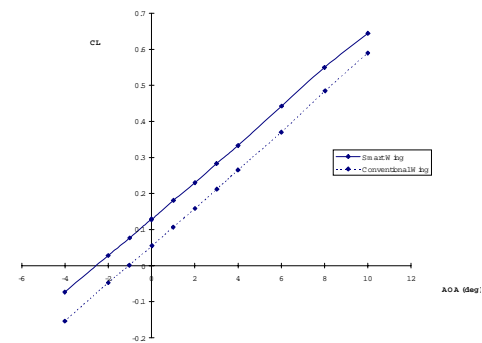
Run 94 vs 5
 $M = 0.25$, $Q = 90$ psf
 Conventional Flap = 5° Aileron = 0°
 Smart Flap = 4.7° Aileron = 0°



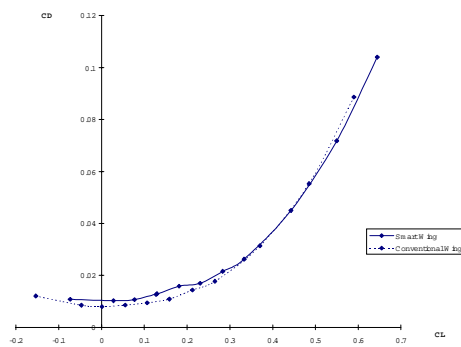
Row C, AOA = 6



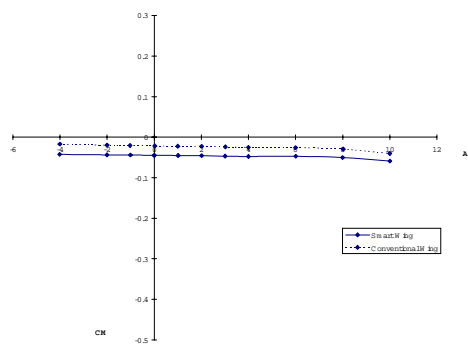
Row D, AOA = 6



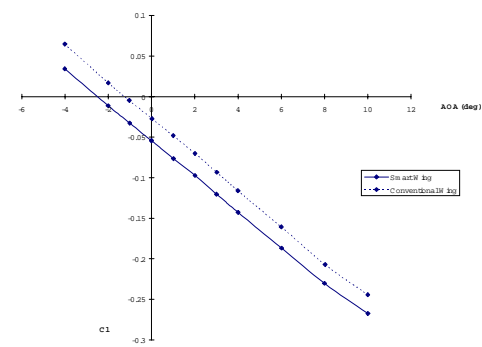
CL vs. AOA



CD vs. Cl

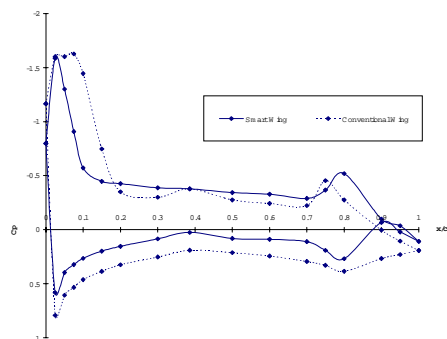


CM vs. AOA

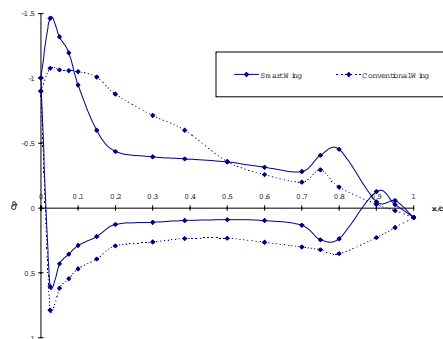


Roll Moment vs. AOA

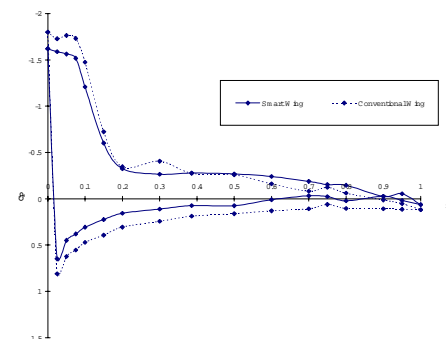
Run 94 vs 5
 $M = 0.25$, $Q = 90$ psf
 Conventional Flap = 5° Aileron = 0°
 Smart Flap = 4.7° Aileron = 0°



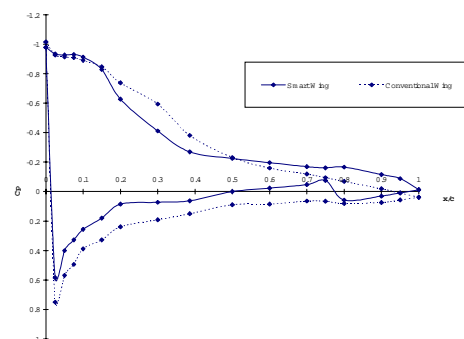
Row A, AOA = 8



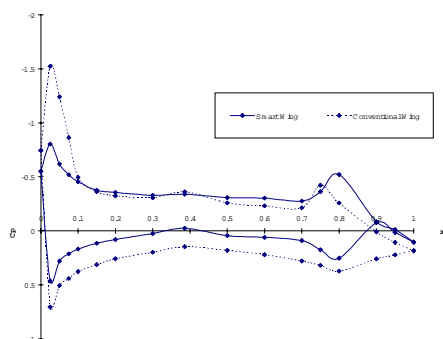
Row B, AOA = 8



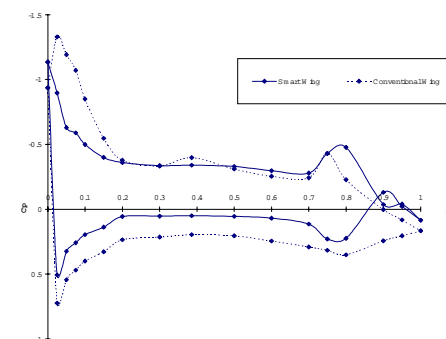
Row C, AOA = 8



Row D, AOA = 8

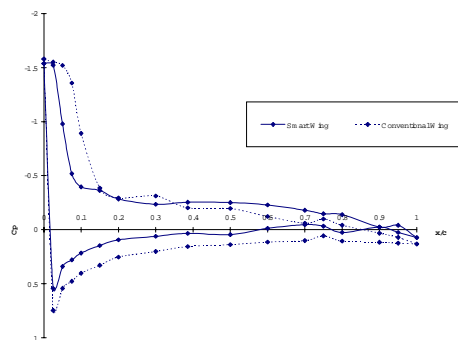


Row A, AOA = 6

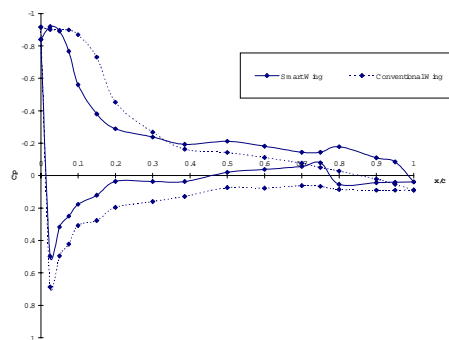


Row B, AOA = 6

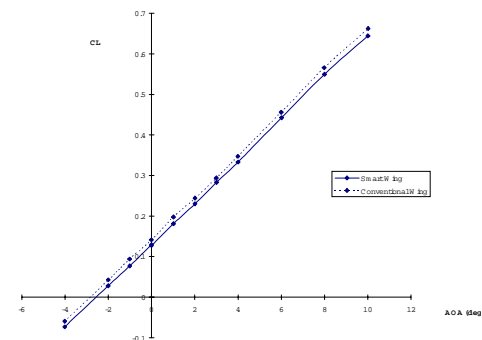
Run 94 vs 11
 $M = 0.25$, $Q = 90$ psf
 Conventional Flap = 10° Aileron = 0°
 Smart Flap = 4.7° Aileron = 0°



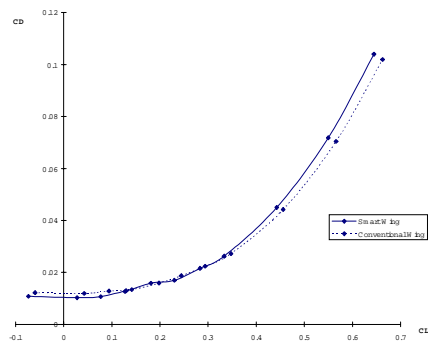
Row C, AOA = 6



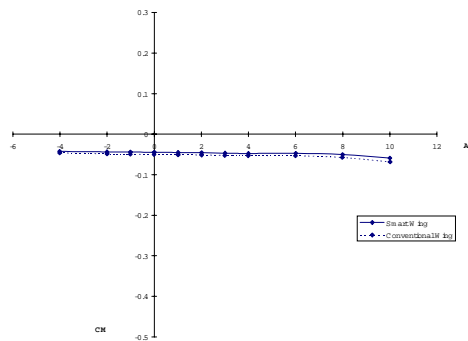
Row D, AOA = 6



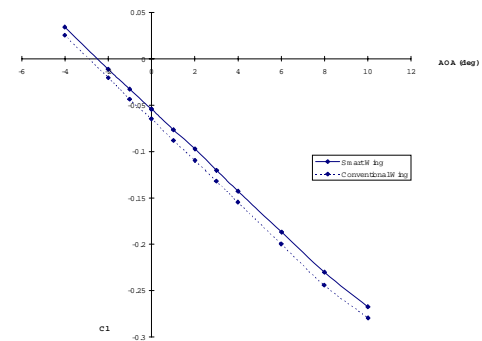
CL vs. AOA



CD vs. Cl

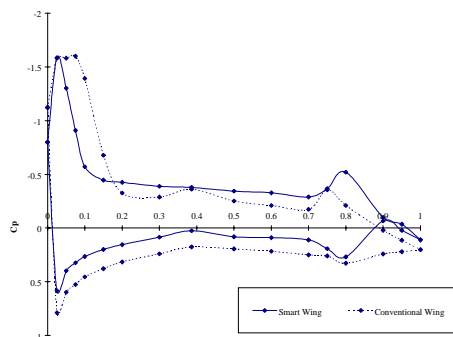


CM vs. AOA

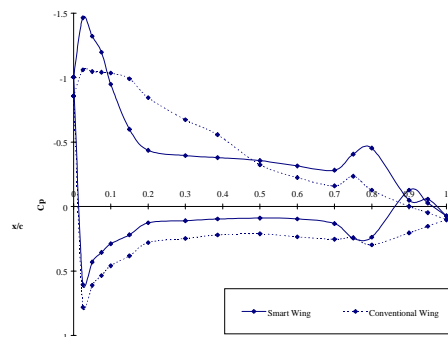


Roll Moment vs. AOA

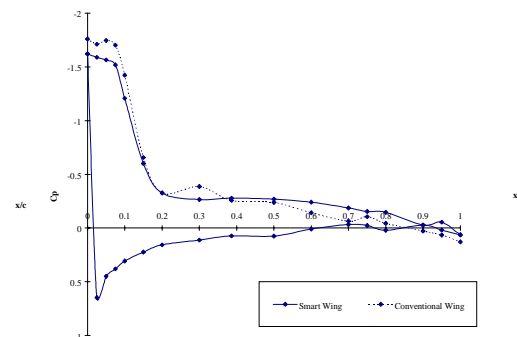
Run 94 vs 11
 $M = 0.25$, $Q = 90$ psf
 Conventional Flap = 10° Aileron = 0°
 Smart Flap = 4.7° Aileron = 0°



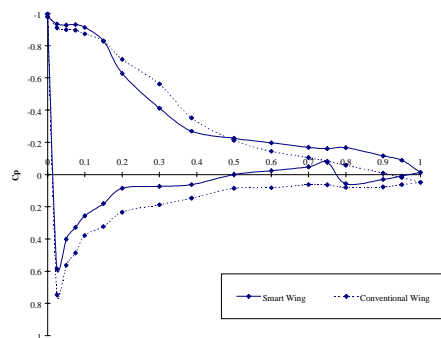
Row A, AOA = 8



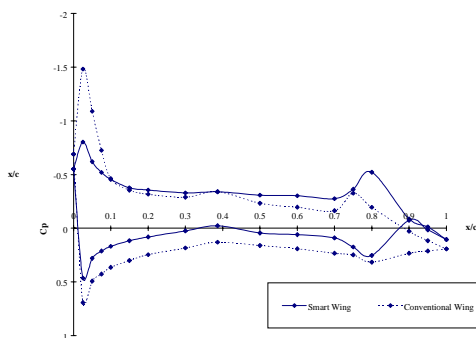
Row B, AOA = 8



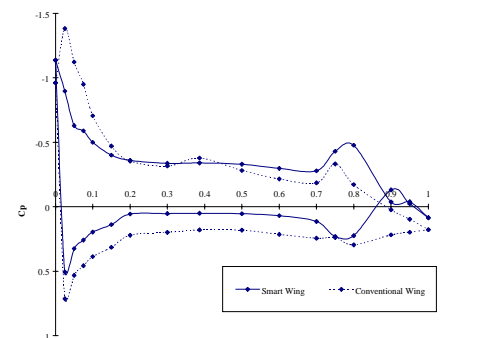
Row C, AOA = 8



Row D, AOA = 8

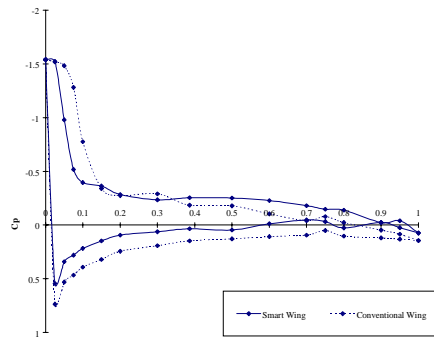


Row A, AOA = 6

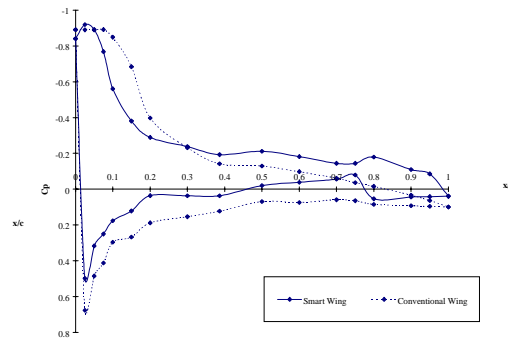


Row B, AOA = 6

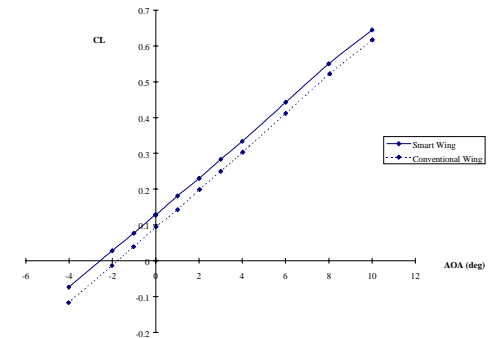
Run 94 vs 14
 $M = 0.25$, $Q = 90$ psf
 Conventional Flap = 7.5° Aileron = 0°
 Smart Flap = 4.7° Aileron = 0°



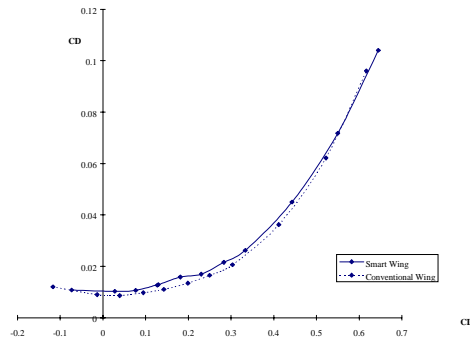
Row C, AOA = 6



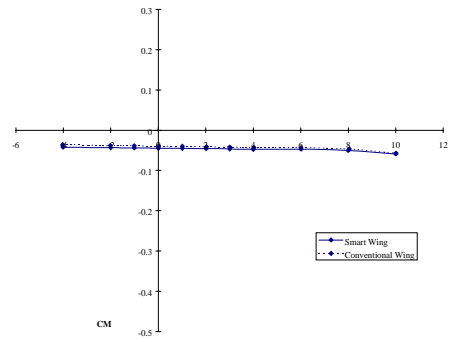
Row D, AOA = 6



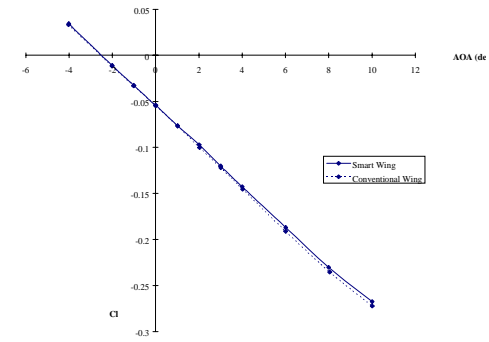
CL vs. AOA



CD vs. CL

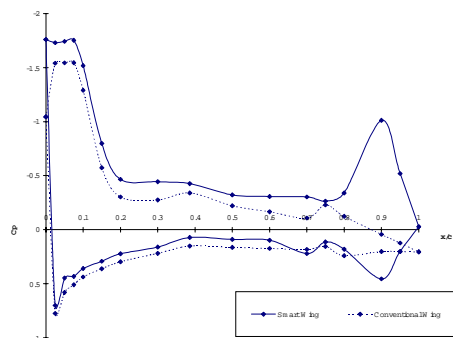


CM vs. AOA

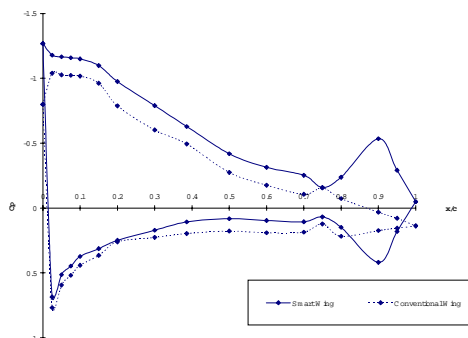


Roll Moment vs. AOA

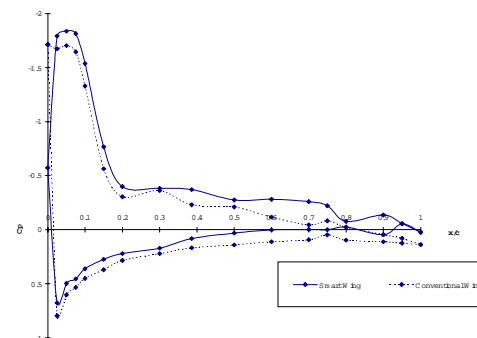
Run 94 vs 14
 $M = 0.25$, $Q = 90$ psf
 Conventional Flap = 7.5° Aileron = 0°
 Smart Flap = 4.7° Aileron = 0°



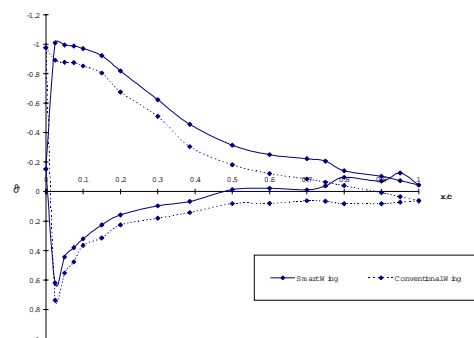
Row A, AOA = 8



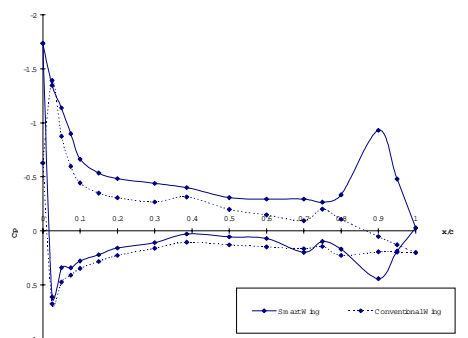
Row B, AOA = 8



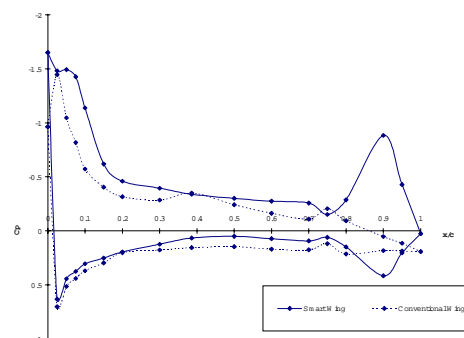
Row C, AOA = 8



Row D, AOA = 8

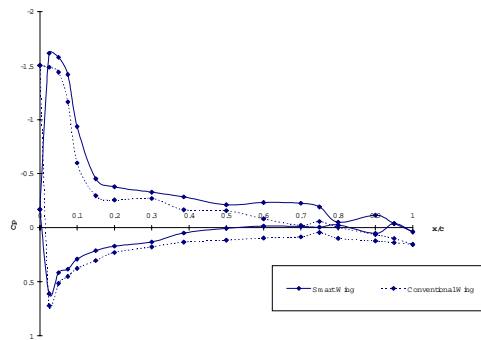


Row A, AOA = 6

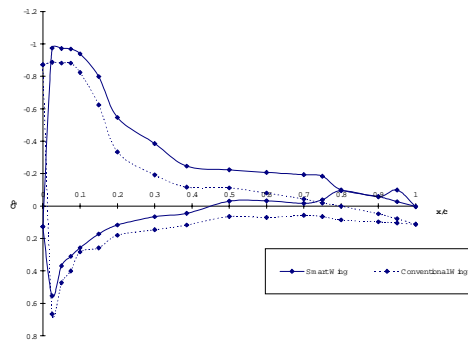


Row B, AOA = 6

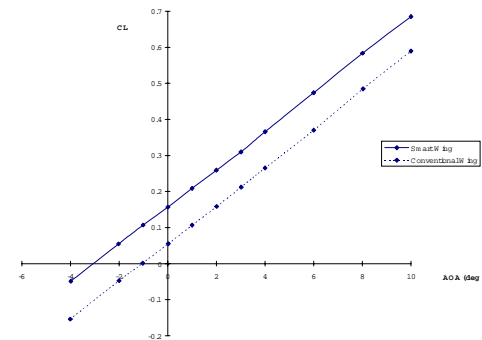
Run 101 vs 5
 $M = 0.25$, $Q = 90$ psf
 Conventional Flap = 5° Aileron = 0°
 Smart Flap = -4° Aileron = 0°



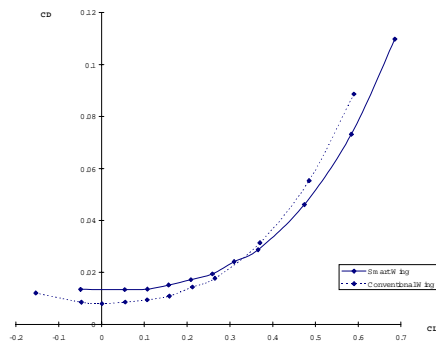
Row C, AOA = 6



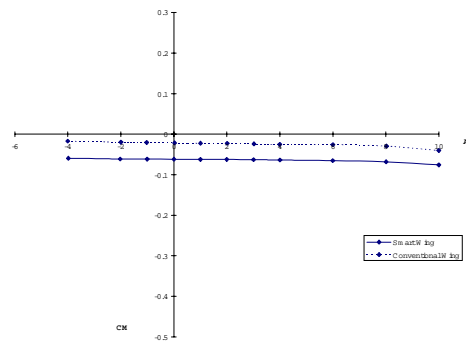
Row D, AOA = 6



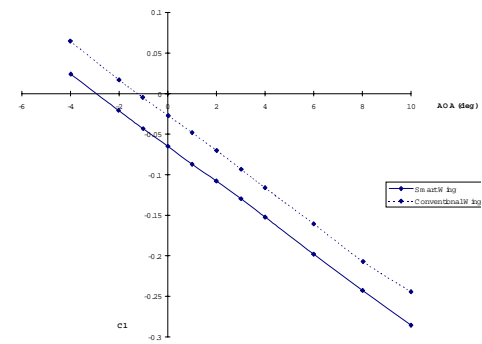
CL vs. AOA



CD vs. CL

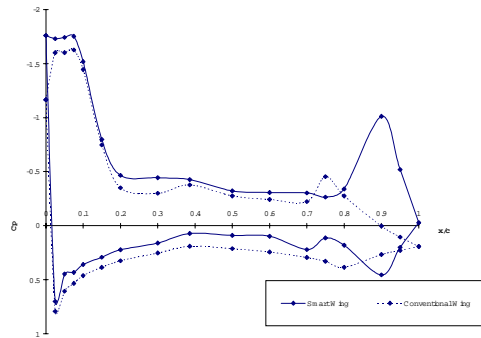


CM vs. AOA

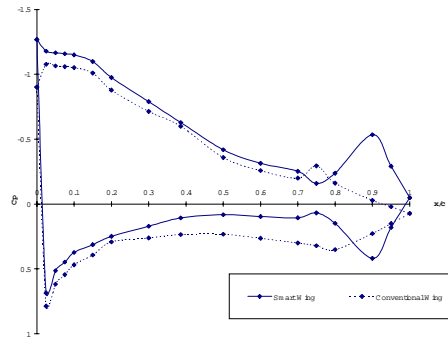


Roll Moment vs. AOA

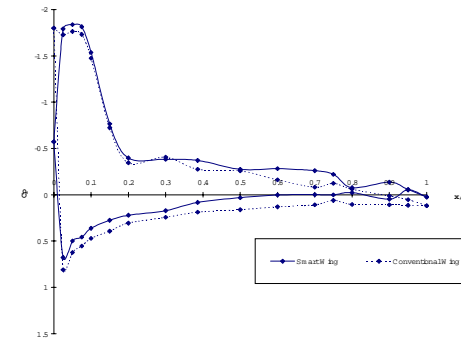
Run 101 vs 5
 $M = 0.25$, $Q = 90$ psf
 Conventional Flap = 5° Aileron = 0°
 Smart Flap = -4° Aileron = 0°



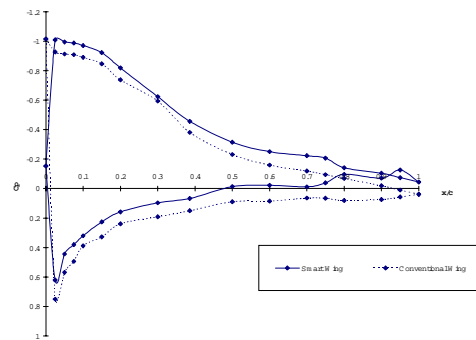
Row A, AOA = 8



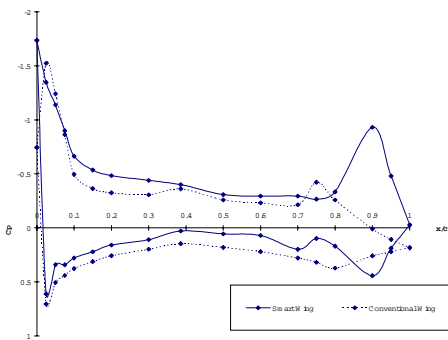
Row B, AOA = 8



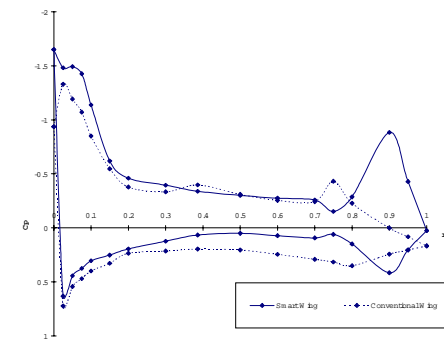
Row C, AOA = 8



Row D, AOA = 8

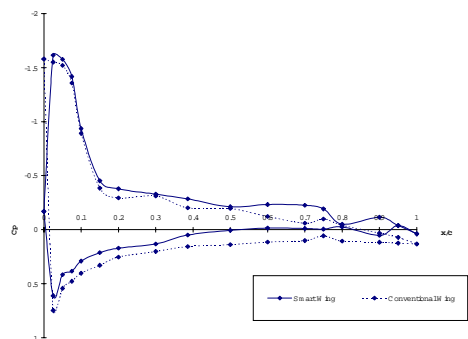


Row A, AOA = 6

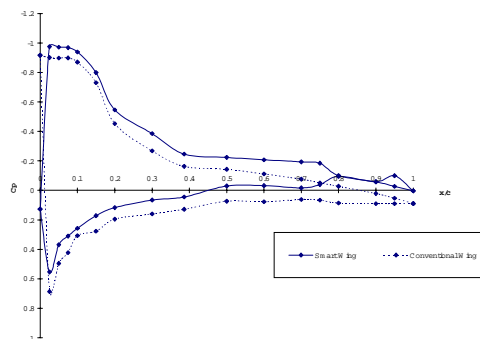


Row B, AOA = 6

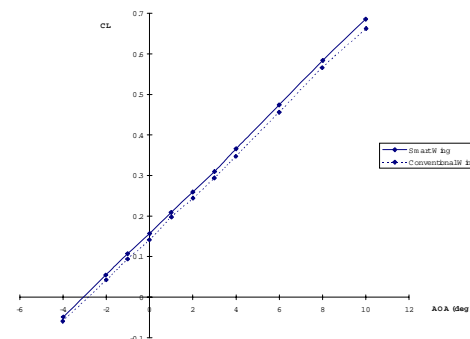
Run 101 vs 11
 $M = 0.25$, $Q = 90$ psf
 Conventional Flap = 10° Aileron = 0°
 Smart Flap = -4° Aileron = 0°



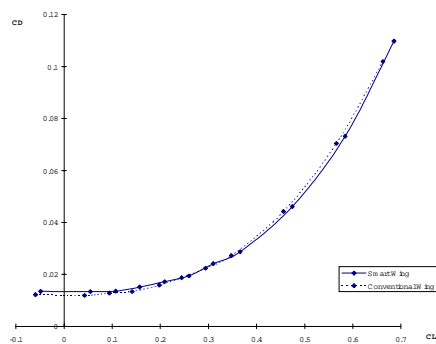
Row C, AOA = 6



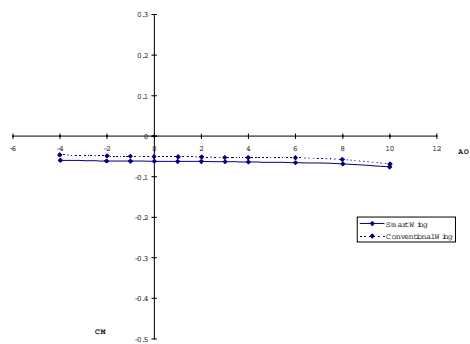
Row D, AOA = 6



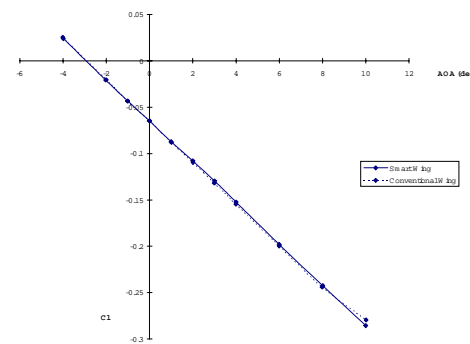
CL vs. AOA



CD vs. CL

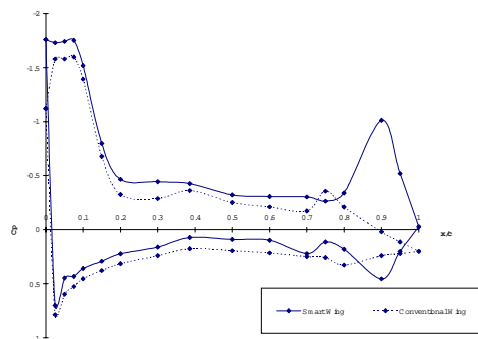


CM vs. AOA

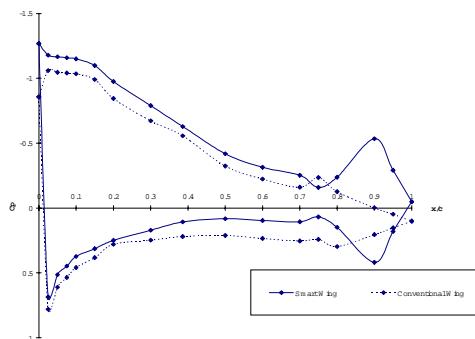


Roll Moment vs. AOA

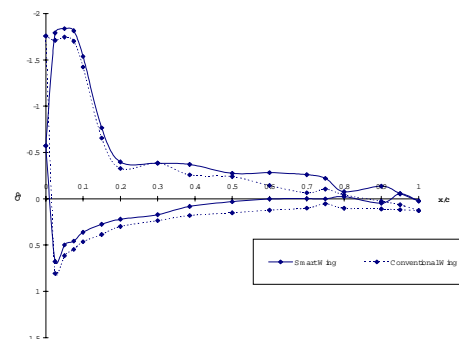
Run 101 vs 11
 $M = 0.25$, $Q = 90$ psf
 Conventional Flap = 10° Aileron = 0°
 Smart Flap = -4° Aileron = 0°



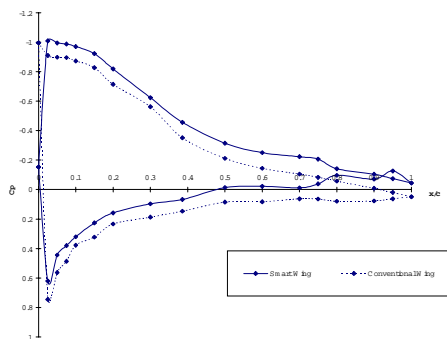
Row A, AOA = 8



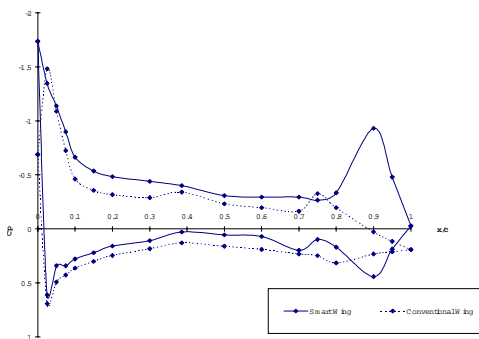
Row B, AOA = 8



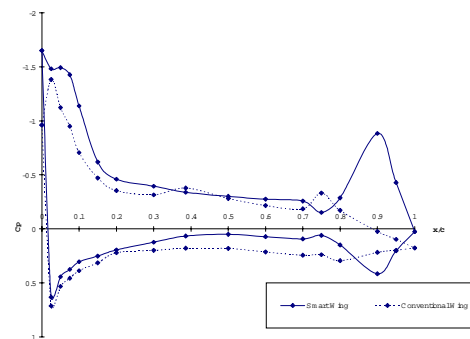
Row C, AOA = 8



Row D, AOA = 8

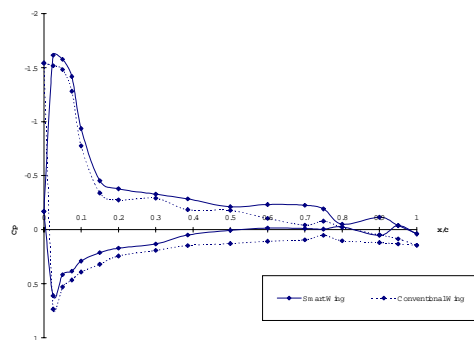


Row A, AOA = 6

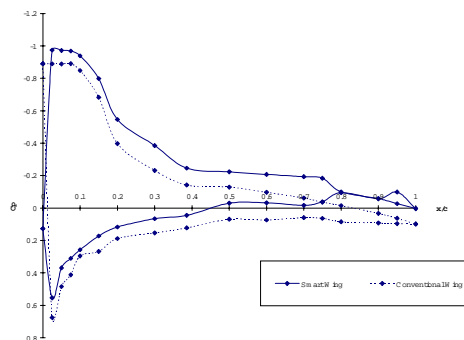


Row B, AOA = 6

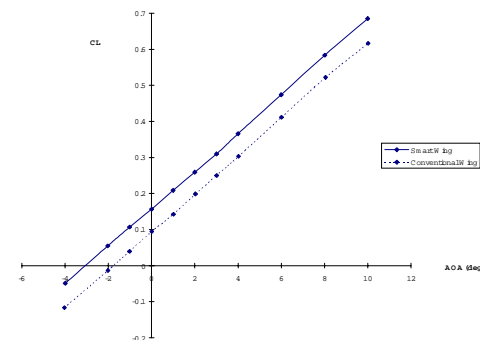
Run 101 vs 14
 $M = 0.25$, $Q = 90$ psf
 Conventional Flap = 7.5° Aileron = 0°
 Smart Flap = -4° Aileron = 0°



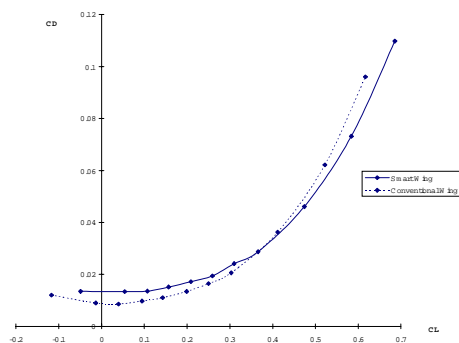
Row C, AOA = 6



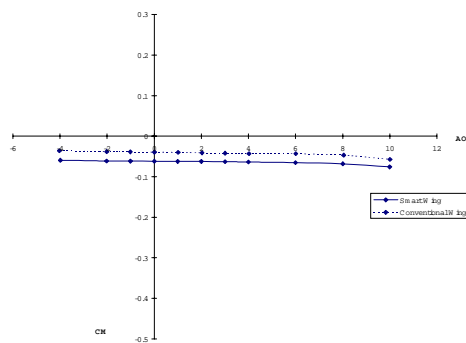
Row D, AOA = 6



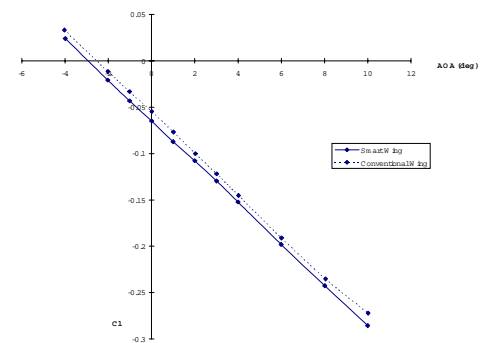
CL vs. AOA



CD vs. CL

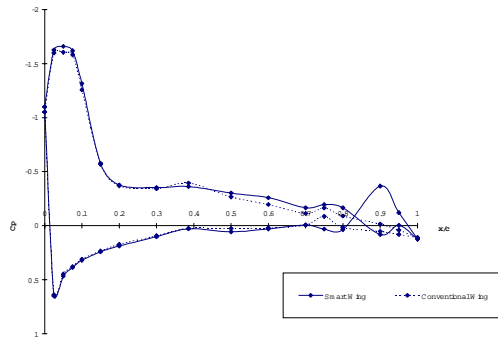


CM vs. AOA

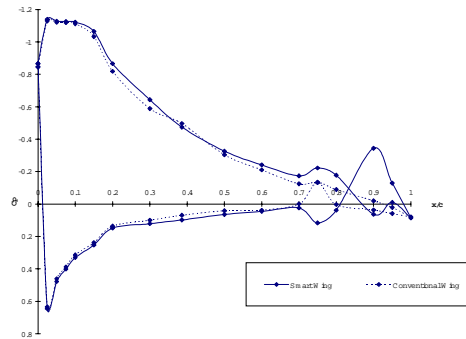


Roll Moment vs. AOA

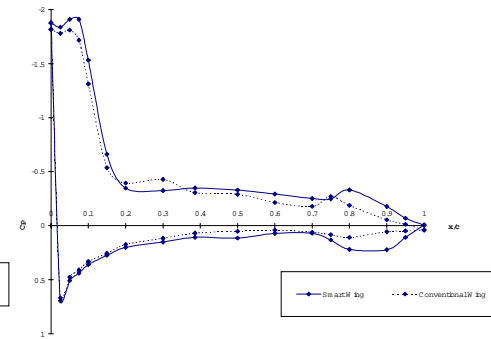
Run 101 vs 14
 $M = 0.25$, $Q = 90$ psf
 Conventional Flap = 7.5° Aileron = 0°
 Smart Flap = -4° Aileron = 0°



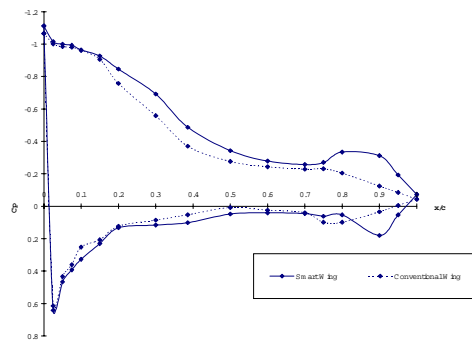
Row A, AOA = 8



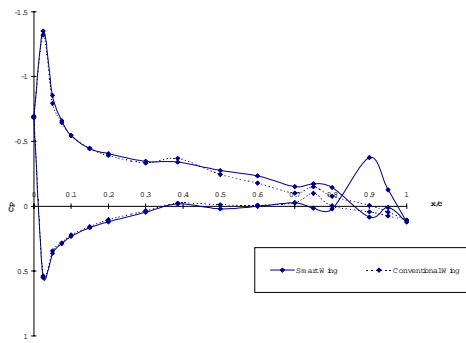
Row B, AOA = 8



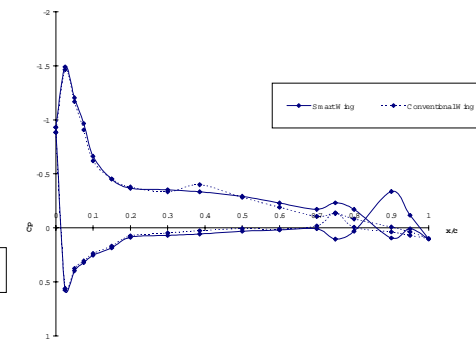
Row C, AOA = 8



Row D, AOA = 8

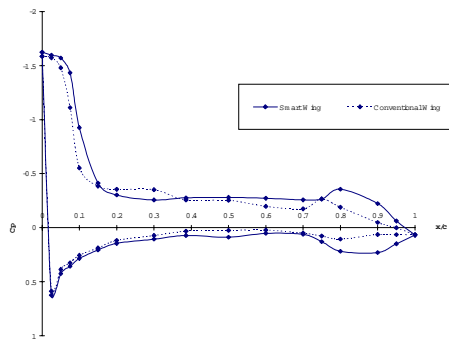


Row A, AOA = 6

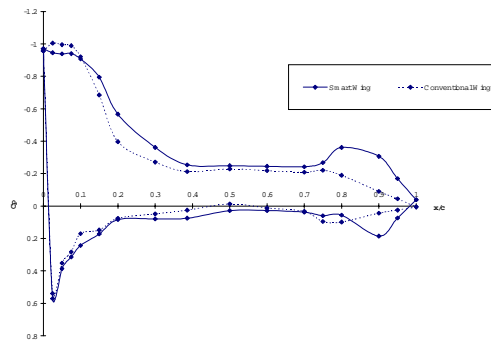


Row B, AOA = 6

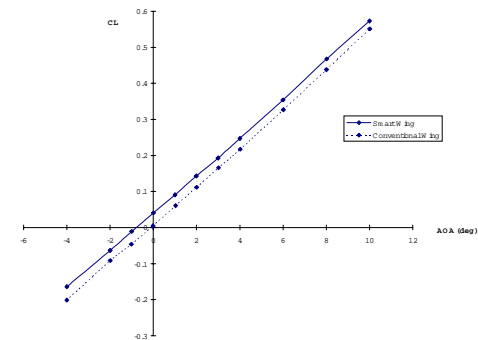
Run 108 vs 19
 $M = 0.25$, $Q = 90$ psf
 Conventional Flap = 0° Aileron = 5°
 Smart Flap = 0° Aileron = 4°



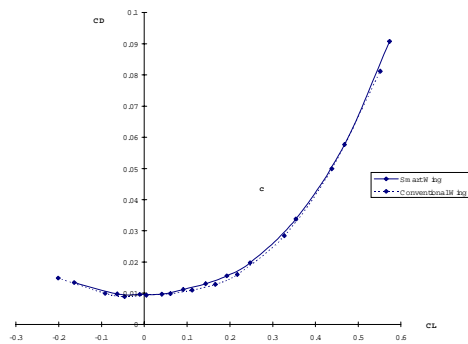
Row C, AOA = 6



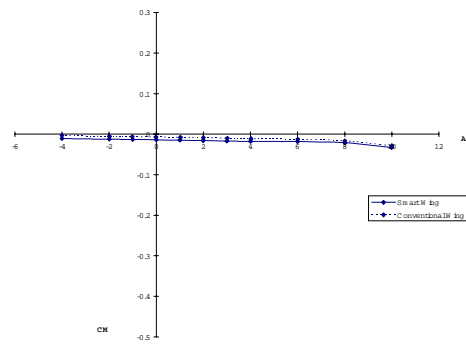
Row D, AOA = 6



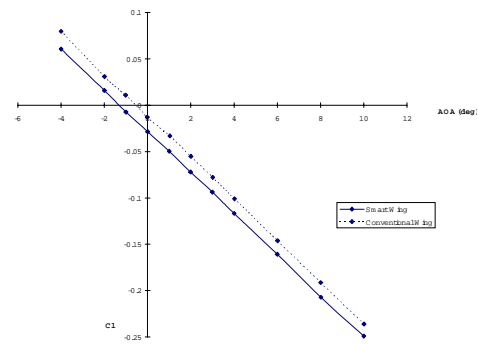
CL vs. AOA



CD vs. CL

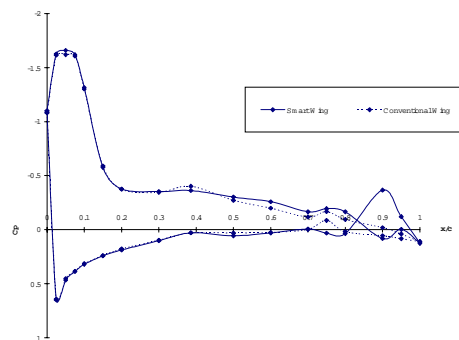


CM vs. AOA

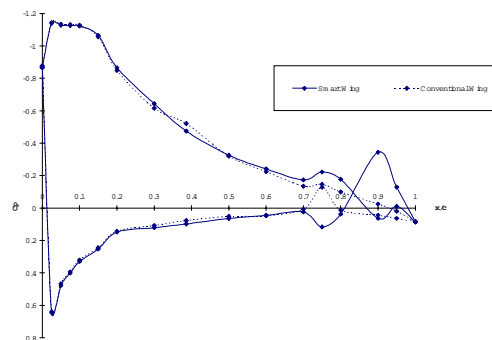


Roll Moment vs. AOA

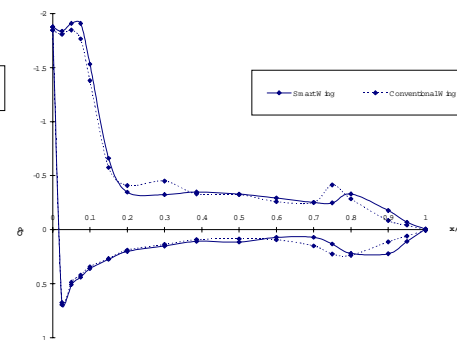
Run 108 vs 19
M = 0.25, Q = 90 psf
Conventional Flap = 0° Aileron = 5°
Smart Flap = 0° Aileron = 4°



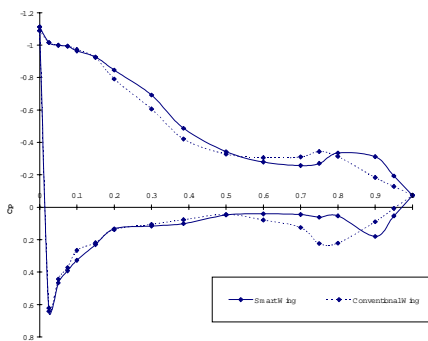
Row A, AOA = 8



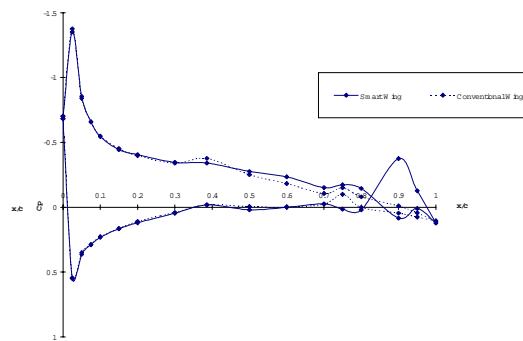
Row B, AOA = 8



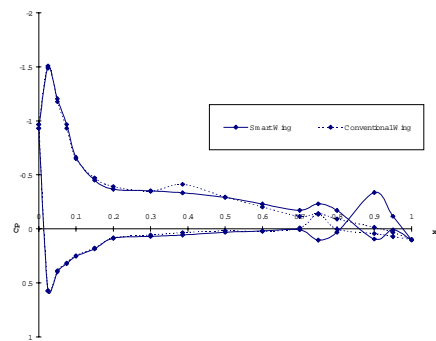
Row C, AOA = 8



Row D, AOA = 8

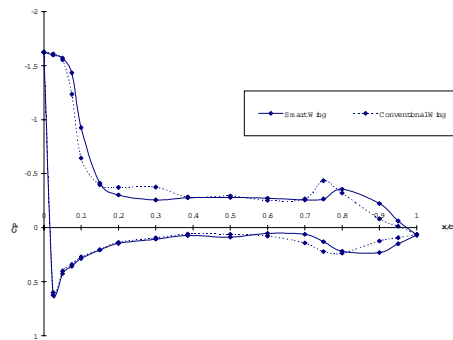


Row A, AOA = 6

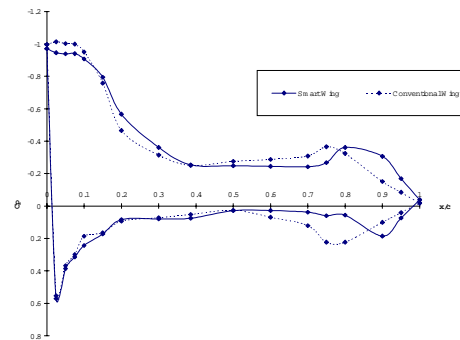


Row B, AOA = 6

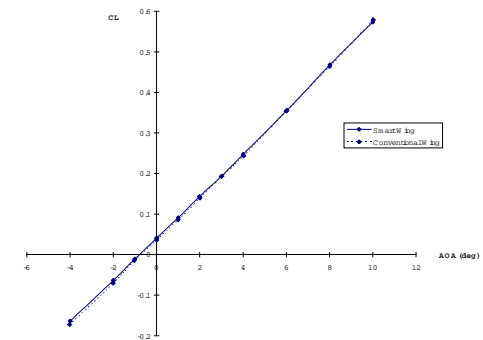
Run 108 vs 31
 $M = 0.25$, $Q = 90$ psf
 Conventional Flap = 0° Aileron = 10°
 Smart Flap = 0° Aileron = 4°



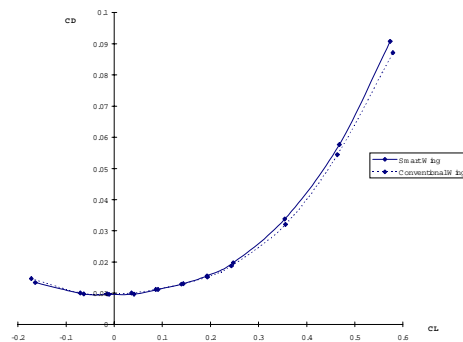
Row C, AOA = 6



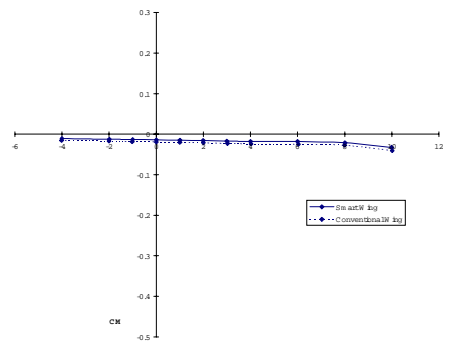
Row D, AOA = 6



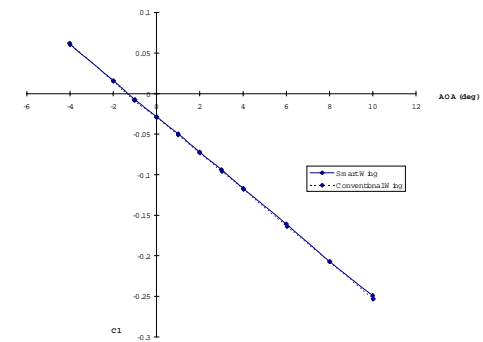
CL vs. AOA



CD vs. CL

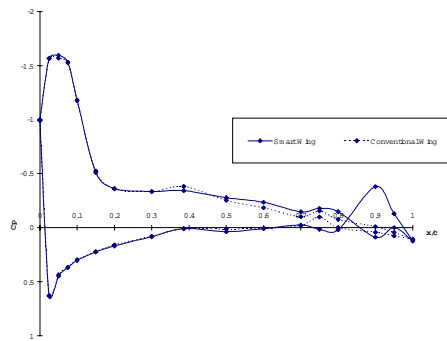


CM vs. AOA

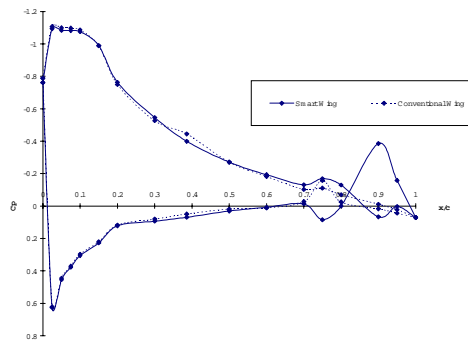


Roll Moment vs. AOA

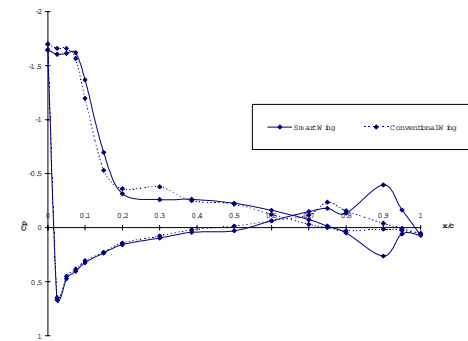
Run 108 vs 31
M = 0.25, Q = 90 psf
Conventional Flap = 0° Aileron = 10°
Smart Flap = 0° Aileron = 4°



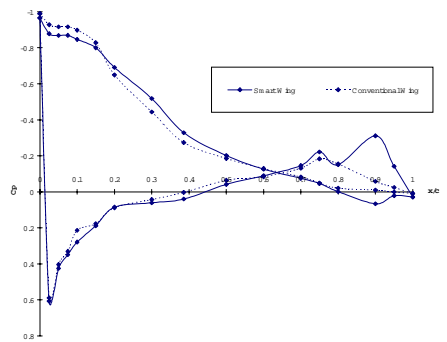
Row A, AOA = 8



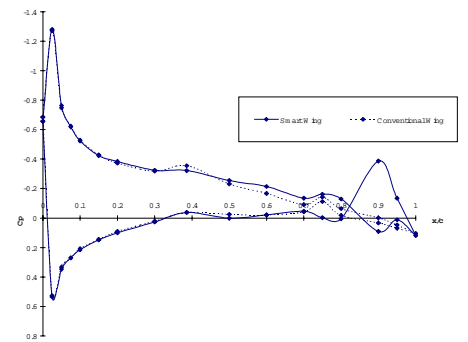
Row B, AOA = 8



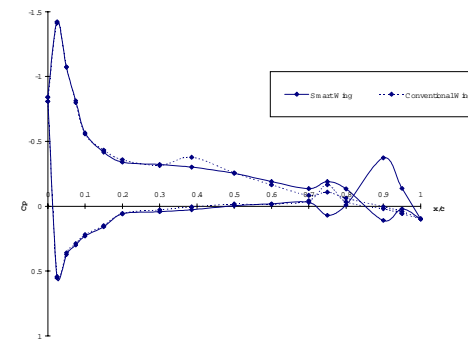
Row C, AOA = 8



Row D, AOA = 8

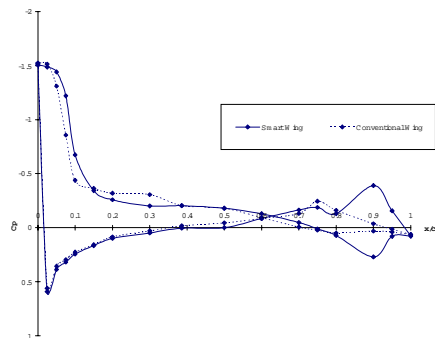


Row A, AOA = 6

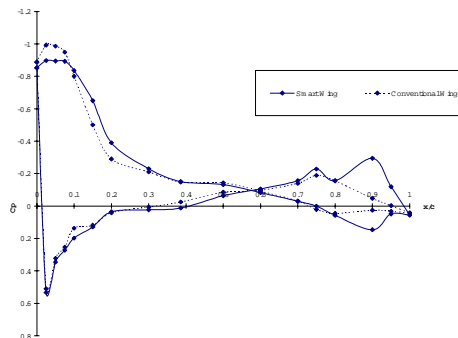


Row B, AOA = 6

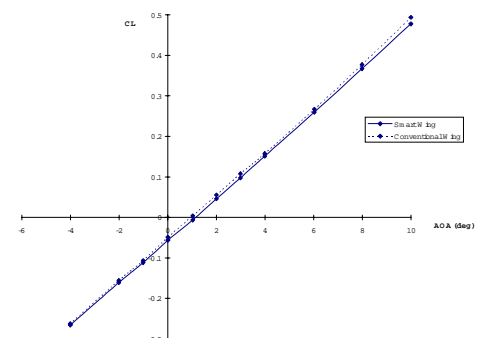
Run 111 vs 45
 $M = 0.25$, $Q = 90$ psf
 Conventional Flap = 0° Aileron = -5°
 Smart Flap = 0° Aileron = -4°



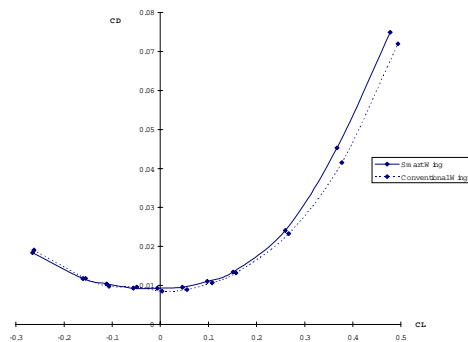
Row C, AOA = 6



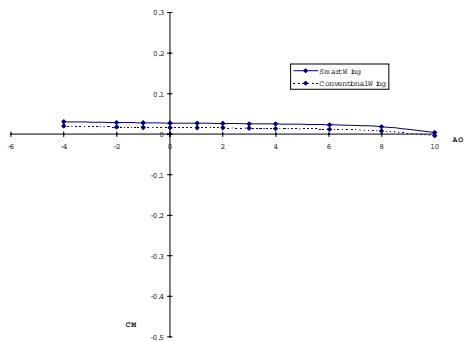
Row D, AOA = 6



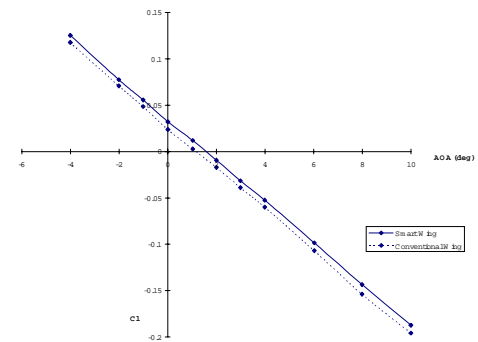
CL vs. AOA



CD vs. Cl

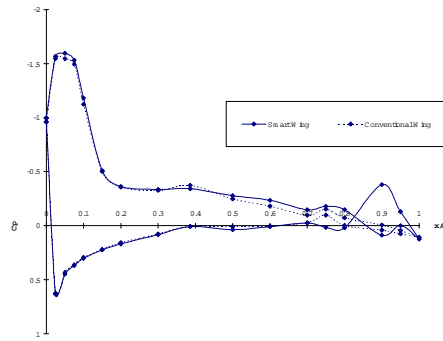


CM vs. AOA

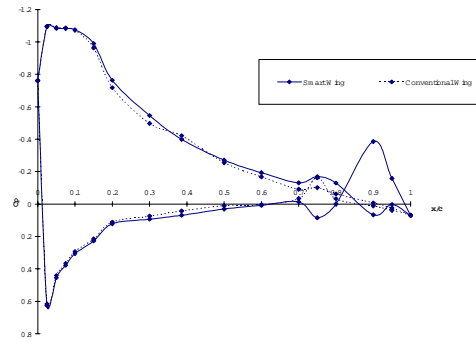


Roll Moment vs. AOA

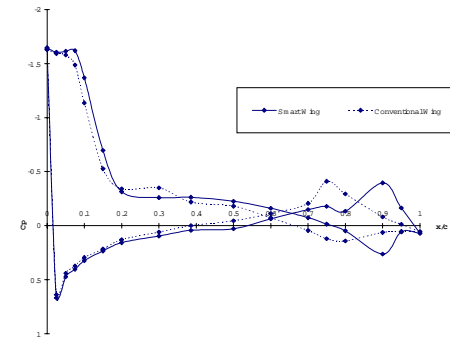
Run 111 vs 45
 $M = 0.25$, $Q = 90$ psf
 Conventional Flap = 0° Aileron = -5°
 Smart Flap = 0° Aileron = -4°



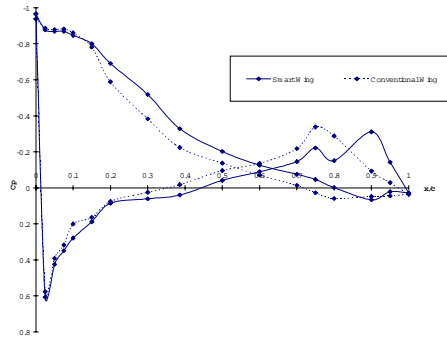
Row A, AOA = 8



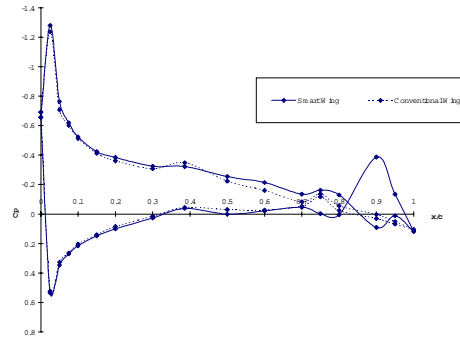
Row B, AOA = 8



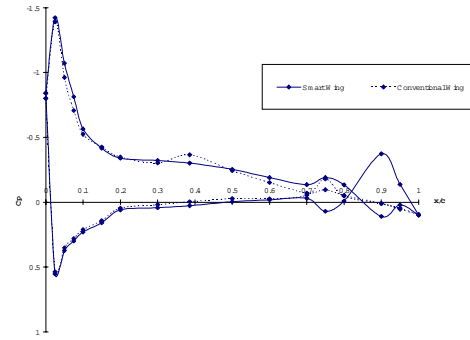
Row C, AOA = 8



Row D, AOA = 8

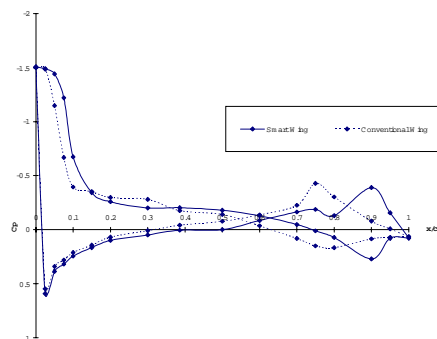


Row A, AOA = 6

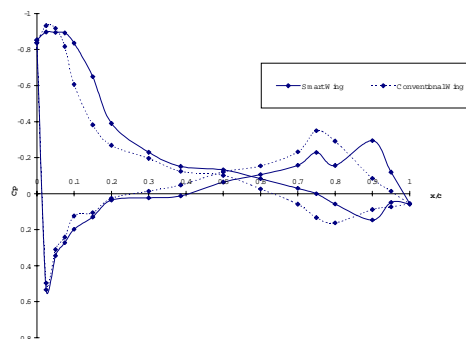


Row B, AOA = 6

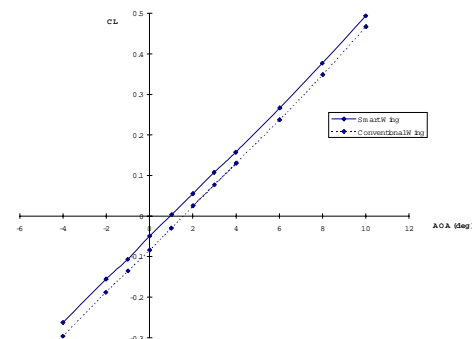
Run 111 vs 57
 $M = 0.25$, $Q = 90$ psf
 Conventional Flap = 0° Aileron = -10°
 Smart Flap = 0° Aileron = -4°



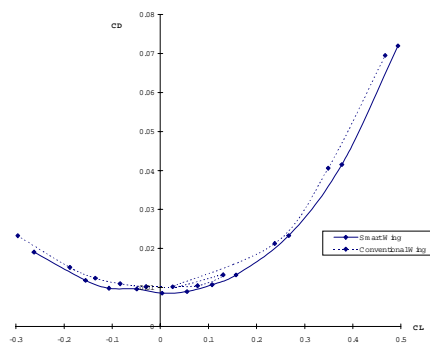
Row C, AOA = 6



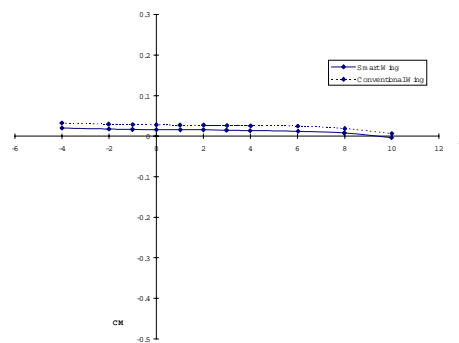
Row D, AOA = 6



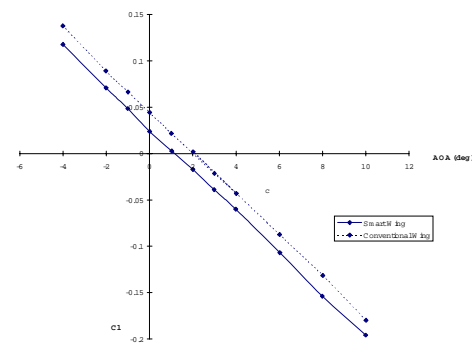
CL vs. AOA



CD vs. Cl

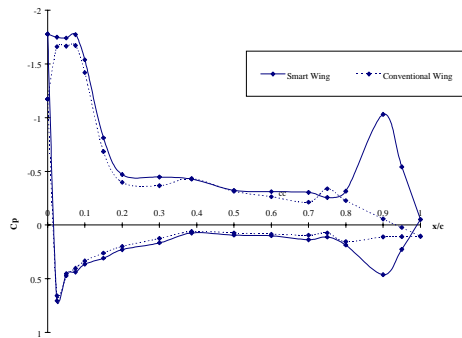


CM vs. AOA

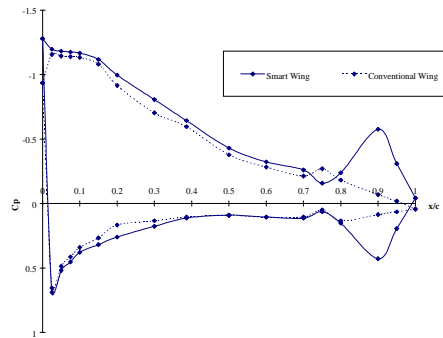


Roll Moment vs. AOA

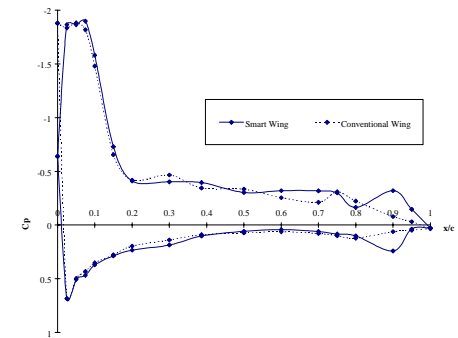
Run 111 vs 57
 $M = 0.25$, $Q = 90$ psf
 Conventional Flap = 0° Aileron = -10°
 Smart Flap = 0° Aileron = -4°



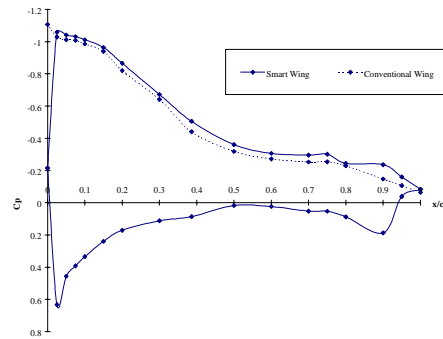
Row A, AOA = 8



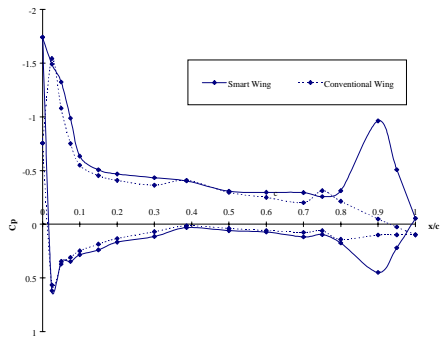
Row B, AOA = 8



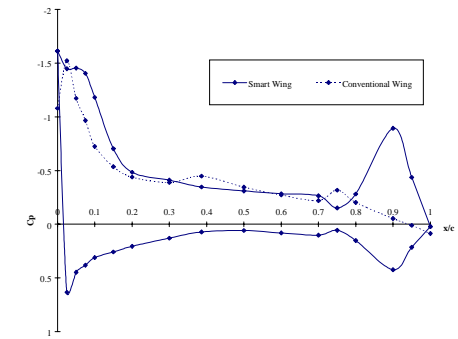
Row C, AOA = 8



Row D, AOA = 8

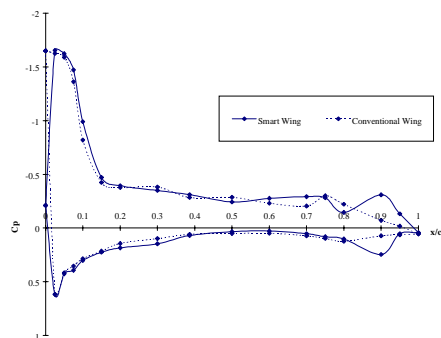


Row A, AOA = 6

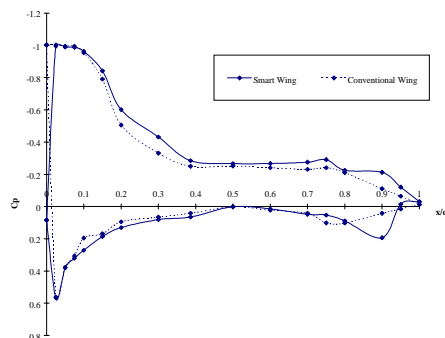


Row B, AOA = 6

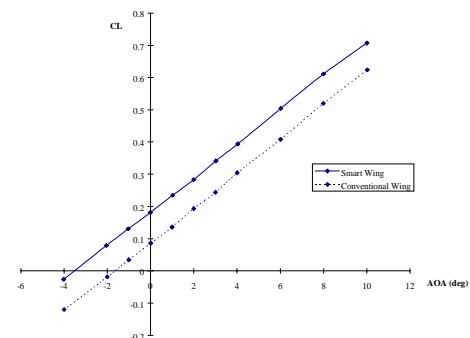
Run 105 vs 22
 $M = 0.25$, $Q = 90$ psf
 Conventional Flap = 5° Aileron = 5°
 Smart Flap = -4° Aileron = -4°



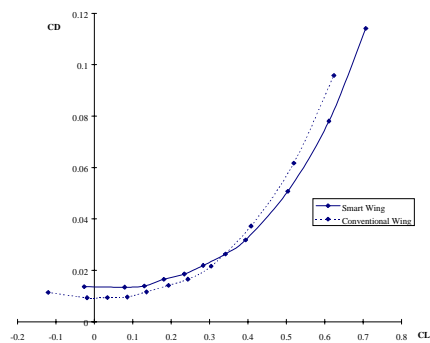
Row C, AOA = 6



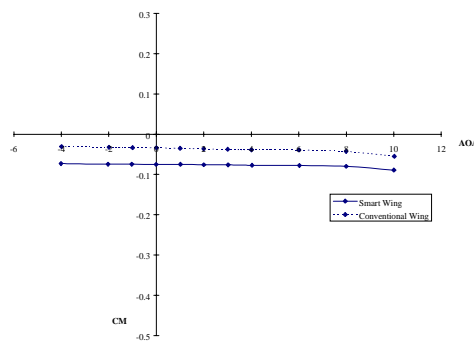
Row D, AOA = 6



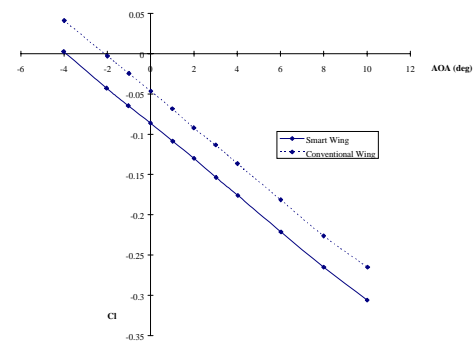
CL vs. AOA



CD vs. CL

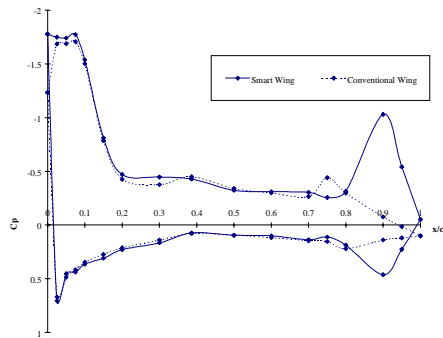


CM vs. AOA

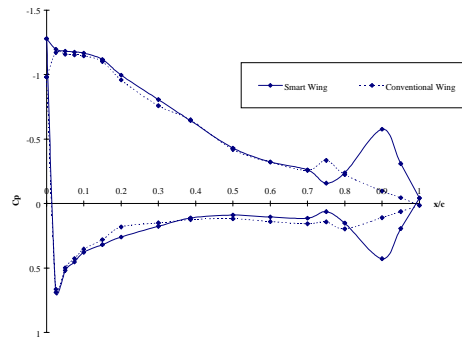


Roll Moment vs. AOA

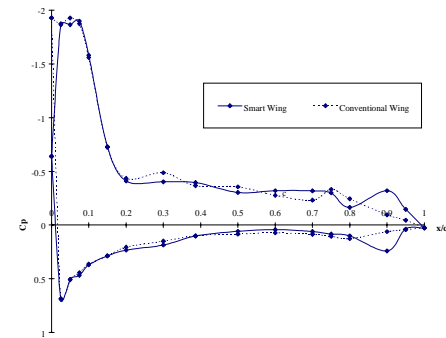
Run 105 vs 22
 $M = 0.25$, $Q = 90$ psf
 Conventional Flap = 5° Aileron = 5°
 Smart Flap = -4° Aileron = -4°



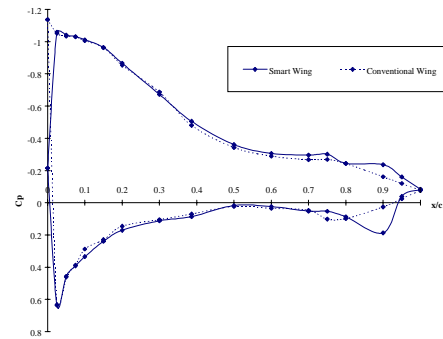
Row A, AOA = 8



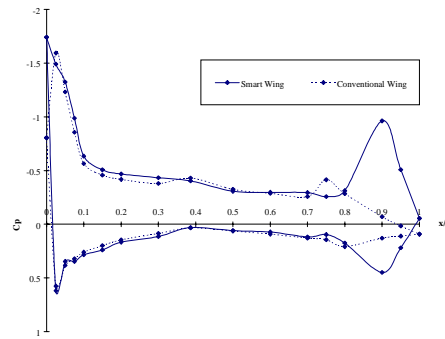
Row B, AOA = 8



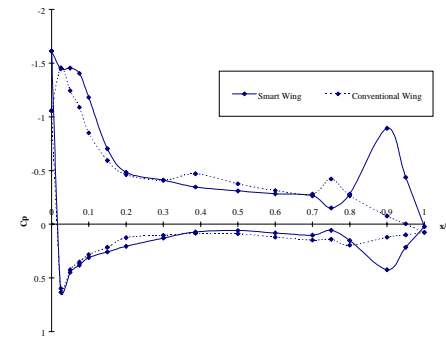
Row C, AOA = 8



Row D, AOA = 8

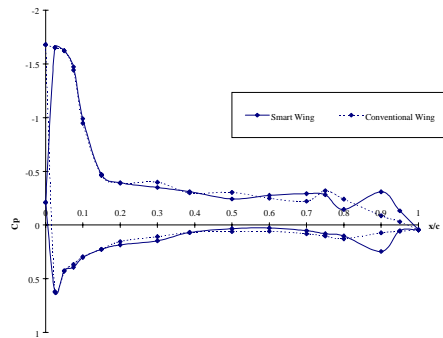


Row A, AOA = 6

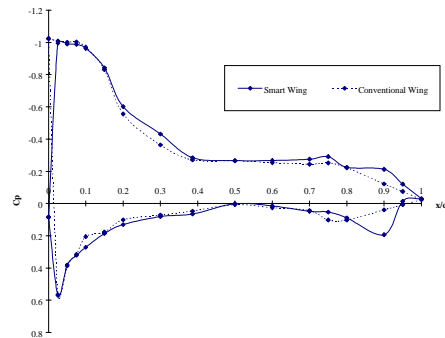


Row B, AOA = 6

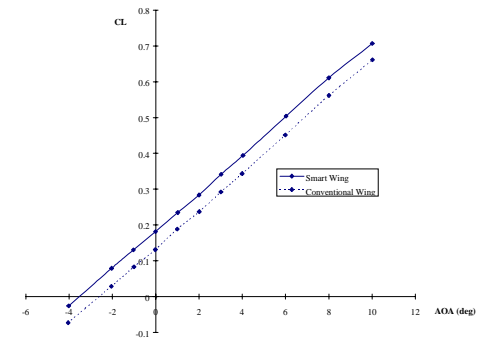
Run 105 vs 25
 $M = 0.25$, $Q = 90$ psf
 Conventional Flap = 7.5° Aileron = 5°
 Smart Flap = -4° Aileron = -4°



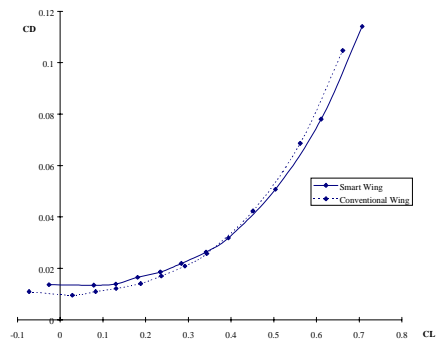
Row C, AOA = 6



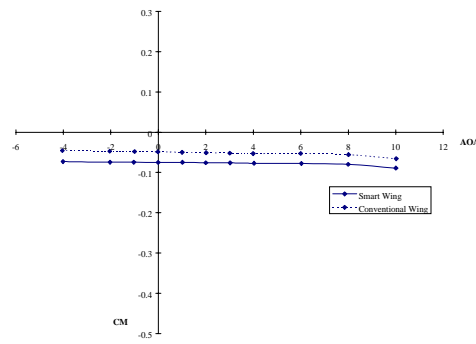
Row D, AOA = 6



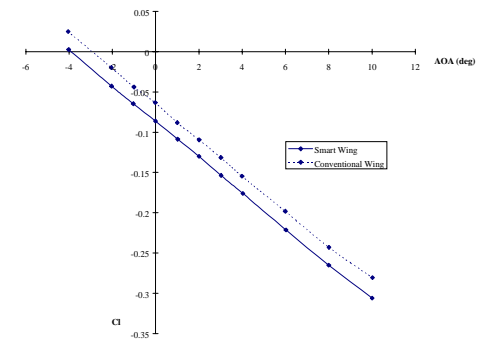
CL vs. AOA



CD vs. CL

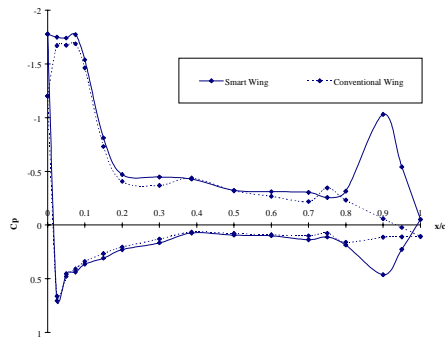


CM vs. AOA

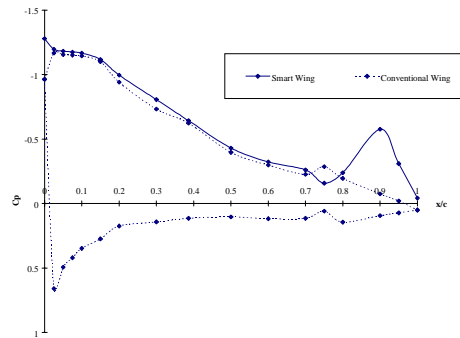


Roll Moment vs. AOA

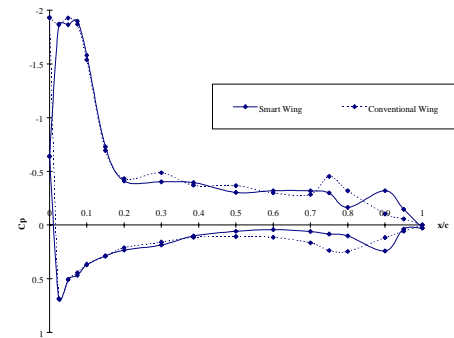
Run 105 vs 25
 $M = 0.25$, $Q = 90$ psf
 Conventional Flap = 7.5° Aileron = 5°
 Smart Flap = -4° Aileron = -4°



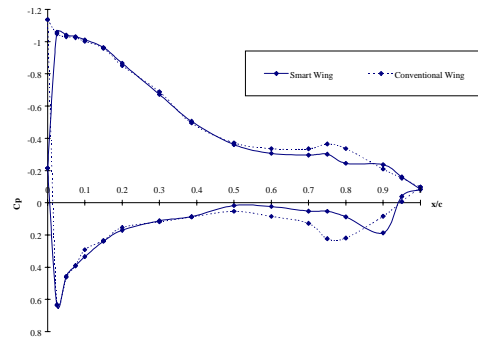
Row A, AOA = 8



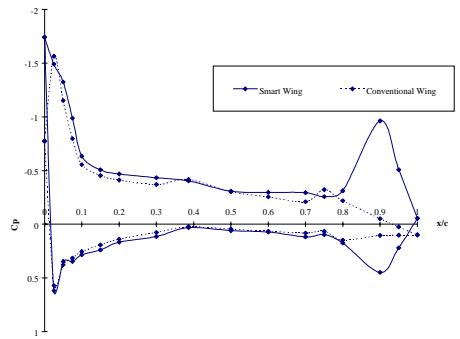
Row B, AOA = 8



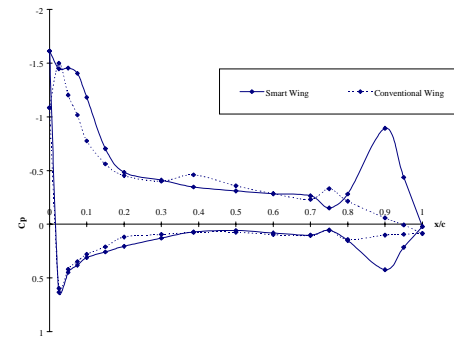
Row C, AOA = 8



Row D, AOA = 8

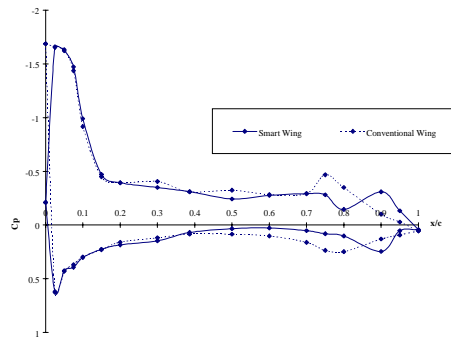


Row A, AOA = 6

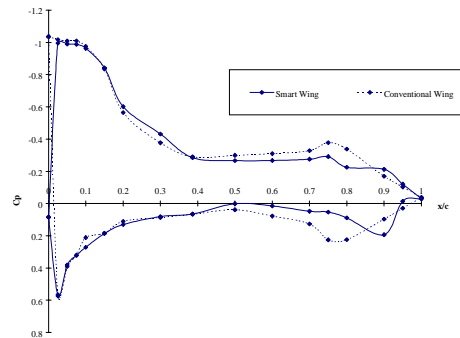


Row B, AOA = 6

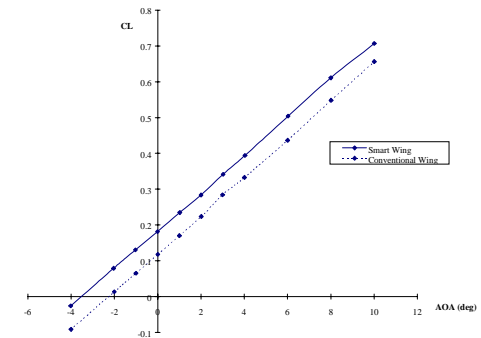
Run 105 vs 34
 $M = 0.25$, $Q = 90$ psf
 Conventional Flap = 5° Aileron = 10°
 Smart Flap = -4° Aileron = -4°



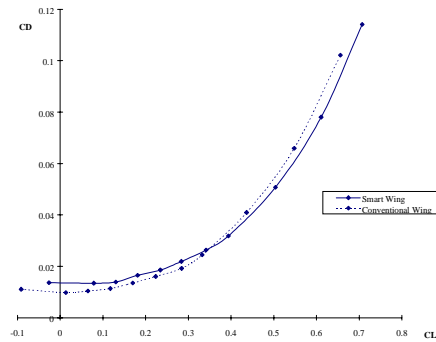
Row C, AOA = 6



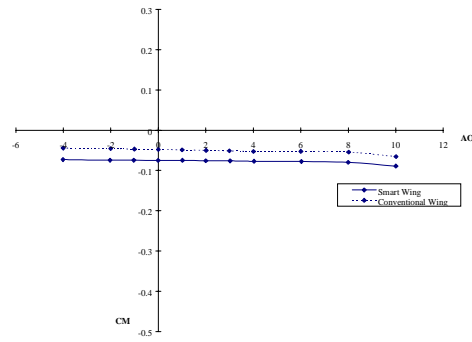
Row D, AOA = 6



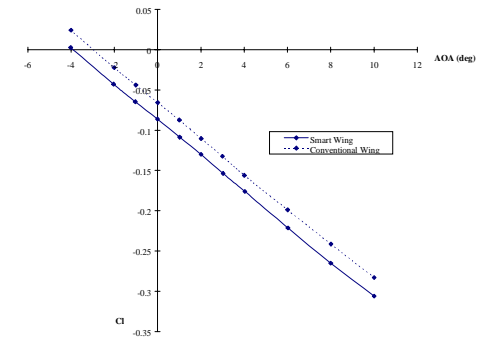
CL vs. AOA



CD vs. CL

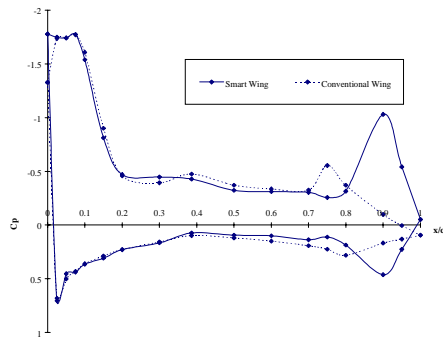


CM vs. AOA

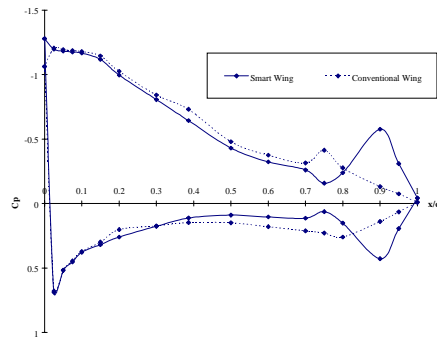


Roll Moment vs. AOA

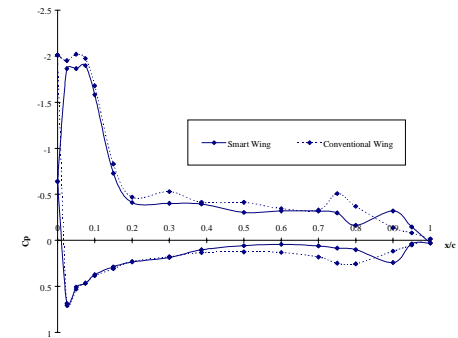
Run 105 vs 34
 $M = 0.25$, $Q = 90$ psf
 Conventional Flap = 5° Aileron = 10°
 Smart Flap = -4° Aileron = -4°



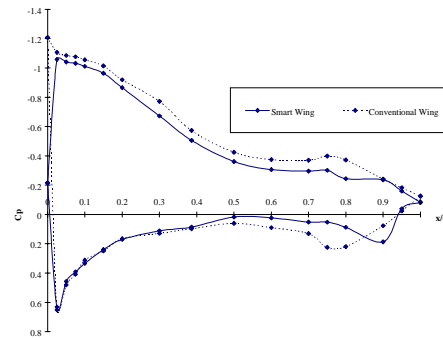
Row A, AOA = 8



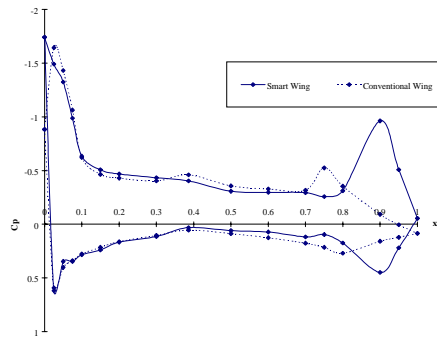
Row B, AOA = 8



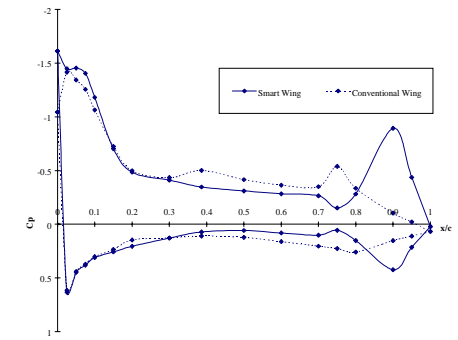
Row C, AOA = 8



Row D, AOA = 8

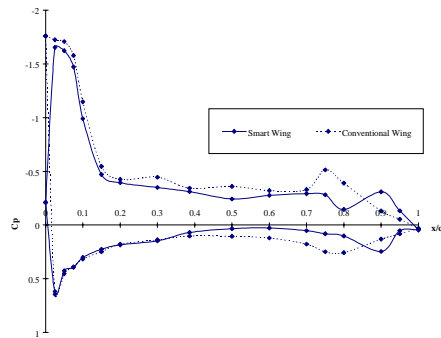


Row A, AOA = 6

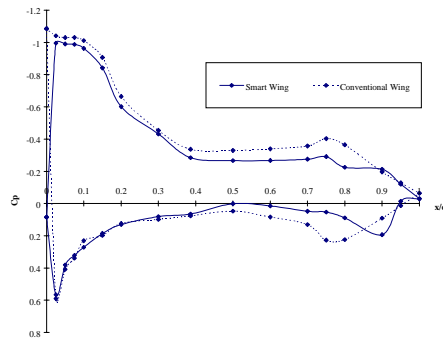


Row B, AOA = 6

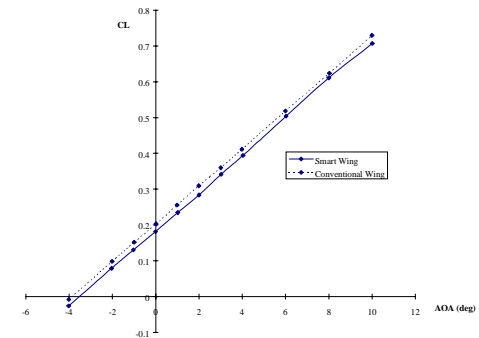
Run 105 vs 40
 $M = 0.25$, $Q = 90$ psf
 Conventional Flap = 10° Aileron = 10°
 Smart Flap = -4° Aileron = -4°



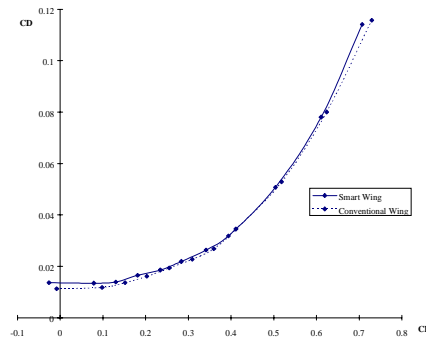
Row C, AOA = 6



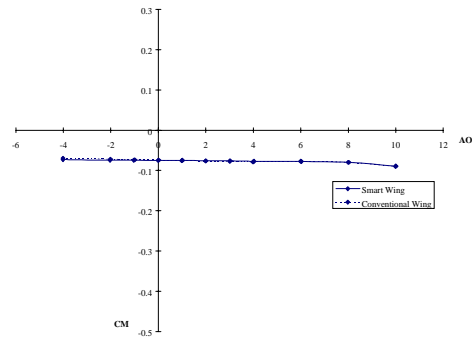
Row D, AOA = 6



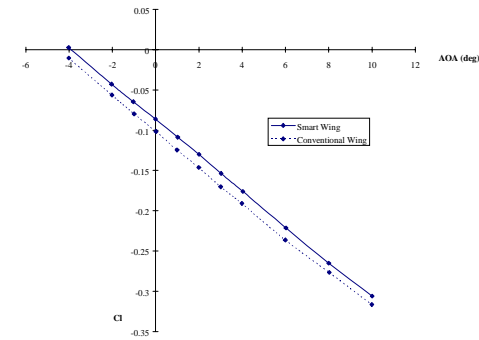
CL vs. AOA



CD vs. CL

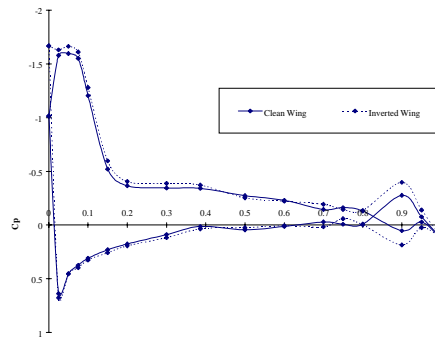


CM vs. AOA

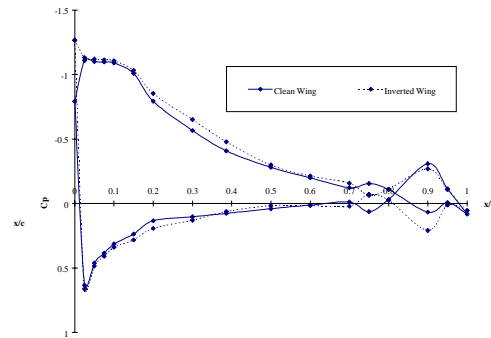


Roll Moment vs. AOA

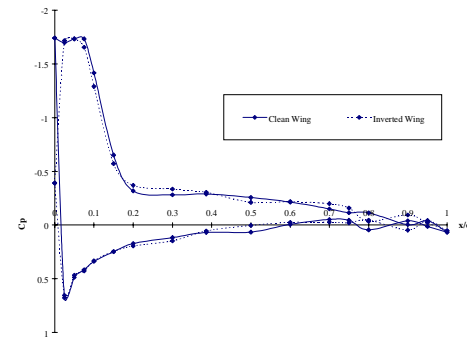
Run 105 vs 40
 $M = 0.25$, $Q = 90$ psf
 Conventional Flap = 10° Aileron = 10°
 Smart Flap = -4° Aileron = -4°



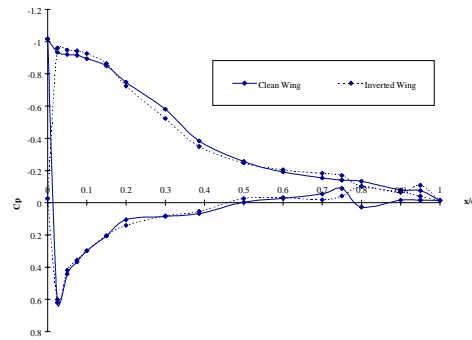
Row A, AOA = 8



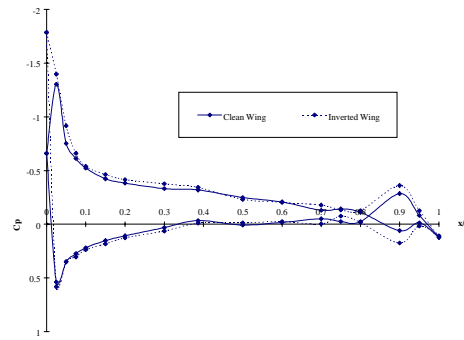
Row B, AOA = 8



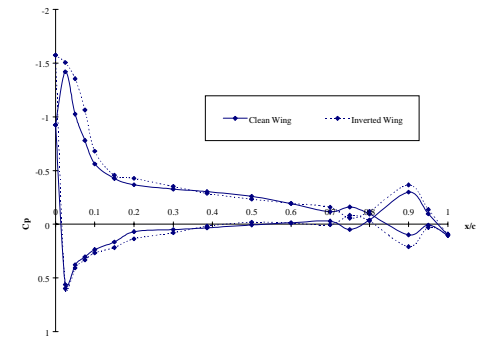
Row C, AOA = 8



Row D, AOA = 8

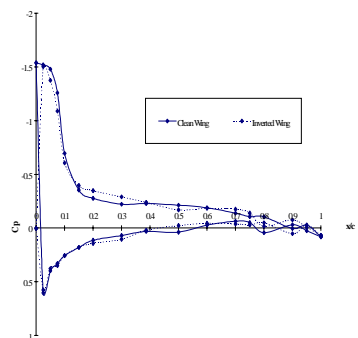


Row A, AOA = 6

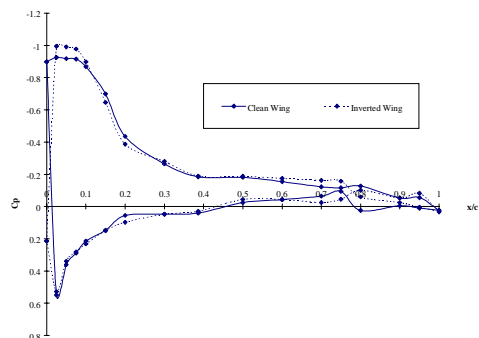


Row B, AOA = 6

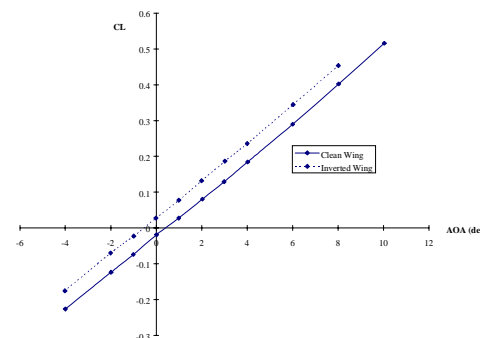
Run 99 vs 88
 $M = 0.25$, $Q = 90$ psf
 Conventional Flap = N/A Aileron = N/A
 Smart Flap = 0° Aileron = 0°



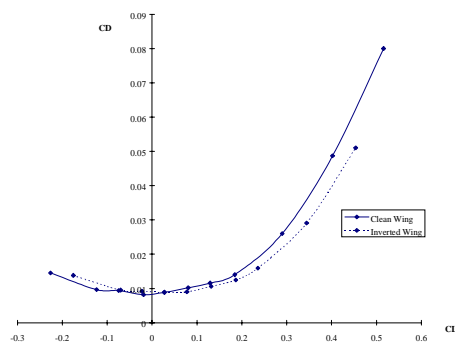
Row C, AOA = 6



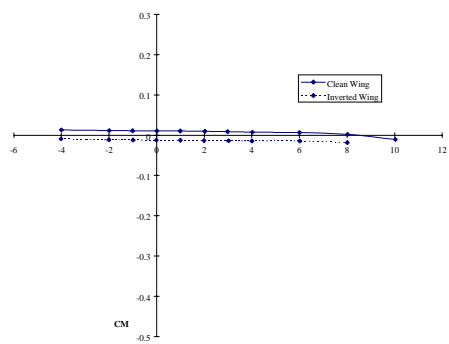
Row D, AOA = 6



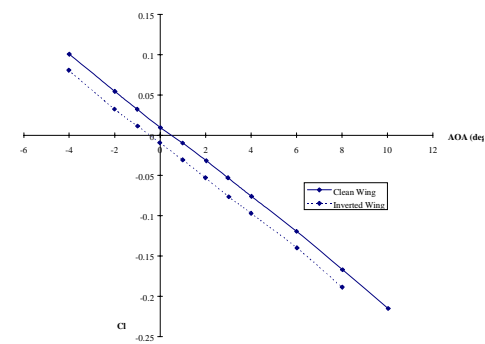
CL vs. AOA



CD vs. CL



CM vs. AOA



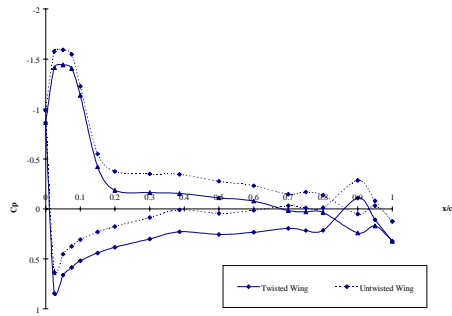
Roll Moment vs. AOA

Run 99 vs 88

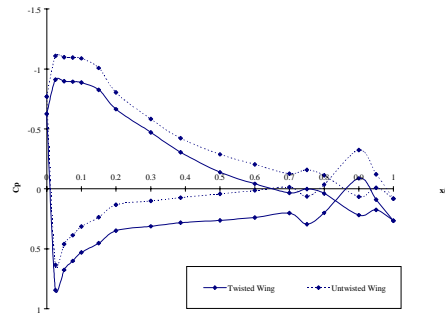
 $M = 0.25$, $Q = 90$ psf

Conventional Flap = N/A Aileron = N/A

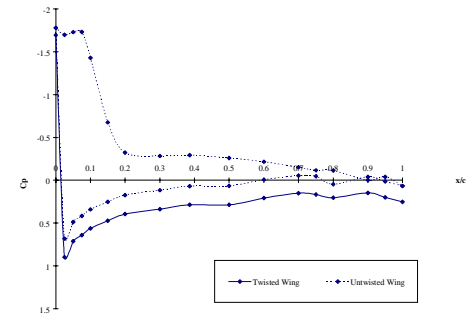
Smart Flap = 0° Aileron = 0°



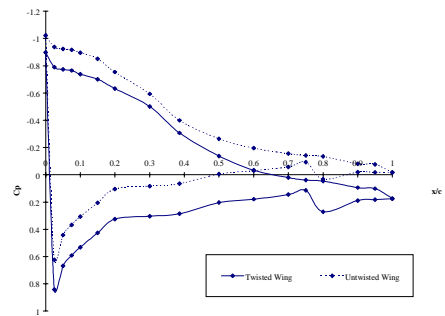
Row A, AOA = 8



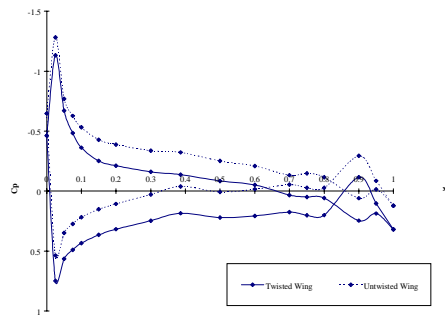
Row B, AOA = 8



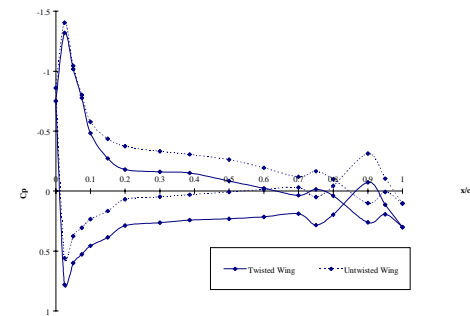
Row C, AOA = 8



Row D, AOA = 8

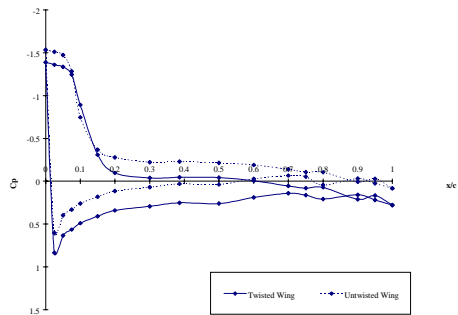


Row A, AOA = 6

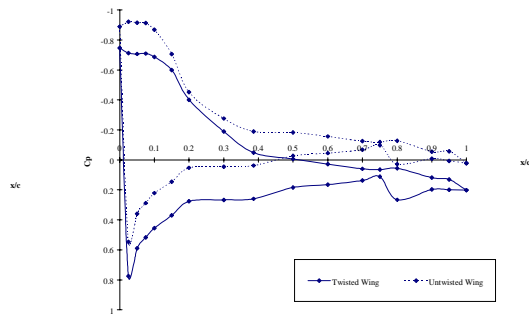


Row B, AOA = 6

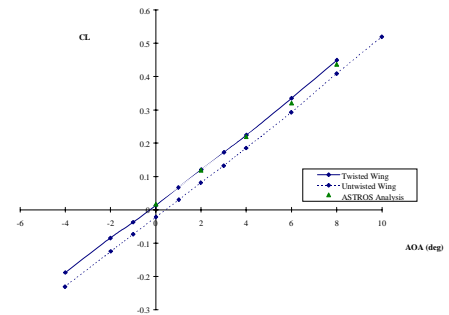
Run 113 vs. 89
 $M = 0.25$, $Q = 90$ psf
 Conventional Flap = 0° Aileron = 0°
 Smart Flap = 0° Aileron = 0°



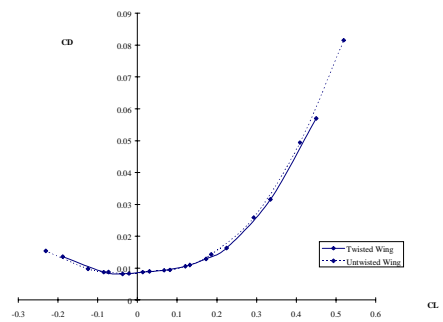
Row C, AOA = 6



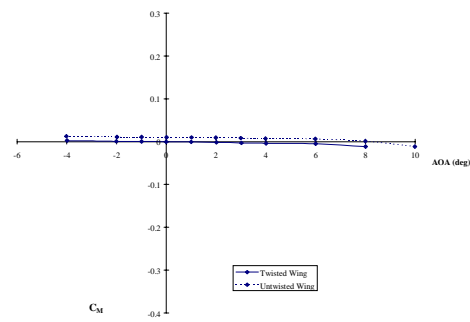
Row D, AOA = 6



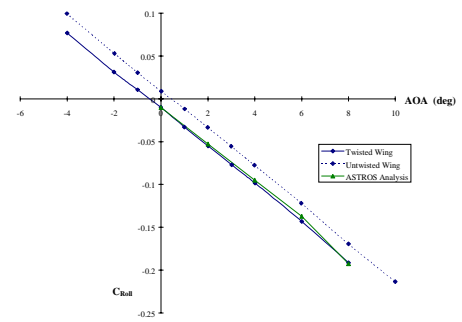
CL vs. AOA



CD vs. CL

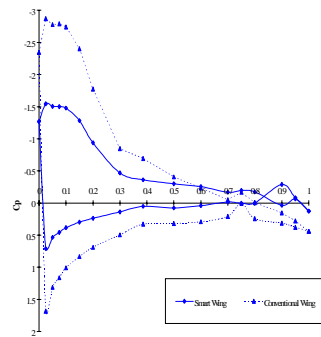


CM vs. AOA

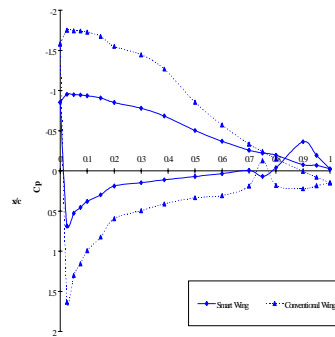


Roll Moment vs. AOA

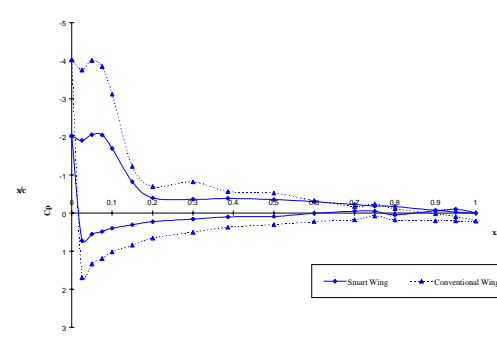
Run 113 vs. 89
 $M = 0.25$, $Q = 90$ psf
 Conventional Flap = 0° Aileron = 0°
 Smart Flap = 0° Aileron = 0°



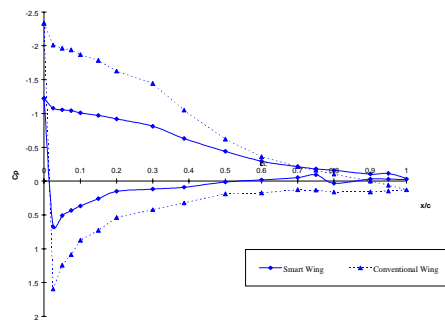
Row A, AOA = 10



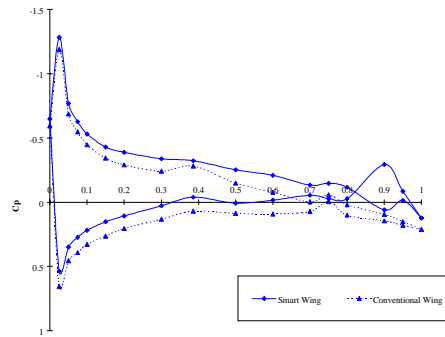
Row B, AOA = 10



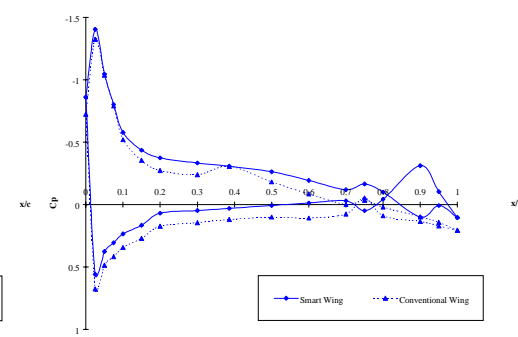
Row C, AOA = 10



Row D, AOA = 10

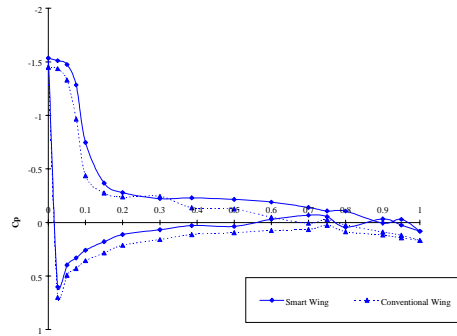


Row A, AOA = 6

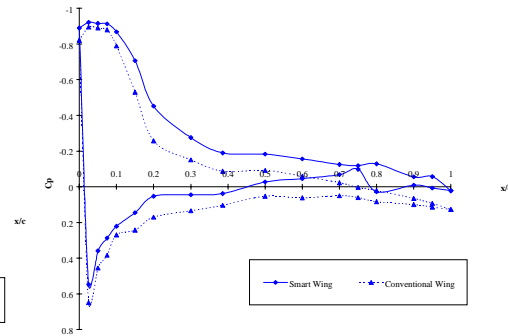


Row B, AOA = 6

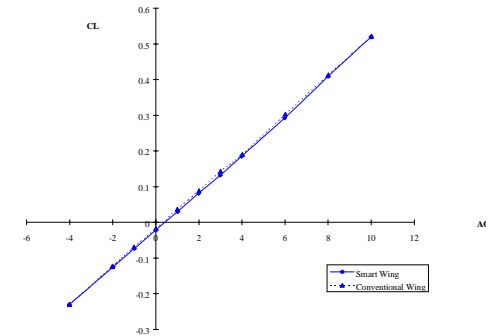
Run 89 vs 3
 $M = 0.29$, $Q = 120$ psf
 Conventional Flap = 0° Aileron = 0°
 Smart Flap = 0° Aileron = 0°



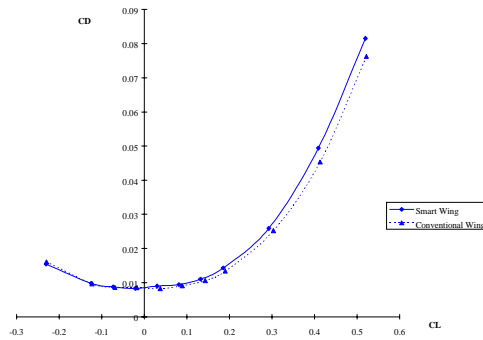
Row C, AOA = 6



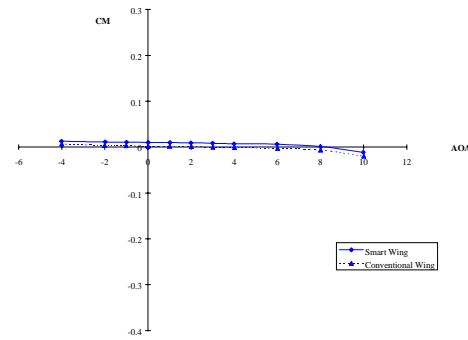
Row D, AOA = 6



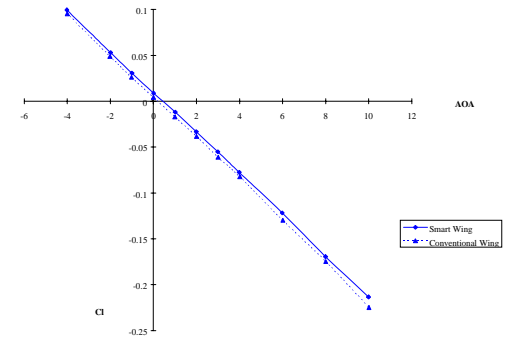
CL vs. AOA



CD vs. CL

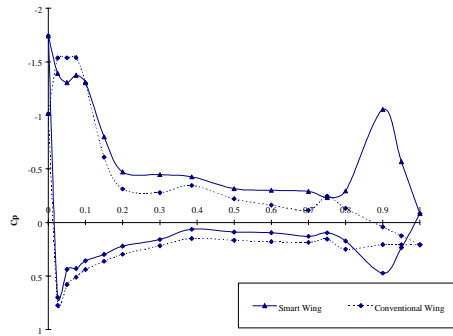


CM vs. AOA

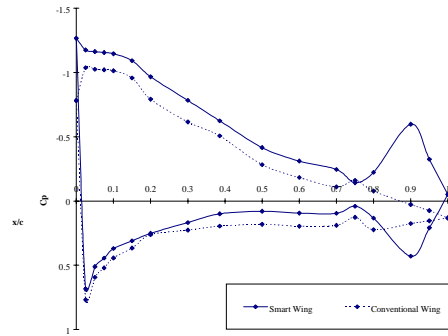


Roll Moment vs. AOA

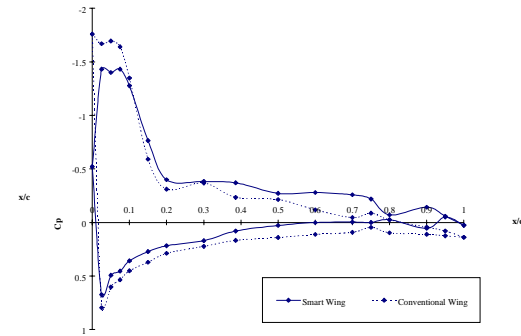
Run 89 vs 3
M = 0.29, Q = 120 psf
Conventional Flap = 0° Aileron = 0°
Smart Flap = 0° Aileron = 0°



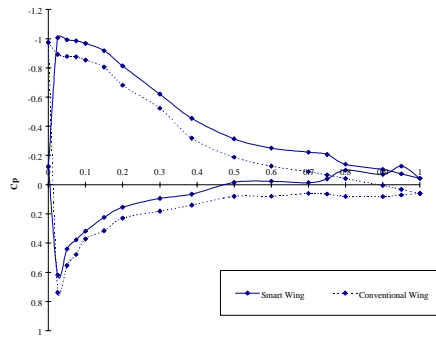
Row A, AOA = 8



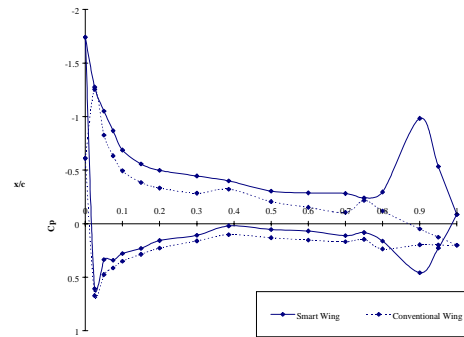
Row B, AOA = 8



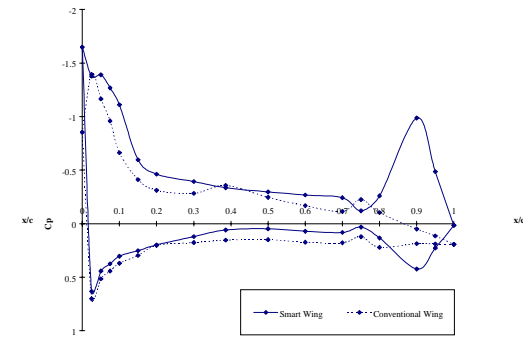
Row C, AOA = 8



Row D, AOA = 8

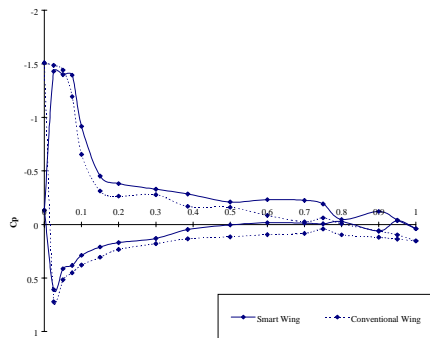


Row A, AOA = 6

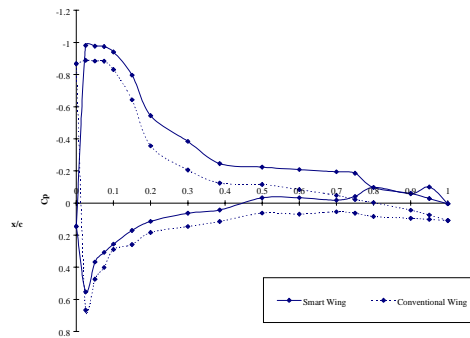


Row B, AOA = 6

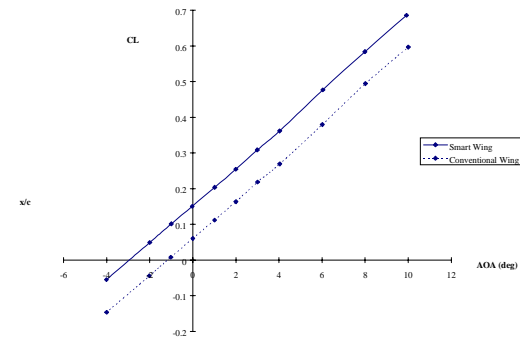
Run 103 vs 8
 $M = 0.29$, $Q = 120$ psf
 Conventional Flap = 5° Aileron = 0°
 Smart Flap = -4° Aileron = 0°



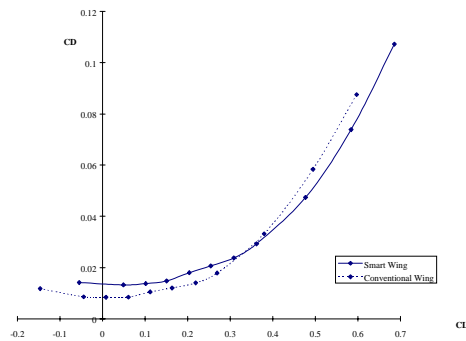
Row C, AOA = 6



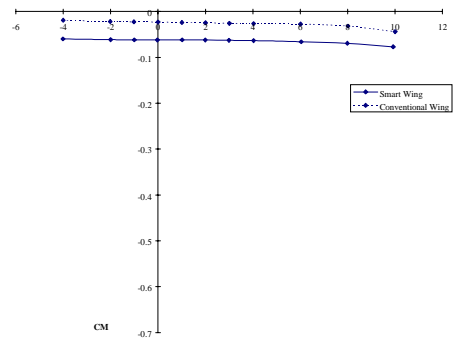
Row D, AOA = 6



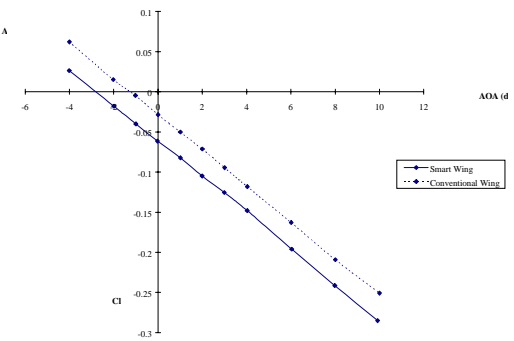
CL vs. AOA



CD vs. CL

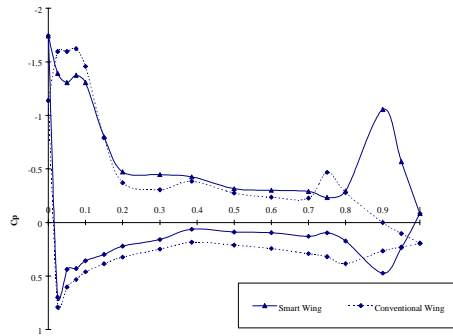


CM vs. AOA

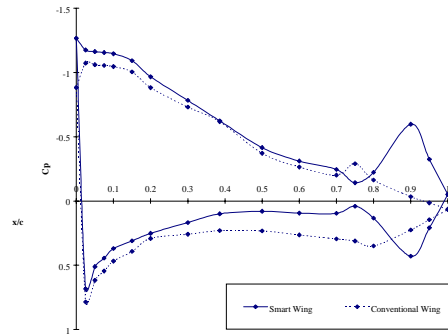


Roll Moment vs. AOA

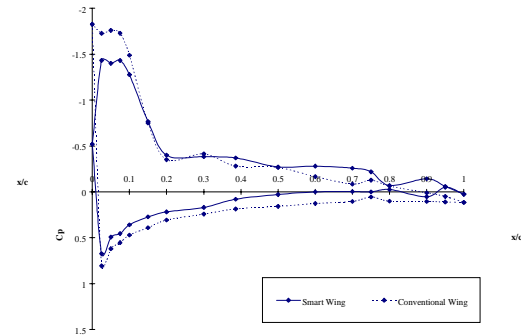
Run 103 vs 8
 $M = 0.29$, $Q = 120$ psf
 Conventional Flap = 5° Aileron = 0°
 Smart Flap = -4° Aileron = 0°



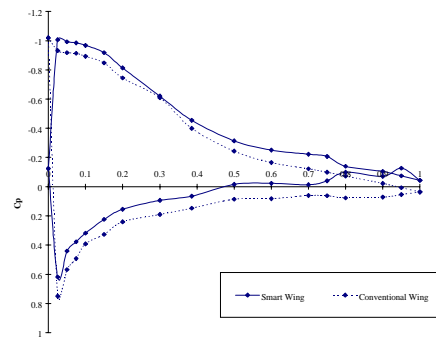
Row A, AOA = 8



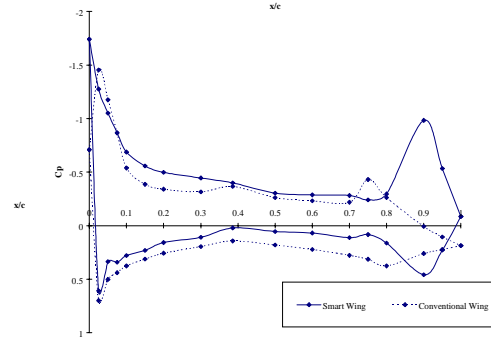
Row B, AOA = 8



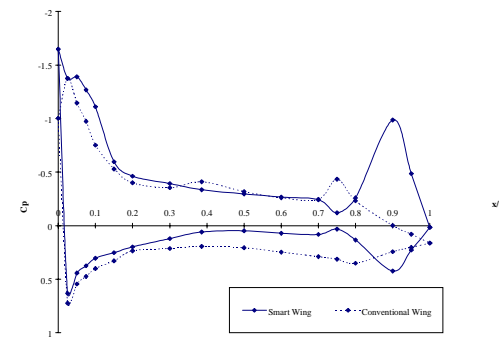
Row C, AOA = 8



Row D, AOA = 8

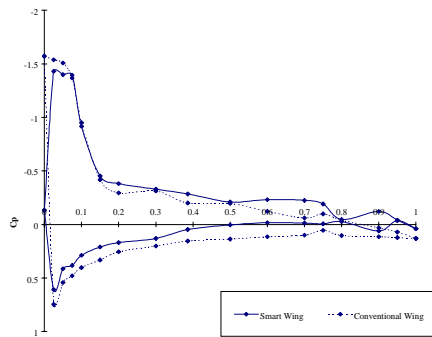


Row A, AOA = 6

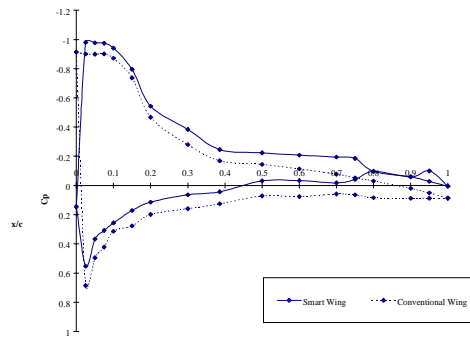


Row B, AOA = 6

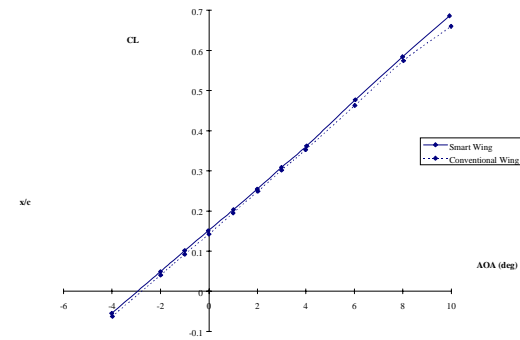
Run 103 vs 12
 $M = 0.29$, $Q = 120$ psf
 Conventional Flap = 7.5° Aileron = 0°
 Smart Flap = -4° Aileron = 0°



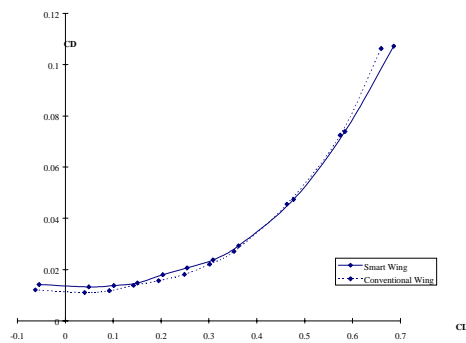
Row C, AOA = 6



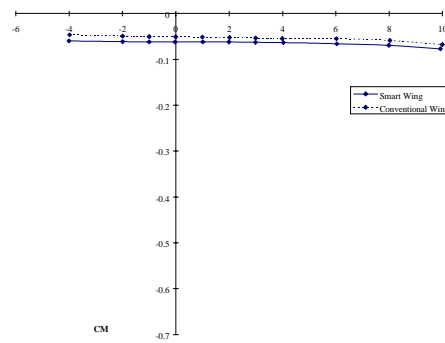
Row D, AOA = 6



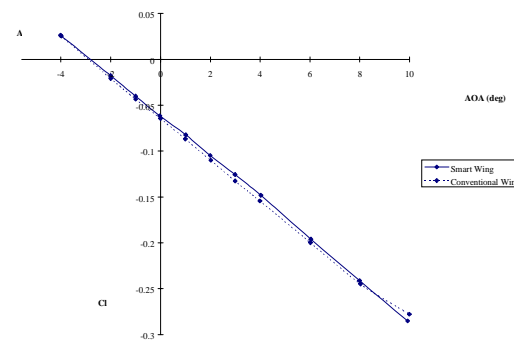
CL vs. AOA



CD vs. Cl

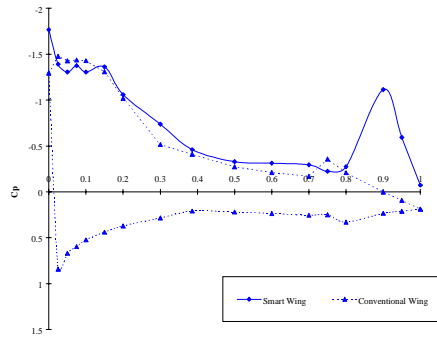


CM vs. AOA

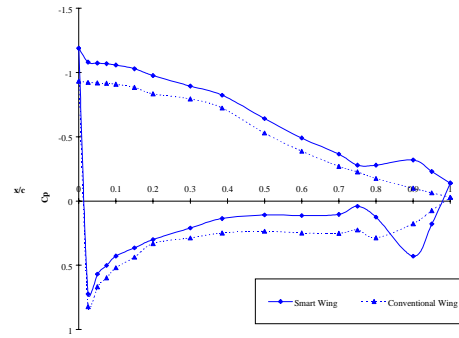


Roll Moment vs. AOA

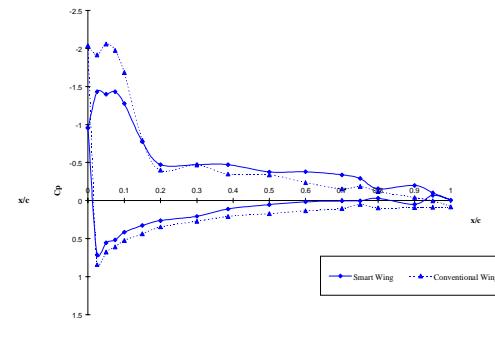
Run 103 vs 12
 $M = 0.29$, $Q = 120$ psf
 Conventional Flap = 10° Aileron = 0°
 Smart Flap = -4° Aileron = 0°



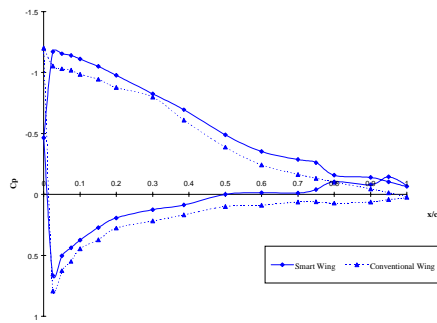
Row A, AOA = 10



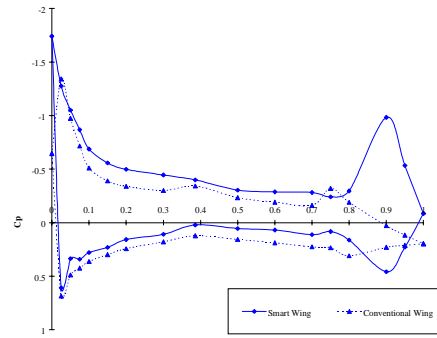
Row B, AOA = 10



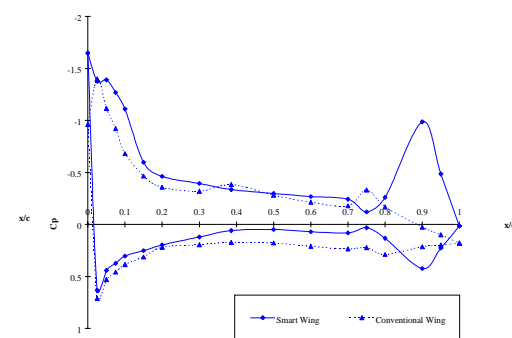
Row C, AOA = 10



Row D, AOA = 10

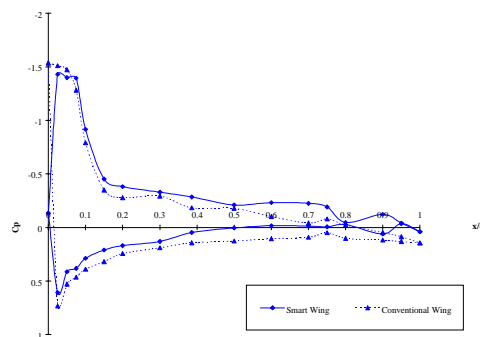


Row A, AOA = 6

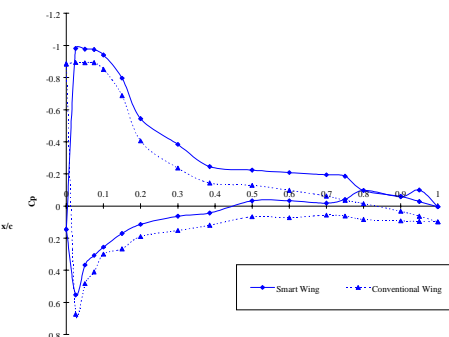


Row B, AOA = 6

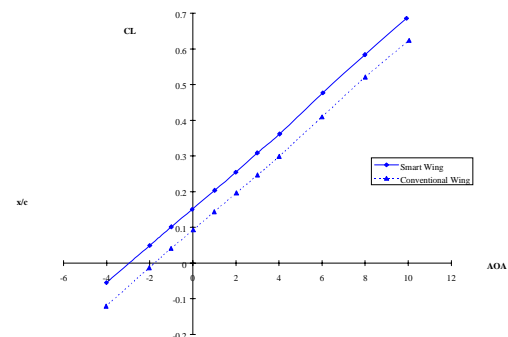
Run 103 vs 13
 $M = 0.29$, $Q = 120$ psf
 Conventional Flap = 7.5° Aileron = 0°
 Smart Flap = -4° Aileron = 0°



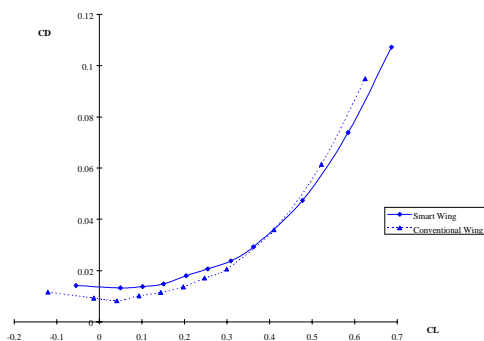
Row C, AOA = 6



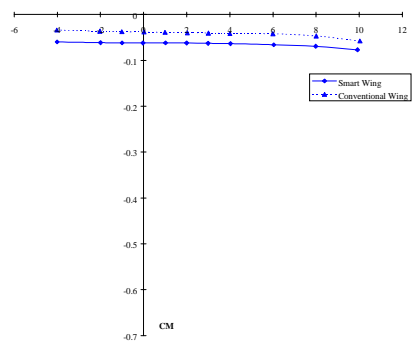
Row D, AOA = 6



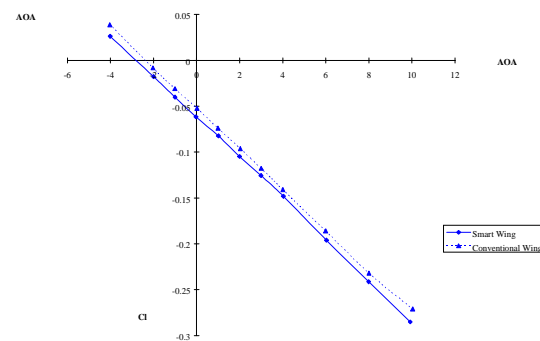
CL vs. AOA



CD vs. CL

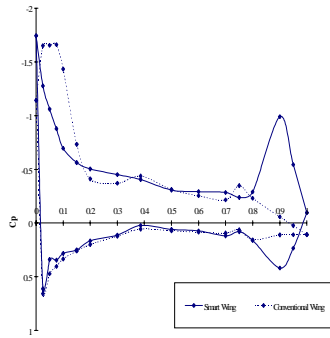


CM vs. AOA

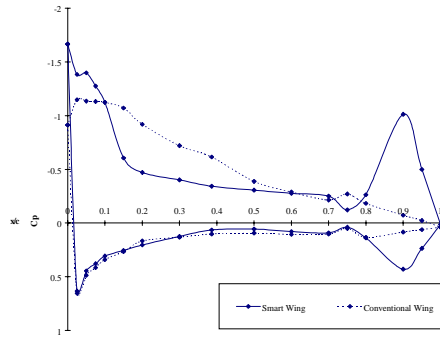


Roll Moment vs. AOA

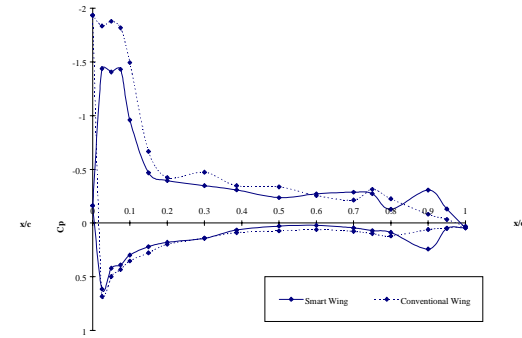
Run 103 vs 13
 $M = 0.29$, $Q = 120$ psf
 Conventional Flap = 7.5° Aileron = 0°
 Smart Flap = -4° Aileron = 0°



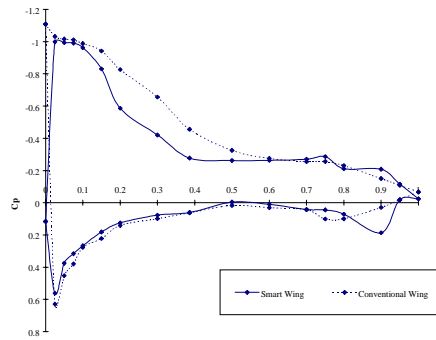
Row A, AOA = 8



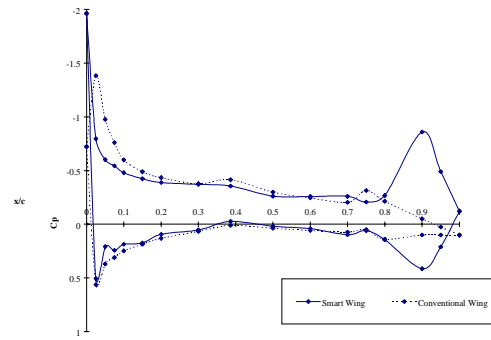
Row B, AOA = 8



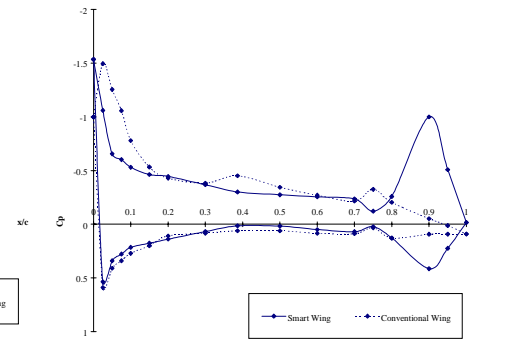
Row C, AOA = 8



Row D, AOA = 8

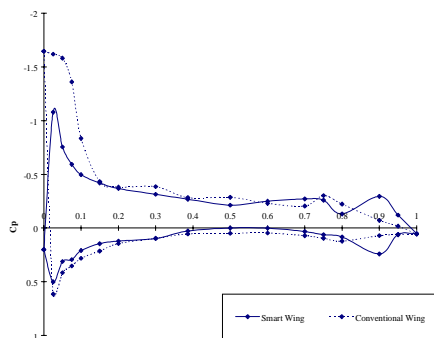


Row A, AOA = 6

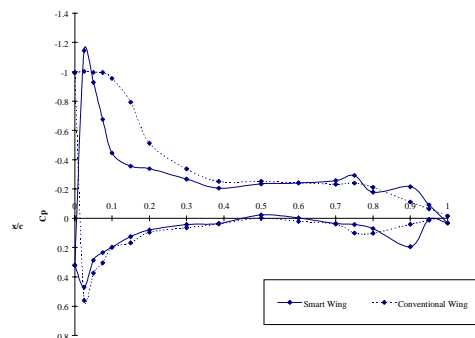


Row B, AOA = 6

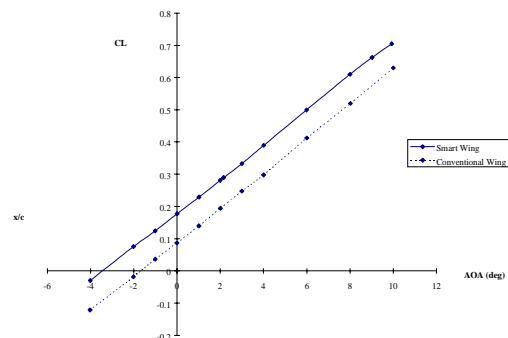
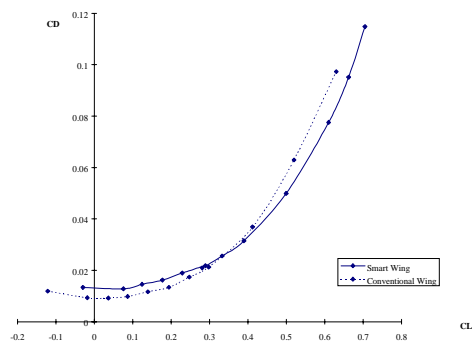
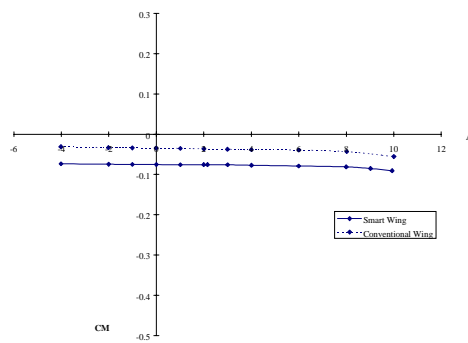
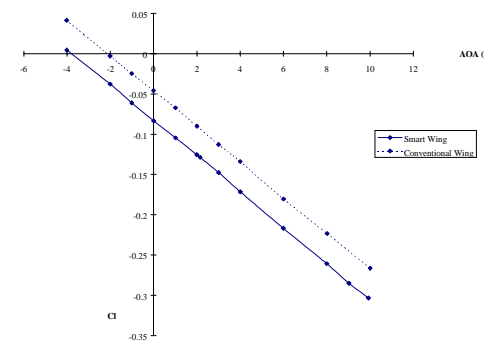
Run 106 vs 21
 $M = 0.29$, $Q = 120$ psf
 Conventional Flap = 5° Aileron = 5°
 Smart Flap = -4° Aileron = -4°



Row C, AOA = 6

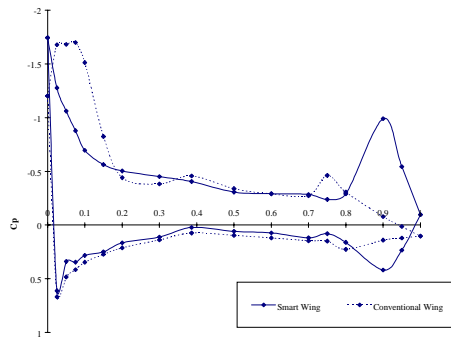


Row D, AOA = 6

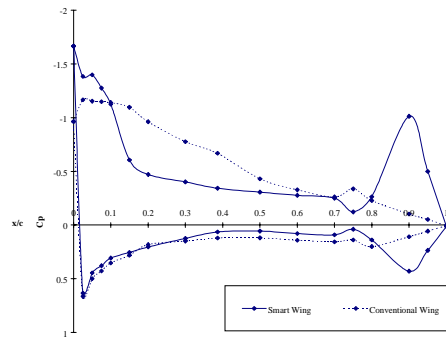
C_L vs. AOAC_D vs. C_LC_M vs. AOA

Roll Moment vs. AOA

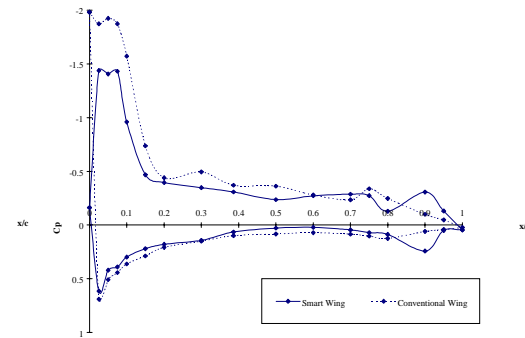
Run 106 vs 21
 $M = 0.29$, $Q = 120$ psf
 Conventional Flap = 5° Aileron = 5°
 Smart Flap = -4° Aileron = -4°



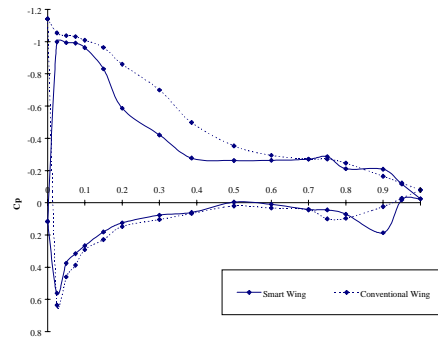
Row A, AOA = 8



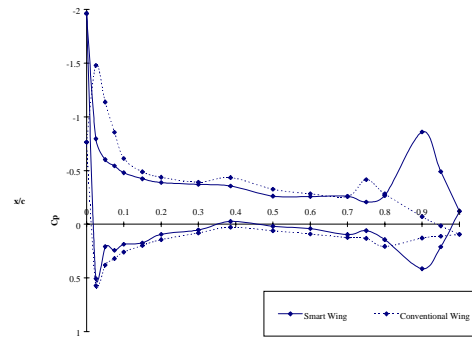
Row B, AOA = 8



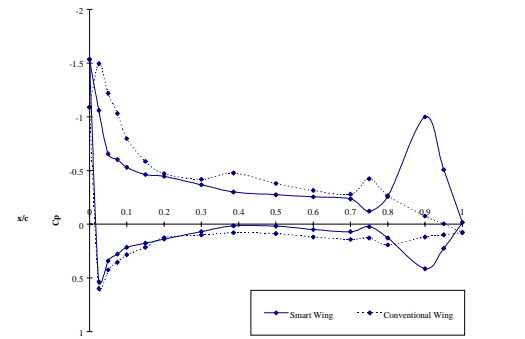
Row C, AOA = 8



Row D, AOA = 8

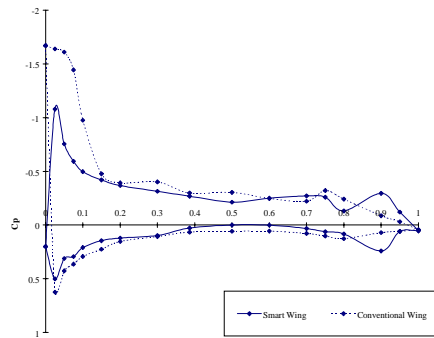


Row A, AOA = 6

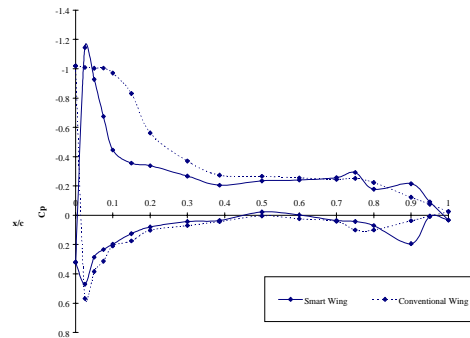


Row B, AOA = 6

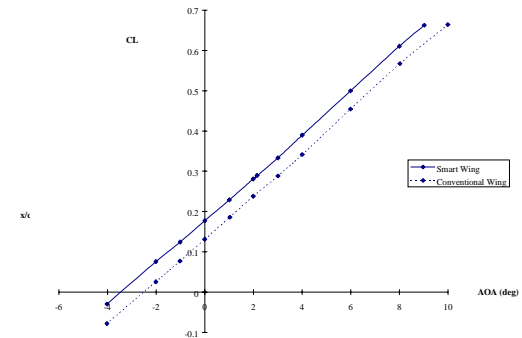
Run 106 vs 26
 $M = 0.29$, $Q = 120$ psf
 Conventional Flap = 7.5° Aileron = 5°
 Smart Flap = -4° Aileron = -4°



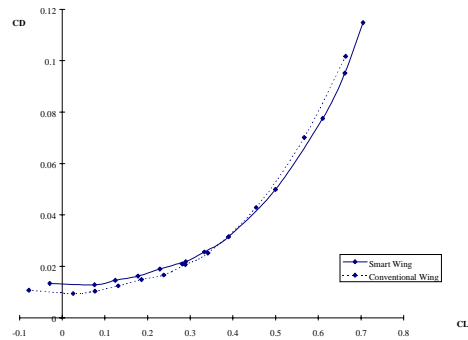
Row C, AOA = 6



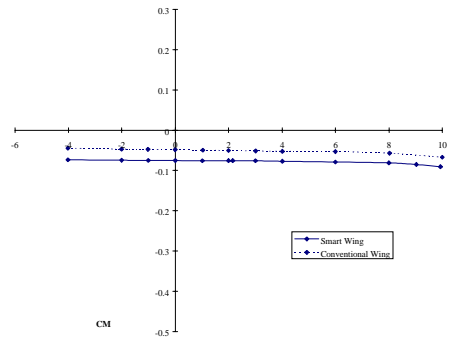
Row D, AOA = 6



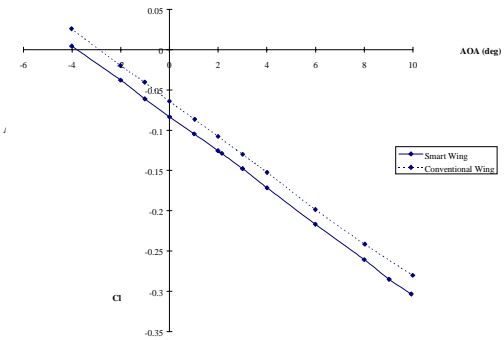
CL vs. AOA



CD vs. CL

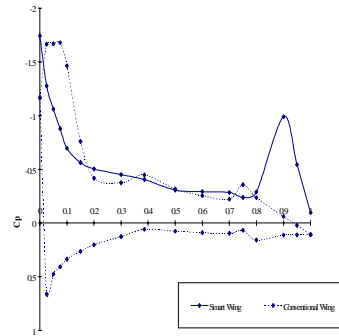


CM vs. AOA

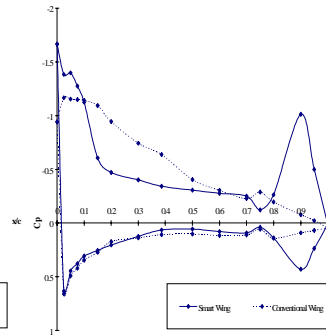


Roll Moment vs. AOA

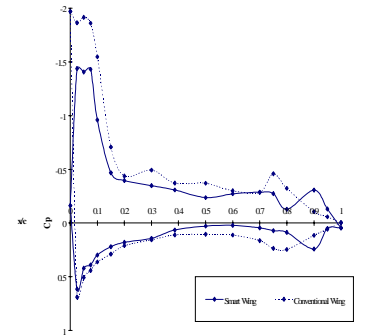
Run 106 vs 26
 $M = 0.29$, $Q = 120$ psf
 Conventional Flap = 7.5° Aileron = 5°
 Smart Flap = -4° Aileron = -4°



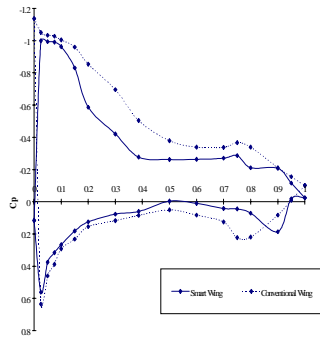
Row A, AOA = 8



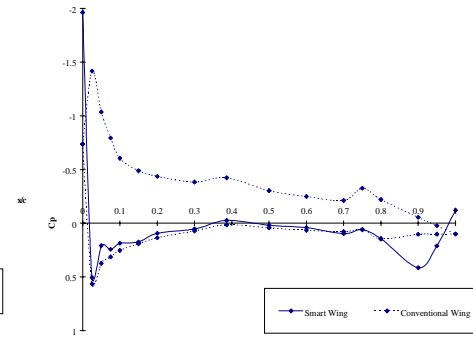
Row B, AOA = 8



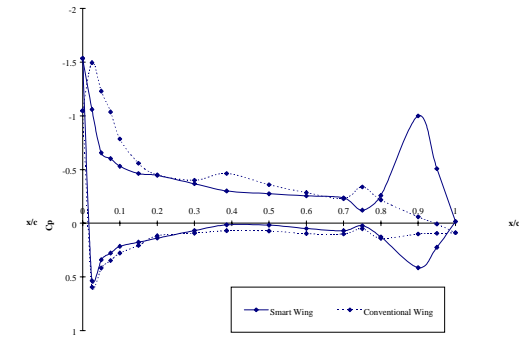
Row C, AOA = 8



Row D, AOA = 8

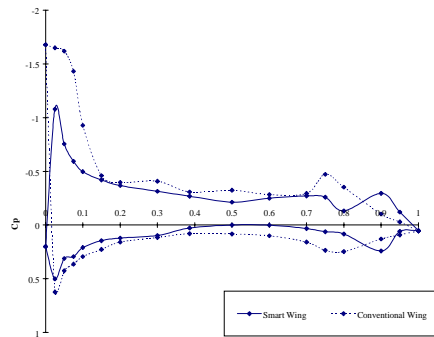


Row A, AOA = 6

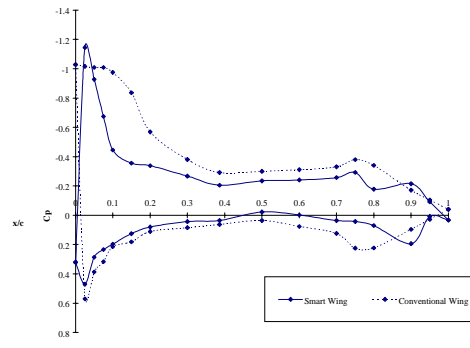


Row B, AOA = 6

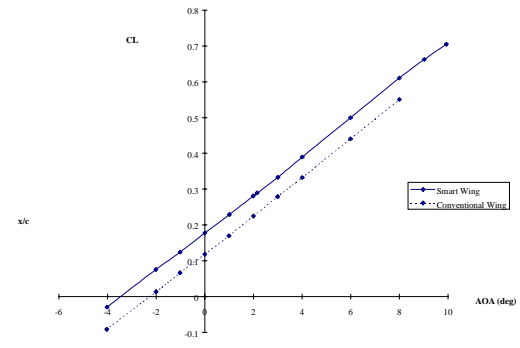
Run 106 vs 33
 $M = 0.29$, $Q = 120$ psf
 Conventional Flap = 5° Aileron = 10°
 Smart Flap = -4° Aileron = -4°



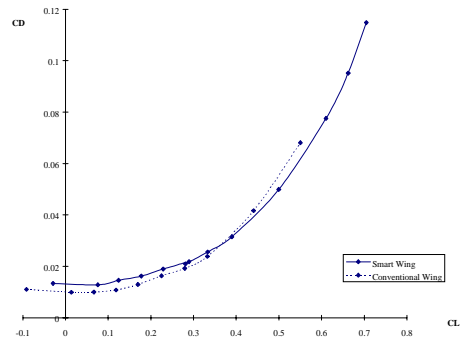
Row C, $AOA = 6$



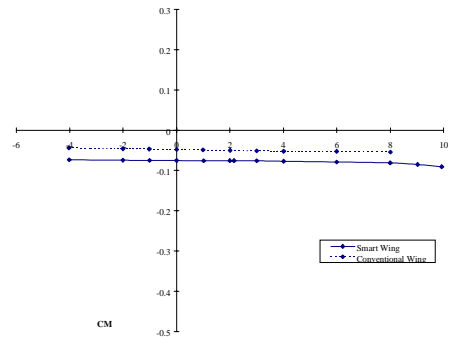
Row D, $AOA = 6$



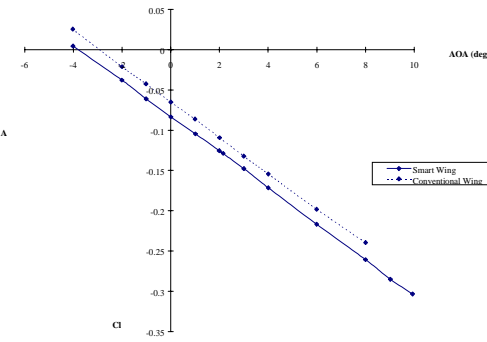
C_L vs. AOA



C_D vs. C_L

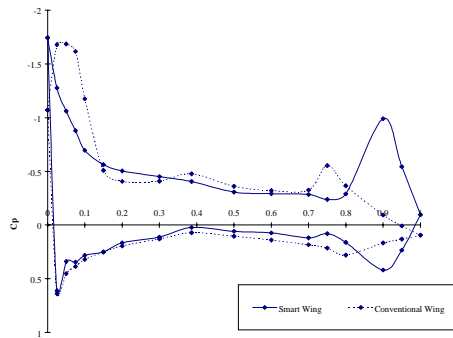


C_M vs. AOA

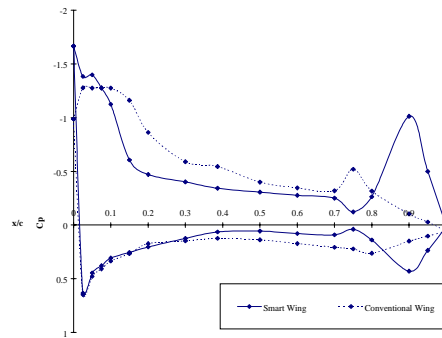


Roll Moment vs. AOA

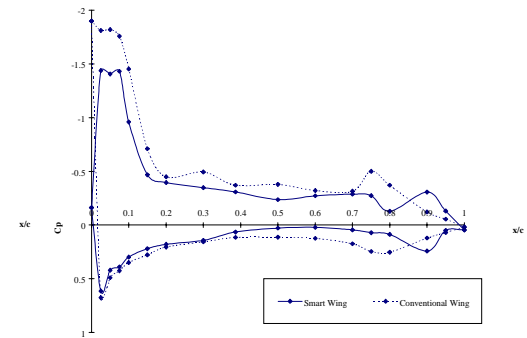
Run 106 vs 33
 $M = 0.29$, $Q = 120$ psf
 Conventional Flap = 5° Aileron = 10°
 Smart Flap = -4° Aileron = -4°



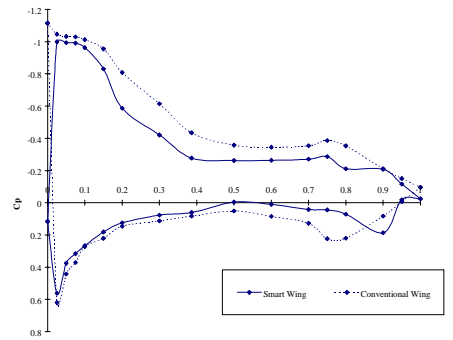
Row A, AOA = 8



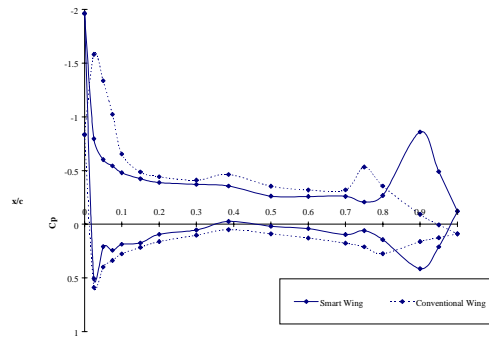
Row B, AOA = 8



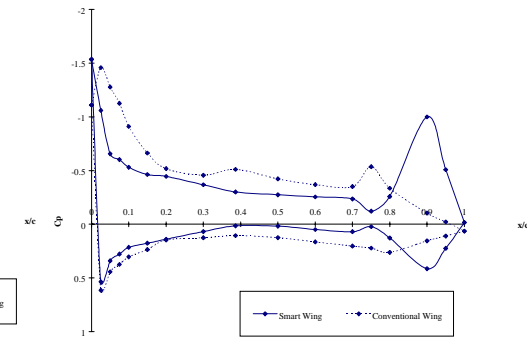
Row C, AOA = 8



Row D, AOA = 8

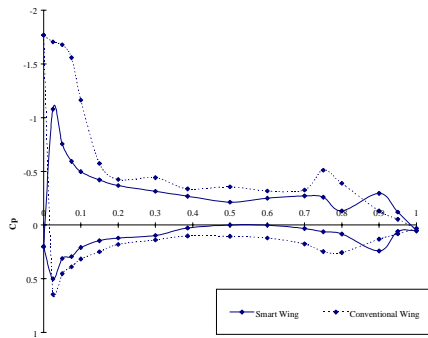


Row A, AOA = 6

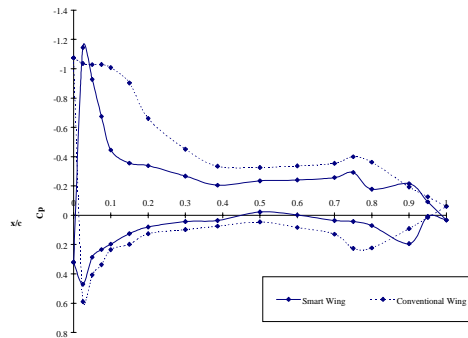


Row B, AOA = 6

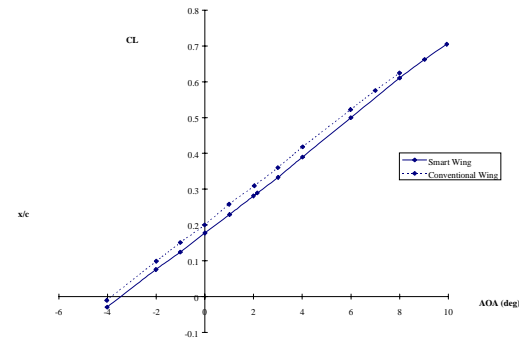
Run 106 vs 41
 $M = 0.29$, $Q = 120$ psf
 Conventional Flap = 10° Aileron = 10°
 Smart Flap = -4° Aileron = -4°



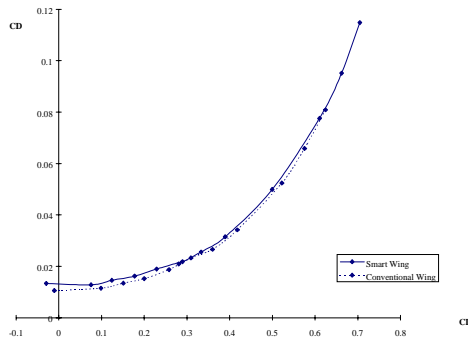
Row C, AOA = 6



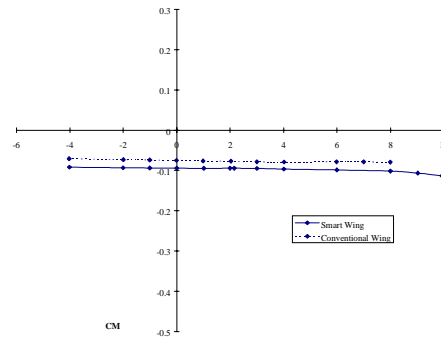
Row D, AOA = 6



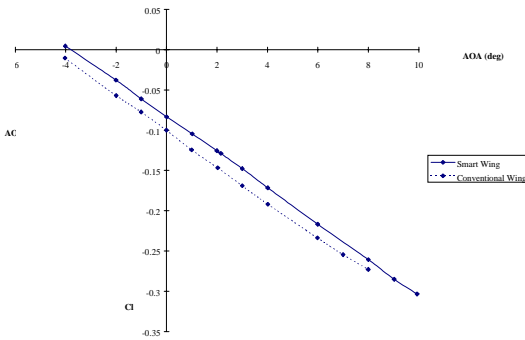
CL vs. AOA



CD vs. CL

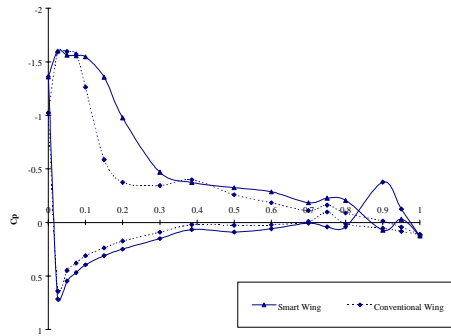


CM vs. AOA

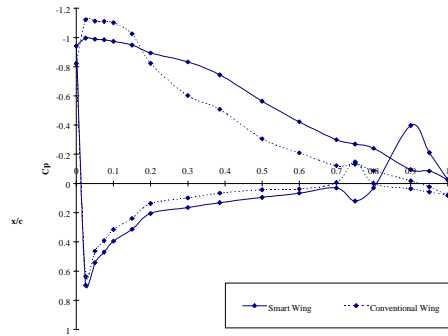


Roll Moment vs. AOA

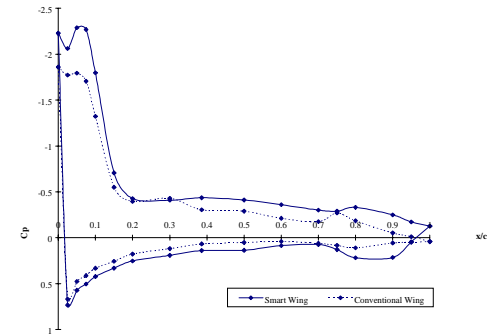
Run 106 vs 41
M = 0.29, Q = 120 psf
Conventional Flap = 10° Aileron = 10°
Smart Flap = -4° Aileron = -4°



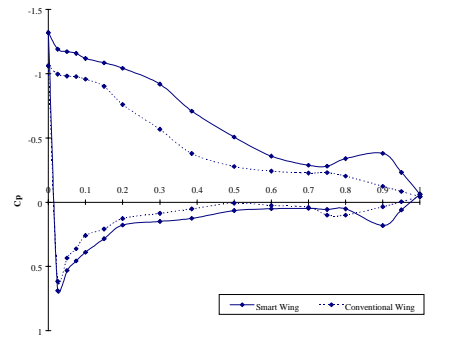
Row A, AOA = 8



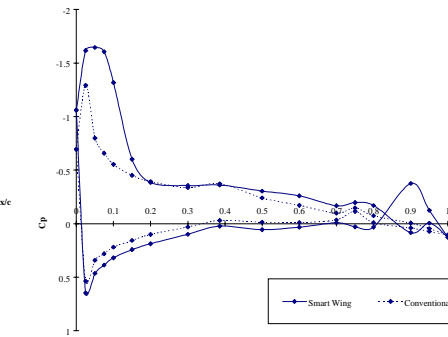
Row B, AOA = 8



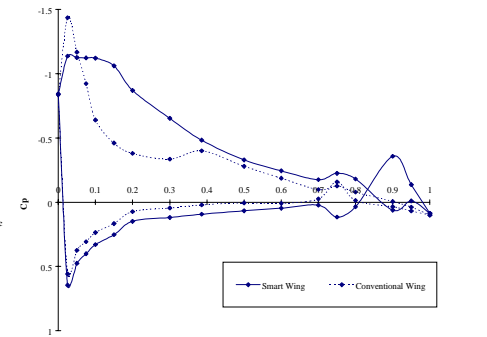
Row C, AOA = 8



Row D, AOA = 8

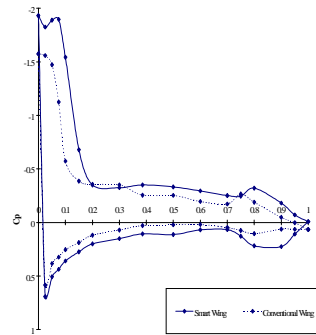


Row A, AOA = 6

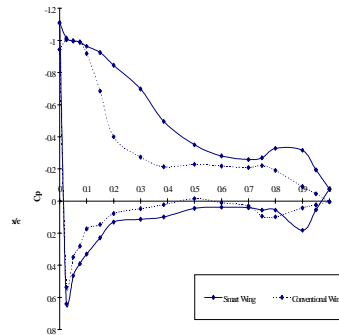


Row B, AOA = 6

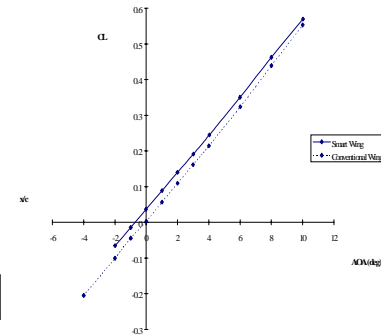
Run 109 vs 20
 $M = 0.29$, $Q = 120$ psf
 Conventional Flap = 0° Aileron = 5°
 Smart Flap = 0° Aileron = 4°



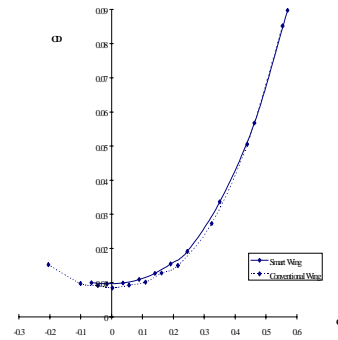
Row C, AOA = 6



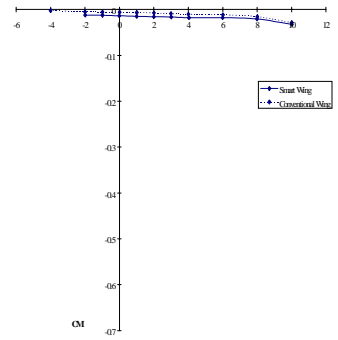
Row D, AOA = 6



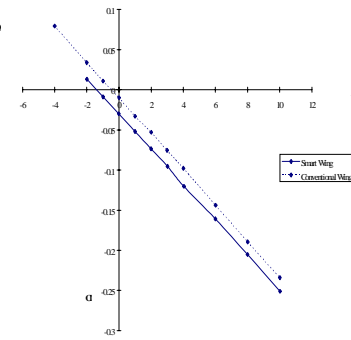
CL vs. AOA



CD vs. CL

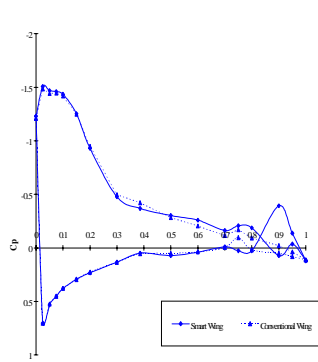


CM vs. AOA

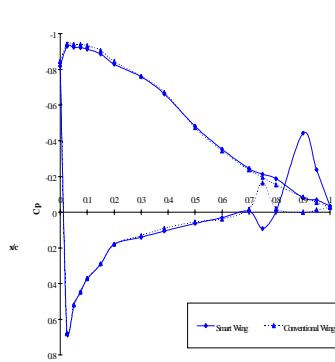


Roll Moment vs. AOA

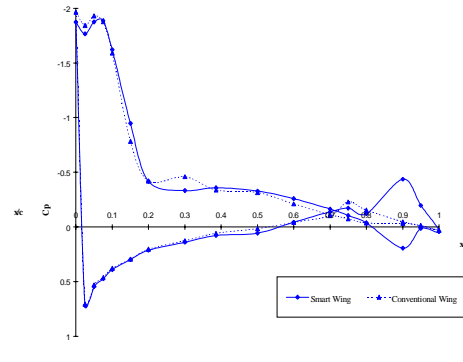
Run 109 vs 20
 $M = 0.29$, $Q = 120$ psf
 Conventional Flap = 0° Aileron = 5°
 Smart Flap = 0° Aileron = 4°



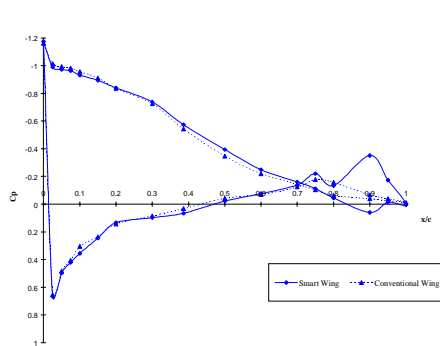
Row A, AOA = 10



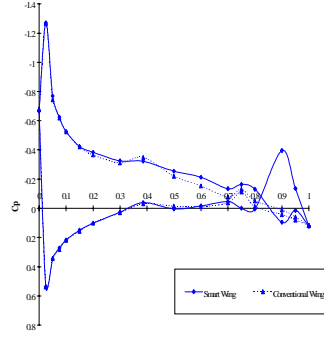
Row B, AOA = 10



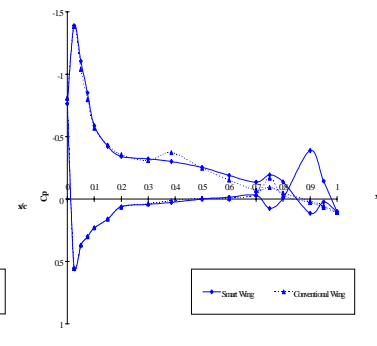
Row C, AOA = 10



Row D, AOA = 10

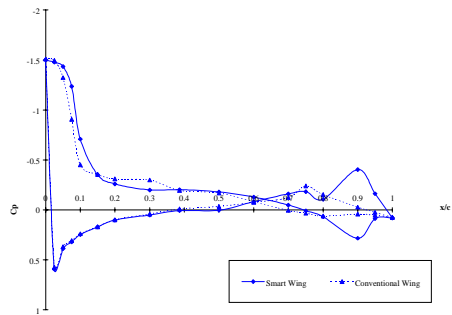


Row A, AOA = 6

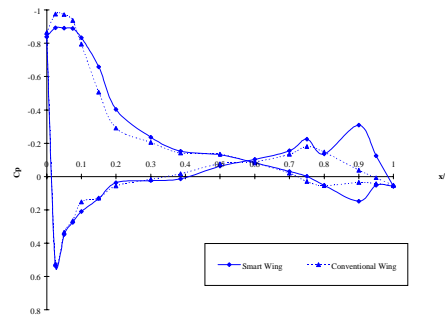


Row B, AOA = 6

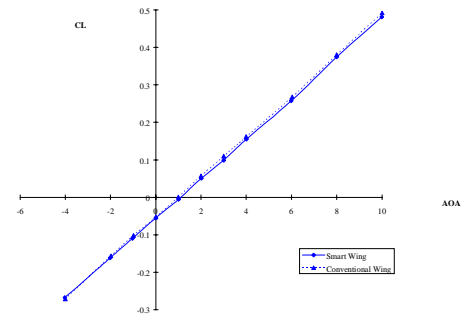
Run 112 vs 46
 $M = 0.29$, $Q = 120$ psf
 Conventional Flap = 0° Aileron = 5°
 Smart Flap = 0° Aileron = 4°



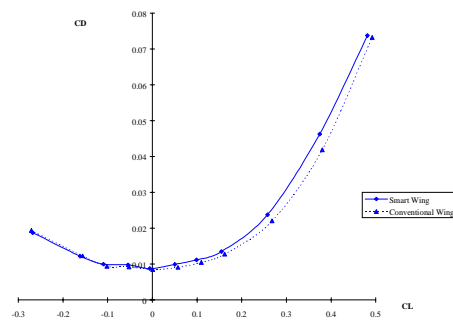
Row C, AOA = 6



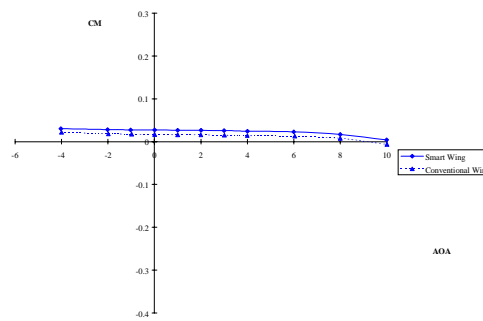
Row D, AOA = 6



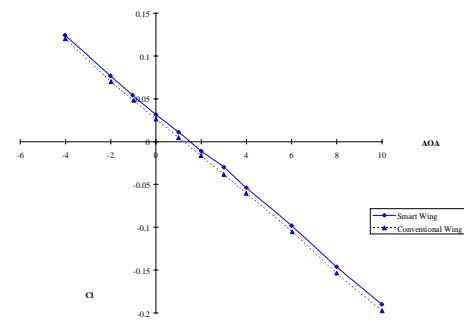
CL vs. AOA



CD vs. CL



CM vs. AOA



Roll Moment vs. AOA

Run 112 vs 46
 $M = 0.29$, $Q = 120$ psf
 Conventional Flap = 0° Aileron = -5°
 Smart Flap = 0° Aileron = -4°

2. WIND TUNNEL TEST 2

Run	Flap Deflection Angle (deg.)		Aileron Deflection Angle (deg.)		Comments	Page
	Conv	Smart	Conv	Smart		
Run 12 VS 110	0	0	0	0		97
Run 12 VS 112	0	0	0	0		99
Run 12 VS 125	0	0	0	0		101
Run 34 VS 110	0	0	0	0	Repeat Runs	103
Run 34 VS 112	0	0	0	0		105
Run 34 VS 125	0	0	0	0		107
Run 59 VS 120	0	0	0	0		109

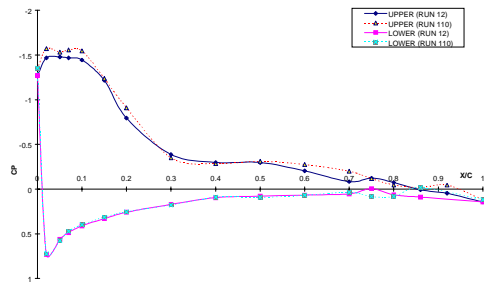
Figure 2-1. Test 2 Data Collected at Q = 60 psf, M = 0.20

Run	Flap Deflection Angle (deg.)		Aileron Deflection Angle (deg.)		Comments	Page
	Conv	Smart	Conv	Smart		
Run 113 VS 134	-----	0	-----	10	Run 134 twist =4.5	111
Run 113 VS 136	-----	0	-----	10	Run 136 twist =4.5	113
Run 113 VS 132, 133	-----	0	-----	0	Run 132 twist = 3 Run 133 twist = 5	115
Run 33 VS 111	0	0	0	0		117
Run 33 VS 113	0	0	0	0		119
Run 33 VS 126	0	0	0	0		121

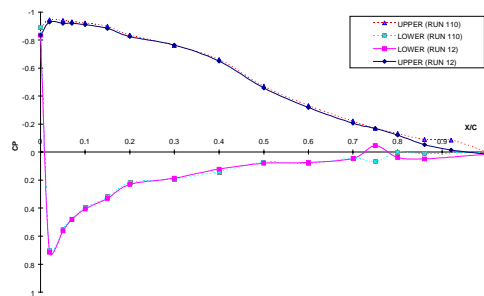
Figure 2-2. Test 2 Data Collected at Q = 90 psf, M = 0.25

Run	Flap Deflection Angle (deg.)		Aileron Deflection Angle (deg.)		Comments	Page
	Conv	Smart	Conv	Smart		
Run 14 VS 127	-10	-10	0	0		123
Run 32 VS 127	0	0	0	0		125
Run 71 VS 127	0	0	0	0		127
Run 76 VS 127	0	0	0	0	back to back repeats	129
Run 77 VS 127	0	0	0	0	back to back repeats	131
Run 78 VS 127	0	0	0	0	back to back repeats	133

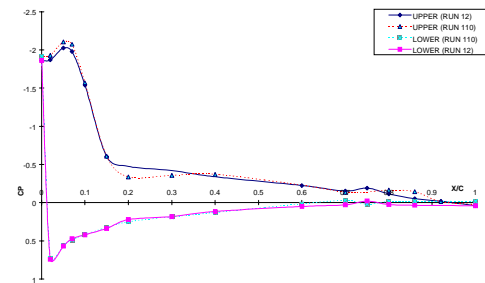
Figure 2-3. Test 2 Data Collected at Q = 120 psf, M = 0.29



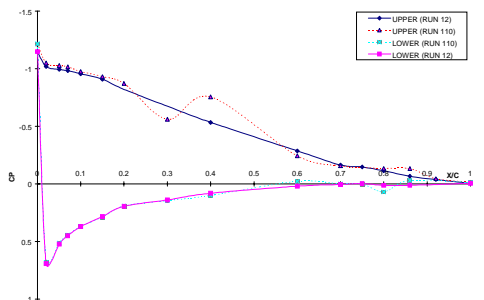
Row A, AOA = 10



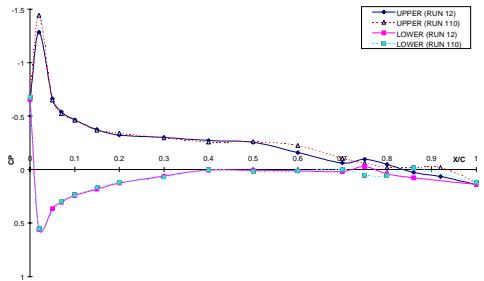
Row B, AOA = 10



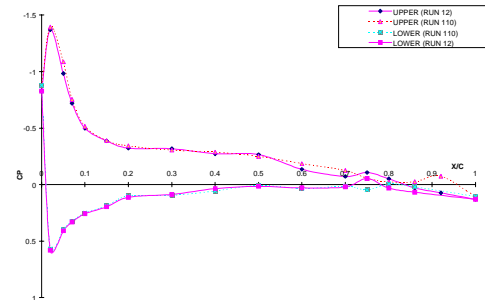
Row C, AOA = 10



Row D, AOA = 10

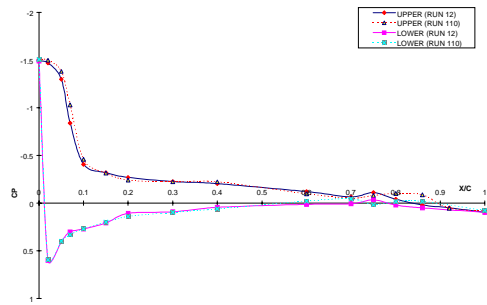


Row A, AOA = 6

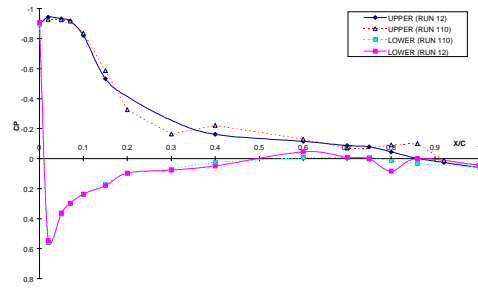


Row B, AOA = 6

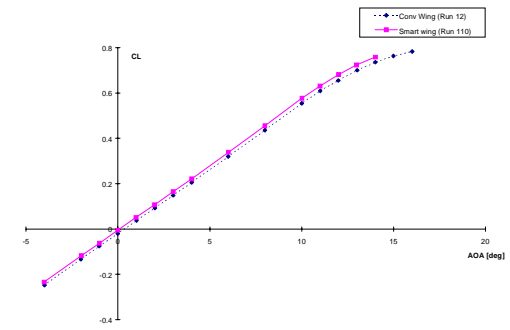
Run 12 vs 110
 $M = 0.20$, $Q = 60$ psf
 Conventional Flap = 0° Aileron = 0°
 Smart Flap = 0° Aileron = 0°



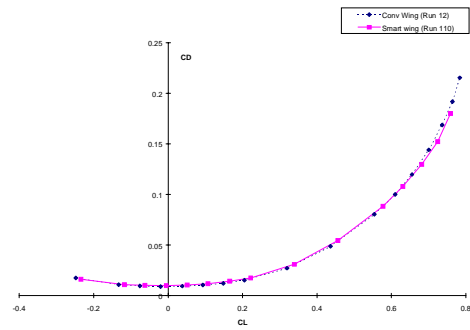
Row C, AOA = 6



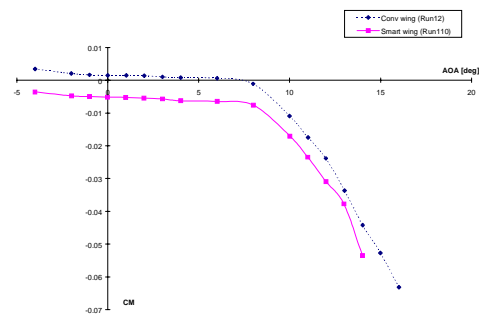
Row D, AOA = 6



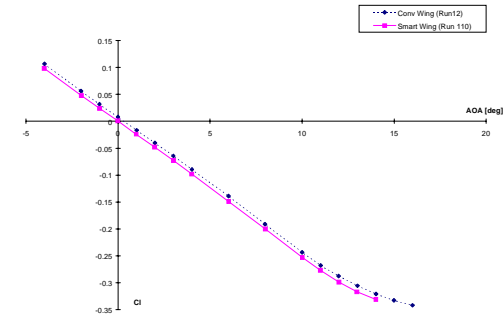
CL vs. AOA



CD vs. CL

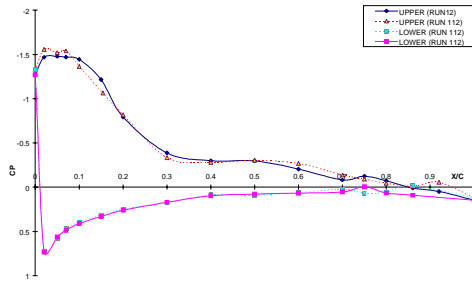


CM vs. AOA

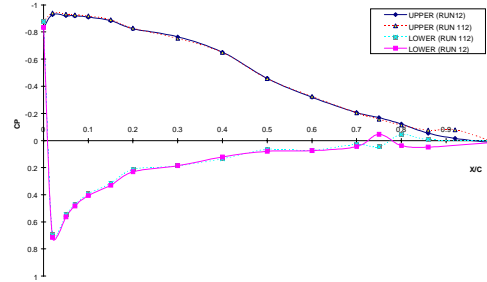


Roll Moment vs. AOA

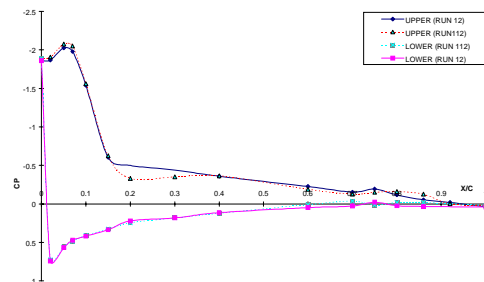
Run 12 vs 110
 $M = 0.20$, $Q = 60$ psf
 Conventional Flap = 0° Aileron = 0°
 Smart Flap = 0° Aileron = 0°



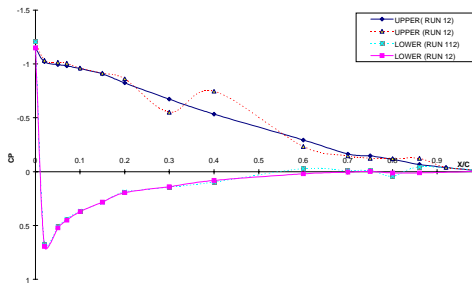
Row A, AOA = 10



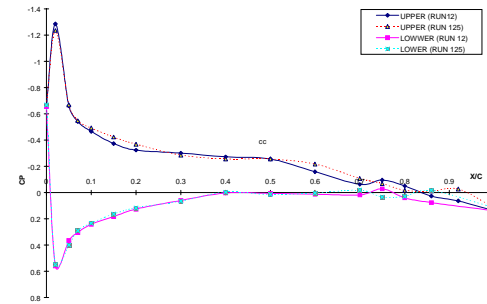
Row B, AOA = 10



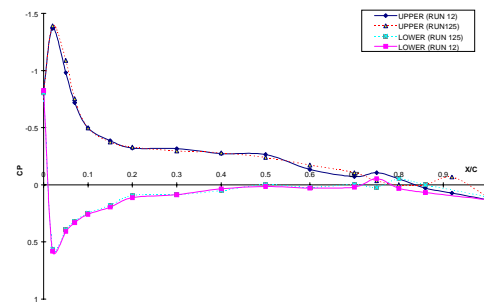
Row C, AOA = 10



Row D, AOA = 10

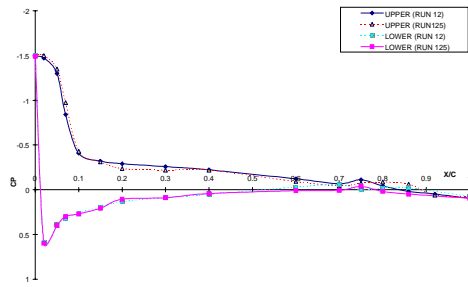


Row A, AOA = 6

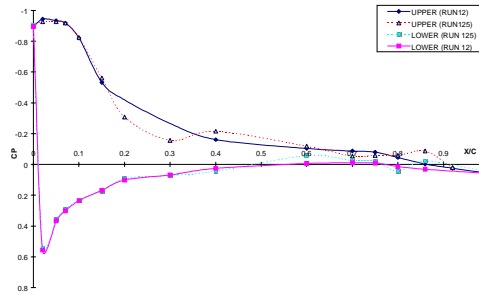


Row B, AOA = 6

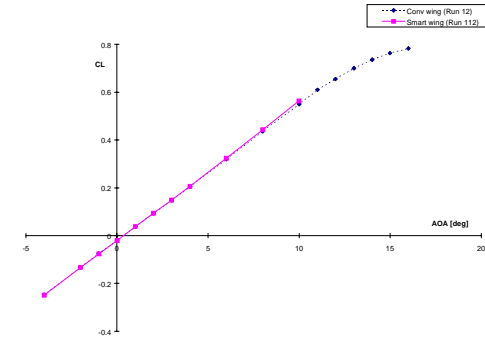
Run 12 vs. 112
 $M = 0.20$, $Q = 60$ psf
 Conventional Flap = 0° Aileron = 0°
 Smart Flap = 0° Aileron = 0°



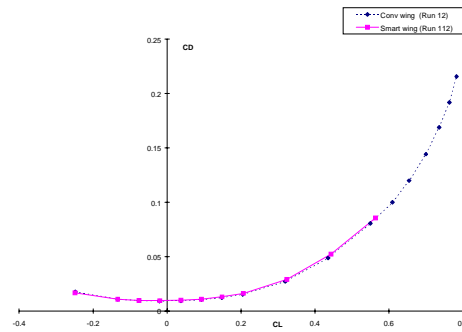
Row C, AOA = 6



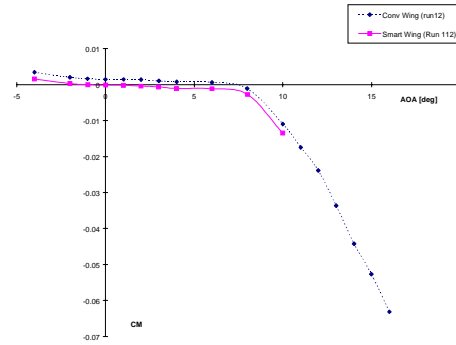
Row D, AOA = 6



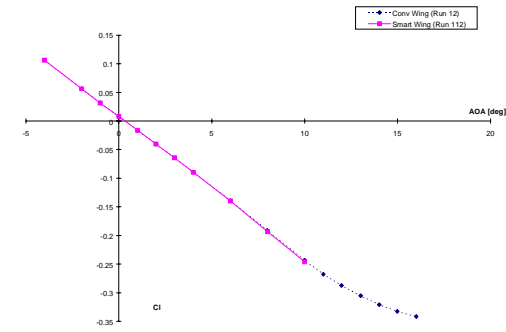
CL vs. AOA



CD vs. CL

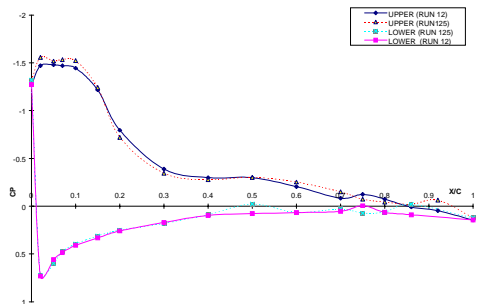


CM vs. AOA

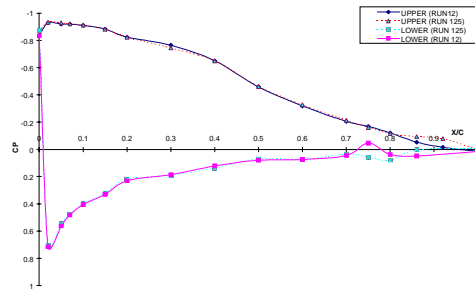


Roll Moment vs. AOA

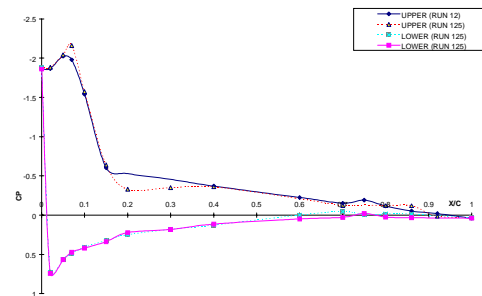
Run 12 vs. 112
 $M = 0.20$, $Q = 60$ psf
 Conventional Flap = 0° Aileron = 0°
 Smart Flap = 0° Aileron = 0°



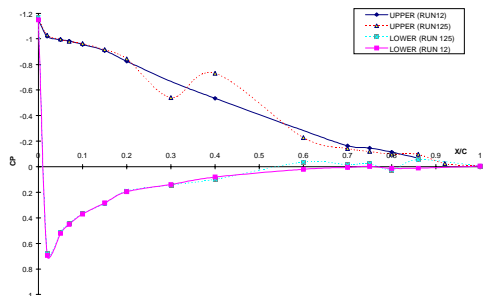
Row A, AOA = 10



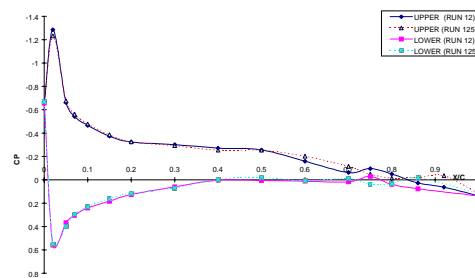
Row B, AOA = 10



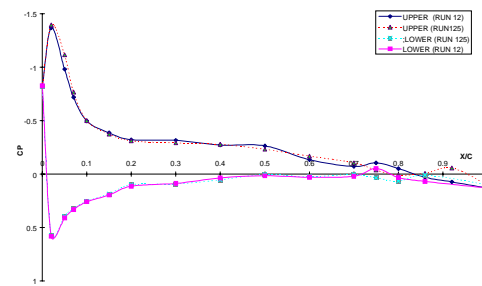
Row C, AOA = 10



Row D, AOA = 10

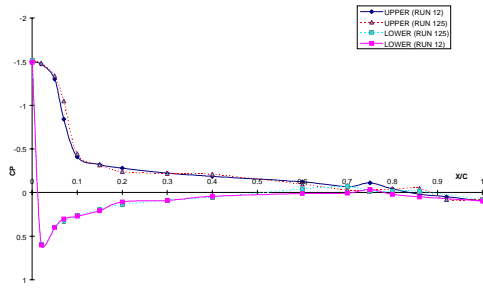


Row A, AOA = 6

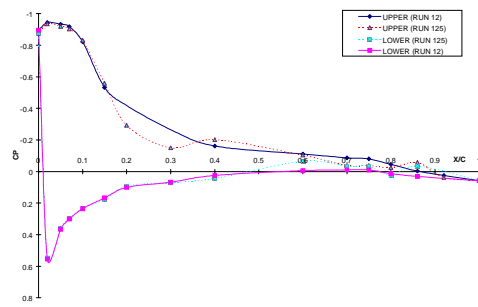


Row B, AOA = 6

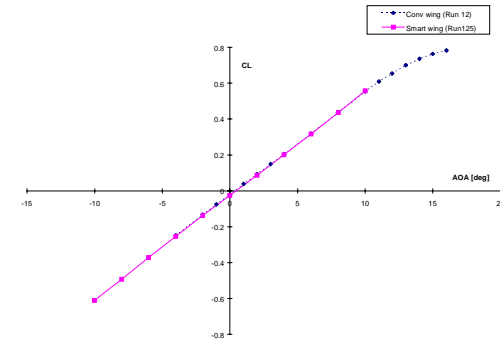
Run 12 vs. 125
 $M = 0.20$, $Q = 60$ psf
 Conventional Flap = 0° Aileron = 0°
 Smart Flap = 0° Aileron = 0°



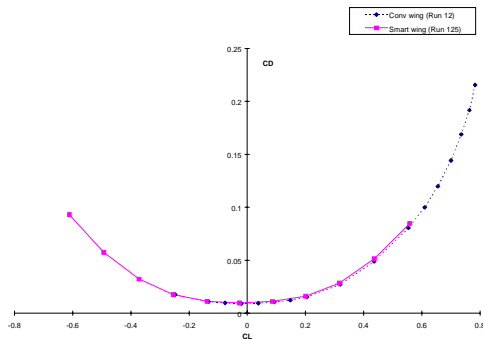
Row C, AOA = 6



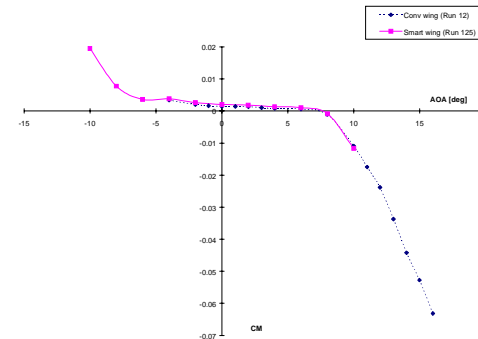
Row D, AOA = 6



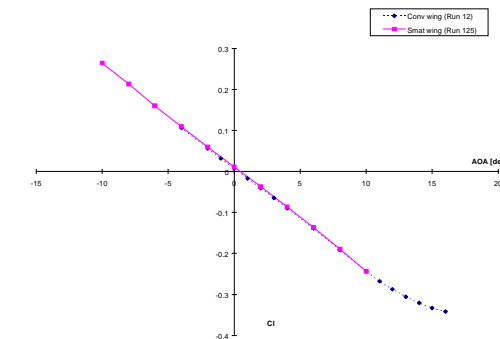
CL vs. AOA



CD vs. CL

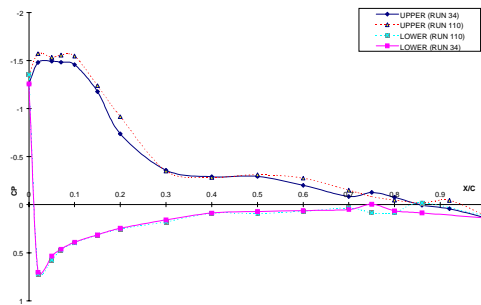


CM vs. AOA

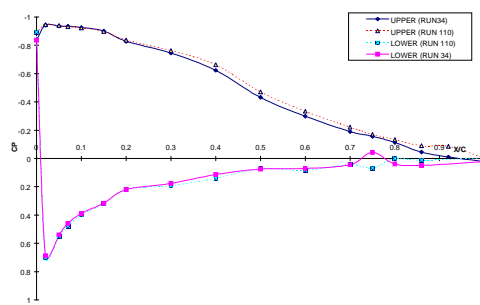


Roll Moment vs. AOA

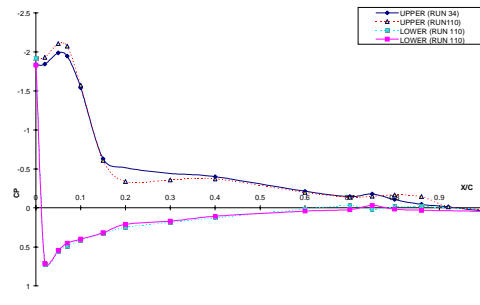
Run 12 vs. 125
 $M = 0.20$, $Q = 60$ psf
 Conventional Flap = 0° Aileron = 0°
 Smart Flap = 0° Aileron = 0°



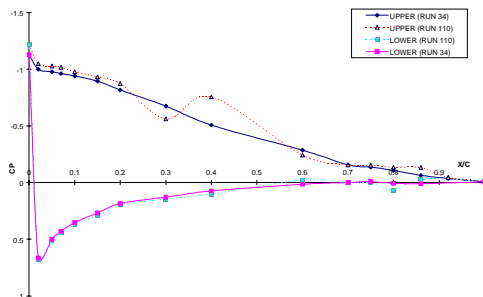
Row A, AOA = 10



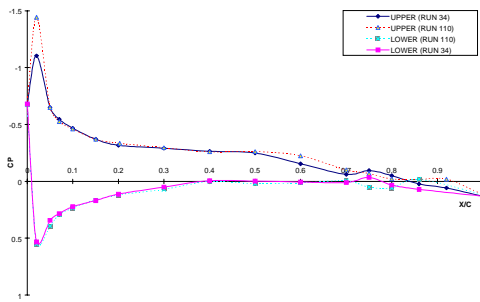
Row B, AOA = 10



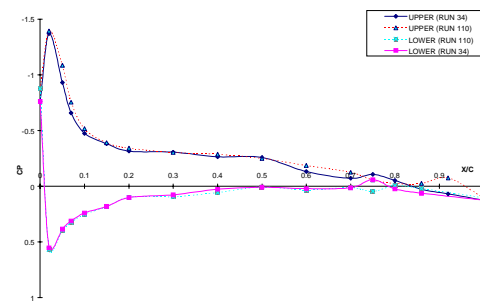
Row C, AOA = 10



Row D, AOA = 10

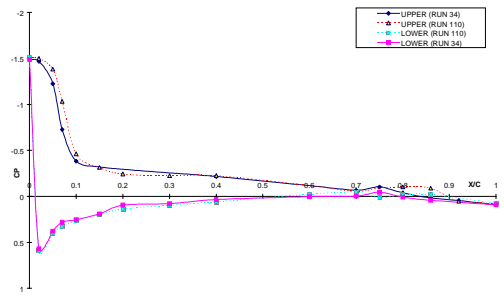


Row A, AOA = 6

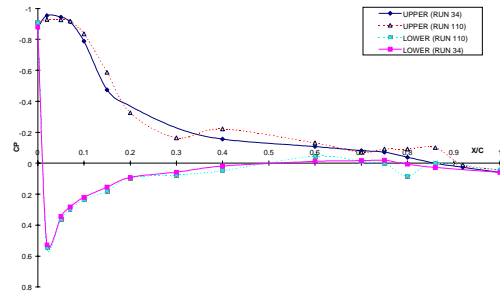


Row B, AOA = 6

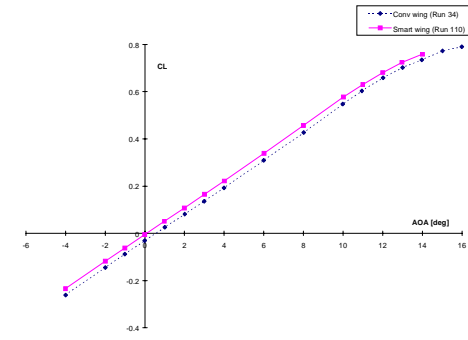
Run 34 vs. 110
 $M = 0.20$, $Q = 60$ psf
 Conventional Flap = 0° Aileron = 0°
 Smart Flap = 0° Aileron = 0°



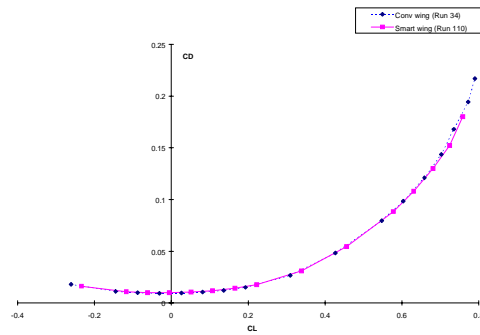
Row C, AOA = 6



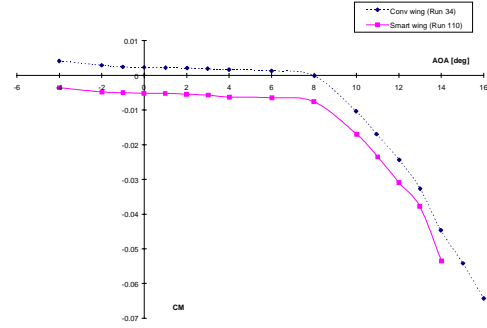
Row D, AOA = 6



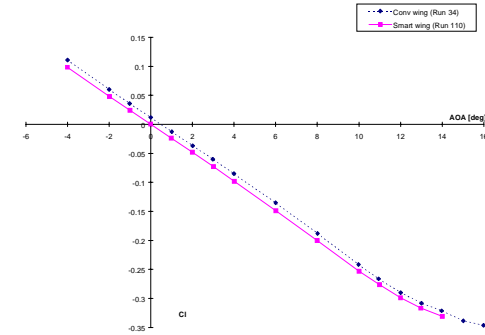
CL vs. AOA



CD vs. CL

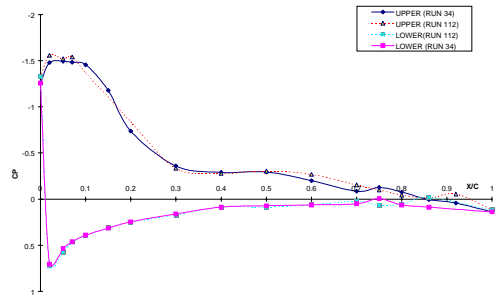


CM vs. AOA

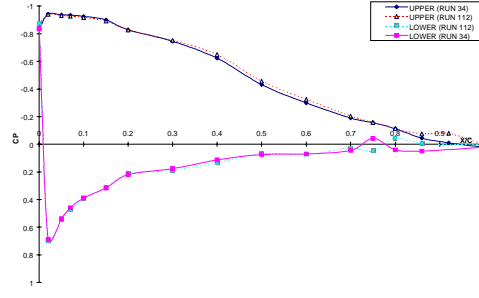


Roll Moment vs. AOA

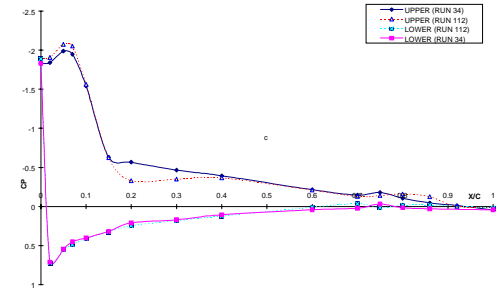
Run 34 vs. 110
 $M = 0.20$, $Q = 60$ psf
 Conventional Flap = 0° Aileron = 0°
 Smart Flap = 0° Aileron = 0°



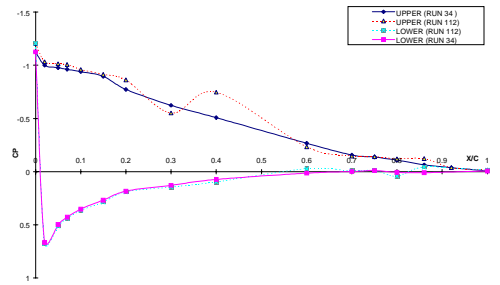
Row A, AOA = 10



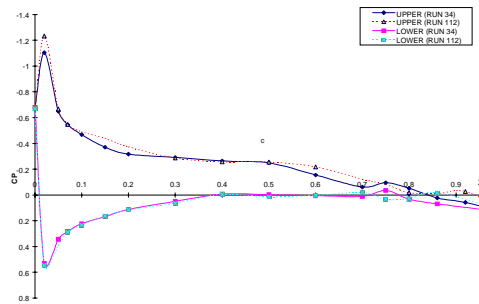
Row B, AOA = 10



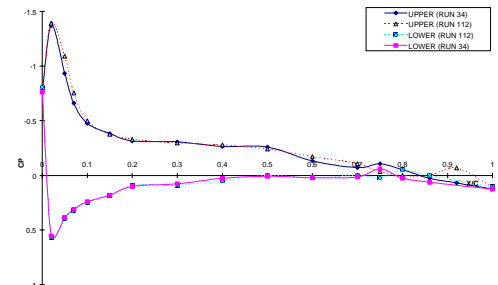
Row C, AOA = 10



Row D, AOA = 10

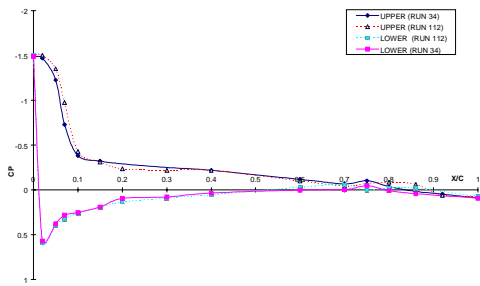


Row A, AOA = 6

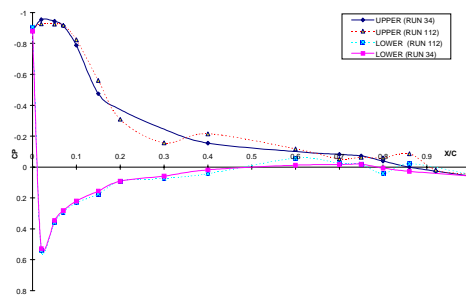


Row B, AOA = 6

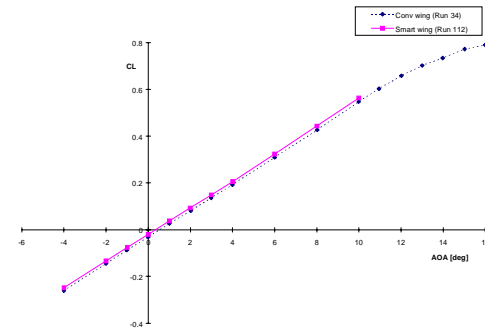
Run 34 vs. 112
 $M = 0.20$, $Q = 60$ psf
 Conventional Flap = 0° Aileron = 0°
 Smart Flap = 0° Aileron = 0°



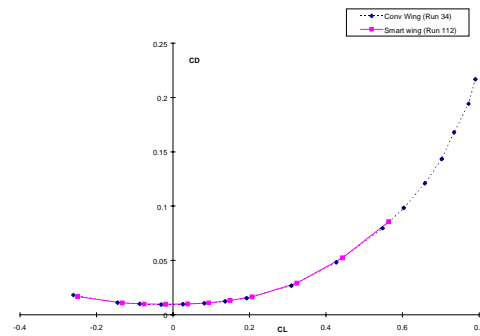
Row C, AOA = 6



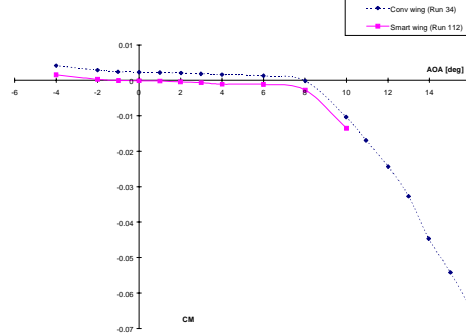
Row D, AOA = 6



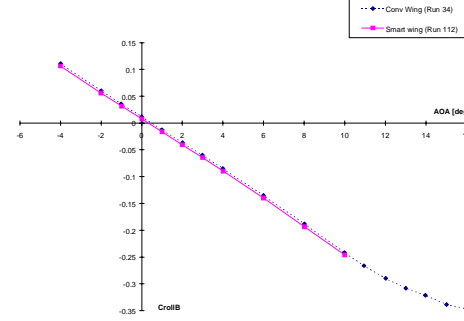
CL vs. AOA



CD vs. CL

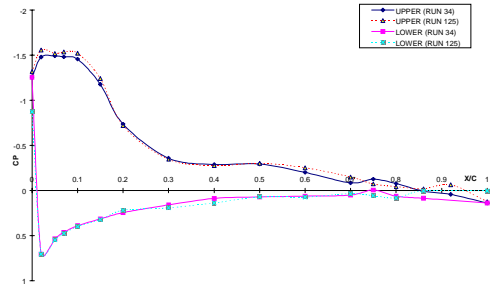


CM vs. AOA

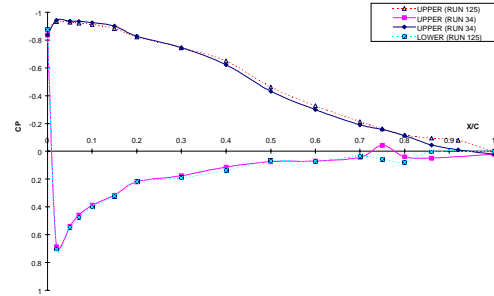


Roll Moment vs. AOA

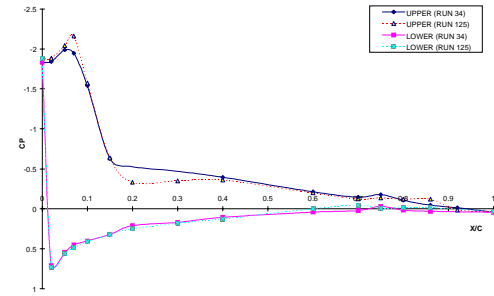
Run 34 vs. 112
 $M = 0.20$, $Q = 60$ psf
 Conventional Flap = 0° Aileron = 0°
 Smart Flap = 0° Aileron = 0°



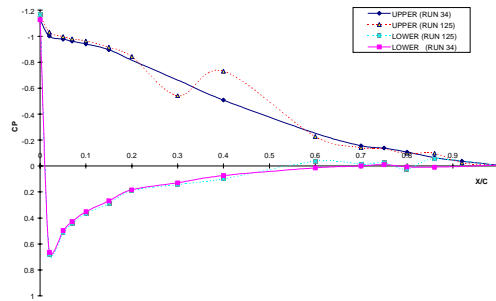
Row A, AOA = 10



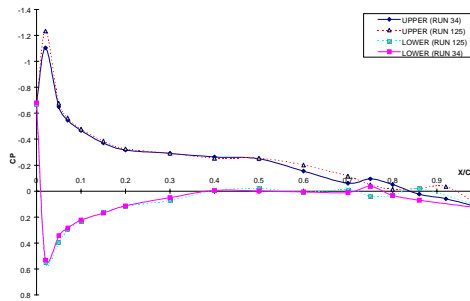
Row B, AOA = 10



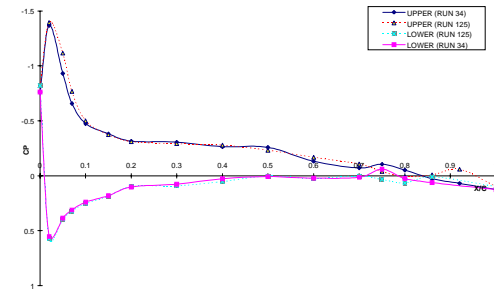
Row C, AOA = 10



Row D, AOA = 10

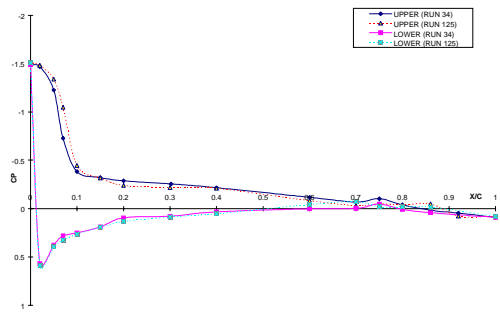
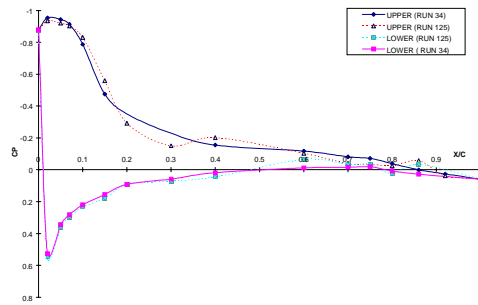
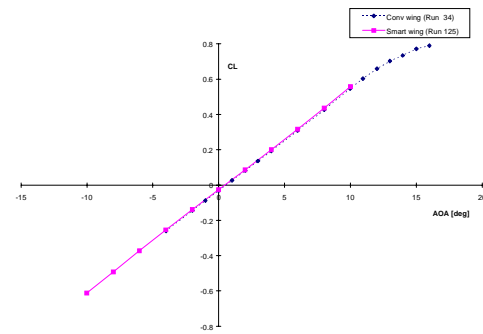


Row A, AOA = 6

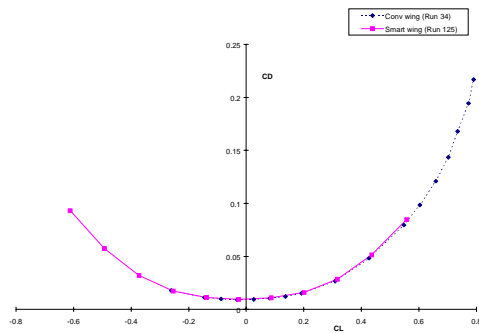


Row B, AOA = 6

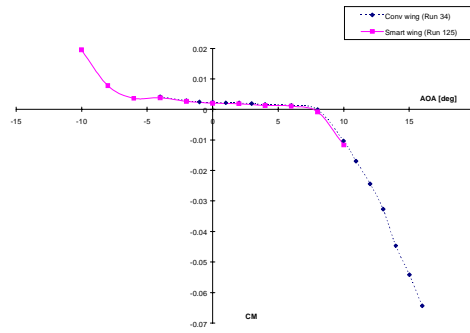
Run 34 vs. 125
 $M = 0.20$, $Q = 60$ psf
 Conventional Flap = 0° Aileron = 0°
 Smart Flap = 0° Aileron = 0°

Row C, $AOA = 6$ Row D, $AOA = 6$ 

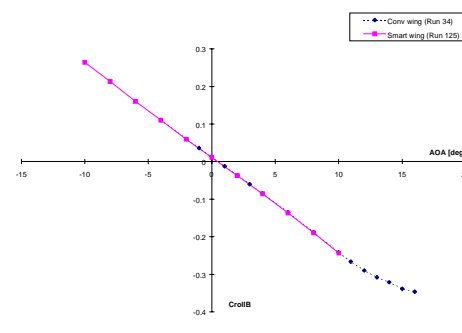
CL vs. AOA



CD vs. CL

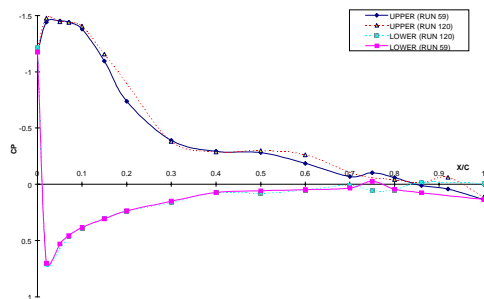


CM vs. AOA

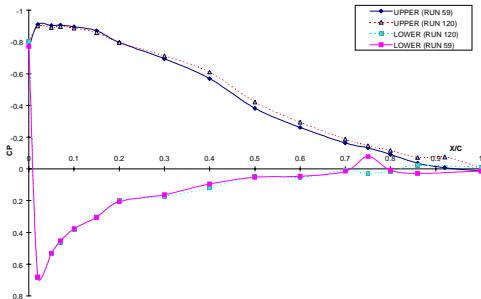


Roll Moment vs. AOA

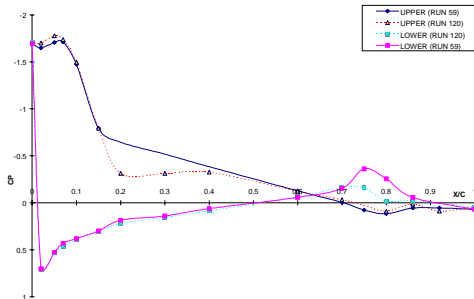
Run 34 vs. 125
 $M = 0.20$, $Q = 60$ psf
 Conventional Flap = 0° Aileron = 0°
 Smart Flap = 0° Aileron = 0°



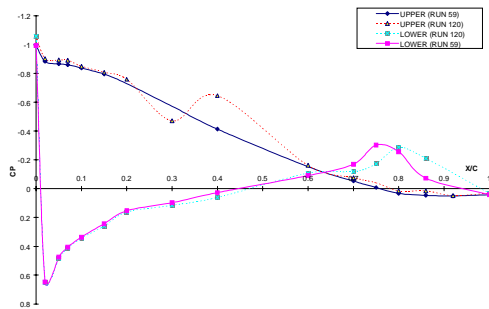
Row A, AOA = 10



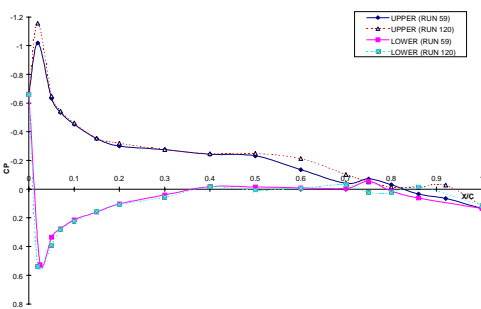
Row B, AOA = 10



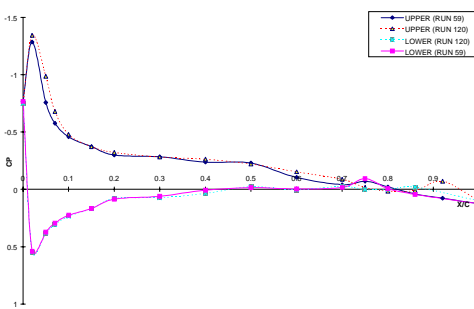
Row C, AOA = 10



Row D, AOA = 10

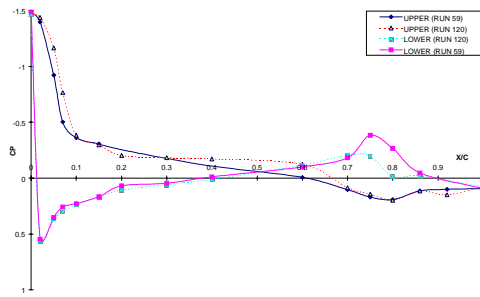


Row A, AOA = 6

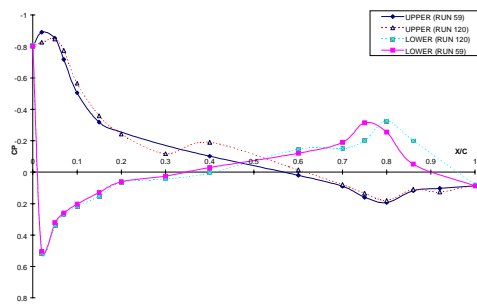


Row B, AOA = 6

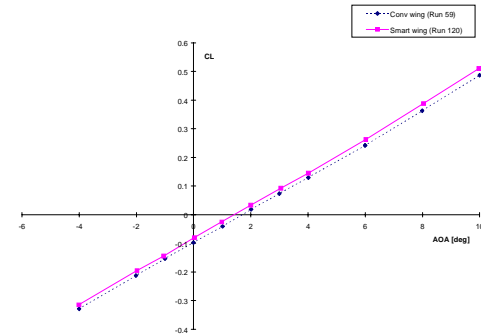
Run 59 vs. 120
 $M = 0.20$, $Q = 60$ psf
 Conventional Flap = 0° Aileron = 0°
 Smart Flap = 0° Aileron = 0°



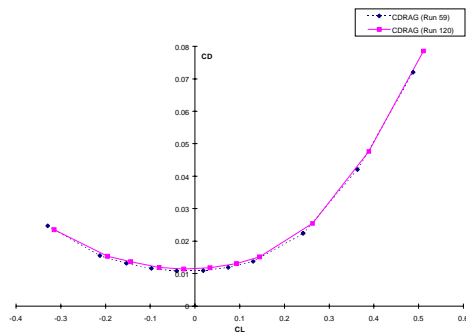
Row C, AOA = 6



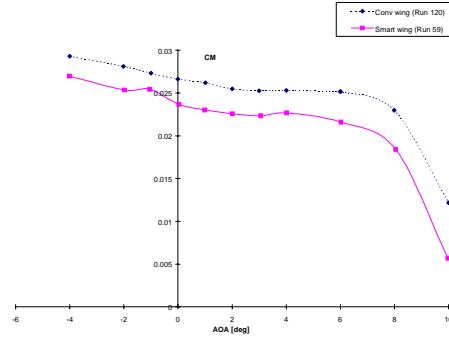
Row D, AOA = 6



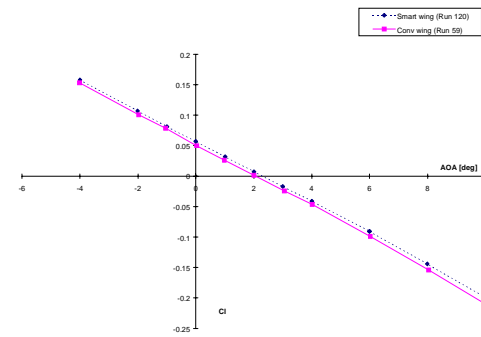
CL vs. AOA



CD vs. Cl

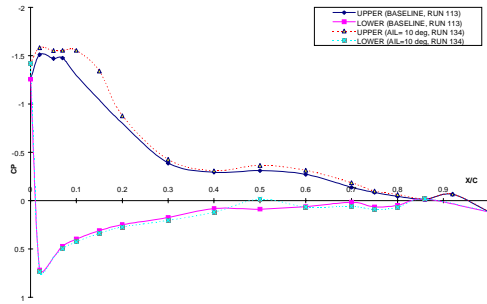


CM vs. AOA

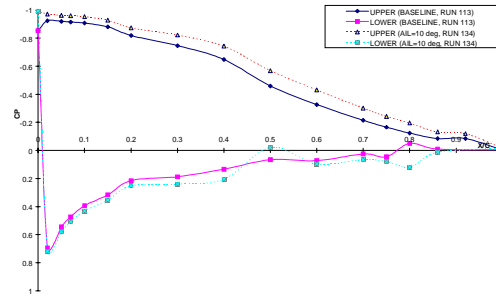


Roll Moment vs. AOA

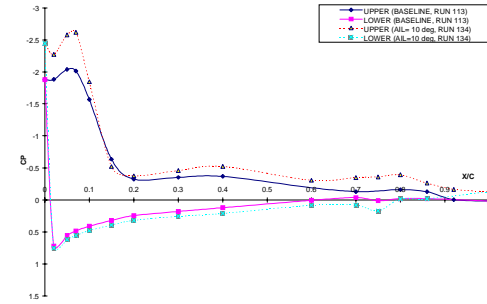
Run 59 vs. 120
 $M = 0.20$, $Q = 60$ psf
 Conventional Flap = 0° Aileron = 0°
 Smart Flap = 0° Aileron = 0°



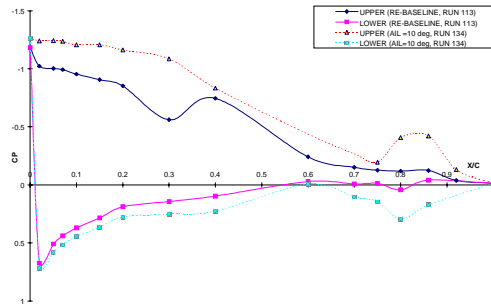
Row A, AOA = 10



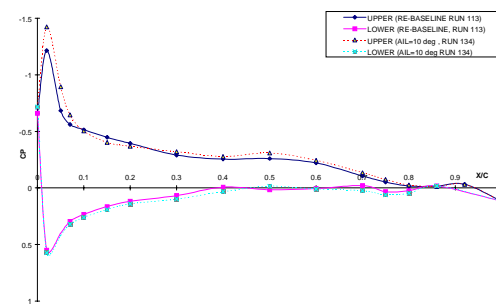
Row B, AOA = 10



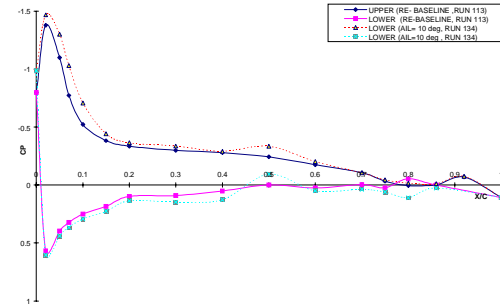
Row C, AOA = 10



Row D, AOA = 10

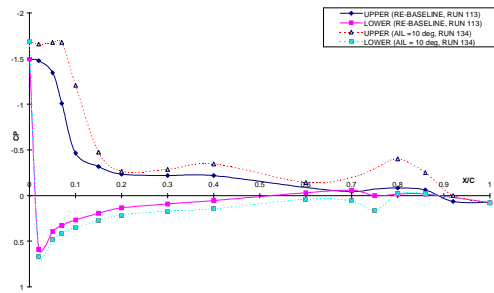


Row A, AOA = 6

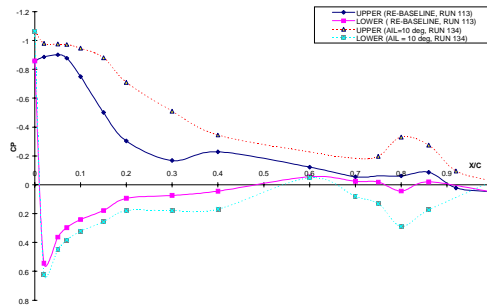


Row B, AOA = 6

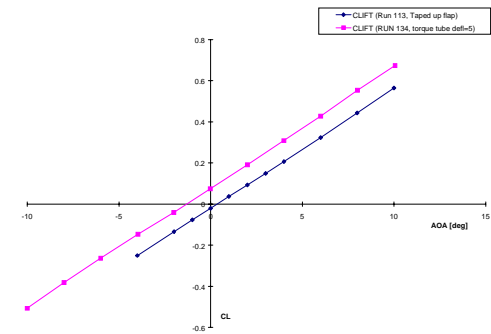
Run 113 vs. 134
 $M = 0.25$, $Q = 90$ psf
 Conventional Flap = N/A Aileron = N/A
 Smart Flap = 0° Aileron = 10°



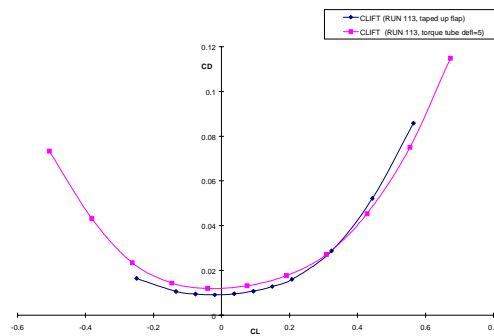
Row C, AOA = 6



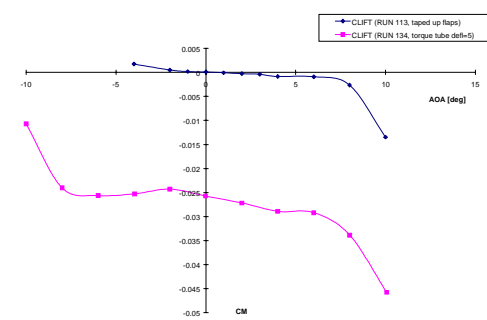
Row D, AOA = 6



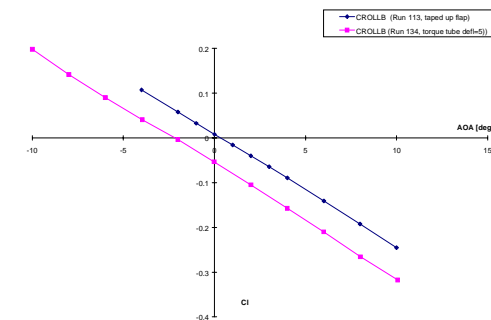
CL vs. AOA



CD vs. CL



CM vs. AOA



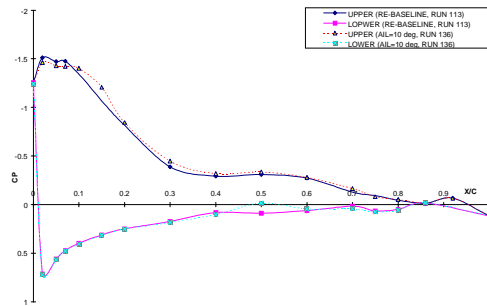
Roll Moment vs. AOA

Run 113 vs. 134

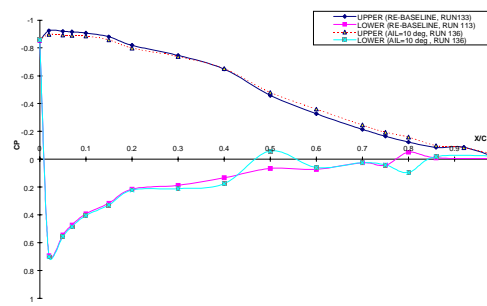
 $M = 0.25$, $Q = 90$ psf

Conventional Flap = N/A Aileron = N/A

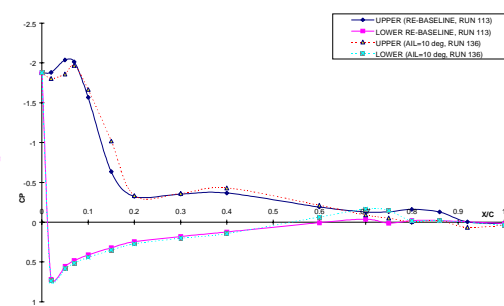
Smart Flap = 0° Aileron = 10°



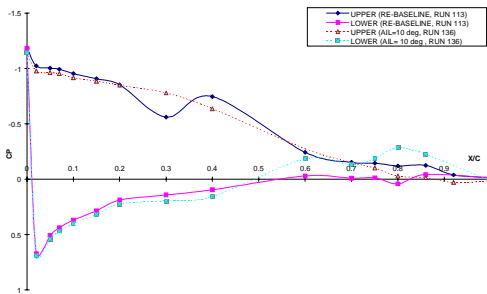
Row A, AOA = 10



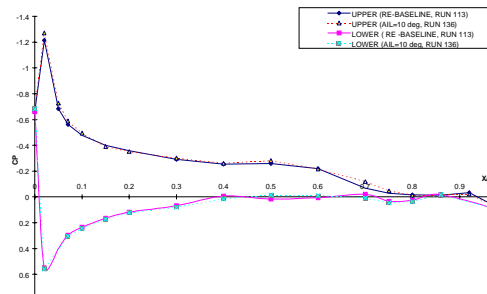
Row B, AOA = 10



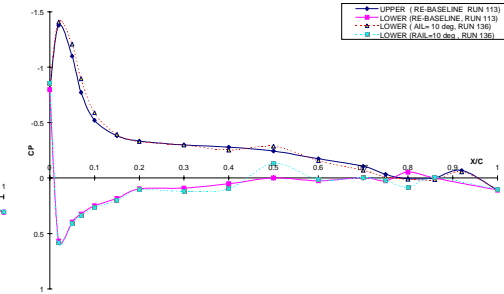
Row C, AOA = 10



Row D, AOA = 10

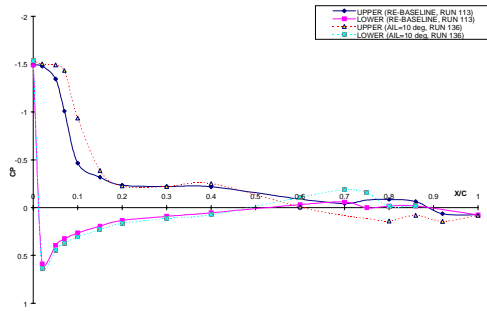


Row A, AOA = 6

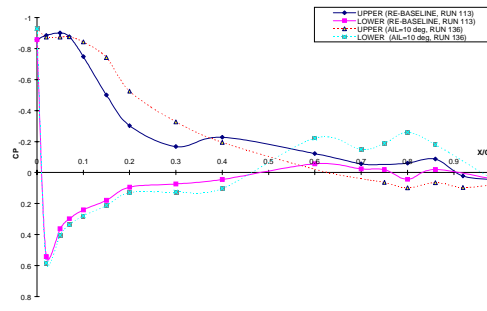


Row B, AOA = 6

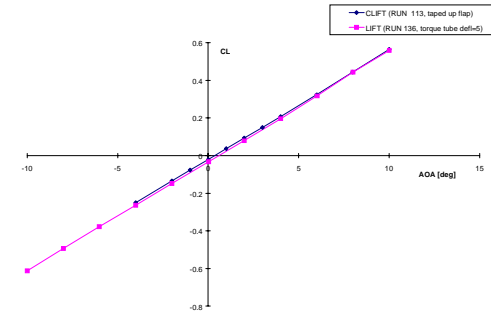
Run 113 vs. 136
 $M = 0.25$, $Q = 90$ psf
 Conventional Flap = N/A Aileron = N/A
 Smart Flap = 0° Aileron = 10°



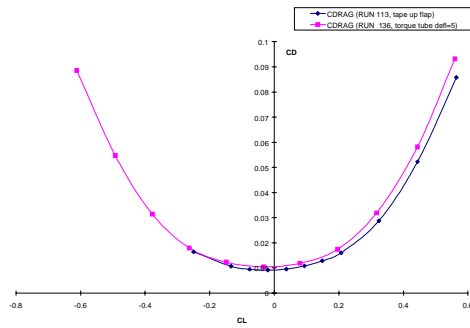
Row C, AOA = 6



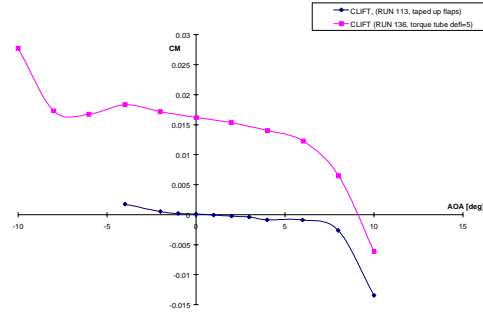
Row D, AOA = 6



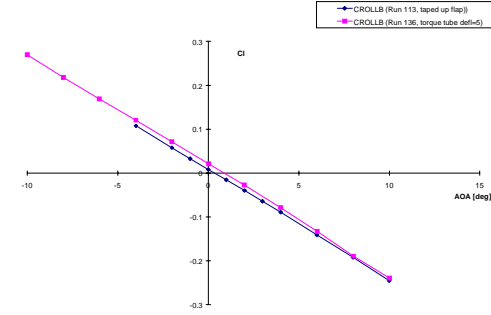
CL vs. AOA



CD vs. CL



CM vs. AOA



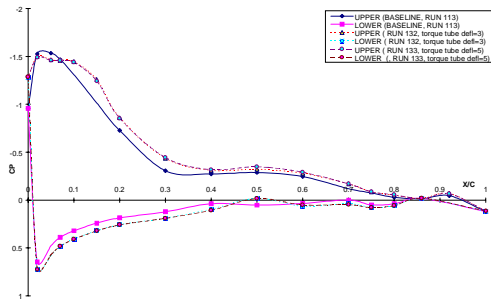
Roll Moment vs. AOA

Run 113 vs. 136

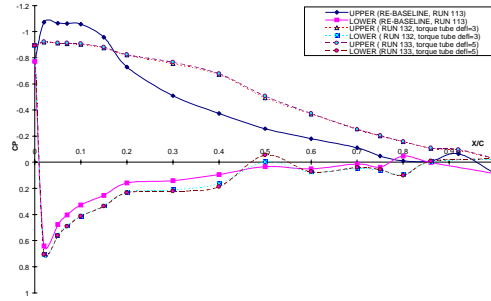
M = 0.25, Q = 90 psf

Conventional Flap = N/A Aileron = N/A

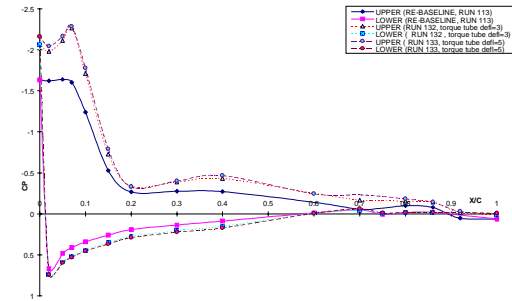
Smart Flap = 0° Aileron = 10°



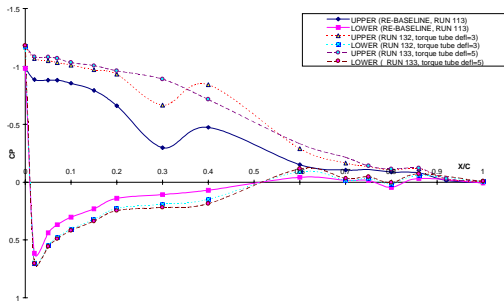
Row A, AOA = 10



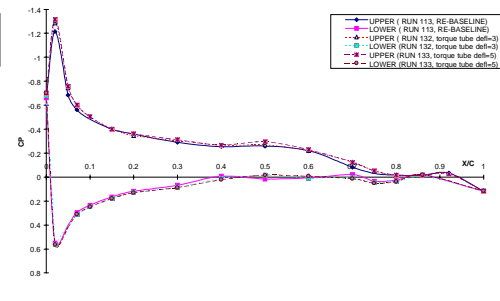
Row B, AOA = 10



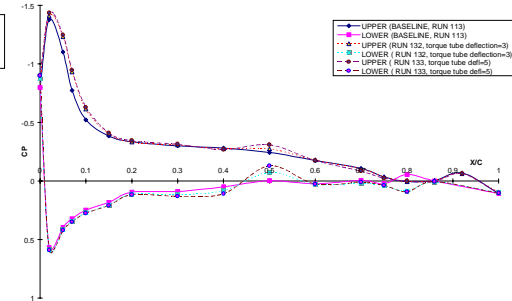
Row C, AOA = 10



Row D, AOA = 10

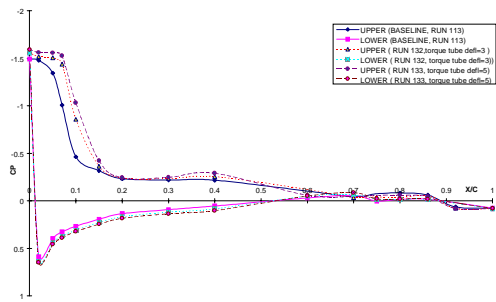


Row A, AOA = 6

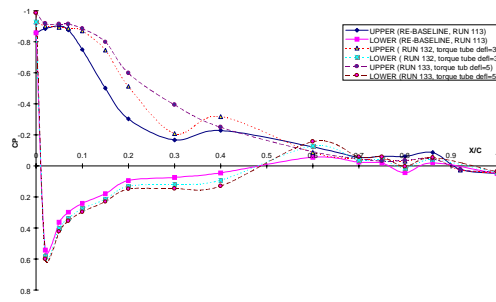


Row B, AOA = 6

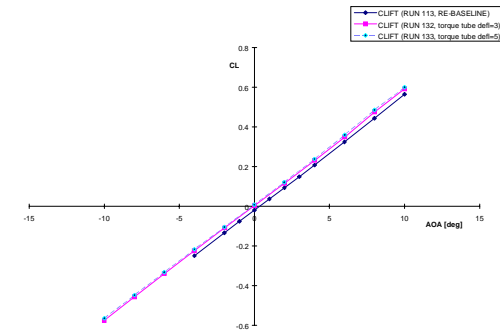
Run 113 vs. 132, 133
M = 0.25, Q = 90 psf
Conventional Flap = N/A Aileron = N/A
Smart Flap = 0° Aileron = 0°



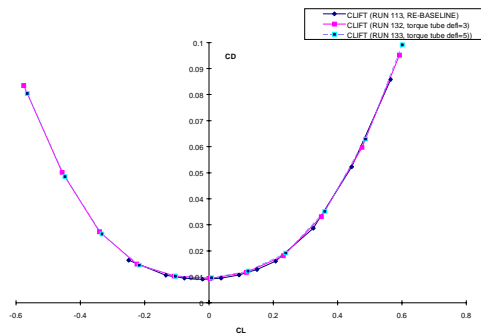
Row C, AOA = 6



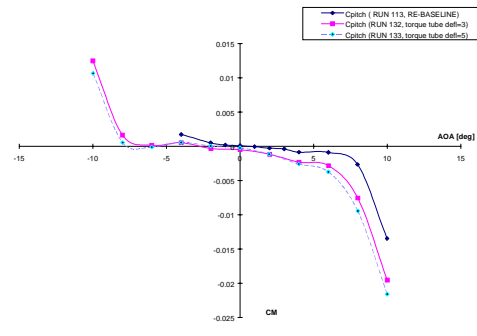
Row D, AOA = 6



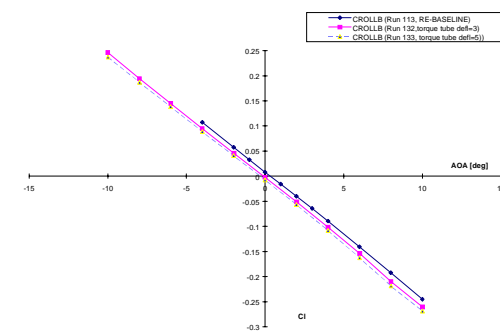
CL vs. AOA



CD vs. Cl

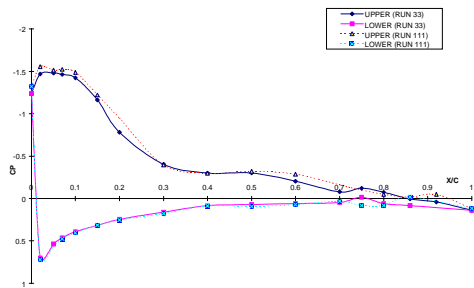


CM vs. AOA

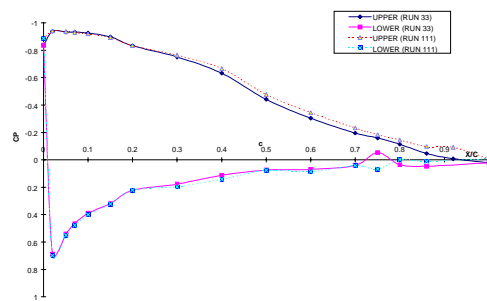


Roll Moment vs. AOA

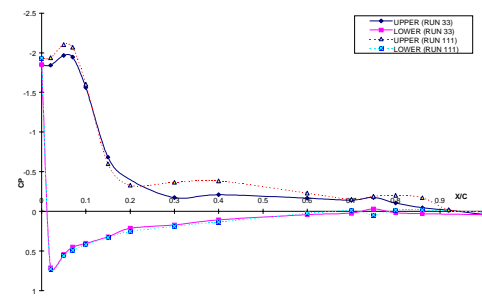
Run 113 vs. 132, 133
M = 0.25, Q = 90 psf
Conventional Flap = N/A Aileron = N/A
Smart Flap = 0° Aileron = 0°



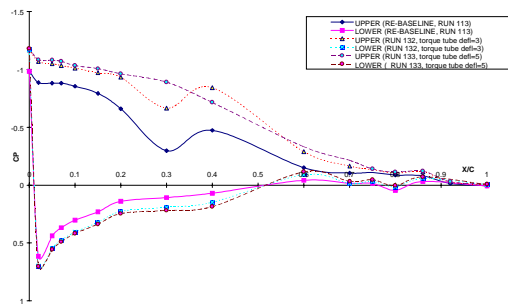
Row A, AOA = 10



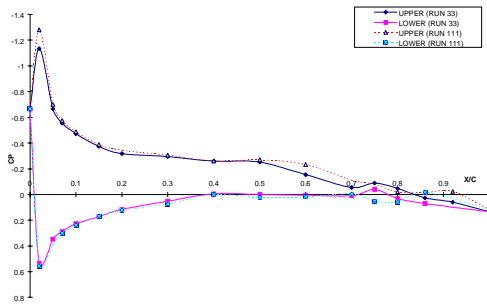
Row B, AOA = 10



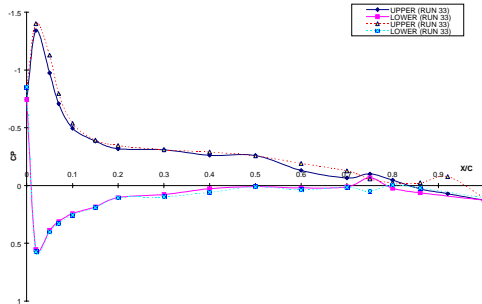
Row C, AOA = 10



Row D, AOA = 10

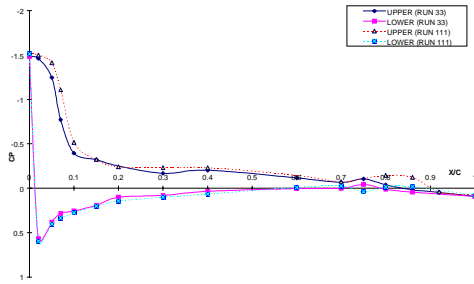


Row A, AOA = 6

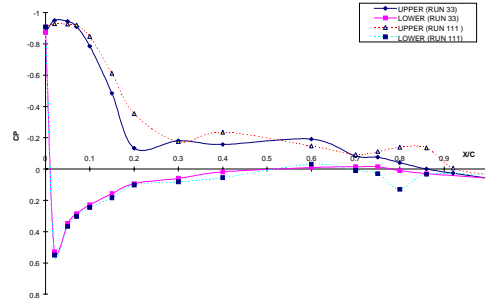


Row B, AOA = 6

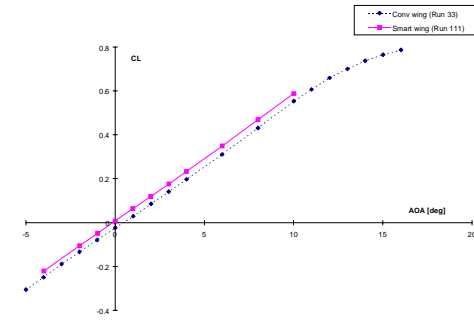
Run 33 vs. 111
 $M = 0.25$, $Q = 90$ psf
 Conventional Flap = 0° Aileron = 0°
 Smart Flap = 0° Aileron = 0°



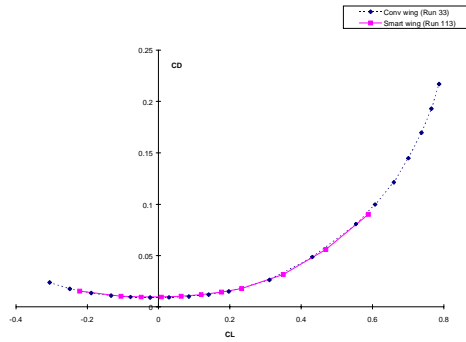
Row C, AOA = 6



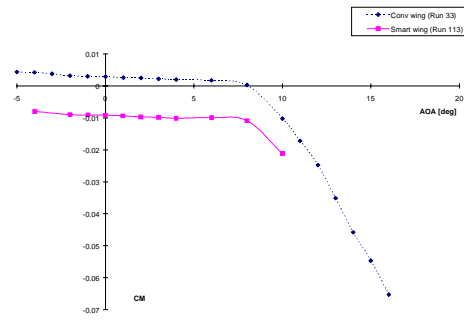
Row D, AOA = 6



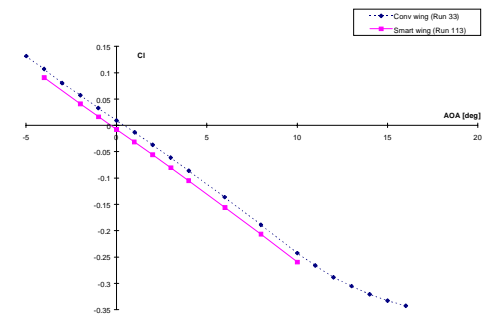
CL vs. AOA



CD vs. CL

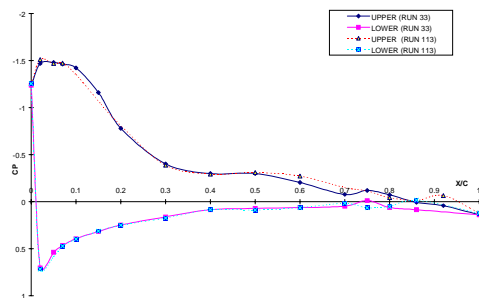


CM vs. AOA

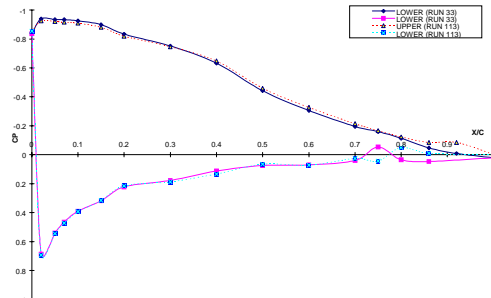


Roll Moment vs. AOA

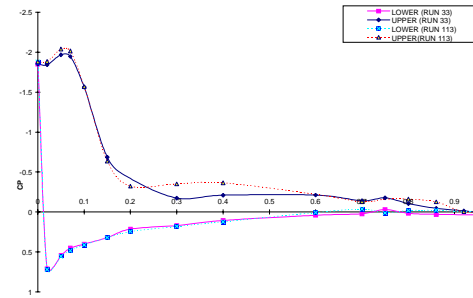
Run 33 vs. 111
 $M = 0.25$, $Q = 90$ psf
 Conventional Flap = 0° Aileron = 0°
 Smart Flap = 0° Aileron = 0°



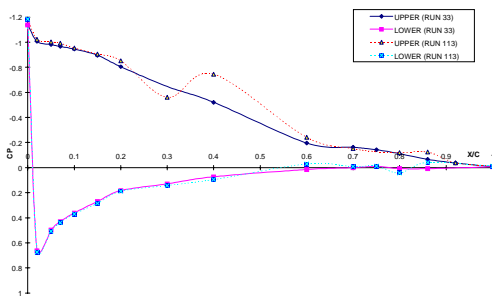
Row A, AOA = 10



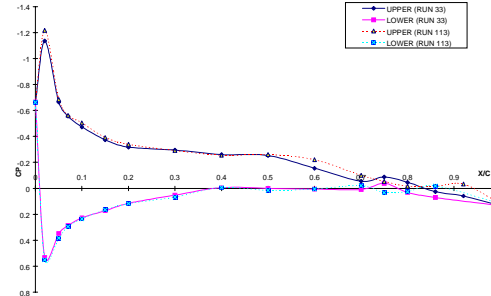
Row B, AOA = 10



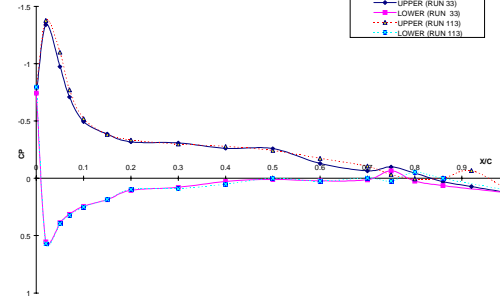
Row C, AOA = 10



Row D, AOA = 10

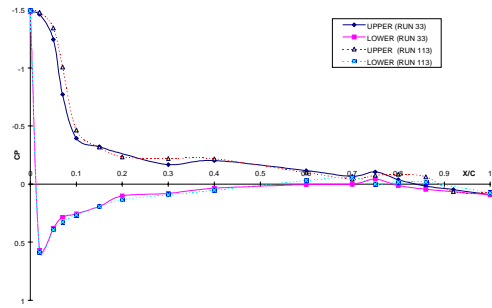


Row A, AOA = 6

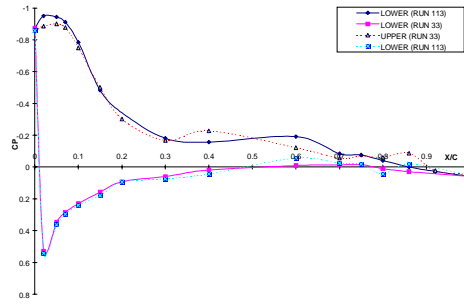


Row B, AOA = 6

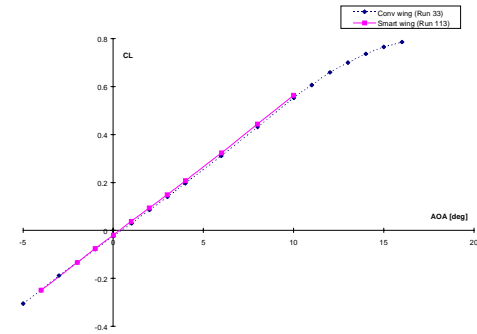
Run 33 vs. 113
 $M = 0.25$, $Q = 90$ psf
 Conventional Flap = 0° Aileron = 0°
 Smart Flap = 0° Aileron = 0°



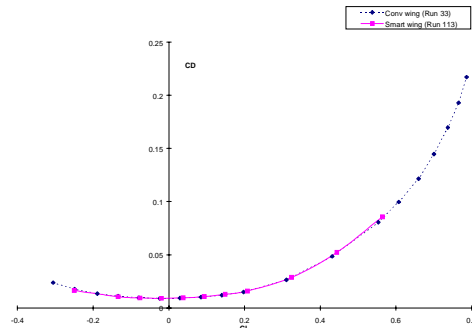
Row C, AOA = 6



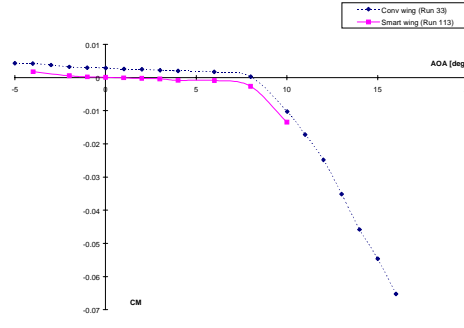
Row D, AOA = 6



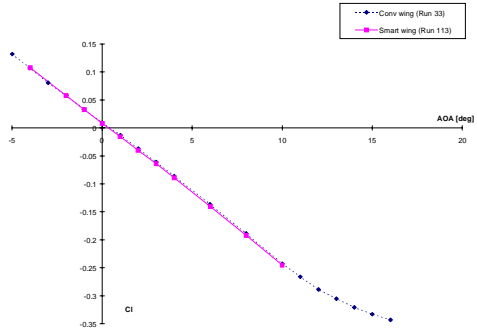
CL vs. AOA



CD vs. CL

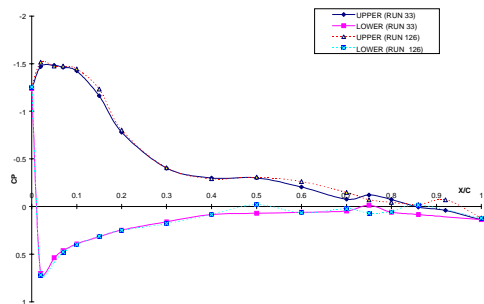


CM vs. AOA

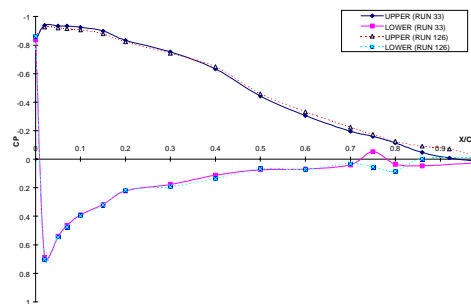


Roll Moment vs. AOA

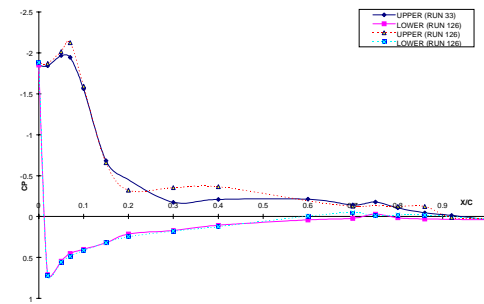
Run 33 vs. 113
 $M = 0.25$, $Q = 90$ psf
 Conventional Flap = 0° Aileron = 0°
 Smart Flap = 0° Aileron = 0°



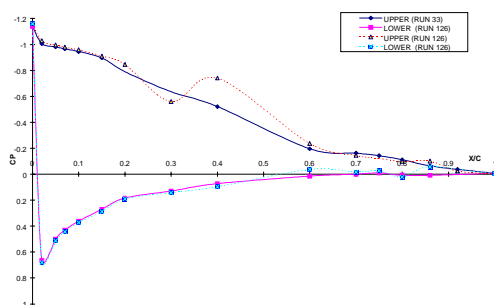
Row A, AOA = 10



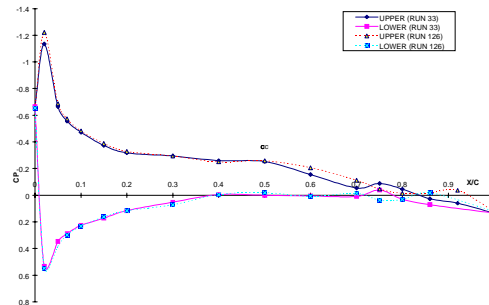
Row B, AOA = 10



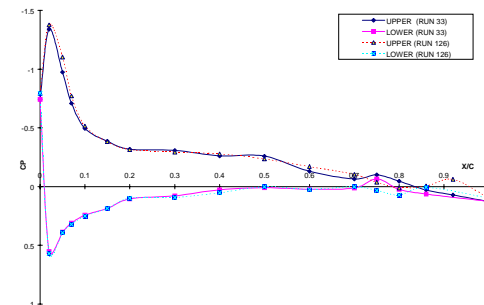
Row C, AOA = 10



Row D, AOA = 10

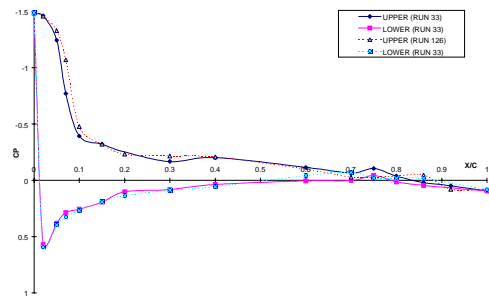


Row A, AOA = 6

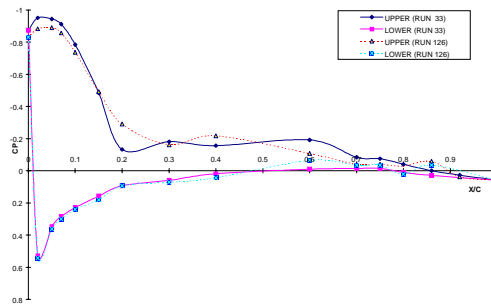


Row B, AOA = 6

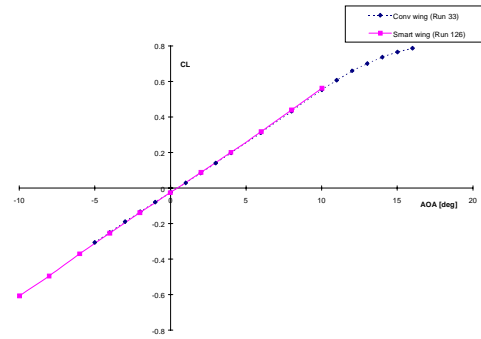
Run 33 vs. 126
 $M = 0.25$, $Q = 90$ psf
 Conventional Flap = 0° Aileron = 0°
 Smart Flap = 0° Aileron = 0°



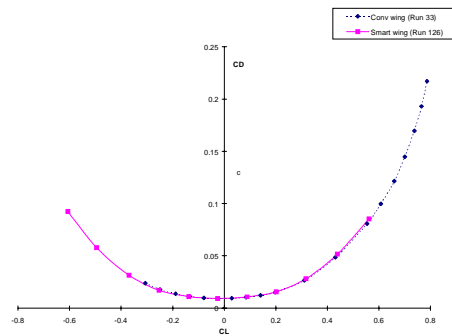
Row C, AOA = 6



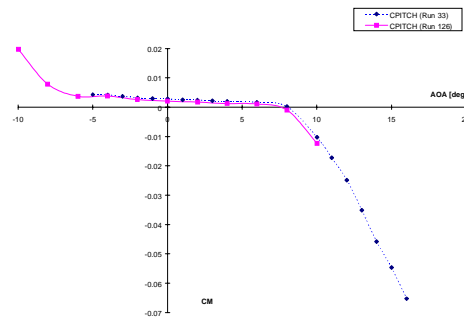
Row D, AOA = 6



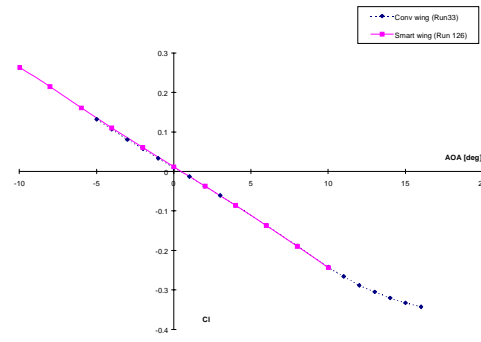
CL vs. AOA



CD vs. CL

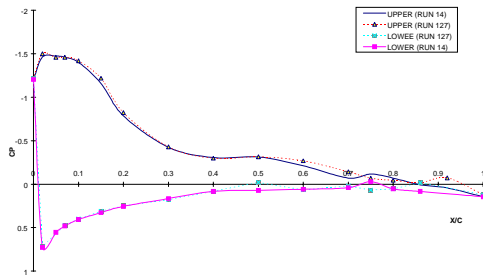


CM vs. AOA

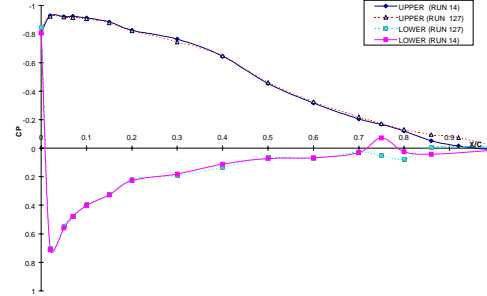


Roll Moment vs. AOA

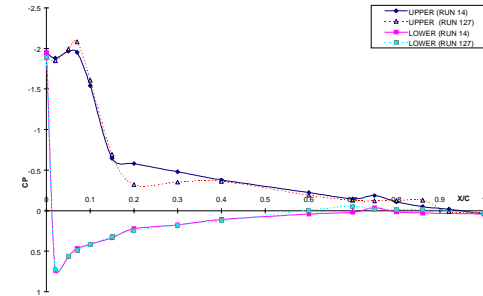
Run 33 vs. 126
 $M = 0.25$, $Q = 90$ psf
 Conventional Flap = 0° Aileron = 0°
 Smart Flap = 0° Aileron = 0°



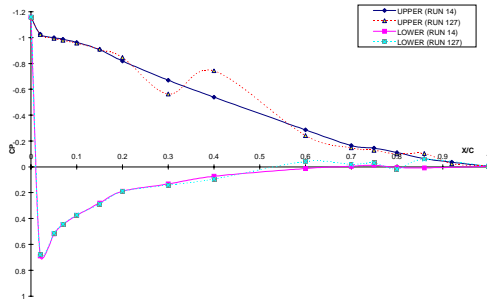
Row A, AOA = 10



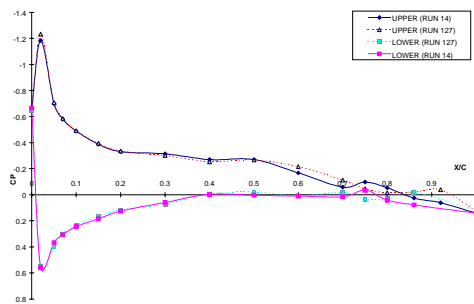
Row B, AOA = 10



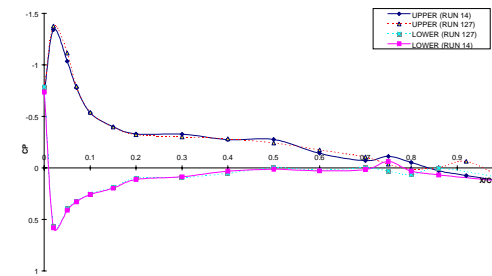
Row C, AOA = 10



Row D, AOA = 10

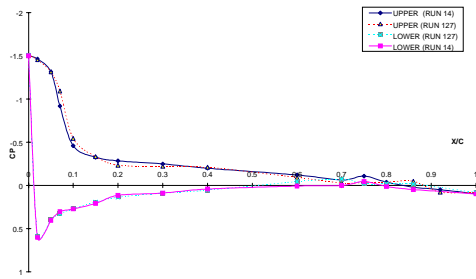


Row A, AOA = 6

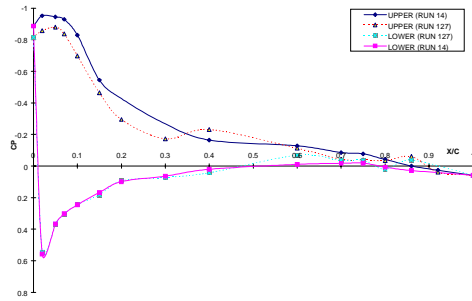


Row B, AOA = 6

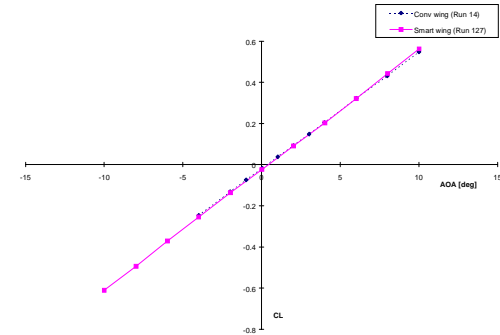
Run 14 vs. 127
 $M = 0.29$, $Q = 120$ psf
 Conventional Flap = -10° Aileron = 0°
 Smart Flap = -10° Aileron = 0°



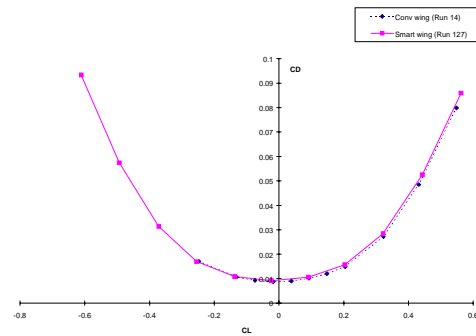
Row C, AOA = 6



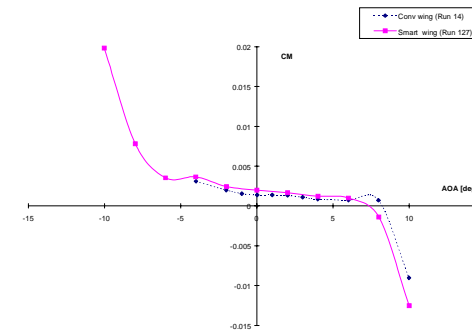
Row D, AOA = 6



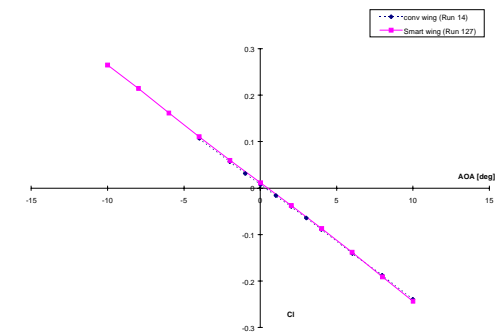
CL vs. AOA



CD vs. CL

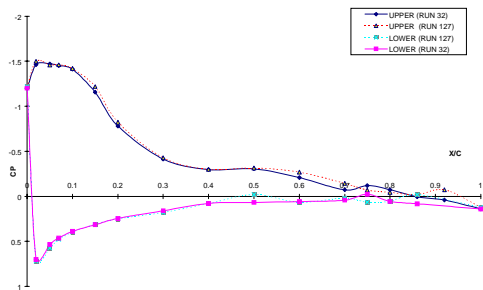


CM vs. AOA

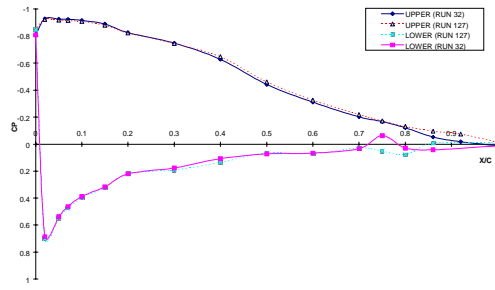


Roll Moment vs. AOA

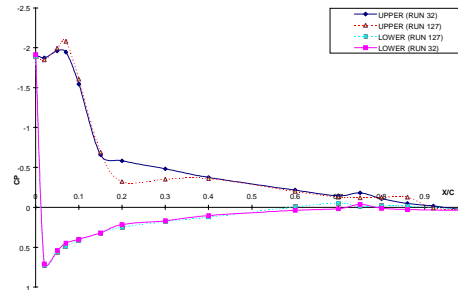
Run 14 vs. 127
 $M = 0.29$, $Q = 120$ psf
 Conventional Flap = -10° Aileron = 0°
 Smart Flap = -10° Aileron = 0°



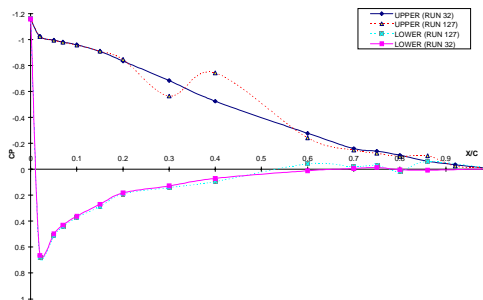
Row A, AOA = 10



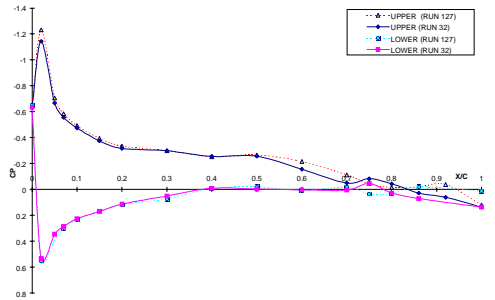
Row B, AOA = 10



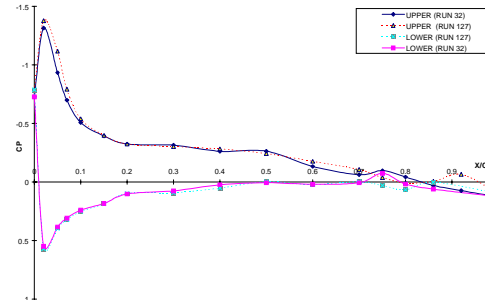
Row C, AOA = 10



Row D, AOA = 10

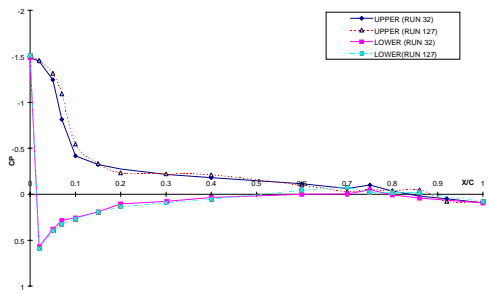


Row A, AOA = 6

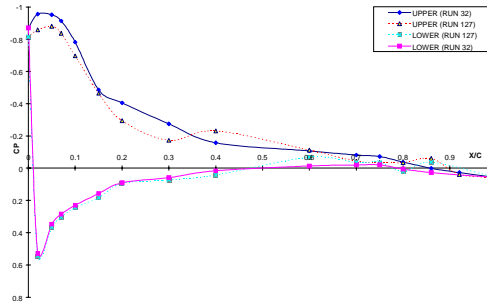


Row B, AOA = 6

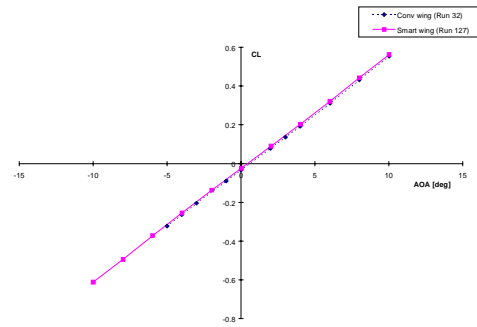
Run 32 vs. 127
 $M = 0.29$, $Q = 120$ psf
 Conventional Flap = 0° Aileron = 0°
 Smart Flap = 0° Aileron = 0°



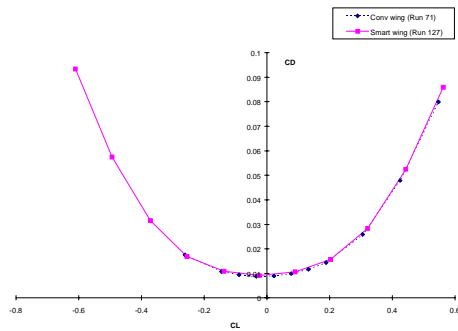
Row C, AOA = 6



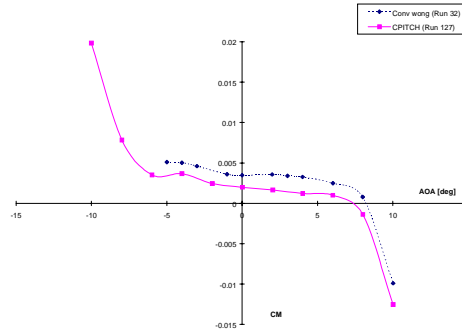
Row D, AOA = 6



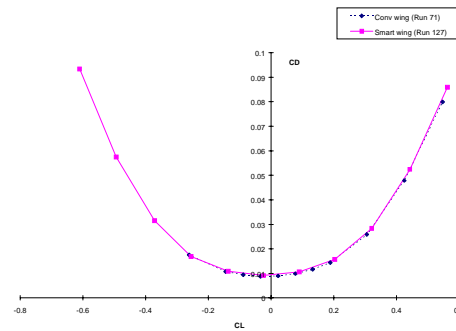
CL vs. AOA



CD vs. CL

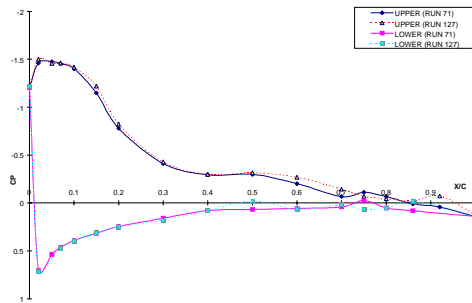


CM vs. AOA

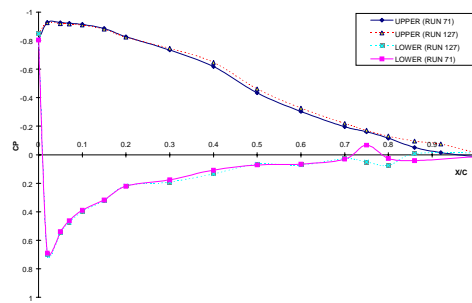


Roll Moment vs. AOA

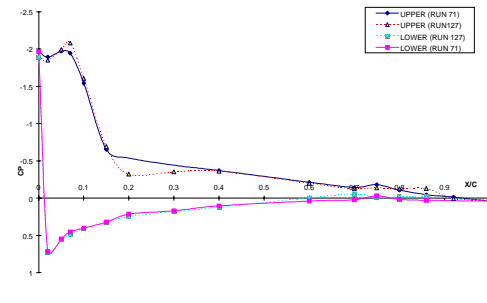
Run 32 vs. 127
 $M = 0.29$, $Q = 120$ psf
 Conventional Flap = 0° Aileron = 0°
 Smart Flap = 0° Aileron = 0°



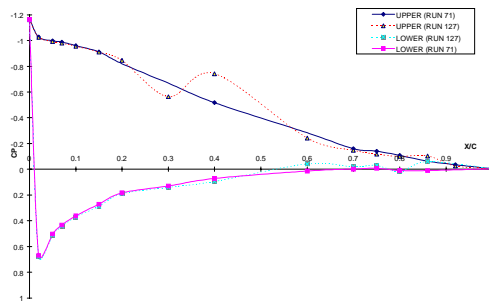
Row A, AOA = 10



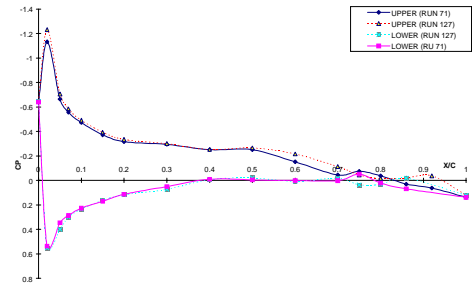
Row B, AOA = 10



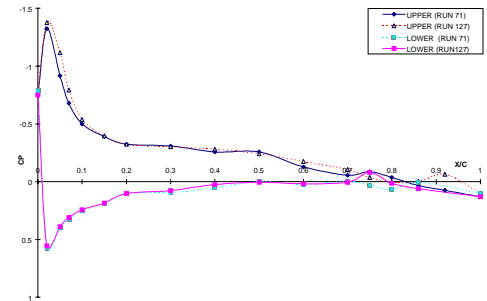
Row C, AOA = 10



Row D, AOA = 10

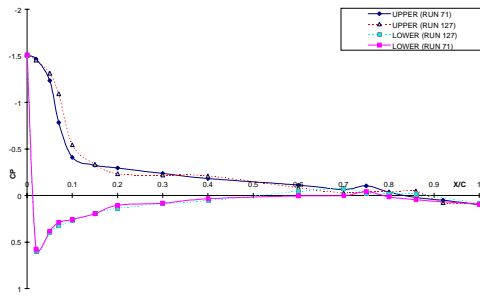


Row A, AOA = 6

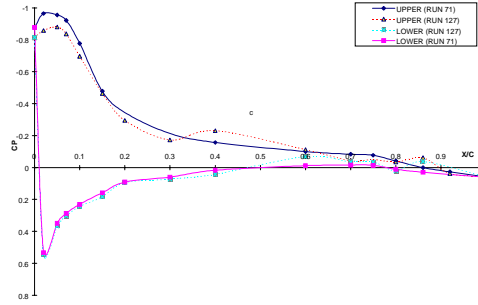


Row B, AOA = 6

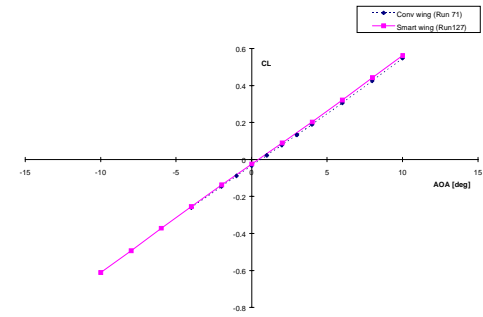
Run 71 vs. 127
 $M = 0.29$, $Q = 120$ psf
 Conventional Flap = 0° Aileron = 0°
 Smart Flap = 0° Aileron = 0°



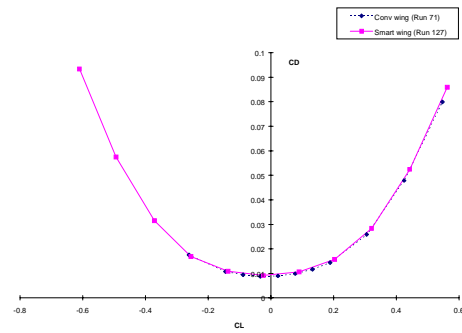
Row C, AOA = 6



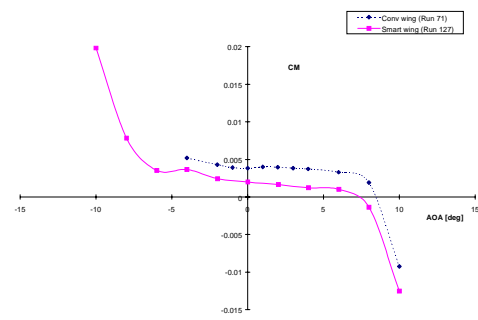
Row D, AOA = 6



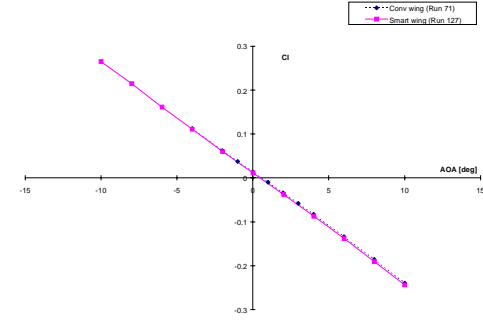
CL vs. AOA



CD vs. CL

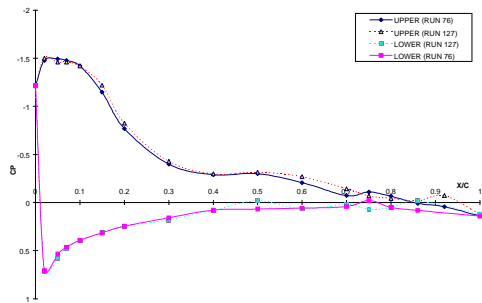


CM vs. AOA

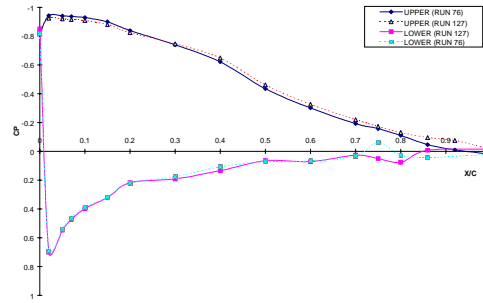


Roll Moment vs. AOA

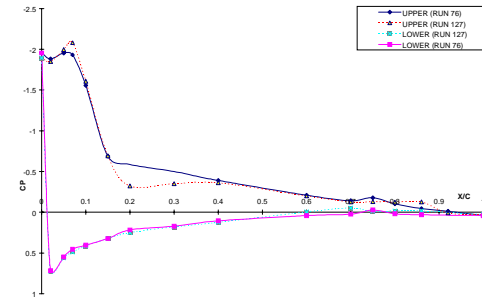
Run 71 vs. 127
 $M = 0.29$, $Q = 120$ psf
 Conventional Flap = 0° Aileron = 0°
 Smart Flap = 0° Aileron = 0°



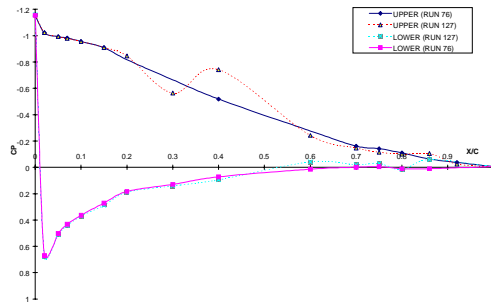
Row A, AOA = 10



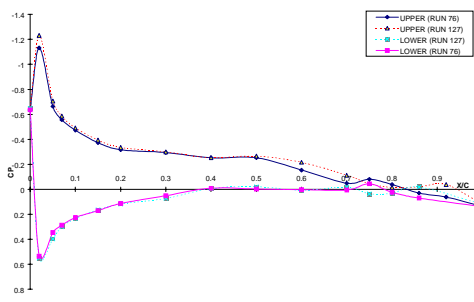
Row B, AOA = 10



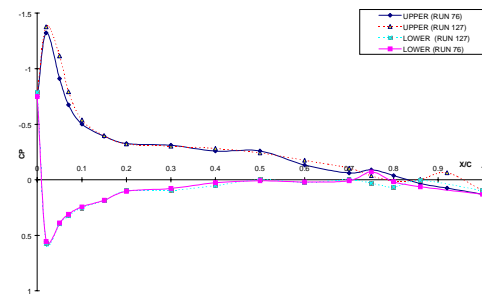
Row C, AOA = 10



Row D, AOA = 10

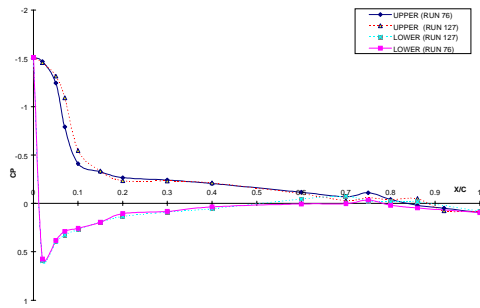


Row A, AOA = 6

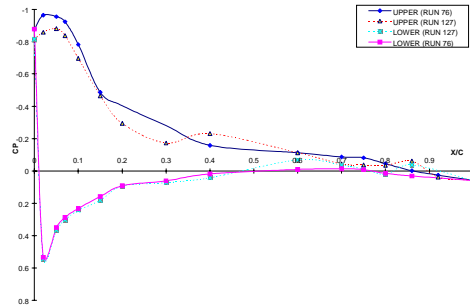


Row B, AOA = 6

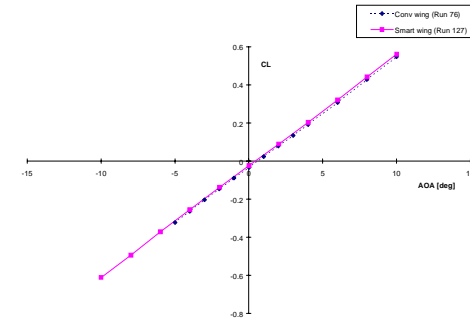
Run 76 vs. 127
 $M = 0.29$, $Q = 120$ psf
 Conventional Flap = 0° Aileron = 0°
 Smart Flap = 0° Aileron = 0°



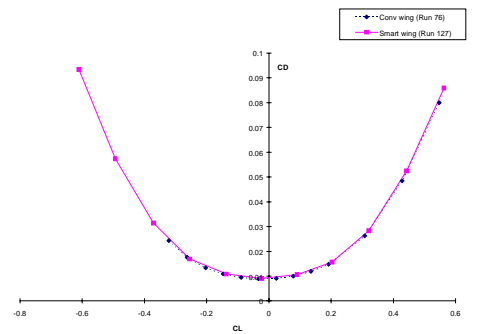
Row C, AOA = 6



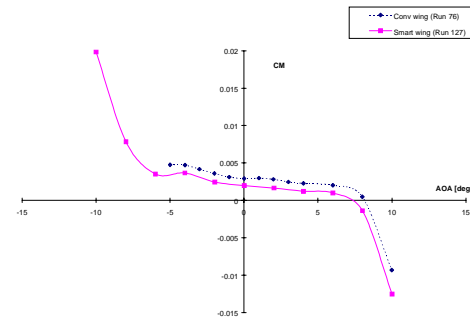
Row D, AOA = 6



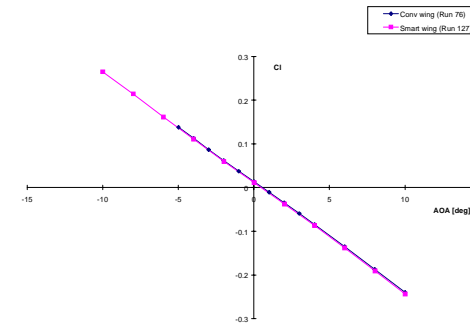
CL vs. AOA



CD vs. CL

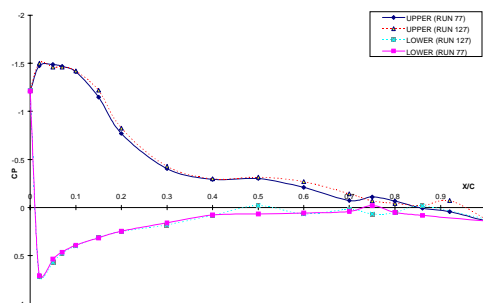


CM vs. AOA

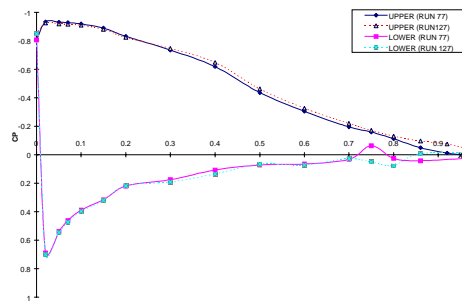


Roll Moment vs. AOA

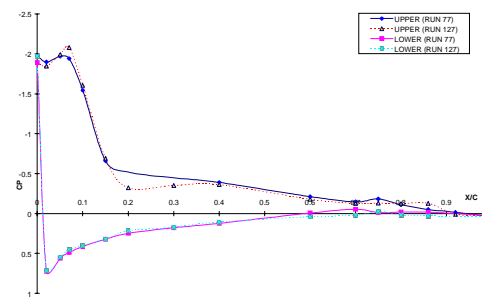
Run 76 vs. 127
 $M = 0.29$, $Q = 120$ psf
 Conventional Flap = 0° Aileron = 0°
 Smart Flap = 0° Aileron = 0°



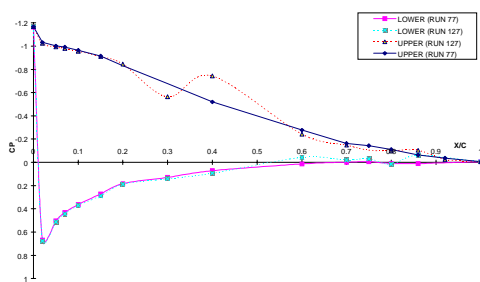
Row A, AOA = 10



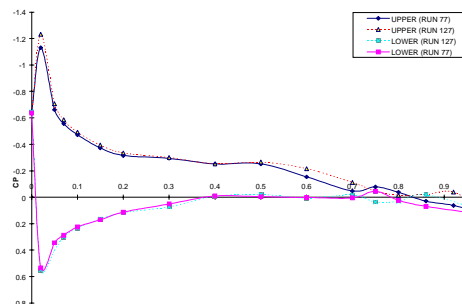
Row B, AOA = 10



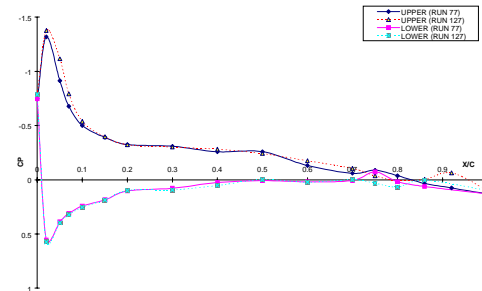
Row C, AOA = 10



Row D, AOA = 10

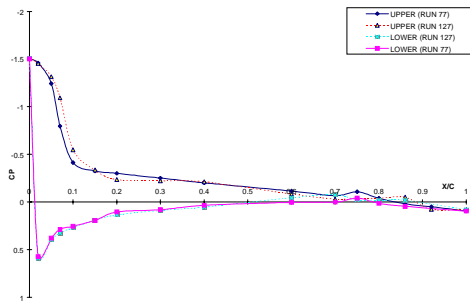


Row A, AOA = 6

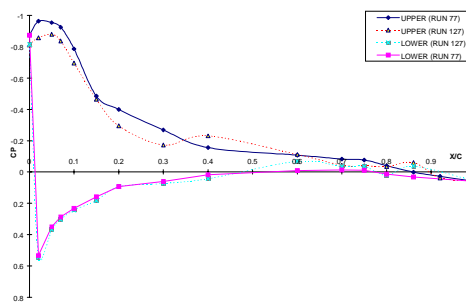


Row B, AOA = 6

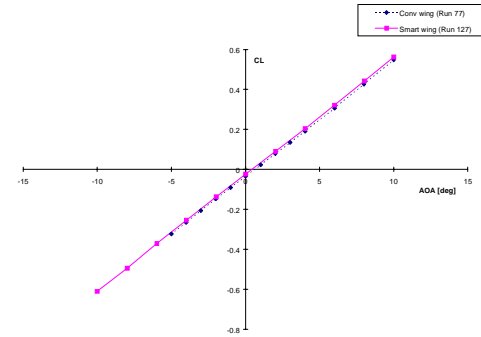
Run 77 vs. 127
 $M = 0.29$, $Q = 120$ psf
 Conventional Flap = 0° Aileron = 0°
 Smart Flap = 0° Aileron = 0°



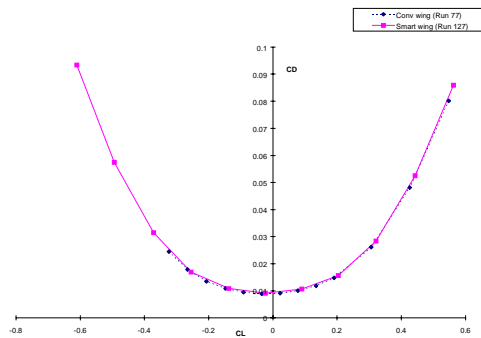
Row C, AOA = 6



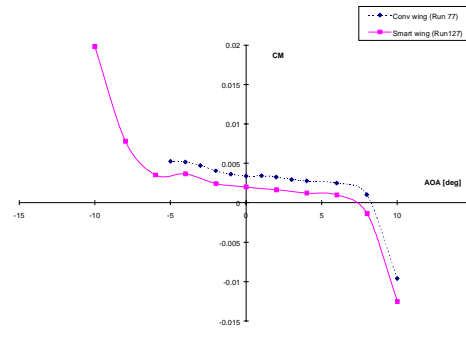
Row D, AOA = 6



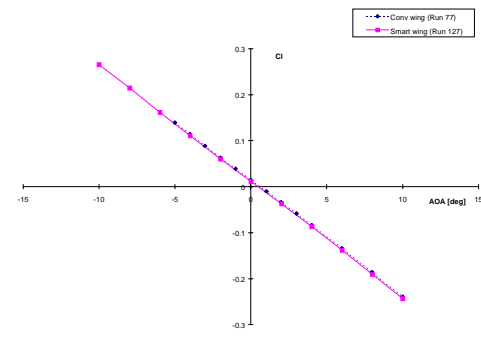
CL vs. AOA



CD vs. CL

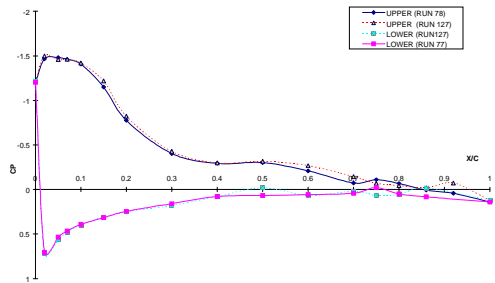


CM vs. AOA

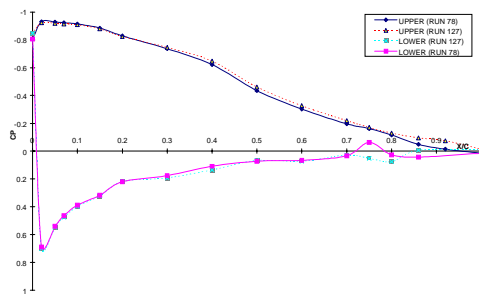


Roll Moment vs. AOA

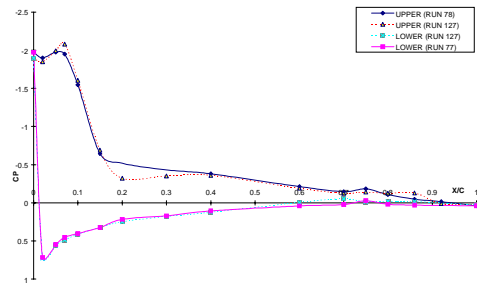
Run 77 vs. 127
 $M = 0.29$, $Q = 120$ psf
 Conventional Flap = 0° Aileron = 0°
 Smart Flap = 0° Aileron = 0°



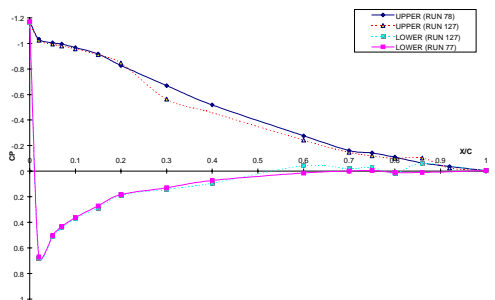
Row A, AOA = 10



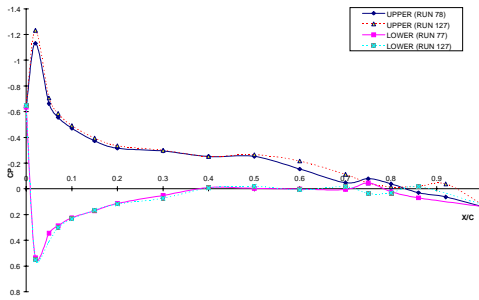
Row B, AOA = 10



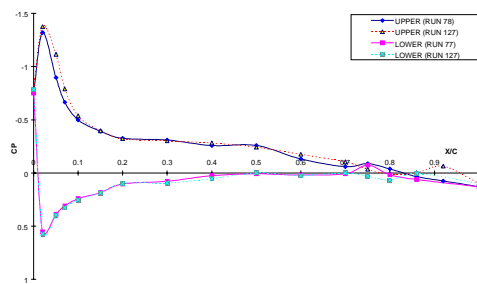
Row C, AOA = 10



Row D, AOA = 10

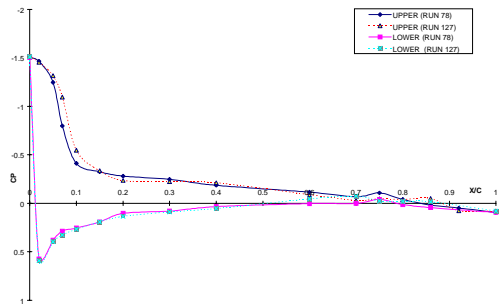


Row A, AOA = 6

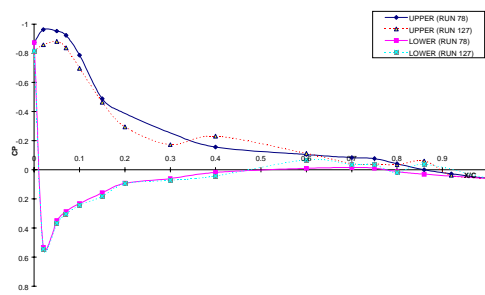


Row B, AOA = 6

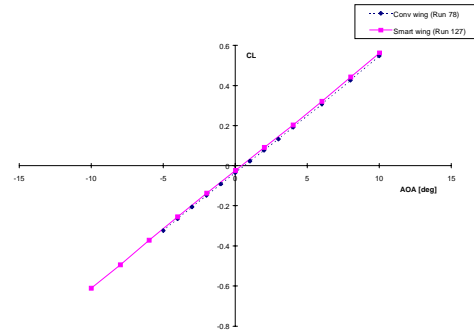
Run 78 vs. 127
 $M = 0.29$, $Q = 120$ psf
 Conventional Flap = 0° Aileron = 0°
 Smart Flap = 0° Aileron = 0°



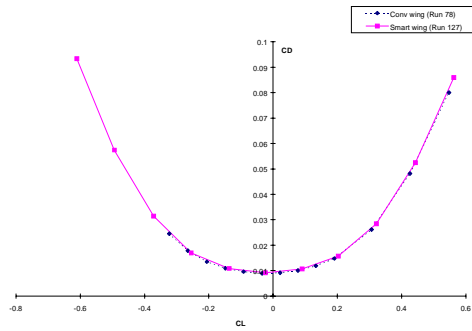
Row C, AOA = 6



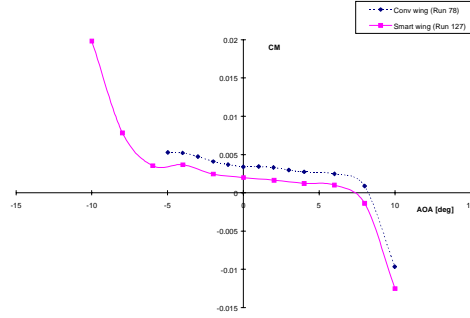
Row D, AOA = 6



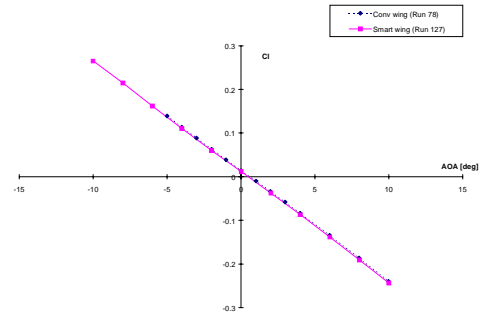
CL vs. AOA



CD vs. CL



CM vs. AOA



Roll Moment vs. AOA

Run 78 vs. 127
 $M = 0.29$, $Q = 120$ psf
 Conventional Flap = 0° Aileron = 0°
 Smart Flap = 0° Aileron = 0°

VOLUME IV

PRE-TEST AND STRESS REPORTS

Table of Contents

VOLUME IV PRE-TEST AND STRESS REPORTS

Pre-Test Report – Test 1 May 1996.....	IV-A-1
Stress Report – Test 1 May 1996	IV-B-84
Pre-Test Report – Test 2 June 1998.....	IV-C-136
Stress Report – Test 2 June 1998.....	IV-D-197

VOLUME IV

PRELIMINARY

PRE-TEST REPORT

**NORTHROP GRUMMAN
SMART WING WIND TUNNEL MODEL**

ARPA / WRIGHT LAB

**SMART STRUCTURES
AND
MATERIALS - SMART WING**

NASA LANGLEY 16 FT. TDT WIND TUNNEL

APRIL/MAY 1996

PREPARED BY;

**L. B. SCHERER
NORTHROP GRUMMAN
WIND TUNNEL ENGINEERING
T611/GS
310-942-5627**

**C. MARTIN
NORTHROP GRUMMAN
STRUCTURAL METHODS AND ADVANCED TECHNOLOGIES
3852/63
310-332-8198**

APPROVALS;

**J KUDVA
PROGRAM MANAGER, SMART WING
NORTHROP GRUMMAN
MANAGER, STRUCTURAL METHODS AND ADVANCED TECHNOLOGIES**

**R.D. SPRINGFIELD
NORTHROP GRUMMAN
MANAGER, WIND TUNNEL ENGINEERING**

TABLE OF CONTENTS

A1. Introduction / Test Objectives	Page 5
A1.1 Program Overview	Page 5
A1.2 Test Objectives and Overview	Page 5
A1.3 Data Objectives and Purpose	Page 5
A2. Test Schedule	Page 6
A2.1 Model Test Schedule	Page 6
A3. Test Program Staffing Requirements	Page 7
A3.1 Tunnel Operation Times	Page 7
A3.2 User Staffing	Page 7
A4. Description of Test Article	Page 8
A4.1 Model Description	Page 8
A4.2 Model Safety Issues	Page 9
A4.3 Model Installation	Page 11
A5. Model Instrumentation	Page 12
A5.1 Common instrumentation to both Smart Wing and Conventional Wing	Page 13
A5.2 Instrumentation Unique to the Conventional Wing	Page 18
A5.3 Instrumentation Unique to the Smart Wing	Page 18
A6. Data Acquisition / Data Reduction	Page 18
A6.1 Data Acquisition	Page 18
A6.2 Data Reduction	Page 20
A7. Data Output/Presentation	Page 20
A7.1 Tab Output	Page 20
A7.2 Real Time Monitoring and Audible Alarms	Page 20
A7.3 Plotted Data Requirements	Page 20
A8. Test Program	Page 21

A9. Facility	Page 26
A9.1 Tunnel Description and Operating Envelope	Page 26
A10. Terms and Constants	Page 30
A11. Points of Contact	Page 41
A12. Flutter and Dynamics	Page 42
A13. Instrumentation List and Pressure List	Page 62
A14. Data Reduction	Page 70

A1. INTRODUCTION / TEST OBJECTIVES

The following report presents the necessary information to conduct the wind tunnel tests of two semi-span models representative of the F/A-18E/F wing. The test is to be conducted in the NASA Langley 16 Transonic Dynamics Tunnel during late April and the month of May 1996. This test is in support of the "Smart Wing" program under contract F33615-C-95-3202 with ARPA and Wright Labs .

A1.1 PROGRAM OVERVIEW

The purpose of the "Smart Wing" program is to explore new materials and technologies in the development of an adaptive wing capable of changing shape to optimize aerodynamic performance at any flight condition. This technology can be used for both commercial and military aircraft. Smart Wing technologies being examined by Northrop Grumman are the use of Shape Memory Alloys (SMA), piezoelectric actuators, and fiber optic sensors for pressure measurement. SMA and piezoelectric actuators would provide for adaptive wing twist and control surfaces with smooth wing surface contours. Aerodynamic performance benefits of such actuators are optimized L/D at varied flight conditions, improved high lift capability at take-off and landing, enhanced maneuvering, and increased range to mention a few. Fiber- optic pressure transducers on a wing surface would provide for improved flight controls and redundancy for the operation of damaged aircraft.

This is the first of two demonstration wind tunnel tests scheduled for the "Smart Wing" program. The second entry is scheduled in April 1997.

A1.2 TEST OBJECTIVES AND OVERVIEW

The purpose of this first wind tunnel entry is to demonstrate the use and benefits of Shape Memory Alloy (SMA) actuators to provide wing twist and control surface deflections under simulated low speed flight conditions. This will be done by constructing two semi-span wing models, 16 percent scale, representative of the F/A-18E/F aircraft. The first model will be representative of the current F/A-18E/F wing with a remotely controlled hinged trailing edge flap and a manually deflected aileron. The second or Smart Wing model will have a SMA deflected, smooth contour, trailing edge flap and aileron. An SMA torque tube, in addition, will be mounted internally to the main wing structure in both the inboard and outboard sections of the conventional and Smart Wing models to provide wing twist capability. This may or may not be used in the conventional wing but is provided to maintain the same bending and torsion characteristics as the Smart Wing. Smart Wing benefits will be demonstrated by comparing aerodynamic data at similar wind tunnel conditions and configurations for both models.

A1.3 DATA OBJECTIVES AND PURPOSE

The data objectives will be to obtain aerodynamic data and stress levels of the wing structure to validate the benefits and SMA actuator performance. Specifically the following data will be obtained;

- Basic aerodynamic coefficient data from the facility provided model balance.
- Pressure coefficients from model surface static pressures measured with PSI pressure transducers and fiber optic pressure transducers. This will further validate the use of fiber optic pressure transducers against a known pressure measurement standard.

- Principal stresses and strains at six locations in the wing structure through the use of strain gaged rosettes.
- Temperature outputs of the SMA torque tubs and SMA control surfaces with the use of thermocouples. This is both for control of the SMA actuators and monitoring of performance.
- Actual torque of the SMA torque tubes from a full strain gaged bridge on each tube.
- Various model positions such as:
 - Model angle of attack with an inclinometer mounted at the wing root and the facility support system.
 - Model wing twist by the use of tilt sensors distributed out the span of the wing
 - Deflection of SMA flaps using fiber optic strain gages.
 - Deflection of conventional trailing edge flap with a potentiometer.

Model dynamics will be monitored closely throughout the test with four to five accelerometers mounted in each of the models as a safety precaution. Specified strain gages and tilt sensors will serve also for the monitoring of model dynamics.

A2. TEST SCHEDULE

A2.1 MODEL TEST SCHEDULE

The model test schedule has been provided in Figure A1. This schedule includes the ground work leading up to the test. Milestone dates concerning the test are as follows;

Ground Vibration Test at Northrop Grumman	March 22 - March 27
Delivery of models to NASA Langley	April 3
Ground Vibration Test at NASA Langley	April 5 - April 12
Model Systems Set-up and Checkout	April 10 - April 28
Model Installation Start	April 29
Testing of Conventional Wing	May 4 - May 8
Testing of Smart Wing	May 4 - May 27
Removal of Model and User Equipment	May 28

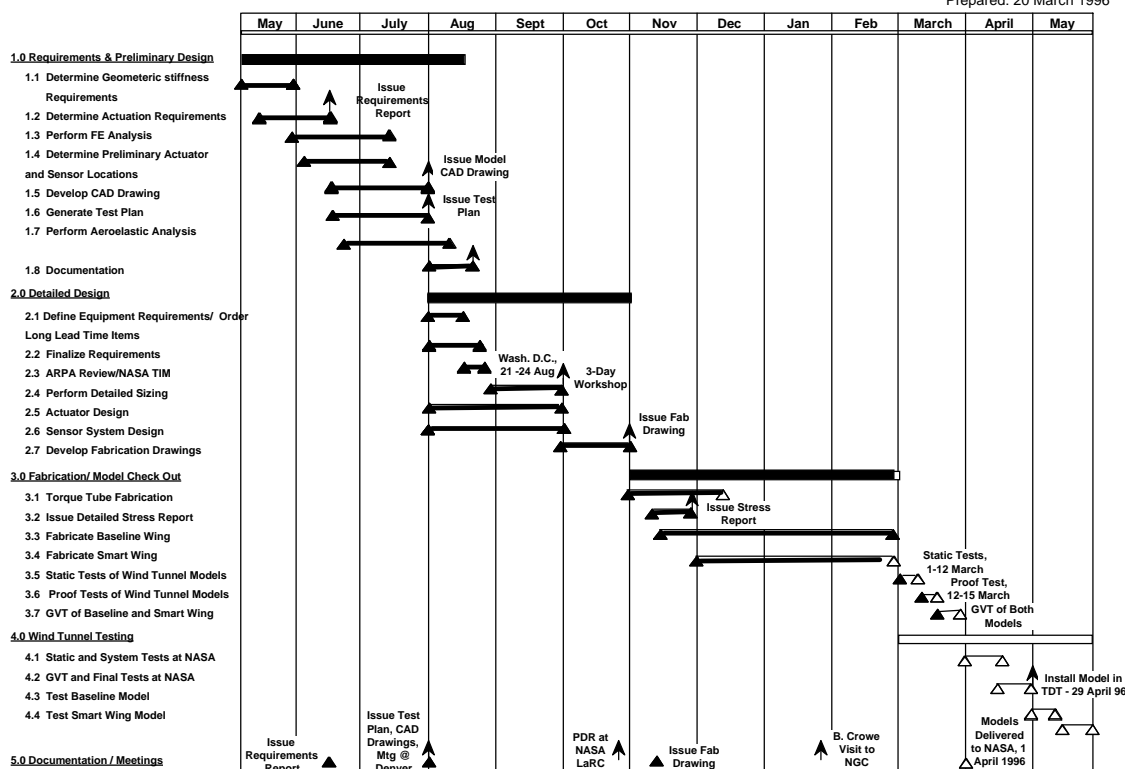


Figure A1. First Wind Tunnel Entry Schedule

A3. TEST PROGRAM STAFFING REQUIREMENTS

A3.1 TUNNEL OPERATION TIMES

The tentative 16 TDT tunnel operation time will be twelve hour days (with the option to decrease to eight), five days a week. Start time will be tentatively 6:30 AM to end of shift at 6:30 PM which includes an approximate one and a half hour for the facility to start up and one hour for the facility to shut down systems (dependent on tunnel conditions) at the end of shift. Model work, data analysis, and instrumentation/ data system set-up work may be done in the off-hours if required.

A3.2 USER STAFFING

Northrop Grumman will support the test on-site with a test engineer, instrumentation engineer, model technician, and two representatives from the Advanced Structural Technologies group. Lockheed Martin and F & S Fiber Optic Technology will each have a representative at the test as well to support their respective systems.

A4. DESCRIPTION OF TEST ARTICLE

A4.1 MODEL DESCRIPTION

Two models of the Smart Wing will be tested. Each of the models are representative of a 16% scale version of the F/A-18E/F right wing. The only modification to the wing contour and planform is the inboard section in which the leading edges have been extended inboard to the fuselage centerline of the F/A-18E/F aircraft. This root section airfoil shape has also been thickened by about 75% for additional model support. Both of the models are identical in construction with the exception of the trailing edge flap and the aileron. The conventional wing has an electrically driven hinged trailing edge flap and a manually deflected aileron identical in planform and contour to the existing F/A-18E/F aircraft. The Smart Wing has an SMA remotely actuated two segment trailing edge control surface/ flap.

The models were designed to provide the capability of twisting the wing inboard and outboard with SMA torque tubes. The main support structures of the models are three aluminum spars out the span of each wing as shown in Figure A2. These spars are joined together by two cross members at the root and at 5.3% span. The model is then covered with aluminum skins with ribs to prevent skin buckling under bending and torsion. The leading edge of the models are rigid and will not be deflected during the test.

On the center wing spar are located two SMA torque tubes, one inboard and one outboard. These torque tubes will have the capability of twisting the wing +5 degrees leading edge up at the wing tip in relation to the wing root. The SMA torque tubes may or may not be used on the conventional wing, but were installed to match the bending and torsion characteristics between the two models.

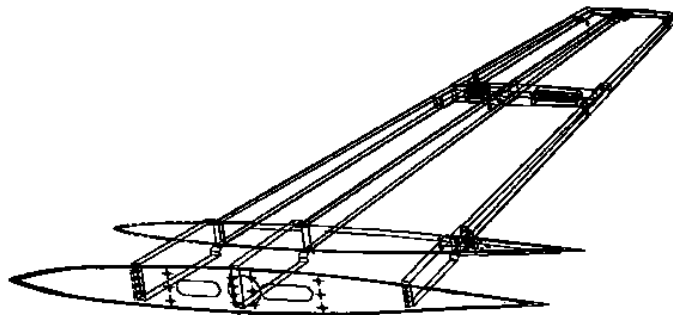


Figure A2. Model Main Spars and Ribs

The conventional wing has a remotely actuated trailing edge flap with a deflection angle range of 0 to +15 degrees trailing edge down. The aileron on the conventional wing is manually deflected by the use of brackets mounted at the end of the control surface. Brackets have been made for the following angles; 0, ± 5 , ± 7.5 , ± 10 , and ± 15 degrees.

The trailing edge flap and aileron on the Smart Wing will be deflected remotely by controlling the actuation of the SMA wires located in the respective RTV skins. The SMA flap and aileron will each have an independently controlled upper and lower SMA wire set. A smooth contour deflection is accomplished by contracting either the upper or lower SMA wire set. Maximum deflection expected is \pm one inch which corresponds to approximately ± 10 degrees.

A4.2 MODEL SAFETY ISSUES - FLUTTER AND STRESS ANALYSIS

Wind Tunnel Dynamics and Flutter Analysis

This report presents vibration and aeroelastic characteristics of the two wind tunnel models which are designed for testing in the NASA Langley's transonic dynamic tunnel (TDT). Conventional Wing represents a basic wing with conventional trailing edge control surfaces. The inboard trailing edge flap is attached to a worm gear assembly which in turn is driven by an electric motor. The out board control surface (aileron) will be set manually to 0, ± 5 , ± 10 degrees. Smart Wing is identical to Conventional Wing except the trailing edge control surfaces are made of SMA materials and are firmly fixed to the rare spare of the wing box. The control surfaces weigh about two pounds more than the conventional control surfaces.

Structural Model

The structural model consists of an assembly of wing box, and trailing edge inboard and outboard control surfaces. The wing box consists of three spars and five ribs, upper and lower skin surfaces. The mid spar is placed along the elastic axis of the wing box. The inboard section of the wing (up to Y station =7.0 inch) is made very stiff. The wing box consists of 345 CBAR elements and 219 CQUAD4 elements. The control surfaces were represented by FEM elements. The leading edge control surfaces are fixed to the front spar in both cases.

Vibration Analysis

Vibration analysis of the structural model discussed above was performed. The first twelve natural vibration modes in the frequency range 1 through 500 Hz were calculated. Figure A3 lists the frequencies of the first twelve modes for Conventional Wing and Smart Wing. Vibration modal deformations for the first six modes are shown in Figures A19 through A24 for Conventional Wing and in Figures A25 through A30 for Smart Wing. The dominating features of the mode shapes are:

Conventional Wing

Mode Number	Mode Type	Frequency
Mode No. 1	first wing bending	33.6 Hz.
Mode No. 2	TE control surface rotation	61.5 Hz.
Mode No. 3	wing torsion + TE flap rotation	87.7 Hz.
Mode No. 4	second wing bending	131.0 Hz.
Mode No. 5	wing bending & torsion	143.0 Hz.
Mode No. 6	second wing bending & TE flap bending	201.0 Hz.

Smart Wing

Mode Number	Mode Type	Frequency
Mode No. 1	first wing bending	35.4 Hz.
Mode No. 2	wing torsion	83.7 Hz.
Mode No. 3	second wing bending	127.0 Hz.
Mode No. 4	second torsion	198.0 Hz.
Mode No. 5	wing bending & torsion	218.0 Hz.
Mode No. 6	wing bending and second torsion	241.0 Hz.

Figure A3. Vibration Mode Frequencies

Aeroelastic Analysis

Aeroelastic analysis (flutter and divergence) was performed using ASTROS, a design software developed by Northrop for the Air Force. The aerodynamic model used in this study is shown in Figure A4. Four spline surfaces were used to relate the structural data and the aerodynamic data. The flutter analysis using 12 vibration modes was conducted for Mach numbers; 0.2, 0.3, 0.5, and 0.6 with density ratios; 0.2, 0.5, and 1.0. These density ratios correspond to tunnel running conditions at $P_T=600, 1100, 2200$ PSF, respectively. Typical flutter solutions in terms of damping vs. equivalent dynamic pressure (Q_{eq} in PSF) and frequency vs. dynamic pressure (Q_{eq} in PSF) are presented in Section A12 and the Stress Report:

Figures A31 through A34 for Mach number 0.5, Conventional Wing
Figures A35 through A37 for Mach number 0.6, Conventional Wing
Figures A39 through A42 for Mach number 0.5, Smart Wing
Figures A43 through A46 for Mach number 0.6, Smart Wing

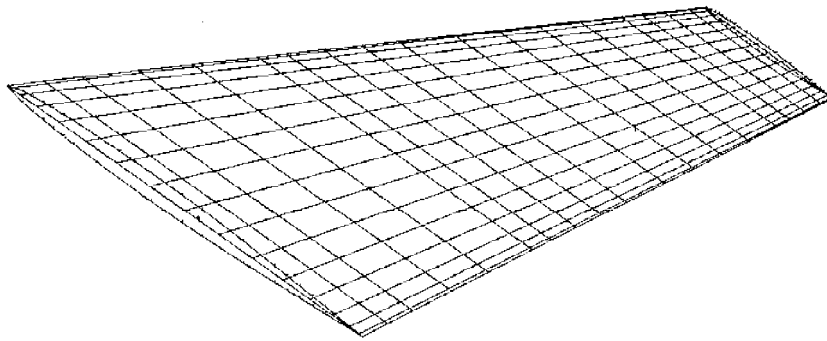


Figure A4. Steady Aerogrid Model

Critical Q is found when the damping curve passes through zero from negative to positive value. At Mach, $M=0.5$, both wings; Conventional Wing and Smart Wing, are free from aeroelastic instability for density ratios 0.25 through 1.0 (i.e. up to $Q = 800$ PSF). However, at Mach, $M=0.6$, Conventional Wing (with conventional flap) flutters in mode two (inboard control surface mode) at $Q_{eq}=158$ PSF with density ratio of 0.2, and at $Q_{eq} = 625$ PSF with density ratio

of 1.0. These, dynamic pressures are well above the test condition which is limited to $Q=120$ PSF. Moreover, the operating Mach number is also limited to $M=0.5$. Hence, the Conventional Wing test model is free of flutter and divergence instabilities. The Smart Wing model with SMA control surfaces, unlike Conventional Wing, is stable at all density ratios up to $M=0.6$. The plots of frequencies vs. equivalent dynamic pressure show very little change in the frequencies. This suggests that the aerodynamic stiffness and aerodynamic damping are small compared to the structural stiffness, and hence, the models are stable in the desired test range.

Stress Analysis

The stress analysis for both of the models is spelled out in detail in the Stress Report (Appendix B).

A4.3 MODEL INSTALLATION

The model(s) will mount to the existing facility semi-span support system which will be located on the west tunnel wall. The installation system as shown in Figure A5 consists of a flow splitter plate mounted 41 inches off the tunnel wall, a turn-table for model pitch rotation located in the tunnel plenum, a spindle between the balance and the turn-table, and a semi-span balance connected to the model via an L-bracket and pedestal. The main flow splitter plate is used to isolate the wing from flow disturbances caused by the support system and to provide a reduced tunnel wall boundary layer at the model. As shown in the Figure A5, there is a round splitter plate, 16.75 inches in diameter attached to the model which provides a larger attachment area for the model and allows larger access for instrumentation cabling. This round splitter however, will add small additional aerodynamic forces to the balance as it is attached to the model and does not touch the main splitter section.

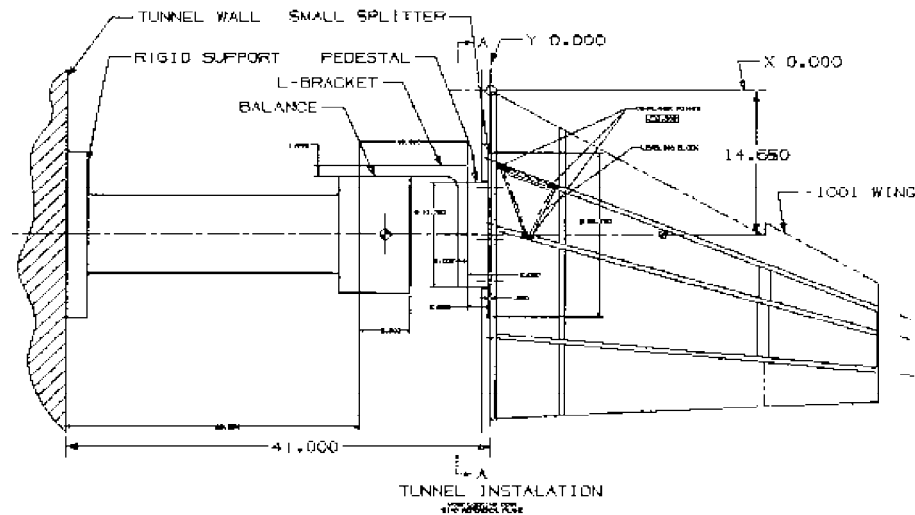


Figure A5. Model Installation

All model electrical instrumentation cabling and pneumatic tubing will route through the pedestal and L-bracket and looped around the balance as not to impose any unwanted load.

A5. MODEL INSTRUMENTATION

Each of the models are extensively instrumented with surface static pressures, strain gages, accelerometers, and various control surface instrumentation. Main aerodynamic data will be obtained from the NASA Langley five-component strain gaged balance designated TDT 01SM. This balance was designed for semi-span models such as the Smart Wing model. The maximum load range for each gage component is as follows;

Normal Force	1500 lbs.
Axial Force	120 lbs
Pitching Moment	6000 in-lb
Yawing Moment	3000 in-lb
Rolling Moment	30,000 in-lb

The balance will mount to the model support located in the “canoe” fairing between the splitter plate and tunnel wall. All model instrumentation cabling will be looped around the balance as not to impart any unwanted loads on the balance.

Much of the model instrumentation is identical in location, number, and type between the “Smart Wing” model and the conventional model. Differences occur in the control surface monitoring and actuation systems. Instrumentation nomenclature and summary has been identified in Section A13 Figure A47.

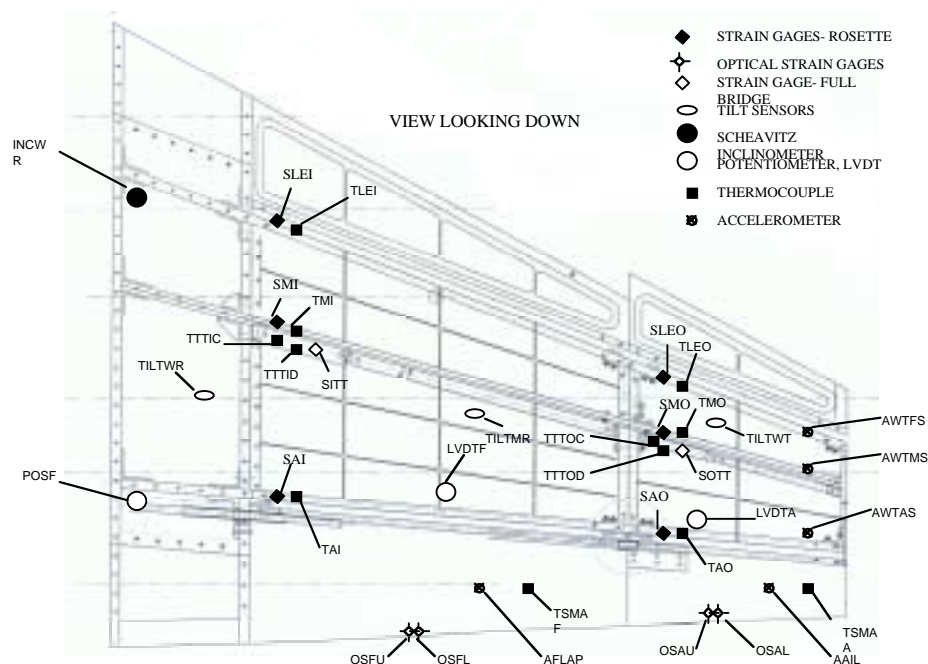
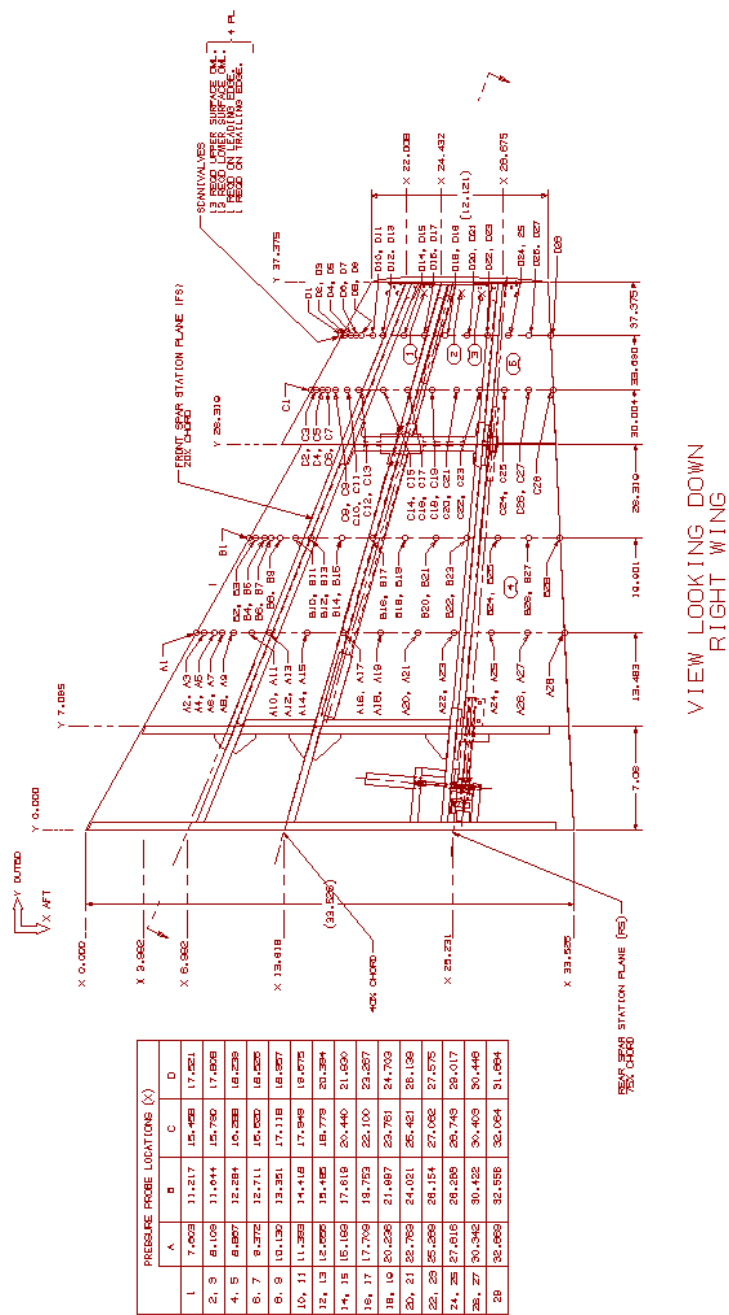


Figure A6. Smart Wing Internal Instrumentation Location

A5.1 COMMON INSTRUMENTATION TO BOTH “SMART WING” AND CONVENTIONAL WING

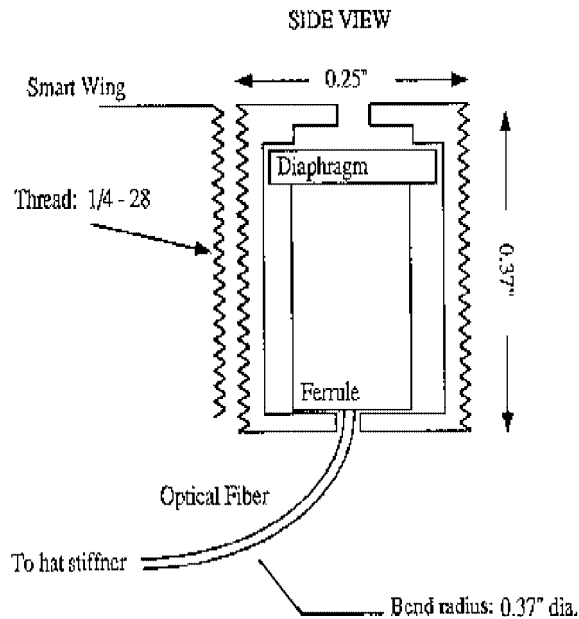
Steady State Pressures

Each of the models will have four chordwise rows of static pressures as shown in Figure A7. The pressure tubing will route through the “canoe” fairing and tunnel wall into the tunnel plenum. Each of the pneumatic tubing will connect to a port on one of five Northrop Grumman supplied PSI modules. Four of the modules contain ± 1 psid rated transducers. The remaining module used will be ± 5 psid rated. static pressures on the upper leading edge surface in each chordwise row will be connected to the ± 5 psid rated module. Pressure hook-up locations are provided in Section A13 Figures A48 thru A52. The modules will be operated and calibrated on-line by the NASA Langley PSI 8400 Control System. A water-cooled plate surrounded by a thermally isolated box will be used to house the modules. This is to maintain a stable temperature which minimizes transducer drift and the need for frequent re-calibration of the modules while running. Ports 1 and 32 on each PSI module will be connected to a known pressure for verification and PSI system health monitoring during the test.



Optical Pressure Transducers

Ten fiber optic pressure transducers will be located in close proximity to the upper surface static pressures in the two inboard chordwise rows. These transducers will be connected to a FOSS system supplied by F & S Fiber Technologies. Pressure data output from this system will be sent to the NASA Mod Comp Acquisition system for recording with other data inputs.



95-368

Figure A8. Detail of Fiber Optic Pressure Hook-Up

Accelerometers

Five accelerometers will be mounted in each model, three in the main wing box and one in each control surface for tracking model dynamics. The Endevco accelerometers model number 2220D-5 are rated at 200 Gs. These accelerometers will be connected to both strip chart and spectrum analyzers for model and control surface dynamic monitoring.

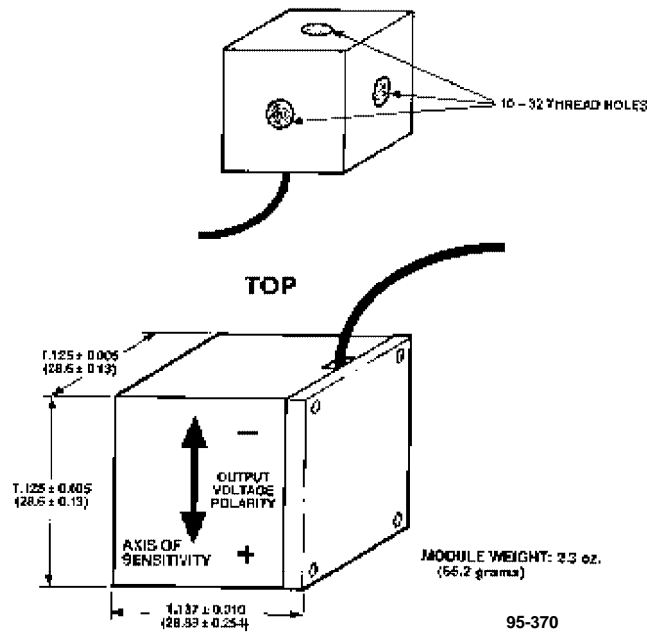


Figure A9. Accelerometer Detail

SMA Torque Tube Actuators

Two SMA torque tube actuators will be located in the wing, one on the inboard center wing spar and one on the outboard center wing spar. The torque tubes will be actuated with Ni-Chrome wire heaters inside of each torque tube. Since the actuation of the SMA torque tubes is temperature dependent, two thermocouples (Type "T" RDX Corp. Model No. 20114-L25) will be attached to each torque tube. One thermocouple for control and one for monitoring into the facility data system. Control of these actuators will be done via a Northrop Grumman supplied control system. Each actuator will also contain a strain gaged bridge to measure the amount of torque being applied. Calibration of these gages will be done prior to test. The outputs of the strain gaged bridges will be fed into the NASA Mod Comp acquisition system.

Tilt Sensors

Three tilt sensors will be mounted in the wing box to measure wing twist. The tilt sensors are Analog Devices ADXL50 accelerometers. The accelerometers work by using a vibrating beam that changes its frequency with the acceleration. The device is sensitive enough to measure its own rotation, and when coupled to the structure will give the structures general tilt. The signal conditioning of these tilt sensors will be done by Northrop Grumman with the output signals being sent to the NASA Mod Comp System.

Strain Gage Rosettes

Six strain gage rosettes shall be mounted on the wing spars, one rosette on the inboard and outboard of each of the three wing spars. The rosettes will measure stress and strain on each of the three spars. Signal conditioning of the strain gages will be Northrop Grumman supplied however, all output signals from these gages will be sent to the NASA Mod Comp Acquisition system for final data reduction. Each rosette shall have a thermocouple (Type "T" RDX Corp. Model No. 20114-L25) for temperature correction if required. The thermocouple outputs will be connected to the NASA thermocouple reference box and the output signals connected to the facility Mod Comp acquisition system.

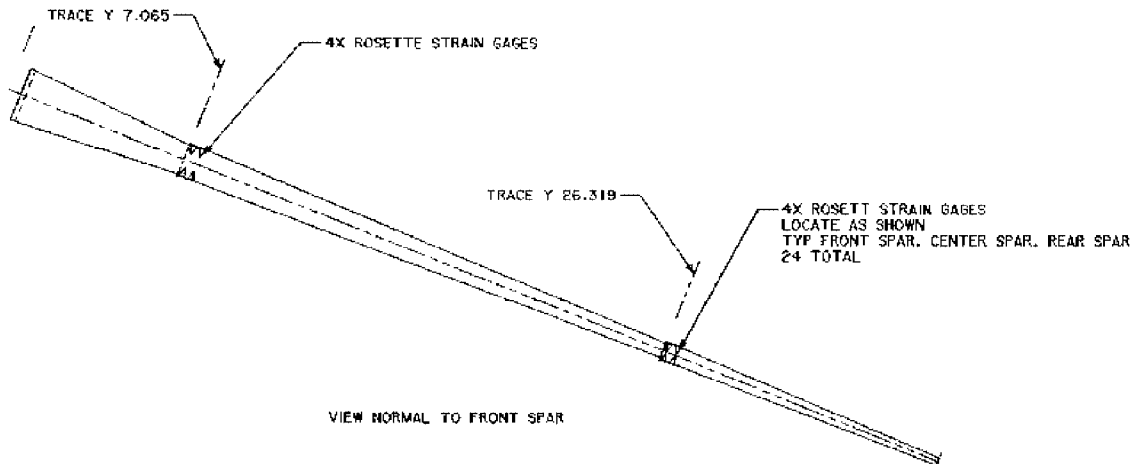


Figure A10. Strain Locations on Spar

Model Attitude

A Scheavitz inclinometer will be mounted in the wing root as shown in Figure A6 to measure model pitch angle. Calibration of the inclinometer will be done with the model installed. In addition, model position will be calculated with the facility support system.

External Optical System for Model Wing Twist and Control Surface Deflection Measurement

A NASA Langley Digital Camera System will be installed in 16 TDT to measure model twist and control surface deflection. This will be done by installing round disks or targets of retro-reflective tape on the lower wing surface. Approximately 27 targets will be used in four rows. The optical camera system will be mounted forward of the model in the tunnel floor with a 45 degree up-look angle to the horizon. The system will measure x, y locations of each of the targets. From that information the system will derive angles, wing twist, and control surface deflections relative to the inboard targets and wind off conditions. The model surface will be painted a flat black to maximize the targets resolution.

A5.2 INSTRUMENTATION UNIQUE TO THE CONVENTIONAL WING

Trailing Edge Flap Actuation System

The inboard trailing edge flap will be controlled via an electric Globe motor and flap position will be measured with a Bourns rotary potentiometer. Control of the flap will be done with a Northrop supplied system located in the control room. Limit switches will be provided to prevent the flap going beyond +15 degrees in the positive direction or 0 degrees in the negative direction.

A5.3 INSTRUMENTATION UNIQUE TO THE SMART WING

SMA Inboard Trailing Edge Flap and Aileron Actuation System

Both the inboard trailing edge flap and the aileron will have a built in SMA actuation system in the skins. The SMA control surfaces will include independent systems in the upper and lower skins in the flap and aileron. Controllers for this system will be provided by Lockheed Martin and will be located in the tunnel control room. A thermocouple (Type "T" RDX Corp. Model No. 20114-L25) will be installed in the flap and aileron for temperature monitoring during operation.

SMA Inboard Trailing Edge Flap and Aileron Actuation System (Cont.)

Real time measurement of the control surfaces deflection will be done by two methods. The first will be the use of linear LVDTs, one for the flap and one for the aileron. The second method will measure deflection through the use of fiber optic strain gages measured on F & S Fiber Optic Technologies System. A fiber optic strain gage will be located near the trailing edge, upper and lower surfaces, of the flap and aileron. All conditioned outputs from the fiber optic strain gages and LVDTs will be sent to the Facility Mod Comp for final data processing.

A6. DATA ACQUISITION / DATA REDUCTION

A6.1 DATA ACQUISITION

All conditioned signal inputs from model instrumentation will be acquired by the facility Mod Comp acquisition system. Northrop Grumman and Lockheed Martin will provide signal conditioning for the model instrumentation with the exception of pressure data from the PSI Modules, thermocouples, and main balance data. Figure A11 shows a block diagram of the wind tunnel set-up with all the inputs to the MODCOMP and responsible party. All data outputs from the facility Mod Comp system will be in engineering units and sent to either a user supplied and/or facility supplied Macintosh computer system. Some of the signal outputs will be split from the facility optical patch panel to user supplied acquisition and control systems for the SMA actuators. (Those instrumentation signals to the optical patch panel have been defined in Figure A10). FNS Technologies will acquire all outputs from the fiber optic pressure transducers and strain gages. Data from the fiber optic system will be sent to the Mod Comp in engineering units.

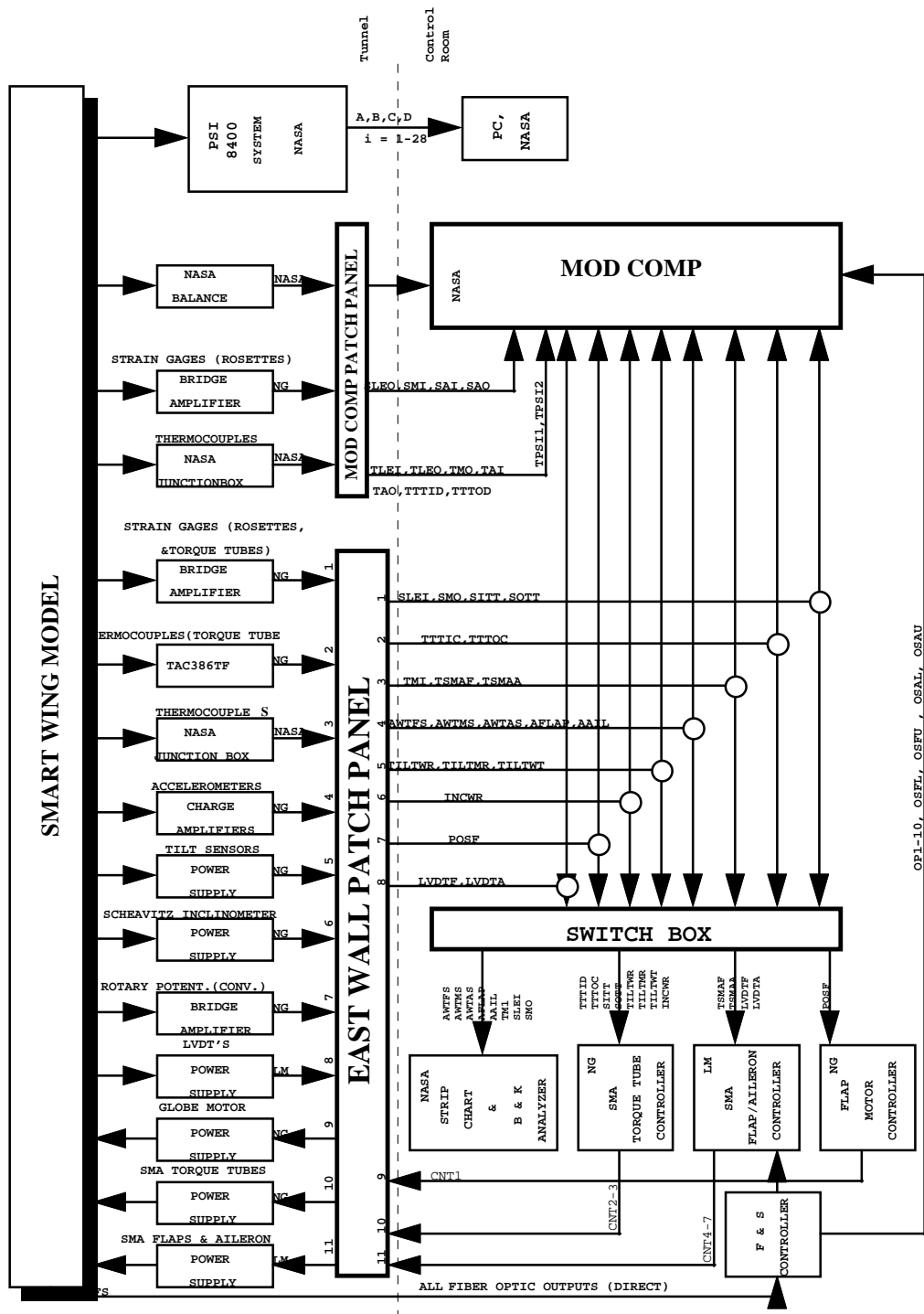


Figure A11. Instrumentation Block Diagram

A6.2 DATA REDUCTION

Data will be reduced to engineering units and coefficient form. Data reduction methodology has been provided in Section A14. A listing of the parameters being calculated has been provided in Section A10 with a constant listing also included in that section.

A7. DATA OUTPUT / PRESENTATION

A7.1 TAB OUTPUT

Data will be printed out in tabulated form after a run by the facility. Those parameters into run, test point no, tunnel parameters, balance output, and model position. In addition, a file in Excel will be created and transferred to a user supplied Macintosh. Excel macros will be provided to further reduce the data to coefficient form for the balance and pressure output, stress and strains from the strain gages, and integration of pressure rows for local coefficient data. This data will be reduced off-line during the test.

A7.2 REAL TIME MONITORING AND AUDIBLE ALARMS

Outputs of certain instrumentation will be monitored for safety purposes. These include the accelerometers, two of the strain gage rosettes (Inboard forward spar, SLEI, and the outboard mid spar, SMO), two thermocouples, and one tilt sensor. This equipment will be monitored on a facility supplied B & K Spectrum Analyzer and a strip chart. Those specific parameters to be connected to the spectrum analyzer and strip chart are called out in Section A12 under the general instrumentation layout.

Other real time systems or controllers for such instrumentation such as the fiber optic pressure transducers and strain gages, the SMA torque tubes, and the SMA flap and aileron will require real time monitoring of specific parameters. The systems needing such parameters and the parameters required are called out in Section A12 under the general instrumentation layout. Those parameters will be used for the real time control of the SMA actuators during the test.

A7.3 PLOTTED DATA REQUIREMENTS

Plotted data formats will be provided by the user on Excel macros prior to the start of the test. Plot formats required are as follows;

Pressure Data

C_{p_i} vs X/C

CN local chord vs ALP1

CA local chord vs ALP1

CM local chord vs ALP1

CN/CA local chord vs ALP1

C_p vs η at the following chord locations $\eta = 10, 30, 50, 60, 80, 90\%$

Balance Force and Moment Data

CN vs ALP1
CL vs ALP1
CL vs CD
CL/CD vs ALP1
CM vs ALP1
Cls vs ALP1

A8. TEST PROGRAM

The principal test variables for the Smart Wing program are as follows:

Tunnel Stagnation Pressure	P_o
Tunnel Dynamic Pressure	Q
Aileron deflection	δ_A
Flap deflection	δ_F
Wing Twist	θ
Angle of Attack	α

A test matrix has been developed to experimentally demonstrate the benefits of warping or bending of aerodynamic surfaces as compared to conventionally hinged control surfaces. The principal measure of success is reduction in drag. Other benefits to be investigated include reduction in control surface deflections for fixed maneuver loads and potential applicability to flutter suppression or gust load alleviation.

Three flap deflections (0, 5, and 15 degrees) and seven aileron deflections (0, ± 5 , ± 10 , and ± 15) are to be tested separately and in combination. The wind tunnel parameters (Q and P_o) are varied to see how performance is effected by dynamic pressure and Mach number. A chart showing the required tunnel conditions is presented in Figure A12. This chart presents a plot of dynamic pressure (Q) versus Mach number (M). Three curves are shown representing the three tunnel stagnation pressures specified: 2100, 1100, and 600 psf. Points on the chart represent the specified dynamic pressure levels to be tested: 40, 60, 80, 100, and 120 psf. An overall variation in Mach number of 0.15 to 0.6 can be obtained. An effort has been made to minimize the number of changes in tunnel stagnation pressure to save on pump-down time. A prioritization of tunnel conditions is yet to be done and this will significantly reduce the number of conditions. High priority conditions are those which give the largest independent variations in Q and Mach number. Maximum Q variation will most likely be obtained at a tunnel stagnation pressure of 2200 psf where the Mach number varies the least (.15 to .28). Maximum Mach number variation, at constant Q , will likely be set at the higher Q levels and the stagnation pressure varied. At Q of 120, the Mach number varies from 0.28 to 0.6.

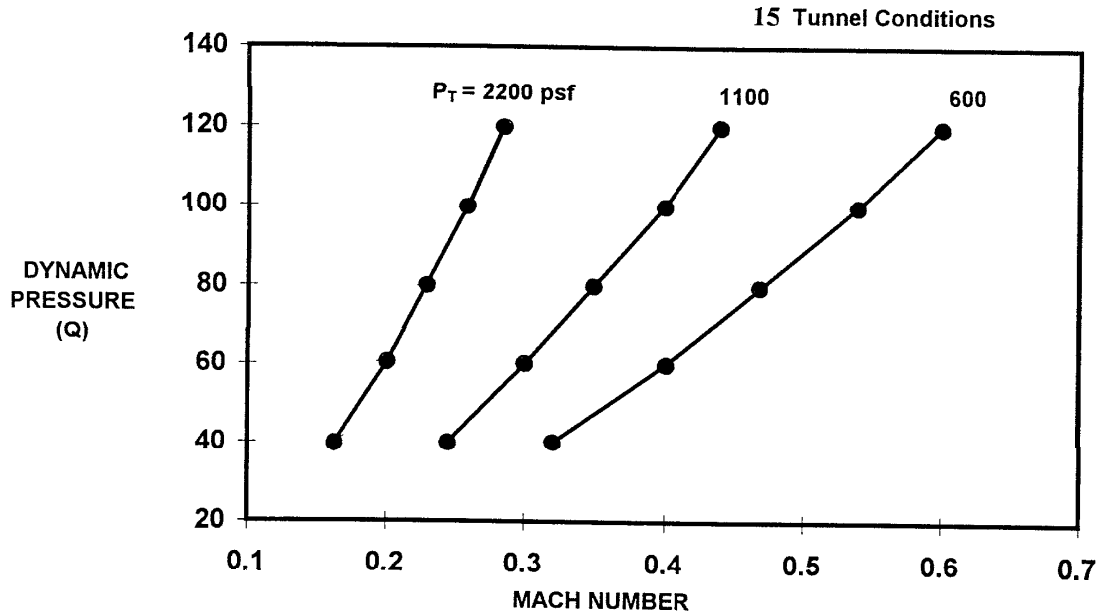


Figure A12. Smart Wing Test Conditions

The test matrices for the Conventional Wing and Smart Wing are presented in Figures A13 and A14 respectively. At the present time the two matrices are identical. Run numbers for each wing model correspond to alpha sweeps and are shown in the first column. Aileron deflection shown in the second column, is set manually with brackets and requires entry into the tunnel. Therefore aileron changes shall be kept to a minimum. Similarly, tunnel pressure changes are slow and therefore kept to a minimum. Flap deflection and wing twist changes are achieved remotely. Alpha sweeps are relatively fast and therefore are repeated for each new condition. It should be noted that the 15-degree flap and ± 15 -degree aileron are shown as optional configurations, to be determined at time of test. Configuration numbers, shown in the last column correspond to any change in model parameters.

The proposed test point sequence is presented in Figure A15. There are 450 test points for each wing if all conditions are tested. Section A shows all test points and how they come about for one aileron deflection (0 degrees) and one tunnel pressure. Five flap deflections are obtained and all Q values are set for each flap deflection. Section B is condensed to show the continuing sequence of test points but shows only for tunnel pressure variation. Section C is a further condensation to show the continuation of test points for variation in aileron deflection. The last 30 points (421 - 450) are devoted to wing twist points which are to be performed as the last configurations of each model entry because of potential re-zeroing problems.

The Conventional wing is to be tested first. A database is to be established. Then the Smart Wing will be tested and performance will be compared to that of the conventional wing.

Model: CONVENTIONAL WING - W17

* indicates tunnel opened for model

Run No. (alpha sweeps)	Aileron (deg)	Po (psf)	Flap (deg)	Twist (deg)	Q (psf)	Alpha (deg)	Notes
1 to 20	0	2200	F1	0	Q1	A1	* configs. 1-4
21 to 40		1100		0			
41 to 60		600		0			
61 to 80	5	2200		0			* configs 5-8
81 to 100		1100		0			
101 to 120		600		0			
121 to 140	10	2200		0			* configs 9-12
141 to 160		1100		0			
161 to 180		600		0			
181 to 200	15	2200		0			* configs 13-16
201 to 220		1100		0			
221 to 240		600		0			
241 to 260	-5	2200		0			* configs. 17-20
261 to 280		1100		0			
281 to 300		600		0			
301 to 320	-10	2200		0			* configs. 21-24
321 to 340		1100		0			
341 to 360		600		0			
361 to 380	(-15)	2200		0			* configs. 25-28
381 to 400		1100		0			
401 to 420		600		0			
421 to 425	0	2200	0	3			* configs. 29-32
427 to 430		1100					
431 to 435		600					
436 to 440		2200		5			* configs. 33-36
441 to 445		1100					
446 to 450		600					

F1 = 0, 5, 10, (15) degrees

Q1 = 40, 60, 80, 100, 120 (psf)

A1 = -4, -2, -1, 0, 1, 2, 3, 4, 6, 8 (degrees)

Items in parentheses () are optional

Figure A13. Conventional Wing Test Matrix

Model: SMART WING - W2

* indicates tunnel opened for model

Run No. (alpha sweeps)	Aileron (deg)	Po (psf)	Flap (deg)	Twist (deg)	Q (psf)	Alpha (deg)	Notes
1 to 20	0	2200	F1	0	Q1	A1	configs. 1-4
21 to 40		1100		0			
41 to 60		600		0			
61 to 80	5	2200		0			configs 5-8
81 to 100		1100		0			
101 to 120		600		0			
121 to 140	10	2200		0			configs 9-12
141 to 160		1100		0			
161 to 180		600		0			
181 to 200	15	2200		0			configs 13-16
201 to 220		1100		0			
221 to 240		600		0			
241 to 260	-5	2200		0			configs. 17-20
261 to 280		1100		0			
281 to 300		600		0			
301 to 320	-10	2200		0			configs. 21-24
321 to 340		1100		0			
341 to 360		600		0			
361 to 380	(-15)	2200		0			configs. 25-28
381 to 400		1100		0			
401 to 420		600		0			
421 to 425	0	2200	0	3			configs. 29-32
427 to 430		1100					
431 to 435		600					
436 to 440		2200		5			configs. 33-36
441 to 445		1100					
446 to 450		600					

F1 = 0, 5, 10, (15) degrees

Q1 = 40, 60, 80, 100, 120 (psf)

A1 = -4, -2, -1, 0, 1, 2, 3, 4, 6, 8 (degrees)

Items in parentheses () are optional

Figure A14. Smart Wing Test Matrix

	Test Point No.	Aileron	Pres	Flap	Twist	Q	Notes
Section A	1	0	2200	0	0	40	
	2					60	
	3					80	
	4					100	
	5					120	
	6			5		40	
	7					60	
	8					80	
	9					100	
	10					120	
	11			10		40	
	12					60	
	13					80	
	14					100	
	15					120	
	16			(15)		40	
	17					60	
	18					80	
	19					100	
	20					120	
Section B	21 - 40		1100	F1		Q1	
	41 - 60		600				
Section C	61 - 120	5	P1				
	121 - 180	10					
	181 - 240	(15)					
	241 - 300	-5					
	301 - 360	-10					
	361 - 420	(-15)					
	421 - 435	0		0	3		
	436 - 450				5		

KEY: P1 = (2200, 1100, 600)

F1 = (0, 5, 10, (15))

Q1 = (40, 60, 80, 100, 120)

Figure A15. Test Points

A9. FACILITY

A9.1 TUNNEL DESCRIPTION AND OPERATING ENVELOPE

The NASA Langley 16 Transonic Dynamics Tunnel was designed to provide the capability of testing large dynamics models at transonic speeds for the study of flutter, aerodynamic loads, and input response. The wind tunnel is a continuous-flow tunnel which operates from Mach numbers near 0 to 1.20 at pressures ranging from 0.2 to atmospheric pressure. The “pressure vessel” design of the tunnel provides for testing medium of either air or Freon 12 (Freon 12 will be replaced with another heavy gas during the tunnel shut-down June 1996 through June 1997). The tests of the Smart Wings will use only air as the testing medium.

Details of the construction of the tunnel and test section have been provided in Figures A16 and A17. The test chamber is 60-feet in diameter with the test section located inside the chamber, 16-feet square with filleted corners. Figure A17 shows the test section cross section with the semi-span mounting system as it will be used with the Smart Wing. Tunnel and model control operation is done in the 32-foot-long control room chamber located alongside the test section. Windows in the control room provide visual access to the test section. There are four quick opening valves, for model safety purposes, located in the by-pass lines which connect the test chamber and the tunnel return leg downstream of the motor nacelle. These will be used in case high model dynamic instabilities to prevent loss of model or components. Details of the 16’ TDT tunnel and operation can be found in the reference NASA Langley Working Paper LWP-799 “The Langley Transonic Dynamics Tunnel”.

The operating envelope with air as the testing medium has been provided in Figure A18. The test program for the Smart Wing was designed to stay within the boundaries of this operating envelope.

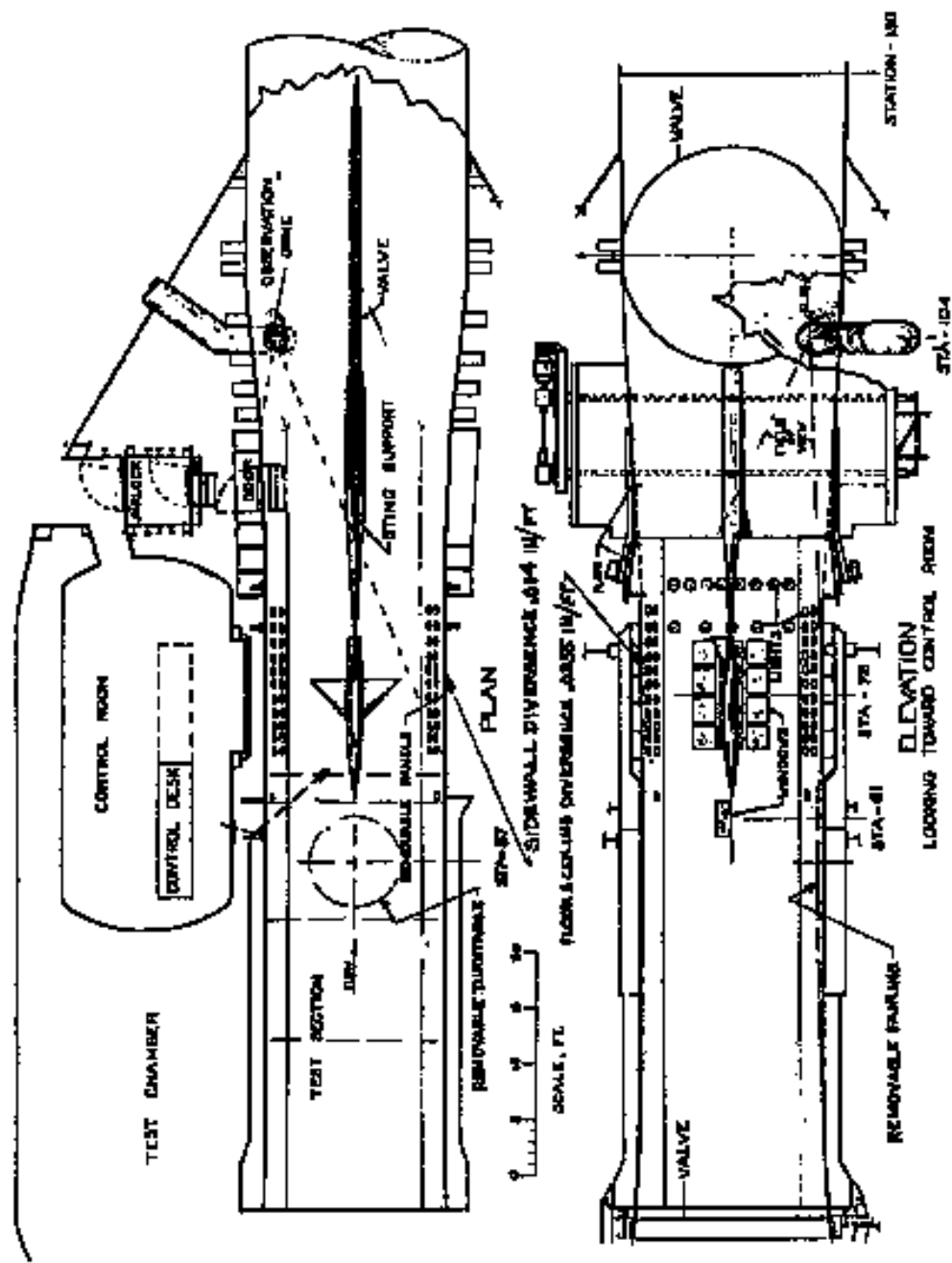


Figure A16. NASA Langley 16 FT TDT
General Arrangement of Test Section

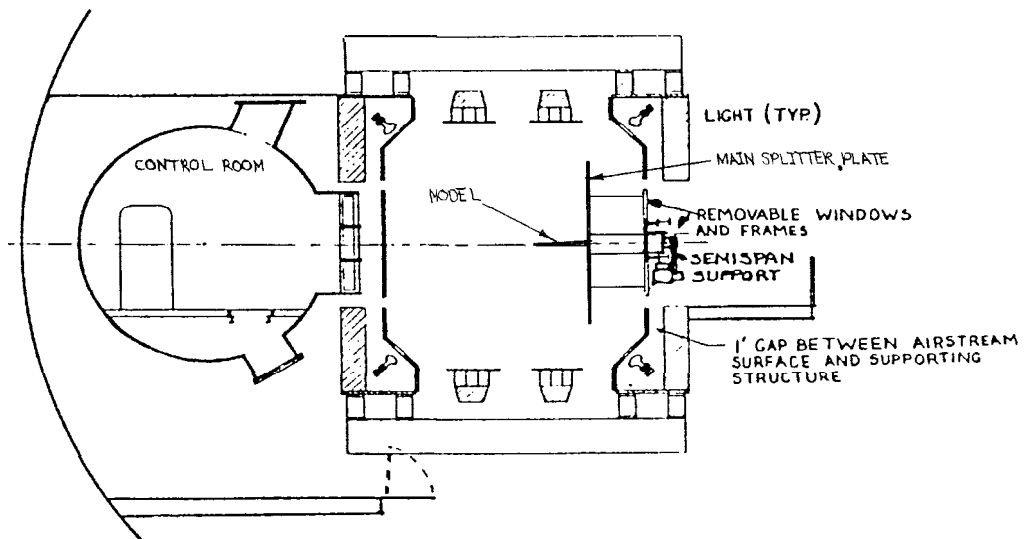


Figure A17. NASA/LaRC Cross-Section at Station 72 of Semi-Span Support System

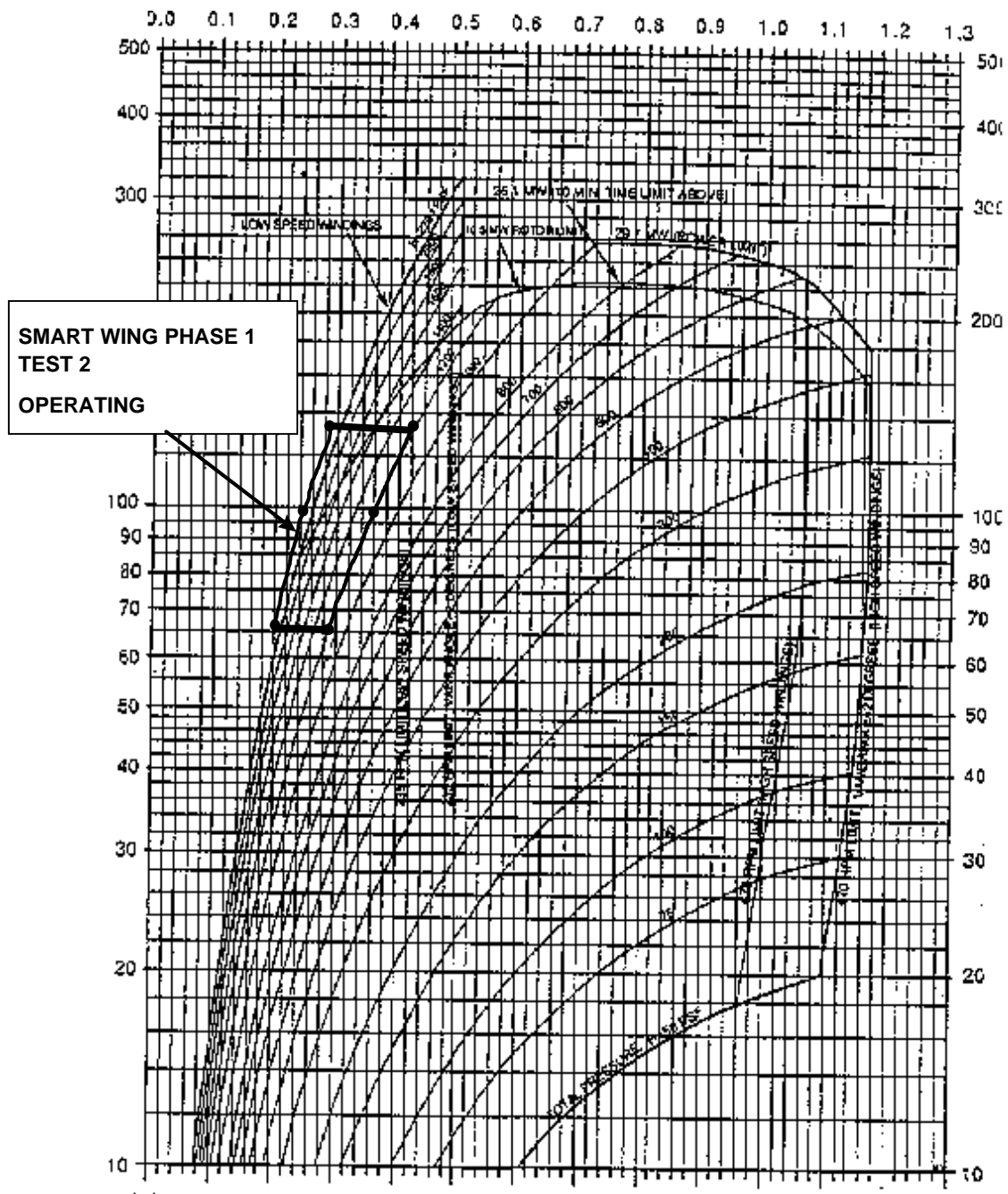


Figure A18. NASA/LaRC 16TDT Transonic Dynamics
Tunnel Operating Boundary in Air
Vane Angle 18 Degrees Unless Noted

A10. TERMS AND CONSTANTS

DATA REDUCTION DEFINITION OF CONSTANTS

TERM	DEFINITION	UNITS	EQN	VALUE
A1	ANGLE OF ATTACK FROM SCHEAVITZ INCLINOMETER	DEG	2	TBD
A2	ANGLE OF ATTACK FROM SCHEAVITZ INCLINOMETER	DEG	2	TBD
AI1	WING TWIST FROM INBOARD TILT SENSOR	DEG	2	TBD
AI2	WING TWIST FROM INBOARD TILT SENSOR	DEG/VOLT	2	TBD
AL0	AILERON POSITION FROM OPTICAL STRAIN GAGE	DEG	14	TBD
AL1	AILERON POSITION FROM OPTICAL STRAIN GAGE	DEG/VOLT	14	TBD
AM1	WING TWIST FROM MID-WING TILT SENSOR	DEG	2	TBD
AM2	WING TWIST FROM MID-WING TILT SENSOR	DEG/VOLT	2	TBD
AO1	WING TWIST FROM OUTBOARD TILT SENSOR	DEG	2	TBD
AO2	WING TWIST FROM OUTBOARD TILT SENSOR	DEG/VOLT	2	TBD
AOPi	PRESSURE MEASUREMENT-OPTICAL PRESSURE TRANS.	PSI	9	TBD
AOP2i	PRESSURE MEASUREMENT-OPTICAL PRESSURE TRANS.	PSI/VOLT	9	TBD

AT0	TORQUE FROM OUTBOARD TORQUE TUBE (SMA)	IN-LB	5	TBD
AT1	TORQUE FROM OUTBOARD TORQUE TUBE (SMA)	IN-LB/VOLT	5	TBD
ATI0	TORQUE FROM INBOARD TORQUE TUBE (SMA)	IN-LB	5	TBD
ATI1	TORQUE FROM INBOARD TORQUE TUBE (SMA)	IN-LB/VOLT	5	TBD
AU0	AILERON DEFLECTION FROM OPTICAL STRAIN GAGE- UPPER SKIN	DEG	14	TBD
AU1	AILERON DEFLECTION FROM OPTICAL STRAIN GAGE- UPPER SKIN	DEG/VOLT	14	TBD
b	WING REFERENCE SPAN	IN	3	TBD
C0	FLAP POTENTIOMETER POSITION	DEG	14	TBD
C1	FLAP POTENTIOMETER POSITION	DEG/VOLT	14	TBD
cbar	WING REFERENCE CHORD	INCHES	3	TBD
clea	REFERENCE CHORD OF INBOARD PRESSURE ROW	INCHES	13	TBD
cleb	REFERENCE CHORD OF MID-INBOARD PRESSURE ROW	INCHES	13	TBD
clec	REFERENCE CHORD OF MID-OUTBOARD PRESSURE ROW	INCHES	13	TBD
cled	REFERENCE CHORD OF OUTBOARD PRESSURE ROW	INCHES	13	TBD

D0	FLAP DEFLECTION LVDT (SMA)	DEG	14	TBD
D1	FLAP DEFLECTION LVDT (SMA)	DEG/VOLT	14	TBD
DA0	AILERON DEFLECTION LVDT (SMA)	DEG	14	TBD
DA1	AILERON DEFLECTION LVDT (SMA)	DEG/VOLT	14	TBD
E	MODULUS OF ELASTICITY	psi/μ-in/in	5	TBD
FL0	FLAP POSITION FROM OPTICAL STRAIN GAGE- LOWER SKIN	DEG	14	TBD
FL1	FLAP POSITION FROM OPTICAL STRAIN GAGE- LOWER SKIN	DEG/VOLT	14	TBD
FU0	FLAP POSITION FROM OPTICAL STRAIN GAGE- UPPER SKIN	DEG	14	TBD
FU1	FLAP POSITION FROM OPTICAL STRAIN GAGE- UPPER SKIN	DEG/VOLT	14	TBD
GF	GAGE FACTOR FOR STANDARD STRAIN	GAG	5	TBD
Imrc	TRANSFER DISTANCE ALONG Y- AXIS FROM BALANCE CENTER TO MRC	INCHES	3	TBD
v	POISSON'S RATIO		6,7,8,9	TBD
S	WING REFERENCE AREA	IN ²	3	TBD
V	EXCITATION VOLTAGE FOR STRAIN GAGES	VOLTS	5	TBD
xca	RATIO OF PRESSURE TAP DISTANCE FROM LE TO LOCAL CHORD- INBOARD PRESSURE ROW		10,11	SEE SECT A14

xcb	RATIO OF PRESSURE TAP DISTANCE FROM LE TO LOCAL CHORD- MID-INBOARD PRESSURE ROW	10,11	SEE SECT A14
xcc	RATIO OF PRESSURE TAP DISTANCE FROM LE TO LOCAL CHORD- MID-OUTBOARD PRESSURE ROW	10,11	SEE SECT A14
xcd	RATIO OF PRESSURE TAP DISTANCE FROM LE TO LOCAL CHORD- OUTBOARD PRESSURE ROW	10,11	SEE SECT A14
yca	RATIO OF PRESSURE TAP DISTANCE FROM SURFACE IN Y- DIRECTION TO LOCAL CHORD- INBOARD PRESSURE ROW	12	SEE SECT A14
ycb	RATIO OF PRESSURE TAP DISTANCE FROM SURFACE IN Y- DIRECTION TO LOCAL CHORD- MID-INBOARD PRESSURE ROW	12	SEE SECT A14
ycc	RATIO OF PRESSURE TAP DISTANCE FROM SURFACE IN Y- DIRECTION TO LOCAL CHORD- MID- OUTBOARD PRESSURE ROW	12	SEE SECT A14
ycd	RATIO OF PRESSURE TAP DISTANCE FROM SURFACE IN Y- DIRECTION TO LOCAL CHORD- OUTBOARD PRESSURE ROW	12	SEE SECT A14

DATA REDUCTION DEFINITION OF TERMS

TERM	DEFINITION	UNITS	EQN.
ALOS	AILERON DEFLECTION LOWER SKIN OPTICAL STRAIN GAGE (SMA)	DEG	14
ALP1	MODEL ALPHA POSITION FROM SCHEAVITZ INCLINOMETER	DEG	2
ALP2	MODEL INBOARD WING TWIST FROM TILT SENSOR	DEG	2
ALP3	MODEL MID-WING TWIST FROM TILT SENSOR	DEG	2
ALP4	MODEL OUTBOARD WING TWIST FROM TILT SENSOR	DEG	2
ALVDT	AILERON DEFLECTION FROM LVDT (SMA)	DEG	14
AOA	MODEL ALPHA POSITION FROM FACILITY SUPPORT SYSTEM	DEG	1
AUOS	AILERON DEFLECTION UPPER SKIN OPTICAL STRAIN GAGE (SMA)	DEG	14
CA	AXIAL COEFFICIENT FROM BALANCE		3
CAA	AXIAL COEFFICIENT FROM INBOARD PRESSURE ROW		13
CAB	AXIAL COEFFICIENT FROM MID INBOARD PRESSURE ROW		13
CAC	AXIAL COEFFICIENT FROM MID OUTBOARD PRESSURE ROW		13
CAD	AXIAL COEFFICIENT FROM OUT- BOARD PRESSURE ROW	----	13
CD	MODEL DRAG COEFFICIENT FROM		

	BALANCE	----	3
CI	MODEL ROLLING MOMENT COEF AT MOMENT REFERENCE CENTER FROM BALANCE- BODY AXIS	----	3
CL	MODEL LIFT COEFFICIENT FROM BALANCE	----	3
Cl _s	MODEL ROLLING MOMENT COEF AT MOMENT REFERENCE CENTER FROM BALANCE- BODY AXIS	----	3
CM	MODEL PITCHING MOMENT COEFFICIENT FROM BALANCE	----	3
CMA	PITCHING MOMENT COEFFICIENT FROM PRESSURES- INBOARD ROW	----	3
CMB	PITCHING MOMENT COEFFICIENT FROM PRESSURES- MID-INBOARD ROW	----	3
CMC	PITCHING MOMENT COEFFICIENT FROM PRESSURES- MID-OUTBOARD ROW	----	3
CMD	PITCHING MOMENT COEFFICIENT FROM PRESSURES-OUTBOARD ROW	----	3
CMRCA	PITCHING MOMENT COEFFICIENT AT MOMENT REFERNCE CENTER FROM PRESSURES- INBOARD ROW	----	12
CMRCB	PITCHING MOMENT COEFFICIENT AT MOMENT REFERNCE CENTER FROM PRESSURES- MID-INBOARD ROW	----	12
CMRCC	PITCHING MOMENT COEFFICIENT AT MOMENT REFERNCE CENTER FROM PRESSURES- MID-OUTBOARD ROW	----	12
CMRCD	PITCHING MOMENT COEFFICIENT AT MOMENT REFERNCE CENTER FROM PRESSURES- OUTBOARD ROW	----	12

CN	NORMAL FORCE COEFFICIENT FROM BALANCE	----	3
Cn	YAWING MOMENT COEFFICIENT ABOUT MOMENT REFERENCE CENTER BODY AXIS	----	3
CNA	NORMAL FORCE COEFFICIENT FROM PRESSURES- INBOARD ROW ----	10	
CNB	NORMAL FORCE COEFFICIENT FROM PRESSURES- MID-INBOARD ROW	----	10
CNC	NORMAL FORCE COEFFICIENT FROM PRESSURES- MID-OUTBOARD ROW	----	10
CND	NORMAL FORCE COEFFICIENT FROM PRESSURES- OUTBOARD ROW	----	10
Cns	YAWING MOMENT COEFFICIENT ABOUT MOMENT REFERENCE CENTER STABILITY AXIS	----	3
CPA _i	PRESSURE COEFFICIENT- INDIVIDUAL PRESSURES- INBOARD ROW	----	9
CPB _i	PRESSURE COEFFICIENT- INDIVIDUAL PRESSURES- MID-INBOARD ROW	----	9
CPC _i	PRESSURE COEFFICIENT- INDIVIDUAL PRESSURES- MID-OUTBOARD ROW	----	9
CPD _i	PRESSURE COEFFICIENT- INDIVIDUAL PRESSURES- OUTBOARD ROW	----	9
CPOP _i	PRESSURE COEFFICIENT - OPTICAL PRESSURE TRANSDUCERS	----	9
DAOAI	WING TWIST MEASUREMENT INBOARD TILT SENSOR TO SCHEAVITZ INCLINOMETER	DEG	2

DAOAM	WING TWIST MEASUREMENT MID WING TILT SENSOR TO SCHEAVITZ INCLINOMETER	DEG	2
DAOAO	WING TWIST MEASUREMENT OUTBOARD TILT SENSOR TO SCHEAVITZ INCLINOMETER	DEG	2
FA	AXIAL FORCE CORRECTED FOR MODEL WEIGHT TARE	LBS	3
FLOS	DEFLECTION OF FLAP FROM OPTICAL STRAIN GAGE ON LOWER SKIN (SMA)	DEG	14
FLVDT	FLAP DEFLECTION (SMA) LVDT	DEG	14
FN	NORMAL FORCE FROM BALANCE	LBS	3
FPOS	FLAP POSITION (CONV.) FROM POTENTIOMETER	DEG	14
FUOS	DEFLECTION OF FLAP FROM OPTICAL STRAIN GAGE ON UPPER SKIN (SMA)	DEG	14
LVDTA	VOLTS FROM AILERON LVDT (SMA)	VOLTS	14
LVDTF	VOLTS FROM FLAP LVDT (SMA)	VOLTS	14
M	TUNNEL FREESTREAM MACH NUMBER	----	1
MI	ROLLING (OR BENDING) MOMENT FROM BALANCE	IN-LB	3
MM	PITCHING MOMENT FROM BALANCE	IN-LB	3
OP _i	OUTPUT FROM OPTICAL PRESSURE TRANSDUCERS	VOLTS	9
OSAL	OUTPUT FROM OPTICAL STRAIN GAGE- LOWER SKIN OF AILERON	VOLTS	14

OSAU	OUTPUT FROM OPTICAL STRAIN GAGE- UPPER SKIN OF AILERON	VOLTS	14
OSFL	OUTPUT FROM OPTICAL STRAIN GAGE- LOWER SKIN OF FLAP	VOLTS	14
OSFU	OUTPUT FROM OPTICAL STRAIN GAGE- UPPER SKIN OF FLAP	VOLTS	14
Po	TUNNEL FREESTREAM STATIC PRESSURE	PSI	1
POSF	OUTPUT OF FLAP POTENTIOMETER (CONV.)	VOLTS	14
PTO	TUNNEL FREESTREAM TOTAL PRESSURE	PSI	1
Q	TUNNEL FREESTREAM DYNAMIC PRESSURE	PSI	1
RN	TUNNEL REYNOLD'S NUMBER	----	1
SAIA	AFT INBOARD SPAR STRAIN GAGE 1 (ROSETTE) OUTPUT	VOLTS	5
SAIB	AFT INBOARD SPAR STRAIN GAGE 2 (ROSETTE) OUTPUT	VOLTS	5
SAIC	AFT INBOARD SPAR STRAIN GAGE 3 (ROSETTE) OUTPUT	VOLTS	5
SAOA	AFT OUTBOARD SPAR STRAIN GAGE 1 (ROSETTE) OUTPUT	VOLTS	5
SAOB	AFT OUTBOARD SPAR STRAIN GAGE 2 (ROSETTE) OUTPUT	VOLTS	5
SAOC	AFT OUTBOARD SPAR STRAIN GAGE 3 (ROSETTE) OUTPUT	VOLTS	5
SLEIA	LEADING EDGE INBOARD SPAR STRAIN GAGE 1 (ROSETTE) OUTPUT	VOLTS	5
SLEIB	LEADING EDGE INBOARD SPAR STRAIN GAGE 2 (ROSETTE) OUTPUT	VOLTS	5

SLEIC	LEADING EDGE INBOARD SPAR STRAIN GAGE 3 (ROSETTE) OUTPUT	VOLTS	5
SLEOA	LEADING EDGE OUTBOARD SPAR STRAIN GAGE 1 (ROSETTE) OUTPUT	VOLTS	5
SLEOB	LEADING EDGE OUTBOARD SPAR STRAIN GAGE 2 (ROSETTE) OUTPUT	VOLTS	5
SLEOC	LEADING EDGE OUTBOARD SPAR STRAIN GAGE 3 (ROSETTE) OUTPUT	VOLTS	5
SMIA	MID-CHORD INBOARD SPAR STRAIN GAGE 1 (ROSETTE) OUTPUT	VOLTS	5
SMIB	MID-CHORD INBOARD SPAR STRAIN GAGE 2 (ROSETTE) OUTPUT	VOLTS	5
SMIC	MID-CHORD INBOARD SPAR STRAIN GAGE 3 (ROSETTE) OUTPUT	VOLTS	5
SMOA	MID-CHORD OUTBOARD SPAR STRAIN GAGE 1 (ROSETTE) OUTPUT	VOLTS	5
SMOB	MID-CHORD OUTBOARD SPAR STRAIN GAGE 2 (ROSETTE) OUTPUT	VOLTS	5
SMOC	MID-CHORD OUTBOARD SPAR STRAIN GAGE 3 (ROSETTE) OUTPUT	VOLTS	5
SOTT	OUTBOARD TORQUE TUBE (SMA) STRAIN GAGE BRIDGE OUTPUT	VOLTS	14
SITT	INBOARD TORQUE TUBE (SMA) STRAIN GAGE BRIDGE OUTPUT	VOLTS	14
TTO	TUNNEL FREESTREAM TOTAL TEMPERATURE	DEG F	1
TORQI	TORQUE VALUE FROM SMA TORQUE TUBE- INBOARD	IN-LB	14
TORQO	TORQUE VALUE FROM SMA TORQUE		

	TUBE- OUTBOARD	IN-LB	14
V_o	VOLTS OUT FROM STRAIN GAGES	VOLTS	5
YM	YAWING MOMENT FROM BALANCE	IN-LB	3
ϵ	STRAIN FROM STRAIN GAGES	μ -in/in	5,6,7,8
σ	STRESS FROM STRAIN GAGES	PSI	5,6,7,8
θ	ANGLE OF PRINCIPAL AXES OF EACH STRAIN GAGE ROSETTE	DEG	6,7,8

A11. POINTS OF CONTACT

Jay Kudva

Northrop Grumman
Program Manager
310-332-8300

Chris Martin

Northrop Grumman
310-332-8198

Lew Scherer

Northrop Grumman
Test Engineer
310-942-5627

Kari Appa

Northrop Grumman
310-332-9609

Peter Jardine

Northrop Grumman
310-332-4020

Bernie Carpenter

Lockheed Martin
303-971-9128

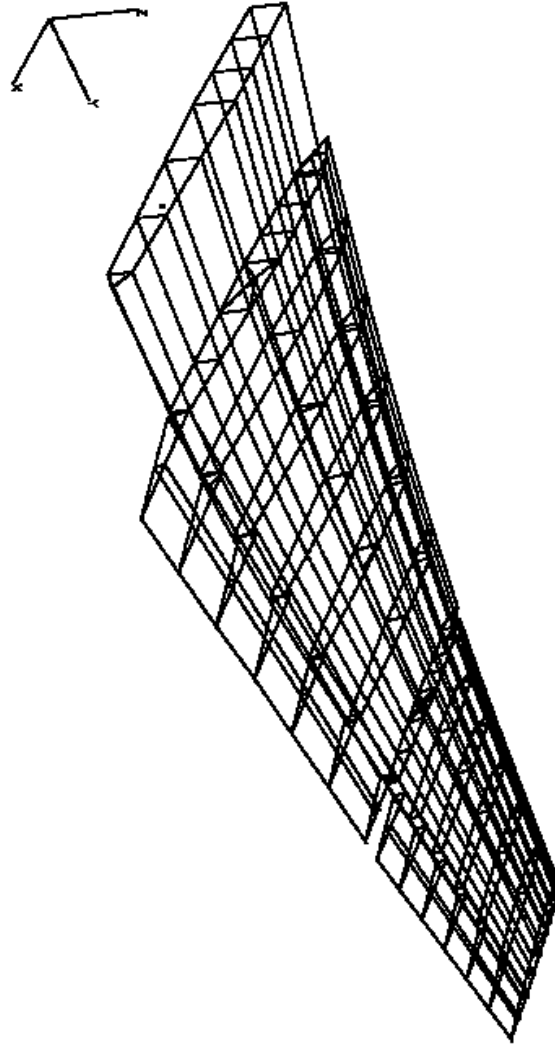
Mark Jones

Fiber and Sensor Technologies
540.953.4268

Anna McGowan

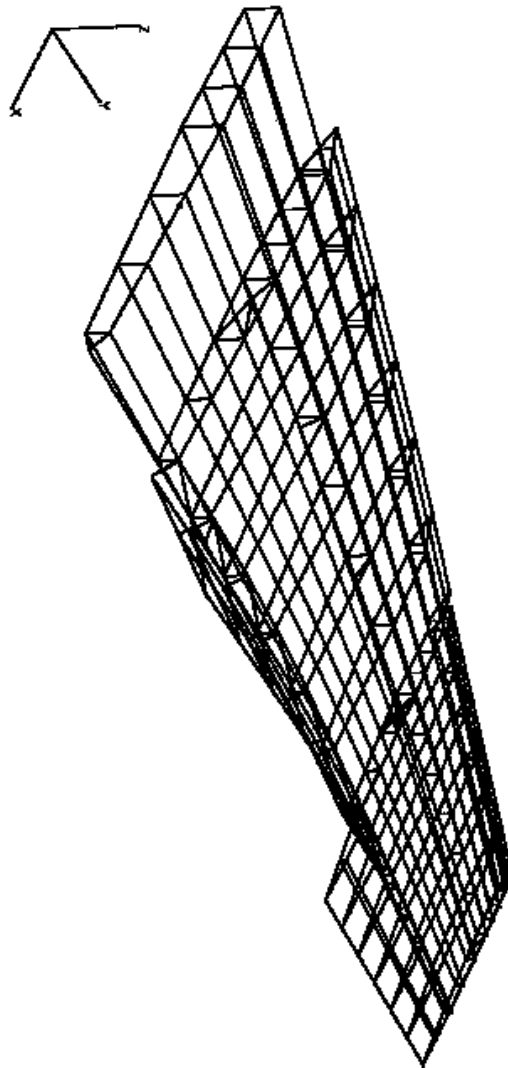
NASA/LaRC
804.864.2846

A12. FLUTTER AND DYNAMICS



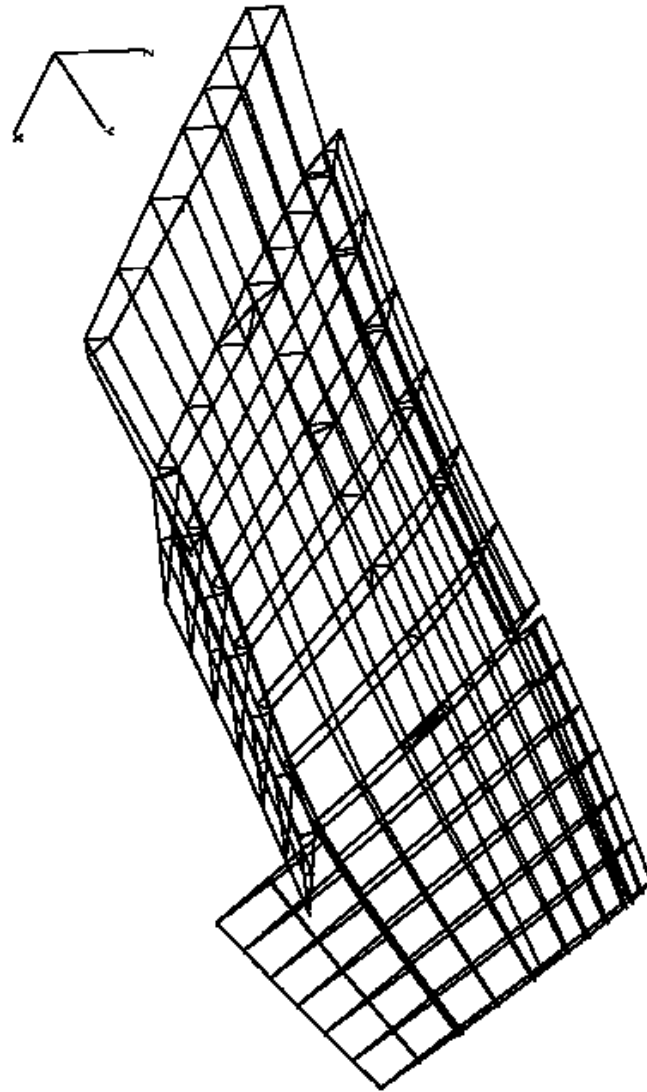
Conventional Wing, Mode 1, 33.6 Hz

Figure A19



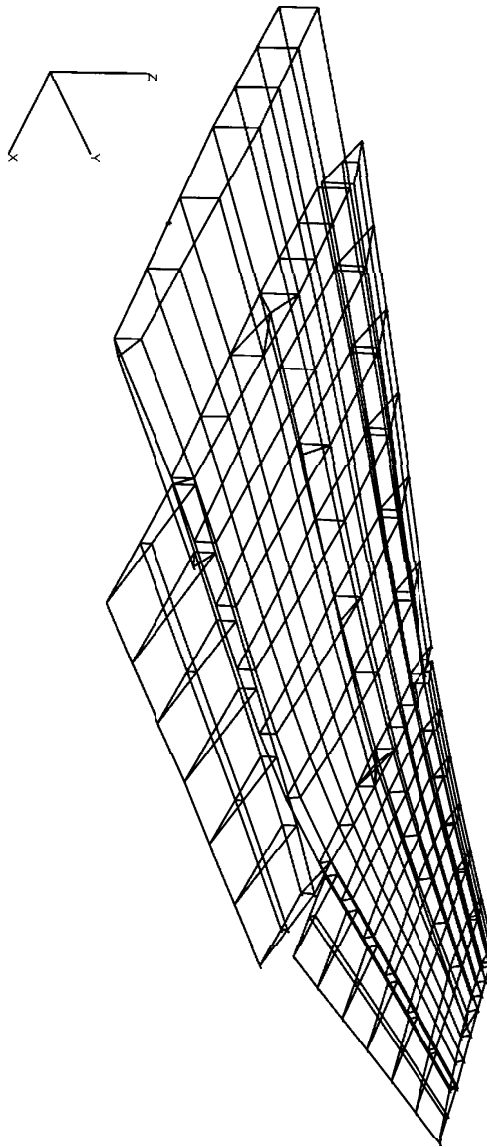
Conventional Wing, Mode 2, 61.5 Hz

Figure A20



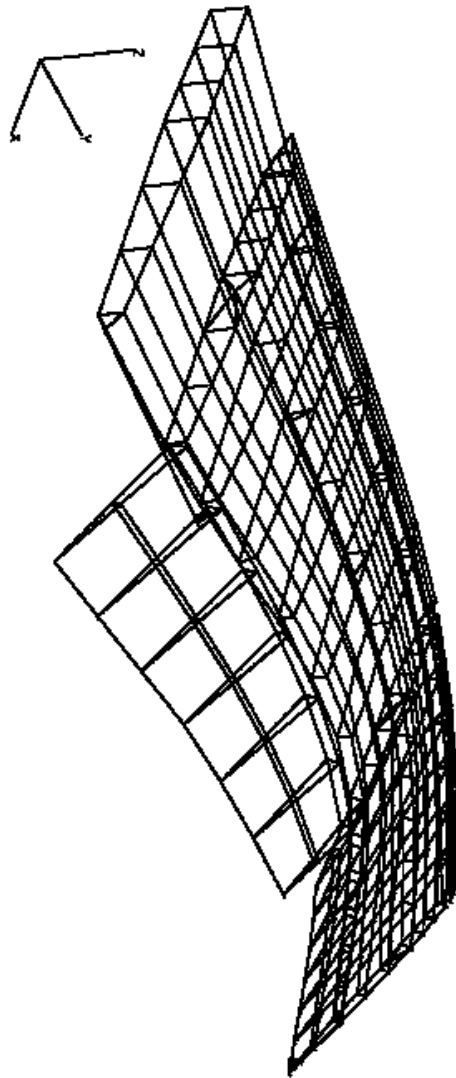
Conventional Wing, Mode 3, 87.7 Hz

Figure A21



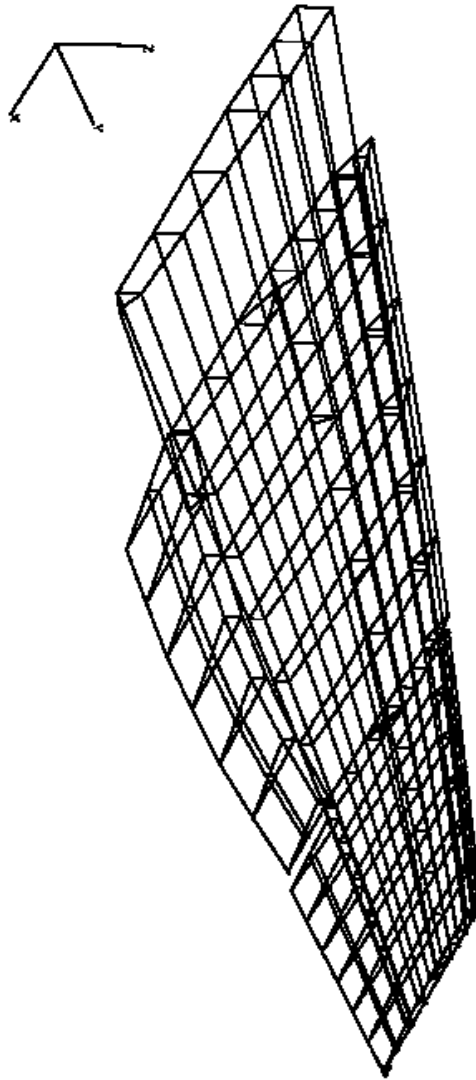
Conventional Wing, Mode 4, 131 Hz

Figure A22



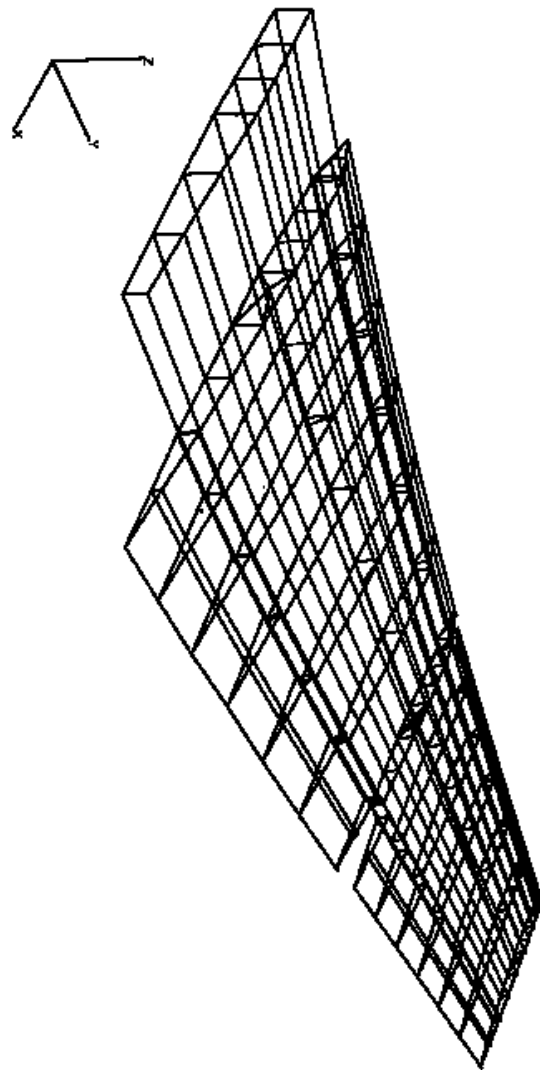
Conventional Wing, Mode 5, 143 Hz

Figure A23



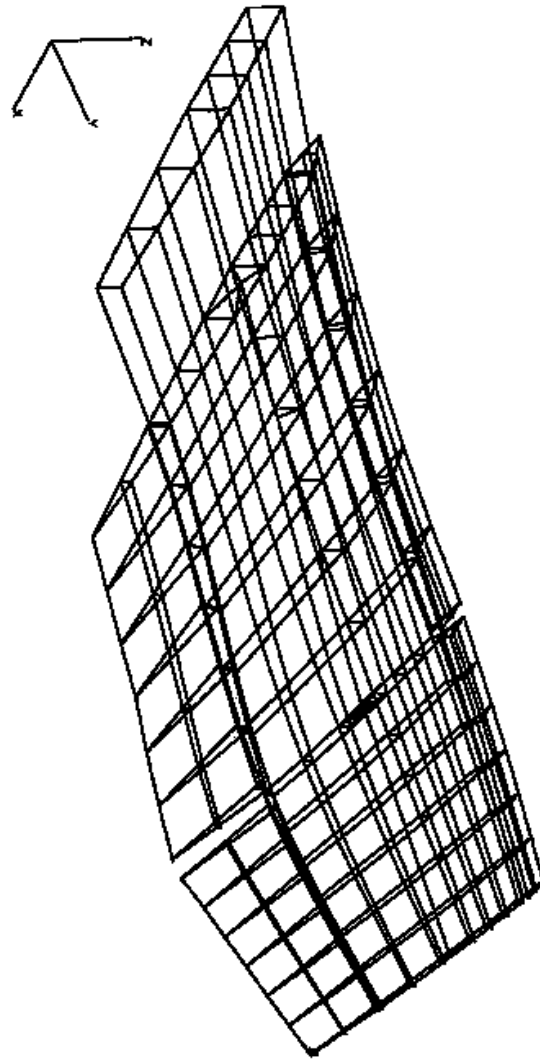
Conventional Wing, Mode 6, 201 Hz

Figure A24



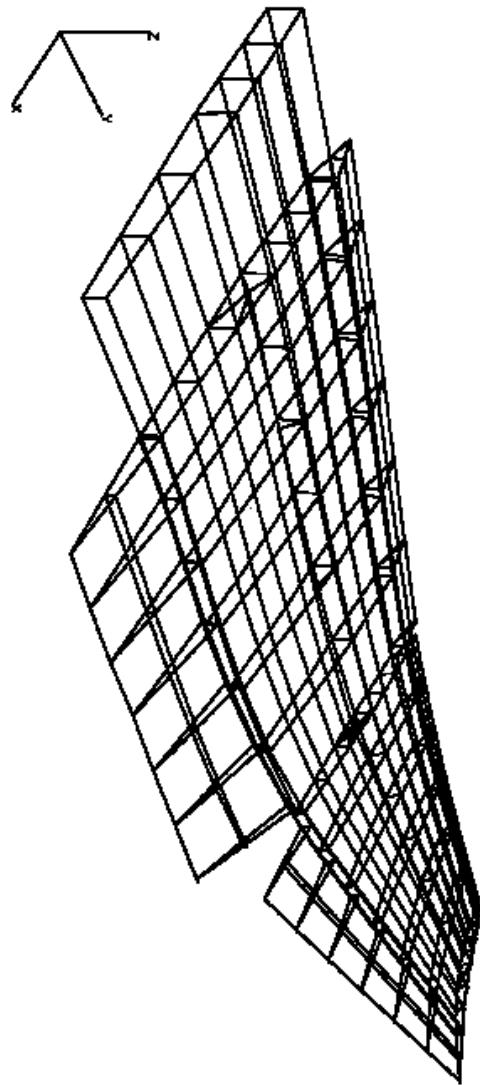
Smart Wing, Mode 1, 35.4 Hz

Figure A25



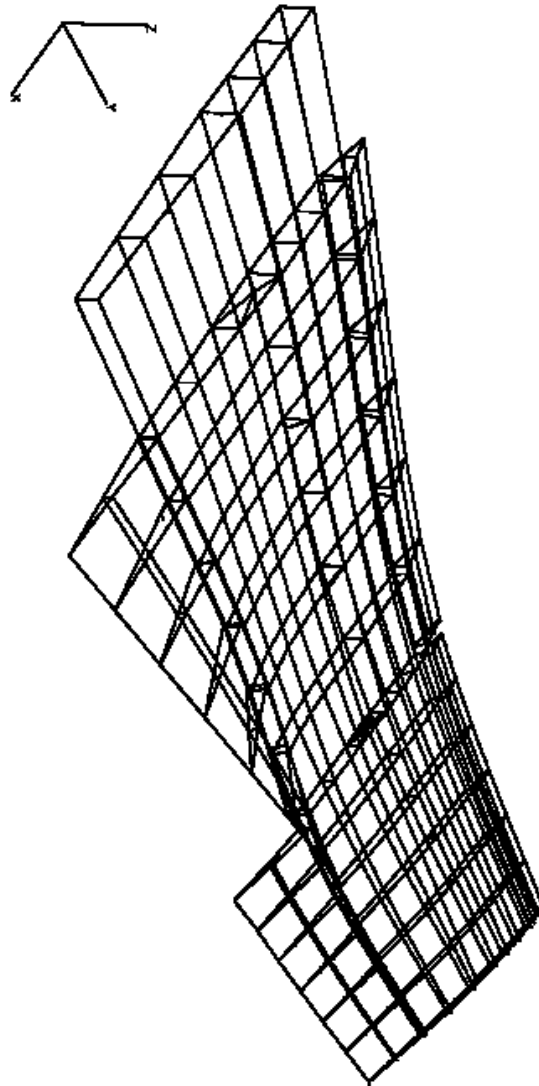
Smart Wing, Mode 2, 83.7 Hz

Figure A26



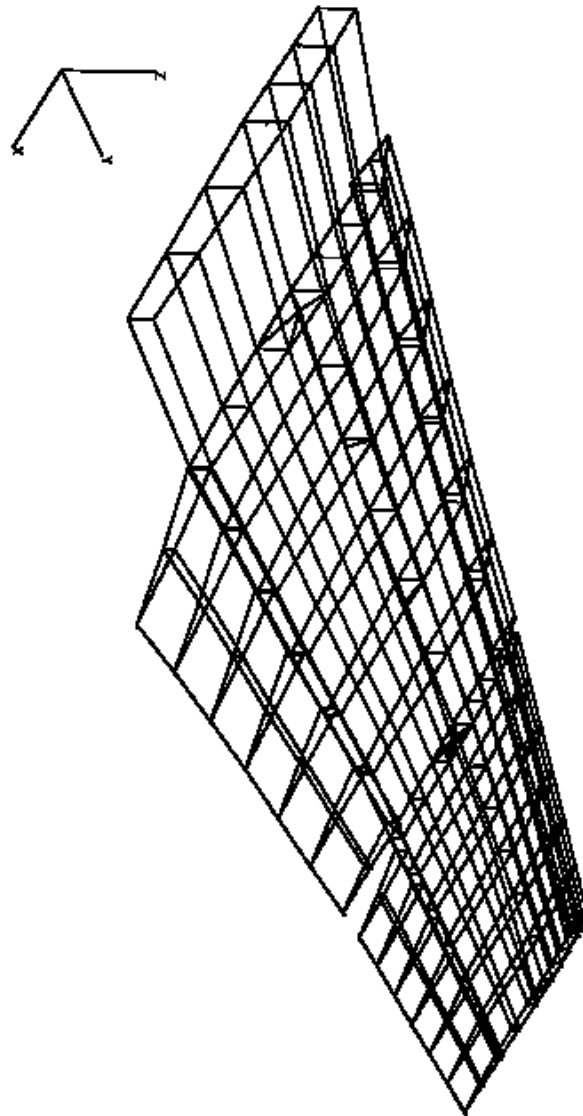
Smart Wing, Mode 3, 127 Hz

Figure A27



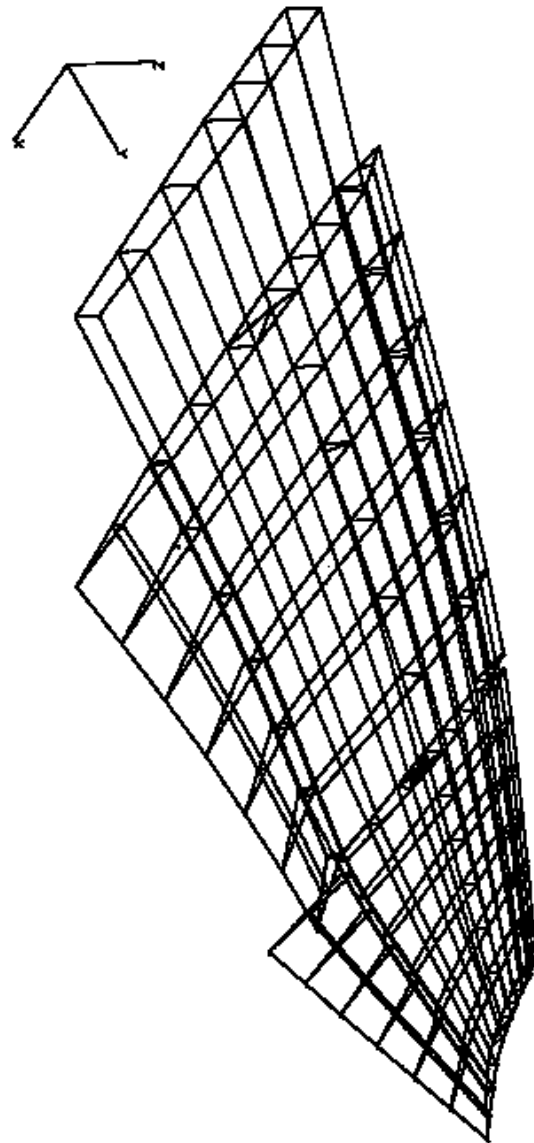
Smart Wing, Mode 4, 198 Hz

Figure A28



Smart Wing, Mode 5, 218 Hz

Figure A29



Smart Wing, Mode 6, 241 Hz

Figure A30

FLUTTER AND DYNAMICS GRAPHS

Included are the graphs for both wind tunnel models at $M = 0.5$ and 0.6 , with density ratios of 0.1 to 1.0 .

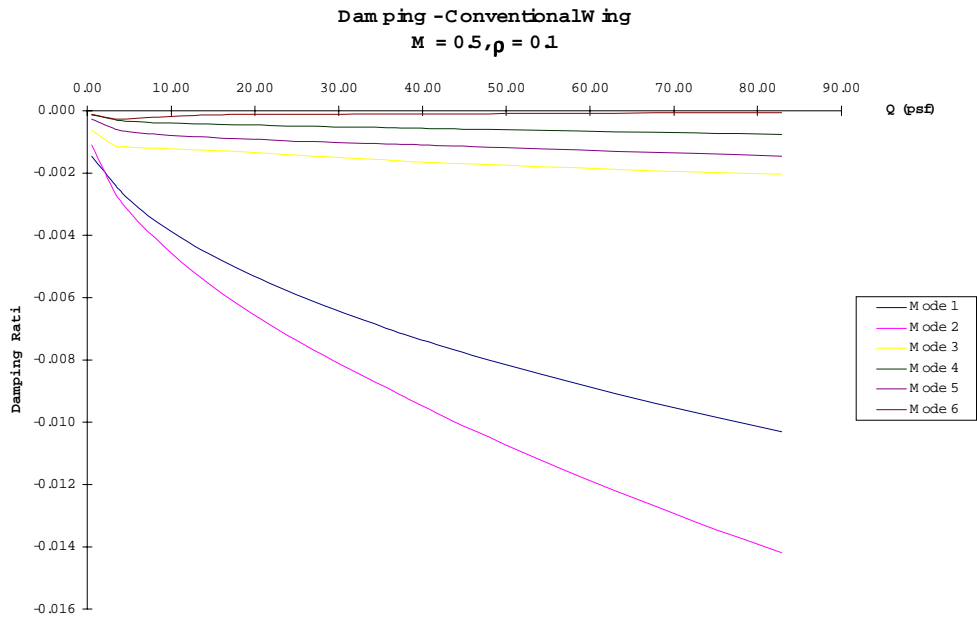


Figure A31

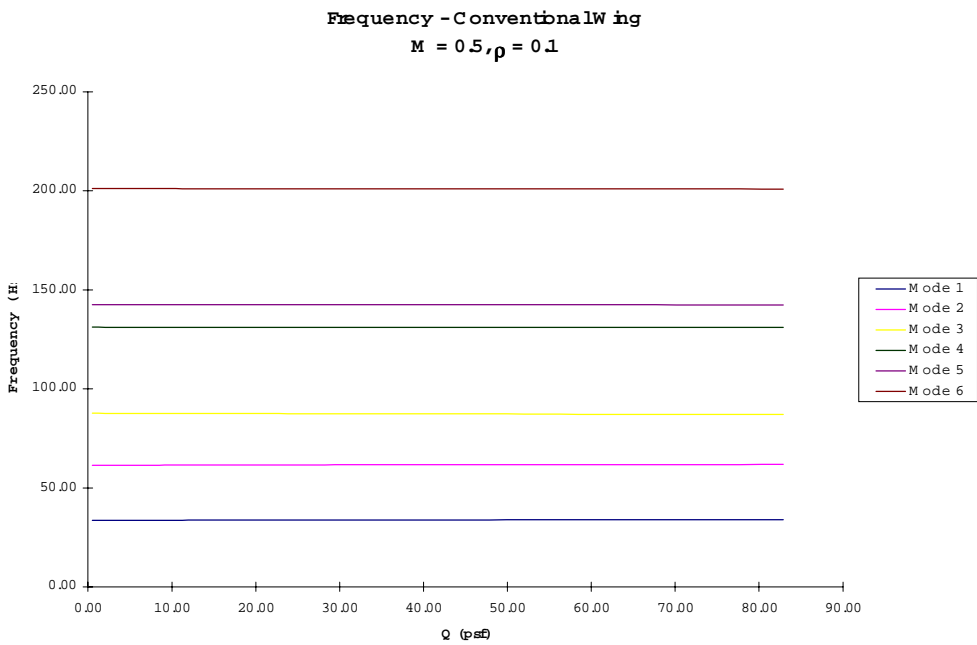


Figure A32

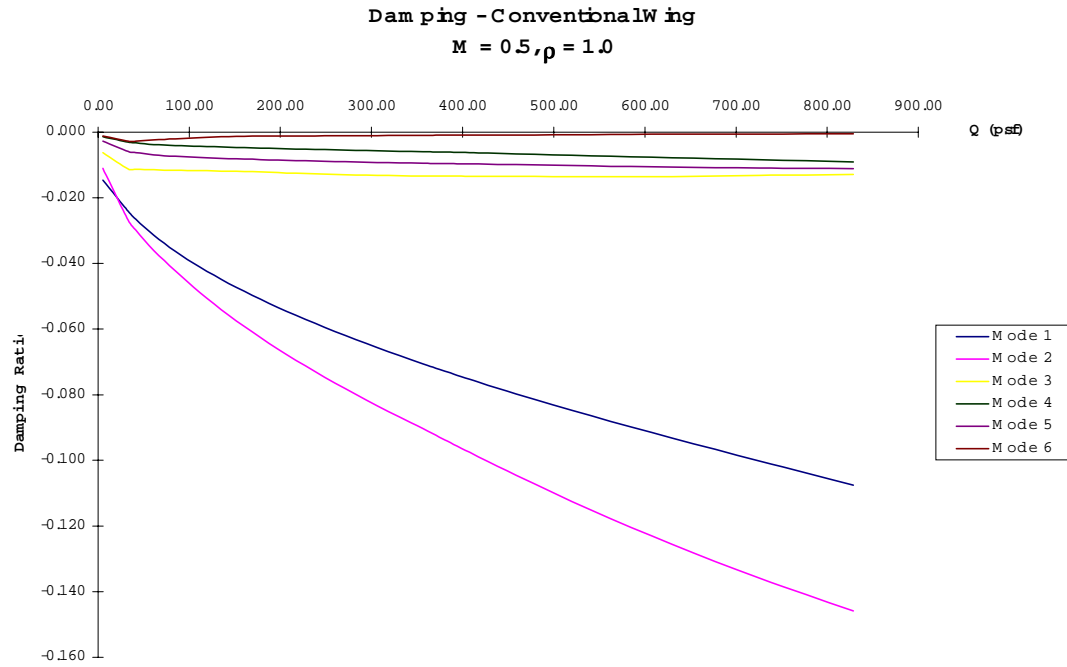


Figure A33

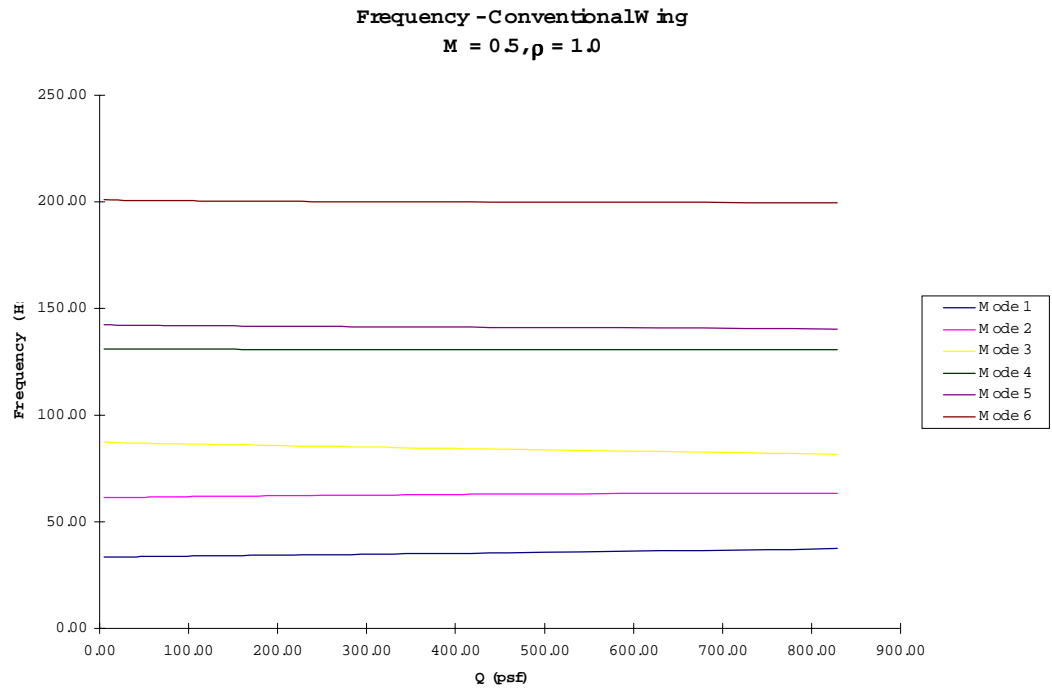


Figure A34

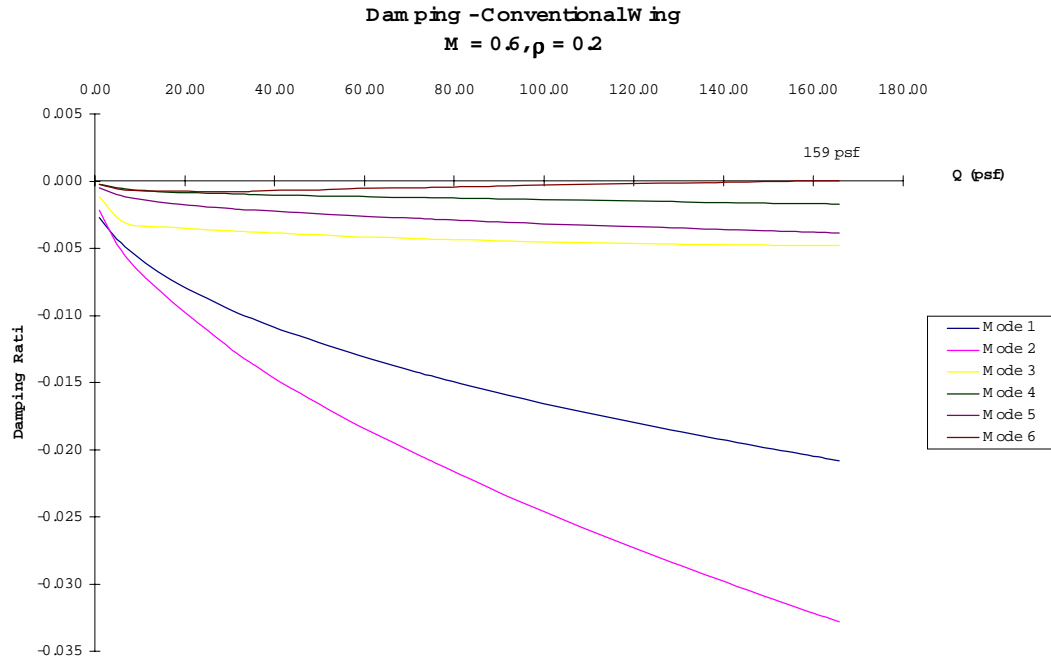


Figure A35

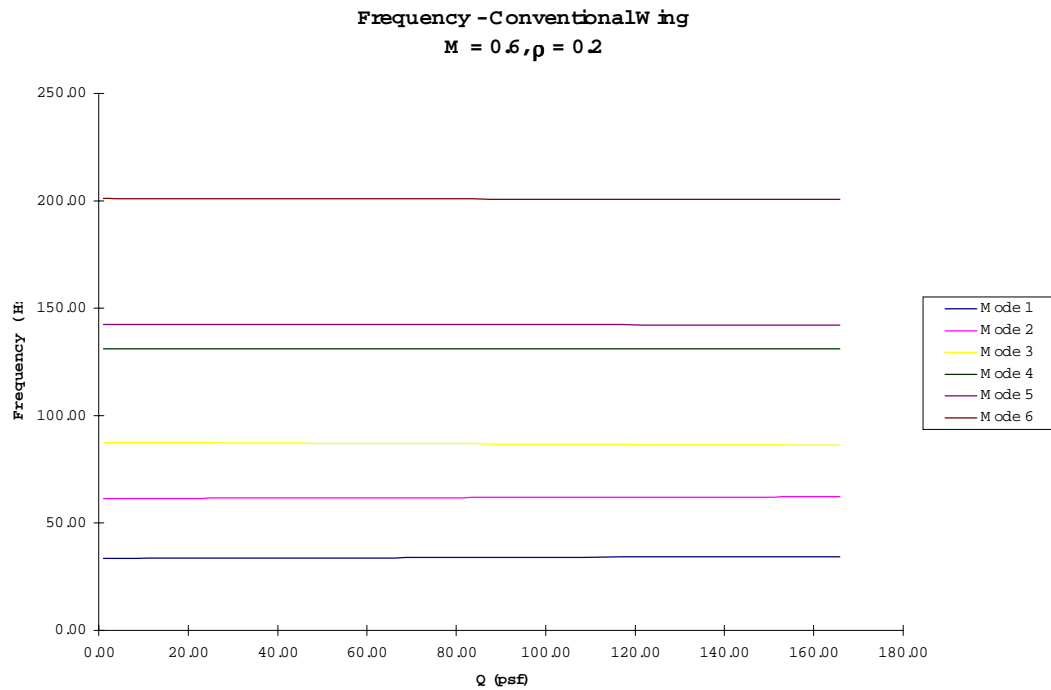


Figure A36

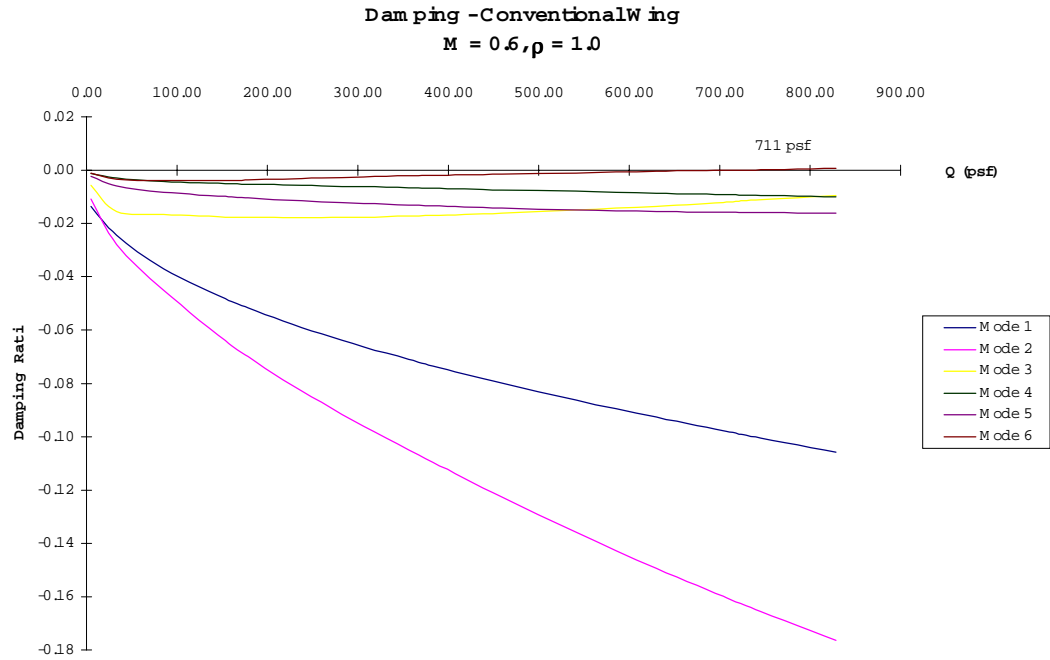


Figure A37

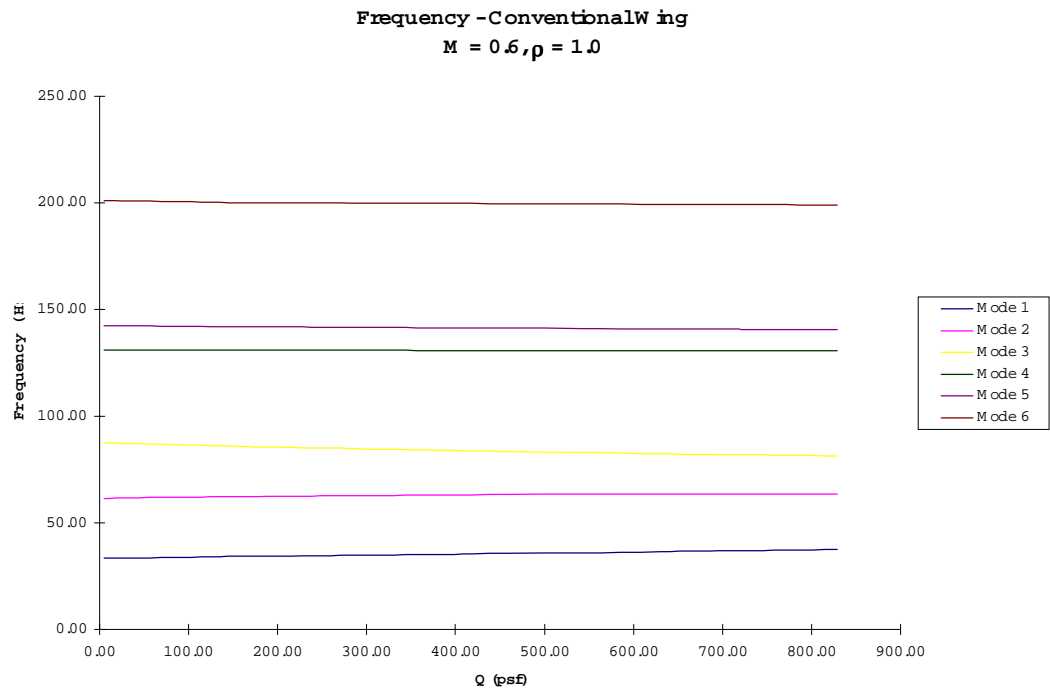


Figure A38

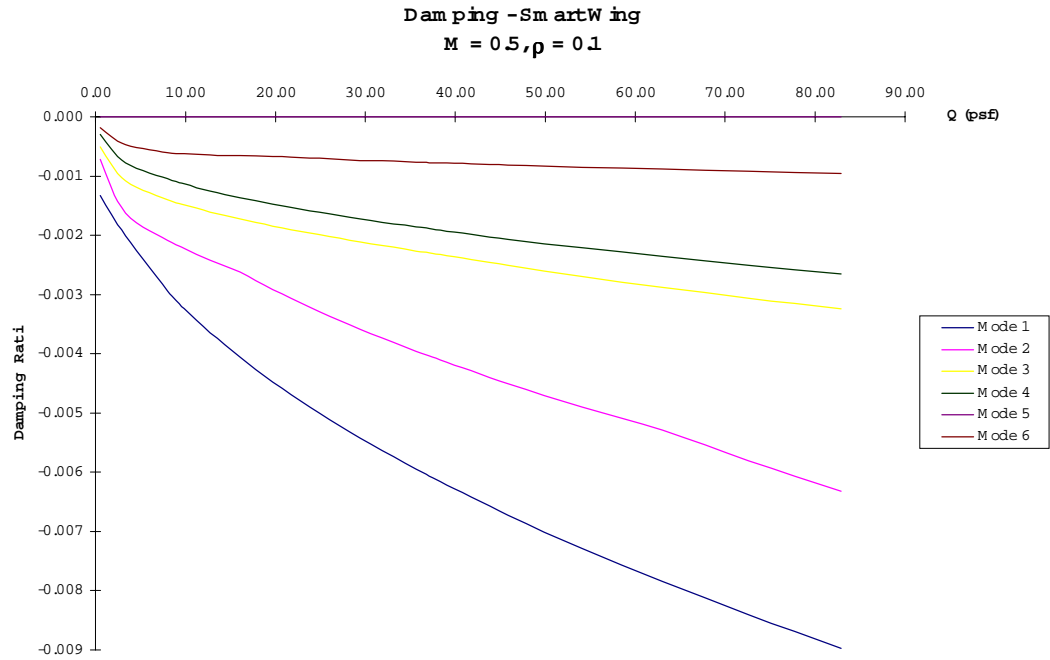


Figure A39

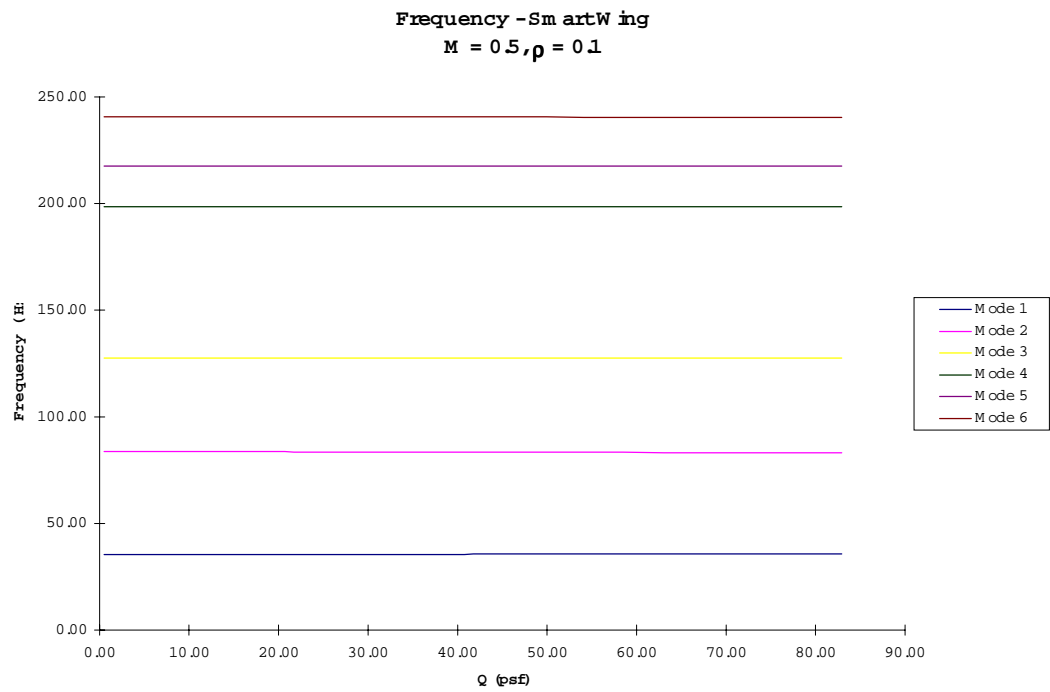


Figure A40

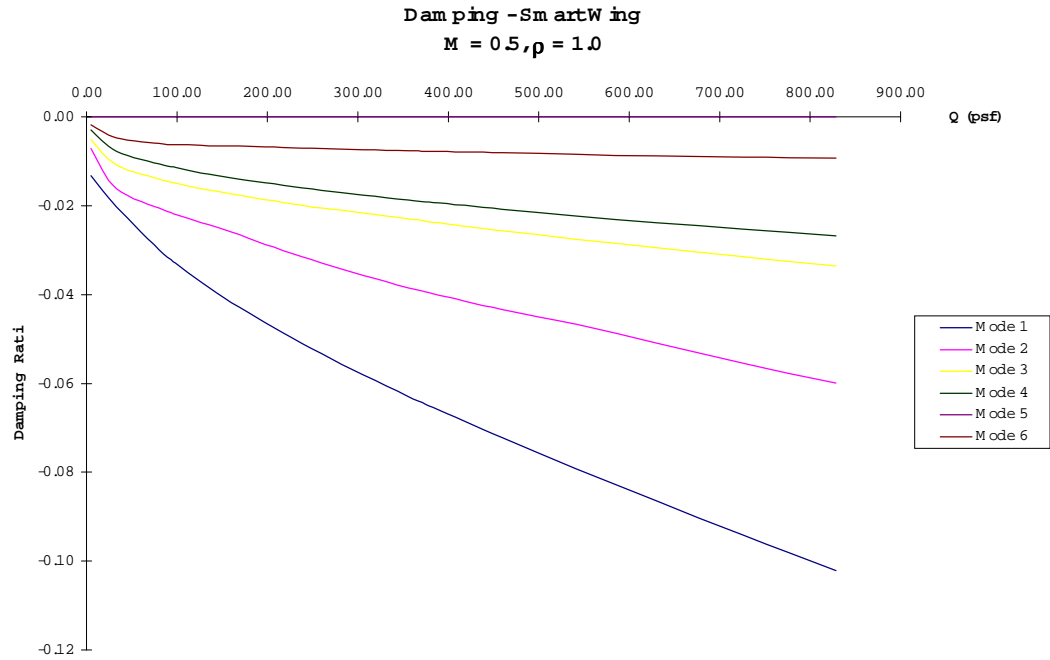


Figure A41

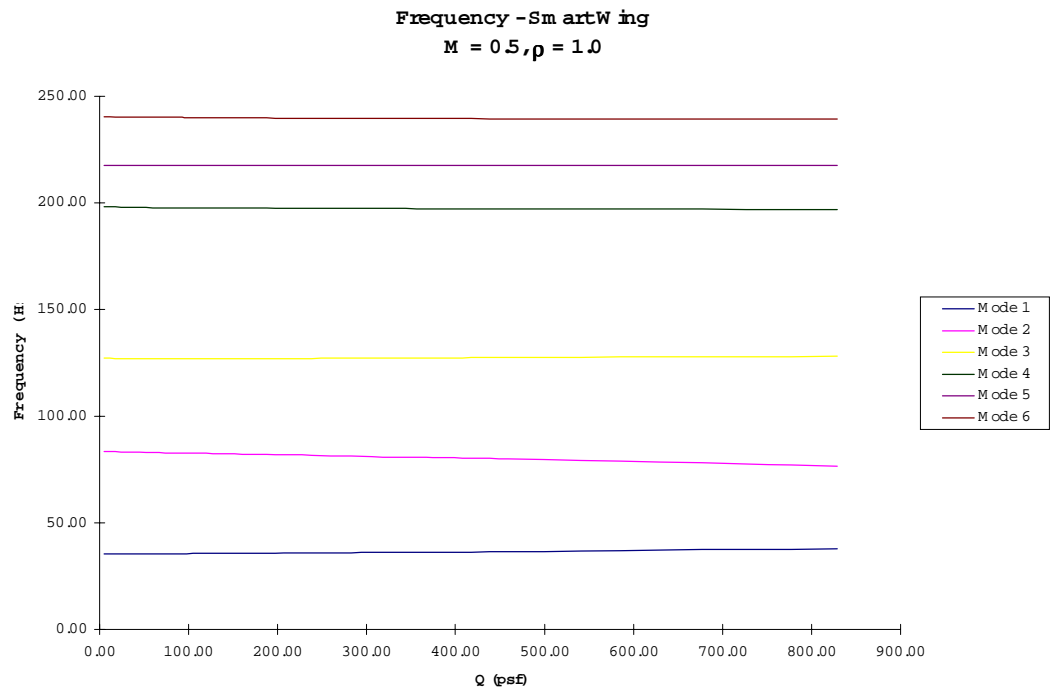


Figure A42

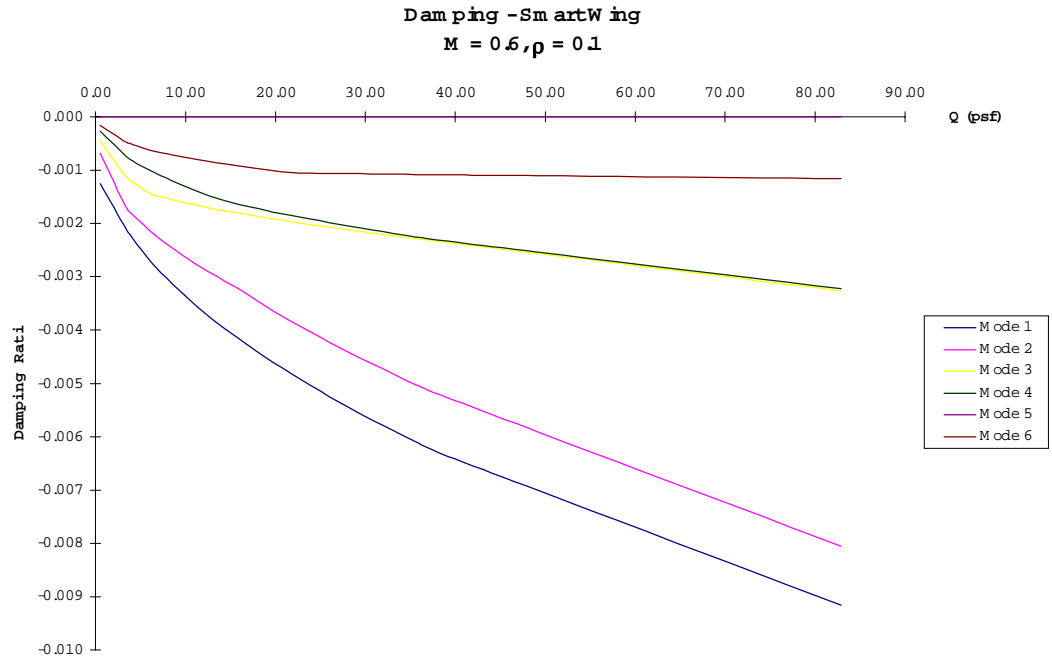


Figure A43

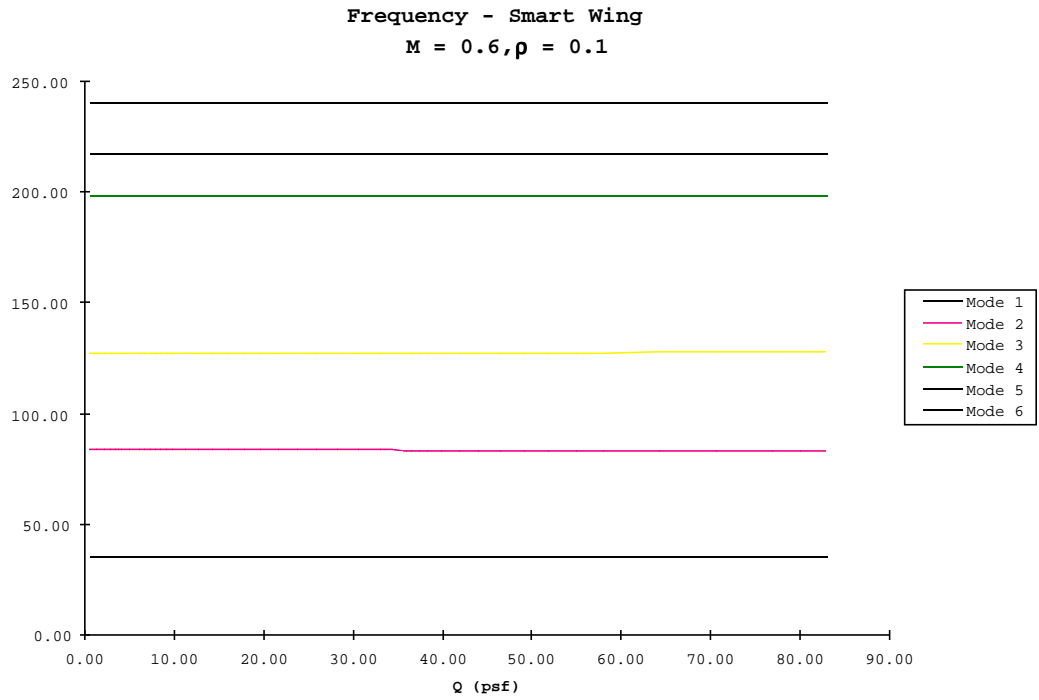


Figure A44

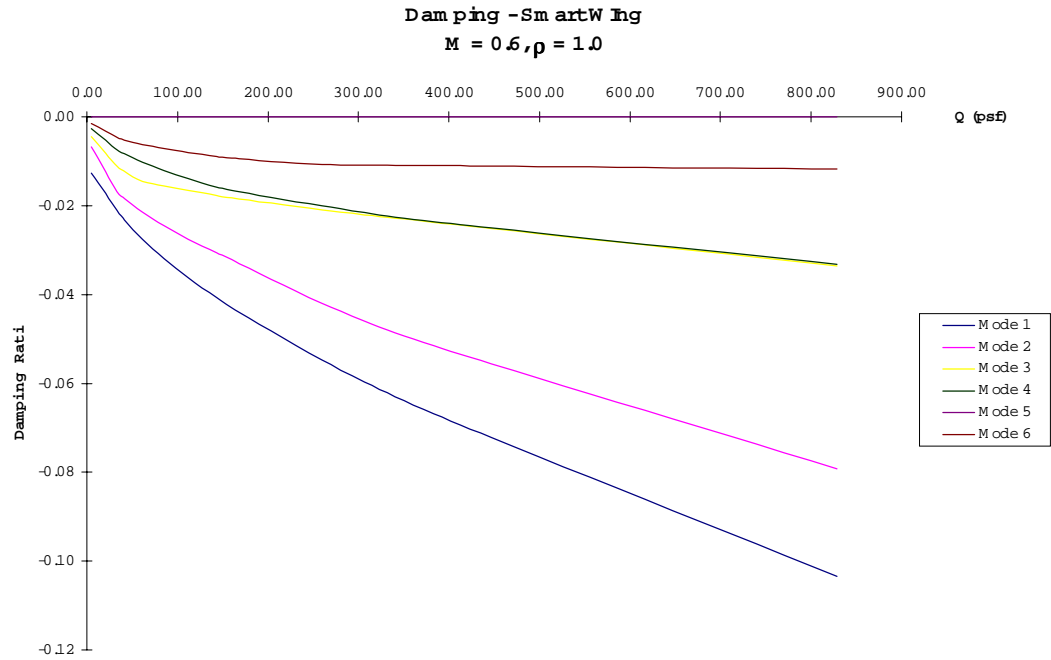


Figure A45

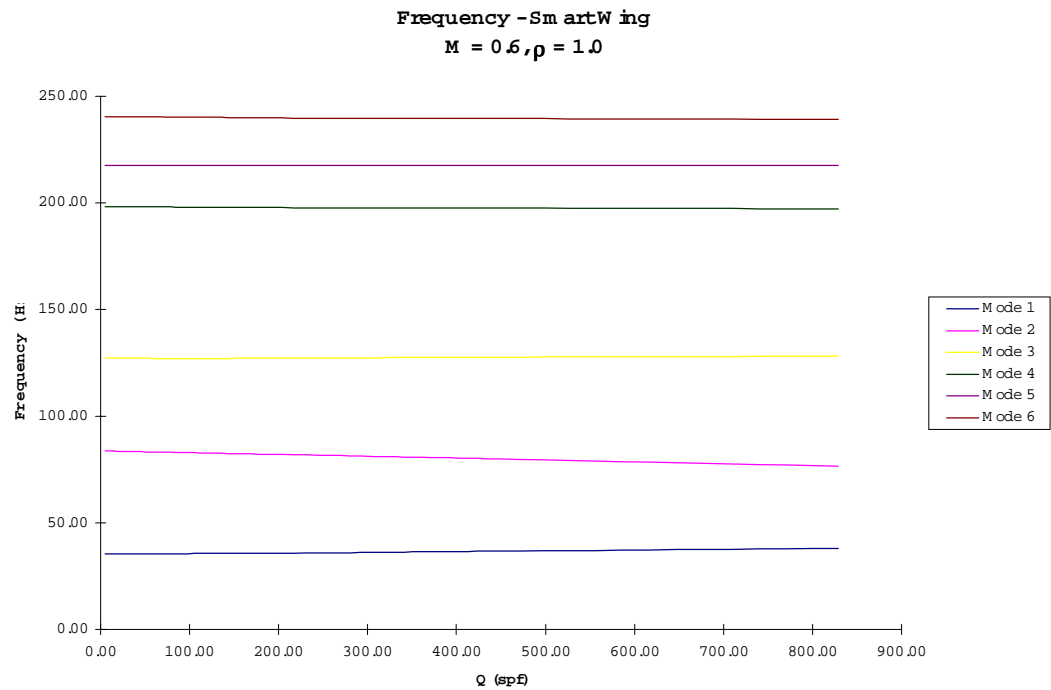


Figure A46

A13. INSTRUMENTATION LIST AND PRESSURE LIST

DESCRIPTION	DATA	APPLIES	RANGE	SIGNAL ⁽¹⁾	MOD COMP	MOD COMP	OPTICAL	STRIP CHART
	DESIGNATION	TO WHICH	(EU)	COND.	CONDITIONED	REAL TIME	SWITCH BOX	OUTPUT
		MODEL		RESPON.	SIGNAL INPUT	MONITORING	CONNECTION	REQ'D ⁽²⁾
OPTICAL PRESSURE TRANSDUCERS								
OPTICAL PRESSURE TRANSDUCER 1	OP1	BOTH		FS	YES	NO	NO	NO
OPTICAL PRESSURE TRANSDUCER 2	OP2	BOTH		FS	YES	NO	NO	NO
OPTICAL PRESSURE TRANSDUCER 3	OP3	BOTH		FS	YES	NO	NO	NO
OPTICAL PRESSURE TRANSDUCER 4	OP4	BOTH		FS	YES	NO	NO	NO
OPTICAL PRESSURE TRANSDUCER 5	OP5	BOTH		FS	YES	NO	NO	NO
OPTICAL PRESSURE TRANSDUCER 6	OP6	BOTH		FS	YES	NO	NO	NO
OPTICAL PRESSURE TRANSDUCER 7	OP7	BOTH		FS	YES	NO	NO	NO
OPTICAL PRESSURE TRANSDUCER 8	OP8	BOTH		FS	YES	NO	NO	NO
OPTICAL PRESSURE TRANSDUCER 8	OP9	BOTH		FS	YES	NO	NO	NO
OPTICAL PRESSURE TRANSDUCER 10	OP10	BOTH		FS	YES	NO	NO	NO
STRAIN GAGES								
INBOARD LEADING EDGE SPAR (ROSETTE)	SLEIA	BOTH		NG	YES	YES	YES	YES
	SLEIB	BOTH		NG	YES	YES	YES	YES
	SLEIC	BOTH		NG	YES	YES	YES	YES
OUTBOARD LEADING EDGE SPAR (ROSETTE)	SLEOA	BOTH		NG	YES	YES	NO	NO
	SLEOB	BOTH		NG	YES	YES	NO	NO
	SLEOC	BOTH		NG	YES	YES	NO	NO
INBOARD MID SPAR (ROSETTE)	SMIA	BOTH		NG	YES	YES	NO	NO
	SMIB	BOTH		NG	YES	YES	NO	NO
	SMIC	BOTH		NG	YES	YES	NO	NO
OUTBOARD MID SPAR (ROSETTE)	SMOA	BOTH		NG	YES	YES	YES	YES
	SMOB	BOTH		NG	YES	YES	YES	YES
	SMOC	BOTH		NG	YES	YES	YES	YES
INBOARD AFT SPAR (ROSETTE)	SAIA	BOTH		NG	YES	YES	NO	NO
	SAIB	BOTH		NG	YES	YES	NO	NO
	SAIC	BOTH		NG	YES	YES	NO	NO
OUTBOARD AFT SPAR (ROSETTE)	SAOA	BOTH		NG	YES	YES	NO	NO
	SAOB	BOTH		NG	YES	YES	NO	NO
	SAOC	BOTH		NG	YES	YES	NO	NO
INBOARD TORQUE TUBE (FULL BRIDGE)	SITT	BOTH		NG	YES	YES	YES	NO

Figure A47 Instrumentation Nomenclature

DESCRIPTION	DATA DESIGNATION	APPLIES TO WHICH MODEL	RANGE (EU)	SIGNAL ⁽¹⁾ COND. RESPON.	MOD COMP CONDITIONED SIGNAL INPUT	MOD COMP REAL TIME MONITORING	OPTICAL SWITCH BOX CONNECTION	STRIP CHART OUTPUT REQ'D ⁽²⁾
STRAIN GAGES (CONT.)								
OUTBOARD TORQUE TUBE (FULL BRIDGE)	SOTT	BOTH		NG	YES	YES	YES	NO
THERMOCOUPLES								
INBOARD LEADING EDGE SPAR	TLEI	BOTH		NASA	YES	YES	NO	NO
OUTBOARD LEADING EDGE SPAR	TLEO	BOTH		NASA	YES	YES	NO	NO
INBOARD MID SPAR	TMI	BOTH		NASA	YES	YES	YES	YES
OUTBOARD MID SPAR	TMO	BOTH		NASA	YES	YES	NO	NO
INBOARD AFT SPAR	TAI	BOTH		NASA	YES	YES	NO	NO
OUTBOARD AFT SPAR	TAO	BOTH		NASA	YES	YES	NO	NO
INBOARD TORQUE TUBE-CONROL	TTTIC	BOTH		NG	YES	YES	YES	NO
OUTBOARD TORQUE TUBE- CONTROL	TTTOC	BOTH		NG	YES	YES	YES	NO
INBOARD TORQUE TUBE-DATA	TTTID	BOTH		NASA	YES	YES	NO	NO
OUTBOARD TORQUE TUBE-DATA	TTTOD	BOTH		NASA	YES	YES	NO	NO
SMA-TRAILING EDGE FLAP	TSMAF	SMA		NASA	YES	YES	YES	NO
SMA-AILERON	TSMAA	SMA		NASA	YES	YES	YES	NO
PSI MODULE 1	TPSI1	BOTH		NASA	YES	YES	NO	NO
PSI MODULE 2	TPSI2	BOTH		NASA	YES	YES	NO	NO
ACCELEROMETERS								
WING TIP- FORWARD SPAR	AWTFS	BOTH		NG	YES	NO	YES	YES
WING TIP- MID SPAR	AWTMS	BOTH		NG	YES	NO	YES	YES
WING TIP- AFT SPAR	AWTAS	BOTH		NG	YES	NO	YES	YES
TRAILING EDGE FLAP	AFLAP	BOTH		NG	YES	NO	YES	YES
AILERON	AAIL	BOTH		NG	YES	NO	YES	YES
TILT SENSORS								
WING ROOT	TILTW R	BOTH		NG	YES	YES	YES	NO
MID RIB	TILTM R	BOTH		NG	YES	YES	YES	NO
WING TIP	TILTW T	BOTH		NG	YES	YES	YES	NO

Figure A47 Instrumentation Nomenclature (cont.)

DESCRIPTION	DATA DESIGNATION	APPLIES TO WHICH MODEL	RANGE (EU)	SIGNAL ⁽¹⁾ COND. RESPON.	MOD COMP CONDITIONED SIGNAL INPUT	MOD COMP REAL TIME MONITORING	OPTICAL SWITCH BOX CONNECTION	STRIP CHART OUTPUT REQ'D ⁽²⁾
INCLINOMETER								
SCHEAVITZ INCLINOMETER- WING ROOT	INCWR	BOTH	+30 DEG	NG	YES	YES	YES	NO
POTENTIOMETER								
TRAILING EDGE FLAP POTENTIOMETER	POSF	CONV.	0-15 DEG	NG	YES	YES	YES	NO
OPTICAL STRAIN GAGES								
			(USTRAIN)					
TRAILING EDGE FLAP UPPER	OSFU	SMA	15000	FS	YES	YES	NO	NO
TRAILING EDGE FLAP LOWER	OSFL	SMA	15000	FS	YES	YES	NO	NO
LOWER AILERON	OSAL	SMA	15000	FS	YES	YES	NO	NO
UPPER AILERON	OSAU	SMA	15000	FS	YES	YES	NO	NO
LVDT								
			INCHES					
TRAILING EDGE FLAP LVDT	LVDTF	SMA	+0.2	LM	YES	YES	YES	NO
AILERON LVDT	LVDTA	SMA	+0.2	LM	YES	YES	YES	NO
CONTROLS (NO DATA INPUTS REQ'D) (WIRE ID ONLY)								
GLOBE MOTOR CONTROL- FLAP ROTATION	CNT1	CONV.		NG	N/A	N/A	N/A	N/A
TORQUE TUBE INBOARD	CNT2	BOTH		NG	N/A	N/A	N/A	N/A
TORQUE TUBE OUTBOARD	CNT3	BOTH		NG	N/A	N/A	N/A	N/A
SMA TRAILING EDGE FLAP- UPPER	CNT4	SMA		LM	N/A	N/A	N/A	N/A
SMA TRAILING EDGE FLAP- LOWER	CNT5	SMA		LM	N/A	N/A	N/A	N/A
SMA AILERON- UPPER	CNT6	SMA		LM	N/A	N/A	N/A	N/A
SMA AILERON-LOWER	CNT7	SMA		LM	N/A	N/A	N/A	N/A
OTHER								
REMOTE RCAL COMMAND		BOTH		NG				

Figure A47 Instrumentation Nomenclature (cont.)

MODULE NO. 1

RANGE ± 5 PSID

PORT NO	TAP NO.	DESCRIPTION	X/C	Q-D PORT
1	VERIF.			
2	A1	LEADING EDGE -INBOARD ROW		
3	A2	UPPER SURFACE -INBOARD ROW		
4	A4			
5	A6			
6	A8			
7	A10			
8	A12			
9	B1	LEADING EDGE - MID INBOARD ROW		
10	B2	UPPER SURFACE- MID INBOARD ROW		
11	B4			
12	B6			
13	B8			
14	B10			
15	B12			
16	C1	LEADING EDGE - MID OUTBOARD ROW		
17	C2	UPPER SURFACE - MID OUTBOARD ROW		
18	C4			
19	C6			
20	C8			
21	C10			
22	C12			
23	D1	LEADING EDGE - OUTBOARD ROW		
24	D2	UPPER SURFACE - OUTBOARD ROW		
25	D4			
26	D6			
27	D8			
28	D10			
29	D12			
30				
31				
32	VERIF.			

Figure A48

MODULE NO. 2

RANGE ± 1 PSID

PORT NO	TAP NO.	DESCRIPTION	X/C	Q-D PORT
1	VERIF.			
2	A14	UPPER SURFACE PRESSURES - INBOARD ROW		
3	A16			
4	A18			
5	A20			
6	A22			
7	A24			
8	A26	▼		
9	A28	TRAILING EDGE PRESSURE - INBOARD ROW		
10	A3	LOWER SURFACE PRESSURES - INBOARD ROW		
11	A5			
12	A7			
13	A9			
14	A11			
15	A13			
16	A15			
17	A17			
18	A19			
19	A21			
20	A23			
21	A25			
22	A27	▼		
23				
24				
25				
26				
27				
28				
29				
30				
31				
32	VERIF.			

Figure A49

MODULE NO. 3

RANGE ± 1 PSID

PORT NO	TAP NO.	DESCRIPTION	X/C	Q-D PORT
1	VERIF.			
2	B14	UPPER SURFACE PRESSURES - MID INBOARD ROW		
3	B16			
4	B18			
5	B20			
6	B22			
7	B24			
8	B26	▼		
9	B28	TRAILING EDGE PRESSURE - MID INBOARD ROW		
10	B3	LOWER SURFACE PRESSURES - MID INBOARD ROW		
11	B5			
12	B7			
13	B9			
14	B11			
15	B13			
16	B15			
17	B17			
18	B19			
19	B21			
20	B23			
21	B25			
22	B27	▼		
23				
24				
25				
26				
27				
28				
29				
30				
31				
32	VERIF.			

Figure A50

MODULE NO. 4

RANGE ± 1 PSID

PORT NO	TAP NO.	DESCRIPTION	X/C	Q-D PORT
1	VERIF.			
2	C14	UPPER SURFACE PRESSURES - MID OUTBOARD ROW		
3	C16			
4	C18			
5	C20			
6	C22			
7	C24			
8	C26	▼		
9	C28	TRAILING EDGE PRESSURE - MID OUTBOARD ROW		
10	C3	LOWER SURFACE PRESSURES - MID OUTBOARD ROW		
11	C5			
12	C7			
13	C9			
14	C11			
15	C13			
16	C15			
17	C17			
18	C19			
19	C21			
20	C23			
21	C25			
22	C27	▼		
23				
24				
25				
26				
27				
28				
29				
30				
31				
32	VERIF.			

Figure A51

MODULE NO. 5

RANGE ± 1 PSID

PORT NO	TAP NO.	DESCRIPTION	X/C	Q-D PORT
1	VERIF.			
2	D14	UPPER SURFACE PRESSURES - OUTBOARD ROW		
3	D16			
4	D18			
5	D20			
6	D22			
7	D24			
8	D26	▼		
9	D28	TRAILING EDGE PRESSURE - OUTBOARD ROW		
10	D3	LOWER SURFACE PRESSURES - OUTBOARD ROW		
11	D5			
12	D7			
13	D9			
14	D11			
15	D13			
16	D15			
17	D17			
18	D19			
19	D21			
20	D23			
21	D25			
22	D27	▼		
23				
24				
25				
26				
27				
28				
29				
30				
31				
32	VERIF.			

Figure A52

SMART WING DATA REDUCTION PROBLEM STATEMENT

PROGRAM: SMART WING TEST NO. ENGINEER: SCHERER DATE: 3/16/96 PAGE B70

NO.	EQUATION	TERM	UNIT	SOURCE	DISPOSITION
1	<u>TUNNEL PARAMETERS REQUIRED</u> PTO TUNNEL TOTAL PRESSURE PO TUNNEL STATIC PRESSURE TTO TUNNEL TOTAL TEMPERATURE RN TUNNEL REYNOLD'S NUMBER PER FOOT M MACH NUMBER QO TUNNEL DYNAMIC PRESSURE	PTO	PSIA	EQ 1	TAB
		PO	PSIA	EQ 1	TAB
		TTO	DEGR	EQ 1	TAB
		QO	PSIA	EQ 1	TAB
		MACH	---	EQ 1	TAB
		RN	---	EQ 1	TAB

IV-A-70

SMART WING DATA REDUCTION PROBLEM STATEMENT

PROGRAM: SMART WING TEST NO. _____ ENGINEER: SCHERER DATE: 3/16/96 PAGE B71

NO.	EQUATION	TERM	UNIT	SOURCE	DISPOSITION
2	<u>MODEL POSITION</u>	AOA	DEG	MC OUTPUT	TAB
		ALP1	DEG	EQ 2	TAB
	<u>ALPHA</u> MODEL ANGLE OF ATTACK CALCULATED AS FOLLOWS:	ALP2	DEG	EQ 2	TAB
		ALP3	DEG	EQ 2	TAB
	AOA - ALPHA CALCULATED FROM MODEL SUPPORT SYSTEM	ALP4	DEG	EQ 2	TAB
		INCWR	VOLTS	MC OUTPUT	TAB
	ALP1 = $A1 * \sin(A2 * \text{INCWR})$ FROM SCHEAVITZ INCLINOMETER	TILTWR	VOLTS	MC OUTPUT	TAB
		TILTMR	VOLTS	MC OUTPUT	TAB
	ALP2 = $A1 + A2 * \text{TILTWR}$ FROM INBOARD TILT SENSOR	TILTW	VOLTS	MC OUTPUT	TAB
		A1	DEG	CONST	
	ALP3 = $AM1 + AM2 * \text{TILTMR}$ FROM MID WING TILT SENSOR	A2	DEG/V	CONST	
		A11	DEG	CONST	
	ALP4 = $AO1 + AO2 * \text{TILTW}$ FROM OUTBOARD TILT SENSOR	A12	DEG/V	CONST	
		AM1	DEG	CONST	
	<u>WING TWIST CALCULATIONS</u>	AM2	DEG/V	CONST	
		AO1	DEG	CONST	
	DAOAI = $ALP2 - ALP1$	AO2	DEG/V	CONST	
		DAOAI	DEG	EQ 2	TAB
	DAOAM = $ALP3 - ALP1$	DAOAM	DEG	EQ 2	TAB
		DAOAO	DEG	EQ 2	TAB
	DAOAO = $ALP4 - ALP1$				

IV-A-71

SMART WING DATA REDUCTION PROBLEM STATEMENT

PROGRAM: SMART WING TEST NO. _____ ENGINEER: SCHERER DATE: 3/16/96 PAGE B73

NO.	EQUATION	TERM	UNIT	SOURCE	DISPOSITION
5	<p>STRAIN GAGE OUTPUTS - STRESSES, STRAINS, AND TORQUES</p> <p><u>CALCULATE INDIVIDUAL STRAINS AND STRESSES FROM GAGES FROM ALL ROSETTES</u></p> <p>If i = 1, refer to gage SLEIA 2, refer to gage SLEIB 3, refer to gage SLEIC 4, refer to gage SLEOA 5, refer to gage SLEOB 6, refer to gage SLEOC 7, refer to gage SMIA 8, refer to gage SMIB 9, refer to gage SMIC</p> <p>If i = 10, refer to gage SMOA 11, refer to gage SMOB 12, refer to gage SMOC 13, refer to gage SAIA 14, refer to gage SAIB 15, refer to gage SAIC 16, refer to gage SAOA 17, refer to gage SAOB 18, refer to gage SAOC</p> <p>$\epsilon_i = (4 * V_{oi}) / (GF_i * V)$ for i = 1- 18</p> <p>$\sigma_i = E * \epsilon_i$ for i = 1- 18</p> <p>where V = Excitation Voltage V_{oi} = Output Voltage for each gage (corresponds to above nomenclature) GF_i = Gage Factor for each gage</p>	SLEIA	VOLTS	MC-OUTPUT	TAB TAB
		SLEIB	VOLTS	MC-OUTPUT	
		SLEIC	VOLTS	MC-OUTPUT	
		SLEOA	VOLTS	MC-OUTPUT	
		SLEOB	VOLTS	MC-OUTPUT	
		SLEOC	VOLTS	MC-OUTPUT	
		SMIA	VOLTS	MC-OUTPUT	
		SMIB	VOLTS	MC-OUTPUT	
		SMIC	VOLTS	MC-OUTPUT	
		SMOA	VOLTS	MC-OUTPUT	
		SMOB	VOLTS	MC-OUTPUT	
		SMOC	VOLTS	MC-OUTPUT	
		SAIA	VOLTS	MC-OUTPUT	
		SAIB	VOLTS	MC-OUTPUT	
		SAIC	VOLTS	MC-OUTPUT	
		SAOA	VOLTS	MC-OUTPUT	
		SAOB	VOLTS	MC-OUTPUT	
		SAOC	VOLTS	MC-OUTPUT	
		e_i	m-in/in	EQ 5	
		s_i	psi	EQ 5	
		E	psi/m-in/in	CONST	
		V_{oi}	VOLTS	MC-OUTPUT	
		V	VOLTS	CONST	
		Gf_i	in/ m-in	CONST	

IV-A-73

SMART WING DATA REDUCTION PROBLEM STATEMENT

PROGRAM: SMART WING TEST NO. _____ ENGINEER: SCHERER DATE: 3/16/96 PAGE B74

NO.	EQUATION	TERM	UNIT	SOURCE	DISPOSITION
6.	<p><u>CALCULATE PRINCIPAL STRESSES AND STRAINS FOR EACH ROSETTE</u></p> <p><u>ROSETTE SLEI (LEADING EDGE INBOARD)</u></p> $\epsilon_{SLEI} = 1 / 2 \left[\epsilon_1 + \epsilon_3 \pm \sqrt{(\epsilon_1 - \epsilon_3)^2 + (2 * \epsilon_2 - \epsilon_1 - \epsilon_3)^2} \right]$ $\sigma_{SLEI} = \frac{E}{2} \left[\frac{\epsilon_1 + \epsilon_3}{1 - \nu} \pm \frac{1}{1 + \nu} * \sqrt{(\epsilon_1 - \epsilon_3)^2 + (2 * \epsilon_2 - \epsilon_1 - \epsilon_3)^2} \right]$ $\theta_{SLEI} = \frac{1}{2} * \text{TAN}^{-1} \frac{2 * \epsilon_2 - \epsilon_1 - \epsilon_3}{\epsilon_1 - \epsilon_3}$ <p><u>ROSETTE SLEO (LEADING EDGE OUTBOARD)</u></p> $\epsilon_{SLEO} = 1 / 2 \left[\epsilon_4 + \epsilon_6 \pm \sqrt{(\epsilon_4 - \epsilon_6)^2 + (2 * \epsilon_5 - \epsilon_4 - \epsilon_6)^2} \right]$ $\sigma_{SLEO} = \frac{E}{2} \left[\frac{\epsilon_4 + \epsilon_6}{1 - \nu} \pm \frac{1}{1 + \nu} * \sqrt{(\epsilon_4 - \epsilon_6)^2 + (2 * \epsilon_5 - \epsilon_4 - \epsilon_6)^2} \right]$ $\theta_{SLEO} = \frac{1}{2} * \text{TAN}^{-1} \frac{2 * \epsilon_5 - \epsilon_4 - \epsilon_6}{\epsilon_4 - \epsilon_6}$	<p>eSLE</p> <p>sSLEI</p> <p>qSLEI</p> <p>eSLEO</p> <p>sSLEO</p> <p>qSLEO</p> <p>E</p> <p>n</p> <p>e_i</p>	<p>m-in/in</p> <p>psi</p> <p>deg</p> <p>m-in/in</p> <p>psi</p> <p>deg</p> <p>psi/m-in/in</p> <p>---</p> <p>m-in/in</p>	<p>Eq 6</p> <p>Eq 6</p> <p>Eq 6</p> <p>Eq 6</p> <p>Eq 6</p> <p>Eq 6</p> <p>CONST</p> <p>CONST</p> <p>Eq 5</p>	<p>TAB</p> <p>TAB</p> <p>TAB</p> <p>TAB</p> <p>TAB</p> <p>TAB</p>

IV-A-74

SMART WING DATA REDUCTION PROBLEM STATEMENT

PROGRAM: SMART WING TEST NO. _____ ENGINEER: SCHERER DATE: 3/16/96 PAGE B75

NO.	EQUATION	TERM	UNIT	SOURCE	DISPOSITION
7	<p><u>CALCULATE PRINCIPAL STRESSES AND STRAINS FOR EACH ROSETTE</u></p> <p><u>ROSETTE SMI</u></p> $\epsilon_{SMI} = 1 / 2 \left[\epsilon_7 + \epsilon_9 \pm \sqrt{(\epsilon_7 - \epsilon_9)^2 + (2 * \epsilon_8 - \epsilon_7 - \epsilon_9)^2} \right]$ $\sigma_{SMI} = \frac{E}{2} \left[\frac{\epsilon_7 + \epsilon_9}{1 - \nu} \pm \frac{1}{1 + \nu} * \sqrt{(\epsilon_7 - \epsilon_9)^2 + (2 * \epsilon_8 - \epsilon_7 - \epsilon_9)^2} \right]$ $\theta_{SMI} = \frac{1}{2} * \text{TAN}^{-1} \frac{2 * \epsilon_8 - \epsilon_7 - \epsilon_9}{\epsilon_7 - \epsilon_9}$ <p><u>ROSETTE SMO</u></p> $\epsilon_{SMO} = 1 / 2 \left[\epsilon_{10} + \epsilon_{13} \pm \sqrt{(\epsilon_{10} - \epsilon_{13})^2 + (2 * \epsilon_{12} - \epsilon_{10} - \epsilon_{13})^2} \right]$ $\sigma_{SMO} = \frac{E}{2} \left[\frac{\epsilon_{10} + \epsilon_{13}}{1 - \nu} \pm \frac{1}{1 + \nu} * \sqrt{(\epsilon_{10} - \epsilon_{13})^2 + (2 * \epsilon_{12} - \epsilon_{10} - \epsilon_{13})^2} \right]$ $\theta_{SMO} = \frac{1}{2} * \text{TAN}^{-1} \frac{2 * \epsilon_{12} - \epsilon_{10} - \epsilon_{13}}{\epsilon_{10} - \epsilon_{13}}$	eSMI sSMI qSMI eSMO sSMO qSMO E n e _i	m-in/in psi deg m-in/in psi deg psi/m-in/in --- m-in/in	Eq 7 Eq 7 Eq 7 Eq 7 Eq 7 Eq 7 CONST CONST Eq 5	TAB TAB TAB TAB TAB TAB

IV-A-75

SMART WING DATA REDUCTION PROBLEM STATEMENT

PROGRAM: SMART WING TEST NO. _____ ENGINEER: SCHERER DATE: 3/16/96 PAGE B76

NO.	EQUATION	TERM	UNIT	SOURCE	DISPOSITION
8	<p><u>CALCULATE PRINCIPAL STRESSES AND STRAINS FOR EACH ROSETTE</u></p> <p><u>ROSETTE SAI</u></p> $\epsilon_{SAI} = 1 / 2 \left[\epsilon_{13} + \epsilon_{15} \pm \sqrt{(\epsilon_{13} - \epsilon_{15})^2 + (2 * \epsilon_{14} - \epsilon_{13} - \epsilon_{15})^2} \right]$ $\sigma_{SAI} = \frac{E}{2} \left[\frac{\epsilon_{13} + \epsilon_{15}}{1 - \nu} \pm \frac{1}{1 + \nu} * \sqrt{(\epsilon_{13} - \epsilon_{15})^2 + (2 * \epsilon_{14} - \epsilon_{13} - \epsilon_{15})^2} \right]$ $\theta_{SAI} = \frac{1}{2} * \text{TAN}^{-1} \frac{2 * \epsilon_{14} - \epsilon_{13} - \epsilon_{15}}{\epsilon_{13} - \epsilon_{15}}$ <p><u>ROSETTE SAO</u></p> $\epsilon_{SAO} = 1 / 2 \left[\epsilon_{16} + \epsilon_{18} \pm \sqrt{(\epsilon_{16} - \epsilon_{18})^2 + (2 * \epsilon_{17} - \epsilon_{16} - \epsilon_{18})^2} \right]$ $\sigma_{SAO} = \frac{E}{2} \left[\frac{\epsilon_{16} + \epsilon_{18}}{1 - \nu} \pm \frac{1}{1 + \nu} * \sqrt{(\epsilon_{16} - \epsilon_{18})^2 + (2 * \epsilon_{17} - \epsilon_{16} - \epsilon_{18})^2} \right]$ $\theta_{SAO} = \frac{1}{2} * \text{TAN}^{-1} \frac{2 * \epsilon_{17} - \epsilon_{16} - \epsilon_{18}}{\epsilon_{16} - \epsilon_{18}}$	<p>eSAI</p> <p>sSAI</p> <p>qSAI</p> <p>eSAO</p> <p>sSAO</p> <p>qSAO</p> <p>E</p> <p>n</p> <p>e_i</p>	<p>m-in/in</p> <p>psi</p> <p>deg</p> <p>m-in/in</p> <p>psi</p> <p>deg</p> <p>psi/m-in/in</p> <p>---</p> <p>m-in/in</p>	<p>Eq 8</p> <p>Eq 8</p> <p>Eq 8</p> <p>Eq 8</p> <p>Eq 8</p> <p>Eq 8</p> <p>CONST</p> <p>CONST</p> <p>Eq 5</p>	<p>TAB</p> <p>TAB</p> <p>TAB</p> <p>TAB</p> <p>TAB</p> <p>TAB</p> <p></p> <p></p> <p></p>

IV-A-76

SMART WING DATA REDUCTION PROBLEM STATEMENT

PROGRAM: SMART WING TEST NO. _____ ENGINEER: SCHERER DATE: 3/16/96 PAGE B79

NO.	EQUATION	TERM	UNIT	SOURCE	DISPOSITION
11	PITCHING MOMENT COEFFICIENT FOR EACH CHORDWISE STATION $CMA = \left[\sum_{i=2}^N 0.5 * \left(CPA_{(i-1)} - CPA_i \right) * \left(xca_i - xca_{(i-1)} \right) * 0.5 * \left(xca_i + xca_{(i-1)} \right) \right] -$ $\left[\sum_{j=2}^N 0.5 * \left(CPA_{(j-1)} - CPA_j \right) * \left(xca_j - xca_{(j-1)} \right) * 0.5 * \left(xca_j + xca_{(j-1)} \right) \right]$ $CMB = \left[\sum_{i=2}^N 0.5 * \left(CPB_{(i-1)} - CPB_i \right) * \left(xcb_i - xcb_{(i-1)} \right) * 0.5 * \left(xcb_i + xcb_{(i-1)} \right) \right] -$ $\left[\sum_{j=2}^N 0.5 * \left(CPB_{(j-1)} - CPB_j \right) * \left(xcb_j - xcb_{(j-1)} \right) * 0.5 * \left(xcb_j + xcb_{(j-1)} \right) \right]$ $CMC = \left[\sum_{i=2}^N 0.5 * \left(CPC_{(i-1)} - CPC_i \right) * \left(xcc_i - xcc_{(i-1)} \right) * 0.5 * \left(xcc_i + xcc_{(i-1)} \right) \right] -$ $\left[\sum_{j=2}^N 0.5 * \left(CPC_{(j-1)} - CPC_j \right) * \left(xcc_j - xcc_{(j-1)} \right) * 0.5 * \left(xcc_j + xcc_{(j-1)} \right) \right]$ $CMD = \left[\sum_{i=2}^N 0.5 * \left(CPD_{(i-1)} - CPD_i \right) * \left(xcd_i - xcd_{(i-1)} \right) * 0.5 * \left(xcd_i + xcd_{(i-1)} \right) \right] -$ $\left[\sum_{j=2}^N 0.5 * \left(CPD_{(j-1)} - CPD_j \right) * \left(xcd_j - xcd_{(j-1)} \right) * 0.5 * \left(xcd_j + xcd_{(j-1)} \right) \right]$	CMA CMB CMC CMD CPA CPB CPC CPD xca xcb xcc xcd	--- --- --- --- --- --- --- --- --- --- --- --	Eq 11 Eq 11 Eq 11 Eq 11 Eq 9 Eq 9 Eq 9 Eq 9 CONST CONST CONST CONST	TAB TAB TAB TAB

IV-A-79

IV-A-80

PROGRAM: SMART WING TEST NO. ENGINEER: SCHERER DATE: 3/16/96 PAGE B80

NO.	EQUATION	TERM	UNIT	SOURCE	DISPOSITION
11.	<p>PITCHING MOMENT COEFFICIENT FOR EACH CHORDWISE STATION (CONT.)</p> <p>N = 15</p> <p>where i =1 corresponds to tap 1 and j=1 corresponds to tap 1</p> <p>2 corresponds to tap 3 2 corresponds to tap 2</p> <p>3 corresponds to tap 5 3 corresponds to tap 4</p> <p>4 corresponds to tap 7 4 corresponds to tap 6</p> <p>5 corresponds to tap 9 5 corresponds to tap 8</p> <p>6 corresponds to tap 11 6 corresponds to tap 10</p> <p>7 corresponds to tap 13 7 corresponds to tap 12</p> <p>8 corresponds to tap 15 8 corresponds to tap 14</p> <p>9 corresponds to tap 17 9 corresponds to tap 16</p> <p>10 corresponds to tap 19 10 corresponds to tap 18</p> <p>11 corresponds to tap 21 11 corresponds to tap 20</p> <p>12 corresponds to tap 23 12 corresponds to tap 22</p> <p>13 corresponds to tap 25 13 corresponds to tap 24</p> <p>14 corresponds to tap 27 14 corresponds to tap 26</p> <p>15 corresponds to tap 28 15 corresponds to tap 28</p>				

SMART WING DATA REDUCTION PROBLEM STATEMENT

PROGRAM: SMART WING TEST NO. ENGINEER: SCHERER DATE: 3/16/96 PAGE B81

NO.	EQUATION	TERM	UNIT	SOURCE	DISPOSITION
12.	SECTION PITCHING MOMENT CORRECTED TO MOMENT REFERENCE CENTER $CMRCA = CNA * \frac{clea}{cbar} + CMA$ $CMRCC = CNC * \frac{clec}{cbar} + CMC$ $CMRCB = CNB * \frac{cleb}{cbar} + CMB$ $CMRCD = CND * \frac{cled}{cbar} + CMB$	CMRCA	---	Eq 12	TAB
		CMRCB	---	Eq 12	TAB
		CMRCC	---	Eq 12	TAB
		CMRCD	---	Eq 12	TAB
		CNA	---	Eq 9	
		CNB	---	Eq 9	
		CNC	---	Eq 9	
		CND	---	Eq 9	
		clea	in	CONST	
		cleb	in	CONST	
		clec	in	CONST	
		cled	in	CONST	
		cbar	in	CONST	

IV-A-81

SMART WING DATA REDUCTION PROBLEM STATEMENT

PROGRAM: SMART WING TEST NO. _____ ENGINEER: SCHERER DATE: 3/16/96 PAGE B83

NO.	EQUATION	TERM	UNIT	SOURCE	DISPOSITION
14	CONTROL SURFACE POSITIONS	FPOS	DEG	Eq 14	TAB
		FLVDT	DEG	Eq 14	TAB
	<u>FLAP POTENTIOMETER (CONVENTIONAL WING ONLY)</u>	ALVDT	DEG	Eq 14	TAB
		FLOS	DEG	Eq 14	TAB
	FPOS = C0 + C1 * POSF	FUOS	DEG	Eq 14	TAB
		ALOS	DEG	Eq 14	TAB
	<u>LVDT (SMA WING ONLY)</u>	AUOS	DEG	Eq 14	TAB
		POSF	VOLTS	MC-OUTPUT	
	FLVDT = D0 + D1 * LVDTF	LVDTF	VOLTS	MC-OUTPUT	
		LVDTA	VOLTS	MC-OUTPUT	
	ALVDT = E0 + E1 * LVDTA	OSFU	VOLTS	MC-OUTPUT	
		OSFL	VOLTS	MC-OUTPUT	
	<u>OPTICAL STRAIN GAGES (SMA WING ONLY)</u>	OSAL	VOLTS	MC-OUTPUT	
		OSAU	VOLTS	MC-OUTPUT	
	FLOS = FL0 + FL1 * OSFU	C0	DEG	CONST	
		C1	DEG/V	CONST	
	FUOS = FU0 + FU1 * OSFL	D0	DEG	CONST	
		D1	DEG/V	CONST	
	ALOS = AL0 + AL1 * OSAL	E0	DEG	CONST	
		E1	DEG/V	CONST	
	AUOS = AU0 + AU1*OSAU	FL0	DEG	CONST	
		FL1	DEG/V	CONST	
		FU0	DEG	CONST	
		FU1	DEG/V	CONST	
		ALO	DEG	CONST	
		AL1	DEG/V	CONST	
		AU0	DEG	CONST	
		AU1	DEG/V	CONST	

IV-A-83

VOLUME IV

**STRESS REPORT
NORTHROP GRUMMAN SMART WING PROGRAM
FOR TESTING IN NASA LaRC
16 FT TRANSONIC DYNAMIC TUNNEL
29 APRIL 1996 - 24 MAY 1996**

PREPARED BY: K. APPA

C. A. MARTIN

APPROVED BY: J. N. KUDVA

REVISION 1

7 MAY 1996

B1. INTRODUCTION AND BACKGROUND

The use of wing warping and contoured control surfaces to control aircraft is not a new idea. It was used by the Wright brothers for their Flyer, and more recently on the Mission Adaptive Wing program. The drawback of the latter design was the complexity and weight added to the aircraft by the actuators used. The Northrop Grumman Smart Wing program (F33615-C-95-3202, from ARPA / WL) will use new actuators that are both smaller and lighter to twist and contour the flap and aileron on a 16% F/A-18 E/F wind tunnel model. The construction of wind tunnel models permits integration issues to be worked out at a more manageable scale, and allows us to foresee potential problems with scaling up to full scale aircraft.

Two wind tunnel models have been fabricated, each with an identical wing box, leading edge control surfaces and rigid inboard section. The difference in the models is the control surfaces. The first model to be tested has conventional hinged flaps and ailerons. This model will be used to gather baseline performance data and provide a reference to gauge performance gains of the smart wing. Figure B1 shows the layout for both wind tunnel models.

The other model, the smart wing, will be constructed identically as the baseline model but with the new actuators and trailing edge control surfaces. A 1.0 in. diameter shape memory alloy (SMA) torque tube will be inserted along the center spar (approx. at 0.40c) to add twist to the model. The trailing edge control surfaces are replaced with a hingeless flap and aileron that have embedded SMA wires that contour the shape of the trailing edge.

In this report a stress analysis of the load bearing structures is presented, along with the analysis of attachment of the model to the balance. Also included in Section B8 is a summary of the flutter and dynamic analysis, with model natural frequencies and damping vs. Q charts.

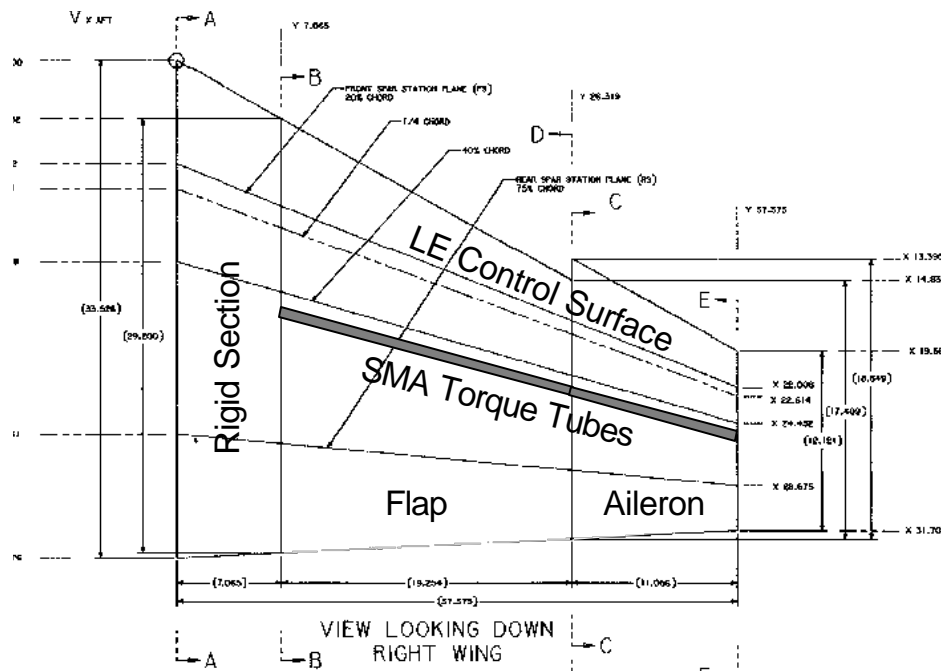


Figure B1. Basic Wind Tunnel Model Planform

B1.1 Summary of Margins of Safety

	Material	Load Type	Margin of Safety	Page Number
Balance Fastener	CRES per ASTM 5737	Shear due to lift	167	9
Balance Fastener	CRES per ASTM 5737	Shear due to Rolling	148	9
Balance Fastener	CRES per ASTM 5737	Shear due to Pitching	16.9	11
Combined Loads on Balance Attachment	CRES per ASTM 5737	Shear	15.2	12
L-Bracket	CRES per ASTM 5737	Shear due to Lift	25	12
L-Bracket	CRES per ASTM 5737	Bending due to Pitching Moment	7.5	12
L Bracket	CRES per ASTM 5737	Bending due to Spanwise Bending	28	13
Combined Loads on L-Bracket	CRES per ASTM 5737	Shear	41.7	13
Combined Loads on L-Bracket	CRES per ASTM 5737	Shear	186	13
LE Inboard Attachment Fastener	CRES per ASTM 5737	Shear	6.36	14
LE Inboard Attachment	7075 Aluminum	Bearing	5.17	15
LE Outboard Attachment Fastener	CRES per ASTM 5737	Shear	8.34	15
LE Outboard Attachment	7075 Aluminum	Bearing	6.83	15
TE Inboard – Outboard Hinge (Conv. Wing)	CRES Rod	Shear	58.9	18

Figure B2 Summary of Margins of Safety

TE Inboard – Inboard Hinge (Conv. Wing)	CRES Rod	Shear	108	18
TE Inboard (Smart Wing) Fastener	CRES per ASTM 5737	Shear	16.1	19
TE Inboard (Smart Wing) Attachment	7075 Aluminum	Bearing	13.4	19
TE Outboard (Smart Wing) Fastener	CRES per ASTM 5737	Shear	6.61	22
TE Outboard (Smart Wing) Attachment	7075 Aluminum	Bearing	5.38	22
TE Outboard (Conv. Wing) Screw	CRES per ASTM 5737	Shear	8.29	21
TE Outboard (Conv. Wing) Pin	CRES per ASTM 5737	Shear	4.36	22
TE Combined Loading	CRES per ASTM 5737	Shear	18.9	23
SMA Torque Tube Fastener	CRES per ASTM 5737	Shear	6.31	23
SMA Torque Tube Fastener Attachment	CRES per ASTM 5737	Bearing	20.4	24
SMA Torque Tube Attachment	17-4 PH	Bearing	20.1	24
LE Spar to Root Rib	7075 Aluminum	Shear due to Lift	180	25
LE Spar to Root Rib	7075 Aluminum	Shear due to Pitching Moment	57.3	25
Combined Loading on LE Spar	7075 Aluminum	Shear	41.0	26

Figure B2 Summary of Margins of Safety (continued)

B1.2 Table of Contents

B1 Introduction and Background	Page 85
B1.1 Summary of Margins of Safety	Page 86
B1.2 Table of Contents	Page 88
B2 Material Properties and Model Parameters	Page 90
B2.1 Model Dimensions and Loads	Page 91
B3 Balance Attachment	Page 91
B3.1 Stress on Wing to Pedestal Attachment	Page 92
B3.1.1 Fastener Shear due to Lift Force	Page 92
B3.1.2 Fastener Tension due to Rolling Moment	Page 93
B3.1.3 Fastener Shear due to Pitching Moment	Page 93
B3.1.4 Combined Loading	Page 94
B3.2 Stress and Deflection of L-Bracket	Page 95
B3.2.1 Stress and Deflection due to Lift Force	Page 95
B3.2.2 Stress and Deflection due to Pitching Moment	Page 95
B3.2.3 Stress and Deflection due to Spanwise Bending	Page 96
B3.2.4 Combined Loading	Page 96
B4 Leading Edge Control Surface Attachment	Page 96
B4.1 Leading Edge Inboard Control Surface	Page 96
B4.2 Leading Edge Outboard Control Surface	Page 98
B5 Trailing Edge Control Surface Attachment	Page 99
B5.1 Flap Attachment	Page 99
B5.1.1 Conventional Flap Attachment	Page 100
B5.1.2 Shape Memory Alloy Actuated Flap Attachment	Page 101
B5.2 Aileron Attachment	Page 103
B5.2.1 Conventional Aileron Attachment	Page 104
B5.2.2 Shape Memory Alloy Actuated Aileron Attachment	Page 105
B5.3 Combined Loading on Flap/Aileron Pin	Page 107
B6 Other Structures	Page 107
B6.1 Shape Memory Alloy Torque Tube Attachment	Page 108

B6.2 Spar Attachment to Root Rib	Page 109
B6.2.1 Combined Loading	Page 110
B7 Conclusions	Page 110
B8 Flutter and Dynamics	Page 111
B8.1 Dynamics and Flutter Analysis	Page 111
B8.2 Summary	Page 115

B2. MATERIAL PROPERTIES AND MODEL PARAMETERS

The allowable membrane stress, S_m , for the materials used in this report are established by using the rules set out in the Wind Tunnel Models Design Criteria. The materials in use for the models structural members are the following:

Construction Materials

$F_{tu} = S_u \equiv$ Ultimate Stress Tension $F_{ty} = S_y \equiv$ Yield Stress Tension

$F_{BR} \equiv$ Bearing Stress

$F_{su} \equiv$ Shear Ultimate

Alloy 7075-T6 Aluminum

$E = 10.3 \times 10^3$ ksi

$G = 3.9 \times 10^3$ ksi

$\nu = 0.33$

$\rho = 0.101$ lb/in³

$F_{tu} = S_u = 76.0$ ksi

$F_{Su} = 46.0$ ksi

$F_{ty} = S_y = 69.0$ ksi

$F_{BR} (e/D = 1.5) = 118$ ksi

4130 Steel

$E = 29.0 \times 10^3$ ksi

$G = 11.0 \times 10^3$ ksi

$\nu = 0.32$

$\rho = 0.283$ lb/in³

$F_{tu} = S_u = 95.0$ ksi

$F_{Su} = 57.0$ ksi

$F_{ty} = S_y = 75.0$ ksi

$F_{BR} = 200.0$ ksi

17-4PH Stainless Steel, H900

$E = 28.5 \times 10^3$ ksi

$G = 11.2 \times 10^3$ ksi

$\nu = 0.27$

$\rho = 0.282$ lb/in³

$F_{tu} = S_u = 190.0$ ksi

$F_{Su} = 123.0$ ksi

$F_{ty} = S_y = 170.0$ ksi

$F_{BR} = 255.0$ ksi

Fasteners (for Leading, Trailing Edges and Skin Attachment)

MS24693C2 and MS24693C3

Diameter = 0.112 in.

Material = CRES per AMS 5737 (A-2286)

Thread Size = 0.112 - 40 UNC - 2A

Head Diameter = 0.317 in.

Tensile Strength = 160 ksi

Locking Nut Plate

Huck Nut Plate FF 6010 L - 4 - A

Thread Size = 0.112 - 40 UNJC - 3B

Inserts

KNCA044OJ

Internal Thread = 4 - 40 UNJC-3B

L = 0.17 in. (Internal Locking Depth)

External Thread = 10 - 32 UNF-2A

T = 0.125 in. (Engagement Depth)

Socket Head Cap Screws

#2-56

Diameter = 0.086

Material = Alloy Steel

Double Shear Strength = 1320 lbs

Head Diameter = 0.140

Tensile Strength (minimum) = 702 lbs

Thread = UNRC

#8-32

Diameter = 0.164

Material = Alloy Steel

Double Shear Strength = 4800 lbs

Head Diameter = 0.270

Tensile Strength (minimum) = 2660 lbs

Thread = UNRC

Installation Torque

4 - 40 = 10 in-lbs

8 - 32 = 36 in-lbs

B2.1 Model Dimensions and Loads

The wind tunnel models are 16 % scale replicas of the F/A - 18 E/F wing with a 7.065 in. inboard section for electric motors and instrumentation. The modified NACA 65A series airfoil used in the model is based on the F/A - 18 design. The thickness varies from 12.4% at the root, to 6.2 % at the inboard rib, and 4.2 % at the tip.

The models were designed to have some flexibility, and lie somewhere between flutter models and rigid force models. This allows a SMA torque tube inserted along the center spar to change the wash-out of the model. The models also have incorporated into them novel trailing edge control surfaces and the instrumentation and power lines to actuate them. These design considerations lead to the decision to construct the models using a conventional wing box technique. Fabricating the models using this technique meant that the stiffness would not be able to be scaled down directly from the full scale aircraft (as is done with flutter models) due to the minimum gage thickness of the materials used in the fabrication. Listed below are the important dimensions and loads that will determine the margins of safety for the wind tunnel models.

Model Scale Factor = 16 %

Model Reference Dimensions

S_w = Wing Area = 887 in.²

b = Wing Span = 37.375 in.

Maximum α = 10°

Maximum Q = 120 psf @ M = 0.4 = 0.833 psi

Balance Forces at α = 10 degrees, Q = 120 psf

Lift = 400 lbs

Pitching Moment = 3000 in-lbs

Yawing Moment = 1000 in-lbs

The test plan calls for wind tunnel runs at N_z = 2.67 to be performed.

c_{root} = Root Chord = 33.526 in.

c_{tip} = Tip Chord = 12.121 in.

Rolling Moment = 7330 in-lbs

Axial = 26.7 lbs

B3. BALANCE ATTACHMENT

Both wing models will be attached to the balance via a 4130 stainless steel L-bracket that will use 9, $\frac{1}{4}$ in. alloy steel screws. The fastener pitch and edge distances are shown in Figure B3 with the applicable loads and their directions, along with a detail drawing of the L-bracket. The fastener pitch was set to the standard of 4 times the diameter while the edge distance was kept to 2 times the diameter of the fasteners.

B3.1 Stress on Wing to Pedestal Attachment

B3.1.1 Fastener Shear due to Lift Force

The models are attached to the balance using 0.25 in., UNRC thread bolts. The installation torque on the fasteners has not been set as of yet. It will be given in the final stress report.

Lift Force = 400 lbs

Assuming that each column of fasteners takes $\frac{1}{3}$ of total load:

Load in Each Fastener Column: $F_L = \text{Lift} / 3 = 400 / 3 = 133.33 \text{ lbs}$

Each Fastener in Shear, Load Evenly Divided

$P = F_L / 3 = 133.33 / 3 = 44.44 \text{ lbs}$

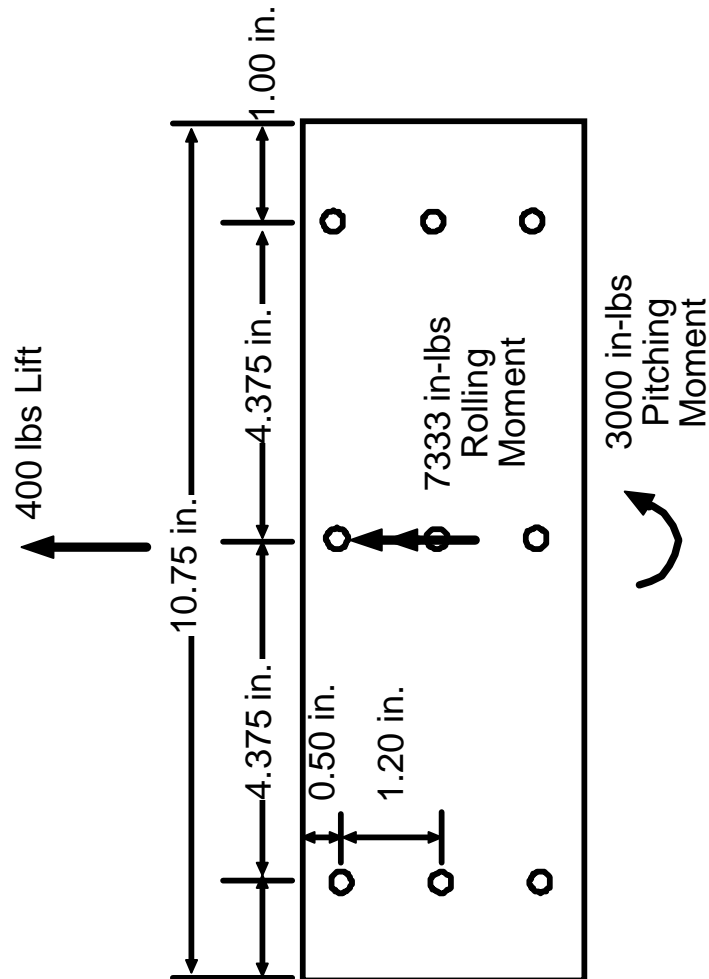


Figure B3. Pedestal to Wing Root Rib Fastener Pattern with maximum applied loads

$$\tau = \frac{4P}{\pi d} = \frac{4(44.44)}{\pi(0.25)^2} = 903.15 \text{ psi}$$

$$M. S. = \frac{\tau_s}{\tau} - 1 = \frac{57000}{903.15} - 1 = \mathbf{62.1}$$

Note: Even if all load in the column is carried by a single fastener (extreme of uneven load distribution), the margin of safety is still sufficient.

Bearing Load on L-Bracket

$$\sigma_{BR} = \frac{P}{dt} = \frac{44.44}{(\frac{1}{4})(1.00)} = 177.81 \text{ psi}$$

B3.1.2 Fastener Tension due to Rolling Moment

The rolling moment on the models is applied down the reference plane of the platform. This causes the bottom row of fasteners to be in tension (Figure B4).

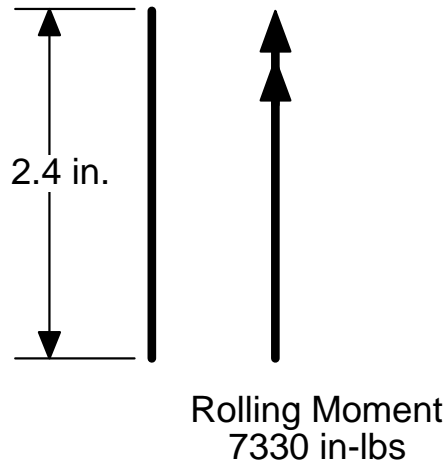


Figure B4. Rolling Moment Diagram

$$M = 7334 \text{ in-lbs}$$

$$x = 2.400 \text{ in.}$$

$$F_R = \frac{M}{x} = \frac{7334}{2.400} = 3.054 \times 10^3 \text{ lbs}$$

Force per fastener = P

$$P = \frac{F_R}{n_f} = \frac{3054}{3} = 1.018 \times 10^3 \text{ lbs}$$

$$M. S. = \frac{P_u}{P} - 1 = \frac{160000}{1018} - 1 = \mathbf{156}$$

B3.1.3 Fastener Shear due to Pitching Moment

Just as the rolling moment is about the center row of fasteners, the pitching moment also causes the model to rotate about the center row of fasteners. The moment is then reacted by the front and rear rows of fasteners (Figure B5).

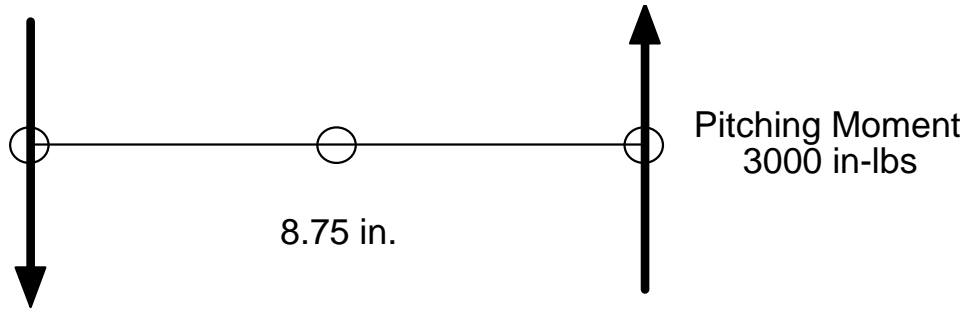


Figure B5. Pitching Moment Diagram

$$M = 3000 \text{ in-lbs}$$

$$x = 8.750 \text{ in.}$$

Force due to the pitching moment, F_P

$$F_P = \frac{M}{x} = \frac{3000}{2.400} = 1250.0 \text{ lbs}$$

$$P = \frac{F_P}{n_f} = \frac{1250.0}{3} = 416.67 \text{ lbs}$$

Thus, the shear load per fastener is given below:

$$\tau = \frac{4P}{\pi d^2} = \frac{(4)(416.67)}{\pi (1/4)^2} = 8.488 \times 10^3 \text{ psi}$$

$$\text{M. S.} = \frac{\tau_u}{\tau} - 1 = \frac{57000}{8488} - 1 = \mathbf{5.72}$$

The bearing stress on the material due to the fastener, σ_{BR} , is given by:

$$\sigma_{BR} = \frac{P}{(d)(t)} = \frac{416.67}{(1/4)(1)} = 1.667 \times 10^3 \text{ psi}$$

$$\text{M. S.} = \frac{\sigma_u}{\sigma_{BR}} - 1 = \frac{118000}{1667} - 1 = \mathbf{70}$$

The shear tear-out stress, τ_{Tear} , is given by:

$$\tau = \frac{P}{2(x)(t)} = \frac{416.67}{2(1)(1)} = 208.4 \text{ psi}$$

$$\text{M. S.} = \frac{\tau_{Tear}}{\tau} - 1 = \frac{25333}{208.4} - 1 = \mathbf{565}$$

B3.1.4 Combined Loading

The combined loads on the wing to pedestal attachment are shown below:

$$F_{Total} = F_{Pitch} + F_{Lift} = 416.67 + 44.44 = 461.11 \text{ lbs}$$

The maximum shear is then:

$$\tau = \frac{4P}{\pi d^2} = \frac{4(461.11)}{\pi (0.25)^2} = 9.394 \times 10^3 \text{ psi}$$

$$\text{M.S.} = \frac{\tau_u}{\tau} - 1 = \frac{57000}{9394} - 1 = \mathbf{5.1}$$

B3.2 Stress and Deflection of L-Bracket

The L-bracket (the piece that connects the pedestal to the balance) is made from a solid piece of 4130 CRES. Figure B6 shows a detail drawing of the L-bracket.

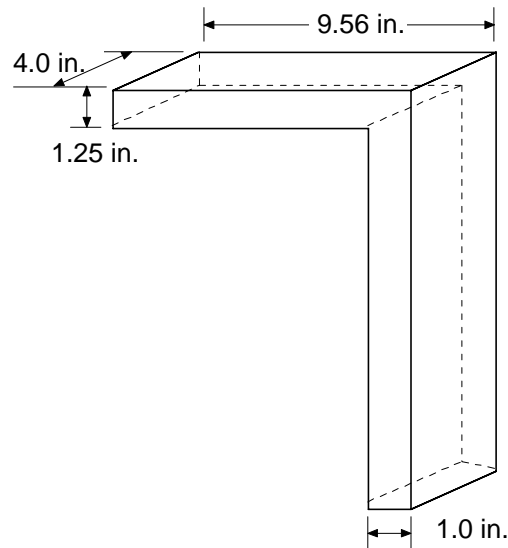


Figure B6. Semi Span Attachment Detail

The moments of inertia for the bracket is:

$$I_1 = \frac{1}{12}(b^3)(h) = \frac{1}{12}(4)^3(1.25) = 6.667 \text{ in.}^4$$

$$I_2 = \frac{1}{12}(h^3)(b) = \frac{1}{12}(1.25)^3(4) = 0.651 \text{ in.}^4$$

$$J = I_1 + I_2 = 6.667 + 0.651 = 7.318 \text{ in.}^4$$

B3.2.1 Stress and Deflection due to Lift Force

For normal operations, the lift is 400 lbs. at a distance of 24 in. from the balance which gives a moment of 9600 in-lbs.

$$\sigma = \frac{My}{I} = \frac{(9600)(2)}{6.667} = 2.88 \times 10^3 \text{ psi}$$

$$\text{M.S.} = \frac{\sigma}{\sigma_{\text{allow}}} - 1 = \frac{2880}{2880} - 1 = 18.8$$

For the nominal lift load, the deflection is:

$$\delta = \frac{Wl^3}{3EI} = \frac{(400)(4.21)^3}{3(2.9 \times 10^7)(6.667)} = 5.15 \times 10^{-5} \text{ in.}$$

B3.2.2 Stress and Deflection due to Pitching Moment

The pitching moment calculated for the models at $\alpha = 10$ degrees is 1100 in-lbs. Using this the stress on the L-bracket and deflection are calculated.

$$\sigma = \frac{My}{I} = \frac{(3000)(2)}{7.318} = 801.7 \text{ psi}$$

$$\text{M.S.} = \frac{\sigma}{\sigma_{\text{allow}}} - 1 = \frac{801.7}{801.7} - 1 = 70$$

For the nominal pitching moment, the deflection is:

$$\delta = \frac{Wl^3}{3EI} = \frac{(801)(4.21)^3}{3(2.9 \times 10^7)(7.318)} = 1.74 \times 10^{-4} \text{ in.}$$

B3.2.3 Stress and Deflection due to Spanwise Bending

$$\sigma = \frac{My}{I} = \frac{(8250)(4)}{6.667} = 2475 \text{ psi}$$

$$\text{M.S.} = \frac{\sigma_y}{\sigma} - 1 = \frac{57000}{2475} - 1 = 22$$

The deflection due to the spanwise bending is:

$$\delta = \frac{Wl^3}{3EI} = \frac{(2063)(4.0)^3}{3(2.9 \times 10^7)(6.667)} = 2.27 \times 10^{-4} \text{ in.}$$

B3.2.4 Combined Loading

The combined stress for the L-bracket is:

$$\sigma_{\text{Max}} = \frac{1}{2}(\sigma_x + \sigma_y) + \sqrt{\left(\frac{\sigma_x - \sigma_y}{2}\right)^2 + \tau_{xy}^2} \text{ psi}$$

$$\sigma_x = 2880 \text{ (Lift)}$$

$$\sigma_y = 2475 \text{ (Spanwise Bending)}$$

$$\tau_{xy} = 800.1 \text{ (Pitch)}$$

$$\sigma_{\text{Max}} = \frac{1}{2}(2880 + 2475) + \sqrt{\left(\frac{2880 - 2475}{2}\right)^2 + (800.1)^2} = 5472 \text{ psi}$$

The shear stress due to combined loading:

$$\tau_{\text{Max}} = \sqrt{\left(\frac{\sigma_x - \sigma_y}{2}\right)^2 + \tau_{xy}^2} = \sqrt{\left(\frac{2880 - 2475}{2}\right)^2 + (800.1)^2} = 825.3 \text{ psi}$$

B4. LEADING EDGE CONTROL SURFACE ATTACHMENT

For both the models the leading edge (LE) control surfaces, both inboard and outboard, will be non-moving, rigid structures. The leading edges will be attached to the front spar on the wing box, constructed from 7075-T6 aluminum, and attached using standard fastener MS24693 #4. The fasteners will be in a single row, with a spacing of one fastener per inch. The area and dimensions for the inboard control are given in Figure B7 and outboard in Figure B8.

B4.1 Leading Edge Inboard Control Surface

The leading edge inboard control surface is divergence critical. Using the maximum Q, and assuming that it is applied at the leading edge tip (the most critical location), the fastener shear stresses and bearing stresses are calculated. For the LE Inboard, there are 19 4/40, 0.112 diameter fasteners that go through a 0.050 in. thick skin. The fasteners are the Huck DPY - 7900 Series at approximately 1 in. spacing in KEEN Inserts set into the leading edge spar.

$$Q = 120 \text{ psf} = 0.833 \text{ psi}$$

$$\text{Area}_{\text{LEI}} = 82.49 \text{ in}^2$$

$$F_{\text{LEI}} = Q \cdot \text{Area} = (0.833)(82.49) = 68.742 \text{ lbs}$$

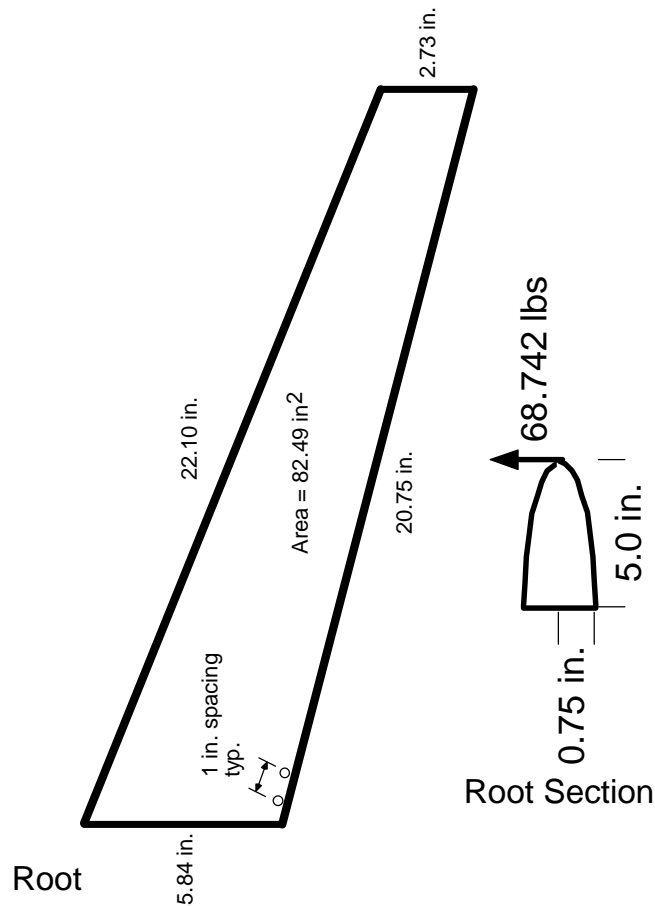


Figure B7. Leading Edge Inboard

For a Factor of Safety of 4:

$$F_{LEI} = (4)(68.742) = 274.97 \text{ lbs}$$

The force on the row of fasteners, T_{LEI} , is:

$$T_{LEI} = F_{LEI} \cdot \frac{5.84}{1.50} = \frac{(274.97)(5.84)}{1.50} = 1.071 \times 10^3 \text{ lbs}$$

Load per Fastener, P , is:

$$P = \frac{T_{LEI}}{n_f} = \frac{1071}{10} = 107.1 \text{ lbs}$$

Shear Load per Fastener, τ_f , :

$$\tau_f = \frac{4P}{\pi d^2} = \frac{4(107.1)}{\pi(0.112)^2} = 1.087 \times 10^4 \text{ psi}$$

$$M. S. = \frac{\tau}{\tau_f} - 1 = \frac{80000}{10871} - 1 = \mathbf{6.36}$$

Bearing Stress:

$$\sigma_{BR} = \frac{P}{dt} = \frac{107.1}{(0.112)(0.05)} = 1.91 \times 10^4 \text{ psi}$$

$$M. S. = \frac{\sigma_m}{\sigma_{BR}} - 1 = \frac{118000}{19125} - 1 = \mathbf{5.17}$$

B4.2 Leading Edge Outboard Control Surface

The attachment method for the LE outboard control surface is similar to that of the inboard control surface. The same fasteners are used with the same spacing. Figure B8 gives a planform view of the LE outboard along with the surface area along with the aerodynamic force applied. The fasteners are the Huck DPY - 7900 Series that are placed with a approximately 2 in. spacing into KEEN Inserts set into the leading edge spar.

$$Q = 120 \text{ psf} = 0.833 \text{ psi}$$

$$\text{Area}_{\text{LEO}} = 36.44 \text{ in}^2$$

The force per row of fastener, F_{LEO} is

$$F_{\text{LEO}} = Q \cdot \text{Area}_{\text{LEO}} = (0.833)(36.44) = 30.355 \text{ lbs}$$

Using a Factor of Safety of 4:

$$F_{\text{LEO}} = (4)(30.355) = 121.42 \text{ lbs}$$

The force on the row of fasteners, T_{LEO} :

$$T_{\text{LEO}} = F_{\text{LEO}} \cdot \frac{4.17}{1.00} = (121.42)(4.17) / 1.00 = 5.063 \times 10^3 \text{ lbs}$$

Load per Fastener, P ,

$$P = T_{\text{LEO}} / n_f = 5063 / 6 = 84.383 \text{ lbs}$$

Shear Load per Fastener, τ_f :

$$\tau_f = \frac{4P}{\pi d^2} = \frac{4(84.383)}{\pi(0.112)^2} = 8.565 \times 10^3 \text{ psi}$$

$$\text{M. S.} = \frac{\tau}{\tau_f} - 1 = \frac{80000}{8565} - 1 = \mathbf{8.34}$$

Bearing Stress:

$$\sigma_{\text{BR}} = \frac{P}{dt} = \frac{84.383}{(0.112)(0.05)} = 1.51 \times 10^4 \text{ psi}$$

$$\text{M. S.} = \frac{\sigma_m}{\sigma_{\text{BR}}} - 1 = \frac{118000}{15068} - 1 = \mathbf{6.83}$$

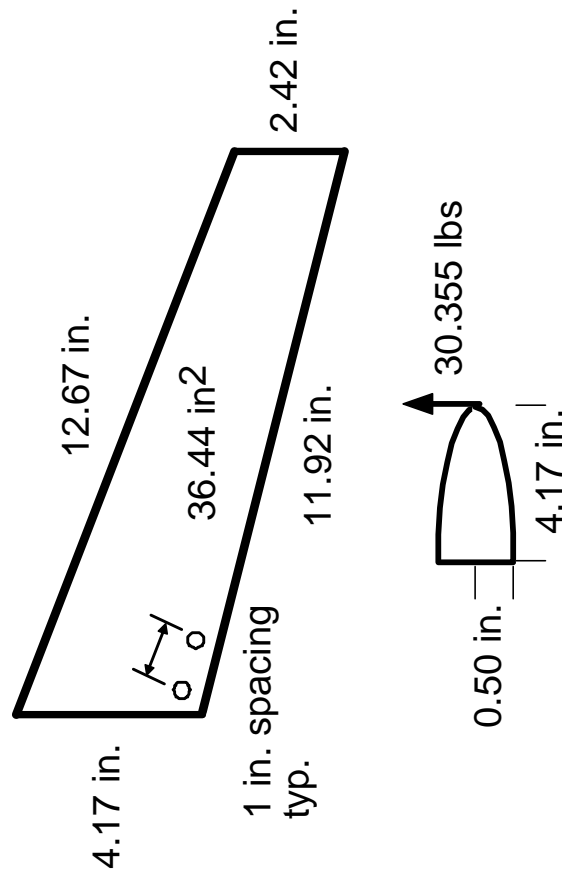


Figure B8. Leading Edge Outboard

B5. TRAILING EDGE CONTROL SURFACE ATTACHMENT

There are two different sets of trailing edge control surfaces. One set uses a conventional globe motor to change the position of the flap and uses pins and bearings to support the flap and brackets to hold on the aileron. The other set of control surfaces contours using shape memory alloy wires is attached similar to the leading edge, with through fasteners. Section B5.1 discusses the attachment of the flap control surfaces while B5.2 addresses the aileron.

B5.1 Flap Attachment

Figure B9 shows the lay-out of the trailing edge flap. Though the attachment methods are different for the two models, the physical dimensions are the same.

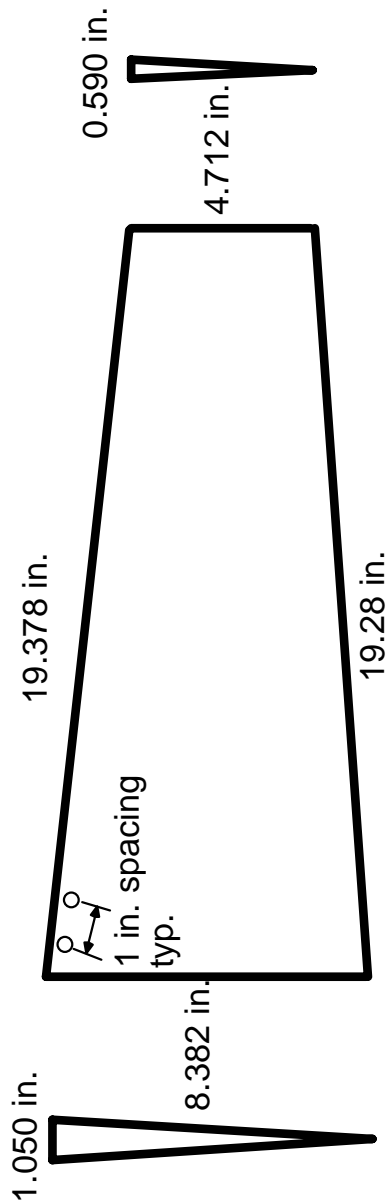


Figure B9. Trailing Edge Inboard - Flap

B5.1.1 Conventional Flap Attachment

The conventional flap is attached in the simplest way possible. A rod runs from the worm gear in the rigid section of the wing, through a bushing, to the flap where it is welded into a plate that is then bolted onto the flap. On the outboard section a similar arrangement is made. The rods that the flap rotates about is 0.5" dia 4340 steel rod from the worm gear to the inboard section of flap, and 0.380" dia 4340 steel rod at the outboard section. Figure B10 shows a detail of the center rib attachment of the flap hinge pin.

The loads that the outboard hinge rod must resist are:

$$Q = 120 \text{ psf} = 0.833 \text{ psi}$$

$$\text{Area}_{\text{TEI}} = 126.06 \text{ in}^2$$

The force on the flap and moment, F_{TEI} and M_{TEI} , is

$$F_{\text{TEI}} = Q \cdot \text{Area}_{\text{TEI}} = (0.833)(126.06) = 105.01 \text{ lbs}$$

$$\tau = \frac{4P}{\pi d^2} = \frac{4(105.05)}{\pi(\frac{3}{8})^2} = 951.1 \text{ psi}$$

$$\text{M.S.} = \frac{\tau_u}{\tau} - 1 = \frac{57000}{951.1} - 1 = 59$$

For the inboard hinge rod, the shear stress, τ , is:

$$F_{\text{TEI}} = Q \cdot \text{Area}_{\text{TEI}} = (0.833)(126.06) = 105.01 \text{ lbs}$$

$$\tau = \frac{4P}{\pi d^2} = \frac{4(105.05)}{\pi(0.5)^2} = 535.02$$

$$\text{M.S.} = \frac{\tau_u}{\tau} - 1 = \frac{57000}{535.02} - 1 = 108$$

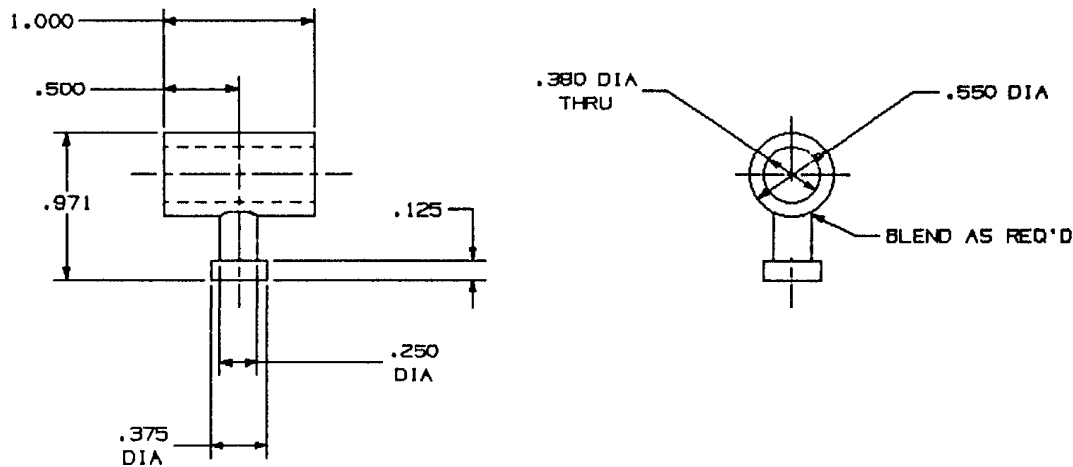


Figure B10. Conventional Flap Attachment Detail

B5.1.2 Shape Memory Alloy Actuated Flap Attachment

The shape memory alloy (SMA) actuated flap is attached in a similar method as the leading edges. Because the control surface does not rotate, the flap can be fastened rigidly to the rear spar. The fasteners are the Huck DPY - 7900 Series that are placed with a approximately 1 in. spacing into KEEN Inserts set into the skin along the trailing edge.

The main difference between the leading the edge and the trailing edge is the material that the control surface is made from. While the leading edge was aluminum, because of the special requirements imposed by the SMA wires, the trailing edges have a thermoset plastic that has inserts placed into it.

$$Q = 120 \text{ psf} = 0.833 \text{ psi}$$

$$\text{Area}_{\text{TEI}} = 126.06 \text{ in}^2$$

The force per row of fastener, F_{TEI} is

$$F_{\text{TEI}} = Q \cdot \text{Area}_{\text{TEI}} = (0.833)(126.06) = 105.01 \text{ lbs}$$

The force on the row of fasteners, T_{TEI} :

$$T_{TEI} = F_{TEI} \cdot x_h = 105.01 \cdot 8.32 / 1.0 = 8.74 \times 10^2 \text{ lbs}$$

Load per fastener, P :

$$P = T_{TEI} / n_f = 873.7 / 19 = 45.98 \text{ lbs}$$

Shear stress per fastener, τ_f :

$$\tau_f = 4P / \pi d^2 = 4(45.98) / \pi (.112)^2 = 4.667 \times 10^3 \text{ psi}$$

$$M. S. = \tau_f / \tau_{allow} - 1 = 80000 / 4667 - 1 = \mathbf{16.1}$$

Bearing Stress on skin, σ_{BR} :

$$\sigma_{BR} = P / dt = 45.98 / (.112)(.05) = 8.21 \times 10^3 \text{ psi}$$

$$M. S. = \sigma_m / \sigma_{BR} - 1 = 118000 / 8210 - 1 = \mathbf{13.4}$$

Surface Loads for SMA Flap

From F/A - 18 aircraft data, the hinge moment for $\delta_{Flap} = 0$ degrees is,

$$HM_{Flap, A/C} = 12,885 \text{ in-lbs}$$

Using scale factors to scale the hinge moments for the 16% model,

$$HM_{Flap, Model} = (HM_{Flap, A/C})(\text{Scale Factor}) = (12885)(4.10 \times 10^{-3})$$

$$HM_{Flap, Model} = 52.83 \text{ in-lbs}$$

The hinge moment is related to the distributed force being applied along the chord length of the flap by the following equation:

$$HM_{Flap, Model} = \frac{1}{2} \cdot w \cdot l^2$$

$$w = 2 \cdot HM / l^2 = 2(52.83) / (6.0)^2 = 2.935 \frac{\text{lb}}{\text{in}}$$

To find the pressure about the entire flap area, divide w by the span of the flap;

$$P_{Flap} = w / b_{Flap} = 2.935 / 19.30 = 0.152 \text{ psi}$$

Determination of Load on Individual Wires

Each SMA wire can withstand a 4 lb. axial force in its austenitic state before it yields. Figure B11 shows the forces and moments on the flap, with the moment broken down into the applied force. The hinge moment, 52.83 in-lbs, is derived from actual F/A-18 data and is not as conservative as the hinge moment used in determining the attachment margins of safety, but more realistically reflects the loads the flap will see in this wind tunnel test.

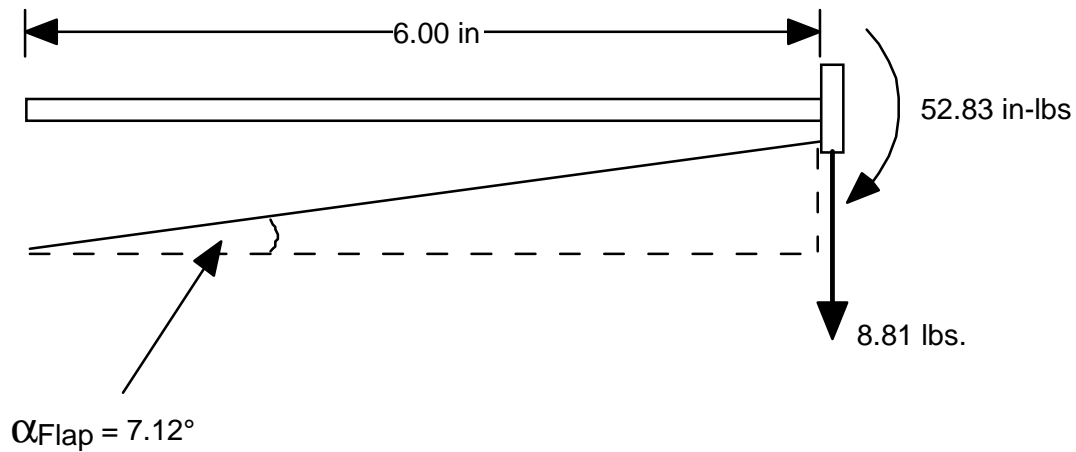


Figure B11. SMA Wire Force Diagram, Flap

Decomposing the moment into forces, F_{Flap}

$$F_{\text{Flap}} = \frac{M_{\text{Flap}}}{x_{\text{Flap}}} = \frac{52.83}{6.00} = 8.805 \text{ lbs}$$

The force on the wires is then,

$$F_{\text{Wire}} = \frac{F_{\text{Flap}}}{\tan \alpha} = \frac{8.805}{\tan(7.12^\circ)} = 70.49 \text{ lbs}$$

There are 92 lengths of wires on the flap, the force per wire is,

$$F_{n_{\text{Wire}}} = \frac{F_{\text{Wire}}}{n_{\text{Wire}}} = \frac{70.49}{92} = 0.766 \text{ lbs}$$

$$\text{M.S.} = \frac{F_{\text{yield}}}{F_{n_{\text{Wire}}}} - 1 = \frac{4}{0.766} - 1 = 4.22$$

B5.2 Aileron Attachment

Figure B12 shows the planform of both ailerons.

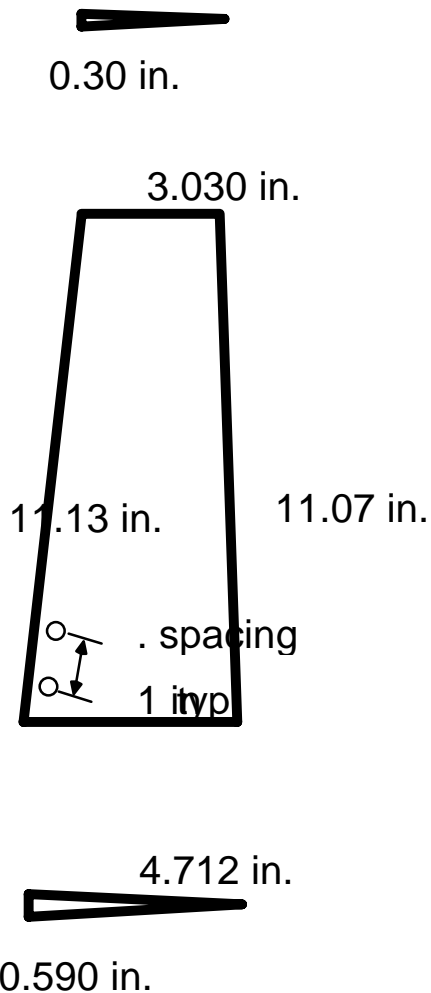


Figure B12. Trailing Edge Outboard - Aileron

B5.2.1 Conventional Aileron Attachment

The conventional aileron is attached using brackets. The initial test plan was to use a globe motor to actuate the aileron (like the flap), but because of aeroelastic reasons the plan was changed. The aileron was to be connected to the globe motor via a 3/8 in. steel rod. When aerodynamic simulations were run using ASTROS, it was found that the even though the rod was strong enough to withstand the maximum aerodynamic loading without failing, the rotational stiffness was not large enough to keep the rod from acting like a 28 in. long rotational spring. This lead to a very low flutter speed. To insure the safety of the tunnel and the model, it was decided to fix the aileron to the rear wing box spar with brackets. The bracket consist of plate that has a bend in it at certain degrees (± 0 , ± 5 , and ± 10 degrees) and a pin that slips from a special close-out rib into the aileron.

Figure B13 shows the design of the conventionally attached aileron. The aileron rotates about a 3/8 in. diameter rod on the inboard portion and a 1/8 pin outboard. To hold the angles of deflection, a screw and a pin are inserted into the outboard tip. There is also an angle bracket which bolts onto the upper surface and to the cap of the trailing edge spar.

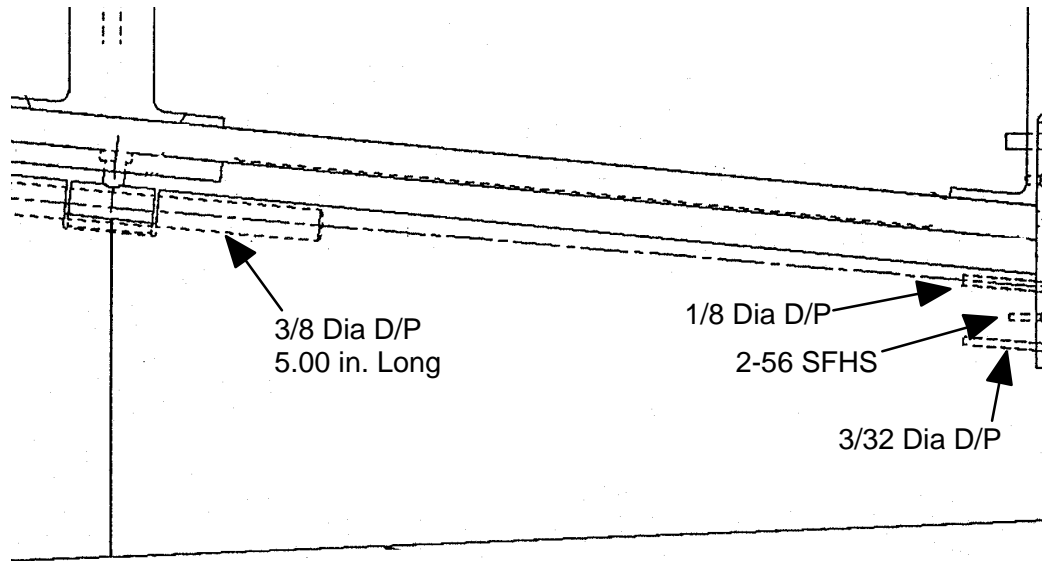


Figure B13. Aileron Attachment

Forces on aileron:

$$Q = 120 \text{ psf} = 0.833 \text{ psi}$$

$$\text{Area}_{\text{TEO}} = 42.80 \text{ in}^2$$

The force on the aileron and moment, F_{TEO} and M_{TEO} , is

$$F_{\text{TEO}} = Q \cdot \text{Area}_{\text{TEO}} = (0.833)(42.80) = 35.651 \text{ lbs}$$

$$M_{\text{TEO}} = F_{\text{TEO}} \cdot 3.03 \text{ in.} = 108.07 \text{ in-lbs}$$

The pin and the screw split the load 34/66, so:

$$F_{\text{SCREW}} = \left(\frac{M}{x_{\text{SCREW}}} \right) \cdot 0.34 = \left(\frac{107.93}{0.5} \right) \cdot 0.34 = 73.49 \text{ lbs}$$

$$F_{\text{PIN}} = \left(\frac{M}{x_{\text{PIN}}} \right) \cdot 0.66 = \left(\frac{107.93}{0.75} \right) \cdot 0.66 = 95.102 \text{ lbs}$$

The shear stress, τ_{SCREW} and τ_{PIN} , on each part is then:

$$\tau_{\text{SCREW}} = \frac{4P}{\pi d^2} = \frac{4(73.49)}{\pi(0.086)^2} = 1.265 \times 10^4 \text{ psi}$$

$$\tau_{\text{PIN}} = \frac{4P}{\pi d^2} = \frac{4(95.102)}{\pi(0.0938)^2} = 1.376 \times 10^4 \text{ psi}$$

The margin of safety for the screw and pin are:

$$\text{M.S.}_{\text{SCREW}} = \frac{\tau_U}{\tau_{\text{SCREW}}} - 1 = \frac{57000}{12651} - 1 = 3.5$$

$$\text{M.S.}_{\text{PIN}} = \frac{\tau_U}{\tau_{\text{PIN}}} - 1 = \frac{57000}{13762} - 1 = 3.14$$

B5.2.2. SMA Aileron Attachment

The SMA aileron is attached in a fashion similar to both the leading edge control surface (Section B4) and the flap (Section B5.1.2). Also similar to the flap, inserts will be used in the thermoset plastic to lock the fasteners in.

Forces on aileron:

$$Q = 120 \text{ psf} = 0.833 \text{ psi}$$

$$\text{Area}_{\text{TEO}} = 42.80 \text{ in}^2$$

The force per row of fastener, F_{TEO} is

$$F_{\text{TEO}} = Q \cdot \text{Area}_{\text{TEO}} = (0.833)(42.80) = 35.651 \text{ lbs}$$

Using Factor of Safety of 4:

$$F_{\text{TEO}} = (4)(35.651) = 142.60 \text{ lbs}$$

The force on the row of fasteners, T_{TEO} :

$$T_{\text{TEO}} = \frac{F_{\text{TEO}} \cdot x}{h} = \frac{(142.60)(4.712)}{.59} = 1.139 \times 10^3 \text{ lbs}$$

Load per fastener, P :

$$P = \frac{T_{\text{TEO}}}{n_f} = \frac{1138.9}{11} = 103.53 \text{ lbs}$$

Shear stress per fastener, τ_f :

$$\tau_f = \frac{4P}{\pi d^2} = \frac{4(103.53)}{\pi(0.112)^2} = 1.051 \times 10^4 \text{ psi}$$

$$\text{M. S.} = \frac{\tau}{\tau_f} - 1 = \frac{80000}{10509} - 1 = \mathbf{6.61}$$

Bearing stress of skin, σ_{BR} :

$$\sigma_{\text{BR}} = \frac{P}{dt} = \frac{103.53}{(.0112)(.05)} = 1.849 \times 10^4 \text{ psi}$$

$$\text{M. S.} = \frac{\sigma_m}{\sigma_{\text{BR}}} - 1 = \frac{118000}{18488} - 1 = \mathbf{5.38}$$

Surface Loads for SMA Aileron

From F/A - 18 aircraft data, the hinge moment for $\delta_{\text{Aileron}} = 0$ degrees is,

$$\text{HM}_{\text{Aileron, A/C}} = 3658.8 \text{ in-lbs}$$

Using scale factors to scale the hinge moments for the 16% model,

$$\text{HM}_{\text{Aileron, Model}} = (\text{HM}_{\text{Aileron A/C}})(\text{Scale Factor}) = (3658.8)(4.10 \times 10^{-3})$$

$$\text{HM}_{\text{Aileron, Model}} = 15.00 \text{ in-lbs}$$

The hinge moment is related to the distributed force being applied along the chord length of the aileron by the following equation:

$$\text{HM}_{\text{Aileron, Model}} = \frac{1}{2} \cdot w \cdot l^2$$

$$w = \frac{2 \cdot \text{HM}}{l^2} = \frac{2(15.00)}{(3.8)^2} = 2.08 \frac{\text{lb}}{\text{in}}$$

To find the pressure about the entire aileron area, divide w by the span of the aileron;

$$P_{\text{Aileron}} = \frac{w}{b_{\text{Aileron}}} = \frac{2.08}{11.10} = 0.187 \text{ psi}$$

Determination of Load on Individual Wires

Each SMA wire can withstand a 4 lb. axial force in its austenitic state before it yields. Figure B14 shows the forces and moments on the aileron, with the moment broken down into the applied force. The hinge moment, 14.96 in-lbs, is derived from actual F/A-18 data and is not as conservative as the hinge moment used in determining the attachment margins of safety, but more realistically reflects the loads the aileron will see in this wind tunnel test.

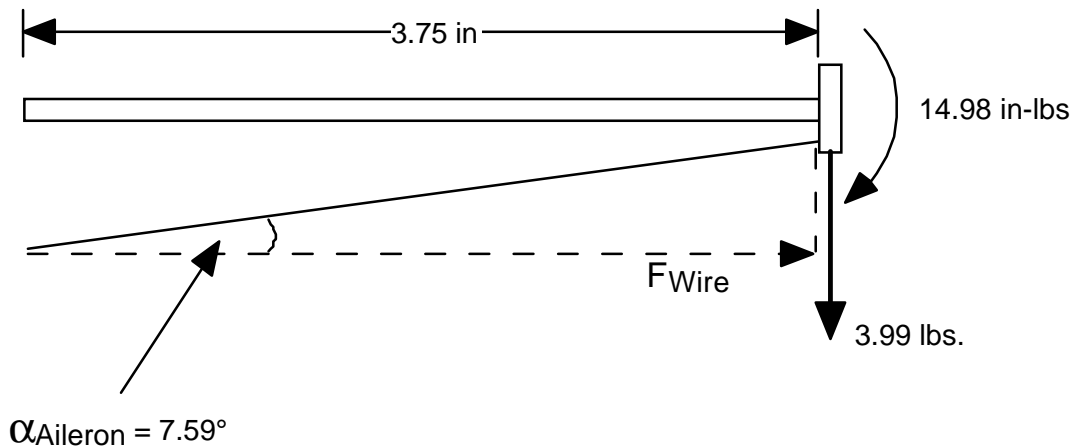


Figure B14. SMA Wire Force Diagram, Aileron

Decomposing the moment into forces, F_{Aileron}

$$F_{\text{Aileron}} = \frac{M_{\text{Aileron}}}{x_{\text{Aileron}}} = \frac{14.98}{3.75} = 3.99 \text{ lbs}$$

The force on the wires is then,

$$F_{\text{Wire}} = \frac{F_{\text{Aileron}}}{\tan \alpha} = \frac{3.99}{\tan(7.59^\circ)} = 29.94 \text{ lbs}$$

There are 52 lengths of wires on the aileron, the force per wire is,

$$F_{n_{\text{Wire}}} = \frac{F_{\text{Wire}}}{n_{\text{Wire}}} = \frac{29.94}{52} = 0.576 \text{ lbs}$$

$$\text{M.S.} = \frac{F_{\text{yield}}}{F_{n_{\text{Wire}}}} - 1 = \frac{4}{0.576} - 1 = 5.95$$

B5.3 Combined Loading on Flap/Aileron Pin

$$A_{\text{total}} = A_{\text{flap}} + A_{\text{aileron}} = 42.80 + 126.06 = 168.86 \text{ in.}^2$$

$$Q = 120 \text{ psf} = 0.833 \text{ psi}$$

$$F = Q \cdot A_{\text{Total}} = (0.833)(168.86) = 140.71$$

$$\tau = \frac{4P}{\pi d^2} = \frac{4(140.71)}{\pi(0.25)^2} = 2.867 \times 10^3 \text{ psi}$$

$$\text{M.S.} =$$

$$\frac{\tau_u}{\tau} - 1 = \frac{57000}{2866} - 1 = 18.9$$

B6. OTHER STRUCTURES

Along with the structures analyzed above, there are many other parts that, while not ultimate safety critical, require analysis to insure a successful test. Among these are the SMA torque tube attachment, aluminum skins, spar clips, and other assorted components. The first issue of the stress report will not include every piece (due to in progress design), but by tunnel entry. Analysis of most of the components has been completed and reported before. The remaining will be documented in the final stress report which will be issued prior to tunnel entry.

B6.1 SMA Torque Tube Attachment

To transfer the moment developed by SMA torque tube to the rest of the structure, a heavy bracket connects the tube to the mid-rib. The bracket must be able to transfer the approximately 2100 in-lbs of torque.

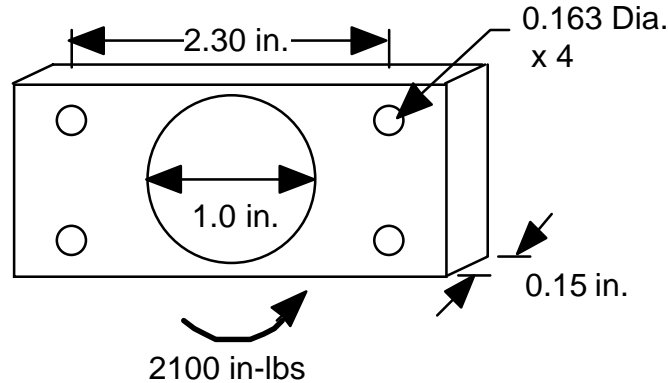


Figure B15. Main SMA Torque Tube Attachment

Moment applied by SMA torque tube, M_{SMA} , is

$$M_{SMA} = 2100 \text{ in-lbs}$$

$$x = 2.3 \text{ in.}$$

$$F_{SMA} = \frac{M}{x} = \frac{2100}{2.3} = 913.04 \text{ lbs}$$

The amount of force taken by each fastener, P , is:

$$P = \frac{F_{SMA}}{n_f} = \frac{913.04}{4} = 228.3 \text{ lbs}$$

Shear stress:

$$\tau_{SMA} = \frac{4P}{\pi d^2} = \frac{4(228.3)}{\pi(0.163)^2} = 1.094 \times 10^4 \text{ psi}$$

$$M.S. = \frac{\tau_u}{\tau} - 1 = \frac{80000}{10941} - 1 = 6.31$$

Bearing stress:

$$\sigma_{BR} = \frac{P}{dt} = \frac{228.3}{(0.163)(0.15)} = 9.337 \times 10^3 \text{ psi}$$

$$M.S. = \frac{\sigma_{BRu}}{\sigma_{BR}} - 1 = \frac{200000}{9337} - 1 = 20.4$$

B6.2 Spar Attachment to Root Rib

For the two models being constructed, the three main spars run from the root rib to the tip (Figure B16). Each spar is attached to the rib via 2 pins and 2 bolts. Below the diagram is the analysis of the leading edge spar joints. The leading edge spar is the most highly loaded spar in the model and was chosen to show the strength of joints.

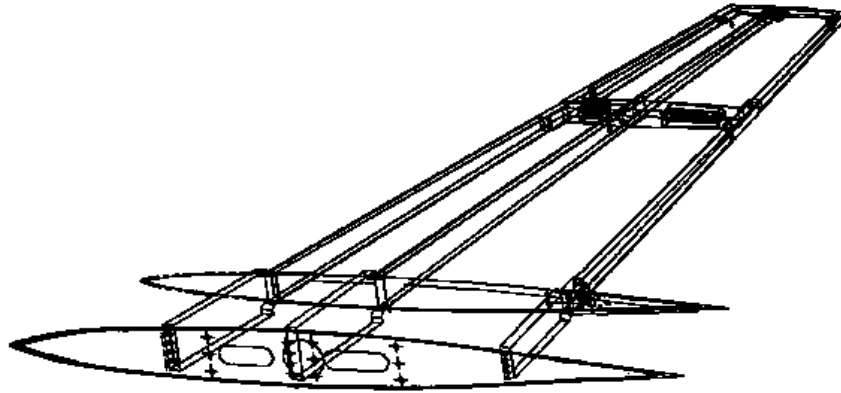


Figure B16. Wing Box Spars and Ribs

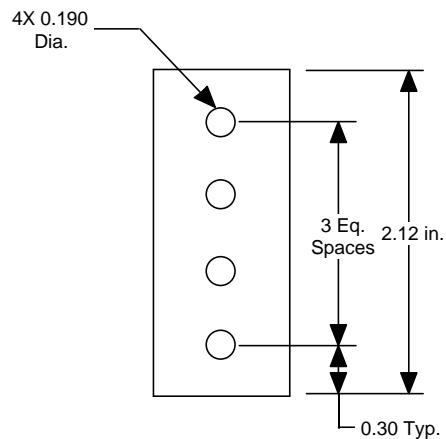


Figure B17. Leading Edge Spar Attachment

Front (Leading Edge) Spar:

The forces on the spar are:

Pitching Moment is 3000 in-lbs

$$F_{LERib} = \frac{M}{x} = \frac{3000}{6.636} = 452.1 \text{ lbs}$$

The shear force of each fastener , P, is:

$$P = F_{LEspar} / n_f = 452.1 / 4 = 113.03 \text{ lbs}$$

$$\tau_{LEspar} = 4P / \pi d^2 = 4(113.03) / \pi(0.190)^2 = 3.98 \times 10^3 \text{ psi}$$

$$M.S. = \tau_u / \tau_{LEspar} - 1 = 80000 / 3980 - 1 = 19$$

For the Lift, the three spars split the load equally, with each taking 133.33 lbs.

For the leading edge spar, the load can also be considered to be distributed evenly among the four fasteners. Hence, P is:

$$F_{LE} = \text{Lift} / \# \text{ Spars} = 400 / 3 = 133.33 \text{ lbs}$$

$$P = F_{LE} / n_f = 133.33 / 4 = 33.33 \text{ lbs}$$

The shear stress on each fastener due to the Lift force is:

$$\tau_{LE} = 4P / \pi d^2 = 4(33.33) / \pi(0.190)^2 = 1.176 \times 10^3 \text{ psi}$$

$$M.S. = \tau_u / \tau_{LE} - 1 = 80000 / 1176 - 1 = 67$$

B6.2.1 Combined Loading - Leading Edge Spar

The combined shear stress on the leading found by adding the shear stress due to lift and pitch:

$$\tau_{Combined} = \tau_{Pitch} + \tau_{Lift} = 1176 + 3980 = 5156$$

$$M.S. = \tau_u / \tau = 80000 / 5156 = 14.5$$

B7 CONCLUSIONS

The above report outlines the margins of safety for the two wind tunnel models that have been fabricated for the ARPA / WL Smart Materials and Structures - Smart Wing contract. The margins of safety are all sufficient to insure safety of both the NASA TDT wind tunnel and of the Northrop Grumman models. The margins are large for some of the structures (e.g. the attachment of the model to the balance, or the attachment of the spars to the ribs) due to the moderate loads being applied and because of the minimum gage thickness of the materials used to construct the models.

B8. FLUTTER AND DYNAMICS

B8.1 Dynamics and Flutter Analysis

This report presents vibration and aeroelastic characteristics of the two wind tunnel models which are designed for testing in the NASA Langley's transonic dynamic tunnel (TDT). Conventional Wing represents a basic wing with conventional trailing edge control surfaces. The inboard trailing edge flap is attached to a worm gear assembly which in turn is driven by an electric motor. The out board control surface (aileron) will be set manually to 0, ± 5 , ± 10 degrees. Smart Wing is identical to Conventional Wing except the trailing edge control surfaces are made of SMA materials and are firmly fixed to the rear spar and skin of the wing box. The control surfaces weigh about two pounds more than the conventional control surfaces.

STRUCTURAL MODEL

The structural model consists of an assembly of wing box, and trailing edge inboard and outboard control surfaces. The wing box consists of three spars and five ribs, and upper and lower skin surfaces. The mid spar is placed along the elastic axis of the wing box. The inboard section of the wing (up to Y station = 7.0 inch) is made very stiff. The wing box consists of 345 CBAR elements and 219 CQUAD4 elements. The control surfaces were represented by FEM elements, not by rigid bars as was done in the original analysis. The leading edge control surfaces are fixed to the front spar in both cases.

VIBRATION ANALYSIS

Vibration analysis of the structural model discussed above was performed. First twelve natural vibration modes in the frequency range 1 through 500 Hz were calculated. Figures B18 thru B22 list the natural frequencies and mode shapes of the Conventional Wing and Smart Wing. Vibration modal deformations for first six modes are shown in Figures B24 through B29 for Conventional Wing and in Figures B30 through B35 for Smart Wing. Listed below are the natural frequencies obtained from both ground vibration testing (GVT) and analysis.

Conventional Wing

Mode	Frequency (Hz)	Damping (%)	Shape
1	30.1	<i>Structural</i>	1st Bending
2	72.1	<i>Damping</i>	1st Torsion
3	108.8	<i>is</i>	2nd Bending
4	113.3	<i>Assumed</i>	2nd Torsion
5	138.5	<i>to be</i>	
6	157.9	<i>Zero</i>	
7	175.0		

Figure B18. Natural Frequencies and Mode Shapes for Conventional Wing, ASTROS Analysis

Mode	Frequency (Hz)	Damping (%)	Amplitude (g's)	Shape
1	24.33	0.507	5.85×10^4	1st Bending, Model
2	63.64	0.380	1.61×10^3	1st Bending, Spindle
3	80.84	0.737	1.72×10^3	1st Torsion, Model
4	108.33	0.683	2.92×10^3	2nd Bending, Model
5	140.43	0.392	1.40×10^3	1st Torsion, Spindle
6	166.68	0.421	2.78×10^3	Combined Torsion and Flap Rotation
7	174.64	1.861	2.63×10^3	2nd Torsion, Model
8	193.42	1.185	8.44×10^2	Control Surface Rotation

Figure B19. Natural Frequencies and Mode Shapes for Conventional Wing, NASA LaRC Ground Vibration Test

Mode	Frequency (Hz)	Damping (%)	Shape
1	28.9	1.05	1st Bending
2	89.4	1.99	1st Torsion
3	109.0	1.55	2nd Bending
4	175.9	3.63	2nd Torsion
5	197.5	2.22	Control Surface Rotation
6	218.6	3.06	3rd Bending

Figure B20. Natural Frequencies and Mode Shapes for Conventional Wing, Northrop Grumman Ground Vibration Test

Smart Wing

Mode	Frequency (Hz)	Damping (%)	Mode Shape
1	27.84	<i>Damping</i>	1st Bending
2	70.11	<i>Assumed</i>	1st Torsion
3	106.74	<i>to be</i>	2nd Bending
4	166.69	<i>Zero</i>	2nd Torsion
5	171.39	<i>in</i>	2nd Torsion and 3rd Bending
6	220.32	<i>Analysis</i>	2nd Torsion and 3rd Bending
7	247.72		

Figure B21. Natural Frequencies and Mode Shapes for Smart Wing, ASTROS Analysis

Mode	Frequency (Hz)	Damping (%)	Amplitude	Mode Shape
1	26.76	0.319	2.67×10^4	1st Bending, Model
2	56.69	0.386	3.03×10^2	1st Spindle
3	73.65	2.161	6.88×10^2	1st Torsion, Model
4	90.06	3.599	3.25×10^2	Flap Bending
5	104.78	1.905	8.37×10^1	2nd Bending, Model
6	118.35	2.556	4.47×10^3	Flap Rotation
7	130.387	2.803	2.67×10^3	Combined Rotation, 2nd Bending, Model
8	159.57	2.234	4.88×10^2	Aileron Rotation
9	170.31	0.382	3.18×10^1	2nd Torsion, Model
10	172.31	0.636	8.73×10^1	Combined Torsion - L-Bracket
11	192.01	2.436	1.92×10^4	Flap/Aileron Rotation

Figure B22. Natural Frequencies and Mode Shapes for Smart Wing, NASA LaRC Ground Vibration Test

AEROELASTIC ANALYSIS

Aeroelastic analysis (flutter and divergence) was performed using ASTROS, a design software developed by Northrop for the Air Force. The aerodynamic model used in this study is shown in Figure B23. Four spline surfaces were used to relate the structural data and the aerodynamic data. The flutter analysis using 12 vibration modes was conducted for Mach numbers 0.2, 0.3, 0.5, and 0.6 with density ratios; 0.2, 0.5, and 1.0. These density ratios correspond to tunnel running conditions at $P_T = 600, 1100, 2200$ PSF, respectively. Typical flutter solutions in terms of damping vs. equivalent dynamic pressure (Q_{eq} in PSF) and frequency vs. dynamic pressure (Q_{eq} in PSF) are presented in the following figures:

Figures B36 through B39 for Mach number 0.5, Conventional Wing

Figures B40 through B43 for Mach number 0.6, Conventional Wing

Figures B44 through B47 for Mach number 0.5, Smart Wing

Figures B48 through B51 for Mach number 0.6, Smart Wing

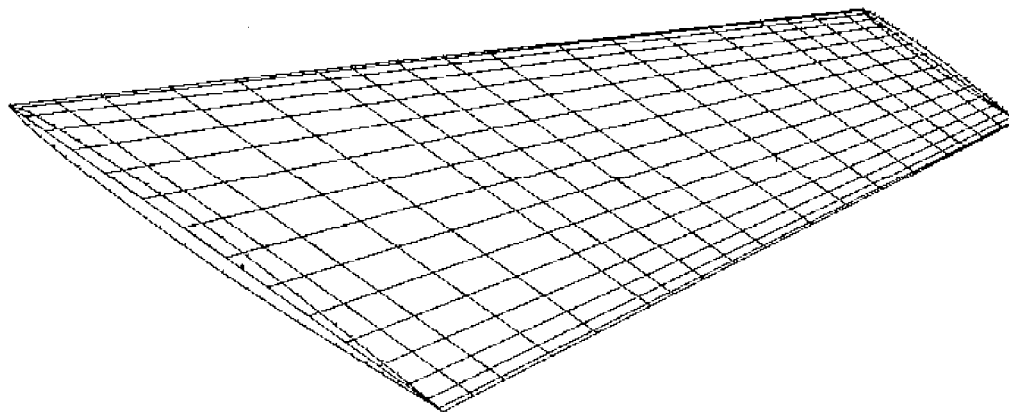


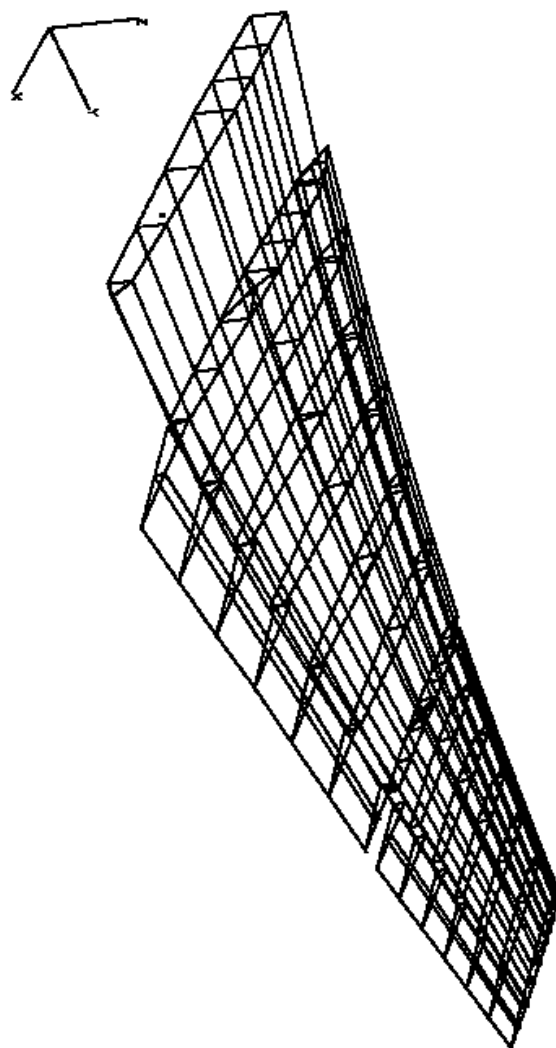
Figure B23. Steady Aerogrid Model

Critical Q is found when the damping curve passes through zero from negative to positive value. At Mach, $M=0.5$, both wings; Conventional Wing and Smart Wing, are free from aeroelastic instability for density ratios 0.25 through 1.0 (i.e. up to $Q = 800$ PSF). However, at Mach, $M=0.6$, Conventional Wing (with conventional flap) flutters in mode two (inboard control surface mode) at $Q_{eq} = 158$ PSF with density ratio of 0.2, and at $Q_{eq} = 625$ PSF with density ratio of 1.0. These, dynamic pressures are well above the test condition which is limited to $Q=120$ PSF. Moreover, the operating Mach number is also limited to $M=0.5$. Hence, the Conventional Wing test model is free of flutter and divergence instabilities. The Smart Wing model with SMA control surfaces, unlike Conventional Wing, is stable at all density ratios up to $M=0.6$. The plots of frequencies vs. equivalent dynamic pressure show very little change in the frequencies. This suggests that the aerodynamic stiffness and aerodynamic damping are small compared to the structural stiffness, and hence, the models are stable in the desired test range.

B8.2 Summary

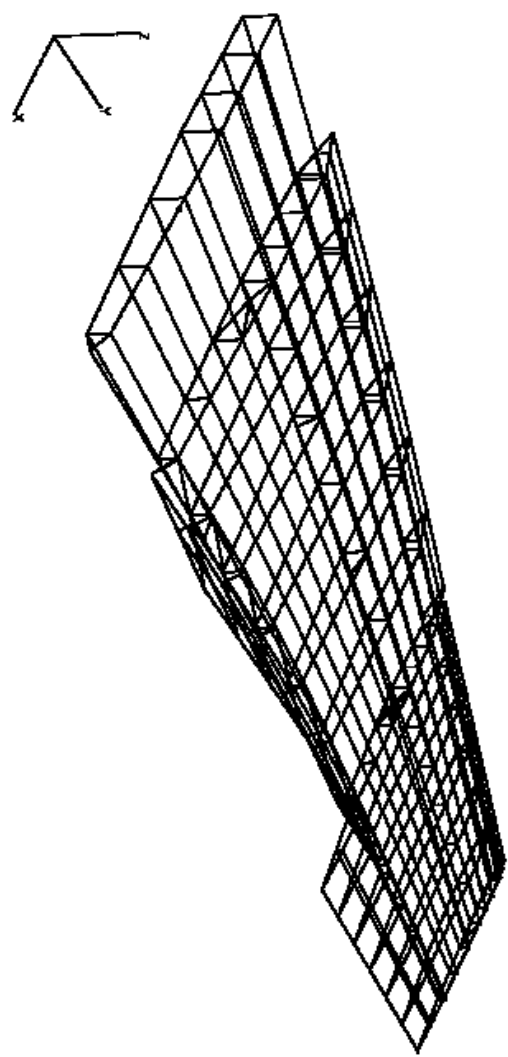
The above appendix outlines the analysis done to insure the models are free from flutter for the tunnel environments of the tests. The only region of instability is at a $M = 0.6$ for the conventional wing. The damping of the 6th mode turns positive at $Q = 160$ psf and $\rho = 0.2$; and at $Q = 711$ psf for $\rho = 1.0$ (Figures B40 – B43). The Smart Wing, on the other hand, showed no flutter until $M = 0.8$, which is well outside the region of these tests. Since the maximum Q that will be run at is 120 psf at $M = 0.5$, the analysis shows that both models are clear for the tests.

Leading edge control surface divergence is also not a concern for either model. The original design had called for the leading edges to be moveable, but model complexity and a large test matrix led to the leading edges to be rigidly fixed to the leading edge spars.



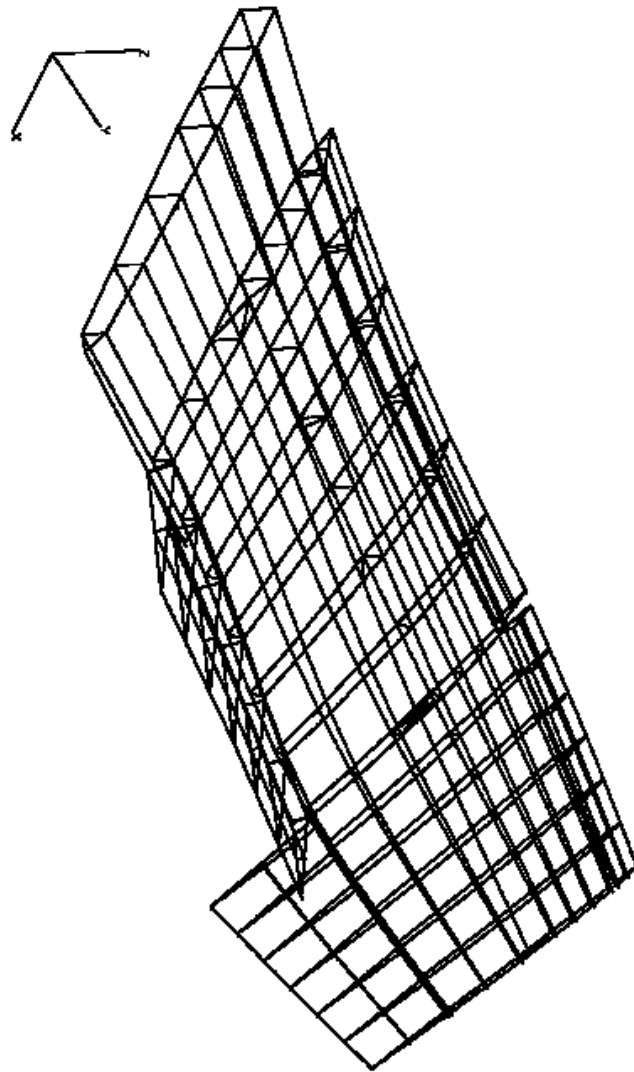
Conventional Wing, Mode 1, 33.6 Hz

Figure B24



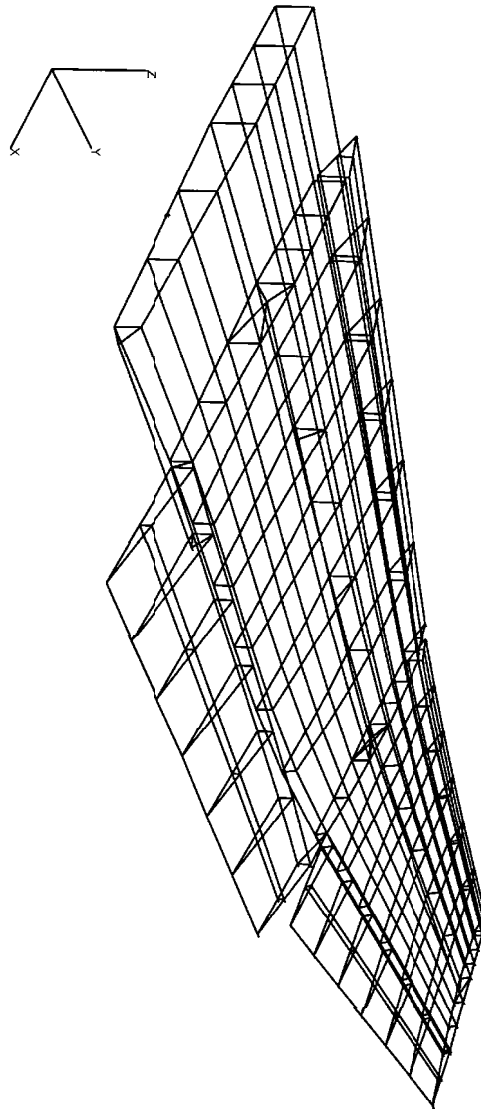
Conventional Wing, Mode 2, 61.5 Hz

Figure B25



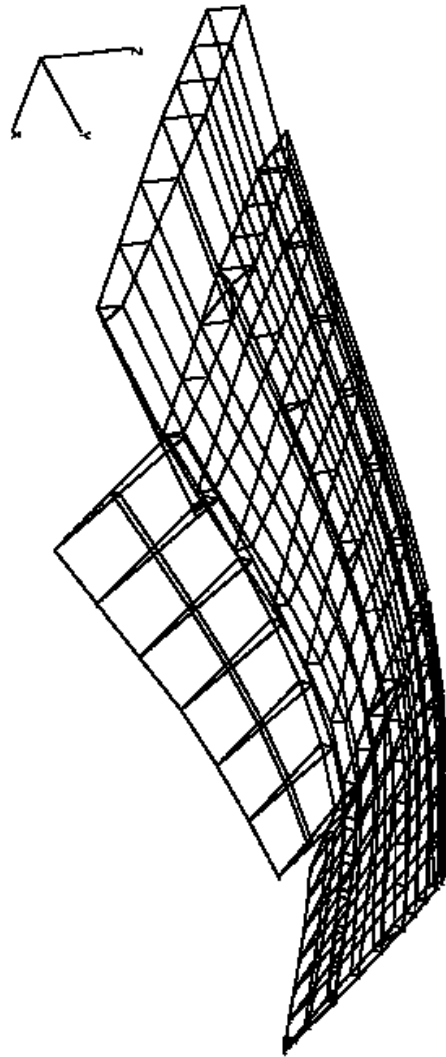
Conventional Wing, Mode 3, 87.7 Hz

Figure B26



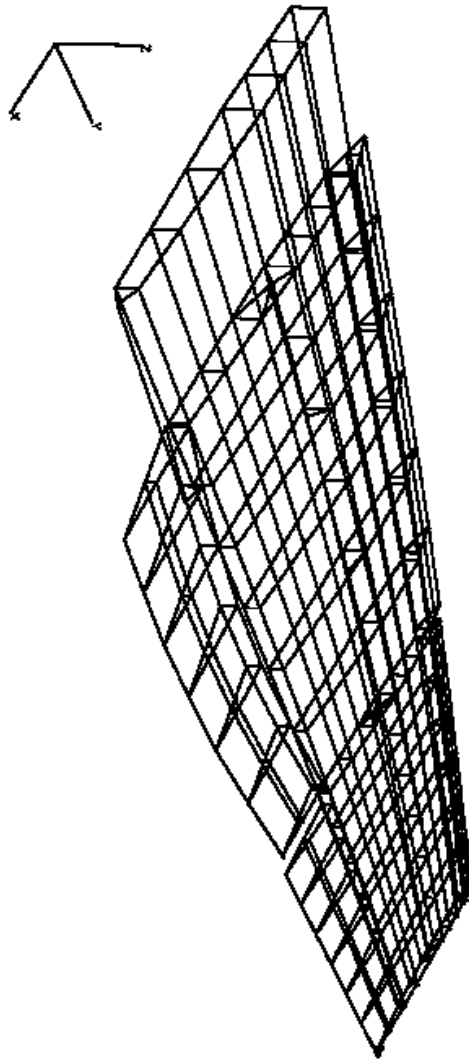
Conventional Wing, Mode 4, 131 Hz

Figure B27



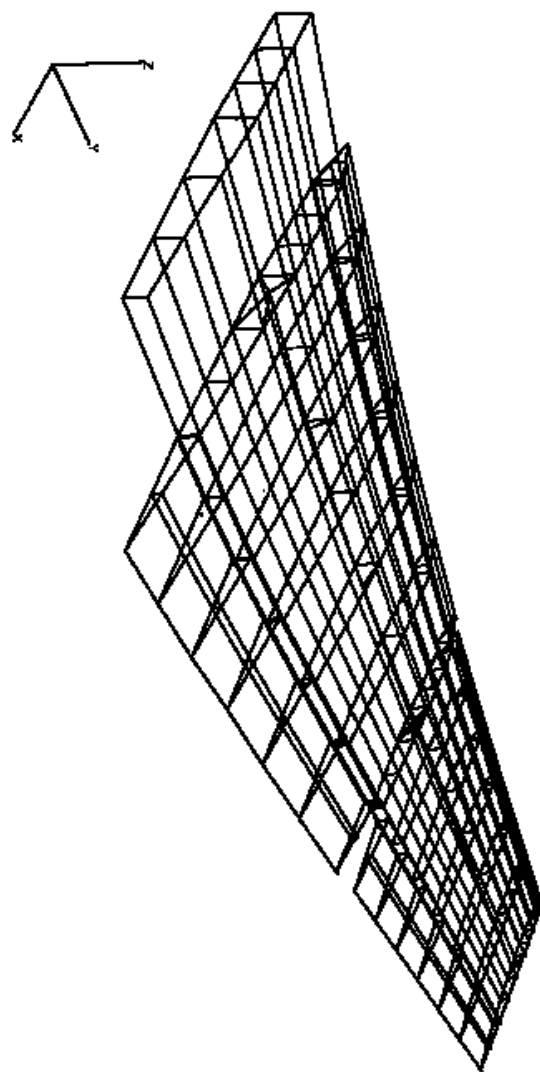
Conventional Wing, Mode 5, 143 Hz

Figure B28



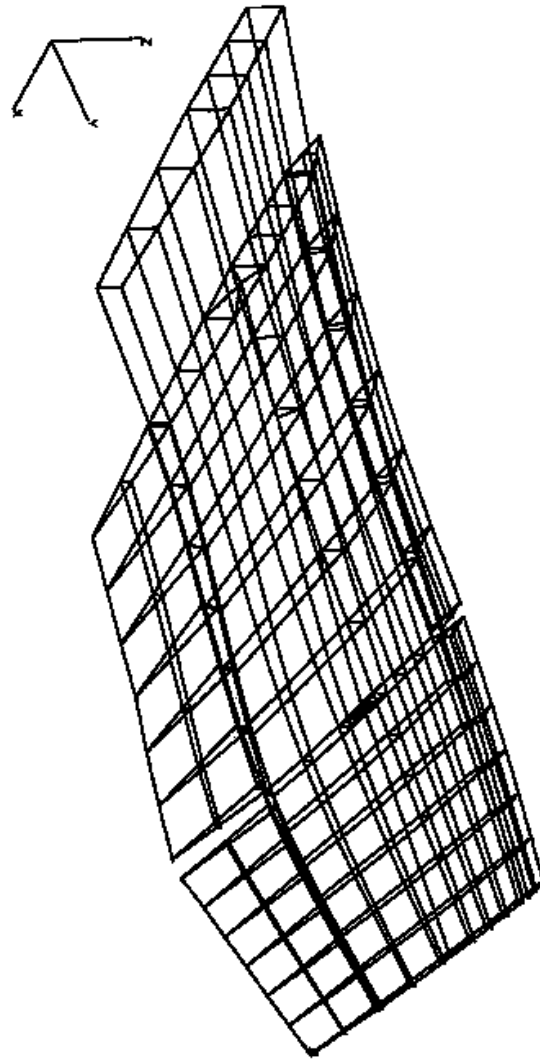
Conventional Wing, Mode 6, 201 Hz

Figure B29



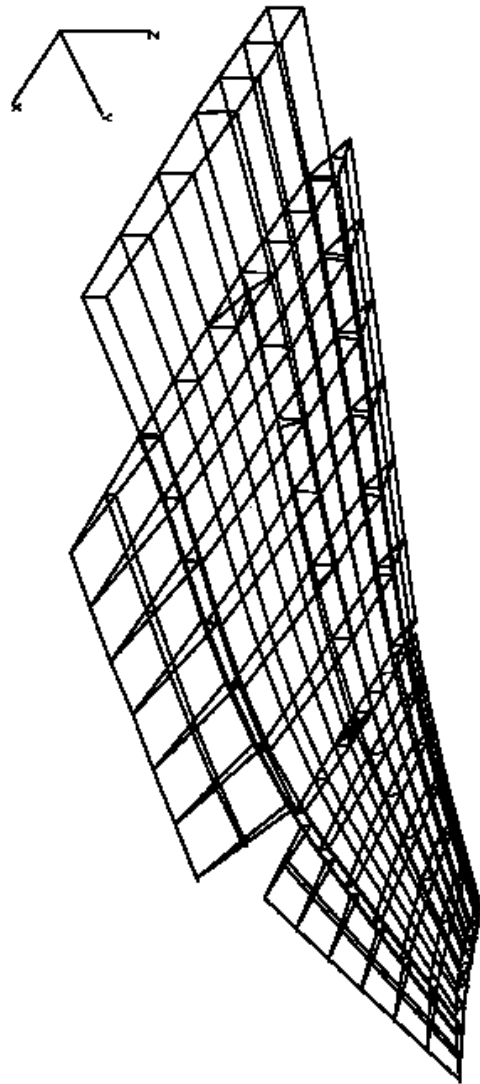
Smart Wing, Mode 1, 35.4 Hz

Figure B30



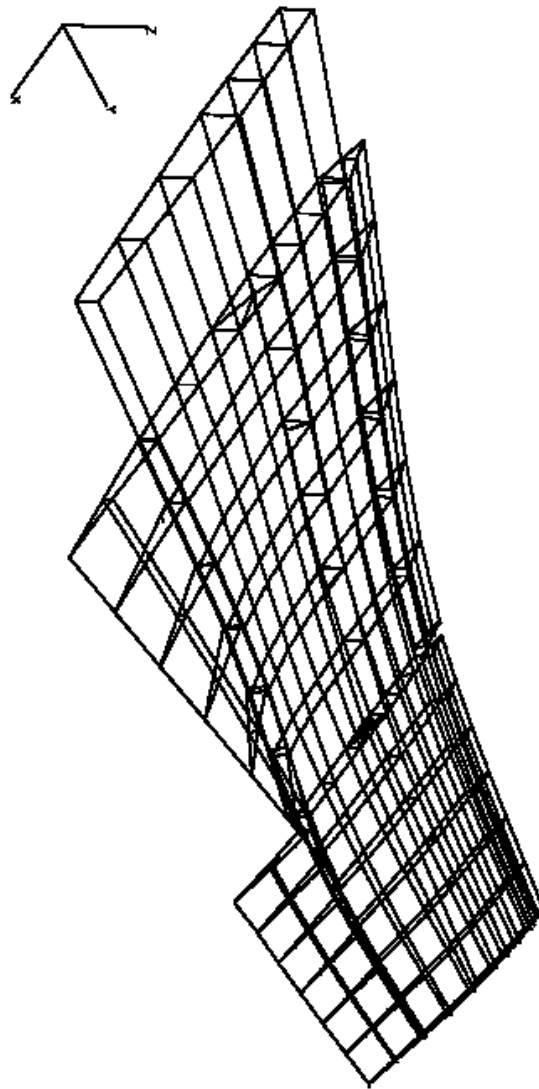
Smart Wing, Mode 2, 83.7 Hz

Figure B31



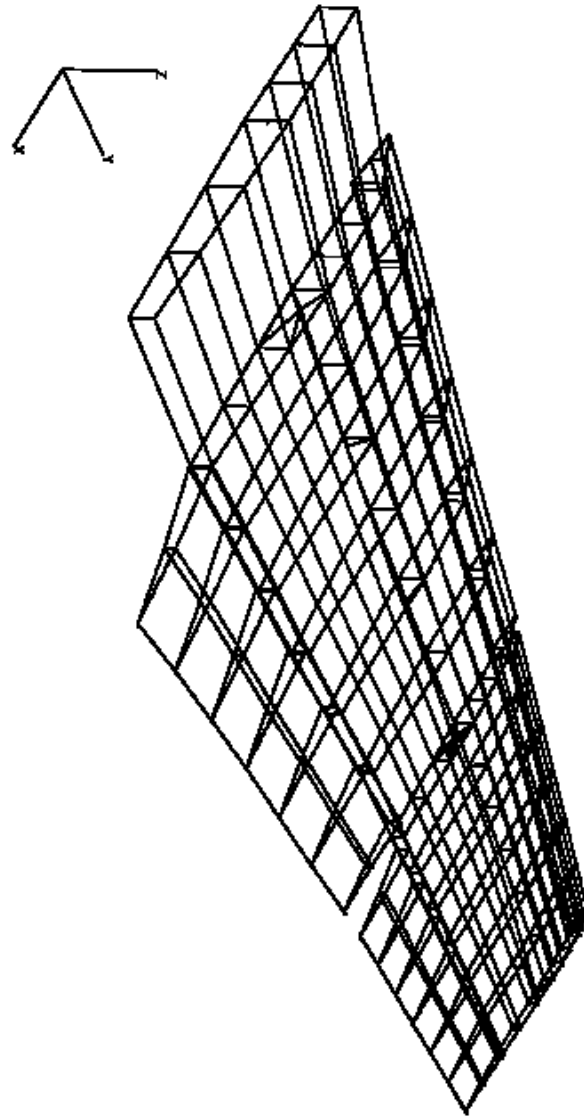
Smart Wing, Mode 3, 127 Hz

Figure B32



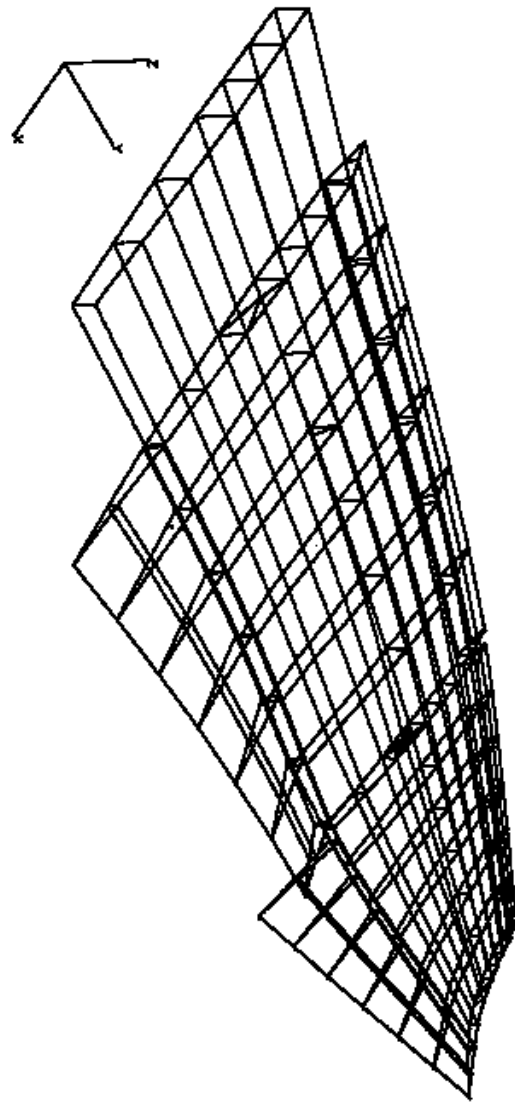
Smart Wing, Mode 4, 198 Hz

Figure B33



Smart Wing, Mode 5, 218 Hz

Figure B34

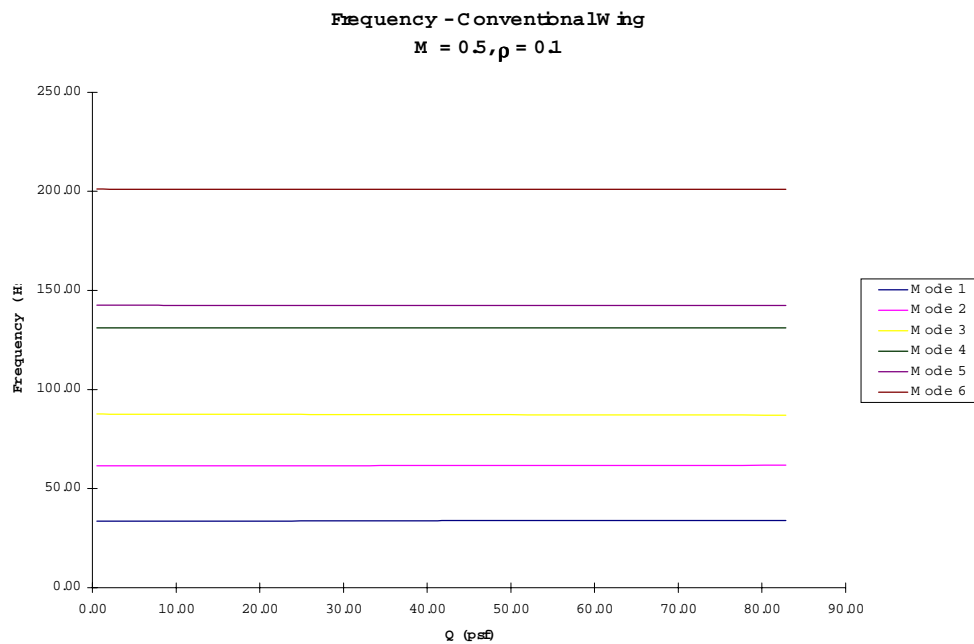
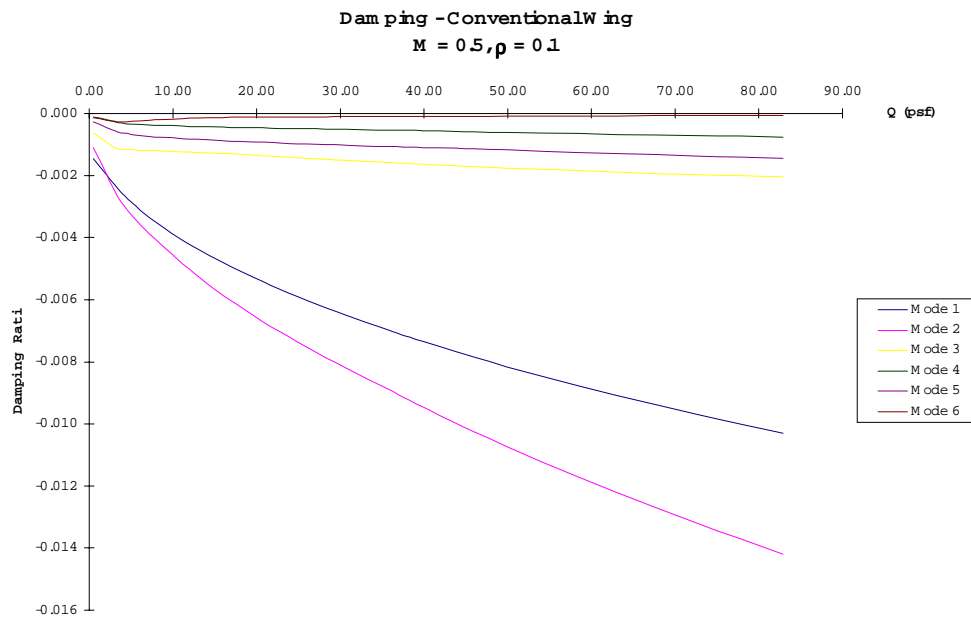


Smart Wing, Mode 6, 241 Hz

Figure B35

B8.3 Flutter and Dynamics Graphs

Included are the graphs for both wind tunnel models at $M = 0.5$ and 0.6 , with density ratios of 0.1 to 1.0 .



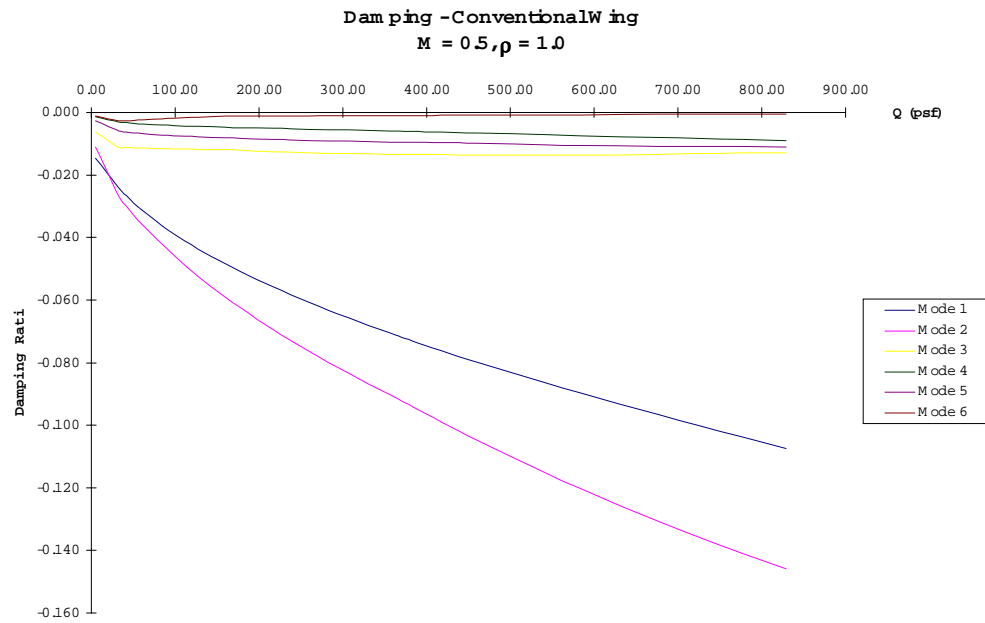


Figure B38

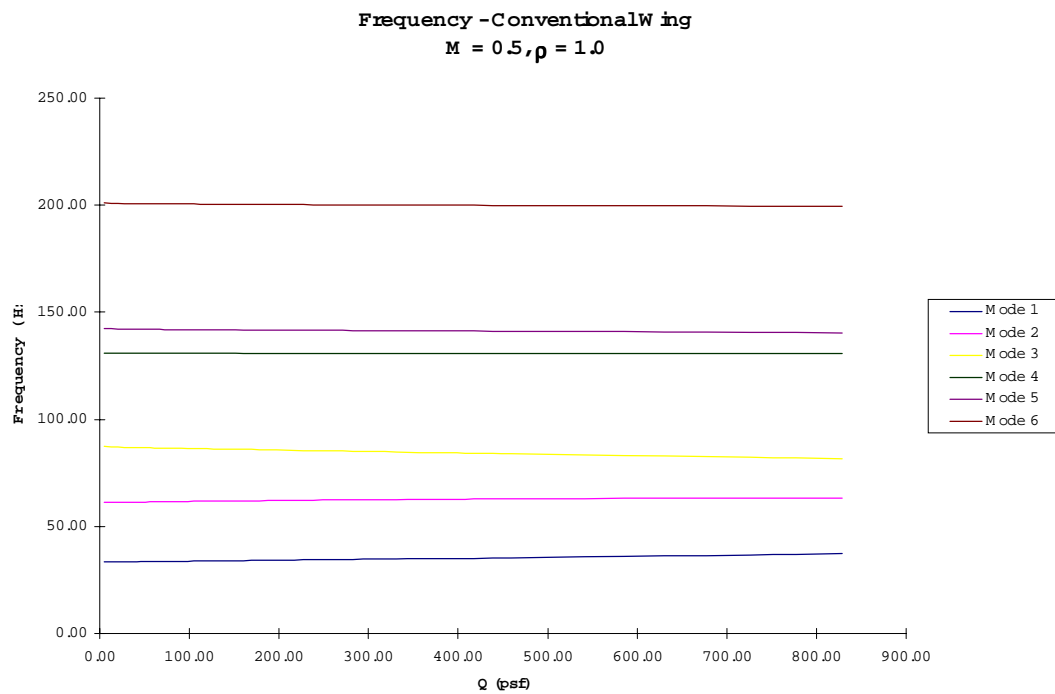


Figure B39

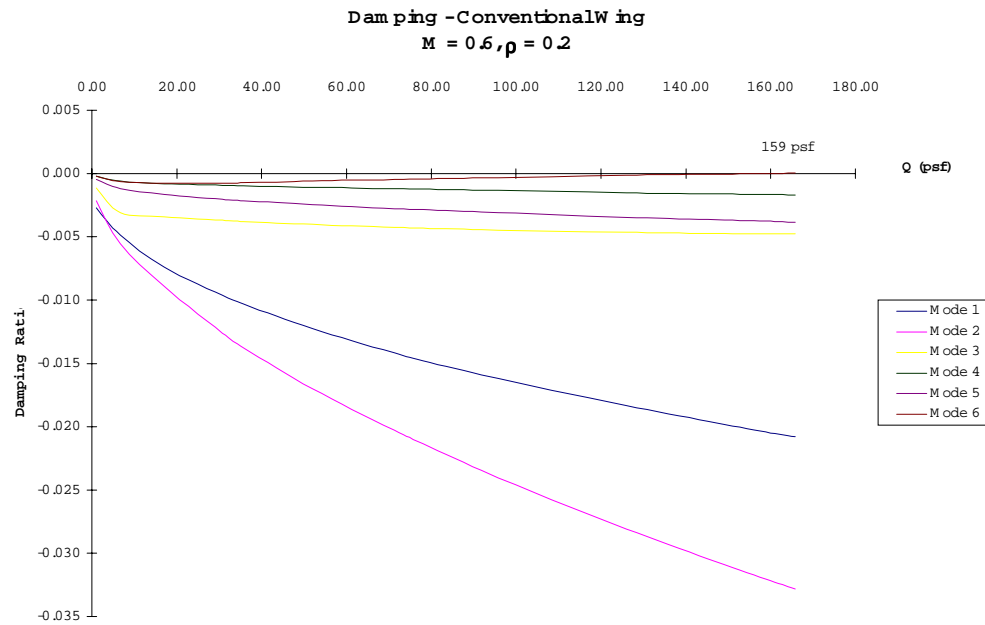


Figure B40

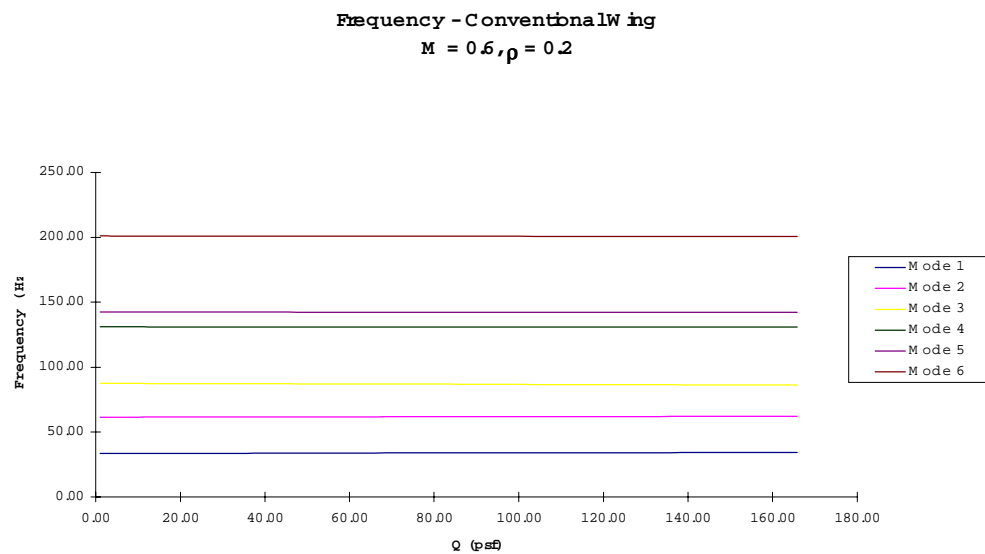


Figure B41

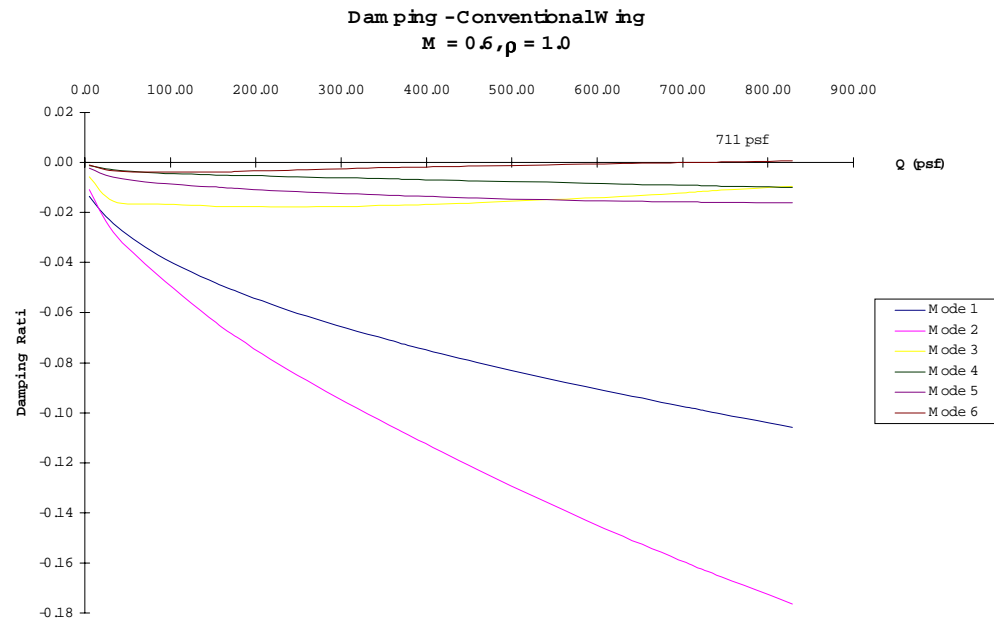


Figure B42

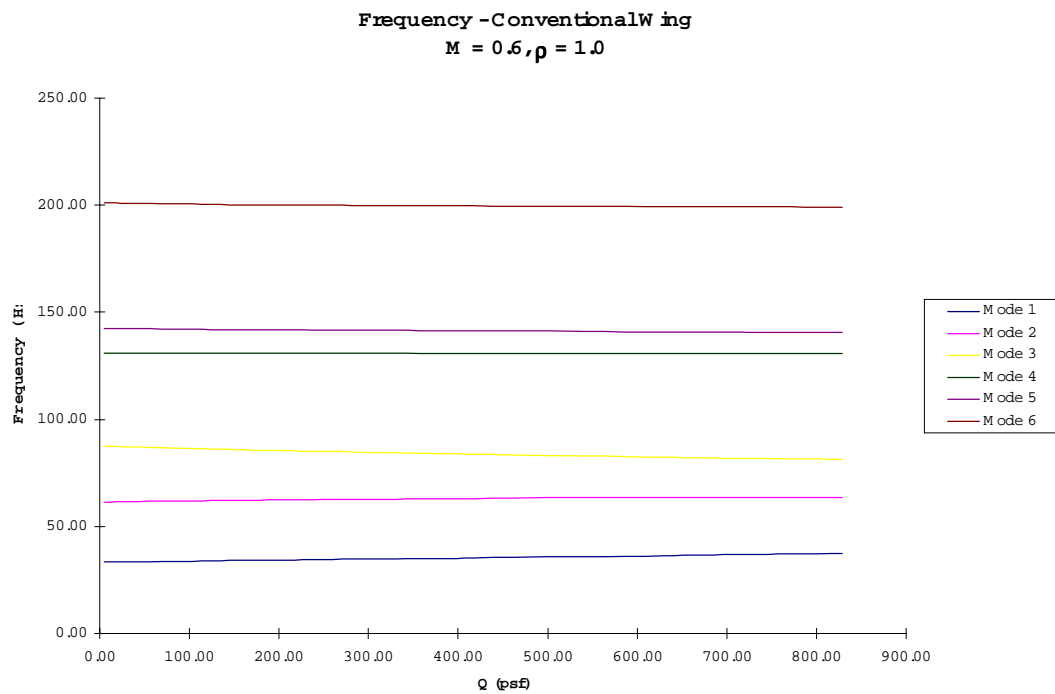


Figure B43

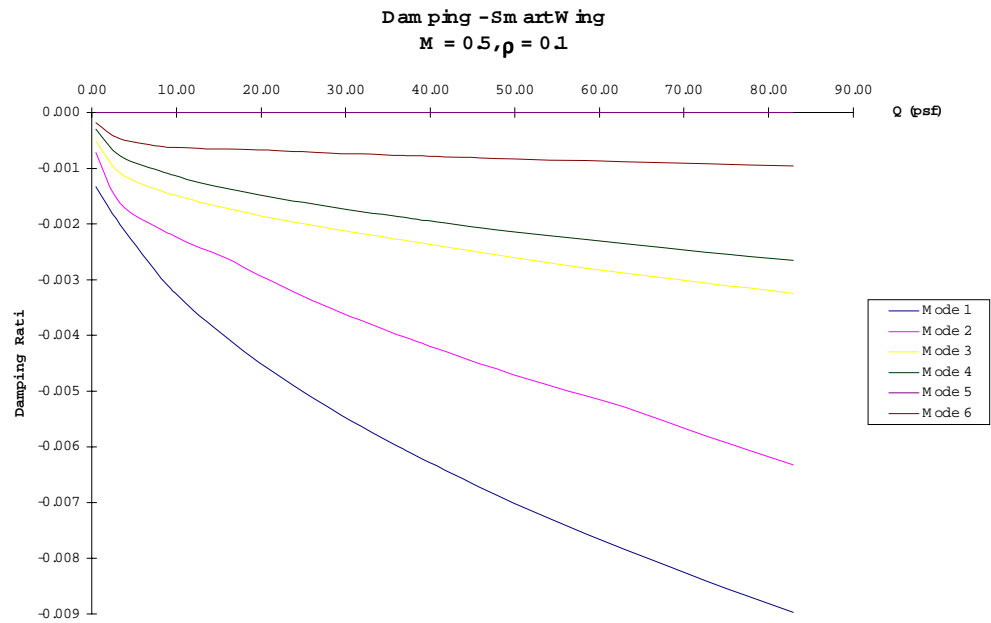


Figure B44

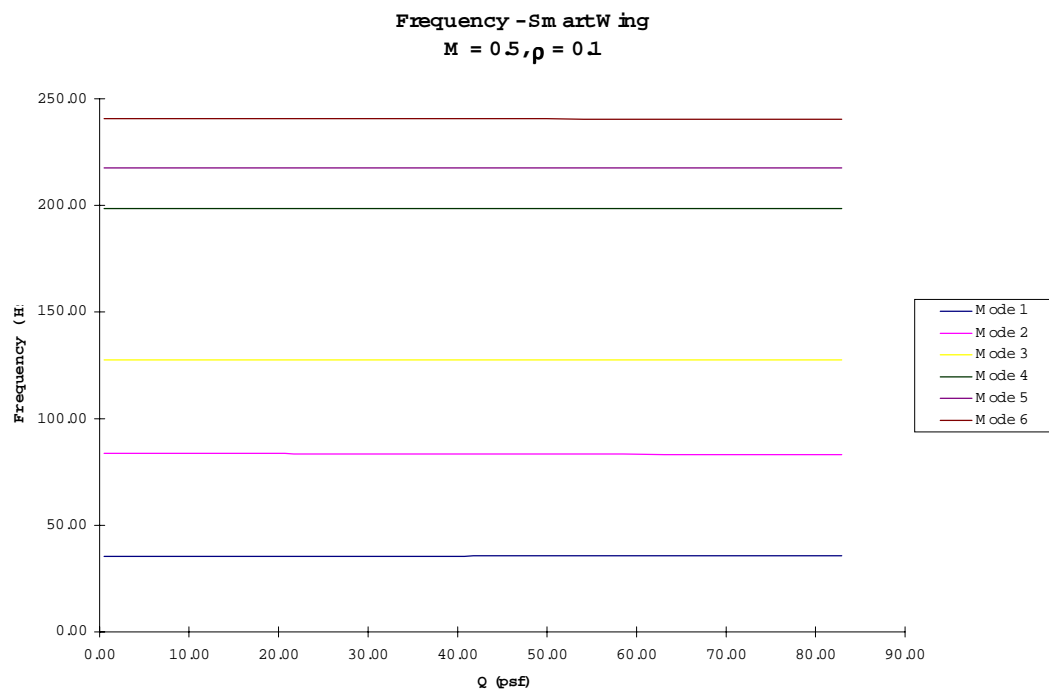


Figure B45

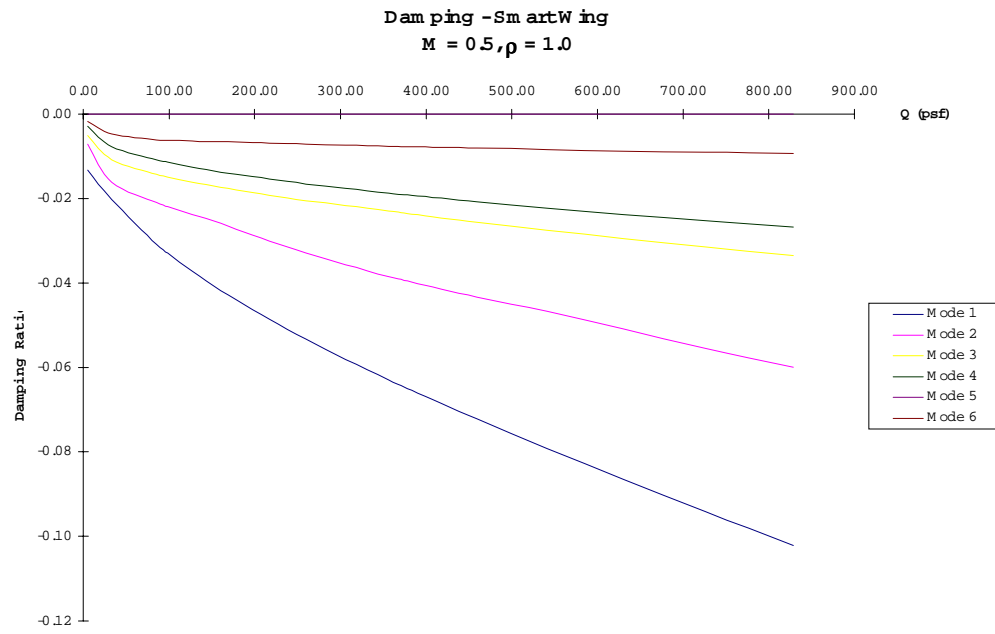


Figure B46

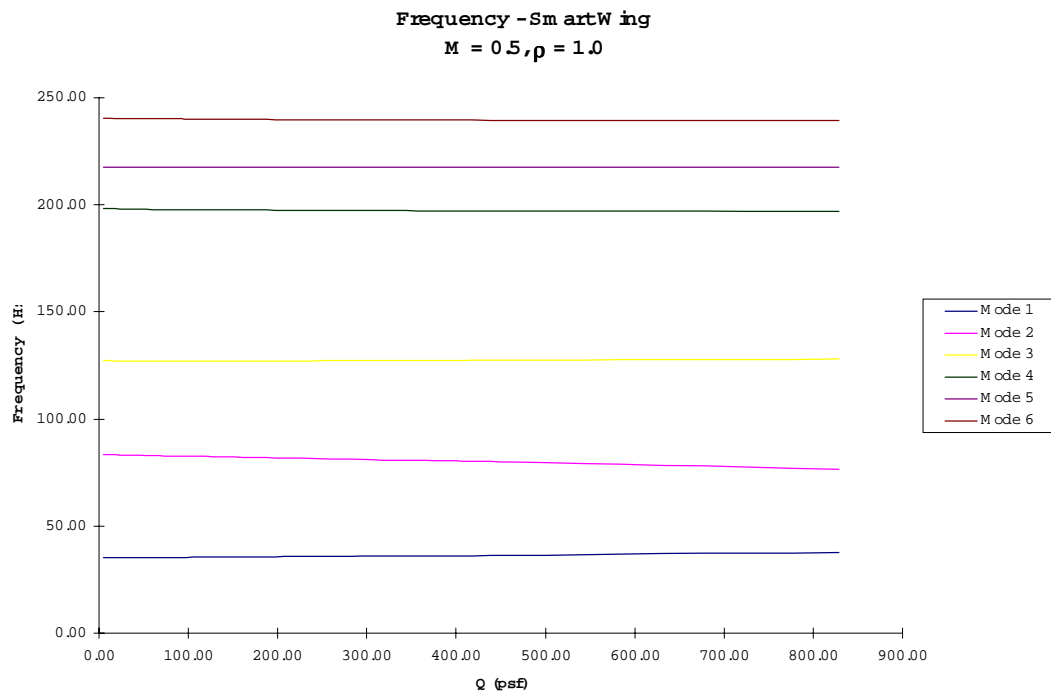


Figure B47

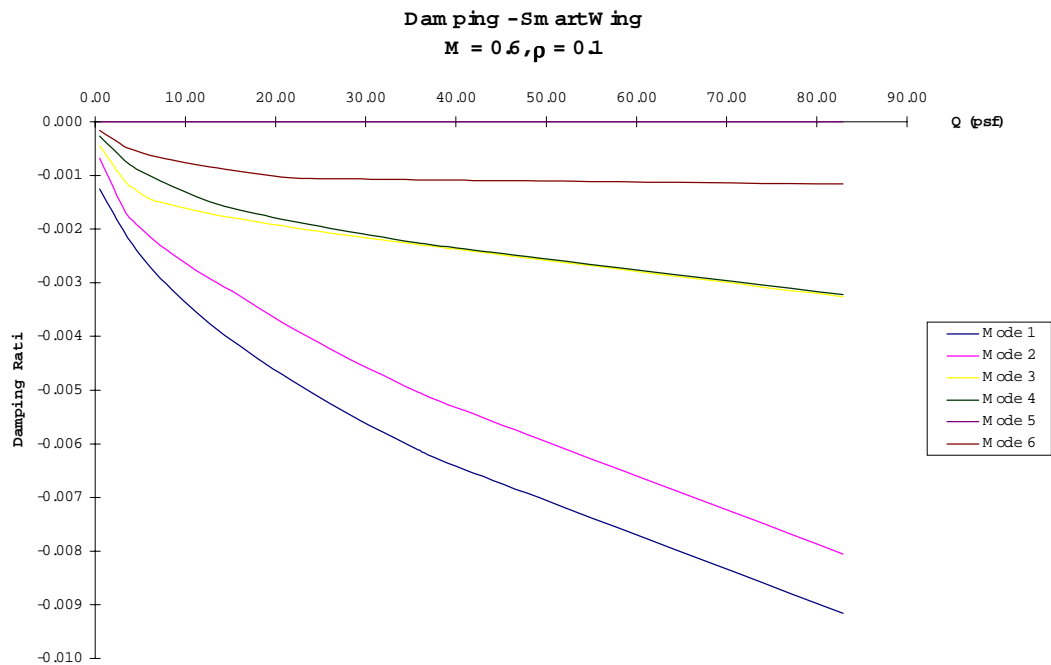


Figure B48

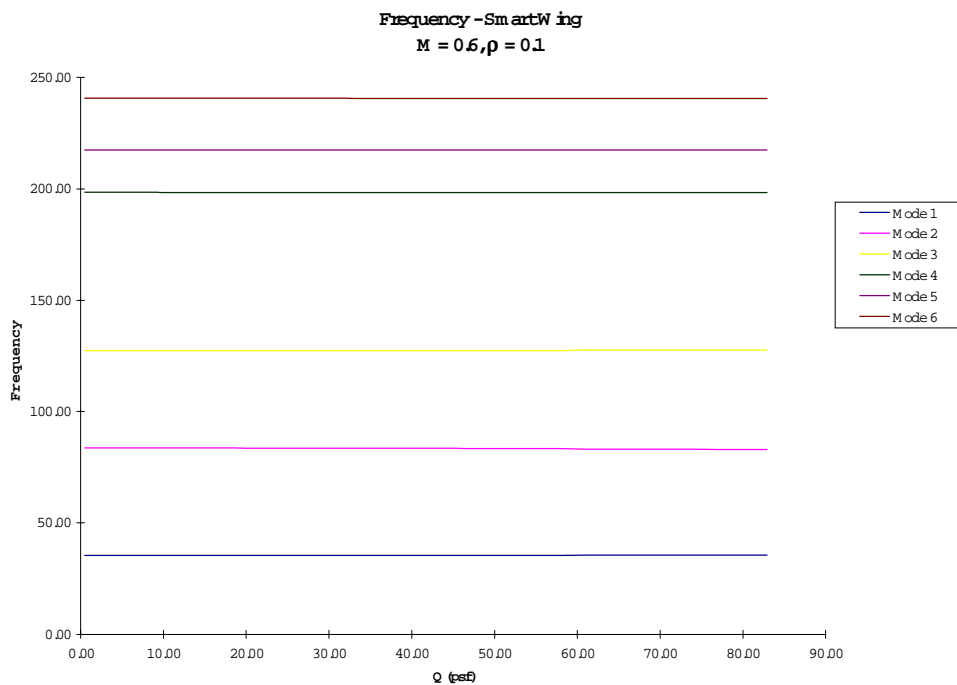


Figure B49

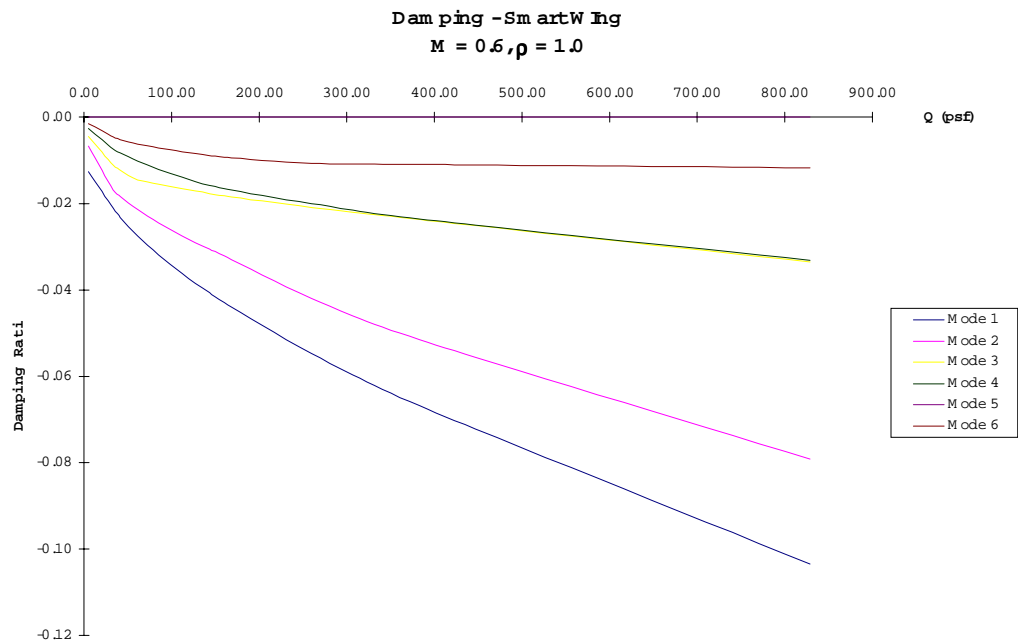


Figure B50

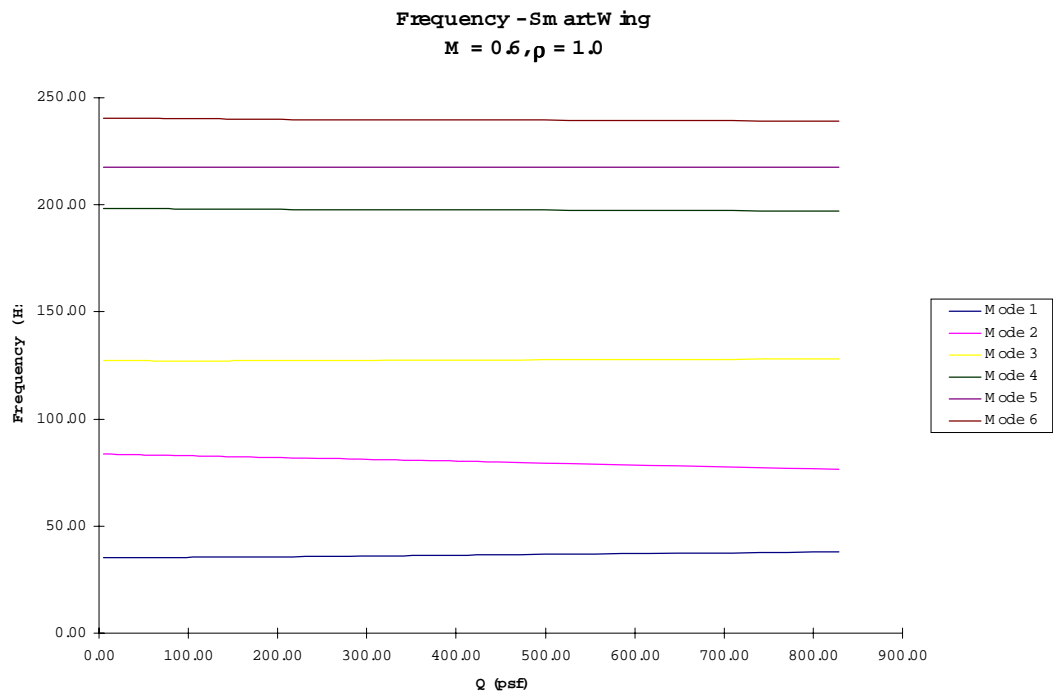


Figure B51

VOLUME IV

PRE-TEST REPORT

**NORTHROP GRUMMAN
SMART WING WIND TUNNEL MODEL
TEST II**

DARPA / WRIGHT LAB

**SMART STRUCTURES
AND
MATERIALS - SMART WING**

NASA LANGLEY 16 FT. TDT WIND TUNNEL

22 JUNE 1998 - 25 JULY 1998

PREPARED BY;

L. B. SCHERER
NORTHROP GRUMMAN
WIND TUNNEL ENGINEERING
9G23/GS
562-942-5627
scherle@mail.northgrum.com

C. MARTIN
NORTHROP GRUMMAN
STRUCTURAL METHODS AND ADVANCED TECHNOLOGIES
9B71/63
310-332-8198
martich3@mail.northgrum.com

APPROVALS;

J KUDVA
PROGRAM MANAGER, SMART WING
NORTHROP GRUMMAN
MANAGER, STRUCTURAL METHODS AND ADVANCED TECHNOLOGIES
kudvaja@mail.northgrum.com

R.D. SPRINGFIELD
NORTHROP GRUMMAN
MANAGER, WIND TUNNEL ENGINEERING

TABLE OF CONTENTS

C1. Introduction / Test Objectives	Page 140
C1.1 Program Overview	Page 140
C1.2 Test Objectives and Overview	Page 140
C1.3 Data Objectives and Purpose	Page 141
C2. Test Schedule	Page 141
C2.1 Model Test Schedule	Page 141
C3. Test Programming Staffing Requirements	Page 142
C3.1 Tunnel Operation Times	Page 142
C3.2 User Staffing	Page 142
C4. Description of Test Article	Page 143
C4.1 Model Description	Page 143
C4.2 Model Installation	Page 144
C5. Model Instrumentation	Page 144
C5.1 Common to both “Smart Wing” and Conventional Wing	Page 146
C5.2 Instrumentation Unique to the Conventional Wing	Page 148
C5.3 Instrumentation Unique to the Smart Wing	Page 149
C6. Data Acquisition / Data Reduction	Page 149
C6.1 Data Acquisition	Page 149
C6.2 Data Reduction	Page 149
C7. Data Output/Presentation	Page 151
C7.1 Tab Output	Page 151
C7.2 Real Time Monitoring and Audible Alarms	Page 151
C7.3 Plotted Data Requirements	Page 151
C8. Test Program	Page 151
C9. Facility	Page 154
C9.1 Tunnel Description and Operating Envelope	Page 154
C10. Terms and Constants	Page 158

C11. Points of Contact	Page 164
C12. Smart Wing Instrumentation Summary, Acquisition, and Hook-ups	Page 165
C13. Smart Wing Surface Static Pressure Locations and Hook-ups	Page 178
C14. Smart Wing Data Reduction Problem Statement	Page 186

C1. INTRODUCTION / TEST OBJECTIVES

The following report presents the necessary information to conduct the wind tunnel tests of two semi-span models representative of the F/A-18E/F wing. The test is to be conducted in the NASA Langley 16 Transonic Dynamics Tunnel during the month of February 1998. This is the second of two tests of the Smart Wing Model in support of the "Smart Wing" program under contract F33615-C-95-3202 with ARPA and Wright Labs .

C1.1 Program Overview

The purpose of the "Smart Wing" program is to explore new materials and technologies in the development of an adaptive wing capable of changing shape to optimize aerodynamic performance at any flight condition. This technology can be used for both commercial and military aircraft. Smart Wing technologies being examined by Northrop Grumman are the use of Shape Memory Alloys (SMA), piezoelectric actuators, and fiber optic sensors for pressure measurement. SMA and piezoelectric actuators would provide for adaptive wing twist and control surfaces with smooth wing surface contours. Aerodynamic performance benefits of such actuators are optimized L/D at varied flight conditions, improved high lift capability at take-off and landing, enhanced maneuvering, and increased range to mention a few. Fiber- optic pressure transducers on a wing surface would provide for improved flight controls and redundancy for the operation of damaged aircraft.

Phase 1 of the Smart Wing Program required two wind tunnel tests to be conducted to demonstrate the use and benefits of using Smart Wing Materials in a working aircraft model. The first test was completed in the NASA Langley 16 TDT Tunnel in April 1997. The results of the first entry demonstrated substantial aerodynamic performance improvements of smooth contoured trailing edge control surfaces and wing twist.

This is the second of two demonstration wind tunnel tests scheduled for the "Smart Wing" Phase 1 program.

C1.2 Test Objectives and Overview

The purpose of this second wind tunnel entry is to further optimize the Shape Memory Alloy (SMA) actuator concepts to provide wing twist and control surface deflections under simulated low speed flight conditions. This optimization includes providing higher and more uniform control surface deflections and greater wing twist than what was achieved during the first entry. Maximum Mach number will be increased from 0.29 to 0.42 during the second entry. The second entry will also provide aerodynamic drag data which was not possible during the first entry due to balance limitations. A new, more accurate balance will be used for this second entry.

The two wind tunnel models to be tested will be the same as the first entry with some modifications. The semi-span wing models are 16 percent scale, representative of the F/A-18E/F aircraft. The first model will be representative of the current F/A-18E/F wing with a remotely controlled hinged trailing edge flap and a manually deflected aileron. The second or Smart Wing model will have a SMA deflected, smooth contour, trailing edge flap and aileron. An SMA torque tube, in addition, will be mounted internally to the main wing structure in both the conventional and Smart Wing models to provide wing twist capability. Both the SMA flap/aileron and the torque tube designs have been improved for this tunnel entry over the first. Smart Wing benefits will be demonstrated by comparing aerodynamic data at similar wind tunnel conditions and configurations for both models.

C1.3 Data Objectives and Purpose

The data objectives will be to obtain aerodynamic data and stress levels of the wing structure to validate the benefits and SMA actuator performance. Specifically the following data will be obtained;

- Basic aerodynamic coefficient data from the facility provided model balance.
- Pressure coefficients from model surface static pressures measured with PSI pressure transducers.
- Principal stresses and strains at six locations in the wing structure through the use of strain gaged rosettes.
- Temperature outputs of the SMA torque tube and SMA control surfaces with the use of thermocouples. This is both for control of the SMA actuators and monitoring of performance.
- Actual torque of the SMA torque tube from a full strain gaged bridge.
- Various model positions such as-
 - Model angle of attack with an inclinometer mounted at the wing root and the facility support system.
 - Model wing twist by the use of tilt sensors distributed out the span of the wing
 - Deflection of SMA flaps using potentiometers.
 - Deflection of conventional trailing edge flap with a potentiometer.

Model dynamics will be monitored closely throughout the test with four to five accelerometers mounted in each of the models as a safety precaution. Specified strain gages and tilt sensors will serve also for the monitoring of model dynamics.

C2. TEST SCHEDULE

C2.1 Model Test Schedule

The model test schedule has been provided in Figure C1. This schedule includes the ground work leading up to the test. Milestone dates concerning the test are as follows;

Delivery of models to NASA Langley	Jan 15
Ground Vibration Test at NASA Langley	Jan 26-30
Model Systems Set-up and Checkout	Jan. 15- Feb. 6
Model Installation Start	Feb. 9
Testing of Conventional Wing	Feb. 16- Feb.20
Testing of Smart Wing	Feb. 23 - March 6
Removal of Model and User Equipment	March 7

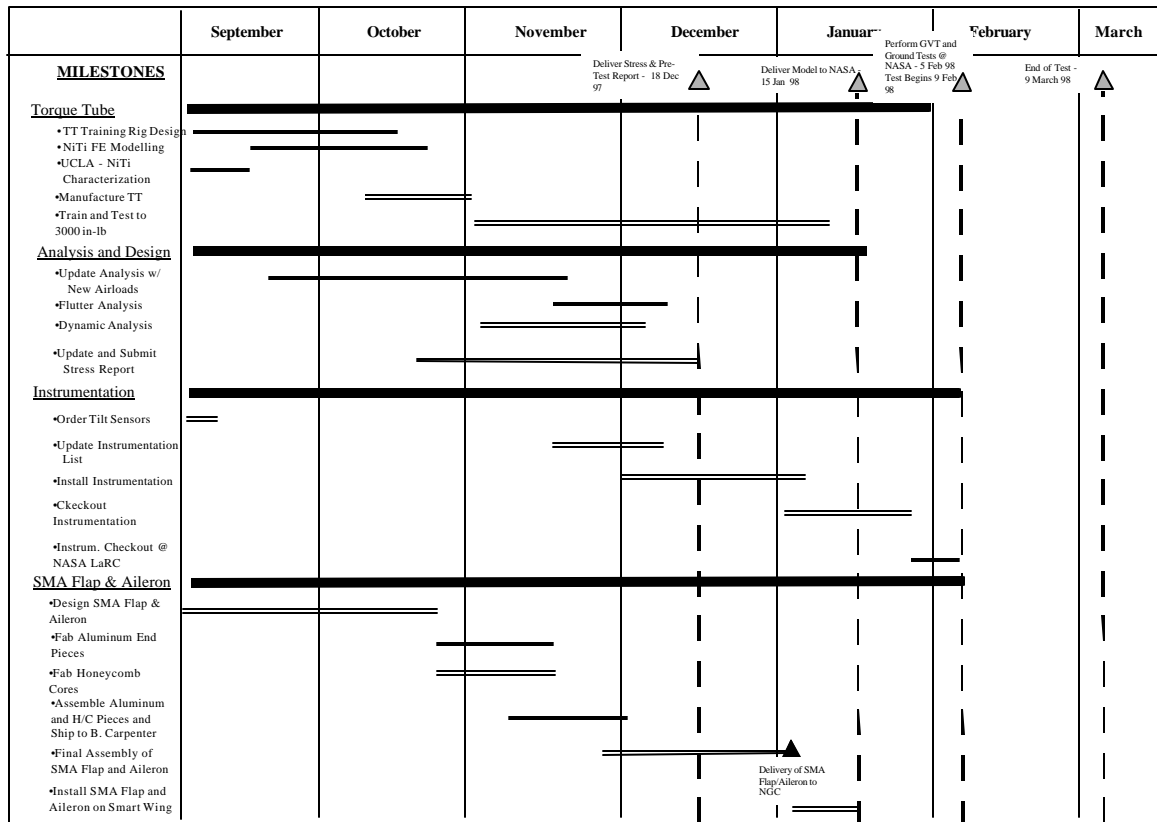


Figure C1. Second Wind Tunnel Entry Schedule

C3. TEST PROGRAM STAFFING REQUIREMENTS

C3.1 Tunnel Operation Times

The tentative 16 TDT tunnel operation time will be twelve hour days (with the option to decrease to eight), five days a week. Start time will be tentatively 6:30 AM to end of shift at 6:30 PM which includes an approximate one and a half hour for the facility to start up and one hour for the facility to shut down systems (dependent on tunnel conditions) at the end of shift. Model work, data analysis, and instrumentation/ data system set-up work may be done in the off-hours if required.

C3.2 User Staffing

Northrop Grumman will support the test on-site with a test engineer, model technician, and two representatives from the Advanced Structural Technologies group. Lockheed Martin will have a representative at the test site as well to support their respective systems. Instrumentation support will be provided by a representative from Mission Research Corp.

C4. DESCRIPTION OF TEST ARTICLE

C4.1 Model Description

Two models of the Smart Wing will be tested. Each of the models are representative of a 16% scale version of the F/A-18 E/F right wing. The only modification to the wing contour and planform is the inboard section in which the leading edges have been extended inboard to the fuselage centerline of the F/A-18 E/F aircraft. This root section airfoil shape has also been thickened by about 75% for additional model support. Both of the models are identical in construction with the exception of the trailing edge flap and the aileron. The conventional wing has an electrically driven hinged trailing edge flap and a manually deflected aileron identical in planform and contour to the existing F/A-18 E/F aircraft. The Smart Wing has an SMA remotely actuated two segment trailing edge control surface/flap.

The models were designed to provide the capability of twisting the wing inboard to outboard with an SMA torque tube. The main support structures of the models are three aluminum spars out the span of each wing as shown in Figure C2. These spars are joined together by two cross members at the root and at 5.3 % span. The model is then covered with aluminum skins with ribs designed to prevent skin buckling under bending and torsion. The leading edge of the models are rigid and will not be deflected during the test.

On the center wing spar is located an SMA torque tube assembly. The torque tube will have the capability of twisting the wing +3 degrees leading edge up at the wing tip in relation to the wing root. The SMA torque tube assembly will not be installed on the conventional wing.

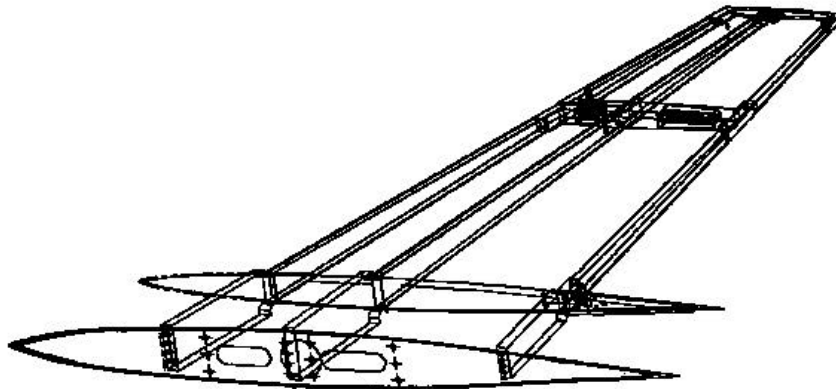


Figure C2. Model Main Spars and Ribs

The conventional wing has a remotely actuated trailing edge flap with a deflection angle range of 0 to +15 degrees trailing edge down. The aileron on the conventional wing is manually deflected by the use of brackets mounted at the end of the control surface. Brackets have been made for the following angles; 0, ± 5 , ± 7.5 , ± 10 , and ± 15 degrees.

The trailing edge flap and aileron on the Smart Wing will be deflected remotely by controlling the actuation of the SMA wires located in the respective RTV skins. The SMA flaps and aileron internally will be constructed of a fiberglass center laminate and an honeycomb core. The SMA flap and aileron will each have an independently controlled upper and lower SMA wire set. A smooth contour deflection is accomplished by contracting either the upper or lower SMA wire set. Maximum deflection expected is \pm one inch which corresponds to approximately ± 10 degrees.

Model safety issues including flutter and stress analysis can be found in the Smart Wing Test 2 Stress Report.

C4.2 Model Installation

The model(s) will mount to the existing facility semi-span support system which will be located on the west tunnel wall. The installation system as shown in Figure C3 consists of a flow splitter plate mounted 41 inches off the tunnel wall, a turn-table for model pitch rotation located in the tunnel plenum, a spindle between the balance and the turn-table, and a semi-span balance connected to the model via an adapter and pedestal. The main flow splitter plate is used to isolate the wing from flow disturbances caused by the support system and to provide a reduced tunnel wall boundary layer at the model. As shown in the Figure C3, there is a round splitter plate, 16.75 inches in diameter attached to the model which provides a larger attachment area for the model and allows larger access for instrumentation cabling. This round splitter however, will add small additional aerodynamic forces to the balance as it is attached to the model and does not touch the main splitter section.

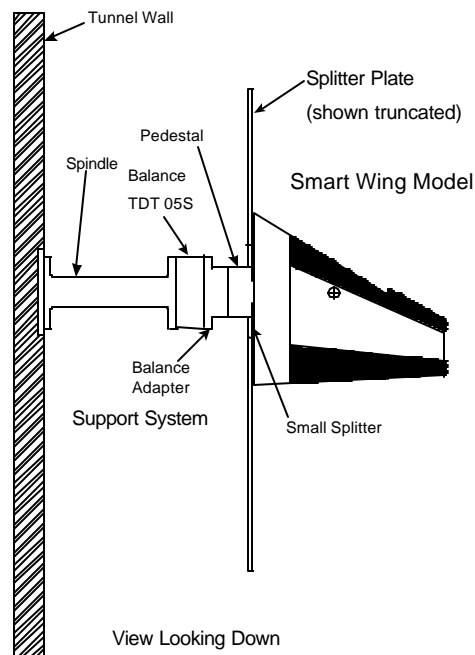


Figure C3. Model Installation

All model electrical instrumentation cabling and pneumatic tubing will route through the pedestal and looped around the balance adapter and balance as not to impose any unwanted load.

C5. MODEL INSTRUMENTATION

Each of the models are extensively instrumented with surface static pressures, strain gages, accelerometers, and various control surface instrumentation. Main aerodynamic data will be obtained from the NASA Langley five-component strain gaged balance designated TDT 05S. This balance was designed for semi-span models such as the Smart Wing model. The maximum load range for each gage component is as follows;

Normal Force	± 1500 lbs
Axial Force	± 120 lbs
Pitching Moment	± 6500 in-lb
Yawing Moment	± 4000 in-lb
Rolling Moment	$\pm 50,000$ in-lb

The balance will mount to the model support located in the “canoe” fairing between the splitter plate and tunnel wall. All model instrumentation cabling will be looped around the balance as not to impart any unwanted loads on the balance.

Much of the model instrumentation is identical in location, number, and type between the “Smart Wing” model and the conventional model. Differences occur in the control surface monitoring and actuation systems. Instrumentation nomenclature, summary, and facility panel hook-ups have been identified in Section C12.

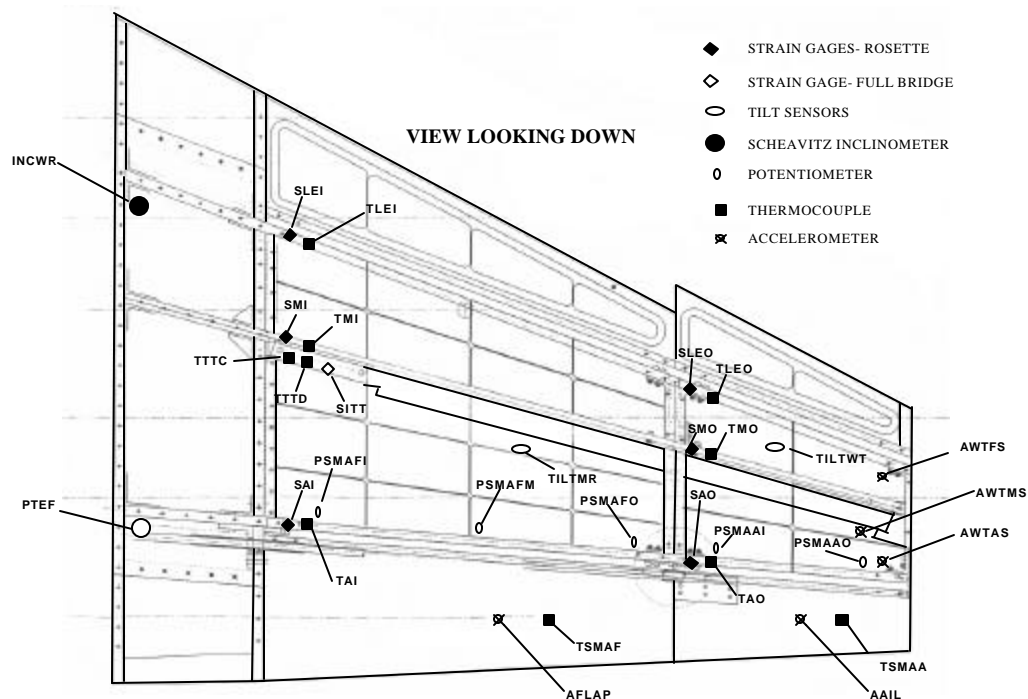


Figure C4. Smart Wing Internal Instrumentation Location

C5.1 COMMON INSTRUMENTATION TO BOTH “SMART WING” AND CONVENTIONAL WING

Steady State Pressures

Each of the models will have four full chordwise rows of static pressures as shown in Figure C5. The Smart Wing will have an additional four partial chordwise rows E,F,G, and H on the aft upper surface as can be seen in Figure C5. The pressure tubing in each model will route through the “canoe” fairing and tunnel wall into the tunnel plenum. Each of the pneumatic tubing will connect to a port on one of five Northrop Grumman supplied PSI modules. Four of the modules contain ± 1 psid rated transducers. The remaining module used will be ± 5 psid rated. Static pressures on the upper leading edge surface in each chordwise row will be connected to the ± 5 psid rated module. Pressure hook-up and exact locations are provided in Section C12. The modules will be operated and calibrated on-line by the NASA Langley PSI 8400 Control System. A water-cooled plate surrounded by a thermally isolated box will be used to house the modules. This is to maintain a stable temperature which minimizes transducer drift and the need for frequent re-calibration of the modules while running. Ports 1 and 32 on each PSI module will be connected to a known pressure for verification and PSI system health monitoring during the test.

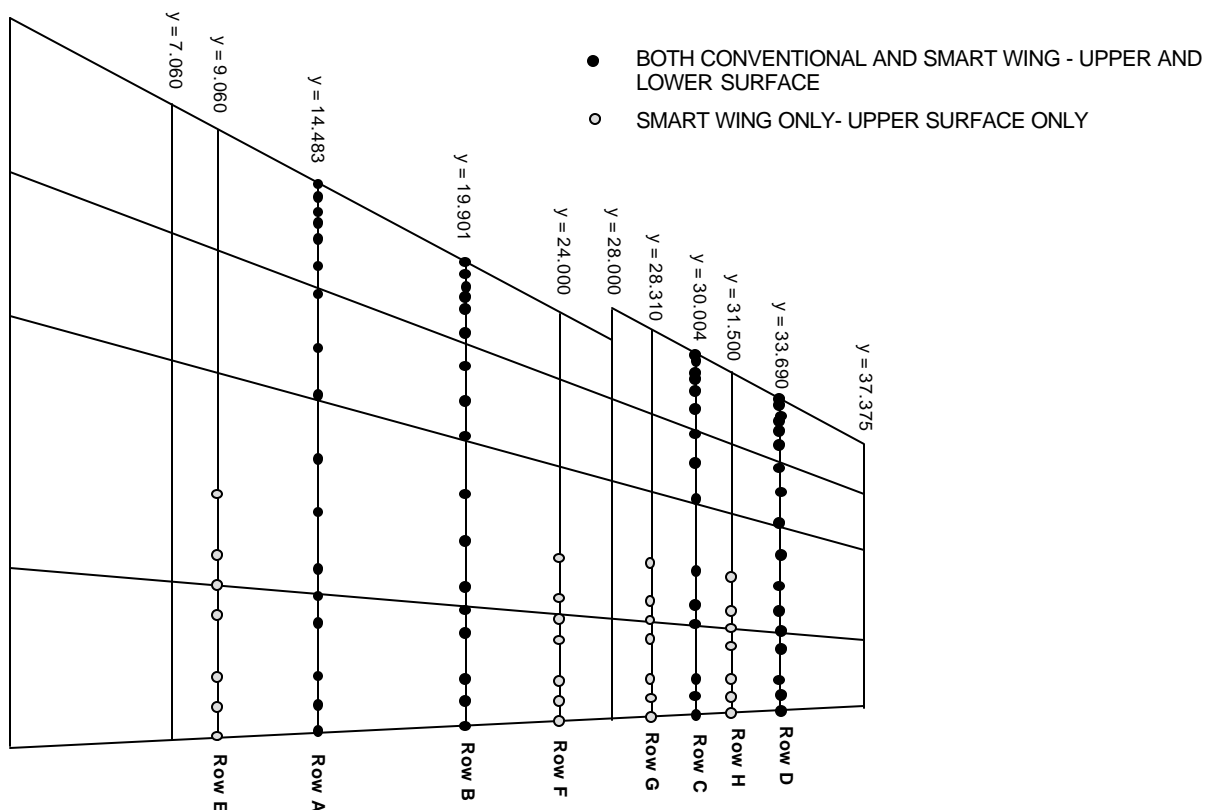
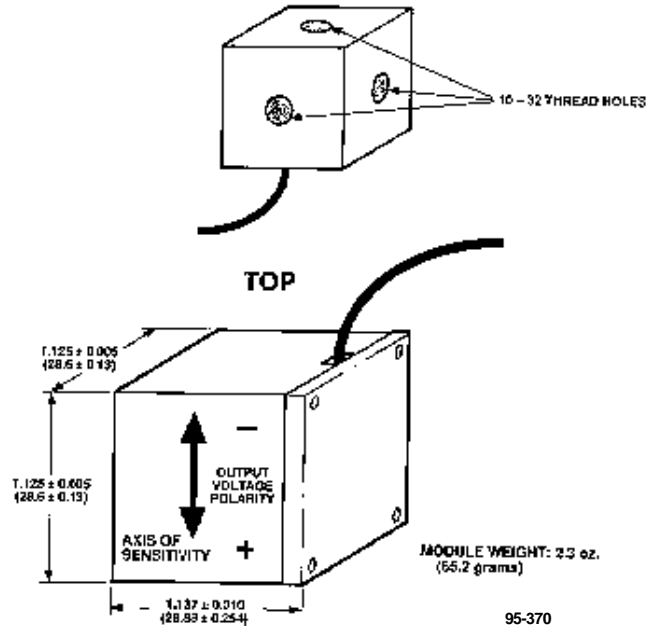


Figure C5. Conventional and Smart Wing Static Pressure Locations

Accelerometers

Five accelerometers will be mounted in each model, three in the main wing box and one in each control surface for tracking model dynamics. The Endevco accelerometers model number 2220D-5 are rated at 200 Gs. These accelerometers will be connected to both strip chart and spectrum analyzers for model and control surface dynamic monitoring.



SMA Torque Tube Actuators

One SMA torque tube actuator will be located in the wing along the center spar. The torque tube will be actuated with Ni-Chrome wire heater on the outside of the torque tube. Since the actuation of the SMA torque tube is temperature dependent, two thermocouples (Type "T" RDX Corp. Model No. 20114-L25) will be attached to the torque tube. One thermocouple for control and one for monitoring into the facility data system. Control of the SMA actuator will be done via a Northrop Grumman supplied control system. The actuator will also contain a strain gaged bridge to measure the amount of torque being applied. Calibration of these gauges will be done prior to test. The outputs of the strain gauged bridges will be fed into the NASA Mod Comp acquisition system.

Tilt Sensors

Two tilt sensors will be mounted in the wing box to measure wing twist. The tilt sensors are Advanced Orientation Systems Model EZ-TILT-3000-045. The tilt sensors work by using an electrolytic sensor. The signal conditioning of these tilt sensors will be done by Northrop Grumman with the output signals being sent to the NASA Mod Comp System.

Strain Gage Rosettes

Six strain gage rosettes shall be mounted on the wing spars, one rosette on the inboard and outboard of each of the three wing spars. The rosettes will measure stress and strain on each of the three spars. Signal conditioning of the strain gages will be Northrop Grumman supplied however, all output signals from these gages will be sent to the NASA Mod Comp Acquisition system for final data reduction. Each rosette shall have a thermocouple (Type "T" RDX Corp. Model No. 20114-L25) for temperature correction if required. The thermocouple outputs will be

connected to the NASA thermocouple reference box and the output signals connected to the facility Mod Comp acquisition system.

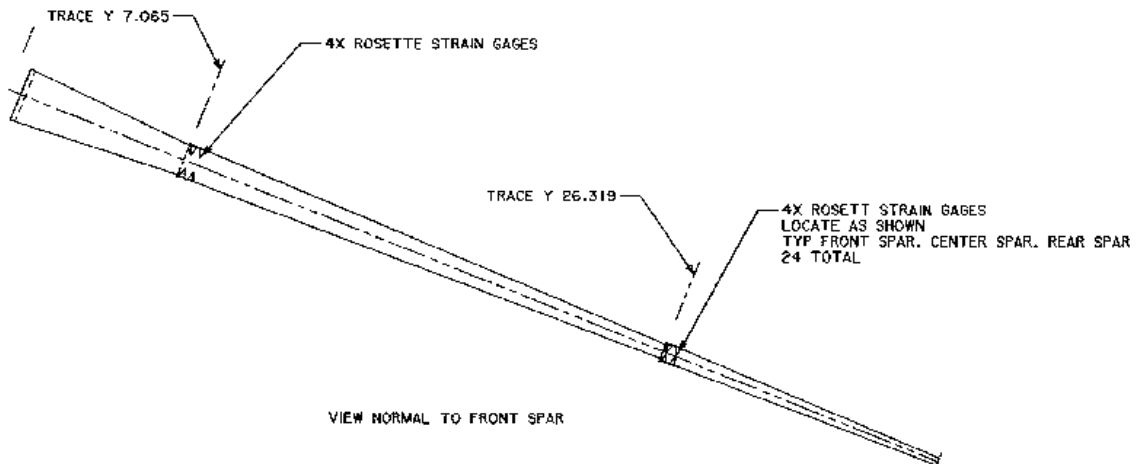


Figure C7. Strain Locations on Spar

Model Attitude

Scheavitz inclinometer will be mounted in the wing root as shown in Figure C4 to measure model pitch angle. Calibration of the inclinometer will be done with the model installed. In addition, model position will be calculated with the facility support system.

External Optical System for Model Wing Twist and Control Surface Deflection Measurement

A NASA Langley Digital Camera System will be installed in 16 TDT to measure model twist and control surface deflection. This will be done by installing round disks or targets of retro-reflective tape on the lower wing surface. Approximately 27 targets will be used in four rows. The optical camera system will be mounted forward of the model in the tunnel floor with a 45 degree up-look angle to the horizon. The system will measure x, y locations of each of the targets. From that information the system will derive angles, wing twist, and control surface deflections relative to the inboard targets and wind off conditions. The model surface will be painted a flat black on the lower surface to maximize the targets resolution.

C5.2 INSTRUMENTATION UNIQUE TO THE CONVENTIONAL WING

Trailing Edge Flap Actuation System

The inboard trailing edge flap will be controlled via an electric Globe motor (Model No. 43A153-2) and flap position will be measured with a Bourns rotary potentiometer (Model No. 3585S-1-203). Control of the flap will be done with a Northrop supplied system located in the control room. Limit switches will be provided to prevent the flap going beyond +15 degrees in the positive direction or 0 degrees in the negative direction.

C5.3 INSTRUMENTATION UNIQUE TO THE SMART WING

SMA Inboard Trailing Edge Flap and Aileron Actuation System

Both the inboard trailing edge flap and the aileron will have a built in SMA actuation system in the skins. The SMA control surfaces will include independent systems in the upper and lower skins in the flap and aileron. Controllers for this system will be provided by Lockheed Martin and will be located in the tunnel control room. A thermocouple (Type "T" RDX Corp. Model No. 20114-L25) will be installed in the flap and aileron for temperature monitoring during operation.

Real time measurement of the control surfaces deflection will be with linear potentiometers (Duncan model 9605). The flap will have three potentiometers one inboard, one midspan and one outboard. The aileron will have an inboard and outboard potentiometer. All conditioned outputs from the potentiometers will be sent to both Lockheed Martin SMA control system and the Facility Mod Comp for final data processing.

C6. DATA ACQUISITION / DATA REDUCTION

C6.1 Data Acquisition

All conditioned signal inputs from model instrumentation will be acquired by the facility Mod Comp acquisition system. Northrop Grumman and Lockheed Martin will provide signal conditioning for the model instrumentation with the exception of pressure data from the PSI Modules, thermocouples, and main balance data. Figure C8 shows a block diagram of the wind tunnel set-up with all the inputs to the MODCOMP and responsible party. All data outputs from the facility Mod Comp system will be in engineering units and sent to either a user supplied and/or facility supplied workstation or PC computer system. Some of the signal outputs will be split from the facility optical patch panel to user supplied acquisition and control systems for the SMA actuators. (Those instrumentation signals to the optical patch panel have been defined in Figure C8).

C6.2 Data Reduction

Data will be reduced to engineering units and coefficient form. Data reduction methodology has been provided in Section C14. A listing of the parameters being calculated has been provide in Section 10 with a constant listing also included in that section.

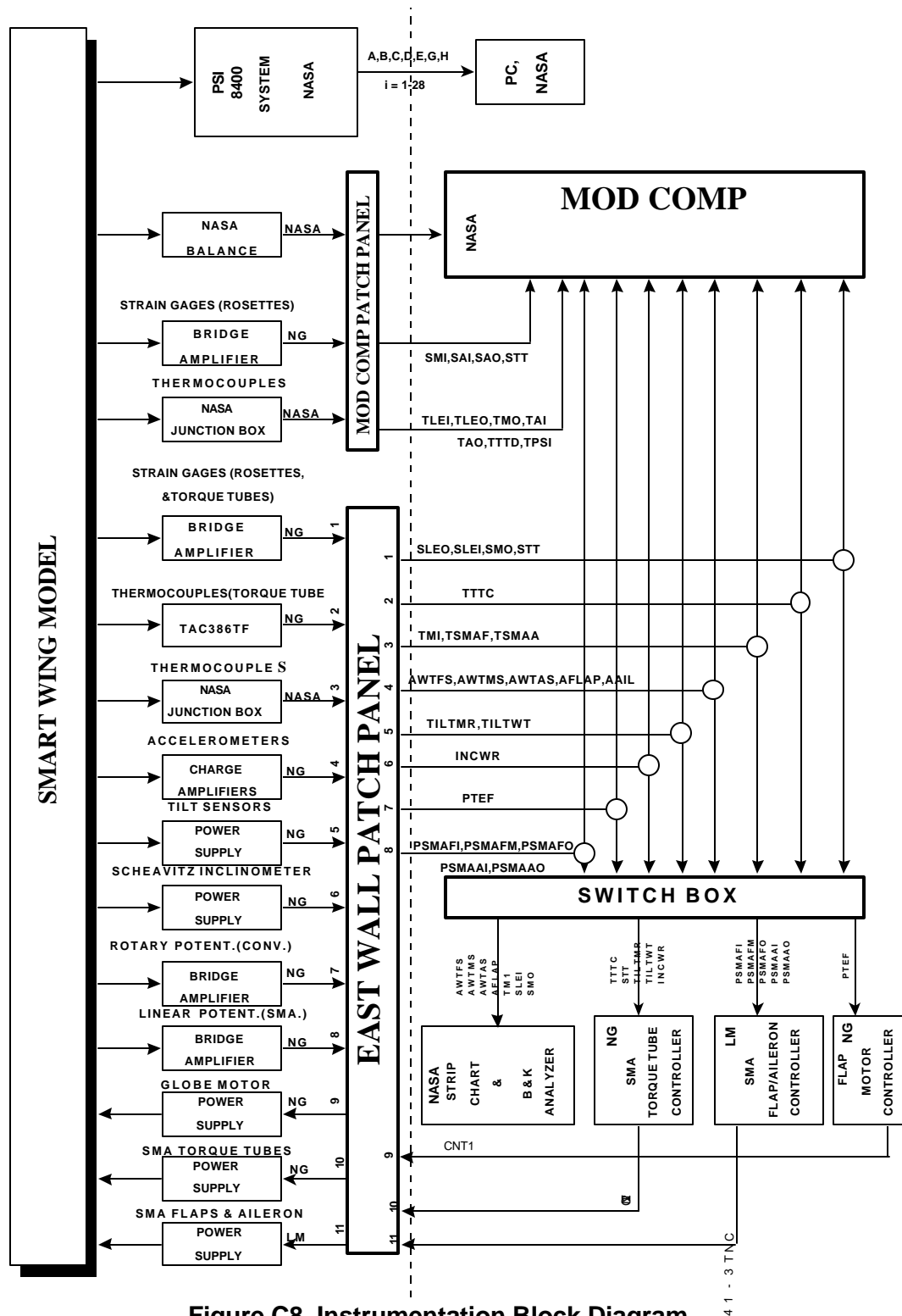


Figure C8. Instrumentation Block Diagram

C7. DATA OUTPUT / PRESENTATION

C7.1 Tab Output

Data will be printed out in tabulated form after a run by the facility. Those parameters into run, test point no., tunnel parameters, balance output, and model position. In addition, a file in Excel will be created and transferred to a user and/ or a facility supplied PC Computer or workstation. Excel macros will be provided to further reduce the data to coefficient form for the balance and pressure output, stress and strains from the strain gages. and integration of pressure rows for local coefficient data. This data will be reduced off-line during the test.

C7.2 Real Time Monitoring and Audible Alarms

Outputs of certain instrumentation will be monitored for safety purposes. These include the accelerometers, two of the strain gage rosettes (Inboard forward spar, SLEI, and the outboard mid spar, SMO), two thermocouples, and one tilt sensor. This equipment will be monitored on a facility supplied B & K Spectrum Analyzer and a strip chart. Those specific parameters to be connected to the spectrum analyzer and strip chart are called out in Section C12 under the general instrumentation layout.

Other real time systems or controllers for such instrumentation such as the strain gages, the SMA torque tube, and the SMA flap and aileron will require real time monitoring of specific parameters. The systems needing such parameters and the parameters required are called out in Section C12 under the general instrumentation layout. Those parameters will be used for the real time control of the SMA actuators during the test.

C7.3 Plotted Data Requirements

Plotted data formats will be provided by the user on Excel macros prior to the start of the test. Plot formats required are as follows;

Pressure Data

C_{p_i} vs. X/C

C_p vs. η at the following chord locations $\eta = 10, 30, 50, 60, 80, 90\%$

Balance Force and Moment Data

CN vs. ALP1

CL vs. ALP1

CL vs. CD

CL/CD vs. ALP1

CM vs. ALP1

Cl_s vs. ALP1

C8. TEST PROGRAM

The principal test variables for the Smart Wing program are as follows:

Tunnel Stagnation Pressure P_o

Tunnel Dynamic Pressure	Q
Aileron deflection	δ_A
Flap deflection	δ_F
Wing Twist	θ
Angle of Attack	α

A test matrix has been developed to experimentally demonstrate the benefits of warping or bending of aerodynamic surfaces as compared to conventionally hinged control surfaces. Benefits to be investigated include drag reduction, reduction in control surface deflections for fixed maneuver loads and potential applicability to flutter suppression or gust load alleviation.

The general mode of test operation will be to set model configuration, tunnel parameters, and lastly model angle of attack. Data will be recorded at specified angles of attack.

Four flap deflections (0, 5, 7.5 and 10 degrees) and five aileron deflections (0, ± 5 , and ± 10) are to be tested separately and in combination. The wind tunnel parameters (Q and P_o) are varied to see how performance is effected by dynamic pressure and Mach number. A chart showing the required tunnel conditions is presented in Figure C9. This chart presents a plot of dynamic pressure (Q) versus Mach number (M). Two curves are shown representing the two tunnel stagnation pressures specified: 2100 and 1100 psf. Points on the chart represent the specified dynamic pressure levels to be tested: 60, 90, and 120 psf. An overall variation in Mach number of 0.15 to 0.42 can be obtained. The matrices are set up to maximize run time and minimize downtime (such as model changes).

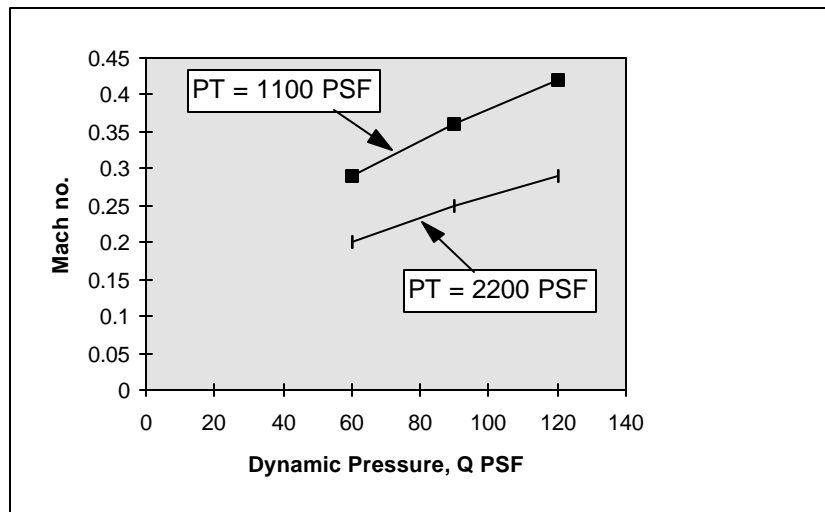


Figure C9. Smart Wing Test Conditions

The test matrices for the Conventional Wing and Smart Wing are presented in Figures C10 and C11 respectively. The matrices are set up to maximize run time and minimize downtime (such as model changes). Run numbers for each wing model correspond to alpha sweeps and are shown in the first column. Aileron deflection shown in the second column, is set manually with brackets and requires entry into the tunnel. Therefore aileron changes shall be kept to a minimum. Similarly, tunnel pressure changes are slow and are also kept to a minimum. Flap deflection and wing twist changes are achieved remotely. Alpha sweeps are relatively fast and therefore are repeated for each new condition. Configuration numbers, shown in the last column correspond to any change in model parameters. There are approximately 120 alpha polars for the Conventional Wing and about 172 alpha polars for the Smart Wing.

The Conventional wing is to be tested first. A database will be established. Then the Smart Wing will be tested and performance will be compared to that of the conventional wing.

Model: CONVENTIONAL WING - W1

* tunnel opened for model change

Run No. (alpha sweeps)	Aileron (deg)	Po (psf)	Flap (deg)	Twist (deg)	Q (psf)	Alpha (deg)	Notes
1 to 12	0	2200	F1	0	Q1	A1	* configs. 1-4
13 to 24		1100		0			
25 to 36	5*	2200		0			* configs 5-8
37 to 48		1100		0			
49 to 60	10*	2200		0			* configs 9-12
61 to 72		1100		0			
73 to 84	-5*	2200		0			* configs 13-16
84 to 95		1100		0			
96 to 107	-10*	2200		0			* configs. 17-20
108 to 119		1100		0			

F1 = 0, 5, 7.5, 10 degrees
Q1 = 60, 90, 120 (psf)
A1 = -4, -2, -1, 0, 1, 2, 3, 4, D 2 deg. to Stall

Figure C10. Conventional Wing Test Matrix

Model: SMART WING - W2

Run No. (alpha sweeps)	Aileron (deg)	Po (psf)	Flap (deg)	Twist (deg)	Q (psf)	Alpha (deg)	Notes
1 to 12	0	2200	F1	0	Q1	A1	configs. 1-4
13 to 24		1100		0			
25 to 36	5*	2200		0			configs 5-8
37 to 48		1100		0			
49 to 60	10*	2200		0			configs 9-12
61 to 72		1100		0			
73 to 84	-5*	2200		0			configs 13-16
84 to 95		1100		0			
96 to 107	-10*	2200		0			configs. 17-20
108 to 119		1100		0			
120 to 131	0	2200		1.2	Q1	A2	config 21
132 to 143		1100		1.2			
144 to 155		2200		3	Q1	A2	config 22
156 to 167		1100		3			
168 to 171	0	2200	10	3	Q1	A1	config 23

Q1 = 60,90,120 PSF
F1 = 0,5,7.5,10 degrees
A1 = -4, -3,-2,-1,0,1,2,3,4 D2 deg. to Stall A2 = -8,-6,-4,-3,-2,-1,0,1,2,3,4,6,8

Figure C11. Smart Wing Test Matrix

C9. FACILITY

C9.1 Tunnel Description and Operating Envelope

The NASA Langley 16 Transonic Dynamics Tunnel was designed to provide the capability of testing large dynamics models at transonic speeds for the study of flutter, aerodynamic loads, and input response. The wind tunnel is a continuous-flow tunnel which operates from Mach numbers near 0 to 1.20 at pressures ranging from 0.2 to atmospheric pressure. The “pressure vessel” design of the tunnel provides for testing medium of either air or Freon 12 (Freon 12 was replaced with Freon 134 during the tunnel shut-down June 1996 through June 1997). The tests of the Smart Wings however, will use only air as the testing medium.

Details of the construction of the tunnel and test section have been provided in Figures C12 and C13. The test chamber is 60-feet in diameter with the test section located inside the chamber, 16-feet square with filleted corners. Figure C13 shows the test section cross section with the semi-span mounting system as it will be used with the Smart Wing. Tunnel and model control operation is done in the 32-foot-long control room chamber located alongside the test section. Windows in the control room provide visual access to the test section. There are four quick opening valves, for model safety purposes, located in the by-pass lines which connect the test chamber and the tunnel return leg downstream of the motor nacelle. These will be used in case high model dynamic instabilities to prevent loss of model or components. Details of the 16 TDT tunnel and operation can be found in the reference NASA Langley Working Paper LWP-799 “The Langley Transonic Dynamics Tunnel”.

The operating envelope with air as the testing medium has been provided in Figure C14. The test program for the Smart Wing was designed to stay within the boundaries of this operating envelope.

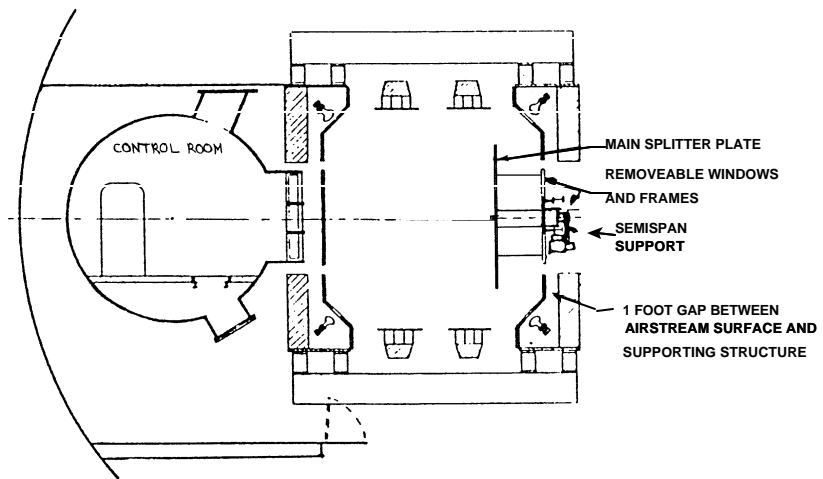


Figure C13. NASA/LaRc Cross-section at Station 72 of Semi-span Support System

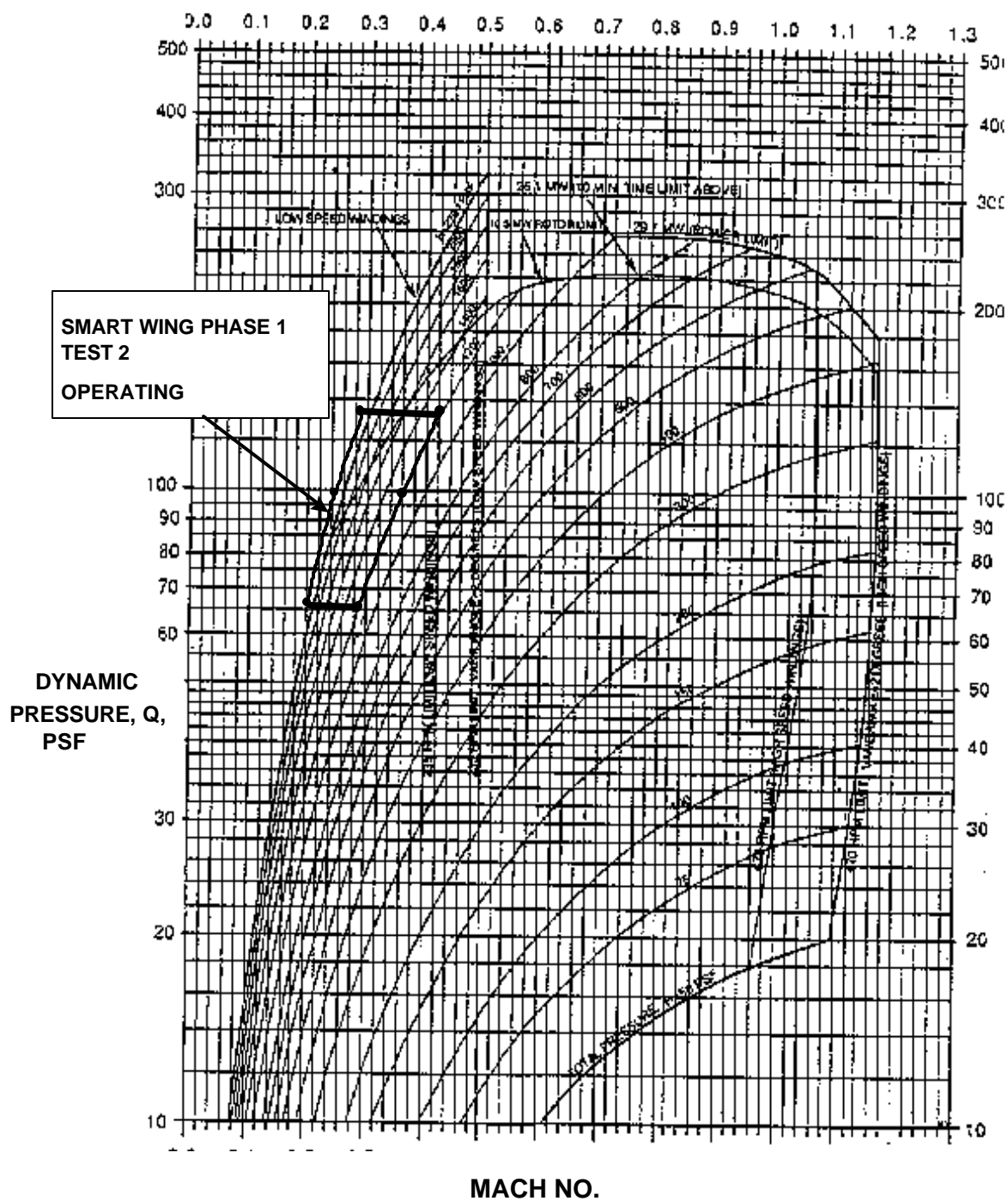


Figure C14. NASA/LaRc 16tdt Transonic Dynamics
Tunnel Operating Boundary in Air
Vane Angle 18 Degrees Unless Noted

C10. TERMS AND CONSTANTS

DATA REDUCTION DEFINITION OF CONSTANTS

TERM	DEFINITION	UNITS	EQN.	VALUE
A1	ANGLE OF ATTACK FROM SCHEAVITZ INCLINOMETER	DEG	2	TBD
A2	ANGLE OF ATTACK FROM SCHEAVITZ INCLINOMETER	DEG	2	TBD
AM1	WING TWIST FROM MID-WING TILT SENSOR	DEG	2	TBD
AM2	WING TWIST FROM MID-WING TILT SENSOR	DEG/VOLT	2	TBD
AO1	WING TWIST FROM OUTBOARD TILT SENSOR	DEG	2	TBD
AO2	WING TWIST FROM OUTBOARD TILT SENSOR	DEG/VOLT	2	TBD
ATI0	TORQUE FROM TORQUE TUBE (SMA)	IN-LB	5	TBD
ATI1	TORQUE FROM TORQUE TUBE (SMA)	IN-LB/VOLT	5	TBD
b	WING REFERENCE SPAN	IN	3	37.375
C0	FLAP POTENTIOMETER POSITION (CONV. WING)	DEG	14	TBD
C1	FLAP POTENTIOMETER POSITION (CONV. WING)	DEG/VOLT	14	TBD
cbar	WING REFERENCE CHORD	IN	3	23.439
D0	FLAP DEFLECTION INBOARD (SMA)	DEG	14	TBD

D1	FLAP DEFLECTION INBOARD (SMA)	DEG/VOLT	14	TBD
E	MODULUS OF ELASTICITY	psi/μ-in/in	5	10.3x10 ⁶
E0	FLAP DEFLECTION MID (SMA)	DEG	14	TBD
E1	FLAP DEFLECTION MID (SMA)	DEG/VOLT	14	TBD
F0	FLAP DEFLECTION OUTBOARD (SMA)	DEG	14	TBD
F1	FLAP DEFLECTION OUTBOARD (SMA)	DEG/VOLT	14	TBD
G0	AILERON DEFLECTION INBOARD (SMA)	DEG	14	TBD
G1	AILERON DEFLECTION INBOARD (SMA)	DEG/VOLT	14	TBD
GF	GAGE FACTOR FOR STANDARD STRAIN GAGE	----	5	TBD
H0	AILERON DEFLECTION OUTBOARD (SMA)	DEG	14	TBD
H1	AILERON DEFLECTION OUTBOARD (SMA)	DEG/VOLT	14	TBD
lmrc	TRANSFER DISTANCE ALONG Y- AXIS FROM BALANCE CENTER TO MRC	IN	3	19.81
v	POISSON'S RATIO		6,7,8,9	0.33
S	WING REFERENCE AREA	IN ²	3	887
V	EXCITATION VOLTAGE FOR STRAIN GAGES	VOLTS		5
TBD				

DATA REDUCTION DEFINITION OF TERMS

TERM	DEFINITION	UNITS	EQN.
ALP1	MODEL ALPHA POSITION FROM SCHEAVITZ INCLINOMETER	DEG	2
ALP2	MODEL MID-WING TWIST FROM TILT SENSOR	DEG	2
ALP3	MODEL OUTBOARD WING TWIST FROM TILT SENSOR	DEG	2
AOA	MODEL ALPHA POSITION FROM FACILITY SUPPORT SYSTEM	DEG	1
CA	AXIAL COEFFICIENT FROM BALANCE	----	3
CD	MODEL DRAG COEFFICIENT FROM BALANCE	----	3
CI	MODEL ROLLING MOMENT COEF. AT MOMENT REFERENCE CENTER FROM BALANCE- BODY AXIS	----	3
CL	MODEL LIFT COEFFICIENT FROM BALANCE	----	3
Cl _s	MODEL ROLLING MOMENT COEF. AT MOMENT REFERENCE CENTER FROM BALANCE- BODY AXIS	----	3
CM	MODEL PITCHING MOMENT COEFFICIENT FROM BALANCE	----	3
C _{ns}	YAWING MOMENT COEFFICIENT ABOUT MOMENT REFERENCE CENTER STABILITY AXIS	----	3
CPA _i	PRESSURE COEFFICIENT- INDIVIDUAL PRESSURES- INBOARD ROW	----	9

CPB _i	PRESSURE COEFFICIENT- INDIVIDUAL PRESSURES- MID-INBOARD ROW	----	9
CPC _i	PRESSURE COEFFICIENT- INDIVIDUAL PRESSURES- MID-OUTBOARD ROW	----	9
CPD _i	PRESSURE COEFFICIENT- INDIVIDUAL PRESSURES- OUTBOARD ROW	----	9
DAOAM	WING TWIST MEASUREMENT MID WING TILT SENSOR TO SCHEAVITZ INCLINOMETER	DEG	2
DAOAO	WING TWIST MEASUREMENT OUTBOARD TILT SENSOR TO SCHEAVITZ INCLINOMETER	DEG	2
FA	AXIAL FORCE CORRECTED FOR MODEL WEIGHT TARE	LBS	3
FN	NORMAL FORCE FROM BALANCE	LBS	3
M	TUNNEL FREESTREAM MACH NUMBER	----	1
MI	ROLLING (OR BENDING) MOMENT FROM BALANCE	IN-LB	3
MM	PITCHING MOMENT FROM BALANCE	IN-LB	3
P _o	TUNNEL FREESTREAM STATIC PRESSURE	PSI	1
PSMAAI	SMA INBOARD AILERON POSITION FROM POTENTIOMETER	DEG	10
PSMAAO	SMA OUTBOARD AILERON POSITION FROM POTENTIOMETER	DEG	10
PSMAFI	SMA INBOARD FLAP POSITION FROM POTENTIOMETER	DEG	10
PSMAFM	SMA INBOARD FLAP POSITION FROM POTENTIOMETER	DEG	10

PSMAFO	SMA INBOARD FLAP POSITION FROM POTENTIOMETER	DEG	10
PTEF 14	OUTPUT OF FLAP POTENTIOMETER (CONV.)	VOLTS	
PTO 1	TUNNEL FREESTREAM TOTAL PRESSURE	PSI	
Q	TUNNEL FREESTREAM DYNAMIC PRESSURE	PSI	1
RN	TUNNEL REYNOLD'S NUMBER	----	1
SAIA 5	AFT INBOARD SPAR STRAIN GAGE 1 (ROSETTE) OUTPUT	VOLTS	
SAIB 5	AFT INBOARD SPAR STRAIN GAGE 2 (ROSETTE) OUTPUT	VOLTS	
SAIC 5	AFT INBOARD SPAR STRAIN GAGE 3 (ROSETTE) OUTPUT	VOLTS	
SAOA 5	AFT OUTBOARD SPAR STRAIN GAGE 1 (ROSETTE) OUTPUT	VOLTS	
SAOB 5	AFT OUTBOARD SPAR STRAIN GAGE 2 (ROSETTE) OUTPUT	VOLTS	
SAOC 5	AFT OUTBOARD SPAR STRAIN GAGE 3 (ROSETTE) OUTPUT	VOLTS	
SLEIA 5	LEADING EDGE INBOARD SPAR STRAIN GAGE 1 (ROSETTE) OUTPUT	VOLTS	
SLEIB 5	LEADING EDGE INBOARD SPAR STRAIN GAGE 2 (ROSETTE) OUTPUT	VOLTS	
SLEIC	LEADING EDGE INBOARD SPAR		

5	STRAIN GAGE 3 (ROSETTE) OUTPUT	VOLTS
SLEOA 5	LEADING EDGE OUTBOARD SPAR STRAIN GAGE 1 (ROSETTE) OUTPUT	VOLTS
SLEOB 5	LEADING EDGE OUTBOARD SPAR STRAIN GAGE 2 (ROSETTE) OUTPUT	VOLTS

SLEOC 5	LEADING EDGE OUTBOARD SPAR STRAIN GAGE 3 (ROSETTE) OUTPUT	VOLTS	
SMIA 5	MID-CHORD INBOARD SPAR STRAIN GAGE 1 (ROSETTE) OUTPUT	VOLTS	
SMIB 5	MID-CHORD INBOARD SPAR STRAIN GAGE 2 (ROSETTE) OUTPUT	VOLTS	
SMIC 5	MID-CHORD INBOARD SPAR STRAIN GAGE 3 (ROSETTE) OUTPUT	VOLTS	
SMOA 5	MID-CHORD OUTBOARD SPAR STRAIN GAGE 1 (ROSETTE) OUTPUT	VOLTS	
SMOB 5	MID-CHORD OUTBOARD SPAR STRAIN GAGE 2 (ROSETTE) OUTPUT	VOLTS	
SMOC 5	MID-CHORD OUTBOARD SPAR STRAIN GAGE 3 (ROSETTE) OUTPUT	VOLTS	
STT 14	INBOARD TORQUE TUBE (SMA) STRAIN GAGE BRIDGE OUTPUT	VOLTS	
TTO	TUNNEL FREESTREAM TOTAL TEMPERATURE	DEG F	1
TORQ	TORQUE VALUE FROM SMA TORQUE TUBE- INBOARD	IN-LB	14
V _o 5	VOLTS OUT FROM STRAIN GAGES	VOLTS	
YM 3	YAWING MOMENT FROM BALANCE	IN-LB	
ϵ	STRAIN FROM STRAIN GAGES	μ -in/in	5,6,7,8
σ	STRESS FROM STRAIN GAGES	PSI	5,6,7,8

θ	ANGLE OF PRINCIPAL AXES OF EACH STRAIN GAGE ROSETTE	DEG	6,7,8
----------	--	-----	-------

C11. POINTS OF CONTACT

Jay Kudva

Northrop Grumman
Program Manager
310-332-8300

Lew Scherer

Northrop Grumman
Test Engineer
310-942-5627

Peter Jardine

Northrop Grumman
310-332-4020

Bernie Carpenter

Lockheed Martin
303-971-9128

Anna McGowan

NASA/LaRC
804-864-2846

Chris Martin

Northrop Grumman
310-332-8198

Kari Appa

Northrop Grumman
310-332-9609

John Flanagan

Northrop Grumman
310-332-3072

Mark West

Mission Research Corp.
714-754-7212

C12. PHASE 1 TEST 2

**SMART WING INSTRUMENTATION SUMMARY, ACQUISITION, AND
HOOK-UPS**

SMART WING-WIND TUNNEL TEST
INSTRUMENTATION SYSTEM SUMMARY

East Wall Channel Key: M = Modcomp Patch Panel, CR = Control Rm. Patch Panel, CNT = Control Signal Patch Panel
Offset for Thermocouples: 150

ModComp	ANALOG CHANNEL INFO										
CHAN.	EA.WALL CHAN.	NAME	DESCRIPTION	MODEL	ORIGIN	EXCIT VOLTS	AMP GAIN	RCAL VALUE (KOHMS)	RCAL EQUIV VOLT	E.U.	MIN LOAD
			BALANCE								
1	M-0	NORMAL		BOTH	BALANCE TDT05S	5				LB	-1500
2	M-1	AXIAL		BOTH	BALANCE TDT05S	5				LB	-120
3	M-2	PITCH		BOTH	BALANCE TDT05S	5				IN-LB	-6500
4	M-3	ROLL		BOTH	BALANCE TDT05S	5				IN-LB	-50,000
5	M-4	YAW		BOTH	BALANCE TDT05S	5				IN-LB	-4000
6	M-5	AOA	TURNTABLE AOA	BOTH	TURNTABLE					DEG	
7-11		EMPTY	EMPTY CHANNELS	BOTH	NONE						
			STRAIN GAGES								
12	M-11	SLEIA	INBOARD L.E. SPAR (ROSETTE)	BOTH	MODCOMP PATCH PANEL	5	300	50	3.29	MICRO-e	-2000
13	M-12	SLEIB		BOTH	MODCOMP PATCH PANEL	5	300	50	3.25	MICRO-e	-2000
14	M-13	SLEIC		BOTH	MODCOMP PATCH PANEL	5	300	50	3.29	MICRO-e	-2000
15	M-14	SLEOA	OUTBOARD L.E. SPAR (ROSETTE)	BOTH	MODCOMP PATCH PANEL	5	300	20	3.04	MICRO-e	-2000
16	M-15	SLEOB		BOTH	MODCOMP PATCH PANEL	5	300	20	3.03	MICRO-e	-2000
17	M-16	SLEOC		BOTH	MODCOMP PATCH PANEL	5	300	20	3.04	MICRO-e	-2000
18	M-17	SMA	INBOARD MID SPAR (ROSETTE)	BOTH	MODCOMP PATCH PANEL	5	300	50	3.29	MICRO-e	-2000
19	M-18	SMIB		BOTH	MODCOMP PATCH PANEL	5	300	50	3.25	MICRO-e	-2000
20	M-19	SMIC		BOTH	MODCOMP PATCH PANEL	5	300	50	3.29	MICRO-e	-2000
21	M-20	SMOA	OUTBOARD MID SPAR (ROSETTE)	BOTH	MODCOMP PATCH PANEL	5	300	20	3.36	MICRO-e	-2000
22	M-21	SMOB		BOTH	MODCOMP PATCH PANEL	5	300	20	3.28	MICRO-e	-2000
23	M-22	SMOC		BOTH	MODCOMP PATCH PANEL	5	300	20	3.36	MICRO-e	-2000
24	M-23	SAIA	INBOARD AFT SPAR (ROSETTE)	BOTH	MODCOMP PATCH PANEL	5	300	50	3.36	MICRO-e	-2000
25	M-24	SAIB		BOTH	MODCOMP PATCH PANEL	5	300	50	3.28	MICRO-e	-2000
26	M-25	SAIC		BOTH	MODCOMP PATCH PANEL	5	300	50	3.36	MICRO-e	-2000
27	M-26	SAOA	OUTBOARD AFT SPAR (ROSETTE)	BOTH	MODCOMP PATCH PANEL	5	300	50	3.04	MICRO-e	-2000
28	M-27	SAOB		BOTH	MODCOMP PATCH PANEL	5	300	50	3.03	MICRO-e	-2000
29	M-28	SAOC		BOTH	MODCOMP PATCH PANEL	5	300	50	3.04	MICRO-e	-2000
30	M-29	STT	TORQUE TUBE (FULL BRIDGE)	BOTH	MODCOMP PATCH PANEL	5	300			IN-LB	-2500
			THERMOCOUPLES								
31	M-30	TLEI	INBOARD LEADING EDGE SPAR	BOTH	JUNC.BOX-MODCOMP PATCH PANE	NA				°F	40
32	M-31	TLEO	OUTBOARD LEADING EDGE SPAR	BOTH	JUNC.BOX-MODCOMP PATCH PANE	NA				°F	40
33	CR-32	TMI	INBOARD MID SPAR	BOTH	JUNC.BOX -EA.WALL -PSB	NA				°F	40
34	M-33	TMO	OUTBOARD MID SPAR	BOTH	JUNC.BOX-MODCOMP PATCH PANE	NA				°F	40
35	M-34	TAI	INBOARD AFT SPAR	BOTH	JUNC.BOX-MODCOMP PATCH PANE	NA				°F	40
36	M-35	TAO	OUTBOARD AFT SPAR	BOTH	JUNC.BOX-MODCOMP PATCH PANE	NA				°F	40
37	CR-36	TTTC	TORQUE TUBE - CONTROL	BOTH	TAC386TF-EA.WALL-PSB	NA				°F	40
38	M-37	TTTD	TORQUE TUBE - DATA	BOTH	JUNC.BOX-MODCOMP PATCH PANE	NA				°F	40
39	M-38	TPSI1	PSI MODULE 1	BOTH	JUNC.BOX-MODCOMP PATCH PANE	NA				°F	40
40	M-39	TPSI2	PSI MODULE 2	BOTH	JUNC.BOX-MODCOMP PATCH PANE	NA				°F	40
41	M-40	TPSI3	PSI MODULE 3	BOTH	JUNC.BOX-MODCOMP PATCH PANE	NA				°F	40
42	M-41	TPSI4	PSI MODULE 4	BOTH	JUNC.BOX-MODCOMP PATCH PANE	NA				°F	40
43	M-42	TPSI5	PSI MODULE 4	BOTH	JUNC.BOX-MODCOMP PATCH PANE	NA				°F	40
44	M-43	TPSI6	PSI MODULE 6	BOTH	JUNC.BOX-MODCOMP PATCH PANE	NA				°F	40

SMART WING-WIND TUNNEL TEST INSTRUMENTATION SYSTEM SUMMARY

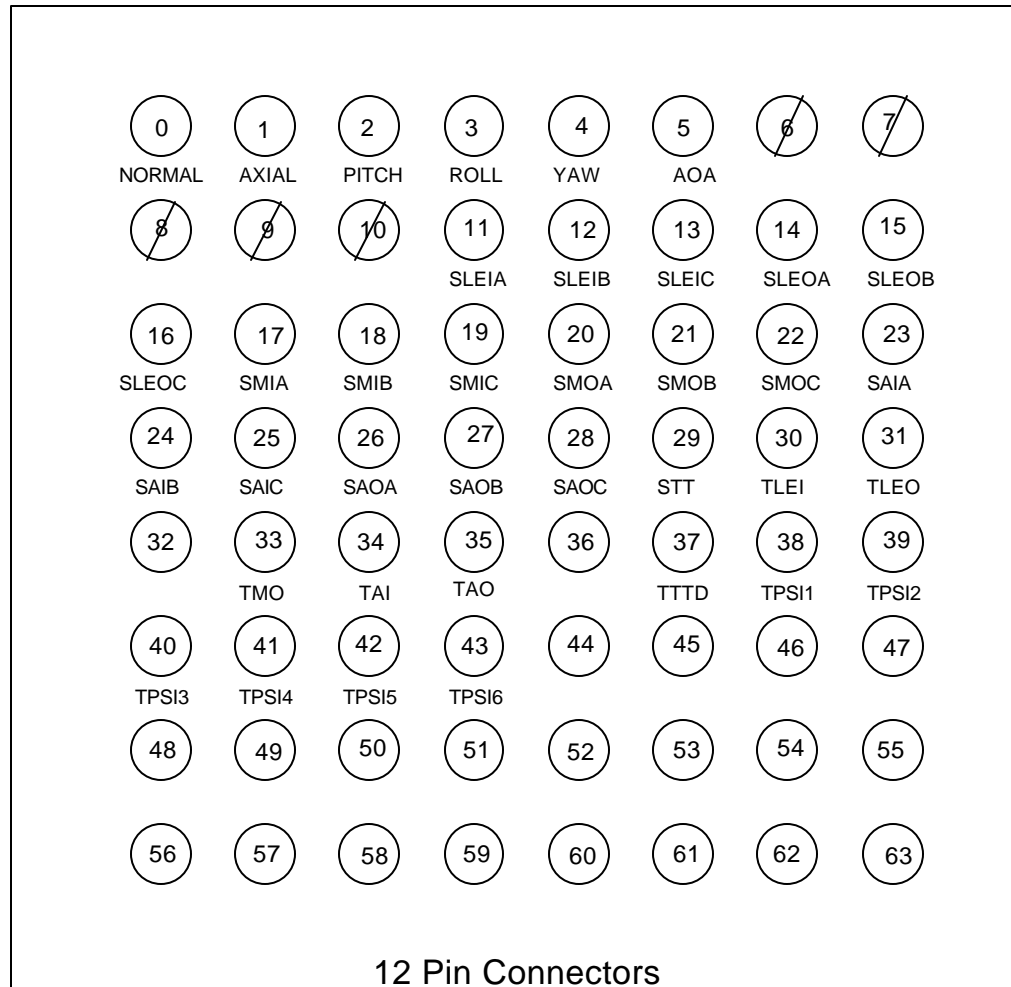
ModComp	ANALOG CHANNEL INFO					EXCIT	AMP	RCAL	RCAL	
CHAN.	EA.WALL CHAN.	NAME	DESCRIPTION	MODEL	ORIGIN	VOLTS	GAIN	VALUE KOHMS	EQUIV VOLI	E.U.
			TILT SENSORS							
45	CR-44	TILTMR	MID RIB	BOTH	PWR SUPPLY-EA.WALL-PSB					DEG
46	CR-45	TILTWT	WING TIP	BOTH	PWR SUPPLY-EA.WALL-PSB					DEG
			INCLINOMETER							
47	CR-46	INCWR	SCHEAVITZ INCLINOMETER - WING ROOT	BOTH	PWR SUPPLY-EA.WALL-PSB	+15				DEG
			ACCELEROMETERS							
48	CR-47	AWTFS	WING TIP-FORWARD SPAR	BOTH	CHARGE AMP-EA.WALL-PSB					G's
49	CR-48	AWTMS	WING TIP- MID SPAR	BOTH	CHARGE AMP-EA.WALL-PSB					G's
50	CR-49	AWTAS	WING TIP - AFT SPAR	BOTH	CHARGE AMP-EA.WALL-PSB					G's
51	CR-50	AFLAP	TRAILING EDGE FLAP	BOTH	CHARGE AMP-EA.WALL-PSB					G's
			POTENTIOMETERS							
52	CR-51	PIEF	TRAILING EDGE FLAP	CONV.	PWR SUPPLY-EA.WALL-PSB					DEG
53	CR-52	PSMAFI	SMA FLAP INBOARD	SMA	PWR SUPPLY-EA.WALL-PSB					DEG
54	CR-53	PSMAFM	SMA FLAP MIDDLE	SMA	PWR SUPPLY-EA.WALL-PSB					DEG
55	CR-54	PSMAFO	SMA FLAP OUTBOARD	SMA	PWR SUPPLY-EA.WALL-PSB					DEG
56	CR-55	PSMAAI	SMA AILERON INBOARD	SMA	PWR SUPPLY-EA.WALL-PSB					DEG
57	CR-56	PSMAAO	SMA AILERON OUTBOARD	SMA	PWR SUPPLY-EA.WALL-PSB					DEG
			CONTROL FEEDBACK							
58	CR-57	FBTT	TORQUE TUBE - WING TWIST	BOTH	HEATING ELEMENT VOLTAGE					VOLTS
59	CR-58	FBSMAFI	SMA TRAILING EDGE FLAP - INBOARD	SMA	SMA ACTUATOR VOLTAGE					VOLTS
60	CR-59	FBSMAFM	SMA TRAILING EDGE FLAP - MIDDLE	SMA	SMA ACTUATOR VOLTAGE					VOLTS
61	CR-60	FBSMAFO	SMA TRAILING EDGE FLAP - OUTBOARD	SMA	SMA ACTUATOR VOLTAGE					VOLTS
62	CR-61	FBSMAAI	SMA AILERON - INBOARD	SMA	SMA ACTUATOR VOLTAGE					VOLTS
63	CR-62	FBSMAAO	SMA AILERON - OUTBOARD	SMA	SMA ACTUATOR VOLTAGE					VOLTS
NEFF "B"										
			CONTROLS							
66	CNT-0	CNT1	GLOBE MOTOR CONTROL- FLAP ROTATION	CONV.	PWR. SUPPLY-EA.WALL-NG	+28				VOLTS
67	CNT-1	CNT2	TORQUE TUBE - WING TWIST	BOTH	PWR. SUPPLY-EA.WALL-NG					VOLTS
68	CNT-2	CNT3	SMA TRAILING EDGE FLAP - INBOARD	SMA	PWR. SUPPLY-EA.WALL-NG					VOLTS
69	CNT-3	CNT4	SMA TRAILING EDGE FLAP - MIDDLE	SMA	PWR. SUPPLY-EA.WALL-NG					VOLTS
70	CNT-4	CNT5	SMA TRAILING EDGE FLAP - OUTBOARD	SMA	PWR. SUPPLY-EA.WALL-NG					VOLTS
71	CNT-5	CNT6	SMA AILERON - INBOARD	SMA	PWR. SUPPLY-EA.WALL-NG					VOLTS
72	CNT-5	CNT6	SMA	SMA	PWR. SUPPLY-EA.WALL-NG					VOLTS
73	MEMSRT-1	MEMSRT-1	MEMS Tilt Sensor - Root Rib	SMA	PWR. SUPPLY-EA.WALL-NG	5				VOLTS
74	MEMSWT-1	MEMSWT-1	MEMS Tilt Sensor - Wing Tip	SMA	PWR. SUPPLY-EA.WALL-NG	5				VOLTS

DESCRIPTION	CHAN NAME	APPLIES TO WHICH MODEL	RANGE EU	SIGNAL COND. RESPON.	MODCOMP CONDITIONED SIGNAL INPUT	MODCOMP REAL TIME MONITORING	PSB	STRIP CHART	B&K ANALYZER
STRAIN GAGES									
INBOARD LEADING EDGE SPAR (ROSETTE)	SLEIA	BOTH	+/- 2000 ue	NG	YES	YES	YES	YES	NO
	SLEIB	BOTH	+/- 2000 ue	NG	YES	YES	YES	YES	YES
	SLEIC	BOTH	+/- 2000 ue	NG	YES	YES	YES	YES	NO
OUTBOARD LEADING EDGE SPAR (ROSETTE)	SLEOA	BOTH	+/- 2000 ue	NG	YES	YES	NO	NO	NO
	SLEOB	BOTH	+/- 2000 ue	NG	YES	YES	NO	NO	NO
	SLEOC	BOTH	+/- 2000 ue	NG	YES	YES	NO	NO	NO
INBOARD MID SPAR (ROSETTE)	SMIA	BOTH	+/- 2000 ue	NG	YES	YES	NO	NO	NO
	SMIB	BOTH	+/- 2000 ue	NG	YES	YES	NO	NO	NO
	SMIC	BOTH	+/- 2000 ue	NG	YES	YES	NO	NO	NO
OUTBOARD MID SPAR (ROSETTE)	SMOA	BOTH	+/- 2000 ue	NG	YES	YES	YES	YES	NO
	SMOB	BOTH	+/- 2000 ue	NG	YES	YES	YES	YES	YES
	SMOC	BOTH	+/- 2000 ue	NG	YES	YES	YES	YES	NO
INBOARD AFT SPAR (ROSETTE)	SAIA	BOTH	+/- 2000 ue	NG	YES	YES	NO	NO	NO
	SAIB	BOTH	+/- 2000 ue	NG	YES	YES	NO	NO	NO
	SAIC	BOTH	+/- 2000 ue	NG	YES	YES	NO	NO	NO
OUTBOARD AFT SPAR (ROSETTE)	SAOA	BOTH	+/- 2000 ue	NG	YES	YES	NO	NO	NO
	SAOB	BOTH	+/- 2000 ue	NG	YES	YES	NO	NO	NO
	SAOC	BOTH	+/- 2000 ue	NG	YES	YES	NO	NO	NO
TORQUE TUBE (FULL BRIDGE)	STT	BOTH	+/- 2000 ue	NG	YES	YES	YES	NO	NO
THERMOCOUPLES									
INBOARD LEADING EDGE SPAR	TLEI	BOTH	40-175 F	NASA	YES	YES	NO	NO	NO
OUTBOARD LEADING EDGE SPAR	TLEO	BOTH	40-175 F	NASA	YES	YES	NO	NO	NO
INBOARD MID SPAR	TMI	BOTH	40-210 F	NASA	YES	YES	YES	YES	NO
OUTBOARD MID SPAR	TMO	BOTH	40-210 F	NASA	YES	YES	NO	NO	NO
INBOARD AFT SPAR	TAI	BOTH	40-175 F	NASA	YES	YES	NO	NO	NO
OUTBOARD AFT SPAR	TAO	BOTH	40-175 F	NASA	YES	YES	NO	NO	NO
TORQUE TUBE-CONROL	TTTC	BOTH	40-250 F	NG	YES	YES	YES	NO	NO
TORQUE TUBE-DATA	TTTD	BOTH	40-250 F	NASA	YES	YES	NO	NO	NO
PSI MODULE 1	TPSI1	BOTH	40-120 F	NASA	YES	YES	NO	NO	NO
PSI MODULE 2	TPSI2	BOTH	40-120 F	NASA	YES	YES	NO	NO	NO
PSI MODULE 3	TPSI3	BOTH	40-120 F	NASA	YES	YES	NO	NO	NO
PSI MODULE 4	TPSI4	BOTH	40-120 F	NASA	YES	YES	NO	NO	NO
PSI MODULE 4	TPSI4	BOTH	40-120 F	NASA	YES	YES	NO	NO	NO
PSI MODULE 6	TPSI6	BOTH	40-120 F	NASA	YES	YES	NO	NO	NO

DESCRIPTION	CHAN NAME	APPLIES TO WHICH MODEL	RANGE EU	SIGNAL COND. RESPON.	MODCOMP CONDITIONED SIGNAL INPUT	MODCOMP REAL TIME MONITORING	PSB	STRIP CHART	B&K ANALYZER
TILT SENSORS									
MID RIB	TILTMR	BOTH	+/- 15 Deg	NG	YES	YES	YES	NO	NO
WING TIP	TILTWI	BOTH	+/- 15 Deg	NG	YES	YES	YES	NO	NO
ACCELEROMETERS									
WING TIP- FORWARD SPAR	AWTFS	BOTH	+/- 50 G	NG	YES	NO	YES	YES	YES
WING TIP- MID SPAR	AWTMS	BOTH	+/- 50 G	NG	YES	NO	YES	YES	YES
WING TIP- AFT SPAR	AWTAS	BOTH	+/- 50 G	NG	YES	NO	YES	YES	YES
TRAILING EDGE FLAP	AFLAP	BOTH	+/- 50 G	NG	YES	NO	YES	YES	YES
INCLINOMETER									
SCHEAVITZ INCLINOMETER- WING ROOT	INCWR	BOTH	±30 DEG	NG	YES	YES	YES	NO	NO
POTENTIOMETERS									
TRAILING EDGE FLAP POTENTIOMETER	POSF	CONV.	0-15 DEG	NG	YES	YES	YES	NO	NO
SMA FLAP INBOARD	PSMAFI	SMA		NG	YES	YES	YES	NO	NO
SMA FLAP MIDDLE	PSMAFM	SMA		NG	YES	YES	YES	NO	NO
SMA FLAP OUTBOARD	PSMAFO	SMA		NG	YES	YES	YES	NO	NO
SMA AILERON INBOARD	PSMAAI	SMA		NG	YES	YES	YES	NO	NO
SMA AILERON OUTBOARD	PSMAAO	SMA		NG	YES	YES	YES	NO	NO

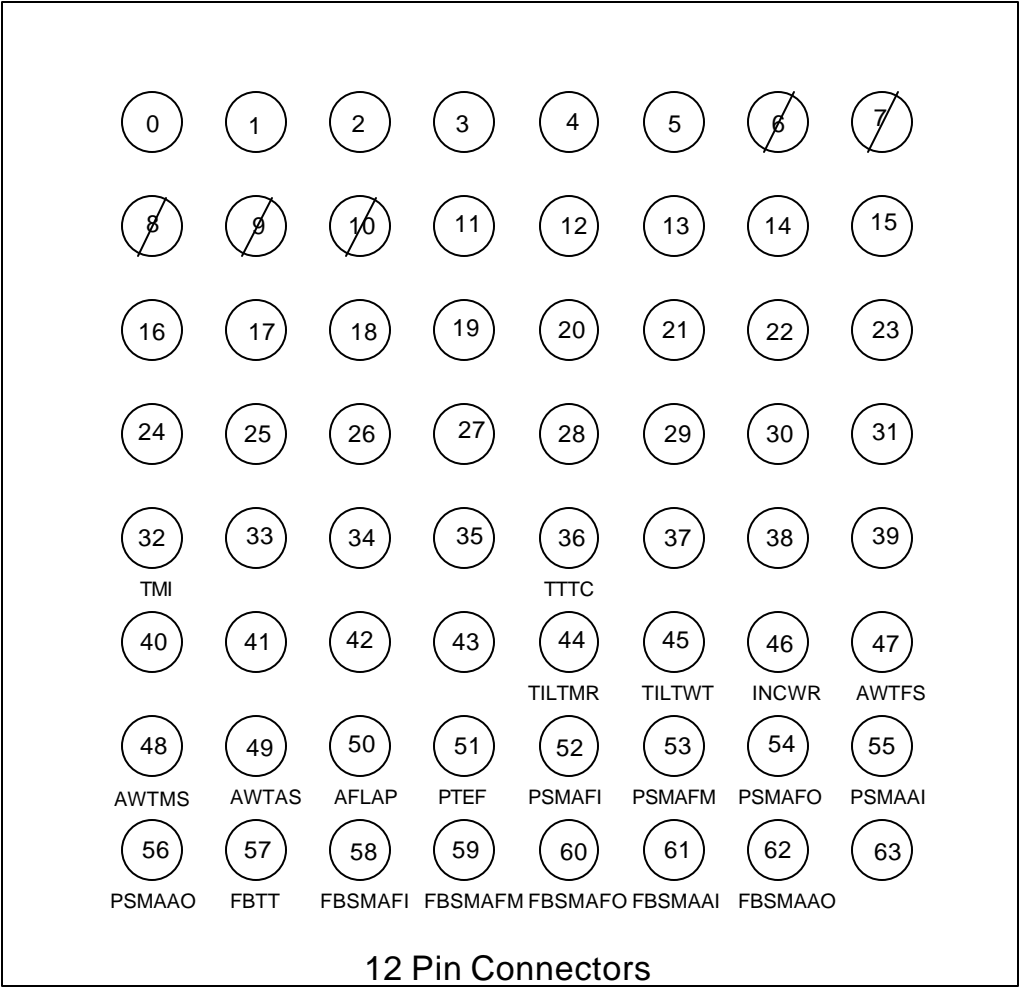
DESCRIPTION	CHAN NAME	APPLIES TO WHICH MODEL	RANGE EU	SIGNAL COND. RESPON.	MODCOMP CONDITIONED SIGNAL INPUT	MODCOMP REAL TIME MONITORING	PSB	STRIP CHART	B&K ANALYZER
CONTROLS (NO DATA INPUTS REQ'D)	(WIRE ID ONLY)				N/A	N/A	N/A	N/A	N/A
GLOBE MOTOR CONTROL- FLAP ROTATION	CNT1	CONV	+/- 5 V	NG	N/A	N/A	N/A	N/A	N/A
TORQUE TUBE - WING TWIST	CNT2	BOTH	+/- 5 V	NG	N/A	N/A	N/A	N/A	N/A
SMA TRAILING EDGE FLAP - INBOARD UPPER	CNT3	SMA	+/- 5 V	LM	N/A	N/A	N/A	N/A	N/A
SMA TRAILING EDGE FLAP - MIDDLE	CNT4	SMA	+/- 5 V	LM	N/A	N/A	N/A	N/A	N/A
SMA TRAILING EDGE FLAP - OUTBOARD	CNT5	SMA	+/- 5 V	LM	N/A	N/A	N/A	N/A	N/A
SMA AILERON - INBOARD	CNT6	SMA	+/- 5 V	LM	N/A	N/A	N/A	N/A	N/A
SMA AILERON - OUTBOARD	CNT7	SMA	+/- 5 V	LM	N/A	N/A	N/A	N/A	N/A
CONTROL FEEDBACK									
TORQUE TUBE - WING TWIST	FBTT	BOTH	+/- 20 V	NG	YES	YES	YES	NO	NO
SMA TRAILING EDGE FLAP - INBOARD UPPER	FBSMAFI	SMA	+/- 20 V	LM	YES	YES	YES	NO	NO
SMA TRAILING EDGE FLAP - MIDDLE	FBSMAFM	SMA	+/- 20 V	LM	YES	YES	YES	NO	NO
SMA TRAILING EDGE FLAP - OUTBOARD	FBSMAFO	SMA	+/- 20 V	LM	YES	YES	YES	NO	NO
SMA AILERON - INBOARD	FBSMAAI	SMA	+/- 20 V	LM	YES	YES	YES	NO	NO
SMA AILERON - OUTBOARD	FBSMAAO	SMA	+/- 20 V	LM	YES	YES	YES	NO	NO
OTHER									
REMOTE RCAL COMMAND		BOTH		NG					

NASA East Wall Platform - MODCOMP NEFF "A" Patch Panel



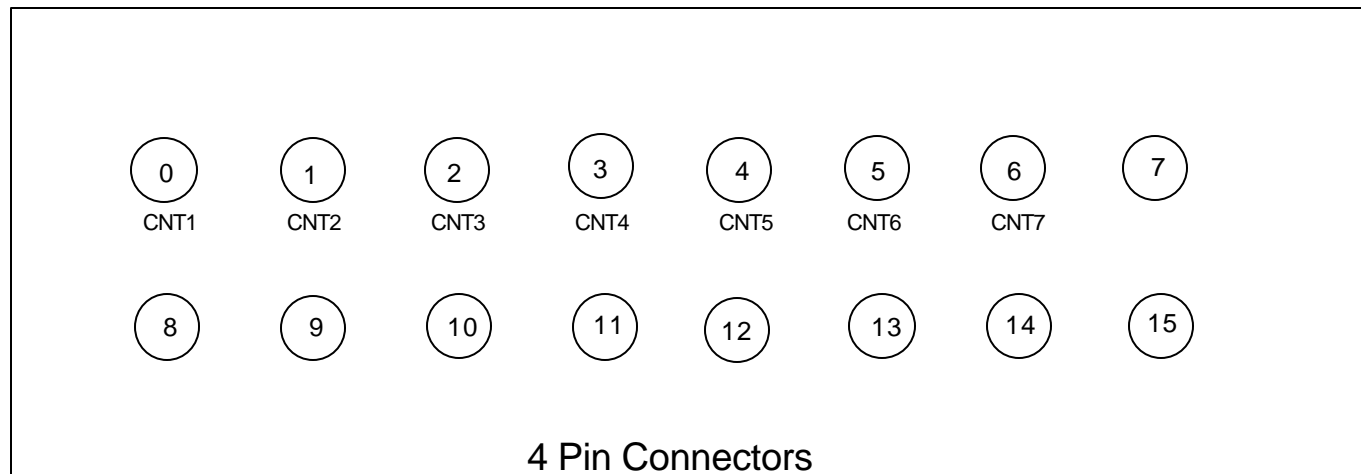
From Model to MODCOMP

NASA East Wall Platform - Control Room Patch Panel



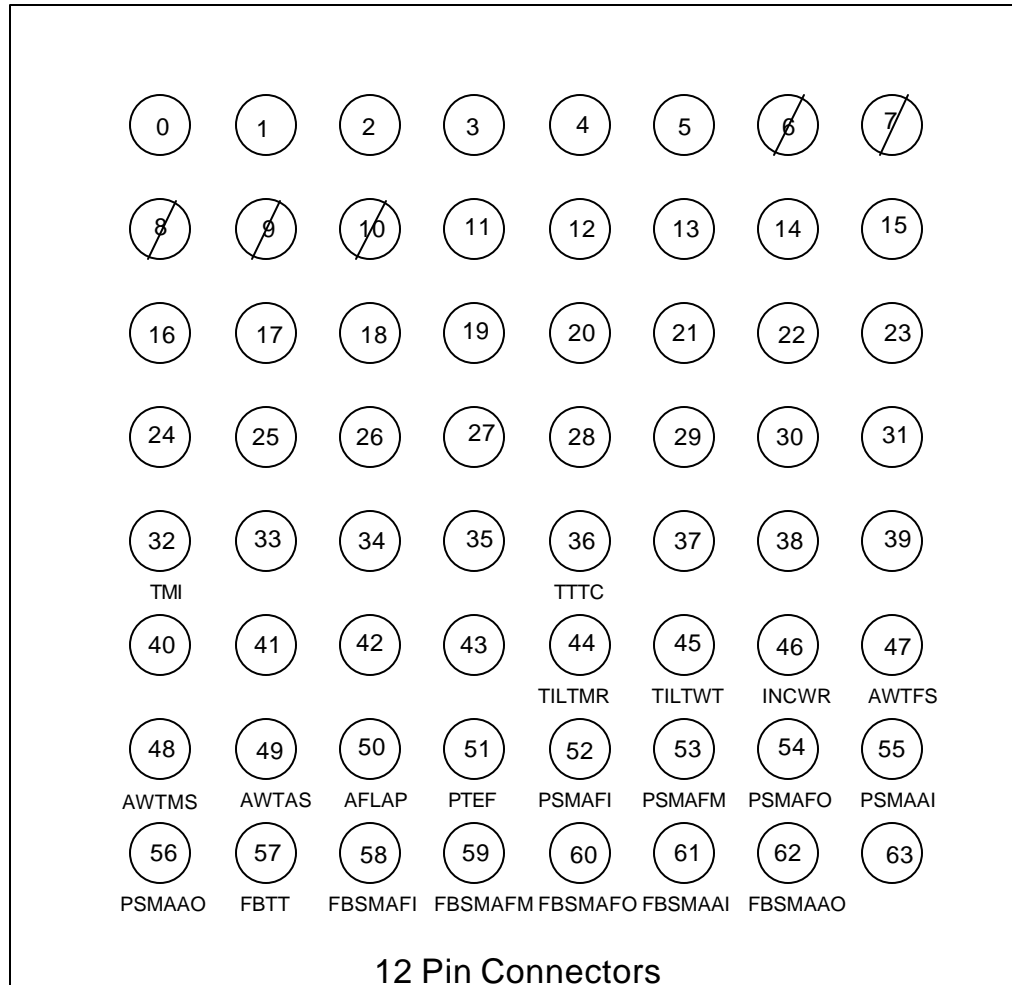
From Model to Control Room
(PSB and MODCOMP)

NASA East Wall Platform - Control Patch Panel



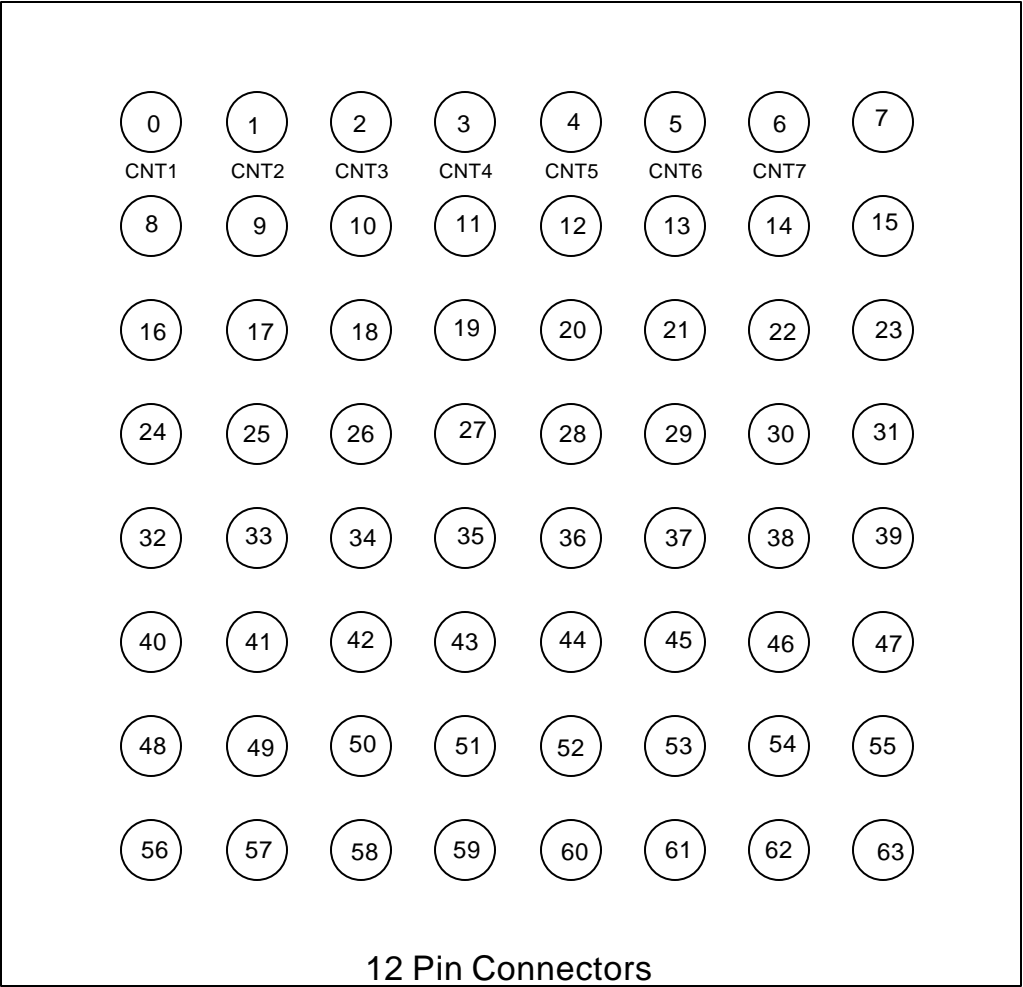
From Model to Control Room
(PSB and MODCOMP)

NASA Control Room - MODCOMP NEFF "A" Patch Panel



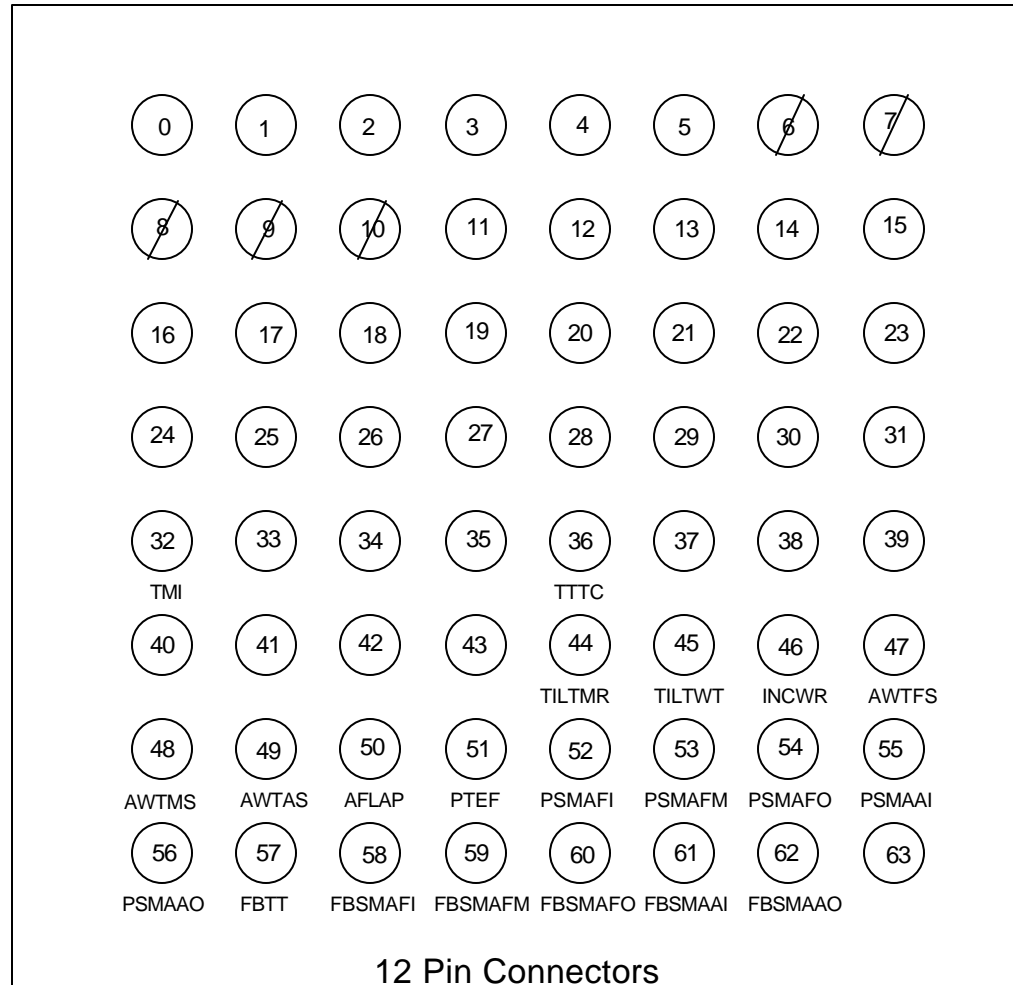
From East Wall Patch in Control Room to MODCOMP

NASA Control Room - MODCOMP NEFF “B” Patch Panel



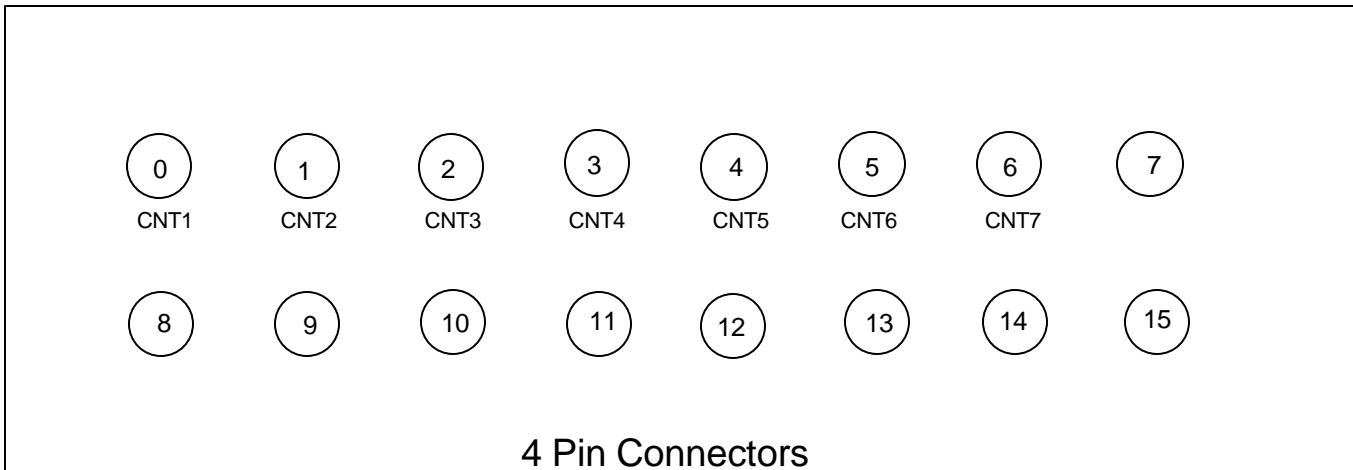
From Control Patch in Control Room to MODCOMP

NASA Control Room - Control Room Patch Panel - East Wall



Inside Control Room "East Wall Patch" to Both PSB and MODCOMP

NASA Control Room - Control Patch Panel



Inside Control Room "Control Patch" to Both PSB and MODCOMP

C13. PHASE 1 TEST 2

SMART WING MODEL

SURFACE STATIC PRESSURE LOCATIONS AND HOOK-UPS

MODULE NO. 1

RANGE ± 5 PSID

NO.	PORT NO	TAP NO.	DESCRIPTION	X/C	Q-D PORT	
1	1	VERIF.				
2	2	A 1	LEADING EDGE - INBOARD ROW			
3	3	A 2	UPPER SURFACE - INBOARD ROW			
4	4	A 4				
5	5	A 6				
6	6	A 8				
7	7	A 10				
8	8	A 12	▼			
9	9	B 1	LEADING EDGE - MID INBOARD ROW			
10	10	B 2	UPPER SURFACE - MID INBOARD ROW			
11	11	B 4				
12	12	B 6				
13	13	B 8				
14	14	B 10				
15	15	B 12	▼			
16	16	C 1	LEADING EDGE - MID OUTBOARD ROW			
17	17	C 2	UPPER SURFACE - MID OUTBOARD ROW			
18	18	C 4				
19	19	C 6				
20	20	C 8				
21	21	C 10				
22	22	C 12	▼			
23	23	D 1	LEADING EDGE - OUTBOARD ROW			
24	24	D 2	UPPER SURFACE - OUTBOARD ROW			
25	25	D 4				
26	26	D 6				
27	27	D 8				
28	28	D 10				
29	29	D 12	▼			
30	30					
31	31					
32	32	VERIF.				

MODULE NO. 2

RANGE ± 1 PSID

NO.	PORT NO	TAP NO.	DESCRIPTION	X/C	Q-D PORT	
33	1	VERIF.				
34	2	A14	UPPER SURFACE PRESSURES - INBOARD ROW			
35	3	A16				
36	4	A18				
37	5	A20				
38	6	A22				
39	7	A24				
40	8	A26				
41	9	A28				
42	10	A30	▼			
43	11	A32	TRAILING EDGE PRESSURE - INBOARD ROW			
44	12	A3	LOWER SURFACE PRESSURES - INBOARD ROW			
45	13	A5				
46	14	A7				
47	15	A9				
48	16	A11				
49	17	A13				
50	18	A17				
51	19	A19				
52	20	A21				
53	21	A23				
54	22	A25				
55	23	A27				
56	24	A29	▼			
57	25	B14	UPPER SURFACE PRESSURES - MID INBOARD ROW			
58	26	B16				
59	27	B18				
60	28	B20				
61	29	B22				
62	30	B30				
63	31	B26				
64	32	B28	▼			

MODULE NO. 3

RANGE ± 1 PSID

NO.	PORT NO	TAP NO.	DESCRIPTION	X/C	Q-D PORT	
65	1	VERIF.				
66	2	B24	UPPER SURFACE PRESSURE - MID INBOARD ROW			
67	3	B32	TRAILING EDGE PRESSURE - MID INBOARD ROW			
68	4	B3	LOWER SURFACE PRESSURES - MID INBOARD ROW			
69	5	B5				
70	6	B7				
71	7	B9				
72	8	B11				
73	9	B13				
74	10	B17				
75	11	B19				
76	12	B21				
77	13	B23				
78	14	B25				
79	15	B27				
80	16	B29	▼			
81	17	C 14	UPPER SURFACE PRESSURES - MID OUTBOARD ROW			
82	18	C 16				
83	19	C 18	* NO HOOKUP			
84	20	C 20				
85	21	C 22				
86	22	C 24				
87	23	C 26				
88	24	C 28				
89	25	C 30	▼			
90	26	C 32	TRAILING EDGE PRESSURE - MID OUTBOARD ROW			
91	27	C 3	LOWER SURFACE PRESSURES - MID OUTBOARD ROW			
92	28	C 5				
93	29	C 7				
94	30	C 9				
95	31	C 11				
96	32	C 13	▼			

MODULE NO. 4

RANGE ± 1 PSID

NO.	PORT NO	TAP NO.	DESCRIPTION	X/C	Q-D PORT
97	1	VERIF.			
98	2	C17	LOWER SURFACE PRESSURES - MID OUTBOARD ROW		
99	3	C19	* NO HOOKUP		
100	4	C21			
101	5	C23			
102	6	C25			
103	7	C27			
104	8	C29	▼		
105	9	D14	UPPER SURFACE PRESSURES - OUTBOARD ROW		
106	10	D16			
107	11	D18	* NO HOOKUP		
108	12	D20			
109	13	D22			
110	14	D24			
111	15	D26			
112	16	D28			
113	17	D30	▼		
114	18	D32	TRAILING EDGE PRESSURE - OUTBOARD ROW		
115	19	D3	LOWER SURFACE PRESSURES - OUTBOARD ROW		
116	20	D5			
117	21	D7			
118	22	D9			
119	23	D11			
120	24	D13			
121	25	D17			
122	26	D19	* NO HOOKUP		
123	27	D21			
124	28	D23			
125	29	D25			
126	30	D27			
127	31	D29	▼		
128	32	VERIF.			

MODULE NO. 5

RANGE ± 1 PSID

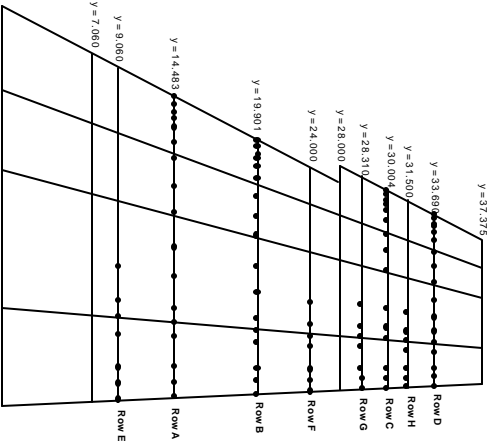
NO.	PORT NO	TAP NO.	DESCRIPTION	X/C	Q-D PORT	
129	1	VERIF.				
130	2	E20	UPPER SURFACE PRESSURES ROW E			
131	3	E22				
132	4	E24				
133	5	E26				
134	6	E28				
135	7	E30				
136	8	E32	▼			
137	9	E21	LOWER SURFACE PRESSURES ROW E			
138	10	E23				
139	11	E25				
140	12	E27				
141	13	E29	▼			
142	14	F20	UPPER SURFACE PRESSURES ROW F			
143	15	F22				
144	16	F24				
145	17	F26				
146	18	F28				
147	19	F30				
148	20	F32	▼			
149	21	F21	LOWER SURFACE PRESSURES ROW F			
150	22	F23				
151	23	F25				
152	24	F27				
153	25	F29	▼			
154	26	G20	UPPER SURFACE PRESSURES ROW G			
155	27	G22				
156	28	G24				
157	29	G26				
158	30	G28				
159	31	G30	▼			
160	32	VERIF.				

MODULE NO. 6

RANGE ± 1 PSID

NO.	PORT NO	TAP NO	DESCRIPTION	X/C	Q-D PORT
129	1	VERIF.			
130	2	G32	UPPER SURFACE PRESSURES ROW G		
131	3	G21	LOWER SURFACE PRESSURES ROW G		
132	4	G23			
133	5	G25			
134	6	G27			
135	7	G29	▼		
136	8	H20	UPPER SURFACE PRESSURES ROW H		
137	9	H22			
138	10	H24			
139	11	H26			
140	12	H28			
141	13	H30			
142	14	H32	▼		
143	15	H21	LOWER SURFACE PRESSURES ROW H		
144	16	H23			
145	17	H25			
146	18	H27			
147	19	H29	▼		
148	20	A15	30% CHORD LOWER SURFACE		
149	21	B15			
150	22	C15			
151	23	D15	▼		
152	24				
153	25				
154	26				
155	27				
156	28				
157	29				
158	30				
159	31				
160	32	VERIF.			

Y - STATION		9.060		13.483		19.901		24.000				28.000		30.004		31.500		33.690	
FLAP		MID ROW - ROW E		INBD ROW - ROW A		OUTBD ROW - ROW B		MID ROW - ROW F		AILERON		MID ROW - ROW G		OUTBD ROW - ROW C		MID ROW - ROW H		OUTBD ROW - ROW D	
% CHORD	TAP NO.	X	Z	X	Z	X	Z	X	Z	% CHORD	TAP NO.	X	Z	X	Z	X	Z	X	Z
0	1			7.603	0.000	11.217	0.000			0	1			15.46	0			17.52	0
2	2.3			8.108	0.198	11.644	0.161			2	2.3			15.79	0.106			17.81	0.082
5	4.5			8.966	0.327	12.284	0.266			5	4.5			16.29	0.176			18.24	0.139
7	6.7			9.372	0.391	12.711	0.318			7	6.7			16.62	0.211			18.53	0.167
10	8.9			10.130	0.466	13.351	0.379			10	8.9			17.12	0.251			18.96	0.199
15	10.11			11.393	0.560	14.418	0.455			15	10.11			17.95	0.302			19.68	0.239
20	12.13			12.656	0.631	15.999	0.513			20	12.13			19.15	0.339			20.70	0.268
30	14.15			15.183	0.724	17.619	0.589			30	14.15			20.44	0.384			21.83	0.304
40	16.17			17.358	0.762	18.200	0.624			40	16.17			22.10	0.396			23.20	0.313
50	18.19			20.236	0.744	21.887	0.606			50	18.19			23.76	0.394			24.70	0.312
60	20.21	21.893	0.733	22.763	0.662	24.020	0.544	24.825	0.493	60	20.21	25.03	0.429	25.42	0.363	25.72	0.373	26.14	0.289
70	22.23	24.691	0.598	25.289	0.531	26.154	0.432	26.708	0.396	70	22.23	26.82	0.344	27.00	0.299	27.29	0.299	27.30	0.239
75	24.25	26.090	0.491	26.553	0.443	27.221	0.361	27.650	0.330	75	24.25	27.71	0.287	27.75	0.252	28.07	0.250	28.29	0.202
80	26.27	27.489	0.393	27.816	0.355	28.289	0.290	28.592	0.265	80	26.27	28.60	0.230	28.74	0.202	28.86	0.200	29.01	0.162
86	28.29	29.168	0.199	29.332	0.180	29.570	0.147	29.722	0.134	90	28.29	30.38	0.117	30.40	0.103	30.43	0.101	30.45	0.083
92	30"	30.847	0.102	30.849	0.092	30.851	0.076	30.852	0.069	95	30"	31.27	0.060	31.23	0.054	31.21	0.052	31.17	0.044
100	32	33.086	0.000	32.871	0.000	32.559	0.000	32.359	0.000	100	32	32.17	0.000	32.06	0	32.00	0.000	31.88	0
* UPPER ONLY		Local Chord		Local Chord		Local Chord		Local Chord		Local Chord		Local Chord		Local Chord		Local Chord		Local Chord	
EVEN NUMBERS ARE UPPER SURFACE		27.981		25.274		21.346		18.837		16.389		15.163		14.247		12.907			



SMART WING DATA REDUCTION PROBLEM STATEMENT

PROGRAM: SMART WING TEST NO. _____ ENGINEER: SCHERER DATE: 3/16/96 PAGE B188

NO.	EQUATION	TERM	UNIT	SOURCE	DISPOSITION
1.	<u>TUNNEL PARAMETERS REQUIRED</u> PTO TUNNEL TOTAL PRESSURE PO TUNNEL STATIC PRESSURE TTO TUNNEL TOTAL TEMPERATURE RN TUNNEL REYNOLD'S NUMBER PER FOOT M MACH NUMBER QO TUNNEL DYNAMIC PRESSURE	PTO PO TTO QO MACH RN	PSIA PSIA DEGR PSIA --- ---	EQ 1 EQ 1 EQ 1 EQ 1 EQ 1 EQ 1	TAB TAB TAB TAB TAB TAB
2.	<u>MODEL POSITION</u> <u>ALPHA</u> MODEL ANGLE OF ATTACK CALCULATED AS FOLLOWS: AOA - ALPHA CALCULATED FROM MODEL SUPPORT SYSTEM $ALP1 = A1 * SIN (A2 * INCWR)$ FROM SCHEAVITZ INCLINOMETER $ALP2 = AM1 + AM2 * TILTMR$ FROM MID WING TILT SENSOR $ALP3 = AO1 + AO2 * TILTTWT$ FROM OUTBOARD TILT SENSOR <u>WING TWIST CALCULATIONS</u> $DAOAM = ALP2 - ALP1$ $DAOAO = ALP3 - ALP1$	AOA ALP1 ALP2 ALP3 INCWR TILTMR TILTTWT A1 A2 AI1 AI2 AM1 AM2 AO1 AO2 IDAOAM DAOAO	DEG DEG DEG DEG VOLTS VOLTS VOLTS DEG DEG/V DEG DEG/V DEG DEG/V DEG DEG/V DEG DEG	MC OUTPUT EQ 2 EQ 2 EQ 2 MC OUTPUT MC OUTPUT MC OUTPUT CONST CONST CONST CONST CONST CONST CONST EQ 2 EQ 2	TAB TAB TAB TAB TAB TAB TAB CONST CONST CONST CONST CONST CONST CONST CONST CONST TAB TAB

C14. PHASE 1 TEST 2 SMART WING DATA REDUCTION PROBLEM STATEMENT

SMART WING DATA REDUCTION PROBLEM STATEMENT

PROGRAM: SMART WING TEST NO. _____ ENGINEER: SCHERER DATE: 3/16/96 PAGE B189

NO.	EQUATION	TERM	UNIT	SOURCE	DISPOSITION
3.	<p>FORCE AND MOMENT COEFFICIENT DATA (MAIN BALANCE)</p> <p>BALANCE INPUTS (CORRECTED FOR WEIGHT TARE AND ABOUT THE BALANCE CENTER):</p> <p>FN NORMAL FORCE</p> <p>FA AXIAL FORCE</p> <p>MM PITCHING MOMENT</p> <p>ML ROLLING MOMENT</p> <p>YM YAWING MOMENT</p> <p><u>BODY AXIS COEFFICIENTS CORRECTED ABOUT THE MODEL MOMENT REFERENCE CENTER</u></p> $CN = \frac{FN}{Q * S} \quad CA = \frac{FA}{Q * S} \quad CM = \frac{PM}{Q * S * CBAR} \quad Cn = \frac{YM - FA * l_{mrc}}{Q * S * b}$ $Cl = \frac{RM + FN * l_{mrc}}{Q * S * b}$ <p><u>COEFFICIENTS IN STABILITY AXIS</u></p> <p>$CL = CN * \cos(ALP1) - CA * \sin(ALP1)$</p> <p>$CD = CN * \sin(ALP1) + CA * \cos(ALP1)$</p> <p>$Cls = Cl * \cos(ALP1) + CN * \sin(ALP1)$</p> <p>$Cns = Cn * \cos(ALP1) - Cl * \sin(ALP1)$</p> <p><u>CALCULATE</u></p> <p>CL / CD</p>	<p>CN</p> <p>CA</p> <p>CM</p> <p>Cn</p> <p>Cl</p> <p>CL</p> <p>CD</p> <p>Cls</p> <p>Cns</p> <p>Q</p> <p>S</p> <p>CBAR</p> <p>b</p> <p>ALP1</p> <p>l_{mrc}</p> <p>FN</p> <p>FA</p> <p>MM</p> <p>ML</p> <p>YM</p>	<p>---</p> <p>---</p> <p>---</p> <p>---</p> <p>---</p> <p>---</p> <p>---</p> <p>---</p> <p>---</p> <p>psi</p> <p>sqin</p> <p>in</p> <p>in</p> <p>deg</p> <p>in</p> <p>lbs</p> <p>lbs</p> <p>in-lb</p> <p>in-lb</p> <p>in-lb</p>	<p>Eq 3</p> <p>Eq 3</p> <p>Eq 3</p> <p>Eq 3</p> <p>Eq 3</p> <p>Eq 3</p> <p>Eq 3</p> <p>Eq 3</p> <p>Eq 1</p> <p>CONST</p> <p>CONST</p> <p>CONST</p> <p>Eq 2</p> <p>CONST</p> <p>MC-OUTPUT</p> <p>MC-OUTPUT</p> <p>MC-OUTPUT</p> <p>MC-OUTPUT</p> <p>MC-OUTPUT</p>	<p>TAB</p> <p>TAB</p> <p>TAB</p> <p>TAB</p> <p>TAB</p> <p>TAB</p> <p>TAB</p> <p>TAB</p> <p>TAB</p>

C14. PHASE 1 TEST 2 SMART WING DATA REDUCTION PROBLEM STATEMENT

SMART WING DATA REDUCTION PROBLEM STATEMENT

PROGRAM: SMART WING TEST NO. _____ ENGINEER: SCHERER DATE: 3/16/96 PAGE B190

NO.	EQUATION	TERM	UNIT	SOURCE	DISPOSITION
5.	STRAIN GAGE OUTPUTS - STRESSES, STRAINS, AND TORQUES	SLEIA	VOLTS	MC-OUTPUT	
		SLEIB	VOLTS	MC-OUTPUT	
		SLEIC	VOLTS	MC-OUTPUT	
		SLEOA	VOLTS	MC-OUTPUT	
		SLEOB	VOLTS	MC-OUTPUT	
		SLEOC	VOLTS	MC-OUTPUT	
		SMIA	VOLTS	MC-OUTPUT	
		SMIB	VOLTS	MC-OUTPUT	
		SMIC	VOLTS	MC-OUTPUT	
		SMOA	VOLTS	MC-OUTPUT	
		SMOB	VOLTS	MC-OUTPUT	
		SMOC	VOLTS	MC-OUTPUT	
		SAIA	VOLTS	MC-OUTPUT	
		SAIB	VOLTS	MC-OUTPUT	
		SAIC	VOLTS	MC-OUTPUT	
		SAOA	VOLTS	MC-OUTPUT	
		SAOB	VOLTS	MC-OUTPUT	
		SAOC	VOLTS	MC-OUTPUT	
		e_i	m-in/in	EQ 5	TAB
		s_i	psi	EQ 5	TAB
		E	psi/m-in/in	CONST	
		V_{o_i}	VOLTS	MC-OUTPUT	
		V	VOLTS	CONST	
		GF_i	in/ m-in	CONST	
	<u>CALCULATE INDIVIDUAL STRAINS AND STRESSES FROM GAGES FROM ALL ROSETTES</u>				
	If i = 1, refer to gage SLEIA	If i = 10, refer to gage SMOA			
	2, refer to gage SLEIB	11, refer to gage SMOB			
	3, refer to gage SLEIC	12, refer to gage SMOC			
	4, refer to gage SLEOA	13, refer to gage SAIA			
	5, refer to gage SLEOB	14, refer to gage SAIB			
	6, refer to gage SLEOC	15, refer to gage SAIC			
	7, refer to gage SMIA	16, refer to gage SAOA			
	8, refer to gage SMIB	17, refer to gage SAOB			
	9, refer to gage SMIC	18, refer to gage SAOC			
	$\epsilon_i = (4 * V_{o_i}) / (GF_i * V)$	for i = 1- 18			
	$\sigma_i = E * \epsilon_i$	for i = 1- 18			
	where V = Excitation Voltage				
	V_{o_i} = Output Voltage for each gage (corresponds to above nomenclature)				
	GF_i = Gage Factor for each gage				

C14. PHASE 1 TEST 2 SMART WING DATA REDUCTION PROBLEM STATEMENT

SMART WING DATA REDUCTION PROBLEM STATEMENT

PROGRAM: SMART WING TEST NO. _____ ENGINEER: SCHERER DATE: 3/16/96 PAGE B191

NO.	EQUATION	TERM	UNIT	SOURCE	DISPOSITION
6.	<p><u>CALCULATE PRINCIPAL STRESSES AND STRAINS FOR EACH ROSETTE</u></p> <p><u>ROSETTE SLEI (LEADING EDGE INBOARD)</u></p> $\epsilon_{nSLEI} = 1/2 \left[\epsilon_1 + \epsilon_3 \pm \sqrt{(\epsilon_1 - \epsilon_3)^2 + (2 * \epsilon_2 - \epsilon_1 - \epsilon_3)^2} \right]$ $\sigma_{SLEI} = \frac{E}{2} \left[\frac{\epsilon_1 + \epsilon_3}{1 - \nu} \pm \frac{1}{1 + \nu} * \sqrt{(\epsilon_1 - \epsilon_3)^2 + (2 * \epsilon_2 - \epsilon_1 - \epsilon_3)^2} \right]$ $\theta_{SLEI} = \frac{1}{2} * \text{TAN}^{-1} \frac{2 * \epsilon_2 - \epsilon_1 - \epsilon_3}{\epsilon_1 - \epsilon_3}$ <p><u>ROSETTE SLEO (LEADING EDGE OUTBOARD)</u></p> $\epsilon_{SLEO} = 1/2 \left[\epsilon_4 + \epsilon_6 \pm \sqrt{(\epsilon_4 - \epsilon_6)^2 + (2 * \epsilon_5 - \epsilon_4 - \epsilon_6)^2} \right]$ $\sigma_{SLEO} = \frac{E}{2} \left[\frac{\epsilon_4 + \epsilon_6}{1 - \nu} \pm \frac{1}{1 + \nu} * \sqrt{(\epsilon_4 - \epsilon_6)^2 + (2 * \epsilon_5 - \epsilon_4 - \epsilon_6)^2} \right]$ $\theta_{SLEO} = \frac{1}{2} * \text{TAN}^{-1} \frac{2 * \epsilon_5 - \epsilon_4 - \epsilon_6}{\epsilon_4 - \epsilon_6}$	<p>eSLE</p> <p>sSLEI</p> <p>qSLEI</p> <p>eSLEO</p> <p>sSLEO</p> <p>qSLEO</p> <p>E</p> <p>n</p> <p>e_i</p>	<p>m-in/in</p> <p>psi</p> <p>deg</p> <p>m-in/in</p> <p>psi</p> <p>deg</p> <p>psi/m-in/in</p> <p>---</p> <p>m-in/in</p>	<p>Eq 6</p> <p>Eq 6</p> <p>Eq 6</p> <p>Eq 6</p> <p>Eq 6</p> <p>Eq 6</p> <p>CONST</p> <p>CONST</p> <p>Eq 5</p>	<p>TAB</p> <p>TAB</p> <p>TAB</p> <p>TAB</p> <p>TAB</p> <p>TAB</p>

SMART WING DATA REDUCTION PROBLEM STATEMENT

PROGRAM: SMART WING TEST NO. _____ ENGINEER: SCHERER DATE: 3/16/96 PAGE B192

NO.	EQUATION	TERM	UNIT	SOURCE	DISPOSITION
7.	<p><u>CALCULATE PRINCIPAL STRESSES AND STRAINS FOR EACH ROSETTE</u></p> <p><u>ROSETTE SMI</u></p> $\epsilon_{SMI} = 1/2 \left[\epsilon_7 + \epsilon_9 \pm \sqrt{(\epsilon_7 - \epsilon_9)^2 + (2 * \epsilon_8 - \epsilon_7 - \epsilon_9)^2} \right]$ $\sigma_{SMI} = \frac{E}{2} \left[\frac{\epsilon_7 + \epsilon_9}{1 - \nu} \pm \frac{1}{1 + \nu} * \sqrt{(\epsilon_7 - \epsilon_9)^2 + (2 * \epsilon_8 - \epsilon_7 - \epsilon_9)^2} \right]$ $\theta_{SMI} = \frac{1}{2} * \text{TAN}^{-1} \frac{2 * \epsilon_8 - \epsilon_7 - \epsilon_9}{\epsilon_7 - \epsilon_9}$ <p><u>ROSETTE SMO</u></p> $\epsilon_{SMO} = 1/2 \left[\epsilon_{10} + \epsilon_{13} \pm \sqrt{(\epsilon_{10} - \epsilon_{13})^2 + (2 * \epsilon_{12} - \epsilon_{10} - \epsilon_{13})^2} \right]$ $\sigma_{SMO} = \frac{E}{2} \left[\frac{\epsilon_{10} + \epsilon_{13}}{1 - \nu} \pm \frac{1}{1 + \nu} * \sqrt{(\epsilon_{10} - \epsilon_{13})^2 + (2 * \epsilon_{12} - \epsilon_{10} - \epsilon_{13})^2} \right]$ $\theta_{SMO} = \frac{1}{2} * \text{TAN}^{-1} \frac{2 * \epsilon_{12} - \epsilon_{10} - \epsilon_{13}}{\epsilon_{10} - \epsilon_{13}}$	<p>eSMI</p> <p>sSMI</p> <p>qSMI</p> <p>eSMO</p> <p>sSMO</p> <p>qSMO</p> <p>E</p> <p>n</p> <p>e_i</p>	<p>m-in/in</p> <p>psi</p> <p>deg</p> <p>m-in/in</p> <p>psi</p> <p>deg</p> <p>psi/m-in/in</p> <p>---</p> <p>m-in/in</p>	<p>Eq 7</p> <p>Eq 7</p> <p>Eq 7</p> <p>Eq 7</p> <p>Eq 7</p> <p>Eq 7</p> <p>CONST</p> <p>CONST</p> <p>Eq 5</p>	<p>TAB</p> <p>TAB</p> <p>TAB</p> <p>TAB</p> <p>TAB</p> <p>TAB</p>

SMART WING DATA REDUCTION PROBLEM STATEMENT

PROGRAM: SMART WING TEST NO. _____ ENGINEER: SCHERER DATE: 3/16/96 PAGE B193

NO.	EQUATION	TERM	UNIT	SOURCE	DISPOSITION
8.	<p><u>CALCULATE PRINCIPAL STRESSES AND STRAINS FOR EACH ROSETTE</u></p> <p><u>ROSETTE SAI</u></p> $\epsilon_{SAI} = 1/2 \left[\epsilon_{13} + \epsilon_{15} \pm \sqrt{(\epsilon_{13} - \epsilon_{15})^2 + (2 * \epsilon_{14} - \epsilon_{13} - \epsilon_{15})^2} \right]$ $\sigma_{SAI} = \frac{E}{2} \left[\frac{\epsilon_{13} + \epsilon_{15}}{1 - \nu} \pm \frac{1}{1 + \nu} * \sqrt{(\epsilon_{13} - \epsilon_{15})^2 + (2 * \epsilon_{14} - \epsilon_{13} - \epsilon_{15})^2} \right]$ $\theta_{SAI} = \frac{1}{2} * \text{TAN}^{-1} \frac{2 * \epsilon_{14} - \epsilon_{13} - \epsilon_{15}}{\epsilon_{13} - \epsilon_{15}}$ <p><u>ROSETTE SAO</u></p> $\epsilon_{SAO} = 1/2 \left[\epsilon_{16} + \epsilon_{18} \pm \sqrt{(\epsilon_{16} - \epsilon_{18})^2 + (2 * \epsilon_{17} - \epsilon_{16} - \epsilon_{18})^2} \right]$ $\sigma_{SAO} = \frac{E}{2} \left[\frac{\epsilon_{16} + \epsilon_{18}}{1 - \nu} \pm \frac{1}{1 + \nu} * \sqrt{(\epsilon_{16} - \epsilon_{18})^2 + (2 * \epsilon_{17} - \epsilon_{16} - \epsilon_{18})^2} \right]$ $\theta_{SAO} = \frac{1}{2} * \text{TAN}^{-1} \frac{2 * \epsilon_{17} - \epsilon_{16} - \epsilon_{18}}{\epsilon_{16} - \epsilon_{18}}$	eSAI SSAI QSAI eSAO SSAO QSAO E n e _i	m-in/in psi deg m-in/in psi deg psi/m-in/in --- m-in/in	Eq 8 Eq 8 Eq 8 Eq 8 Eq 8 Eq 8 CONST CONST Eq 5	TAB TAB TAB TAB TAB TAB

SMART WING DATA REDUCTION PROBLEM STATEMENT

PROGRAM: SMART WING TEST NO. _____ ENGINEER: SCHERER DATE: 3/16/96 PAGE B194

NO.	EQUATION	TERM	UNIT	SOURCE	DISPOSITION
-----	----------	------	------	--------	-------------

9.	PRESSURE COEFFICIENT DATA FROM MODEL SURFACE PRESSURES	CPA_i	---	Eq 9	TAB
		CPB_i	---	Eq 9	TAB
	<u>MODEL SURFACE STATIC PRESSURES</u>	CPC_i	---	Eq 9	TAB
		CPD_i	---	Eq 9	TAB
	INPUTS: Pressures A_{1-28} , B_{1-28} , C_{1-28} , & D_{1-28}	P_o	psi	Eq 1	
		Q	psi	Eq 1	
	$CPA_i = (A_i - P_o) / Q$ for $i = 1-28$	A_i	psi	MC-OUTPUT	
		B_i	psi	MC-OUTPUT	
	$CPB_i = (B_i - P_o) / Q$ for $i = 1-28$	C_i	psi	MC-OUTPUT	
		D_i	psi	MC-OUTPUT	
	$CPC_i = (C_i - P_o) / Q$ for $i = 1-28$	AOP_i	psi	CONST	
	$CPD_i = (D_i - P_o) / Q$ for $i = 1-28$	$AOP2_i$	psi/volt	CONST	

C14. PHASE 1 TEST 2 SMART WING DATA REDUCTION PROBLEM STATEMENT

SMART WING DATA REDUCTION PROBLEM STATEMENT

PROGRAM: SMART WING TEST NO. _____ ENGINEER: SCHERER DATE: 3/16/96 PAGE B195

NO.	EQUATION	TERM	UNIT	SOURCE	DISPOSITION
10.	CONTROL SURFACE POSITIONS	PTEF	DEG	Eq 10	TAB
		PSMAFI	DEG	Eq 10	TAB
	<u>FLAP POTENTIOMETER (CONVENTIONAL WING ONLY)</u>	PSMAFM	DEG	Eq 10	TAB
		PSMAFO	DEG	Eq 10	TAB
	PTEF = C0 + C1 * POSF	PSMAAI	DEG	Eq 10	TAB
		PSMAAO	DEG	Eq 10	TAB
	<u>POTENTIOMETER (SMA WING ONLY)</u>	POSF	VOLTS	MC-OUTPUT	
		VPOTFI	VOLTS	MC-OUTPUT	
	PSMAFI = D0 + D1 * VPOTFI	VPOTFM	VOLTS	MC-OUTPUT	
		VPOTFO	VOLTS	MC-OUTPUT	
	PSMAFM = E0 + E1 * VPOTFM	VPOTAI	VOLTS	MC-OUTPUT	
		VPOTAO	VOLTS	MC-OUTPUT	
	PSMAFO = F0 + F1 * VPOTFO	C0	DEG	CONST	
		C1	DEG/V	CONST	
	PSMAAI = G0 + G1 * VPOTAI	D0	DEG	CONST	
		D1	DEG/V	CONST	
	PSMAAO = H0 + H1 * VPOTAO	E0	DEG	CONST	
		E1	DEG/V	CONST	
		F0	DEG	CONST	
		F1	DEG/V	CONST	
		G0	DEG	CONST	
		G1	DEG/V	CONST	
		H0	DEG	CONST	
		H1	DEG/V	CONST	

C14. PHASE 1 TEST 2 SMART WING DATA REDUCTION PROBLEM STATEMENT

SMART WING DATA REDUCTION PROBLEM STATEMENT

PROGRAM: SMART WING **TEST NO.** **ENGINEER:** SCHERER **DATE:** 3/16/96 **PAGE** B196

NO.	EQUATION	TERM	UNIT	SOURCE	DISPOSITION
-----	----------	------	------	--------	-------------

IV-C-196

VOLUME IV

**STRESS REPORT
DARPA / AFRL / NORTHROP GRUMMAN
SMART WING PHASE 1 PROGRAM
NASA LaRC 16 FT TRANSONIC DYNAMIC TUNNEL
22 JUNE 1998 - 17 JULY 1998**

**PREPARED BY: K. APPA
 C. A. MARTIN
 J. BARTLEY - CHO
APPROVED BY: J. N. KUDVA**

**Preliminary Release: 17 December 1997
Revised: 16 February 1998**

D1. INTRODUCTION AND BACKGROUND

In the first wind tunnel test on the DARPA / AFRL “Smart Materials and Structures - Smart Wing Phase 1” program (F33615-95-C-3202), two 16% scale models of the F/A-18 E/F starboard wing were tested. The two models were identical in internal structure and outer mold line. Their differences came in the trailing edge control surface. The conventional model had hinged flap and aileron (flap being actuated by a globe motor, and fixed aileron using a bracket), while the smart model had smoothly contouring trailing edges that contained shape memory alloy (SMA) wire. Both models were fitted with two, SMA torque tubes along the center spar (at approximately 0.4c). The tests were very successful, with 10% improvement in lift due to the contoured control surfaces and 8% improvement in roll moment due to increased spanwise wing twist.

In the second wind tunnel test on Smart Wing Phase 1 program, these two models will once again be tested. The conventional model will be tested to provide a baseline against which the smart wing is compared (it is necessary to test the conventional model again because the balance to be used during the second test, TDT - 05S, will be different than the balance used the first entry, and a common reference is required). The smart model contains some differences. It has second generation SMA flap and aileron with improved fatigue, deflection repeatability, and deflected shape control. The smart model will also now have only one SMA torque tube that runs the entire span, and provides up to 3000 in-lbs of torque, which results in approximately 3 degrees of spanwise twist.

In this report a stress analysis of the load bearing structures is presented, along with the analyses of attachment of the model to the balance. Also included in Section D9 is a summary of the flutter and dynamic analysis, with model analytical natural frequencies and damping vs. Q charts.

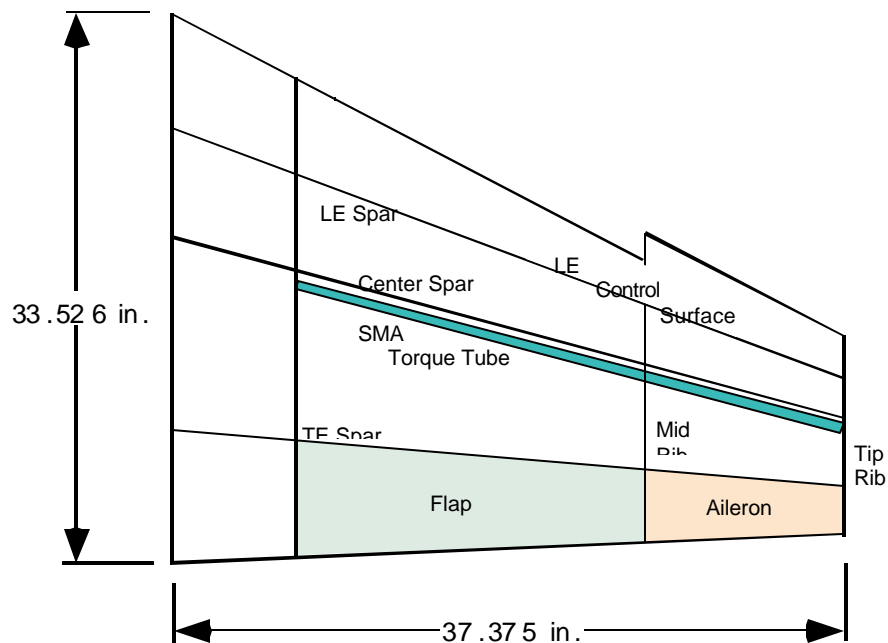


Figure D1. Basic Wind Tunnel Model Planform

D1.1 Summary of Margins of Safety

	Material	Load Type	Margin of Safety	Page Number
Balance Fastener	CRES per ASTM 5737	Shear due to lift	38.3	10
Balance Fastener	CRES per ASTM 5737	Shear due to Rolling	120	11
Balance Fastener	CRES per ASTM 5737	Shear due to Pitching	156	12
Combined Loads on Balance Attachment	CRES per ASTM 5737	Shear	18.9	12
LE Inboard Attachment Fastener	CRES per ASTM 5737	Shear	26.2	13
LE Inboard Attachment	7075 Aluminum	Bearing	21.8	13
LE Outboard Attachment Fastener	CRES per ASTM 5737	Shear	33.5	14
LE Outboard Attachment	7075 Aluminum	Bearing	27.8	14
TE Inboard - Outboard Hinge (Conv. Wing)	CRES Rod	Shear	86.3	16
TE Inboard - Inboard Hinge (Conv. Wing)	CRES Rod	Shear	154.2	16
TE Inboard (Smart Wing) Fastener	CRES per ASTM 5737	Shear	14.8	17
TE Inboard (Smart Wing) Attachment	7075 Aluminum	Bearing	12.3	17

Figure D2 Summary of Margins of Safety

TE Outboard (Smart Wing) Fastener	CRES per ASTM 5737	Shear	30.6	21
TE Outboard (Smart Wing) Attachment	7075 Aluminum	Bearing	22.5	21
TE Outboard (Conv. Wing) Screw	CRES per ASTM 5737	Shear	5.56	22
TE Outboard (Conv. Wing) Pin	CRES per ASTM 5737	Shear	5.04	22
TE Combined Loading	CRES per ASTM 5737	Shear	27.9	23
SMA Torque Tube Fastener	CRES per ASTM 5737	Shear	6.31	23
SMA Torque Tube Fastener Attachment	CRES per ASTM 5737	Bearing	20.4	24
SMA Torque Tube Attachment	17-4 PH	Bearing	20.1	24
Tip Rib - Torque Tube (Leading Edge) Pin	4340	Shear	6.27	34
Tip Rib - Torque Tube (Leading Edge) Screw	4340	Shear	6.87	35
Tip Rib - Torque Tube (Leading Edge) Pin	4340	Bearing	7.10	35
Tip Rib - Torque Tube (Leading Edge) Screw	4340	Bearing	10.4	35

Figure D2. Summary of Margins of Safety (continued)

Tip Rib - Torque Tube (Trailing Edge) Pin	4340	Shear	7.20	35
Tip Rib - Torque Tube (Trailing Edge) Screw	4340	Shear	7.63	35
Tip Rib - Torque Tube (Trailing Edge) Pin	4340	Bearing	8.10	35
Tip Rib - Torque Tube (Trailing Edge) Screw	4340	Bearing	13.20	36
LE Spar to Root Rib	7075 Aluminum	Shear due to Lift	96	37
LE Spar to Root Rib	7075 Aluminum	Shear due to Pitching Moment	17.7	37
Combined Loading on LE Spar	7075 Aluminum	Shear	7.91	37

Figure D2. Summary of Margins of Safety (continued)

D1.2 Table of Contents

D1. Introduction and Background	Page 198
D1.1 Summary of Margins of Safety	Page 199
D1.2 Table of Contents	Page 202
D2. Material Properties and Model Parameters	Page 204
D2.1 Model Dimensions and Loads	Page 205
D3. Balance Attachment	Page 206
D3.1 Pin Shear due to Lift Force	Page 207
D3.2 Fastener Shear due to Rolling Moment	Page 207
D3.3 Pitching Moment	Page 208
D3.4 Combined Lift and Pitch on Shear Pins	Page 208
D4. Leading Edge Control Surface Attachment	Page 208
D4.1 Leading Edge Inboard Control Surface	Page 208
D4.2 Leading Edge Outboard Control Surface	Page 209
D5. Trailing Edge Control Surface Attachment	Page 210
D5.1 Flap Attachment	Page 211
D5.1.1 Conventional Flap Attachment	Page 211
D5.1.2 Shape Memory Alloy Actuated Flap Attachment	Page 212
D5.2 Aileron Attachment	Page 214
D5.2.1 Conventional Aileron Attachment	Page 215
D5.2.2 Shape Memory Alloy Actuated Aileron Attachment	Page 217
D5.3 Combined Loading on Conventional Flap/Aileron Pin	Page 218
D6. Other Structures	Page 219
D6.1 Torque Tube	Page 219
D6.1.1 Torque Tube Transmission Rod Twist	Page 219
D6.1.2 SMA Torque Tube Attachment	Page 220
D6.1.3 Torque Tube Keyway	Page 223
D6.1.4 Mesh Gear	Page 225
D6.1.5 Outboard Rib Attachment	Page 227

D6.1.6 Tip Rib	Page 229
D6.2 Spar Attachment to Root Rib	Page 231
D6.2.1 Combined Loading- Leading Edge Spar	Page 232
D7. Conclusions	Page 233
D8. References	Page 233
D9. Dynamics and Flutter Analyses	Page 233
D10. Summary	Page 239

D2. MATERIAL PROPERTIES AND MODEL PARAMETERS

The allowable membrane stress, S_m , for the materials used in this report are established by using the rules set out in the Wind Tunnel Models Design Criteria. The materials in use for the model's structural members are the following:

Construction Materials

$F_{tu} = S_u = \sigma_u$ = Ultimate Stress Tension

$F_{BR} = \sigma_{BR}$ = Bearing Stress

$F_{ty} = S_y = \sigma_y$ = Yield Stress Tension

$F_{su} = \tau_u$ = Shear Ultimate

7075-T6 Aluminum

$E = 10.3 \times 10^3$ ksi

$G = 3.9 \times 10^3$ ksi

$\nu = 0.33$

$\rho = 0.101$ lb/in³

$F_{tu} = S_u = \sigma_u = 76.0$ ksi

$F_{su} = \tau_u = 46.0$ ksi

$F_{ty} = S_y = \sigma_y = 69.0$ ksi

$F_{BR} (e/D = 1.5) = \sigma_{BR} = 118$ ksi

4340 Steel (Quenched and Tempered to 800°F)

$E = 29.0 \times 10^3$ ksi

$G = 11.0 \times 10^3$ ksi

$\nu = 0.32$

$\rho = 0.283$ lb/in³

$F_{tu} = S_u = \sigma_u = 200$ ksi

$F_{su} = \tau_u = 120$ ksi

$F_{ty} = S_y = \sigma_y = 176$ ksi

$F_{BR} (e/D = 1.5) = \sigma_{BR} = 272$ ksi

4130 Steel

$E = 29.0 \times 10^3$ ksi

$G = 11.0 \times 10^3$ ksi

$\nu = 0.32$

$\rho = 0.283$ lb/in³

$F_{tu} = S_u = \sigma_u = 95.0$ ksi

$F_{su} = \tau_u = 57.0$ ksi

$F_{ty} = S_y = \sigma_y = 75.0$ ksi

$F_{BR} = \sigma_{BR} = 200.0$ ksi

17-4PH Stainless Steel, H900

$E = 28.5 \times 10^3$ ksi

$G = 11.2 \times 10^3$ ksi

$\nu = 0.27$

$\rho = 0.282$ lb/in³

$F_{tu} = S_u = \sigma_u = 190.0$ ksi

$F_{su} = \tau_u = 123.0$ ksi

$F_{ty} = S_y = \sigma_y = 170.0$ ksi

$F_{BR} = \sigma_{BR} = 255.0$ ksi

Fasteners (for Leading, Trailing Edges and Skin Attachment)

MS24693C2 and MS24693C3

Diameter = 0.112 in.

Material = CRES per AMS 5737 (A-2286)

Thread Size = 0.112 - 40 UNC - 2A

Head Diameter = 0.317 in.

Tensile Strength = 160 ksi

Locking Nut Plate

Huck Nut Plate FF 6010 L - 4 - A

Thread Size = 0.112 - 40 UNJC - 3B

Keen Inserts

KNCA0440J

Internal Thread = 4 - 40 UNJC-3B
L = 0.17 in. (Internal Locking Depth)

External Thread = 10 - 32 UNF-2A
T = 0.125 in. (Engagement Depth)

Socket Head Cap and Flathead Screws

#2-56 - Socket

Diameter = 0.086
Material = Alloy Steel
Double Shear Strength = 1320 lbs

Head Diameter = 0.140
Tensile Strength (minimum) = 702 lbs
Thread = UNRC

#6-32 - Socket

Diameter = 0.138
Material = Alloy Steel
Double Shear Strength = 3400 lbs

Head Diameter = 0.307
Tensile Strength (minimum) = 1730 lbs
Thread = UNRC

#8-32 - Socket

Diameter = 0.164
Material = Alloy Steel
Double Shear Strength = 4800 lbs

Head Diameter = 0.270
Tensile Strength (minimum) = 2660 lbs
Thread = UNRC

#10-32 - Socket

Diameter = 0.190
Material = Alloy Steel
Double Shear Strength = 6450 lbs

Head Diameter = 0.312
Tensile Strength (minimum) = 3800 lbs
Thread = UNRC

¼ in. -28

Diameter = 0.250
Material = Alloy Steel
Double Shear Strength = 11,200 lbs

Head Diameter = 0.370
Tensile Strength (minimum) = 6910 lbs
Thread = UNRC

Installation Torque

#4 -40 = 10 in-lbs
#10-32 = 60 in-lbs

#8-32 = 36 in-lbs
¼ in. -28 = 144 in-lbs

D2.1 Model Dimensions and Loads

The wind tunnel models are 16% scale replicas of the F/A-18 E/F wing with a 7.065 in. inboard section for electric motors and instrumentation. The modified NACA 65A series airfoil used in the model is based on the F/A-18 design. The thickness varies from 12.4% at the root, to 6.2% at the inboard rib, and 4.2% at the tip.

The models were designed to have some flexibility, and lie somewhere between flutter models and rigid force models. This allows a SMA torque tube inserted along the center spar to change the wash-out of the model. The models also have incorporated into them novel trailing edge control surfaces and the instrumentation and power lines to actuate them. These design considerations lead to the decision to construct the models using a conventional wing box technique. Fabricating the models using this technique meant that the stiffness would not be able

to be scaled down directly from the full scale aircraft (as is done with flutter models) due to the minimum gage thickness of the materials used in the fabrication. Listed below are the important dimensions and loads that will determine the margins of safety for the wind tunnel models.

Model Scale Factor = 16%	
Model Reference Dimensions	
S_w = Wing Area = 887 in. ²	c_{root} = Root Chord =
33.526 in.	
b = Wing Span = 37.375 in.	c_{tip} = Tip Chord = 12.121 in.
c_{bar} = 23.439 in.	
Maximum α = 15 degrees	
Maximum Q = 130 psf = 0.903 psi @ $M = 0.33$	
Balance Forces at $\alpha = 15$ degrees, $Q = 130$ psf	
Lift = 900 lbs	Rolling Moment = 13,000 in-lbs
Pitching Moment = 1800 in-lbs	Axial = 40 lbs
Yawing Moment = 1000 in-lbs	
The test plan calls for wind tunnel runs at $N_z = 3.25$ to be performed.	

D3. BALANCE ATTACHMENT

Both wing models will be attached to the balance via a 4130 stainless steel pedestal that uses 12, ½ in. alloy steel screws and 2, ½ in. shear pins. The fastener locations and moment lengths are shown in Figure D3 with the applicable loads and their directions.

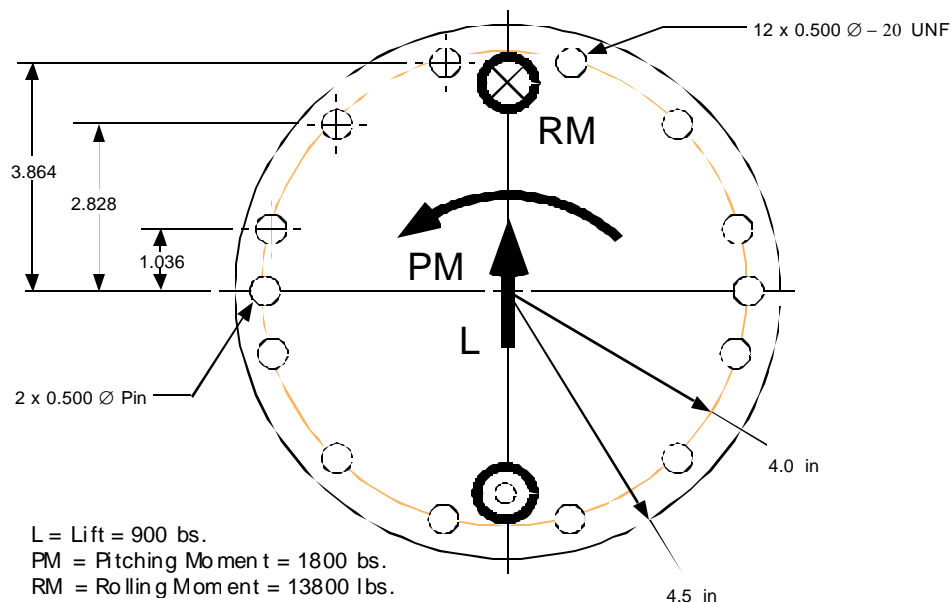


Figure D3. Balance Attachment Drawing

D3.1 Pin Shear Due to Lift Force

The lift force is reacted through the 2, $\frac{1}{2}$ in. shear pins.

$$P = \frac{\text{Lift}}{\# \text{ pins}} = \frac{900}{2} = 450 \text{ lbs}$$

$$\tau = \frac{4P}{\pi d^2} = \frac{4(450)}{\pi(0.5)^2} = 2.292 \times 10^3 \text{ psi}$$

$$\text{M.S.} = \frac{\tau_u}{\tau} - 1 = \frac{90000}{2292} - 1 = 38.3$$

D3.2 Fastener Shear due to Rolling Moment

The rolling moment of 13,800 in-lbs is reacted by the 12, 0.500 in. fasteners in tension. It is assumed that each row of fasteners reacts an equal portion of the moment:

Row 1: $M = 4333 \text{ in-lbs @ } 7.727 \text{ in.}$

Row 2: $M = 4333 \text{ in-lbs @ } 5.657 \text{ in.}$

Row 3: $M = 4333 \text{ in-lbs @ } 2.071 \text{ in.}$

Row 1

$M = 4333 \text{ in-lbs.}$

$x = 7.727 \text{ in.}$

$$F_R = \frac{M}{x} = \frac{4333}{7.727} = 5.608 \times 10^2 \text{ lbs}$$

$$P = \frac{F_R}{n_f} = \frac{5.608 \times 10^2}{2} = 2.804 \times 10^2 \text{ lbs}$$

$$\text{M.S.} = \frac{F_{Tu}}{P} - 1 = \frac{126000}{280.4} - 1 = 450$$

Row 2

$M = 4333 \text{ in-lbs.}$

$x = 5.657 \text{ in.}$

$$F_R = \frac{M}{x} = \frac{4333}{5.657} = 7.660 \times 10^2 \text{ lbs}$$

$$P = \frac{F_R}{n_f} = \frac{7.660 \times 10^2}{2} = 3.830 \times 10^2 \text{ lbs}$$

$$\text{M.S.} = \frac{F_{Tu}}{P} - 1 = \frac{126000}{383.0} - 1 = 329$$

Row 3

$M = 4333 \text{ in-lbs.}$

$x = 2.071 \text{ in.}$

$$F_R = \frac{M}{x} = \frac{4333}{2.071} = 2.092 \times 10^3 \text{ lbs}$$

$$P = \frac{F_R}{n_f} = \frac{2.092 \times 10^3}{2} = 1.046 \times 10^3 \text{ lbs}$$

$$\text{M.S.} = \frac{F_{Tu}}{P} - 1 = \frac{126000}{1046} - 1 = 120$$

D3.3 Pitching Moment

The pitching moment is equal to 1800 in-lbs and is assumed to be reacted solely by the shear pins.

$$M = 1800 \text{ in-lbs}$$

$$x = 8 \text{ in.}$$

$$F_{PM} = M/x = 1800/8 = 2.25 \times 10^2 \text{ lbs}$$

$$P = F_{PM}/n_f = 2.25 \times 10^2 / 1 = 2.25 \times 10^2 \text{ lbs}$$

$$\tau = 4P/\pi d^2 = 4(2.25 \times 10^2)/\pi(0.50)^2 = 1.145 \times 10^3 \text{ psi}$$

$$M.S. = \tau_u/\tau - 1 = 90000/1145 - 1 = 77.54$$

D3.4 Combined Lift and Pitch on Shear Pins

$$P_T = P_{Lift} + P_{PM} = 450 + 112.5 = 562.5 \text{ lbs}$$

$$\tau = 4P/\pi d^2 = 4(562.5)/\pi(0.500)^2 - 1 = 2.865 \times 10^3 \text{ psi}$$

$$M.S. = \tau_u/\tau - 1 = 57000/2865 - 1 = 18.9$$

D4. LEADING EDGE CONTROL SURFACE ATTACHMENT

For both models the inboard and outboard leading edge (LE) control surfaces will be non-moving, rigid structures. The leading edges will be attached to the front spar on the wing box, constructed from 7075-T6 aluminum, and attached using standard fastener MS24693 #4. The fasteners will be in a single row, with a spacing of one fastener per inch. The area and dimensions for the inboard control are given in Figure D4 and outboard in Figure D5.

D4.1 Leading Edge Inboard Control Surface

The leading edge inboard control surface is divergence critical. Using the maximum Q, and assuming that it is applied at the leading edge tip (the most critical location), the fastener shear stresses and bearing stresses are calculated. For the LE Inboard, there are 19 4/40, 0.112 in. diameter fasteners that go through a 0.050 in. thick skin. The fasteners are the Huck DPY - 7900 Series at approximately 1 in. spacing in KEEN Inserts set into the leading edge spar.

$$Q = 130 \text{ psf} = 0.903 \text{ psi}$$

$$Area_{LEI} = 82.49 \text{ in}^2$$

$$F_{LEI} = Q \cdot Area = (0.903)(82.49) = 74.49 \text{ lbs}$$

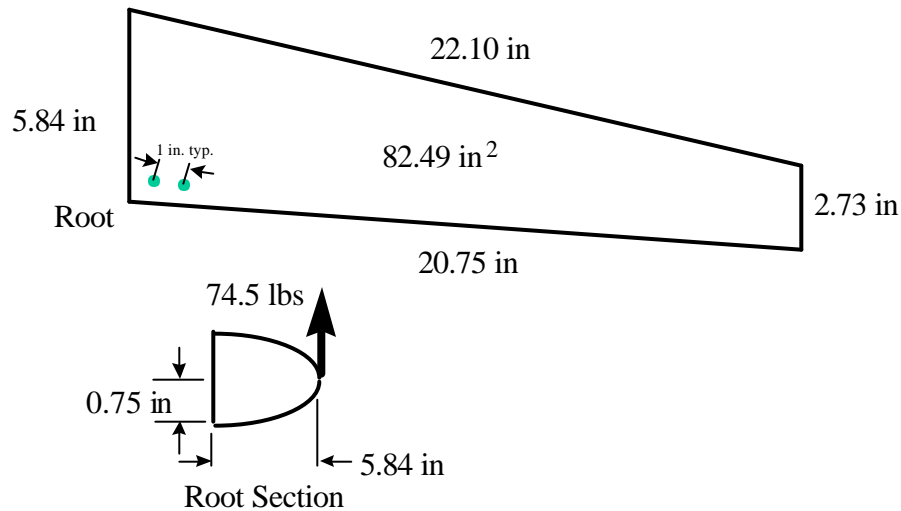


Figure D4. Leading Edge Inboard

The force on the row of fasteners, T_{LEI} , is:

$$T_{LEI} = F_{LEI} \cdot x/h = F_{LEI} \cdot 5.84/1.50 = (74.49)(5.84)/1.50 = 2.90 \times 10^2 \text{ lbs}$$

Load per Fastener, P , is:

$$P = T_{LEI}/n_f = 290/17 = 17.06 \text{ lbs}$$

Shear Load per Fastener, τ_f :

$$\tau_f = 4P/\pi d^2 = 4(29.0)/\pi(0.112)^2 = 1.731 \times 10^3 \text{ psi}$$

$$M. S. = \tau/\tau_f - 1 = 80000/1731 - 1 = 46.2$$

Bearing Stress:

$$\sigma_{BR} = P/dt = 17.06/(0.112)(0.05) = 3.046 \times 10^3 \text{ psi}$$

$$M. S. = \sigma_m/\sigma_{BR} - 1 = 118000/3046 - 1 = 38.7$$

D4.2 Leading Edge Outboard Control Surface

The attachment method for the LE outboard control surface is similar to that of the inboard control surface. The same fasteners are used with the same spacing. Figure D5 gives a planform view of the outboard LE along with the surface area and the aerodynamic force applied. The fasteners are the Huck DPY - 7900 Series that are placed with a approximately 2 in. spacing into KEEN Inserts set into the leading edge spar.

$$Q = 130 \text{ psf} = 0.903 \text{ psi}$$

$$\text{Area}_{\text{LEO}} = 36.44 \text{ in}^2$$

The force per row of fastener, F_{LEO} is

$$F_{\text{LEO}} = Q \cdot \text{Area}_{\text{LEO}} = (0.903)(36.44) = 32.905 \text{ lbs}$$

The force on the row of fasteners, T_{LEO} :

$$T_{\text{LEO}} = F_{\text{LEO}} \cdot \frac{4.17}{1.00} = (32.905)(4.17) / 1.00 = 137 \times 10^2 \text{ lbs}$$

Load per Fastener, P ,

$$P = T_{\text{LEO}} / n_f = 137.2 / 6 = 22.87 \text{ lbs}$$

Shear Load per Fastener, t_b :

$$\tau_f = 4P / \pi d^2 = 4(22.87) / \pi (0.112)^2 = 2.321 \times 10^3 \text{ psi}$$

$$\text{M. S.} = \tau / \tau_f - 1 = 80000 / 2321 - 1 = 33.5$$

Bearing Stress:

$$\sigma_{\text{BR}} = P / dt = 22.87 / (0.112)(0.05) = 4.084 \times 10^3 \text{ psi}$$

$$\text{M. S.} = \sigma_m / \sigma_{\text{BR}} - 1 = 118000 / 4084 - 1 = 27.9$$

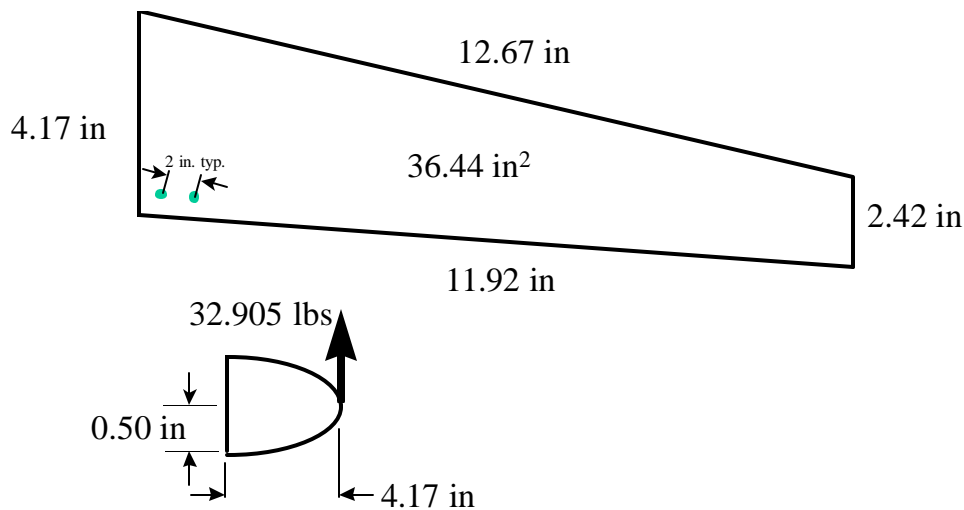


Figure D5. Leading Edge Outboard

D5. TRAILING EDGE CONTROL SURFACE ATTACHMENT

There are two different sets of trailing edge control surfaces. One set uses a conventional globe motor to change the position of the flap and uses pins and bearings to support the flap and brackets to set the aileron deflected position. The other set of control surfaces contoured by shape memory alloy wires is attached similar to the leading edge, with through fasteners. Section D5.1 discusses the attachment of the flap control surfaces while D5.2 addresses the aileron.

D5.1 Flap Attachment

Figure D6 shows the lay-out of the trailing edge flap. Though the attachment methods are different for the two models, the physical dimensions are the same.

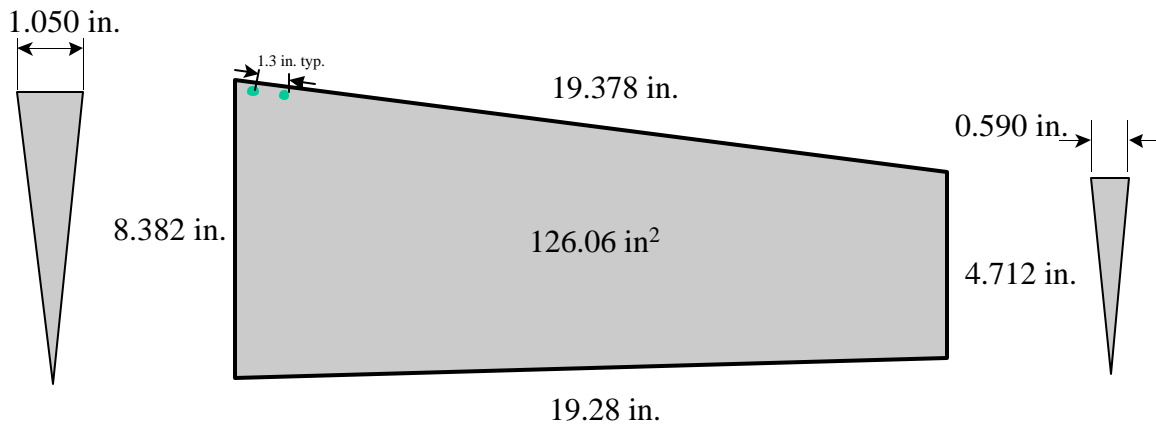


Figure D6. Trailing Edge Inboard - Flap

D5.1.1 Conventional Flap Attachment

The conventional flap attachment is done in the simplest way possible and is shown in Figure D7. A rod runs from the worm gear in the rigid section of the wing, through a bushing, to the flap where it is welded into a plate that is then bolted onto the flap. On the outboard section a similar arrangement is made. The rods that the flap rotates about is 0.500 in. diameter 4340 steel rod from the worm gear to the inboard section of flap, and 0.380 in. diameter 4340 steel rod at the outboard section. Figure D8 shows a detail of the center rib attachment of the flap hinge pin.

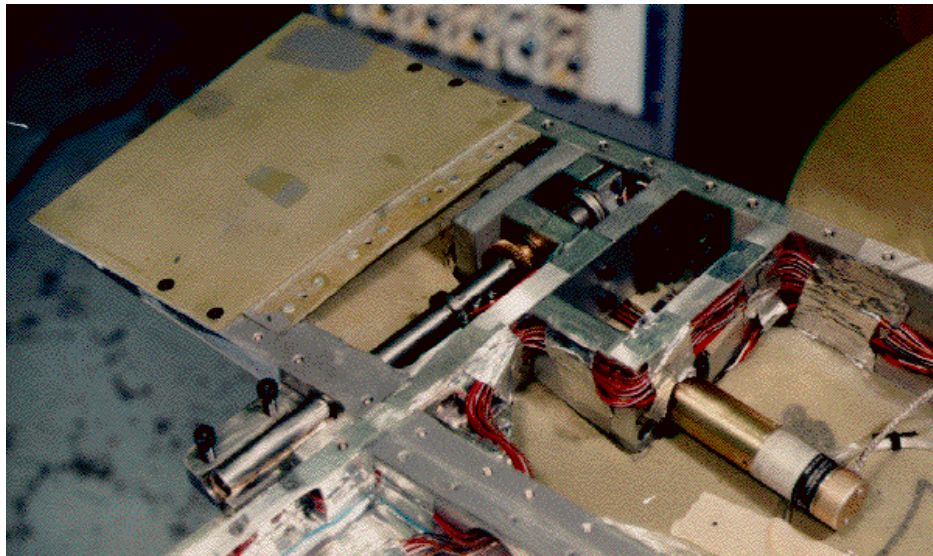


Figure D7. Conventional Flap Motor and Attachment

The loads that the outboard hinge rod must resist are:

$$Q = 130 \text{ psf} = 0.903 \text{ psi}$$

$$\text{Area}_{\text{TEI}} = 126.06 \text{ in}^2$$

The force on the flap, F_{TEI} is

$$F_{\text{TEI}} = Q \cdot \text{Area}_{\text{TEI}} = (0.903)(126.06) = 113.83 \text{ lbs}$$

$$\tau = \frac{4P}{\pi d^2} = \frac{4(113.83)}{\pi(\frac{3}{8})^2} = 1.031 \times 10^3 \text{ psi}$$

$$\text{M.S.} = \frac{\tau_U}{\tau} - 1 = \frac{90000}{1031} - 1 = 86.3$$

For the inboard hinge rod, the shear stress, τ , is:

$$F_{\text{TEI}} = Q \cdot \text{Area}_{\text{TEI}} = (0.903)(126.06) = 113.83 \text{ lbs}$$

$$\tau = \frac{4P}{\pi d^2} = \frac{4(113.83)}{\pi(0.5)^2} = 579.73$$

$$\text{M.S.} = \frac{\tau_U}{\tau} - 1 = \frac{90000}{579.73} - 1 = 154.2$$

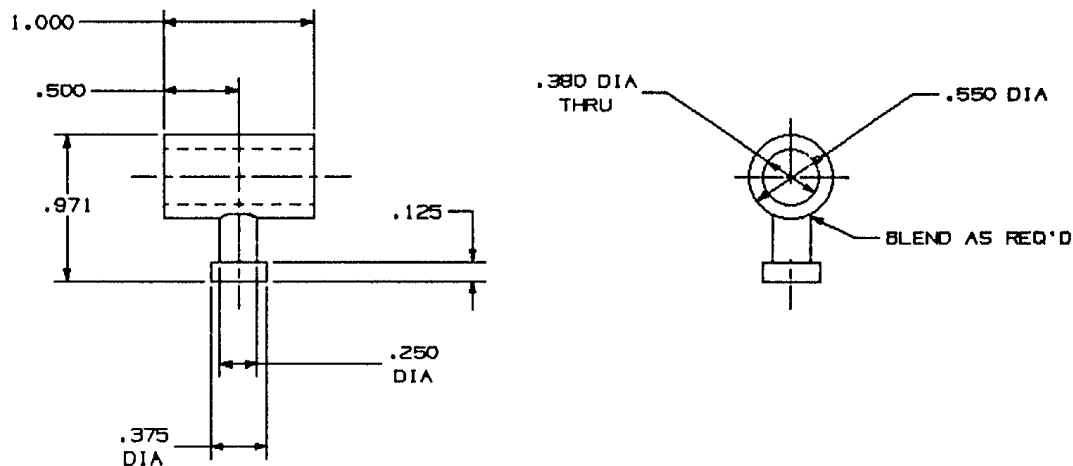


Figure D8. Conventional Flap Attachment Detail

D5.1.2 Shape Memory Alloy Actuated Flap Attachment

The SMA actuated flap is attached in a similar method as the leading edges. Because the control surface does not rotate, the flap can be fastened rigidly to the rear spar and skin. The control surface is fastened through the skin into the SMA close-out. The fasteners used are 0.112 in. diameter Huck DPY - 7900 Series that have a spacing of approximately 1 in. Because ULTEM[®] thermoplastic was used for the close-out on both the flap and aileron (due to the need to electrically isolate the wires from each other and the structure), KEEN inserts were used to lock the fasteners. Figure D9 shows a picture of the SMA trailing edge flap with ULTEM[®] close-out strip and attachment holes with inserts installed. The dark lines in the are the SMA wires

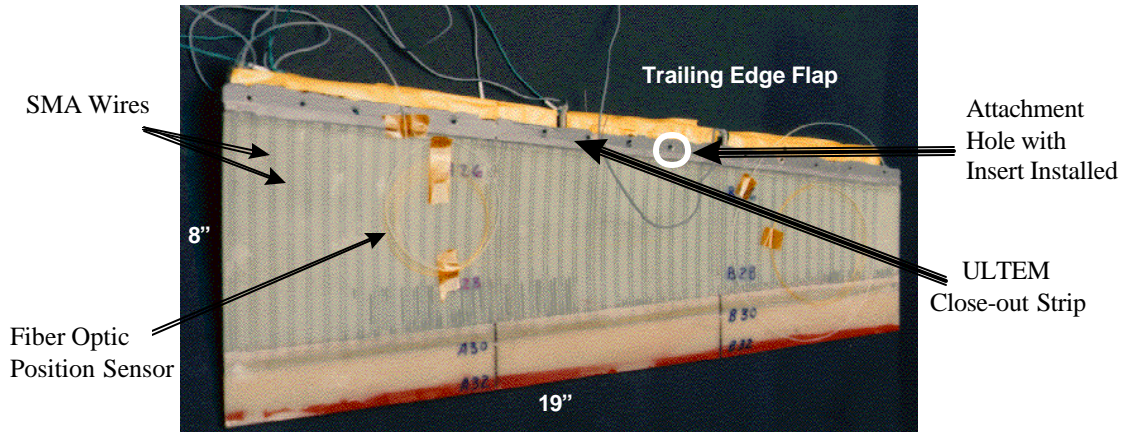


Figure D9. SMA Trailing Edge Flap

$$Q = 130 \text{ psf} = 0.903 \text{ psi}$$

$$\text{Area}_{\text{TEI}} = 126.06 \text{ in}^2$$

The force per row of fastener, F_{TEI} is

$$F_{\text{TEI}} = Q \cdot \text{Area}_{\text{TEI}} = (0.903)(126.06) = 113.83 \text{ lbs}$$

The force on the row of fasteners, T_{TEI} :

$$T_{\text{TEI}} = F_{\text{TEI}} \cdot \frac{x}{h} = 113.83 \cdot \frac{8.382}{1.050} = 9.087 \times 10^2 \text{ lbs}$$

Load per fastener, P :

$$P = \frac{T_{\text{TEI}}}{n_f} = \frac{908.7}{14} = 64.907 \text{ lbs}$$

Shear stress per fastener, τ_f :

$$\tau_f = \frac{4P}{\pi d^2} = \frac{4(64.907)}{\pi (.112)^2} = 6.588 \times 10^3 \text{ psi}$$

$$\text{M. S.} = \frac{\tau}{\tau_f} - 1 = \frac{80000}{6588} - 1 = 11.1$$

Bearing Stress on skin, s_{BR} :

$$\sigma_{\text{BR}} = \frac{P}{dt} = \frac{64.907}{(.112)(.05)} = 1.159 \times 10^4 \text{ psi}$$

$$\text{M. S.} = \frac{\sigma_u}{\sigma_{\text{BR}}} - 1 = \frac{118000}{11590} - 1 = 9.2$$

Surface Loads for SMA Flap

From F/A - 18 aircraft data, the hinge moment for $d_{\text{Flap}} = 0$ degrees is,

$$\text{HM}_{\text{Flap, A/C}} = 12,885 \text{ in-lbs}$$

Using scale factors to scale the hinge moments for the 16% model,

$$\text{HM}_{\text{Flap, Model}} = (\text{HM}_{\text{Flap, A/C}})(\text{Scale Factor}) = (12885)(4.10 \times 10^{-3})$$

$$\text{HM}_{\text{Flap, Model}} = 52.83 \text{ in-lbs}$$

The hinge moment is related to the distributed force being applied along the chord length of the flap by the following equation:

$$\text{HM}_{\text{Flap, Model}} = \frac{1}{2} \cdot w \cdot l^2$$

$w = 2 \cdot HM / l^2 = 2(52.83) / (6.0)^2 = 2.935 \frac{\text{lb}}{\text{in}}$, where w is the force per inch and l is average chord of flap

To find the pressure about the entire flap area, divide w by the span of the flap;

$$P_{\text{Flap}} = w / b_{\text{Flap}} = 2.935 / 19.30 = 0.152 \text{ psi}$$

Determination of Load on Individual Wires

Each SMA wire can withstand a 4 lb. axial force in its austenitic state before it yields. Figure D10 shows the forces and moments on the flap, with the moment broken down into the applied force. The hinge moment, 52.83 in-lbs, is derived from actual $F/A - 18$ data and is not as conservative as the hinge moment used in determining the attachment margins of safety, but more realistically reflects the loads the flap will see in this wind tunnel test.

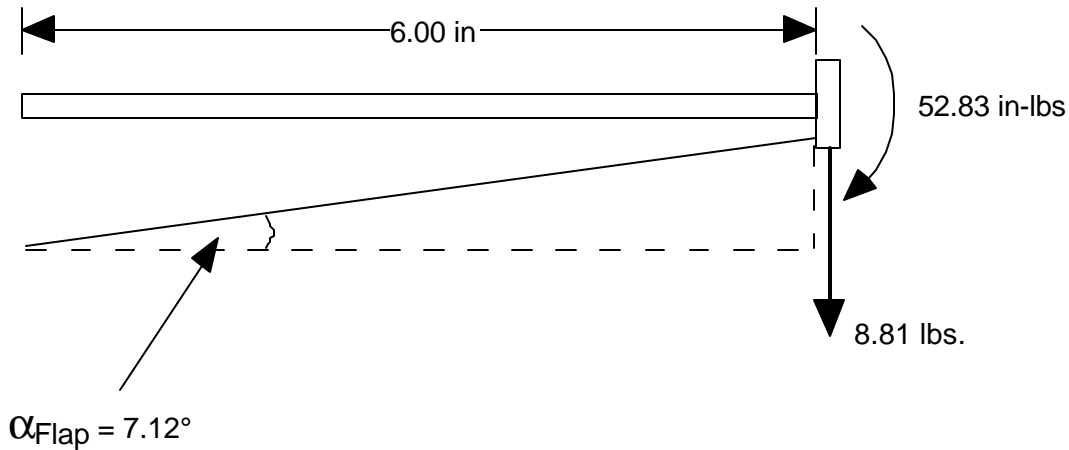


Figure D10. SMA Wire Force Diagram, Flap

Decomposing the moment into forces, F_{Flap}

$$F_{\text{Flap}} = M_{\text{Flap}} / x_{\text{Flap}} = 52.83 / 6.00 = 8.805 \text{ lbs}$$

The force on the wires, F_{wire} , is then,

$$F_{\text{Wire}} = F_{\text{Flap}} / \tan \alpha = 8.805 / \sin(7.12^\circ) = 71.04 \text{ lbs}$$

There are 92 lengths of wires on the flap, the force per wire is,

$$F_{n_{\text{Wire}}} = F_{\text{Wire}} / n_{\text{Wire}} = 71.04 / 92 = 0.772 \text{ lbs}$$

$$\text{M.S.} = F_{\text{yield}} / F_{n_{\text{Wire}}} - 1 = 4 / 0.772 - 1 = 4.18$$

D5.2 Aileron Attachment

Figure D11 shows the planform of both ailerons.

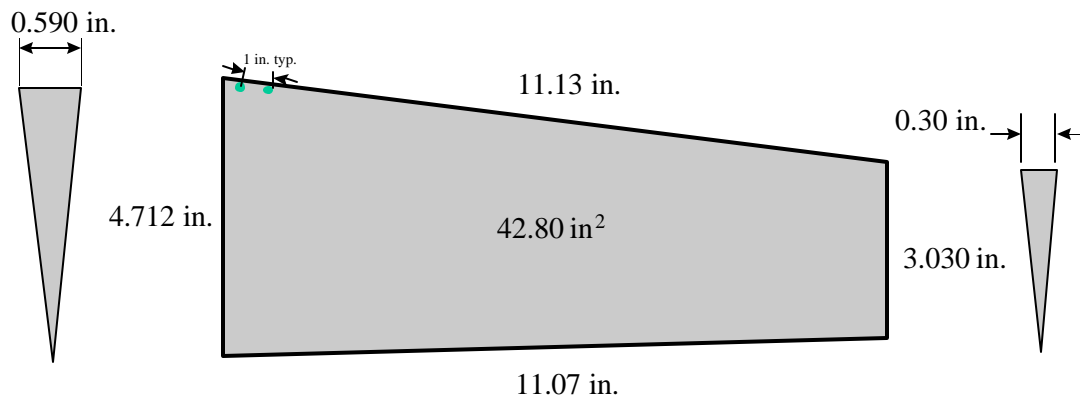


Figure D11. Trailing Edge Outboard - Aileron

D5.2.1 Conventional Aileron Attachment

The conventional aileron is attached using brackets. The initial test plan was to use a globe motor to actuate the aileron (like the flap), but because of aeroelastic reasons the plan was changed. The aileron was to be connected to the globe motor via a 3/8 in. steel rod. When aerodynamic simulations were run using ASTROS, it was found that even though the rod was strong enough to withstand the maximum aerodynamic loading without failing, the rotational stiffness was not large enough to keep the rod from acting like a 28 in. long rotational spring. This led to a very low flutter speed. To insure the safety of the tunnel and the model, it was decided to fix the aileron to the rear wing box spar with brackets. The bracket consists of a plate that is bent at certain degrees (± 0 , ± 5 , and ± 10 degrees) and a pin that slips from a special close-out rib into the aileron.

Figure D12 shows the design of the conventional aileron attachment. The aileron rotates about a 3/8 in. diameter rod on the inboard portion and a 1/8 in. pin outboard. To hold the angles of deflection, a screw and a pin are inserted into the outboard tip. There is also an angle bracket which bolts onto the upper surface and to the cap of the trailing edge spar.

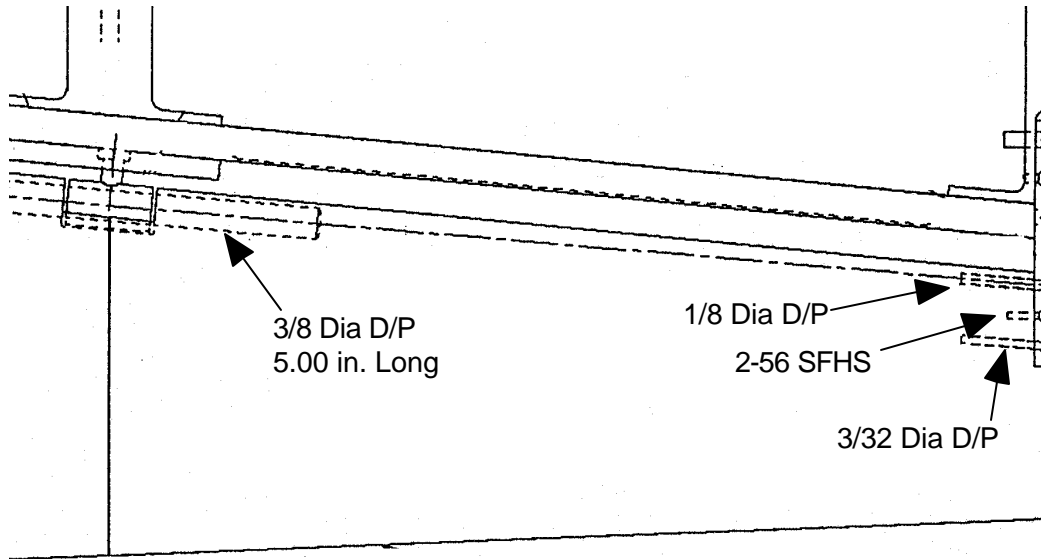


Figure D12. Aileron Attachment

Forces on aileron:

$$Q = 130 \text{ psf} = 0.903 \text{ psi}$$

$$\text{Area}_{\text{TEO}} = 42.80 \text{ in}^2$$

The force on the aileron and moment, F_{TEO} and M_{TEO} , is

$$F_{\text{TEO}} = Q \cdot \text{Area}_{\text{TEO}} = (0.903)(42.80) = 38.648 \text{ lbs}$$

$$M_{\text{TEO}} = F_{\text{TEO}} \cdot 3.03 \text{ in.} = 117.10 \text{ in-lbs}$$

The pin and the screw split the load 34/66, so:

$$F_{\text{SCREW}} = \left(\frac{M}{x_{\text{screw}}} \right) \cdot 0.34 = \left(\frac{117.10}{0.5} \right) \cdot 0.34 = 79.63 \text{ lbs}$$

$$F_{\text{PIN}} = \left(\frac{M}{x_{\text{PIN}}} \right) \cdot 0.66 = \left(\frac{117.10}{0.75} \right) \cdot 0.66 = 103.05 \text{ lbs}$$

The shear stress, τ_{SCREW} and τ_{PIN} , on each part is then:

$$\tau_{\text{SCREW}} = \frac{4P}{\pi d^2} = \frac{4(79.63)}{\pi(0.086)^2} = 1.371 \times 10^4 \text{ psi}$$

$$\tau_{\text{PIN}} = \frac{4P}{\pi d^2} = \frac{4(103.05)}{\pi(0.0938)^2} = 1.491 \times 10^4 \text{ psi}$$

The margin of safety for the screw and pin are:

$$\text{M.S.}_{\text{SCREW}} = \frac{\tau_U}{\tau_{\text{screw}}} - 1 = \frac{90000}{13710} - 1 = 5.56$$

$$\text{M.S.}_{\text{pin}} = \frac{\tau_U}{\tau_{\text{pin}}} - 1 = \frac{90000}{14910} - 1 = 5.04$$

D5.2.2. SMA Aileron Attachment

The SMA aileron is attached in a fashion similar to both the leading edge control surface (Section D4) and the SMA flap (Section D5.1.2). Also similar to the SMA actuated flap, the same Huck fasteners and KEEN inserts will be used to hold the fasteners in.

Forces on aileron:

$$Q = 130 \text{ psf} = 0.903 \text{ psi}$$

$$\text{Area}_{\text{TEO}} = 42.80 \text{ in}^2$$

The force per row of fastener, F_{TEO} is

$$F_{\text{TEO}} = Q \cdot \text{Area}_{\text{TEO}} = (0.903)(42.80) = 38.648 \text{ lbs}$$

The force on the row of fasteners, T_{TEO} :

$$T_{\text{TEO}} = F_{\text{TEO}} \cdot \frac{x}{h} = (38.648)(4.712) / .445 = 4.092 \times 10^2 \text{ lbs}$$

Load per fastener, P :

$$P = T_{\text{TEO}} / n_f = 409.2 / 11 = 37.2 \text{ lbs}$$

Shear stress per fastener, τ_f :

$$\tau_f = 4P / \pi d^2 = 4(37.2) / \pi (0.112)^2 = 3.776 \times 10^3 \text{ psi}$$

$$\text{M. S.} = \tau / \tau_f - 1 = 80000 / 3776 - 1 = \mathbf{20.2}$$

Bearing stress of skin, σ_{BR} :

$$\sigma_{\text{BR}} = P / dt = 37.2 / (0.112)(.05) = 6.643 \times 10^3 \text{ psi}$$

$$\text{M. S.} = \sigma_m / \sigma_{\text{BR}} - 1 = 118000 / 6643 - 1 = \mathbf{16.8}$$

Surface Loads for SMA Aileron

From F/A - 18 aircraft data, the hinge moment for $d_{\text{Aileron}} = 0^\circ$ is,

$$\text{HM}_{\text{Aileron, A/C}} = 3658.8 \text{ in-lbs}$$

Using scale factors to scale the hinge moments for the 16% model,

$$\text{HM}_{\text{Aileron, Model}} = (\text{HM}_{\text{Aileron A/C}})(\text{Scale Factor}) = (3658.8)(4.10 \times 10^{-3})$$

$$\text{HM}_{\text{Aileron, Model}} = 15.00 \text{ in-lbs}$$

The hinge moment is related to the distributed force being applied along the chord length of the aileron by the following equation:

$$\text{HM}_{\text{Aileron, Model}} = \frac{1}{2} \cdot w \cdot l^2$$

$$w = 2 \cdot \text{HM} / l^2 = 2(15.00) / (3.8)^2 = 2.08 \frac{\text{lb}}{\text{in}}$$

To find the pressure about the entire aileron area, divide w by the span of the aileron;

$$P_{\text{Aileron}} = w / b_{\text{Aileron}} = 2.08 / 11.10 = 0.187 \text{ psi}$$

Determination of Load on Individual Wires

Each SMA wire can withstand a 4 lb. axial force in its austenitic state before it yields. Figure D13 shows the forces and moments on the aileron, with the moment broken down into the applied force. The hinge moment, 14.98 in-lbs, is derived from actual F/A-18 data and is not as conservative as the hinge moment used in determining the attachment margins of safety, but more realistically reflects the loads the aileron will see in this wind tunnel test.

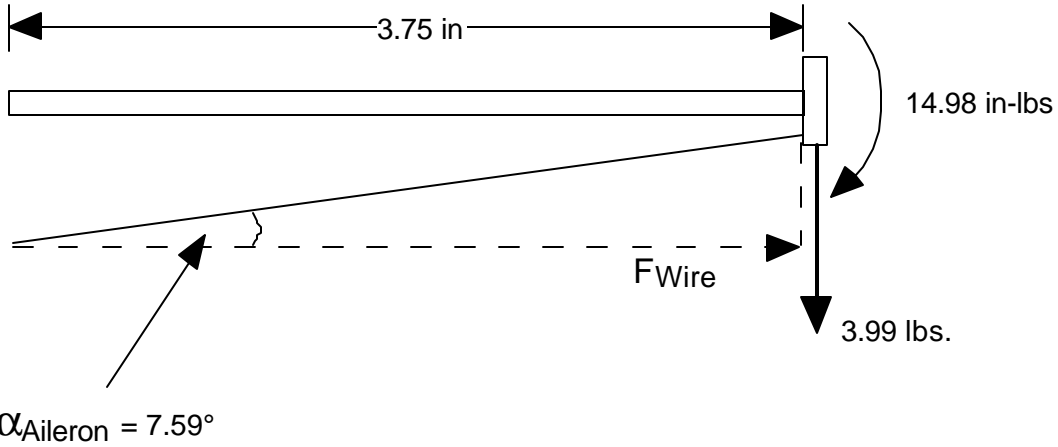


Figure D13. SMA Wire Force Diagram, Aileron

Decomposing the moment into forces, F_{Aileron}

$$F_{\text{Aileron}} = \frac{M_{\text{Aileron}}}{x_{\text{Aileron}}} = \frac{14.98}{3.75} = 3.99 \text{ lbs}$$

The force on the wires is then,

$$F_{\text{Wire}} = \frac{F_{\text{Aileron}}}{\sin \alpha} = \frac{3.99}{\sin(7.59^\circ)} = 30.21 \text{ lbs}$$

There are 52 lengths of wires on the aileron, the force per wire is,

$$F_{n_{\text{Wire}}} = \frac{F_{\text{Wire}}}{n_{\text{Wire}}} = \frac{30.21}{52} = 0.581 \text{ lbs}$$

$$\text{M.S.} = \frac{F_{\text{yield}}}{F_{n_{\text{Wire}}}} - 1 = \frac{4}{0.581} - 1 = 5.89$$

D5.3 Combined Loading on Conventional Flap/Aileron Pin

$$A_{\text{total}} = A_{\text{flap}} + A_{\text{aiileon}} = 126.06 + 42.80 = 168.86 \text{ in.}^2$$

$$Q = 130 \text{ psf} = 0.903 \text{ psi}$$

$$F = Q \cdot A_{\text{Total}} = (0.903)(168.86) = 152.44$$

$$\tau = \frac{4P}{\pi d^2} = \frac{4(152.44)}{\pi(0.25)^2} = 3.106 \times 10^3 \text{ psi}$$

$$\text{M.S.} = \frac{\tau_u}{\tau} - 1 = \frac{90000}{3106} - 1 = 27.9$$

D6. OTHER STRUCTURES

Along with the structures analyzed above, there are many other parts that, while not safety critical, require analysis to insure a successful test. Among these are the SMA torque tube attachment, aluminum skins, spar clips, and other assorted components. The first issue of the stress report will not include every piece (due to in-progress design), but shall by tunnel entry. Analysis of most of the components has been completed and reported before. The remaining will be documented in the final stress report which will be issued prior to tunnel entry.

D6.1 Torque Tube

The torque tube assembly stress analysis is given below. While an important technology to the Smart Wing program, the torque tube and torque tube connection is not a safety critical item in the wind tunnel model construction. Due to space limitations inside the wind tunnel model and a desire to fabricate torque tube connections that weigh as little as possible, it was not reasonably possible to meet a margin of safety of 3 on all parts. All margins are positive, and are above 1 except the torque shaft that has a margin of 0.56. The transfer of applied torque through the tip rib and the attachment of the tip rib to the front and rear spars is safety critical, though. The margins of safety on these joints meet the required value of 3.

D6.1.1 Torque Tube Transmission Rod Twist

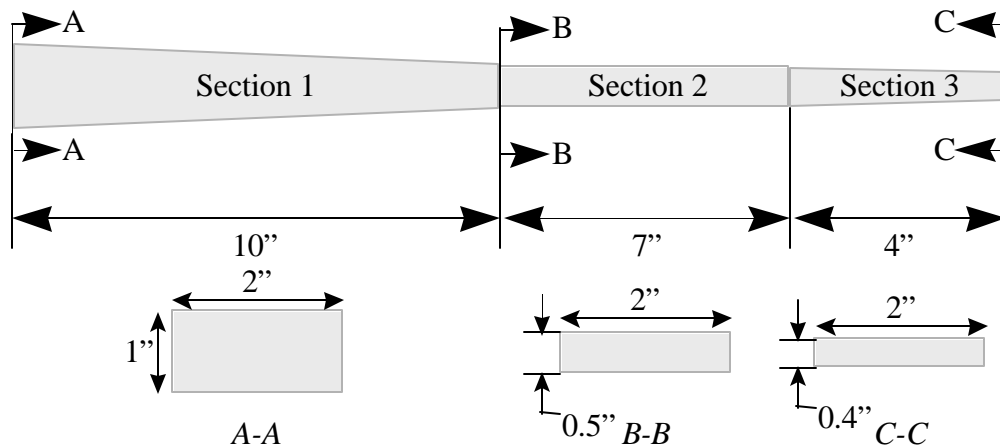


Figure D14. Transmission Rod Dimensions

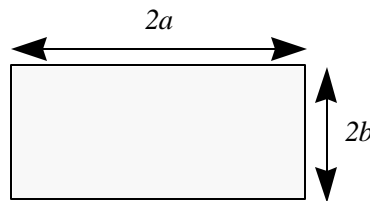


Figure D15. Nomenclature for Rectangular Cross Section Under Torsion

$$\theta = \int \frac{T}{K(x)G} dx$$

where for $a \geq b$, (see Figure D15)

$$K = ab^3 \left[\frac{16}{3} - 3.36 \frac{b}{a} \left(1 - \frac{b^4}{12a^4} \right) \right]$$

∴

$$\theta = \int_0^{10} \frac{T}{K(x)G} dx + \int_0^7 \frac{T}{K(x)G} dx + \int_0^{14} \frac{T}{K(x)G} dx = \theta_1 + \theta_2 + \theta_3$$

Assuming a 10% deviation in shear stiffness (i.e., $G=90\%G$), for an applied torque T of 3,000 in-lbs, the rotation of the connection rod, θ_{Total} , due to T is,

$$\theta_1 = 1.03^\circ \quad \theta_2 = 1.75^\circ \quad \theta_3 = 1.40^\circ$$

$$\theta_{Total} = \theta_1 + \theta_2 + \theta_3 = 1.03^\circ + 1.75^\circ + 1.40^\circ = 4.18^\circ$$

Sample K calculation:

For Section 2, $a = 1.00''$, $b = 0.25''$

$$K = (1)(0.25)^3 \left[\frac{16}{3} - 3.36 \left(\frac{0.25}{1} \right) \left(1 - \frac{0.25^4}{12(1)^4} \right) \right] = 0.0702$$

$$\theta_2 = \int_0^7 \frac{T}{K(x)G} dx = \frac{(7)(3000)}{(0.0702)(0.90)(10.9 \times 10^6)} = 0.03058 \text{ radians} = 1.75^\circ$$

Stress at Tip of Torque Shaft

The outboard-most tip of the transmission rod is the weakest in terms of strength as it is the thinnest.

From Roark and Young [1], (see Figure D15)

$$\tau_{MAX} = \frac{3T}{8ab^2} \left[1 + 0.6095 \left(\frac{b}{a} \right) + 0.8865 \left(\frac{b}{a} \right)^2 - 1.8023 \left(\frac{b}{a} \right)^3 + 0.9100 \left(\frac{b}{a} \right)^4 \right]$$

at the midpoint of each long side for $a \geq b$.

∴ for $a = 1.00''$, $b = 0.20''$, $T = 3,000$ in-lbs,

$$\tau_{MAX} = \frac{3(3000)}{8(1)(0.2)^2} \left[1 + 0.6095 \left(\frac{0.2}{1} \right) + 0.8865 \left(\frac{0.2}{1} \right)^2 - 1.8023 \left(\frac{0.2}{1} \right)^3 + 0.9100 \left(\frac{0.2}{1} \right)^4 \right] = 32.2 \text{ ksi}$$

$$M.S. = \frac{F_{Su}}{\tau_{Max}} - 1 = \frac{120000}{32200} - 1 = 2.73$$

D6.1.2 SMA Torque Tube Attachment

To transfer the moment developed by SMA torque tube to the rest of the structure, a heavy bracket connects the tube to the mid-rib. The bracket must be able to transfer approximately 3000 in-lbs of torque. The torque tube assembly is attached to the root rib by a 4340 steel bracket (Figure D16).

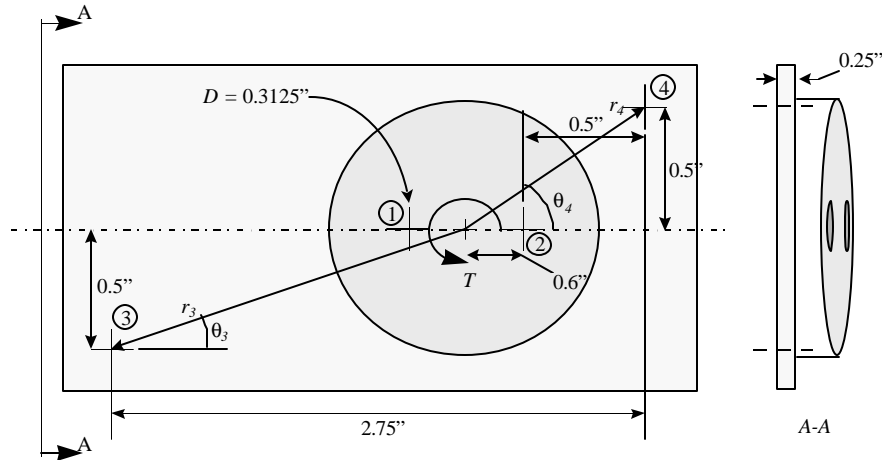


Figure D16. Root Bracket Geometry

Bearing

The reaction of torque towards the root rib occurs in two stages: 1) the 3000 in-lbs is reacted by two 0.3125" pins (pins 1 and 2) that connect one of the mesh gear to the bracket and 2) the 3000 in-lbs is reacted by the root rib via two 0.3125 pins that connect the bracket to the rib (pins 3 and 4).

a). Bearing at Pins 1 and 2

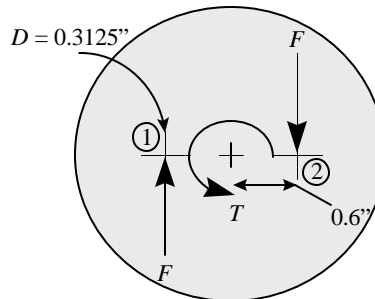


Figure D17. Forces on Pins 1 and 2

Based on Figure D17, the reactions F at the pins are,

$$F = \frac{T}{2r} = \frac{3000}{2(0.6)} = 2500 \text{ lbs}$$

The bearing stress is, σ_f

$$\sigma_{brg} = \frac{F}{dt} = \frac{2500}{(0.3125)(0.25)} = 3.2 \times 10^4 \text{ psi}$$

$$M.S. = \frac{\sigma_{BRU}}{\sigma_{brg}} = \frac{272000}{32000} - 1 = 7.5$$

The shear stress is, τ_ϕ ,

$$\tau_f = \frac{4F}{\pi d^2} = \frac{4(2500)}{\pi(0.3125)^2} = 3.259 \times 10^4 \text{ psi}$$

$$\text{M.S.} = \tau_u / \tau_f - 1 = 90000 / 32590 - 1 = \mathbf{1.76}$$

b. Bearing at Pins 3 and 4

Based on Figure D18,

$$r_3 = \sqrt{0.5^2 + (2.75 - 0.6 - 0.5)^2} = 1.72 \text{ in.}$$

$$r_4 = \sqrt{0.5^2 + 1.1^2} = 1.21 \text{ in.}$$

$$\theta_3 = \tan^{-1} \left(\frac{0.5}{2.75 - 0.6 - 0.5} \right) = 16.9^\circ$$

$$\theta_4 = \tan^{-1} \left(\frac{0.5}{1.1} \right) = 24.4^\circ$$

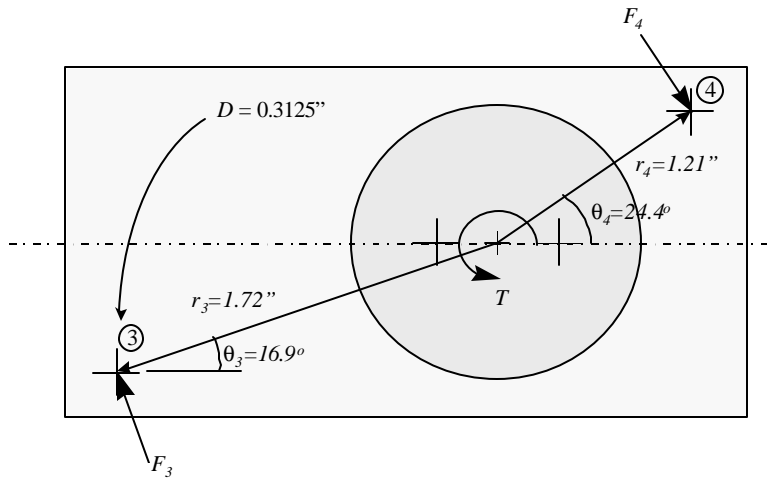


Figure D18. Forces on Pins 3 and 4

Performing equilibrium calculations (see, Figure D18),

$$F_3 = 1167 \text{ lbs}$$

$$F_4 = 821 \text{ lbs}$$

Taking the larger of the two, bearing stress at Pin 3 is,

$$\sigma_{\text{brg}} = F_3 / d t = \frac{1167}{(0.3125)(0.25)} = 1.49 \times 10^4 \text{ psi}$$

$$\text{M.S.} = \sigma_{\text{BRu}} / \sigma_{\text{brg}} = 272000 / 14900 - 1 = \mathbf{17.3}$$

Using Pin 3 as the worst case, the shear stress is, τ_f

$$\tau_f = 4F_3 / \pi d^2 = \frac{4(1167)}{\pi(0.3125)^2} = 1.522 \times 10^4 \text{ psi}$$

$$\text{M.S.} = \tau_u / \tau_f - 1 = 90000 / 15220 - 1 = \mathbf{4.91}$$

D6.1.3 Torque Tube Keyway

A parallel key made from 4340 steel is used to connect the transmission rod to the SMA torque tube.

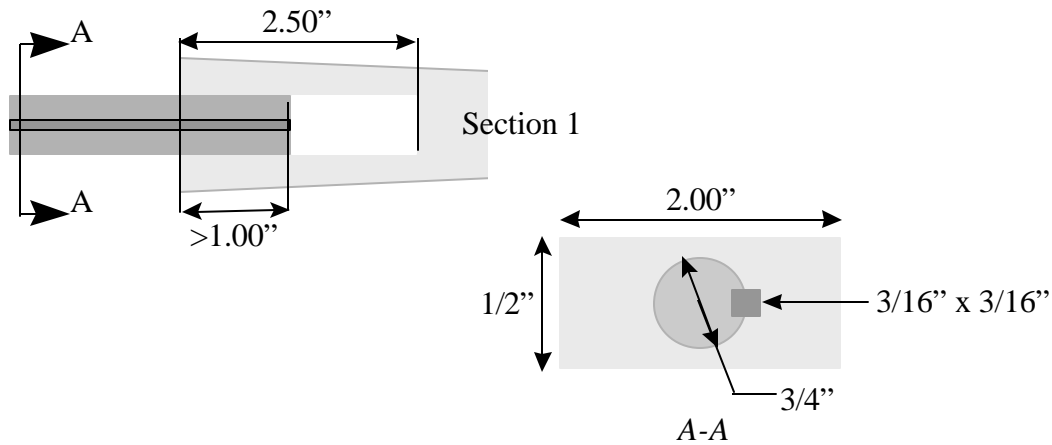


Figure D19. Keyway Dimensions

Maximum Torque Transmitted

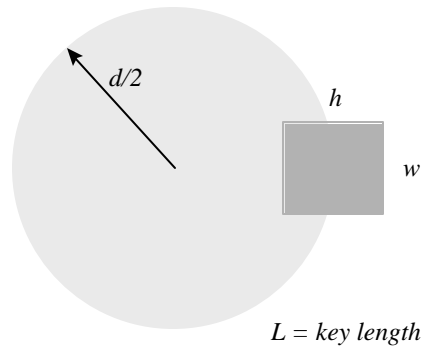


Figure D20. Rothbart's Nomenclature for Parallel Key Max Transmittable Torque Calculation

From Rothbart [2], (see Figure D20 for definition of variables)

$$T \leq \frac{1}{2} dwLF_{Su}, \text{ for shear}$$

$$T \leq \frac{1}{4} dhLF_{Ty}, \text{ for compression}$$

For $d = \frac{3}{4}$ in., $w = h = \frac{3}{16}$ in., $L = 1.00$ in.

$$T_{\text{shear}} = \frac{1}{2} dwLF_{Su} = (0.5)\left(\frac{3}{4}\right)\left(\frac{3}{16}\right)(1)(120000) = 8437 \text{ in} \cdot \text{lbs}$$

$$\text{M.S. Shear} = \frac{T_{\text{Shear}}}{T_{\text{Applied}}} - 1 = \frac{8437}{3000} - 1 = 1.81$$

$$T_{\text{compression}} = \frac{1}{4} d h L F_{tu} = 0.25 \left(\frac{3}{4} \right) \left(\frac{3}{16} \right) (1) (200000) = \mathbf{7031 \text{ in} \cdot \text{lbs}}$$

$$\text{M.S. Compression} = \frac{T_{\text{Compression}}}{T_{\text{Applied}}} - 1 = \frac{7031}{3000} - 1 = \mathbf{1.34}$$

Strength

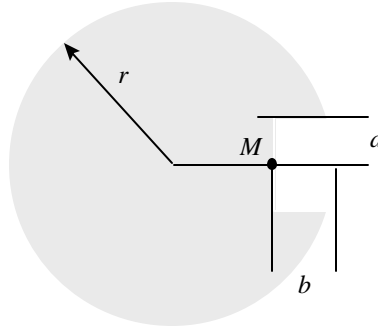


Figure D21. Nomenclature for Keyway Under Torsion

$$\tau_{\text{MAX}} = \frac{TB}{r^3}$$

where,

$$B = K_1 + K_2 \left(\frac{b}{r} \right) + K_3 \left(\frac{b}{r} \right)^2 + K_4 \left(\frac{b}{r} \right)^3, \text{ for } 0.2 \leq \frac{b}{r} \leq 0.5$$

where, for $0.5 \leq \frac{a}{b} \leq 1.5$,

$$K_1 = 1.1690 - 0.3168 \left(\frac{a}{b} \right) + 0.0490 \left(\frac{a}{b} \right)^2$$

$$K_2 = 0.4349 - 1.5096 \left(\frac{a}{b} \right) + 0.8677 \left(\frac{a}{b} \right)^2$$

$$K_3 = -1.1830 + 4.2764 \left(\frac{a}{b} \right) - 1.7024 \left(\frac{a}{b} \right)^2$$

$$K_4 = 0.8812 - 0.2627 \left(\frac{a}{b} \right) - 0.1897 \left(\frac{a}{b} \right)^2$$

For $r = \frac{3}{8}$, $a = b = \frac{3}{32}$,

$$\frac{b}{r} = 0.25, \quad \frac{a}{b} = 1$$

therefore,

$$K_1 = 0.9012; \quad K_2 = -0.2070; \quad K_3 = 1.3910; \quad K_4 = 0.4288 \text{ and } B = 0.9431$$

$$\tau_{MAX} = \frac{(3000)(0.9431)}{\left(\frac{3}{8}\right)^3} = 5.37 \times 10^3 \text{ psi}$$

$$\text{M.S.} = \frac{120000}{53700} - 1 = 1.23$$

D6.1.4 Mesh Gear

Variable prestrain in the SMA torque tube is accommodated by a pair of 4340 steel mesh gears at the root rib. The mesh gear enable a small clocking ability of about 5° .

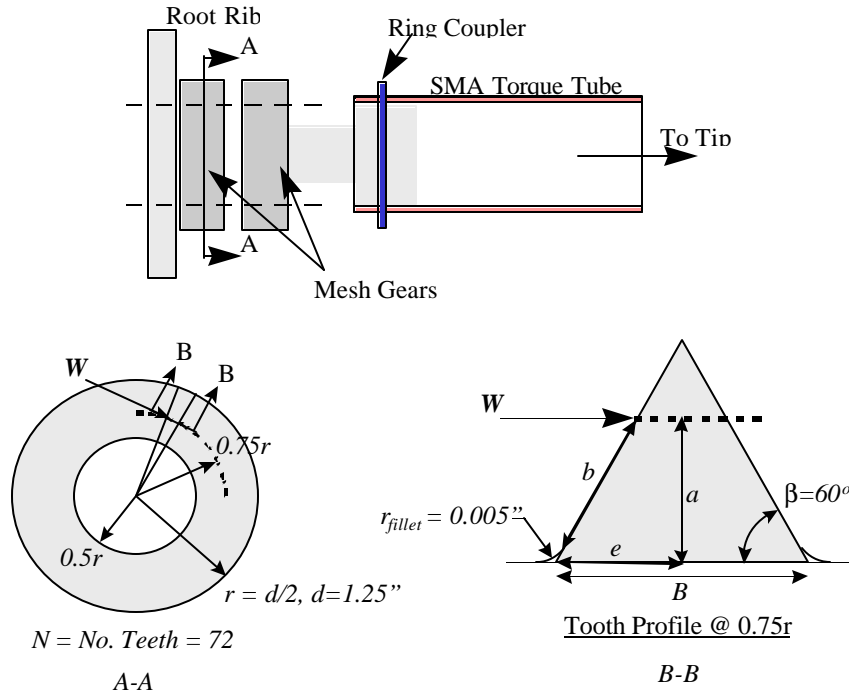


Figure D22. Mesh Gear and SMA Torque Tube Assembly

Stress in Gear Teeth

For one gear tooth,

$$\sigma_{\text{bending}} = \frac{W}{t} \left[1 + 0.26 \left(\frac{e}{r} \right)^{0.7} \right] \left[\frac{1.5a}{e^2} + \frac{\cos \beta}{2e} + \frac{0.45}{(be)^{1/2}} \right]$$

where W = applied load, t = thickness. Other variables are described in Figures D22 and D23.

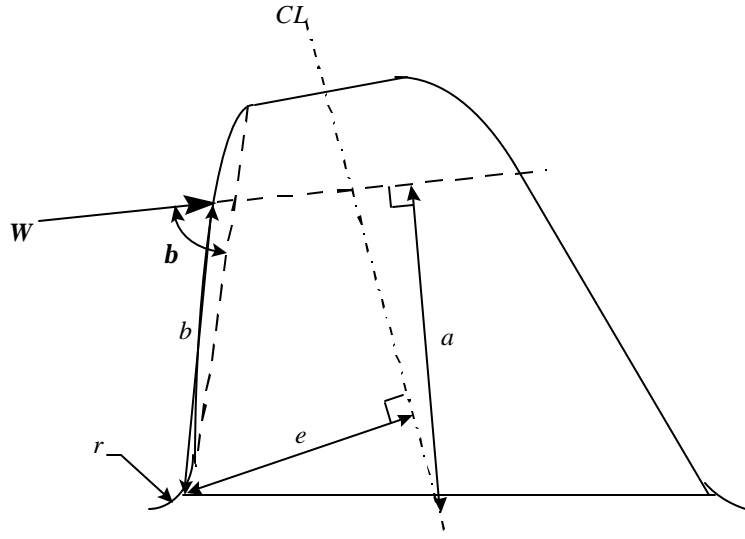


Figure D23. Definition of Variables Defining A Gear Tooth

Based on the gear tooth profile shown in Figure D23,

$$e = 0.0205 \text{ in.}$$

$$a = 0.027 \text{ in.}$$

$$b = 0.031 \text{ in.}$$

$$\beta = 60^\circ$$

$$t = 0.5r = 0.5\left(\frac{1.25}{2}\right) = 0.3125 \text{ in.}$$

$$W = \frac{T}{rN} = \frac{3000}{(0.75)\left(\frac{1.25}{2}\right)(72)} = 88.9 \text{ lbs}$$

Assuming a root radius of 0.005 in.

$$\sigma_{\text{bending}} = \frac{88.9}{0.3125} \left[1 + 0.26 \left(\frac{0.0205}{0.005} \right)^{0.7} \right] \left[\frac{15(0.027)}{0.0205^2} + \frac{\cos(60)}{2(0.0205)} + \frac{0.45}{((0.031)(0.0205))^{1/2}} \right] = 4.63 \times 10^4 \text{ psi}$$

$$\text{M.S.} = \frac{F_{Tu}}{\sigma_{\text{bending}}} - 1 = \frac{200000}{46300} - 1 = 3.32$$

Mesh Gear Clamping Requirement

Because of the triangular teeth profile, any application of torque on the mesh gear will produce a force in the axial direction that will tend to push the gears apart. To keep them together, two fasteners are used to clamp the two.

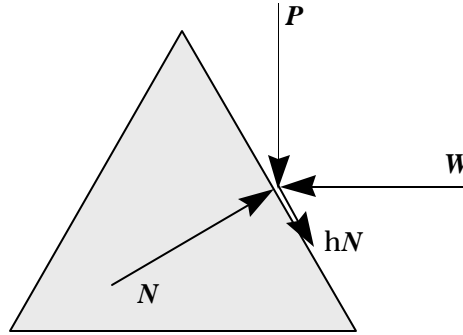


Figure D24. Forces On Gear Teeth

Performing equilibrium calculation based on Figure D24 for no friction ($\mu_o = 0$),

$$P = \frac{W(\cos 60 - \mu \sin 60)}{\sin 60 + \mu \cos 60} = \frac{88.9(\cos 60)}{\sin 60} = 51.3 \text{ lbs}$$

Since this is the pushing force per tooth, the total pushing force is,

$$P_{\text{Total}} = PN = (51.3)(72) = 3694 \text{ lbs}$$

Each fastener will take half the total. The allowable tensile strength is 126 ksi. Hence, for a 1/4 in. fastener,

$$F_f = \frac{P_{\text{Total}}}{n_f} = \frac{3694}{2} = 1847 \text{ lbs}$$

$$\sigma_T = \frac{F_f}{\pi r^2} = \frac{1847}{\pi(0.125)^2} = 3.76 \times 10^3 \text{ psi}$$

$$\text{M.S.} = \frac{\sigma_{Tu}}{\sigma_T} - 1 = \frac{126000}{37600} - 1 = 2.35$$

D6.1.5 Outboard Rib Attachment

The transmission rod is composed of 17" inboard and 4" outboard pieces. They are joined by a double splice with four, 0.25 in. diameter fasteners and two, 3/8 in. diameter pins. The materials used for both the outboard rib and the torque tube connection rod is 4340 steel.

Stress in Tang

Using Roark and Young's [1] equation for maximum shear stress in rectangular section under torsion (see section D6.1.1), for $a = 1.00$ " and $b = 0.125$ ",

$$\tau_{\text{Max}} = \frac{3(3000)}{8(1)(0.125)^2} \left[1 + 0.6095 \left(\frac{0.125}{1} \right) + 0.8865 \left(\frac{0.125}{1} \right)^2 - 1.8023 \left(\frac{0.125}{1} \right)^3 + 0.9100 \left(\frac{0.125}{1} \right)^4 \right] = 7.82 \times 10^3 \text{ psi}$$

$$\text{M.S.} = \frac{F_{\text{Su}}}{\tau_{\text{Max}}} - 1 = \frac{120000}{78200} - 1 = \mathbf{0.53}$$

Required Fastener Clamping Force

When a torque is applied on the transmission rod, the tang will try to open up the tabs. Four ¼ in. fasteners are used to clamp down the tabs and tang from separating. Assuming that the fasteners are 1.5 in. apart (see Figure D25), the force F on each fastener is,

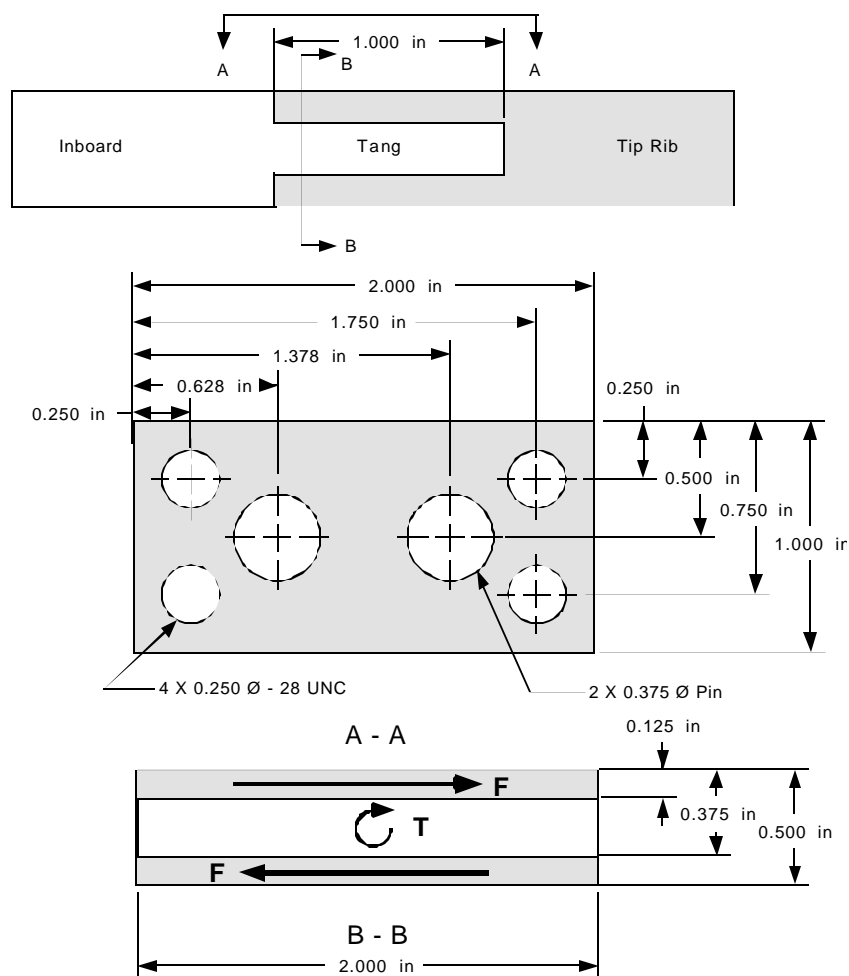


Figure D25. Transmission Rod Connection: Double Splice

$$F = \frac{T}{x} = \frac{3000}{1.5} = 2000 \text{ lbs}$$

$$\sigma_T = \frac{F_f}{\pi r^2} = \frac{2000}{\pi(0.125)^2} = 4.07 \times 10^3 \text{ psi}$$

Assuming a fastener tensile allowable of 126 ksi,

$$M.S. = \frac{F_{Tu}}{\sigma_T} - 1 = \frac{126000}{40700} - 1 = \mathbf{2.09}$$

Tab Bearing, Tab Tear, and Pin Shear

Application of torque will also try to shear the fasteners clamping the tab and tang. To resist the shear, two pins are used in conjunction with the fasteners. Based on Figure D25, Section B-B, the shearing force F on both tabs is,

$$F = \frac{T}{2r} = \frac{3000}{2(0.125 + 0.125/2)} = 8000 \text{ lbs}$$

The force on the shear pins is thus,

$$F_p = \frac{F}{n_f} = \frac{8000}{2} = 4000 \text{ lbs}$$

a) Bearing on Tab

$$\sigma_{brg} = \frac{F_p}{dt} = \frac{4000}{(0.375)(0.25)} = 4.267 \times 10^4 \text{ psi}$$

$$M.S. = \frac{\sigma_{BRu}}{\sigma_{brg}} - 1 = \frac{272000}{42667} - 1 = \mathbf{5.37}$$

b) Tab Tear

If the pins are also 0.75 in. apart, then each pin is 1/2 in. away from the tab edge. The shearing stress is then

$$\tau_{tear} = \frac{F_p}{2dt} = \frac{4000}{2(0.375)(0.125)} = 4.27 \times 10^4 \text{ psi}$$

$$M.S. = \frac{F_{Su}}{\tau_{tear}} - 1 = \frac{120000}{42700} - 1 = \mathbf{1.81}$$

c) Pin Shear

The shearing stress on each pin is 1/2 F_p because the joint is in double shear,

$$\tau_{shear} = \frac{4(\frac{1}{2}F_p)}{\pi d^2} = \frac{4(4000)}{\pi(0.375)^2} = 3.62 \times 10^4 \text{ psi}$$

$$M.S. = \frac{\tau_u}{\tau_{shear}} - 1 = \frac{90000}{36200} - 1 = \mathbf{1.49}$$

D6.1.6 Tip Rib

The torque resulting from the SMA Torque tube is spread to the spars by means of the tip rib shown in Figure D26. The rib is pinned and screwed to the LE spar by two 0.187 in. Ø pins and a #6 screw, while the TE spar connection uses one 0.1875 in. Ø pin and a #6 screw. The load

applied to the LE and TE joints are 857 lbs and 460 bs., respectively, and are shown in Figure D26.

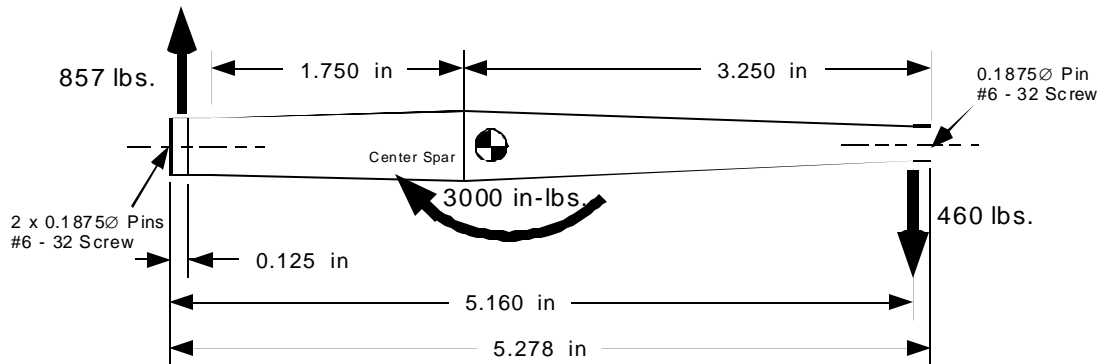


Figure D26. Tip Rib Dimensions and Applied loads

Leading Edge Attachment

The load on the LE joint is assumed to be pure shear, with 80% being taken by the 0.1875 in. Ø pins and 20% to the #6 screw.

Shear Stress

$$P_{pin} = 0.40F_{LE} = 0.40(857) = 342 \text{ lbs}$$

$$P_{screw} = 0.20F_{LE} = 0.20(857) = 171 \text{ lbs}$$

$$\tau_{pin} = \frac{4P_{pin}}{\pi d^2} = \frac{4(342)}{\pi(0.1875)^2} = 1.238 \times 10^4 \text{ psi}$$

$$M.S._{pin} = \frac{\tau_u}{\tau_{pin}} - 1 = \frac{90000}{12380} - 1 = 6.27$$

$$\tau_{screw} = \frac{4P_{screw}}{\pi d^2} = \frac{4(171)}{\pi(0.138)^2} = 1.143 \times 10^4 \text{ psi}$$

$$M.S._{screw} = \frac{\tau_u}{\tau_{screw}} - 1 = \frac{90000}{11430} - 1 = 6.87$$

Bearing Stress

$$\sigma_{BRpin} = \frac{P}{dt} = \frac{342}{(0.1875)(0.125)} = 1.459 \times 10^4 \text{ psi}$$

$$M.S._{pin} = \frac{\sigma_{BRu}}{\sigma_{BRpin}} - 1 = \frac{118000}{14590} - 1 = 7.10$$

$$\sigma_{BRscrew} = \frac{P}{dt} = \frac{171}{(0.1875)(0.125)} = 1.036 \times 10^4 \text{ psi}$$

$$M.S._{screw} = \frac{\sigma_{BRu}}{\sigma_{BRscrew}} - 1 = \frac{118000}{10360} - 1 = 10.4$$

Trailing Edge Attachment

The load on the TE joint is assumed to be pure shear, with 66% being taken by the 0.1875 in. Ø pin and 34% by the #6 screw.

Shear Stress

$$P_{\text{pin}} = 0.66F_{\text{TE}} = 0.66(460) = 303 \text{ lbs}$$

$$P_{\text{screw}} = 0.34F_{\text{TE}} = 0.33(460) = 156 \text{ lbs}$$

$$\tau_{\text{pin}} = \frac{4P_{\text{pin}}}{\pi d^2} = \frac{4(303)}{\pi(0.1875)^2} = 1.0974 \times 10^4 \text{ psi}$$

$$M.S._{\text{pin}} = \frac{\tau_u}{\tau_{\text{pin}}} - 1 = \frac{90000}{10974} - 1 = \mathbf{7.20}$$

$$\tau_{\text{screw}} = \frac{4P_{\text{screw}}}{\pi d^2} = \frac{4(156)}{\pi(0.138)^2} = 1.043 \times 10^4 \text{ psi}$$

$$M.S._{\text{screw}} = \frac{\tau_u}{\tau_{\text{screw}}} - 1 = \frac{90000}{10430} - 1 = \mathbf{7.63}$$

Bearing Stress

$$\sigma_{\text{BRpin}} = \frac{P}{dt} = \frac{303}{(0.1875)(0.125)} = 1.293 \times 10^4 \text{ psi}$$

$$M.S._{\text{pin}} = \frac{\sigma_{\text{BRu}}}{\sigma_{\text{BRpin}}} - 1 = \frac{118000}{12930} - 1 = \mathbf{8.1}$$

$$\sigma_{\text{BRscrew}} = \frac{P}{dt} = \frac{156}{(0.1875)(0.125)} = 8.320 \times 10^3 \text{ psi}$$

$$M.S._{\text{screw}} = \frac{\sigma_{\text{BRu}}}{\sigma_{\text{BRscrew}}} - 1 = \frac{118000}{8320} - 1 = \mathbf{13.2}$$

D6.2 Spar Attachment to Root Rib

For the two models being constructed, the three main spars run from the root rib to the tip (Figure D27). Each spar is attached to the rib via 2 pins and 2 bolts. Below the diagram is the analysis of the leading edge spar joints. The leading edge spar is the most highly loaded spar in the model and was chosen to show the strength of joints.

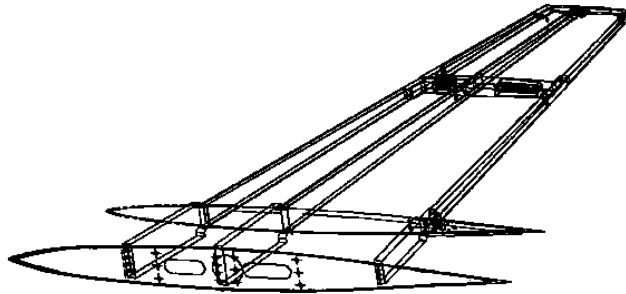


Figure D27. Wing Box Spars and Ribs

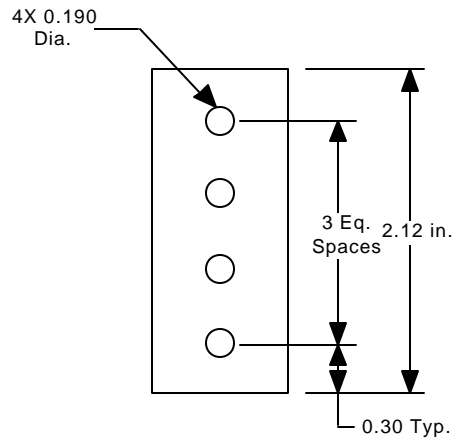


Figure D28. Leading Edge Spar Attachment

Front (Leading Edge) Spar:

The forces on the spar are:

Pitching Moment is 1800 in-lbs

$$F_{LE\text{Rib}} = M/x = 1800/6.636 = 271.25 \text{ lbs}$$

The shear force of each shear pin , P, is:

$$P = F_{LE\text{Spar}} / n_f = 271.25/2 = 135.6 \text{ lbs}$$

$$\tau_{LE\text{Spar}} = 4P / \pi d^2 = 4(135.6) / \pi (0.190)^2 = 4.783 \times 10^3 \text{ psi}$$

$$M.S. = \tau_u / \tau_{LE\text{Spar}} - 1 = 90000 / 4783 - 1 = 17.8$$

For the Lift, the three spars split the load equally, with each taking 300 lbs

For the leading edge spar, the load can also be considered to be distributed evenly among the two shear pins. Hence, P is:

$$F_{LE} = \text{Lift} / \# \text{Spars} = 900/3 = 300 \text{ lbs}$$

$$P = F_{LE} / n_f = 300/2 = 150.00 \text{ lbs}$$

The shear stress on each pin due to the Lift force is:

$$\tau_{LE} = 4P / \pi d^2 = 4(150.00) / \pi (0.190)^2 = 5.291 \times 10^3 \text{ psi}$$

$$M.S. = \tau_u / \tau_{LE} - 1 = 90000 / 5291 - 1 = 16.0$$

D6.2.1 Combined Loading - Leading Edge Spar

The combined shear stress on the leading edge spar found by adding the shear stress due to lift and pitch:

$$\tau_{\text{Combined}} = \tau_{\text{Pitch}} + \tau_{\text{Lift}} = 4811 + 5291 = 1.01 \times 10^4 \text{ psi}$$

$$\text{M.S.} = \frac{\tau_u}{\tau} - 1 = \frac{90000}{10100} - 1 = 7.91$$

D7. CONCLUSIONS

The above report outlines the margins of safety for the two wind tunnel models that have been fabricated for the DARPA / AFRL Smart Materials and Structures - Smart Wing Phase I contract. The margins of safety are all sufficient to insure safety of both the NASA TDT wind tunnel and of the Northrop Grumman models. The margins are large for some of the structures (e.g. the attachment of the model to the balance, or the attachment of the spars to the ribs) due to the moderate loads being applied and because of the minimum gage thickness of the materials used to construct the models.

D8. REFERENCES

- 1) NASA Langley Research Center, Wind Tunnel Design Criteria, Report Number LHB 1710.15, May 1992
- 2) Roark, R. and Young, W., Formulas for Stress and Strain, Fifth Edition, McGraw-Hill, Inc., New York, 1975
- 3) Shigley, J. E., Mechanical Engineering Design, McGraw-Hill, Inc., New York, 1963
- 4) Alexander, M., Subsonic Wind Tunnel Testing, Report Number WL-TR-91-3073, 1991

D9. Dynamics and Flutter Analyses

This report presents vibration and aeroelastic characteristics of the two wind tunnel models which are designed for testing in the NASA Langley's transonic dynamic tunnel (TDT). The Conventional model represents a basic wing with conventional trailing edge control surfaces. The inboard trailing edge flap is attached to a worm gear assembly which in turn is driven by an electric motor. The outboard control surface (aileron) will be set manually to $0, \pm 5, \pm 10$ degrees. The Smart wing is identical to the Conventional wing except the trailing edge control surfaces are made of SMA materials and are firmly fixed to the rear spar and skin of the wing box.

Structural Model

The structural model consists of an assembly of wing box, and trailing edge inboard and outboard control surfaces. The wing box consists of three spars and four ribs, and upper and lower skin surfaces. The mid spar is placed along the elastic axis of the wing box. The inboard section of the wing (up to Y station = 7.0 inch) is made very stiff. The wing box consists of 345 CBAR elements and 219 CQUAD4 elements. The leading edge control surfaces are fixed to the front spar in both cases.

Vibration Analysis

Vibration analysis of the structural model discussed above was performed. The first twelve natural vibration modes in the frequency range 1 through 500 Hz were calculated. Figures D29 and D31 list the natural frequencies and mode shape descriptions of the Conventional Wing and Smart Wing. Listed in Figure D30 are the natural frequencies obtained from the ground vibration testing (GVT) on the conventional model before the first tunnel entry. The GVT will have to be redone for the smart wing due to new control surfaces and torque tube assemblies. A final analysis for the smart wing will be performed in early 1998 after all the trailing edge parts have been fabricated and an exact weight and mass distribution can be obtained.

Conventional Wing

Mode	Frequency (Hz)	Damping (%)	Shape
1	26.0	<i>No Damping Assumed in Analysis</i>	1 st Bending
2	77.4		1 st Torsion
3	106.5		2 nd Bending
4	173.6		2 nd Torsion

Figure D29. Natural Frequencies and Mode Shapes for Conventional Wing, ASTROS Analysis

Mode	Frequency (Hz)	Damping (%)	Shape
1	24.33	0.507	1 st Bending
2	63.64	0.380	1 st Bending, Spindle
2	80.84	0.737	1 st Torsion
4	108.33	0.683	2 nd Bending
5	140.43	0.392	1 st Torsion, Spindle
6	166.68	0.421	Combined Torsion and Flap Rotation
7	174.64	1.861	2 nd Torsion
8	193.42	1.185	Control Surface Rotation

Figure D30. Natural Frequencies and Mode Shapes for Conventional Wing, NASA LaRC Ground Vibration Test

Smart Wing

Mode	Frequency (Hz)	Damping (%)	Shape
1	26.2	<i>No Damping Assumed in Analysis</i>	1 st Bending
2	82.8		1 st Torsion
3	119.4		2 nd Bending
4	162.2		2 nd Torsion

Figure D31. Natural Frequencies and Mode Shapes for Smart Wing, ASTROS Analysis

Aeroelastic Analysis

Aeroelastic analysis (flutter and divergence) was performed using ASTROS, a design software developed by Northrop Grumman for the U. S. Air Force. The aerodynamic model used in this study is shown in Figure D32. Four spline surfaces were used to relate the structural data and the aerodynamic data. The flutter analysis using 12 vibration modes was conducted for Mach number 0.6 with density ratios 0.5 and 1.0. Since the test dynamic pressures run from 60 psf to 120 psf., based on the “Wind Tunnel Model Systems Criteria”, the models must be clear of flutter and divergence up to 240 psf. Typical flutter solutions in terms of damping vs. equivalent dynamic pressure (Q_{eq} in psf) and frequency vs. dynamic pressure (Q_{eq} in psf) are presented in the following figures:

Figures D33 through D36 for Mach number 0.6, Conventional Wing

Figures D37 through D39 for Mach number 0.6, Smart Wing

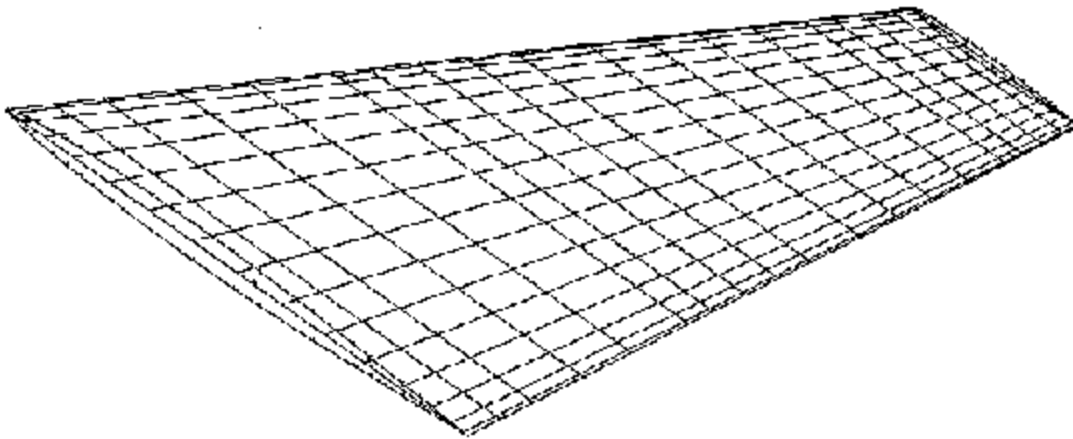


Figure D32. Steady Aerogrid Model

The critical flutter Q is found when the damping curve passes through zero from negative to positive value. While the critical divergence Q is found when the frequency curve passes through zero. At Mach, $M=0.6$, both wings; Conventional Wing and Smart Wing, are free from aeroelastic dynamic and static instability for density ratios 0.5 through 1.5 (i.e. up to $Q = 800$ PSF). Hence, the conventional and smart wing test models are free of flutter and divergence instabilities. The plots of frequencies vs. equivalent dynamic pressure show very little change in the frequencies. This suggests that the aerodynamic stiffness and damping are small compared to the structural stiffness and damping, and hence, the models are stable in the desired test range.

Flutter and Dynamics Graphs

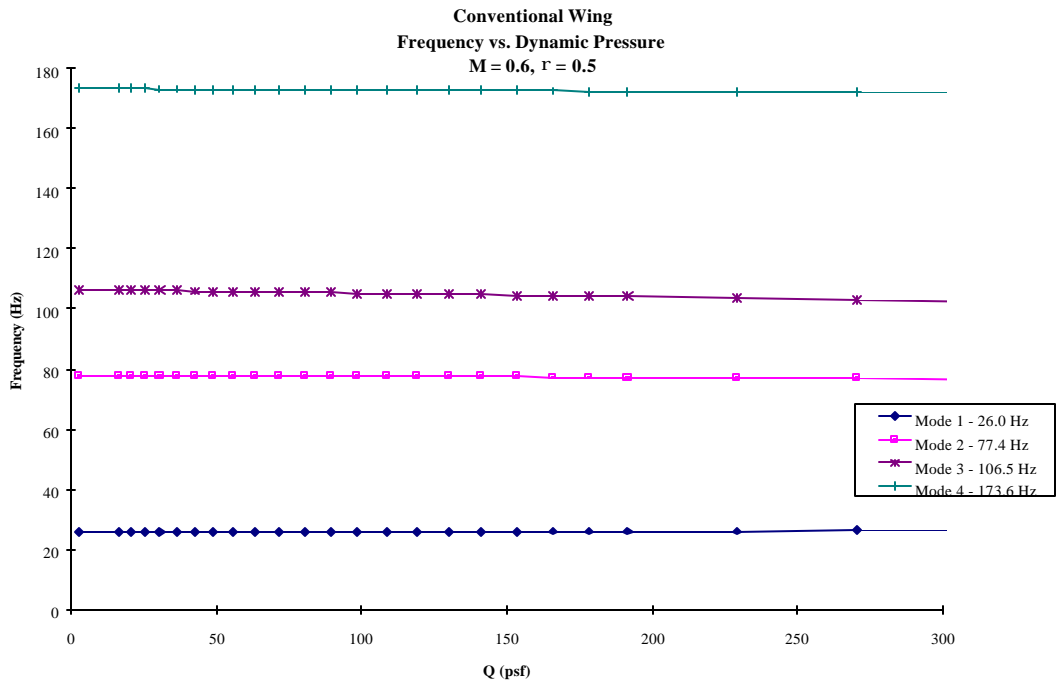


Figure D33

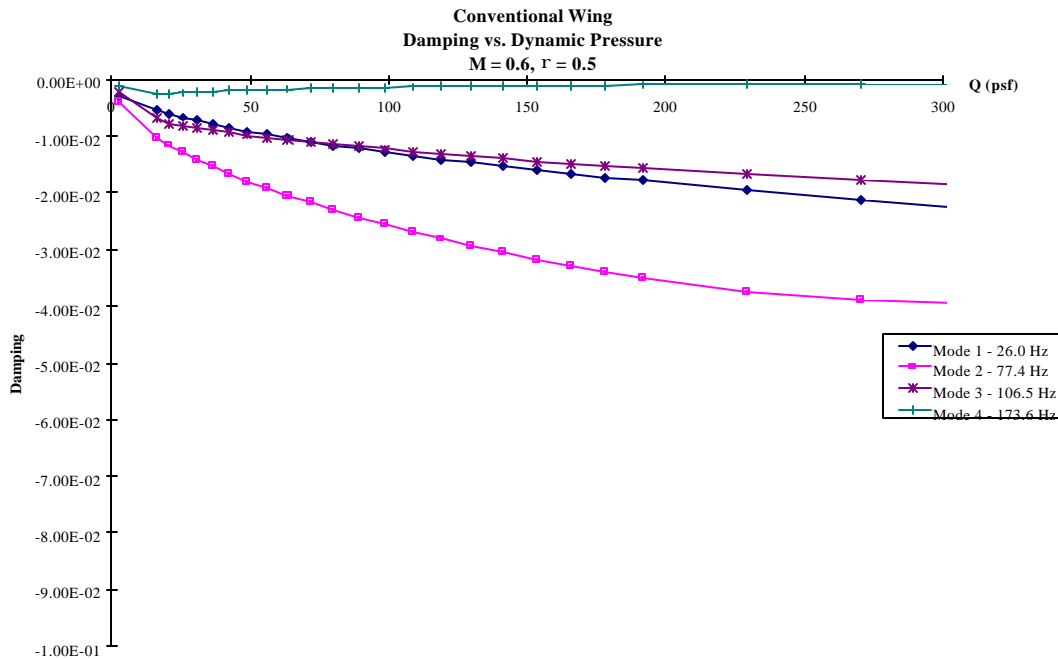


Figure D34

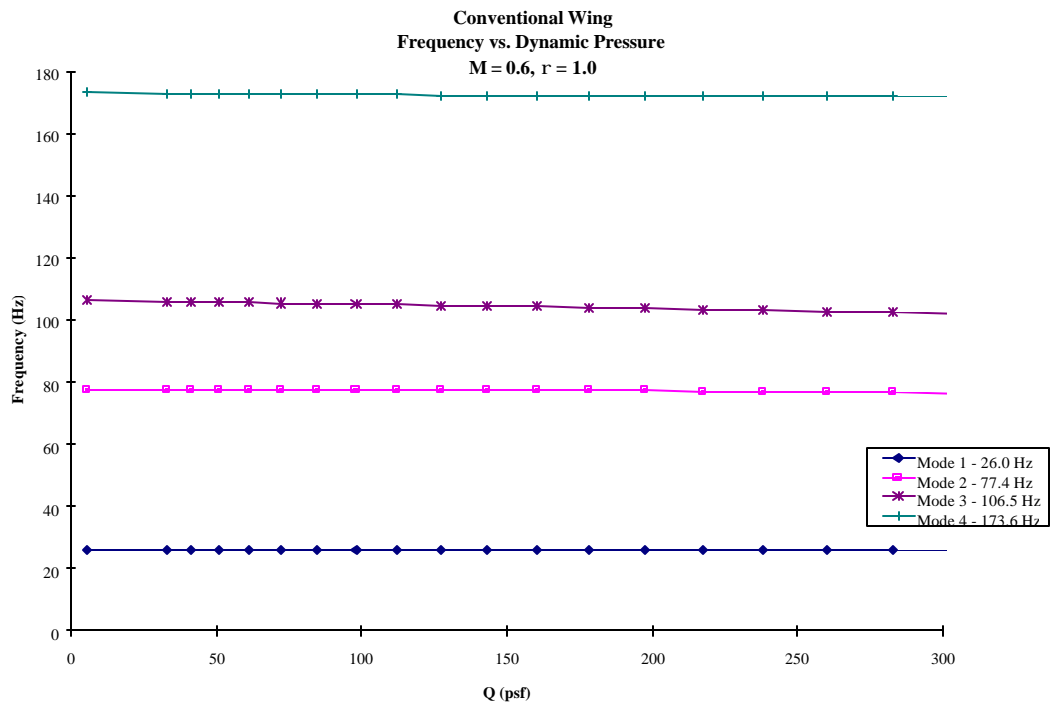


Figure D35

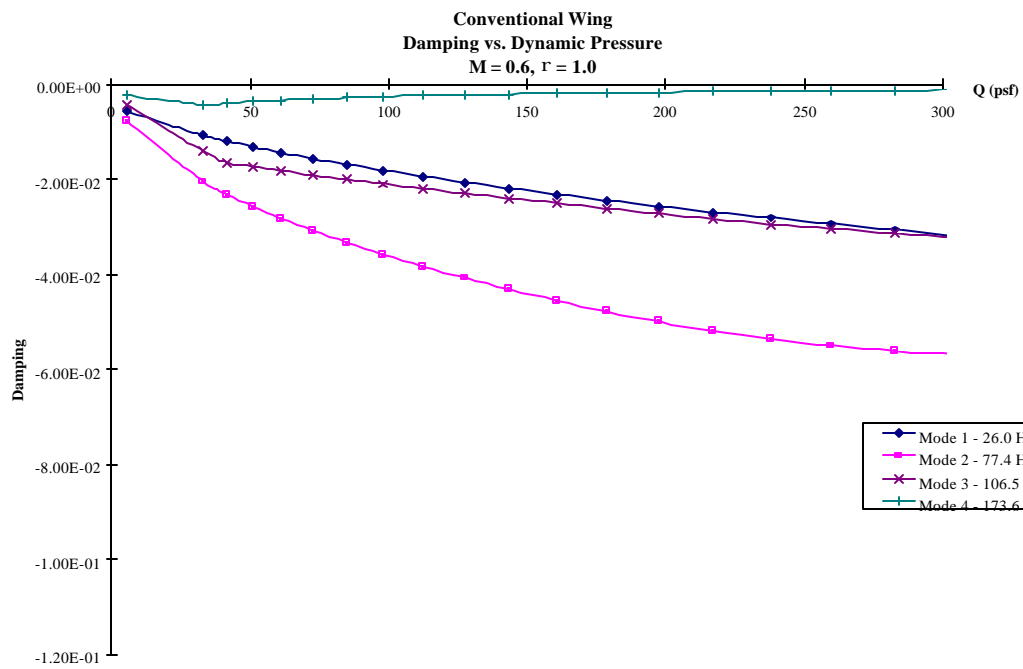


Figure D36

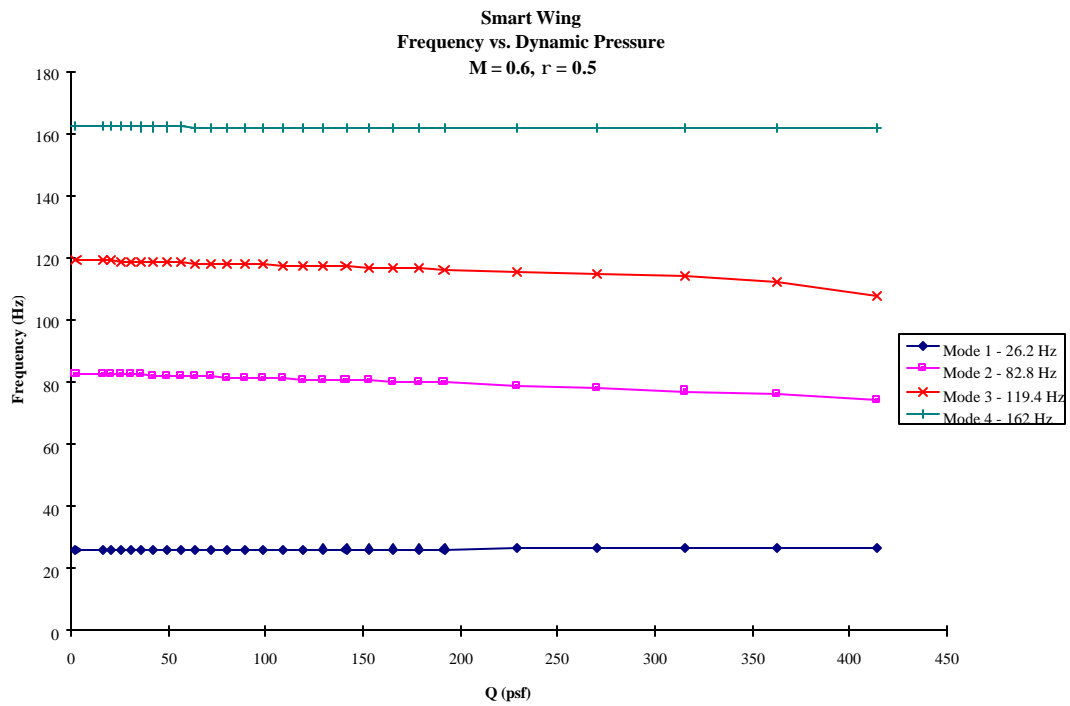


Figure D37

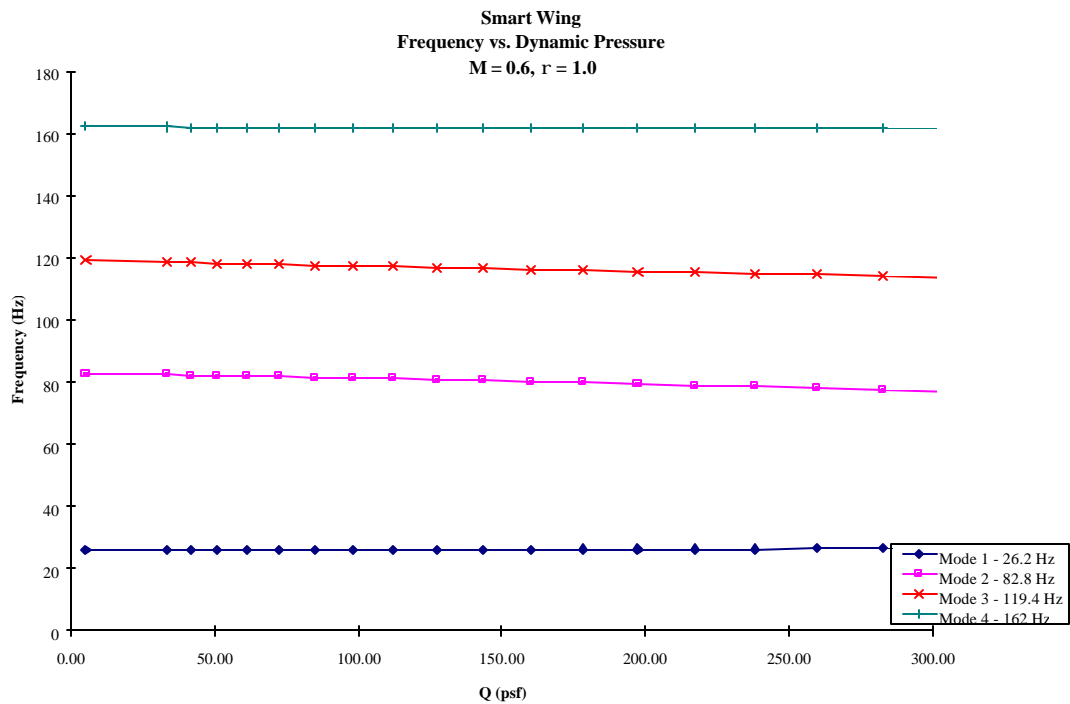


Figure D38

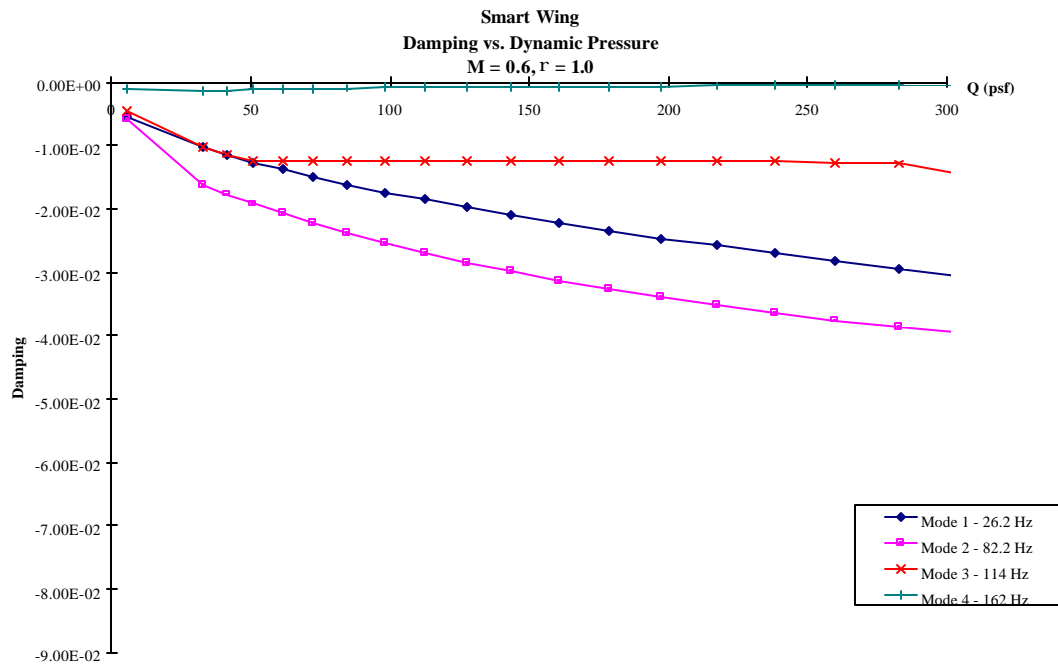


Figure D39

D10. SUMMARY

This appendix outlines the analysis done to insure the models are free from flutter and divergence for the tunnel environments of the tests. Since the maximum Q that will be run at is 130 psf at M = 0.5, the analysis shows that both models are clear of aeroelastic instabilities for the tests. Final analysis for the smart wing will be performed in early 1998 after all of the parts have been fabricated and an exact weight and mass distribution can be obtained.

Leading edge control surface divergence is also not a concern for either model. The original design had called for the leading edges to be moveable, but model complexity and a large test matrix led to the leading edges to be rigidly fixed to the leading edge spars.